Transactions of the ASME

Journal of Engineering for Gas Turbines and Power

Published Quarterly by The American Society of Mechanical Engineers

VOLUME 108 • NUMBER 1 • JANUARY 1986

Technical Editor
ARTHUR J. WENNERSTROM
Senior Associate Editor
G. K. SEROVY
Associate Editors
Air Pollution Control
H. E. HESKETH
Diesel and Gas Engine Power
G. VanDeMARK
Gas Turbine
G. OPDYKE
Power
R. W. PORTER
Advanced Energy Systems
T. M. BARLOW
Fuels
H. C. ORENDER
Nuclear Engineering
J. SUSNIR

BOARD ON COMMUNICATIONS
Chairman and Vice-President
K. N. REID, JR.

Members-at-Large
W. BEGELL
J. T. COKONIS
W. G. GOTTENBERG
F. LANDIS
J. R. LLOYD
R. E. NICKELL
J. E. ORTLOFF
C. F. PHILLIPS
R. E. REDER
F. W. SCHMIDT

President, **L. S. FLETCHER**
Executive Director,
PAUL ALLMENDINGER
Treasurer, **ROBERT A. BENNETT**

PUBLISHING STAFF
Mng. Dir., Publ., **J. J. FREY**
Dep. Mng. Dir., Pub.,
JOS. SANSONE
Managing Editor,
CORNELIA MONAHAN
Production Editor,
VALERIE WINTERS
Editorial Prod. Asst.
MARISOL ANDINO

The Journal of Engineering for Gas Turbines and Power (ISSN 0022-0825) is published quarterly for $100 per year by The American Society of Mechanical Engineers, 345 East 47th Street, New York, NY 10017. Second class postage paid at New York, NY and additional mailing offices. POSTMASTER: Send address change to The Journal of Engineering for Gas Turbines and Power, c/o The AMERICAN SOCIETY OF MECHANICAL ENGINEERS, 22 Law Drive, Box 2300, Fairfield, NJ 07007-2300."

CHANGES OF ADDRESS must be received at Society headquarters seven weeks before they are to be effective. Please send old label and new address.

PRICES: To members, $24.00, annually; to nonmembers, $100.00.

Add $6.00 for postage to countries outside the United States and Canada.

STATEMENT from By-Laws. The Society shall not be responsible for statements or opinions advanced in papers or ... printed in its publications (B 7.1, para. 3).

COPYRIGHT © **1986** by the American Society of Mechanical Engineers. Reprints from this publication may be made on condition that full credit be given the TRANSACTIONS OF THE ASME – JOURNAL OF ENGINEERING FOR POWER, and the author, and date of publication be stated.

INDEXED by Engineering Information

TECHNICAL PAPERS

Downloaded 03 Jun 2010 to 171.66.16.159. Redistribution subject to ASME license or copyright; see http://www.asme.org/terms/Terms_Use.cfm

(Contents Continued)

DISCUSSION

ANNOUNCEMENTS

Annulus Wall Boundary-Layer Measurements in a Four-Stage Compressor

N. A. Cumpsty
Whittle Laboratory,
University of Cambridge,
England

There are few available measurements of the boundary layers in multistage compressors when the repeating-stage condition is reached. These tests were performed in a small four-stage compressor; the flow was essentially incompressible and the Reynolds number based on blade chord was about $5 \cdot 10^4$. Two series of tests were performed; in one series the full design number of blades were installed, in the other series half the blades were removed to reduce the solidity and double the staggered spacing. Initially it was wished to examine the hypothesis proposed by Smith [1] that staggered spacing is a particularly important scaling parameter for boundary layer thickness; the results of these tests and those of Hunter and Cumpsty [2] tend to suggest that it is tip clearance which is most potent in determining boundary-layer integral thicknesses. The integral thicknesses agree quite well with those published by Smith.

Introduction

There are not many measurements of boundary-layer flows in multistage compressors available in the literature. The most useful source is the results given by Smith [1] on a large low-speed compressor. It was in this paper that Smith established the repeating stage model for multistage compressors. This has had a very marked effect on the way in which one thinks about multistage compressors, rendering an otherwise impossibly complicated situation amenable to correlation and consideration. Smith chose to use staggered spacing as a primary length scale for nondimensionalizing lengths and these measurements began with the idea of testing this to see if it was particularly important [2]. Because there are so few sets of measurements in multistage measurements it is believed that these will be of some interest and use.

A large number of tests were run on the four-stage compressor with two types of blading. The compressor has been used extensively before and is described in [3], but is summarized in the following table:

Mean diameter	317 mm
Hub-tip ratio	0.78
Blade chord	17.8 mm (0.7 in.)
Aspect ratio	2.0
Rotor tip clearance	0.46 mm
Stator hub clearance	0.63 mm (approx.)
Degree of reaction	50%
Stagger (measured from axial)	35 deg
Camber	20 deg

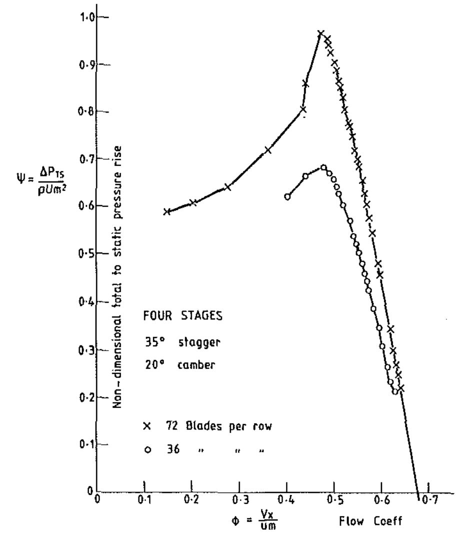

Fig. 1 Nondimensional total-static pressure rise versus nondimensional flow rate

Solidity (midspan)	72 blades per row	1.28
	36 blades per row	0.64
Reynolds number based on blade chord and velocity at mean height for operation at 3000 rev/min		$0.5 \cdot 10^5$

The blades are untwisted and the stators unshrouded. The number of blades per row was 72 in one case and 36 in the other; the larger number of blades, giving a solidity based on pitch of 1.28, is that corresponding to the original design and with this blading the flow coefficient at design is 0.55. Figure 1 shows the nondimensional total-to-static pressure rise versus

---

Contributed by the Gas Turbine Division of The American Society of Mechanical Engineers and presented at the 30th International Gas Turbine Conference and Exhibit, Houston, Texas, March 18–21, 1985. Manuscript received at ASME Headquarters, December 21, 1984. Paper No. 85-GT-61.

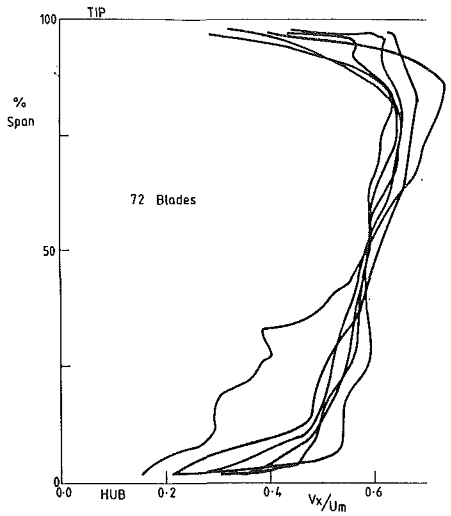

Fig. 2 Axial velocity profiles measured downstream of stator 3 at different circumferential positions across a pitch, $\phi = 0.55$

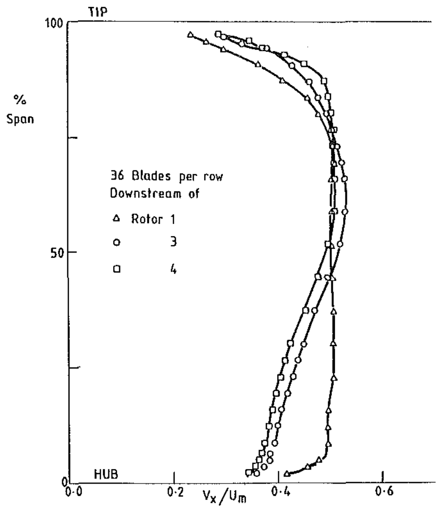

Fig. 3 Axial velocity profiles downstream of rotor 1, 3, and 4 at flow rate close to stall, $\phi = 0.48$

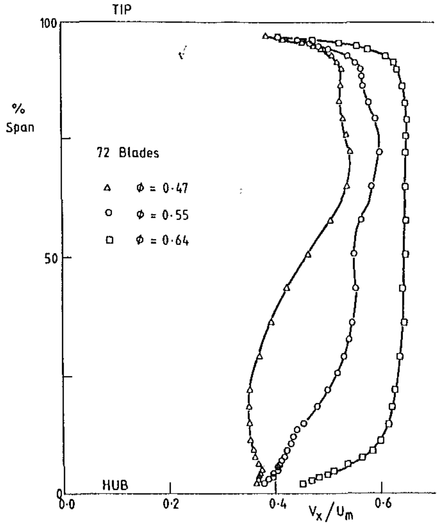

Fig. 4 Axial velocity profiles downstream of rotor 4 for three flow coefficients, 72 blades

flow coefficient $\phi = Vx/U_m$ for each build; stall occurs at a higher flow coefficient ($\phi = 0.48$ compared with 0.47) for the 36-bladed machine and the maximum flow rate which could be achieved was reduced from about $\phi = 0.64$ to 0.63. Accompanying these changes is a pronounced reduction in pressure rise. The boundary-layer tests were accordingly carried out at the following conditions:

72 blades per row: Solidity = 1.28 $\phi = 0.47, 0.55, 0.64$

36 blades per row: Solidity = 0.64 $\phi = 0.48, 0.55, 0.63$

Diffusion factor was calculated from the measurements at blade midheight using DF = $1 - V_2/V_1 + \frac{1}{2}(s/c)\Delta V_\theta/V_1$. At $\phi = 0.55$ the values were approximately equal for rotor 3 and stator 3, 0.32 for the 72-bladed machine and 0.29 for the 36-bladed. The lower diffusion factor with the smaller number of blades is perhaps surprising but reflects the smaller deflection produced by the rather low-solidity blades. It is clear that both sets of blades were conservatively loaded at $\phi = 0.55$ by the criterion of diffusion factor.

The low-flow coefficients correspond to conditions just above stall in both cases.

Some early tests were made with a three-hole cylindrical probe but these showed erroneous trends close to the outer casing and were superseded by measurements with a small three-hole cobra probe; all measurements shown here were obtained with a cobra, the flow angles being found after nulling the probe.

The probe was made of 3-mm hypodermic tubing into which the three 0.5-mm tubes were inserted. The 3-mm outside diameter was tapered down over a length of about 15 mm before the 0.5-mm tubes, soldered together, were bent over to give the cobra head. The head was bent in such a way that the probe would fit through a 3-mm hole in the compressor casing but so that the sensing holes were as far forward of the stem as possible.

When downstream of the rotors it was judged to be sufficient to take a measurement at only one circumferential position, but downstream of stators this was inadequate. For the stators radial traverses were made at a number of circumferential positions so that a reasonable average could be obtained; an example of the various profiles of axial velocity is shown in Fig. 2, using measurements downstream of stator 3 in the 72-bladed build at the design-flow coefficient. At other flow coefficients traverses were made at only three circumferential positions but a reasonable average for the boundary layer thickness could be constructed from these.

It would have been desirable to have taken traverses at more circumferential positions and at different axial positions between blade rows; there was simply not enough time to do this. Nevertheless, the results obtained are interesting and useful trends are shown. The results also appear to be consistent with those given by Smith [2], where these can be compared. (It is to be noted that Smith has taken many more traverses on a much larger machine with blading of better aerodynamic design.)

Results

Velocity Profiles. An important requirement of the present results is that the radial profile should approach the repeating-stage condition. The importance of this condition has been demonstrated by Smith [1]. Figure 3 shows the axial velocity profile downstream of the first, third, and fourth rotors for the 36-bladed compressor at a flow coefficient close to stall. The radial distribution of axial velocity is very similar for the third and fourth rotors but these are very different to the profile after the first rotor; it may be concluded that stage 4 does correspond closely to a repeating stage. The behavior is similar at other flow coefficients and for the 72-bladed machine.

The effect of variation in the flow coefficient in the radial profile of axial velocity is shown in Figs. 4 and 5 for the 72 and 36-bladed machines, respectively. It both cases it is the

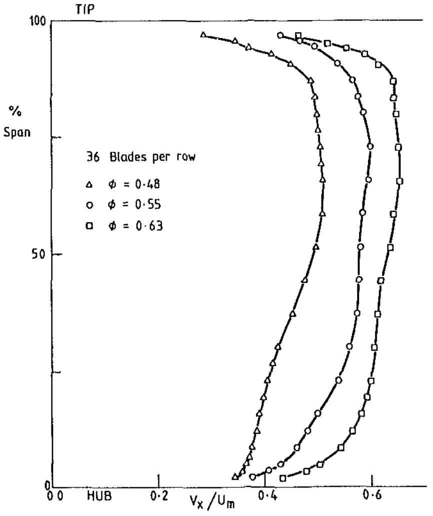

Fig. 5 Axial velocity profiles downstream of rotor 4 for three flow coefficients, 36 blades

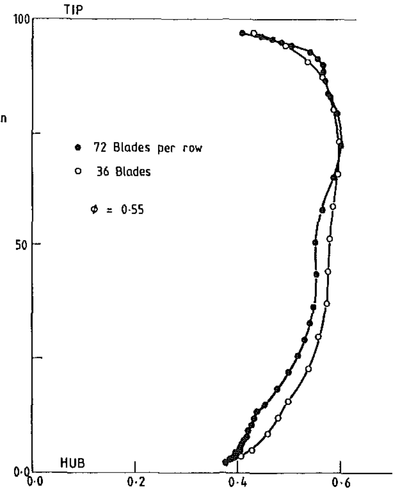

Fig. 6 Axial velocity profiles downstream of rotor 4 for 36 and 72 blades at $\phi = 0.55$

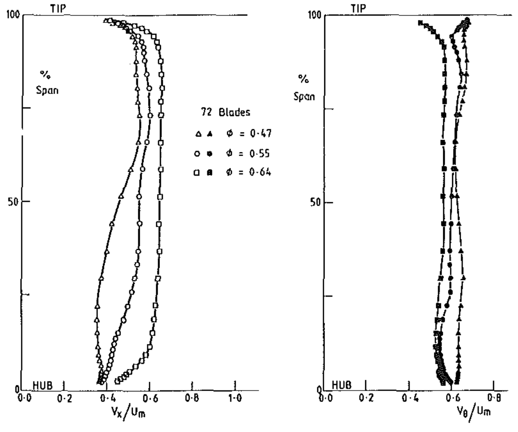

Fig. 7 Axial and whirl velocities downstream of rotor 4 for three flow coefficients, 72 blades

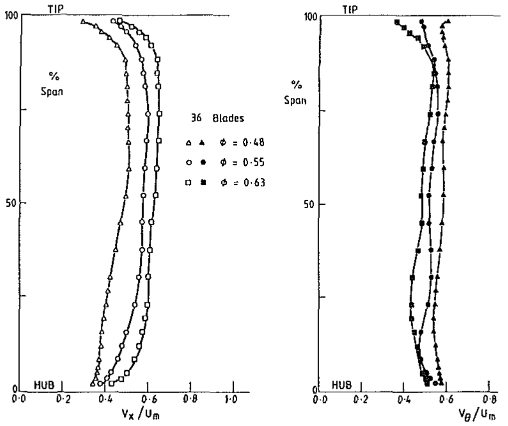

Fig. 8 Axial and whirl velocities downstream of rotor 4 for three flow coefficients, 36 blades

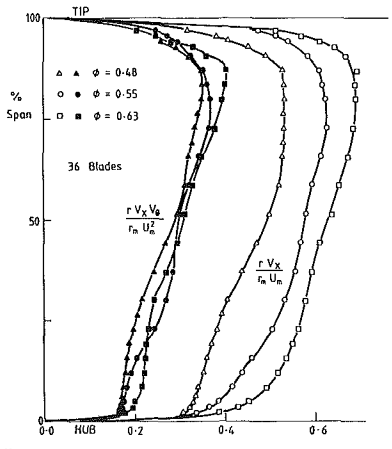

Fig. 9 Radially weighted distribution of axial velocity and $V_x V_\theta$ for three flow coefficients, 36 blades

repeating-stage condition downstream of rotor 4 which is shown. The profiles become markedly nonuniform at the flow coefficient close to stall, $\phi = 0.47$ or 0.48 and it is difficult to determine where the boundary layer ends. This is particularly true near the hub where the boundary layer could be visualized as very thin (2 mm thick) or very thick (about 20 mm); the measurements of velocity do not help to resolve this.

A direct comparison of the axial velocity profile downstream of rotor 4 for the different builds is shown in Fig. 6. The comparison is at the design flow coefficient and the two are generally similar. In fact the velocity seems generally rather higher for the 36-bladed build implying that the flow coefficients were not genuinely equal. The agreement is similarly good for the large flow coefficient but less good near to stall with the results for 72-bladed compressor showing the most nonuniform profile.

The results so far have concentrated on the axial velocity but this, clearly, is only one of the parameters of concern. Figures 7 and 8 show the axial and tangential velocities downstream of rotor 4 for the 72 and 36-bladed builds respectively for the flow coefficients close to stall, at design and the maximum. (The velocity scale is smaller here than in results presented in Figs. 2–6.) The rise in tangential velocity as the flow coefficient falls is pronounced. The boundary layer near the hub behaves in a similar manner for both builds; at high flow coefficients the flow angle increases toward the wall, a trend more pronounced close to design, but near to stall the flow angle is nearly constant until very close to the wall indeed. Close to stall it is, as already remarked, very difficult to determine the boundary-layer edge.

Near the outer wall the behavior shown in Figs. 7 and 8 is quite different for the two builds. At large-flow coefficients the flow angle is approximately invariant with distance from the wall for both builds, but the high-solidity build behaves quite differently at lower flows, showing a marked increase in flow inclination to the axial as the wall is approached. Close to stall both builds show a substantial increase in flow in-

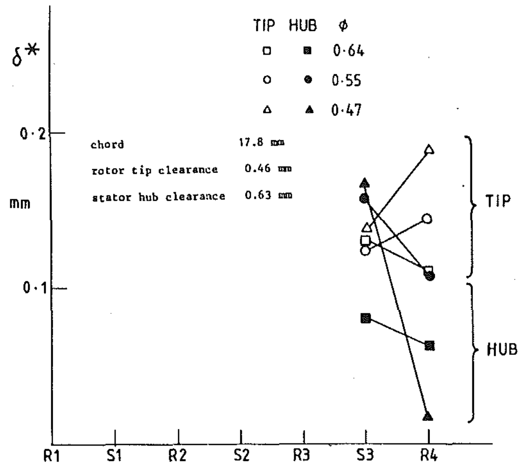

Fig. 10 Displacement thickness from measurements at three flow coefficients in 72-bladed compressor

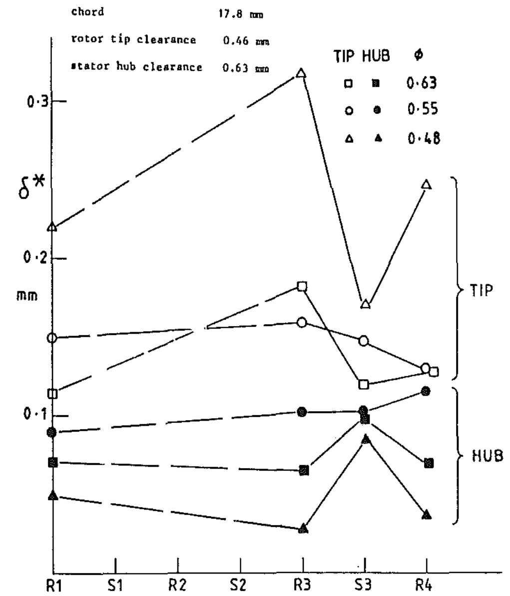

Fig. 11 Displacement thickness from measurements at three flow coefficients in 36-bladed compressor

clination as the wall is approached, the tangential velocity staying constant at about 0.6 of blade speed at mean height.

Integral Parameters. The most useful parameters for assessing the boundary layer are the integral thicknesses. The displacement thickness is defined by:

$$\delta^* = \frac{1}{r_w V_{x_w}} \int (V_x - v_x) r dr \text{ is the most important.}$$

Here r_w denotes the radius at the wall, either hub or tip, $\bar{V}_x$ is the free-stream velocity, and V_{x_w} is the free-stream velocity extrapolated to the wall. The limits of integration are determined as is appropriate. Of comparable importance is the tangential force deficit thickness. Ignoring radial shift of streamlines the tangential force on a blade row per unit span is given by

$$f_\theta = 2\pi r \rho v_x (v_{\theta_2} - v_{\theta_1})$$

and the tangential force deficit thickness is given by

$$\nu = \frac{1}{r_w F_{\theta w}} \int (F_\theta - f_\theta) r dr$$

where $F_{\theta w}$ is again the value of tangential force extrapolated to the wall. Both definitions are essentially those of Smith [1].

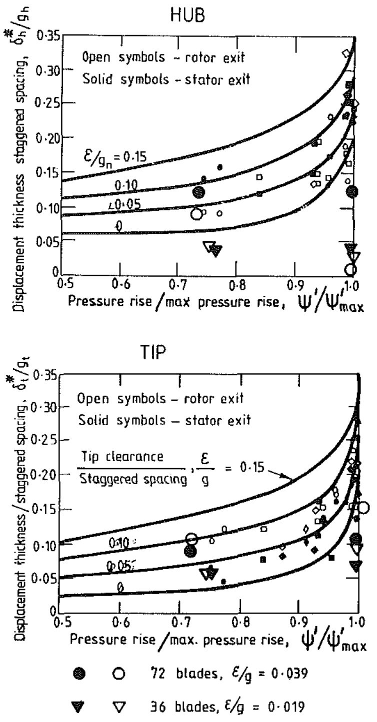

Fig. 12 Tip and hub displacement thicknesses superimposed on correlation of Smith (dath by Smith shown with small symbols, present data with large symbols)

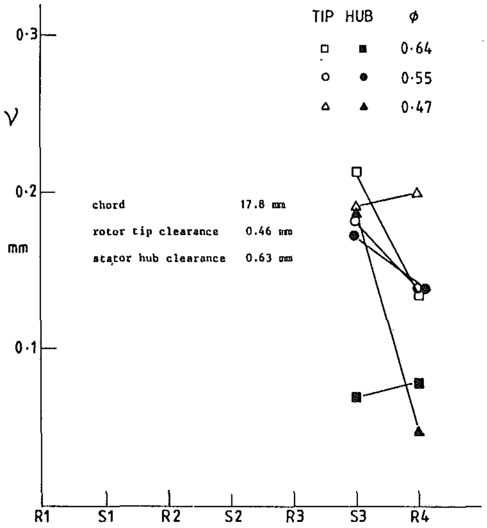

Fig. 13 Tangential force deficit thickness from measurements at three flow coefficients in 72-bladed compressor

The integrals given above involve the product with radius and plots of rV_x and rV_xV_θ; these are shown in Fig. 9 for the 36-bladed machine at three flow coefficients (the plots for the 72-bladed machine are similar). The integrals were obtained using a planimeter to find the area between the measured curve and the extrapolation to the wall. In the case of $\phi = 0.63$ this procedure is largely unambiguous but this is not true at the lower-flow coefficients, particularly for the hub boundary layer, the uncertainty springing from the problem of defining the boundary-layer edge. In fact, it is probable that the ordinary concept of a boundary layer and a free stream is too restrictive for the repeating stage, with shear stress and mixing occurring right across the passage.

Figures 10 and 11 show the displacement thickness distribution for the 72 and 36-bladed machines respectively.

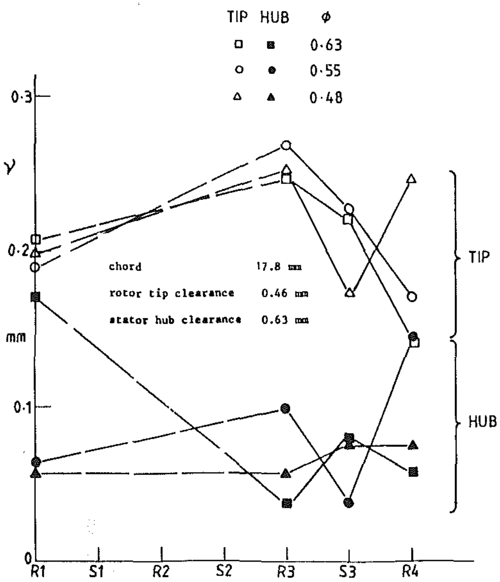

Fig. 14 Tangential force deficit thickness from measurements at three flow coefficients in 36-bladed compressor

For the 72-bladed machine traverses were made after stator 3 and rotor 4 only; for the 36-bladed compressor they were also made after rotor 1. In each case results are shown for three flow coefficients: At the tip the displacement thickness is greatest for the flow coefficient near to stall, at the hub the opposite seems to be generally true although there is an anomaly for the 72-bladed machine after the third stator row. With the 36-bladed build the trends seem to be more consistent showing a rise in δ^* across the rotor and a fall across the stator at the outer wall with the opposite occurring at the hub. This is consistent with Hunter and Cumpsty [2] which emphasizes the clearance as the prime determiner of δ^*.

Figures 12 reproduce the correlation curves prepared by Smith [1] upon which are superimposed the present measurements of δ^* for the two smaller flow coefficients (the largest flows are off the graphs to the left). For the outer wall the agreement is reasonable, except near stall. The smaller displacement thicknesses measured near the outer wall close to stall compared with those of [1] are probably because of the use of untwisted blades for the tests described here. In a letter to the author Smith has pointed out that untwisted blades tend to load the hub region in the repeating stage environment so that the outer-wall region never gets loaded very heavily. Near the hub the comparison with [1] is less satisfactory and this most probably lies with unsatisfactory choice of boundary-layer edge. At the outer wall the boundary layers are certainly thicker for the lower solidity blading but less than would be expected on the basis of scaling with staggered spacing. At the hub no trend is apparent.

The tangential force-deficit thickness is shown in Figs. 13 and 14. The trends are not unlike those for displacement thickness, tending to confirm the result of work by Smith [1] where ν nondimensionalized with respect to δ^* was approximately constant within the scatter evident.

Conclusions

1 The definition of the boundary-layer edge is difficult, particularly when the stage is repeating and particularly on the hub. The boundary layer could, from the velocity profiles, be regarded as very thin or very thick. This led to the conclusion that another technique, foreign gas injection, should be used to investigate repeating-stage boundary layers and a program using the technique is underway.

2 The integral thicknesses measured appear to be more or less in line with those reported by Smith [1] in a much bigger machine at higher Reynolds number. There is considerable scatter, particularly at the hub, but the degree of scatter is comparable to that measured by Smith.

The use of untwisted blades has probably unloaded the outer wall relative to the hub as stall is approached.

3 The staggered gap does not appear to be particularly important variable; it is the clearance at the rotor tip or stator hub which appears to be crucial in determining the integral thicknesses of the end-wall boundary layer, a point stressed by Hunter and Cumpsty [2] and evident from the correlation curves of [1].

Acknowledgments

The measurements described here were made by Dr. Jane Hodson in the very short time she was employed here as a research assistant. The project was supported by the S.E.R.C.

References

1 Smith, L. H., "Casing Boundary Layers in Multistage Axial Compressors," *Flow Research in Blading*, Ed. L.S. Dz-ng, Elsevier, 1970.

2 Hunter, I. H., and Cumpsty, N. A., "Casing Wall Boundary=Layer Development Through an Isolated Compressor Rotor," ASME JOURNAL OF ENGINEERING FOR POWER, Vol. 104, 1982, pp. 805=818.

3 Day, I. J., *Axial Compressor Stall*, Ph.D. Dissertation, University of Cambridge, 1976.

Behavior of Tip Leakage Flow Behind an Axial Compressor Rotor

M. Inoue

M. Kuroumaru

M. Fukuhara

Department of Mechanical
Engineering, Power Division,
Kyushu University,
Fukuoka, Japan

Performance testing and detailed flow measurements were made in an axial compressor rotor with various tip clearances. The experiments were conducted on the condition of the same incidence angle at midspan. Thus, the effect of tip clearance distinguished from that of incidence angle was investigated on the overall performance, work-done factor, blockage factor, and increases in displacement, momentum, and blade-force-deficit thicknesses of the casing wall boundary layer. The phase-locked flow patterns obtained by the multisampling technique show clear evidence of a leakage vortex core behind the rotor. Behavior of the leakage vortex was clarified for various tip clearances by examining loci of the vortex center, decay characteristics of the vorticity at the center, and the total amount of vorticity shed from the blade tip. These results were compared with the leakage vortex model presented by Lakshminarayana.

Introduction

It is well known that a substantial loss in an axial-flow compressor is caused in the casing boundary-layer flow [1]. In spite of the fact that many studies have been done on the casing boundary layer [2-11], it is difficult to predict accurately its development through a rotor with arbitrary design condition. The reason is that, in prediction methods, the development of the boundary layer is described by integral properties over the annulus-wall boundary layer, whereas, in the actual flow, complex phenomena have resulted from the interaction of rotating blades, boundary layer on the wall, tip leakage flow, etc.

Recently, with the development of flow measurement techniques, much effort in experimental studies has been concerned with the better understanding of the complex inviscid and viscous effects in the casing boundary-layer flow [12-15]. These studies will be useful more or less for establishment of the accurate prediction of the casing boundary-layer development available to all design conditions. However, many more experimental studies are desired to attain the final goal.

In this study, detailed flow measurements were made before and behind an axial-flow rotor with various tip clearances to investigate the clearance effect on the end-wall flow development and to elucidate the behavior of the tip leakage flow. The experiments were done at the flow rate corresponding to the same incidence angle of the rotor blade in the middle span (not at the same flow rate) so as to get rid of the effect of incidence variation caused by boundary layer blockage. Tip leakage flows behind the rotor were visualized by a computer-aided flow measurement with a slanted hot wire [16], and the results are compared with the flow model proposed by Lakshminarayana [17].

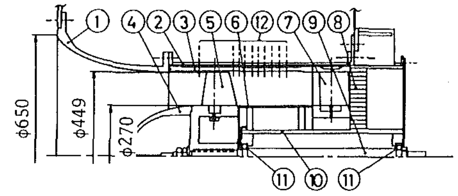

1 Inlet section
2 Outer casing(fixed)
3 Inner casing(changeable)
4 Nose cone
5 Rotor
6 Hub section(changeable)
7 Stator(changeable)
8 Honeycomb
9 Rotating axis
10 Inner hub(fixed)
11 Bearing
12 Surveying taps

Fig. 1 A schematic view of test section

Experimental Equipment and Instrumentation

A schematic view of the test section of the rotating cascade equipment in Kyushu University is shown in Fig. 1. An inlet section ①, an inner casing ③, a rotor ⑤, a hub section ⑥ and a stator ⑦ are changeable so as to make an experiment for any combination of cascade geometries within the limits of the maximum of 460 mm and the minimum hub/tip ratio of 0.3. A large inlet chamber (1500 mm × 1500 mm × 1500 mm) with honeycombs and filters is mounted on the upstream end of the test section. The downstream end is connected to an outlet chamber (1800 mm × 1500 mm × 2350 mm) followed by a nozzle flow meter, a cone-diffuser and a variable exhaust system (an auxiliary fan). The drive shaft ⑨ is coupled with a torque meter inside the outlet chamber and with a d-c motor outside it.

A 449-mm-dia, isolated rotor with hub/tip ratio of 0.6 was used for the experiments reported herein. The rotor comprises 12 blades of NACA 65 series profile designed for free vortex operation with an axial inlet flow condition. The blade-row geometry and operating characteristics at representative sections are given in Table 1. The stator, consisting of 13 blades of NACA 65 series profile, was designed for an axial

---

Contributed by the Gas Turbine Division of The American Society of Mechanical Engineers and presented at the 30th International Gas Turbine Conference and Exhibit, Houston, Texas, March 18-21, 1985. Manuscript received at ASME Headquarters, December 21, 1984. Paper No. 85-GT-62.

Table 1 Geometry and operating characteristics of the rotor

	root	mid-span	tip
radius	135.0 mm	180.0 mm	224.5 mm
chord length	106.1 mm	117.8 mm	117.5 mm
camber (c_{l0})*	1.30	0.62	0.32
solidity	1.50	1.25	1.00
maximum thickness /chord	10.00 %	8.00 %	6.00 %
trailing edge thickness /chord	1.41 %	1.27 %	1.28 %
stagger	31.5 deg	47.2 deg	56.2 deg
inlet flow angle**	49.1 deg	57.0 deg	62.5 deg
exit flow angle**	22.2 deg	44.4 deg	55.8 deg

geometries applied to developed cuts at constant radii.

* isolated airfoil lift coefficient of NACA 65 profile camber line at zero angle of attack in potential flow

** angle between relative flow and axial direction

outlet flow condition, but was set far downstream of the rotor by inserting the hub section ⑥ ahead of the stator ⑦ in order to investigate the behavior of the tip leakage vortex at the rotor exit.

The tests with tip clearances of 0.5, 1.0, 2.0, 3.0, and 5.0 mm were conducted by changing the inner diameter of the casing insert ③, so that the blade geometry at tip section is kept exactly constant. The front and hind parts of each casing insert have gradual slopes of 30 mm axial length to connect the inlet and outlet sections smoothly (the slope varies from 0 deg for 0.5 mm clearance to 8.5 deg for 5.0 mm). A total pressure rise coefficient ψ of 0.4 at the design flow rate coefficient ϕ of 0.5 was obtained for the minimum tip clearance, which agreed well with the design value.

The overall stage performance was evaluated by measurements of pressures and temperatures in the inlet and the outlet chamber, flow rate, and torque. The peripheral-averaged velocity distributions before and behind the rotor were obtained by radial survey of a 5-hole cobra probe 20.4 mm upstream of the leading edge and 28.0 mm downstream of the trailing edge of the tip blade section, respectively (Fig. 2). The measurements for various tip clearances were made at the flow rate corresponding to the same relative inlet flow angle at the midspan as that for the minimum tip clearance ($\tau = 0.5$ mm).

The three-dimensional structure of the exit flow relative to the rotor was determined by a constant-temperature hot-wire anemometer and a periodic multisampling and averaging technique with an on-line microcomputer [16]. The hot-wire surveys were made at the four measuring cross sections parallel to the trailing edge plane of the rotor as shown in Fig. 2. The sensor is a tungsten filament of 5-μm dia, 1-mm effective length and 30-deg slanting angle. At each measuring location, 12 positions of the hot-wire sensor were set by rotating the probe axis. At each sensor position, the hot-wire

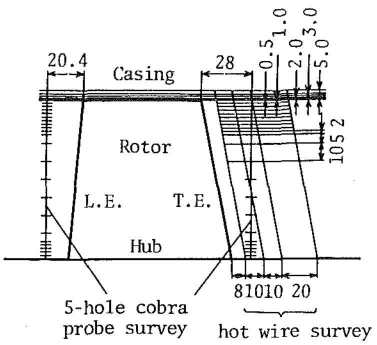

Fig. 2 Illustrations of measuring planes and measuring radial locations

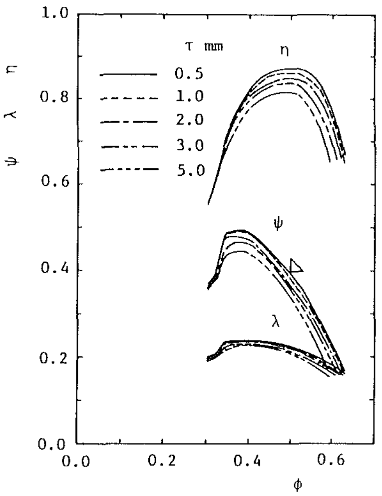

Fig. 3 Effect of tip clearance on stage performance

Nomenclature

c_z = axial velocity
c_θ = absolute tangential velocity
D = casing diameter
D_h = hub diameter
K_B = endwall blockage factor
L = shaft power from torque and speed
l_t = chord length at tip section
ΔP = total pressure rise through the stage
Q = flow rate
r = radius
s = distance from trailing edge along relative streamline
u = peripheral speed of blade
u_t = peripheral speed of blade at tip
z = axial distance from trailing edge
β = relative flow angle
Γ = circulation of blade
$\Delta\Gamma$ = total amount of leakage vorticity in terms of circulation
δ_e = boundary-layer thickness
δ_z^* = axial displacement thickness [equation (8)]
ζ_p = pressure loss coefficient [equation (7)]
η = efficiency
θ_z^* = axial momentum thickness [equation (9)]
λ = shaft power coefficient [equation (3)]
ν_T = tangential force deficit thickness [equation (10)]
ξ_s = streamwise vorticity [equation (11)]
ρ = density
τ = tip clearance
ϕ = flow rate coefficient [equation (1)]
ψ = total pressure rise coefficient [equation (2)]
ω = angular velocity of rotor
Ω = work-done factor

Subscripts

1 = rotor inlet
2 = rotor exit
c = casing
d = design condition
e = boundary-layer edge
h = hub

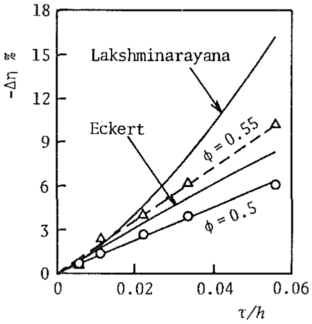

Fig. 4 Reduction of efficiency with tip clearance

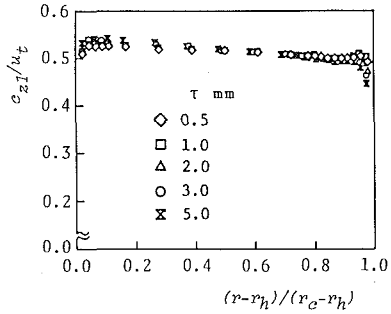

Fig. 5 Velocity distributions at rotor inlet

signals were acquired for 100 circumferential sampling points every rotation as instructed by the microcomputer. The 100 circumferential points cover the progress of two complete blade passages. The data acquisition and the sum of the data were done at the same time for each sampling point during 512 revolutions of the rotor. Therefore a set of 12 ensemble averages of the hot-wire signal, which is the sum of the data divided by 512, is obtained corresponding to the 12 hot-wire orientations. Three components of the flow velocity were determined from the 12 ensemble averages by solving the calibration equation of the hot-wire with the least-mean-square method. Using this technique, it was possible to save measuring time as well as calibrating time, thus preventing substantial change in the hot-wire output owing to wire contamination. As the velocity is determined from 6144 (= 12 × 512) signals, they are accurate in the statistical sense.

Results and Discussion

Overall Performance. Figure 3 shows the stage performance of the rotor with stator, where the flow rate coefficient ϕ, the total pressure coefficient ψ, the shaft power coefficient λ and the stage efficiency η are defined as

$$\phi = Q/\{u_t\pi(D^2 - D_h^2)/4\} \qquad (1)$$

$$\psi = \Delta P/(\rho u_t^2/2) \qquad (2)$$

$$\lambda = L/\{\rho u_t^3\pi(D^2 - D_h^2)/8\} \qquad (3)$$

$$\eta = \phi\psi/\lambda \qquad (4)$$

Increase in the tip clearance (τ) reduces both the efficiency and input power (shaft power coefficient). Therefore, the pressure coefficient decreases multiplicatively with tip clearance. The decrease in ψ was 6.1% when the clearance was raised from τ = 0.5 mm to 2.0 mm and was 13.8% to 5.0 mm. The maximum efficiency is obtained near the design flow rate for all tip clearances.

The reduced amount of efficiency at the design point (ϕ = 0.5) is compared with the predictions by Lakshminarayana [17] and Eckert [18] in Fig. 4. The experimental result is considerably smaller than the predicted one. Generally, the reduced amount depends on the blading and the flow conditions. For example, the efficiency reduction becomes substantially large at ϕ = 0.55 in this experiment. This is due to the fact that there are a few indirect causes to reduce the efficiency. At the same flow rate, a change in the blockage effect of the casing boundary layer brings about a change in the incidence flow angle at the blade midspan. Lift-incidence characteristics depend on the blading. Furthermore, the change in the incidence may affect profile loss and secondary flow loss outside the annulus-wall boundary layers.

In order to exclude the effect of incidence, the experiments on the flow development through the rotor were conducted at

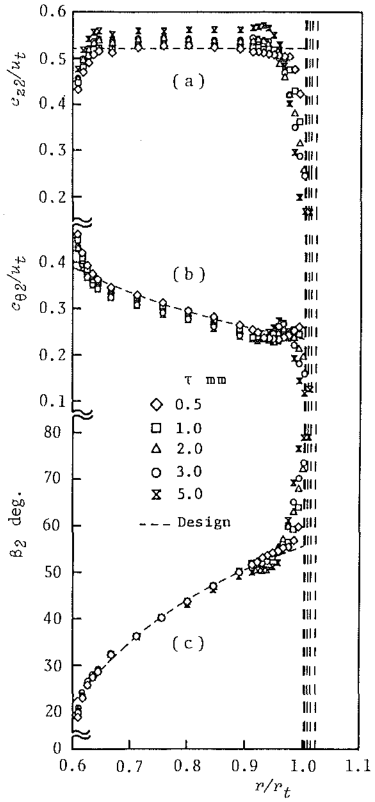

Fig. 6 Distributions of axial velocity, tangential velocity and relative flow angle at rotor exit

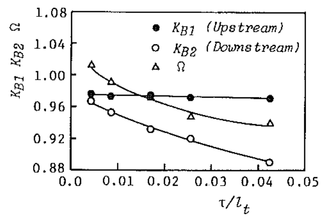

Fig. 7 Variations of blockage factor and work done factor with tip clearance

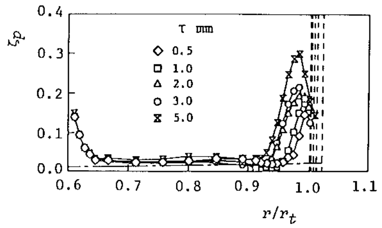

Fig. 8 Distribution of total pressure loss coefficient through rotor

the flow rate which gives the same incidence at the midspan as that for $\tau = 0.5$ mm and $\phi = 0.5$.

Flow Development Through the Rotor. Inlet velocity distributions, measured by the 5-hole cobra probe, are shown in Fig. 5. The flow direction was axial. But an appreciable velocity gradient was observed which gave higher velocity near the hub, although uniform axial inlet flow was intended in the design. This is due to streamline curvature affected by the inlet nose cone. The velocity gradient becomes slightly larger for larger tip clearance on account of variation of the sucking effect of the rotor near the tip region.

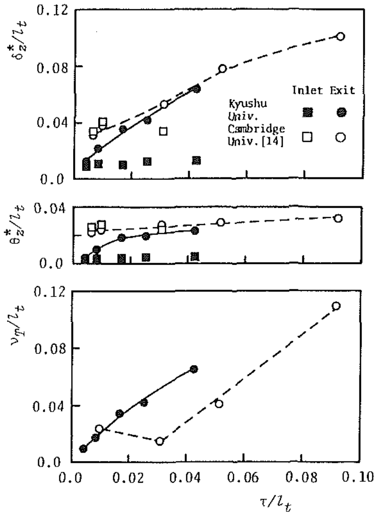

Fig. 9 Variations of displacement, momentum, and tangential force deficit thicknesses with tip clearance

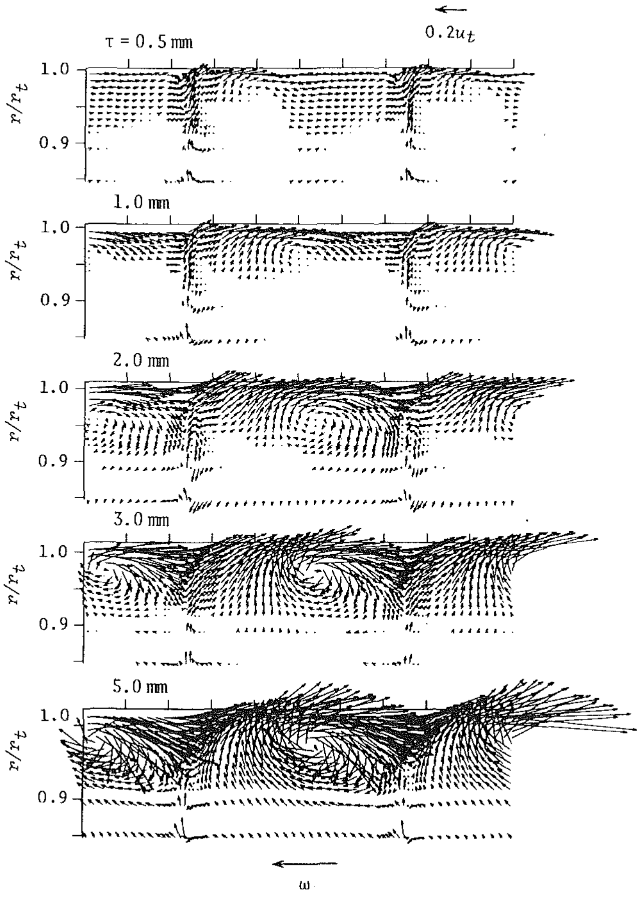

Fig. 10(a) Variation of secondary flow with tip clearance (z/l_t = 0.068)

The boundary layer at the casing wall becomes thicker as the tip clearance rises partially because of different slopes at the front part of the casing insert. In this experiment, however, the flow-rate coefficient changed little on the condition of the same incidence at midspan, since the reduction of flow in the thickened boundary layer was compensated by an increase in velocity near the hub (due to the larger velocity gradient) in the case of the large clearances. Such a compensating effect does not come into existence in a general compressor stage without a nose cone just before the rotor. Therefore, the discussion in the following sections will be restricted to the half-flow passage near the casing.

Figure 6 presents the radial distributions of the axial and tangential velocities and the relative flow angle at the rotor exit measured by the 5-hole cobra probe. Any accounting was not taken of the unsteady effect on the low response data because they were within the scattered band of the circumferentially averaged values of the hot-wire data. Vertical dashed lines in the figure denote the casing wall for various tip clearances. In the case of τ = 0.5 mm, these distributions coincide with the design values except in the annulus-wall boundary layers. As the tip clearance rises, the axial velocity increases in the main stream. Since the inlet axial velocity is almost invariable with tip clearance (except slight increase in velocity gradient), and the development of the hub boundary layer is also invariable, the increment of the axial velocity is mainly caused by the casing boundary layer development

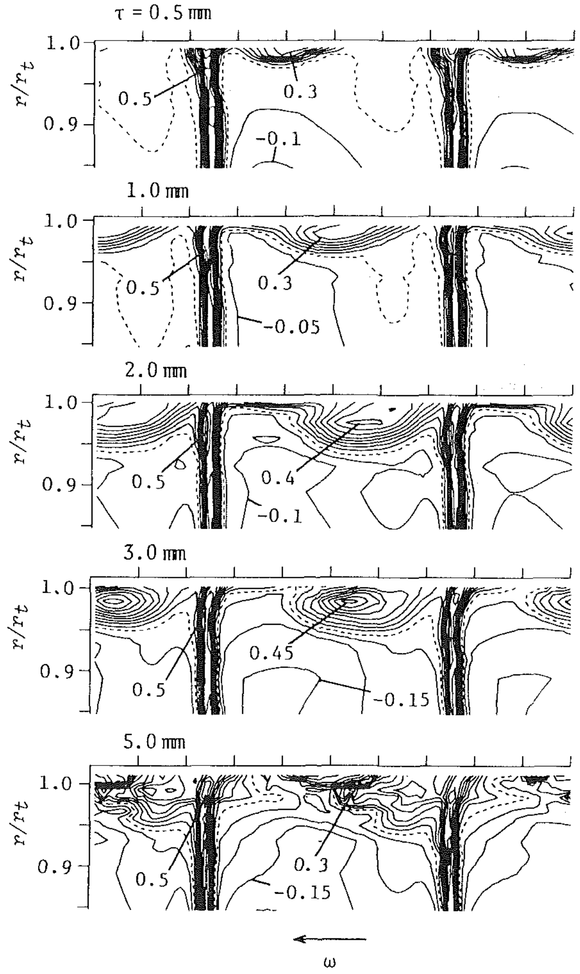

Fig. 10(b) Variation of relative kinetic energy defect with tip clearance (z/l_t = 0.068)

Table 2 Blading details at tip section of the authors' rotor and the "Cambridge" rotor

	ϕ	ψ_{th}+	Hub/tip ratio	β_1	β_2
Kyushu University	0.5	0.469	0.6	62.5 deg	55.8 deg
Cambridge University	0.49*	0.254*	0.4	63.9 deg*	60.7 deg

	Blade profile	Thickness ratio	Camber angle	Solidity	Stagger angle
Kyushu University	NACA 65	6%	8.0**	1.0	56.2 deg
Cambridge University	C 4	8%	8.2	0.7*	60.7 deg

* Recalculated by the authors from [14]
** Equivalent camber angle of NACA65 profile
\+ ψ_{th} = Euler's head coefficient

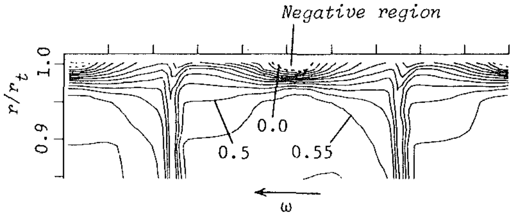

Fig. 11 Contours of axial velocity at rotor exit (τ = 3 mm, z/l_t = 0.068)

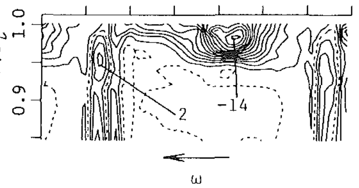

Fig. 12 Contours of streamwise vorticity at rotor exit (τ = 3 mm, z/l_t = 0.068)

through the rotor. The exit relative-flow angle changes little except in the casing boundary layer. Therefore, the absolute tangential velocity in the mainstream decreases with increase in the axial velocity. This is the main reason for input power reduction with tip clearance.

In the casing boundary layer, the tangential velocity has the maximum value and the maximum point is more distant from the wall as the tip clearance rises. This is due to the tip leakage vortex as will be shown in the blade-to-blade flow at the rotor exit. The influence of the clearance is also observed in the exit-flow angle distribution with an inflection point near the casing.

In terms of a design, the increase in axial velocity and the decrease in tangential velocity at the mainstream are represented by an end-wall blockage factor K_B and a work-done factor Ω:

$$K_B=\frac{(r_c-\delta_{zc}^*)^2-(r_h+\delta_{zh}^*)^2}{r_c^2-r_h^2} \tag{5}$$

$$\Omega=\frac{<u_2c_{\theta 2}-u_1c_{\theta 1}>}{<u_2c_{\theta 2,d}-u_1c_{\theta 1,d}>} \tag{6}$$

where < > denotes the average weighted with local flow rate and a subscript d indicates the design value.

Figure 7 presents the blockage factors at the rotor inlet and exit and the work-done factor. The inlet blockage factor changes little with tip clearance in spite of the increase in the inlet boundary-layer thickness. The reason is due to the slight change in the inlet velocity gradient as described earlier. Both the exit blockage factor and the work-done factor reduce remarkably as the clearance becomes large. This rotor was designed with K_B = 0.96 and Ω = 1.0, and these values are obtained at τ/l_t = 0.6% (τ = 0.7 mm) in the figure.

Figure 8 shows the distributions of the pressure loss coefficient defined by

$$\zeta_p=\frac{(u_2c_{\theta 2}-u_1c_{\theta 1})-\Delta P/\rho}{u_t^2/2} \tag{7}$$

A dotted-dash line indicates the predicted value based on two-dimensional cascade data. In the mainstream, the loss coefficient is a little larger than the predicted value, and changes little with tip clearance except for τ = 5.0 mm. It can be seen from the figure that the increase in loss with clearance is mainly attributable to the remarkable rise in the casing boundary layer.

The development of the casing boundary layer is further demonstrated with reference to the integral properties. In order to compare with Hunter and Cumpsty's experiment [14], the axial displacement thickness δ_z^*, the axial momentum thickness θ_z^*, and the tangential force deficit thickness ν_T were taken as the integral properties.

$$\delta_z^*=\frac{1}{r_cc_{ze}}\int_{r_c-\delta_e}^{r_c}(c_{ze}-c_z)rdr \tag{8}$$

$$\theta_z^*=\frac{1}{r_cc_{ze}^2}\int_{r_c-\delta_e}^{r_c}(c_{ze}c_z-c_z^2)rdr \tag{9}$$

$$\nu_T=\frac{1}{r_cc_{ze}c_{\theta e}}\int_{r_c-\delta_e}^{r_c}(c_{ze}c_{\theta e}-c_zc_\theta)rdr \tag{10}$$

where the subscript e indicates the boundary-layer edge, and the boundary-layer thickness δ_e is somewhat arbitrarily taken on the basis of the axial velocity distribution.

Figure 9 presents the variation of δ_z^*, θ_z^*, ν_T with tip clearance before and behind the rotor. In the figure, the experimental data from [14] are replotted by the open symbols. Table 2 shows comparisons of the flow conditions and the bladings at the tip section of the authors' and the "Cambridge" rotor. In this experiment, slight increases in the displacement and momentum thicknesses with tip clearance are shown at the rotor inlet. The larger the tip clearance is, the thicker the displacement, momentum, and force-deficit thickness are at the rotor exit. However, the variation trends differ from the Cambridge data. Substantial differences of the flow condition between the authors' and the Cambridge rotor are the blade loading (pressure-rise coefficient) and the inlet boundary layer thickness. In the case of the Cambridge rotor (low loading and thick inlet boundary layer), there is little change in the displacement and momentum thicknesses through the rotor at the smaller tip clearances. On the other

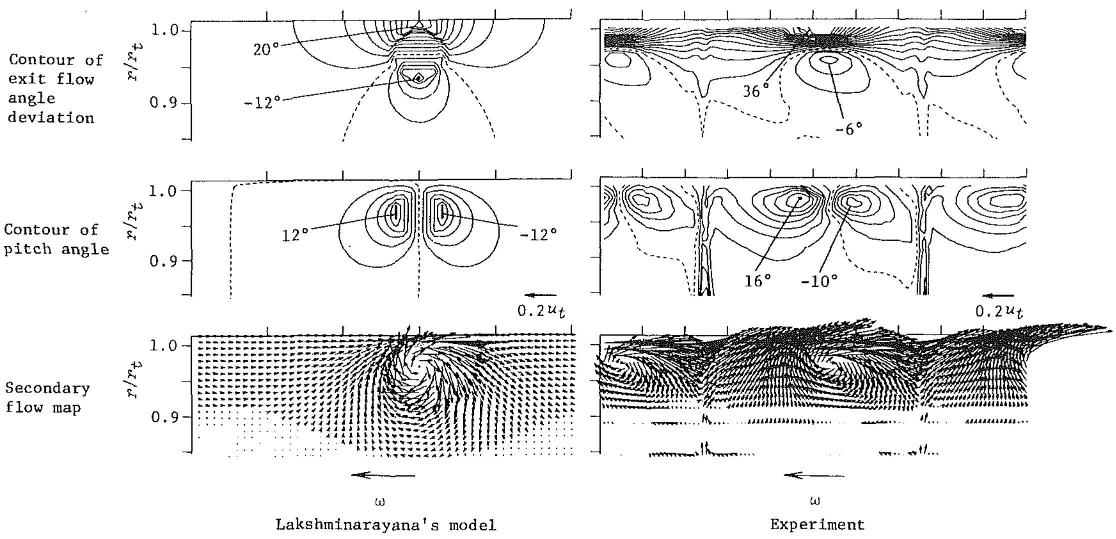

Fig. 13 Comparisons of exit-flow angle deviation, pitch angle, and secondary flow between experiment and Lakshminarayana's model

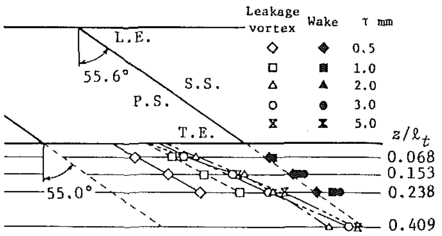

Fig. 14(a) Loci of vortex center for various tip clearances

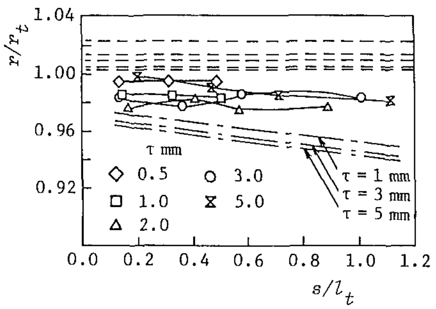

Fig. 14(b) Radial locations of vortex center for various tip clearances

hand, both thicknesses increase remarkably for the authors' rotor (high loading and thin inlet boundary layer). At the larger clearances ($\tau/l_t > 2.5\%$), however, the variation trends of the displacement and momentum thicknesses are quite similar between the authors' data and the Cambridge data.

Unexpected phenomena arise in the case of low loading and thick inlet boundary layers, such as the force-deficit thickness less than the tip clearance and the slight reduction in the force-deficit thickness with tip clearance. For high loading and thin inlet boundary layer, however, the force-deficit thickness is thicker than the tip clearance by 1.5 to 2 times. The force-deficit thickness appears to increase with blade loading at the large clearance.

Blade-to-Blade Flow at Rotor Exit. The phase-locked flow pattern at the rotor exit is obtained by the periodic multisampling technique with a slanted hot-wire. Figures 10(*a*) and (*b*) present the secondary-flow maps and the contour maps of relative kinetic energy defect for various tip clearances. The secondary flow was defined by a velocity component perpendicular to the design relative-flow direction, and the coefficient of kinetic energy defect was defined by the difference of relative kinetic energy between the measured and designed value divided by the design relative kinetic energy. Short vertical segments above the figure are drawn every 20% of the blade spacing. Dotted contour lines in Fig. 10(*b*) indicate the kinetic energy defect being zero, and negative values are due to blockage effect of blade wakes, wall-boundary layers and a leakage vortex.

From the secondary flow maps, it can be seen how the rolling-up of the leakage flow varies with tip clearance. For the minimum clearance case, the existence of the leakage vortex is not clear, but it can be checked from the energy-defect contour map. On the corner between the pressure side of the wake and the casing, downward flow comes into existence on account of scraping the casing boundary layer. This is reconfirmed by the existence of low-energy fluid accumulating at this corner in Fig. 10(*b*). Such a scraping effect is hardly observed for other clearances.

As the tip clearance rises from $\tau = 0.5$ mm to 2.0 mm, the leakage vortex rolls up more clearly, and the position of rolling-up is more distant from the suction side of the blade. For the larger clearances ($\tau > 2.0$ mm), it rolls up more intensely, but the position of rolling-up is almost invariable. On the other hand, clear evidence of a vortex core was not found in [14]. This is probably due to the thicker casing boundary layer at the rotor inlet.

The rolling up of the leakage flow is closely related to the radial distributions of the time-averaged tangential velocity and the relative exit flow angle in the casing boundary layer (Fig. 6). The large vortex motion causes reverse flow in the axial direction locally as shown in Fig. 11, which results in the large pressure loss near the tip region.

It can be seen from Fig. 10(*b*) that the accumulation of low-energy fluid is mainly in the rolling-up of the leakage flow. As the leakage vortex moves from the suction side of the blade to the pressure side of the adjacent blade owing to the interaction of the casing wall, the region of low kinetic energy is apt to appear toward the pressure side of the passage [14], or interact with the adjacent wake. Such a map was obtained from downstream surveys at low flow rates (the figure is omitted in this report and will be presented in a future paper).

Figure 12 shows the contour map of streamwise vorticity normalized by twice the angular velocity of rotor. The streamwise vorticity was evaluated by numerical differentiation using the following equation [19]:

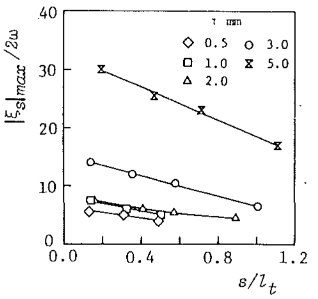

Fig. 15 Decay characteristics of streamwise vorticity

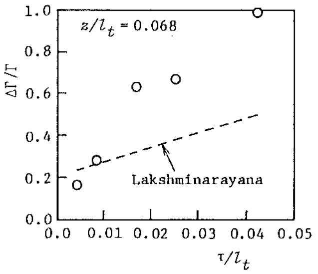

Fig. 16 Total amount of shed vorticity from blade tip

$$\xi_s = \{(1/r)\partial(rc_\theta)/\partial r - (1/r)\partial c_r/\partial\theta\}\cos\beta - \{\partial c_r/\partial z - \partial c_z/\partial r\}\sin\beta \qquad (11)$$

The positive and negative values in the wake region result from the radial velocity caused by centrifugal effects. In the leakage vortex, the magnitude of the vorticity becomes higher toward the vortex center. Lakshminarayana employed a circular solid vortex having constant vorticity within a certain radius for the leakage vortex in his model [17]. In Fig. 13 the contour maps of the relative exit-flow angle deviation from the design value and the pitch angle as well as the secondary flow map are compared with those calculated by Lakshminarayana's model. The exit flow angle deviation near the casing becomes larger on account of the relative motion of the casing wall. Contours of the pitch angle are asymmetric about the vortex center owing to the inclination of the vortex axis. However, his model represents qualitatively the flow induced by the leakage vortex.

Behavior of Leakage Vortex. Behavior of the leakage vortex is investigated by the phase-locked hot-wire surveys at the four measuring sections indicated in Fig. 2. Figure 14(*a*) shows the loci of the vortex center for various tip clearances on the z-θ plane. The vortex center is taken as a position of the maximum kinetic energy defect in Fig. 10(*b*). In the figure, the blade chords at $r/r_t = 0.984$ are drawn for reference since the averaged radial location of the vortex center is at this radius. The filled-in symbols are positions of the wake center at the same radius. The loci of the center agree almost with the averaged exit-flow angle for each tip clearance. The intersection of the extrapolation of the loci inside the rotor is near midpassage at midchord position where the interaction of leakage flow, casing boundary layer, and scraping vortex is the dominant feature according to a recent study by Lakshminarayana [15].

Figure 14(*b*) presents the relative streamwise variation in the radial location of the vortex, where dashed lines indicate the casing wall and dotted-dash lines indicate the vortex centers of Lakshminarayana's model [17] calculated by $r/r_t = 1-(\text{radius of solid vortex})/r_t$. Although the measured radial positions are somewhat scattered, they are larger than the calculated values and have a tendency to decrease in the streamwise direction. The decreasing rate is smaller than that of the model.

The decay of the vorticity was investigated by examining the streamwise variation of the maximum streamwise vorticity in the leakage vortex. As shown in Fig. 15, the larger the maximum vorticity, the faster the decaying rate. However, the change in the total amount of the streamwise vorticity which represents the shed vortex from the blade tip was relatively small in the streamwise direction. The total amount of the shed vorticity was evaluated by integrating the streamwise vorticity over the half-flow passage near the casing since the streamwise vorticity due to the radial flow on the suction side of a wake is cancelled by that on the pressure side. The effect of relative motion of the casing wall was eliminated by subtracting the circulation of the skewed boundary layer on the casing wall. Figure 16 shows the total amount of shed vorticity from the blade tip in comparison with the calculated value of Lakshminarayana's model. For the smaller clearance, the agreement is fairly good, but the experimental values become larger than the calculated ones as the clearance rises.

On the whole, the tip leakage flow can be expressed by Lakshminarayana's model. However, some modifications are desired in order to establish an accurate prediction method applicable for all bladings and flow conditions. For this purpose, there is a need for further experiments on other bladings and flow conditions.

Conclusions

Performance testing and detailed flow measurement have been made in an axial compressor rotor with various tip clearances. The experiments have been conducted not at the same flow rate but at the flow rates which give the same incidence angle to exclude the effect of incidence. Behavior of the tip leakage vortex has been investigated by means of a phase-locked multisampling technique with a slanted hot wire. From the experimental results reported in this paper the following conclusions are drawn.

1 An increase in the tip clearance deteriorates the stage performance by reducing both efficiency and input power.

2 The reduction of efficiency did not agree with the existing predictions in this experiment. This is probably due to some indirect causes depending on the blading and the flow condition.

3 At the same incidence, the relative exit flow angle and the total pressure loss change little with tip clearance except in the casing boundary layer. On the other hand, the free-stream exit axial velocity increases and the exit tangential velocity decreases with tip clearance due to the blockage caused by casing boundary layer development through the rotor.

4 Variations of the end-wall blockage and work-done factor due to the boundary-layer development through the rotor have been presented.

5 Variations of the displacement and momentum thicknesses at the rotor exit with tip clearance almost agree with Hunter and Cumpsty's data at the large tip clearances, in spite of different blading and flow condition. At the small clearances, however, differences in the blade loading and the inlet boundary-layer thickness affect the variation of these thicknesses.

6 The tangential blade force deficit thickness increases with tip clearance unless the blade loading is too low and the inlet boundary layer is thick. Its magnitudes have been about 1.5 to 2 times of the tip clearance in this experiment.

7 A peak in the tangential velocity distribution and an inflection point in the exit flow angle in the casing boundary layer are closely related to rolling-up of the leakage flow.

8 Clear evidence of the leakage vortex core has been found in this experiment. As the tip clearance rises, the

leakage vortex rolls up more intensely and the position of rolling-up is more distant from the suction side of the blade. At large tip clearances, however, the rolling-up position changes little with tip clearance.

9 The large vortex motion causes reverse flow in the axial direction near the casing wall.

10 The vortex model by Lakshminarayana represents qualitatively the tip leakage flow behind the rotor.

11 The locus of the vortex center and the decay characteristics of the vorticity have been investigated.

12 The total amount of leakage vortex in terms of circulation is substantially larger than Lakshminarayana's for large tip clearances.

References

1 Smith, L. H., Jr., "Casing Boundary Layers in Multistage Axial-Flow Compressors," *Flow Research on Blading*, Ed. L. S. Dzung, Elsevier, New York, 1970, pp. 275-304.

2 Stratford, B. S., "The Use of Boundary Layer Techniques to Calculate the Blockage from the Annulus Wall Boundary Layer in a Compressor," ASME Paper No. 67-WA/GT-7, Nov. 1967.

3 Mellor, G. L., and Wood, G. M., "An Axial Compressor End-Wall Boundary Layer Theory," ASME *Journal of Basic Engineering*, Vol. 93, No. 2, June 1971, pp. 300-316.

4 Marsh, H., and Horlock, J. H., "Wall Boundary Layers in Turbomachines," *Journal of Mechanical Engineering Science*, Vol. 14, No. 6, 1972, pp. 411-423.

5 Hirsch, C., "End-Wall Boundary Layers in Axial Compressors," ASME JOURNAL OF ENGINEERING FOR POWER, Vol. 96, No. 4, Oct. 1974, pp. 413-426.

6 Balsa, T. F., and Mellor, G. L., "The Simulation of Axial Compressor Performance Using an Annulus Wall Boundary Layer Theory," ASME JOURNAL OF ENGINEERING FOR POWER, Vol. 97, No. 3, July 1975, pp. 305-318.

7 Railly, J. W., "A Non-Axisymmetric End-Wall Boundary Layer Theory for Axial Compressor Rows," Aeron. Res. Counc., C. P. No.1322, Jan. 1975.

8 Papailion, K., Flot, R., and Mathieu, J., "Secondary Flow in Compressor Bladings," ASME JOURNAL OF ENGINEERING FOR POWER, Vol. 99, No. 2, Apr. 1977, pp. 211-224.

9 De Ruyck, J., Hirsch, C., and Kool, P., "An Axial Compressor End-Wall Boundary Layer Calculation Method," ASME JOURNAL OF ENGINEERING FOR POWER, Vol. 101, No. 2, Apr. 1979, pp. 233-249.

10 De Ruyck, J., and Hirsch, C., "Investigation of an Axial Compressor End-Wall Boundary Layer Prediction Method," ASME JOURNAL OF ENGINEERING FOR POWER, Vol. 103, No. 1, Jan. 1981, pp. 20-33.

11 Adkins, G. G., Jr., and Smith, L. H., Jr., "Spanwise Mixing in Axial-Flow Turbomachines," ASME JOURNAL OF ENGINEERING FOR POWER, Vol. 104, No. 1, Jan. 1982, pp. 97-110.

12 Dring, R. P., Joslyn, H. D., and Hardin, L. W., "An Investigation of Axial Compressor Rotor Aerodynamics," ASME JOURNAL OF ENGINEERING FOR POWER, Vol. 104, No. 1, Jan. 1982, pp. 84-96.

13 Lakshminarayana, B., Pouagare, M., and Davino, R., "Three-Dimensional Flow Field in the Tip Region of a Compressor Rotor Passage. Part I: Mean Velocity Profiles and Annulus Wall Boundary Layer," ASME JOURNAL OF ENGINEERING FOR POWER, Vol. 104, No. 4, Oct. 1982, pp. 760-771.

14 Hunter, I. H., and Cumpsty, N. A., "Casing Wall Boundary Layer Development Through an Isolated Compressor Rotor," ASME JOURNAL OF ENGINEERING FOR POWER, Vol. 104, No. 4, Oct. 1982, pp. 805-818.

15 Pandya, A., and Lakshminarayana, B., "Investigation of the Tip Clearance Flow Inside and at the Exit of a Compressor Rotor Passage. Part I: Mean Velocity Field," ASME JOURNAL OF ENGINEERING FOR POWER, Vol. 105, No. 1, Jan. 1983, pp. 1-12.

16 Kuroumaru, M., Inoue, M., Higaki, T., Abd-Elkhalek, F. A., and Ikui, T., "Measurements of Three-Dimensional Flow Field Behind an Impeller by Means of Periodic Multi-Sampling of a Slanted Hot Wire," *Bulletin of the JSME*, Vol. 25, No. 209, Nov. 1982, pp. 1674-1681.

17 Lakshminarayana, B., "Methods of Predicting the Tip Clearance Effects in Axial Flow Turbomachinery," *ASME Journal of Basic Engineering*, Ser. D, Vol. 92, No. 3, Sept. 1970, pp. 467-482.

18 Eckert, B., and Schnell, E., "Axial und Radial Kompressoren," 5th ed., Springer-Verlag, 1961, p. 193.

19 Inoue, M., and Kuroumaru, M., "Three-Dimensional Structure and Decay of Vortices Behind an Axial Flow Rotating Blade Row," ASME JOURNAL OF ENGINEERING FOR GAS TURBINES AND POWER, Vol. 106, No. 3, July 1984, pp. 561-569.

A Numerical Modeling of Endwall and Tip-Clearance Flow of an Isolated Compressor Rotor

C. Hah
Corporate Research and Development,
General Electric Company,
Schenectady, N.Y. 12301

The current study is aimed at developing and appraising a numerical method for the development of endwall boundary layers through tip-clearances and their effect on the performance of an isolated compressor rotor. The Reynolds-averaged Navier-Stokes equation is solved for the entire flow field in elliptic form. The relative flow is computed on the generalized coordinates fixed on the rotor. Comparison between the numerical results and experimental data indicates that the complex three-dimensional viscous flow phenomena inside the tip region are properly predicted.

Introduction

The flow across tip clearance near the casing wall in turbomachinery is extremely complex and dominated by a three-dimensional viscous effect. The boundary layer that develops across the tip clearance limits both the performance and the aerodynamic efficiency of turbomachinery. However, relatively little progress has been made to understand and to develop a realistic prediction method of the flow.

A large number of experimental studies have been undertaken to understand and to describe the flow field. The influence of endwall flows in actual compressor stages was well described in an earlier paper by Smith [1]. Various pioneering works by Rains [2], Dean [3], Lakshminarayana and Horlock [4], and Lakshminarayana [5], indicated that tip clearance exerts a significant influence on the development of endwall flow. Booth et al. [6] used various water flow rigs to obtain parameters for their correlation of tip clearance modeling. The recent experimental studies by Hunter and Cumpsty [7] and Inoue and Kuroumaru [8], and Murthy and Lakshminarayana [9], show remarkable progress toward understanding the detailed nature of tip-clearance flow. These studies measured detailed flow fields inside rotating blades with hot wire or laser-Doppler velocimetry with various tip clearances and flow conditions; thus, the relative motion between the blade and the casing wall is properly included. Indeed, these results show that high dynamic head exists right down to the casing. Their experimental studies provide verification data for prediction models in addition to clarifying the physical nature of the flow.

On the analytical side, most research efforts have been concerned with the development of various correlation models that attempt to provide the designer with empirical information about the tip-clearance influence. Hawthorne [10] and Horlock and Lakshminarayana [11] developed their theory based on the classical secondary flow theory. Although these models predict useful values of flow outlet angles for simple geometry, no information on aerodynamic losses and viscous effects has been obtained. Horlock and Perkins [12] and Hirsch [13] used boundary layer theory and handled the endwall flow as a viscous flow. To obtain practical solutions, a considerable number of assumptions are made and solutions are provided in the form of integral properties rather than boundary-layer profiles. These solutions are as limited as the ones based on inviscid assumptions. Wadia and Booth [15] used viscous equations to solve flow in the simulated clearance flow with rectangular shapes. Their analysis requires mass flow rate through clearance. Also, geometry and flow conditions are probably oversimplified for realistic study, although their analyses provide very interesting results.

The purpose of the present study is to develop and verify full three-dimensional numerical schemes to predict the entire flow field, including tip-clearance region in an isolated compressor rotor. A three-dimensional viscous flow program developed for a single-blade row [14] has been further modified to handle the tip-clearance flow in the rotating frame.

Governing Equations and Turbulence Closure

The Reynolds-averaged, Navier-Stokes equations are used for the modeling of viscous flow phenomena inside rotating blade passages.

Various conservation equations for the viscous flow inside rotating blade passages can be written as follows using coordinates rotating with angular velocity.

$$\frac{1}{\rho}\,\frac{D\rho}{Dt}+U_{i,i}=0 \qquad (1)$$

Momentum:

$$\frac{\partial(\rho U_i)}{\partial t}+\frac{\partial}{\partial x_i}(\rho U_i U_j)+2\rho\,\epsilon_{ijk}\Omega_j U_K$$

$$=-\frac{\partial p}{\partial x_i}+\frac{\partial}{\partial x_i}\left[\mu\left(\frac{\partial U_i}{\partial x_j}+\frac{\partial U_j}{\partial x_i}-\frac{2}{3}\,\frac{\partial U_k}{\partial x_k}\delta_{ij}\right)-\rho\overline{u_i u_j}\right]+F_i \qquad (2)$$

Contributed by the Gas Turbine Division of The American Society of Mechanical Engineers and presented at the 30th International Gas Turbine Conference and Exhibit, Houston, Texas, March 18–21, 1985. Manuscript received at ASME Headquarters, December 27, 1984. Paper No. 85-GT-116.

Energy:

$$\frac{\partial}{\partial t}(\rho e)+\frac{\partial}{\partial x_j}(\rho U_j e)=\frac{\partial}{\partial x_j}\left(\left(\frac{\mu}{\mathrm{Pr}}\right)_{\mathrm{eff}}\frac{\partial T}{\partial x_j}\right)-\frac{\partial}{\partial x_j}\ (\text{-}U_j)+U_iF_i$$

$$+\frac{\partial}{\partial x_j}\left[U_i\mu\left(\frac{\partial U_i}{\partial x_j}+\frac{\partial U_j}{\partial x_i}-\frac{2}{3}\frac{\partial U_k}{\partial x_k}\delta_{ij}\right)\right] \qquad (3)$$

Gas state:

$$f(p,\rho,T)=0 \qquad (4)$$

where U_i = mean velocity, u_i = fluctuating velocity, e = total energy, R = gas constant, and Ω_i = angular velocity. For the the current test problem, which is steady and adiabatic flow, the time-dependent terms are not formulated and the energy equation is not solved.

An algebraic Reynolds stress model which was previously applied for the separated flow inside a cascade of airfoils [14] is further modified and used for the closure of the governing equations. The modification is to extend the previous model to the viscous sublayer region, which should be properly described for the flow inside very narrow tip clearance. Following studies by Lam and Bremhorst [17] and Rodi et al. [18], rather simple modifications are made for the transport equations of turbulence kinetic energy and dissipation rate as follows.

$$U_i\frac{\partial k}{\partial x_i}=\frac{\partial}{\partial x_i}\left(\frac{\nu_{\mathrm{eff}}}{\sigma_k}\frac{\partial k}{\partial x_i}\right)-\overline{u_iu_j}U_{i,j}-\epsilon \qquad (5)$$

$$U_i\frac{\partial \epsilon}{\partial x_i}=\frac{\partial}{\partial x_i}\left(\frac{\nu_{\mathrm{eff}}}{\sigma_\epsilon}\frac{\partial \epsilon}{\partial x_i}\right)$$

$$+C_S\frac{\epsilon^2}{k^3}(\overline{u_iu_j}-2/3k\delta_{ij})(\overline{u_ju_i}-2/3k\delta_{ji}) \qquad (6)$$

$$-C_Rf_{\epsilon 1}\frac{\epsilon}{k}\overline{u_iu_j}U_{i,j}-C_{\epsilon 2}f_{\epsilon 2}\frac{\epsilon^2}{k}$$

where

$$\nu_{\mathrm{eff}}=\nu+C_\mu f_\mu k^2/\epsilon;\quad k=1/2\delta_{ij}\overline{u_iu_j};$$

$$f_\mu=\left(1-e^{-A_\mu R_l}\right)^2\left(1+\frac{A_t}{R_t}\right)$$

$$f_{\epsilon 1}=1+\left(\frac{A_C}{R_t}\right)^3$$

$$f_{\epsilon 2}=1-e^{-R_e^2}$$

$$R_l=\sqrt{k}l/\nu$$

$$R_t=k^2/\nu\epsilon$$

and 1 is the distance between the node and the nearest solid surface.

The functions f_μ, $f_{\epsilon 1}$, and $f_{\epsilon 2}$ are to extend the preceding transport equations to the viscous sublayer region. Inside the viscous sublayer, the turbulence kinetic energy becomes negligibly small and turbulent shear stress also becomes negligible. For high local Reynolds numbers, R_t (when the node is outside the viscous sublayer), the preceding transport equations return to the original form for the fully turbulent flow.

The Reynolds stress components are estimated using the following algebraic equations with the local values of k, ϵ, and mean shear rate.

$$0=(1+C_1)(-\overline{u_ku_j}U_{i,k}-\overline{u_ku_i}U_{j,k})(1-\gamma)$$

$$-2(\epsilon_{ilm}\Omega_i\overline{u_mu_j}+\epsilon_{jlm}\Omega_l\overline{u_mu_i})-2/3\delta_{ij}(1-\gamma)\epsilon$$

$$-C_{\phi 1}\frac{\epsilon}{k}(\overline{u_iu_j}-2/3\delta_{ij})$$

$$+D_6\Omega_n(\epsilon_{lnj}\overline{u_lu_j}+\epsilon_{lnj}\overline{u_lu_i}) \qquad (7)$$

where γ and $C_{\phi 1}$ are constants in the modeling and C_1 is a variable, which represents the collective effects of the convection and the diffusion terms in the exact transportation equations of the Reynolds stresses. The physical basis of equation (7) is explained in [16], and the model was successfully applied for the prediction of separated flow through the cascade of airfoils [14]. Various constants in the turbulence modeling are not optimized for the present study; the values are: C_μ = 0.09, $C_{\phi 1}$ = 1.5, C_S = 1.8, $C_{\epsilon 2}$ = 1.44, D_6 = 0.7, δ_k = 1.0, δ_ϵ = 1.22, γ = 0.6, C_R = 0.46, A_μ = 0.016, A_t = 19.5, and A_{C1} = 0.06.

Various experimental studies [7, 8, 9] indicate that the flow in tip clearance is highly three-dimensional and involves flow separation near stall condition. As simpler turbulence closure schemes (based on mixing length or eddy viscosity type modeling) cannot be used for separated flow, the above model is used for the current study. However, evaluation of different turbulence closure models for the tip clearance flow is not the purpose of the current study. Perhaps this evaluation can be the subject of a future study.

Nomenclature

$C_S, C_1, C_\epsilon,$
$C_{\epsilon 1}, C_{\epsilon 2},$
γ, D_6 = constants in turbulence closure models
T = mean temperature
c_p = specific heat
D_{ij} = diffusion coefficient in equation (9)
Fi = additional body force in equation (2)
G_1, G_2, G_3 = convection coefficient in equation (9)
k = turbulence kinetic energy
k_c = thermal conductivity
P = $-\overline{u_iu_j}\,U^i_j$
p = static pressure
R = gas constant
W_x, W_r, W_Θ = axial, radial, and tangential mean velocities
W_x, W_r, W_Θ = axial, radial, and tangential fluctuating velocities
U_m = wheel speed at midspan
β = coefficient of thermal expansion
Ω_i = angular velocity of rotor
δ_{ij} = Kronecker delta
ϵ_{ijk} = permutation tensor
ν = kinematic viscosity
ρ = density
θ = dissipation due to viscosity [equation (3)]
ϕ = flow coefficient $(W_X)_0/U_m$

Subscripts

ρ = pressure side
s = suction side
t = total
o = upstream
m = midspan
l = first mode near the wall
w = value at the wall

Superscripts

$-$ = average value

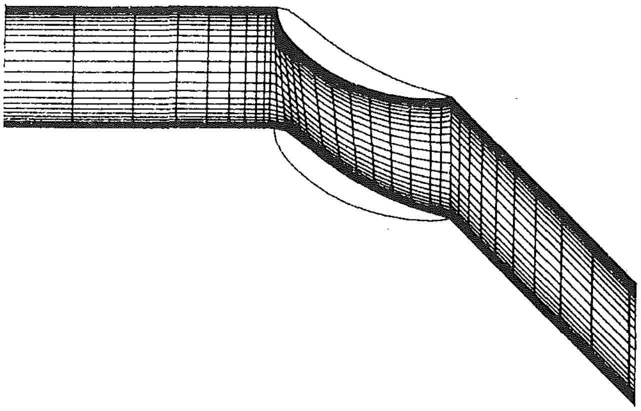

Fig. 1(*a*) Blade-to-blade grid at rotor hub

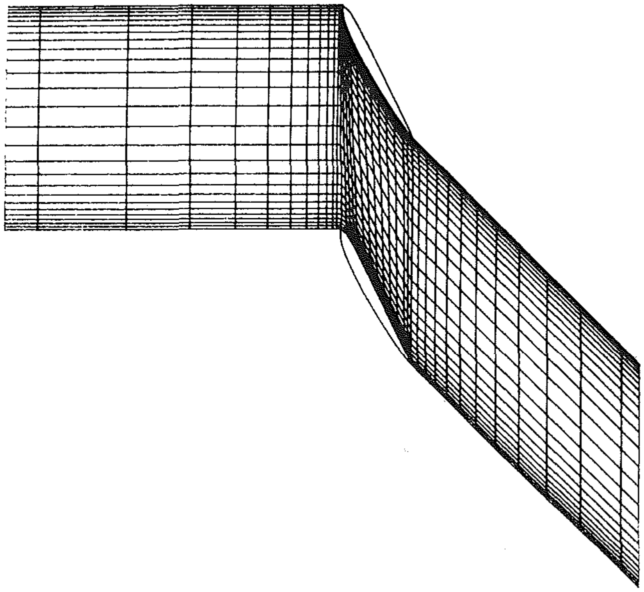

Fig. 1(*b*) Blade-to-blade grid at rotor tip

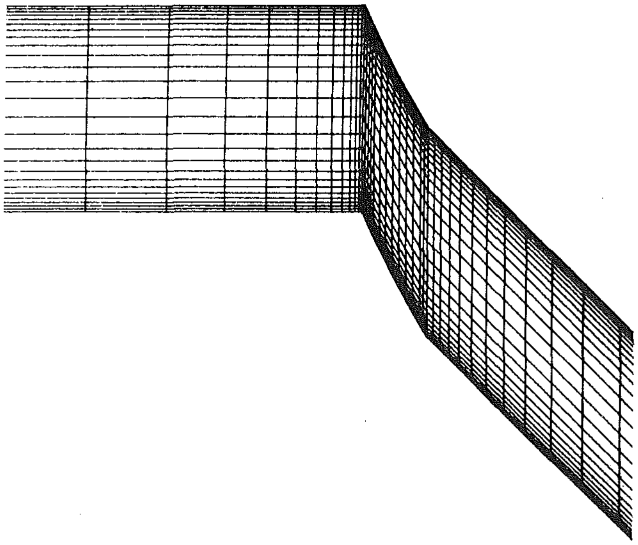

Fig. 1(*c*) Blade-to-blade grid inside tip clearance

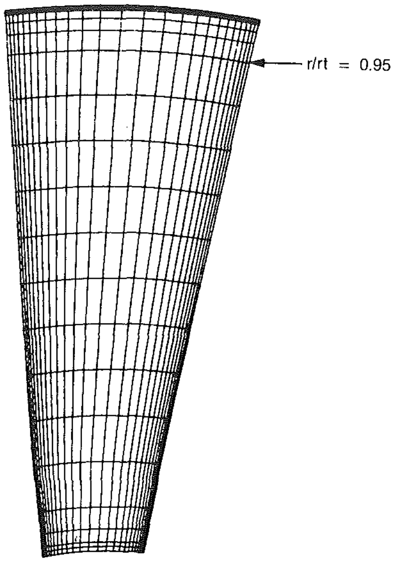

Fig. 1(*d*) Hub-to-tip grid at rotor inlet

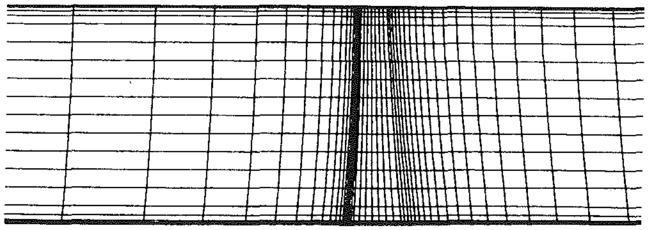

Fig. 1(e) Through flow grid at the middle of passage

Computational Grid

To represent the blade geometry and the tip clearance accurately, nonorthogonal body-fitted coordinates are generated. The grid used for the case with 1 percent chord clearance is shown in Fig. 1. The grid consists of 26 × 28 × 52 nodes in blade-to-blade, spanwise, and streamwise directions. Seven nodes are located between the blade tip and the casing. The nodes in the tip clearance are equally spaced and all the other nodes near solid walls are exponentially stretched. For 5 percent chord clearance, the grid nodes inside the clearance are also exponentially stretched. As the periodicity condition should be maintained for the flow inside tip clearance, the blade-to-blade grid in this region is also built to satisfy periodicity.

Numerical Scheme

The numerical procedure developed previously for the general three-dimensional flow inside blade rows [14] has been further modified for stable and accurate solution of the current problem. For the convenience of formulation, the governing equations are expressed in the following form

$$\frac{\partial}{\partial x}(\rho U\phi)+\frac{\partial}{\partial y}(\rho V\phi)+\frac{\partial}{\partial z}(\rho W\phi)=\frac{\partial}{\partial x}\left(\Gamma_\phi\frac{\partial\phi}{\partial x}\right)+\frac{\partial}{\partial y}\left(\Gamma_\phi\frac{\partial\phi}{\partial y}\right)+\frac{\partial}{\partial z}\left(\Gamma_\phi\frac{\partial\phi}{\partial z}\right)+S_\phi \qquad (8)$$

where ϕ is any of the dependent variables, Γ_ϕ is the diffusion coefficient, and S_ϕ represents all remaining terms. On the transformed curvilinear coordinates (ξ, η, ψ), the following similar form of the equation can be written.

$$\frac{1}{J}\frac{\partial}{\partial\xi}(\rho G_1\phi)+\frac{1}{J}\frac{\partial}{\partial\eta}(\rho G_2\phi)+\frac{1}{J}\frac{\partial}{\partial\psi}(\rho G_3\phi)$$

$$=\frac{1}{J}\frac{\partial}{\partial\xi}\left[\frac{\Gamma_\phi}{J}D_{\xi\xi}\phi_\xi+\frac{\Gamma_\phi}{J}D_{\xi\eta}\phi_\eta+\frac{\Gamma_\phi}{J}D_{\xi\psi}\phi\psi\right]$$

$$+\frac{1}{J}\frac{\partial}{\partial\eta}\left[\frac{\Gamma_\phi}{J}D_{\eta\xi}\phi_\xi+\frac{\Gamma_\phi}{J}D_{\eta\eta}\phi_\eta+\frac{\Gamma_\phi}{J}D_{\eta\psi}\phi\psi\right]$$

$$+\frac{1}{J}\frac{\partial}{\partial\psi}\left[\frac{\Gamma_\phi}{J}D_{\psi\xi}\phi_\xi+\frac{\Gamma_\phi}{J}D_{\psi\eta}\phi_\eta\right.$$

$$\left.+\frac{\Gamma_\phi}{J}D_{\psi\psi}\phi\psi\right]+S_\phi{}' \tag{9}$$

With the divergence theorem, equation (9) can be written as follows for arbitrarily shaped control volume.

$$\int_A \rho\phi^{n+1}G_in_idA=\int_A\frac{\Gamma_{\text{eff}}}{\sigma_{ij}}\phi_i^{n+1}n_jdA+\int_R S_\phi dR \tag{10}$$

Various terms in equation (9) are integrated numerically for arbitrarily shaped control volumes to get finite difference equations for the unknowns at the computational nodes. Second-order-accurate central differencing is used for the diffusion terms. For the discretization of the convection term, a hybrid scheme that combines the central differencing and the quadratic interpolation scheme [19] is used. When the central differencing of the convection term violates stability criteria (cell Peclet number exceeds two), a modified quadratic interpolation scheme [14] is used instead. To reduce any possible numerical diffusion because of the flow and grid skewness, the quadratic interpolation scheme is applied along the computed streamline instead of along the grid direction.

Various studies have indicated that a solution procedure based on the primitive variables of the flow converges rather slowly when applied to separated flows. Furthermore, when finite difference equations for the continuity and momentum are not satisfied closely during iteration, strong coupling between pressure and velocity generate nonphysical oscillations and delay overall convergence with the current numerical scheme. The concept of pressure-implicit split operator by Issa [20] is further extended for three-dimensional curvilinear coordinates. With the proposed concept, one more correction step is added at each iteration to get improved intermediate solutions for the pressure and velocity. The intermediate values of velocity are first obtained with the pressure field of previous iterations

$$A_p\rho^nU_i^*=\Sigma A_{pm}U_{im}^*-\Delta_iP^n+S_i \tag{11}$$

where * denotes intermediate value at this step, A_p and A_{pm} are the finite difference coefficients, and n represents the value at nth iteration. As the values obtained with this predictor step do not satisfy mass conservation, corrective components of pressure and velocity are obtained by combining finite difference equations for pressure and velocity.

$$(\rho^nU_i^{**}-\rho^nU_i^*)=A_p^{-1}\Delta_i(p^*-p^n) \tag{12}$$

In equation (12), the effect of convection [first term in the right hand of equation (11)] is neglected in order to facilitate the solution of this equation. An additional step is to include this convective effect in the intermediate solutions. With the values of *, **, and n

$$\rho^nU_i^{n+1}-\rho^*U^{**} \tag{13}$$

$$=A_p^{-1}\left[\sum A_p^m(U_{im}^{**}-U_{im}^*)\right.$$

$$\left.-\Delta_i(p^{n+1}-p^*)\right]$$

The effect of convection is represented with the values of previous steps and handled as a source term in solving equation (13).

With the generalized curvilinear coordinates, unknown values at 27 surrounding nodes (U_{im}) are used to update the unknown at the center of the control volume. Numerical experiments indicate that overall convergence rates diminish when off-diagonal terms are neglected. For the present problem, fully converged solutions are obtained with $650\approx750$ iterations and the overall computational efficiency is increased about four times when the above scheme is fully implemented. However, the current scheme requires about 30 percent more overall computer storage because of the increased number of nodes for the discretization.

Boundary Conditions

As pointed out by experimental studies [7, 8], endwall flow in a rotor is characterized by the effect of relative motion between the blade and casing. As the coordinates are fixed on the rotor, the casing is moving with constant speed. At the nodes nearest to the casing, the effect of moving boundary conditions is transmitted through the shear stress acting on the control volume surface, which is located on the casing.

Measured profiles for velocity and turbulence intensity are used as upstream boundary conditions. The turbulence energy dissipation rate at upstream is based on the characteristic length scale (1 percent of pitch at midspan). No-slip conditions are used on the blade surface and hub-wall. On the solid wall, the turbulence kinetic energy is specified to be zero and the normal gradient of energy dissipation is also specified to be zero. The periodicity conditions are strictly imposed for the flow upstream and downstream of the blade, and inside the tip clearance. All velocity components, pressure, density, and corrective values of all the variables are the same on the periodic boundary nodes.

Asymptotic conditions are used at the exit of computational domain, i.e., second-order streamwise derivatives of unknown variables are assumed to be zero. Residuals of finite difference equations are monitored along with the total mass flow rate at each computational plane. When these residuals, nondimensionalized with inlet flow quantities (inlet flow rate, momentum flux, and energy flux), are less than 10^{-3}, the solution is assumed to be converged. Using an IBM 3083, the necessary CPU time per grid point per iteration is 14×10^{-3} s.

Results and Analysis

The developed numerical procedure has been tested for tip clearance flows measured by Hunter and Cumpsty [7]. The experimental study includes detailed flow measurements inside casing wall boundary layer with several tip clearances and flow coefficients. Some important parameters of the isolated rotor are:

- Blade chord: 0.152 M
- Hub-to-tip ratio: 0.4
- Number of blades: 22
- Airfoil profile: C4 on circular arc camber line
- Overall span: 0.457 M
- Pitch/chord at tip: 1.428
- Max. thickness/chord at tip: 8.0%
- RPM: 525

The rotor is designed to give free-vortex flow at a flow coefficient of 0.7. Predictions are made for two clearances (1.0 and 5.1 percent chord).

Mean Velocity

To analyze the effect of tip clearance on the mean velocity field, the velocity vectors projected on the cylindrical plane are examined. In Figs. 2, 3, and 4, predicted blade-to-blade velocity distributions are compared. As shown in Fig. 2, the effect of tip clearance is almost negligibly small far away from

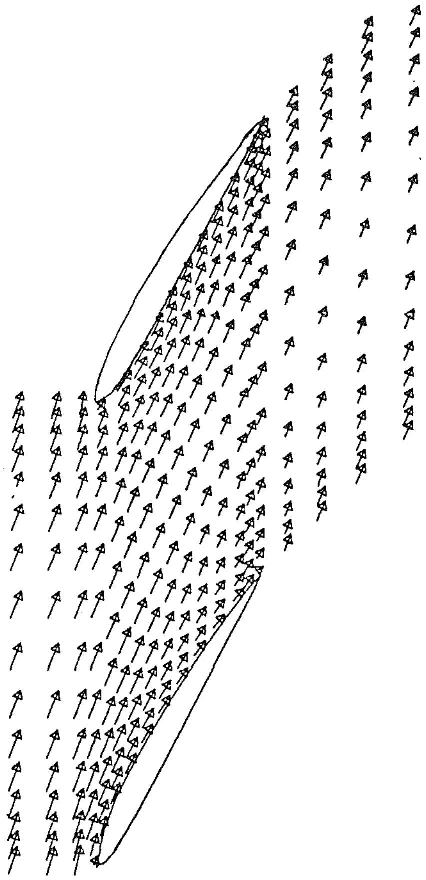

Fig. 2 Velocity vectors $W_{\theta x} = W_\theta + W_x$ at $r/r_t = 0.95$ (25 percent chord inside blade passage from tip)

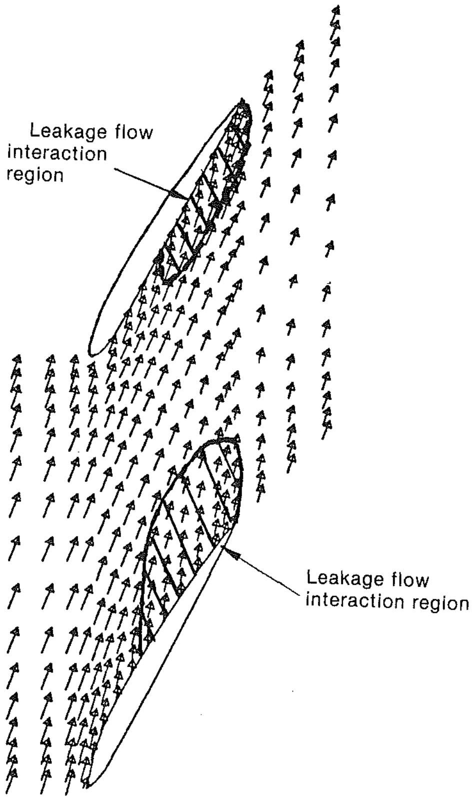

Fig. 3 Velocity vectors $W_{\theta x} = W_\theta + W_x$ at $r/r_t = 0.994$ (2 percent chord inside blade passage from tip)

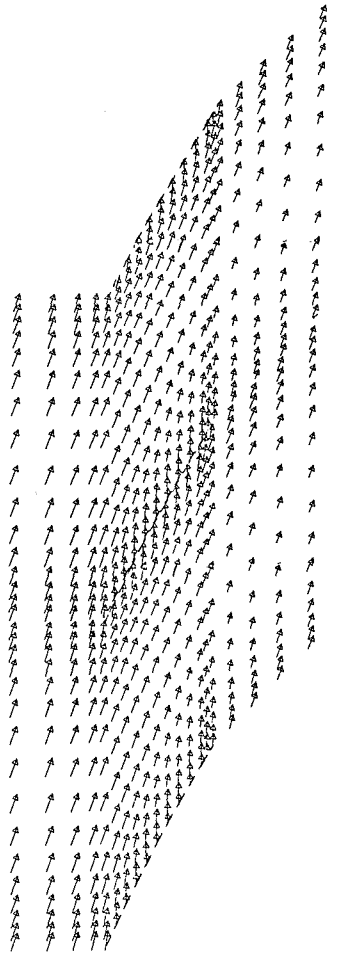

Fig. 4 Velocity vectors $W_{\theta x} = W_\theta + W_x$ at $r/r_t = 0.999$ (middle of tip clearance)

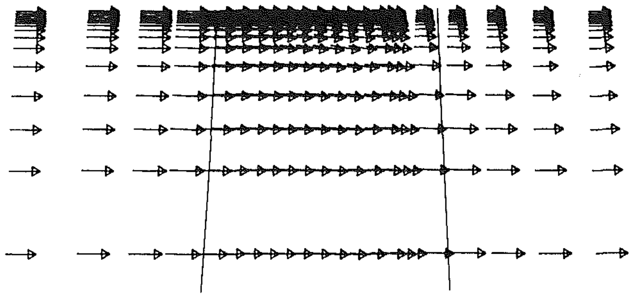

Fig. 5(*a*) Velocity vectors $W_{rx} = W_r + W_x$ at the middle of blade passage

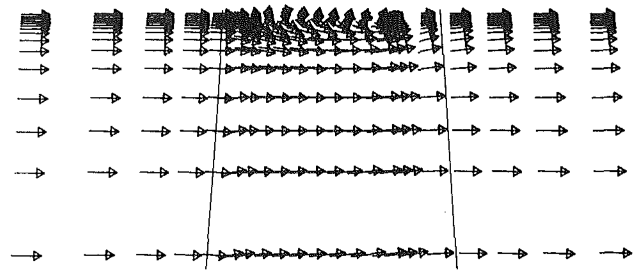

Fig. 5(*b*) Velocity vectors $W_{rx} = W_r + W_x$ near the blade suction surface (5 percent pitch)

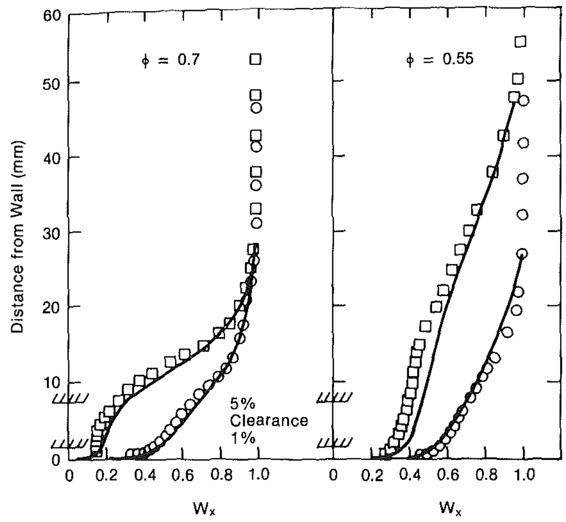

Fig. 6 Comparison of variation of axial velocity downstream of rotor (○: measurement with t/c = 1.0 percent, □: measurement with t/c = 5.1 percent, –: predictions, measurement by Hunter and Cumpsty [7]

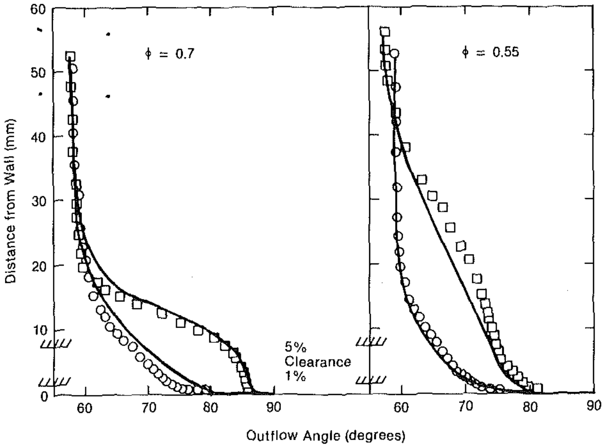

Fig. 7 Comparison of variation of rotor relative outflow angle (measurement by Hunter and Cumpsty [7])

the clearance ($r/r_{\rm tip}-0.95$) and the inviscid effect dominates the flow turning. Near the blade tip (Fig. 3, $r/r_{\rm tip}-0.994$), the effect of leakage jet is clearly shown and the flow is considerably affected by the leakage flow (beyond 50 percent chord from the leading edge). Near the casing wall, the leakage flow is further enhanced by the moving of the casing wall (in relative frame) and blade-to-blade flow is further dominated by the tip clearance flow (25 percent chord beyond leading edge, Fig. 4). The velocity vectors projected to the throughflow plane (axial and radial velocity component) at the middle of passage and near the blade surface are compared in Fig. 5. Near the blade tip and casing wall, where a large vortex motion is induced by the leakage flow and casing wall, a locally reversed flow in axial direction is observed. This local flow separation is moved toward the pressure side when the flow coefficient is reduced.

Time-Averaged Properties of Boundary Layers

Time-averaged axial velocity downstream of the rotor is compared in Fig. 6. As pointed out by Hunter and Cumpsty [7], the profile becomes less full as the gap size is enlarged and this is enhanced at the larger flow coefficient. These effects of tip clearance are well predicted although the numerical results show somewhat less pronounced effect. Comparison of rotor relative flow angles with tip clearance is shown in Fig. 7. Leakage flow, which is moving from the pressure side of the blade surface to the suction side, contributes to the underturning of the flow near the casing. This effect of underturning is further enhanced by the relative motion of the casing wall. The numerical results show that these effects are properly predicted with the current scheme. Here again, the numerical results have a tendency to underpredict these effects. This discrepancy might be due to inadequate physical modeling (turbulence closure) or insufficient grid points to describe complex three-dimensional flow field.

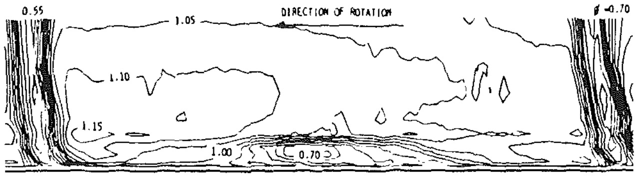

Measurement by Hunter and Cumpsty [7]

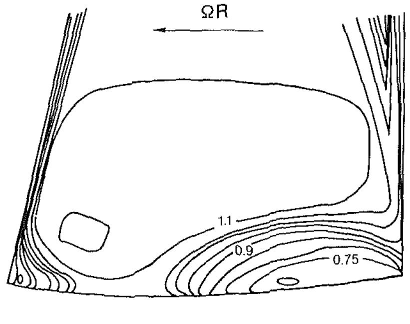

Prediction

Fig. 8 Comparison of rotor exit relative dynamic head at ϕ = 0.7

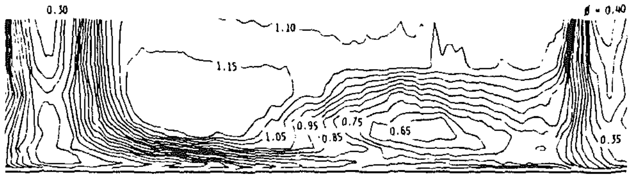

Measurement by Hunter and Cumpsty [7]

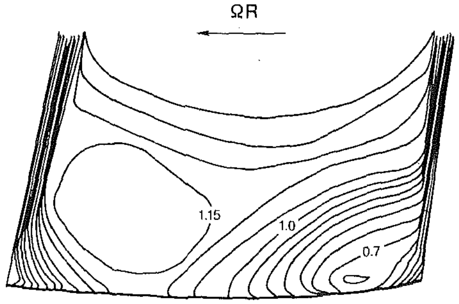

Prediction

Fig. 9 Comparison of rotor exit relative dynamic head at ϕ = 0.4

Three-Dimensional Flow Structure

In Figs. 8 and 9, contours of the rotor exit relative dynamic head are compared for two flow coefficients. As the experimental data indicate, the endwall flow is highly nonuniform and has strong gradients of properties across the entire blade passage. Again, the data indicate that the flow near the casing wall is dominated by the leakage jet and the wall velocity in the relative frame of reference. A core with low relative dynamic head is observed away from the wall and this region grows and moves toward the pressure side of the

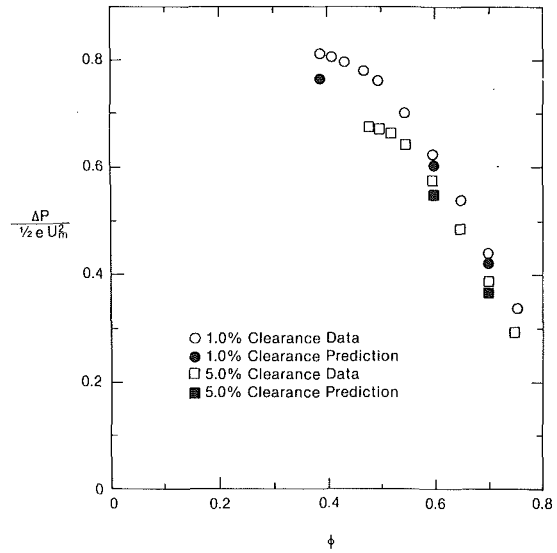

Fig. 10 Comparison of compressor overall performance characteristics

wake with lower flow rate. The numerical results made with current grid size (which is probably too coarse to capture detailed quantitative aspects of flow) and with relatively simple turbulence closure predict the major qualitative aspect of the flow field properly. The formation of low energy region, movement of this region toward pressure side with lower flow rate, and high energy near the immediate wall are all properly shown in the prediction.

Comparison of detailed three-dimensional flow structure indicates that the current numerical precedure, which is based on fully elliptic solution of the entire flow, predicts the overall physical nature reasonably well. For better agreements of quantitative aspects of this highly complicated flow, improved physical modeling and refined computational grids might be further investigated.

Overall Compressor Performance

Figure 10 shows the comparison of static pressure rise characteristics for the rotor with different tip clearance. As pointed out by Hunter and Cumpsty [7], the aerodynamic behavior of the machine is influenced substantially by tip clearance in the investigated unstalled region. For the computed flow coefficients and tip clearances, the numerical results are in good agreement with the measured data.

Concluding Remarks

A numerical procedure is developed for calculation of the tip clearance flow in an isolated compressor rotor. The governing equations are solved using a generalized curvilinear coordinate fixed on the rotor and the casing wall is handled as a moving wall.

The calculated results show the capabilities of the current numerical procedure. The calculated velocity vector inside the tip clearance is in good agreement with previous experimental results. The overall effects of tip-clearance on the outflow are well predicted (casing wall boundary layer development, relative outflow angle, and overall compressor performance). The highly complex three-dimensional nature of tip-clearance flow is also reasonably well predicted. For improved computational results of this complex three-dimensional viscous flow, which includes flow separation, strong interaction between viscous and inviscid flows, and the effects of streamline curvature and rotation on turbulent diffusion, better physical modeling and refined computational grid should be studied further.

References

1 Smith, Jr., L. H., "Casing Boundary Layer in Multistage Axial-Flow Compressors," *Flow Research on Blading*, edited by L. S. Dzung, Elsevier, 1970, pp. 275-304.

2 Rains, D. A., "Tip Clearance Flows in Axial Flow Compressors and Pumps," Report No. 5, Hydrodynamics and Mechanical Engineering Laboratories, California Institute of Technology.

3 Dean, R. C., "The Influence of Tip Clearance on Boundary Layer Flow in a Rectilinear Cascade," Report 27-3, Gas Turbine Laboratory, MIT.

4 Lakshminarayana, B., and Horlock, J. H., "Leakage and Secondary Flows in Compressor Cascades," ARC R and M 3483, 1965.

5 Lakshminarayana, B., "Methods of Predicting the Tip Clearance Effects in Axial Flow Turbomachinery," ASME *Journal of Basic Engineering*, Ser. D, Vol. 92, No. 3, Sept. 1970, pp. 467-482.

6 Booth, T. C., Dodge, P. R., and Hepworth, H. K., "Rotor-Tip Leakage: Part 1—Basic Methodology," ASME Journal of Engineering for Power, Vol. 104, Jan. 1982, pp. 154-161.

7 Hunter, I. H., and Cumpsty, N. A., "Casing Wall Boundary Layer Development Through an Isolated Compressor Rotor," ASME Journal of Engineering for Power, Vol. 104, No. 4.

8 Inoue, M., and Kuroumaru, M., "Three-Dimensional Structure and Decay of Vortices Behind an Axial Flow Rotating Blade Row," ASME Journal of Engineering for Gas Turbines and Power, Vol. 106, No. 3, July 1984, pp. 561-569.

9 Murthy, K. N. S., and Lakshminarayana, B., "Laser Doppler Velocimetry Measurements in the Tip Region of a Compressor Rotor," AIAA Paper No. 84-1602.

10 Hawthorne, W. R., "The Applicability of Secondary Flow Analysis to the Solution of Internal Flow Problems," *Fluid Mechanics of Internal Flow*, edited by G. Sowan, Elsevier, Amsterdam, 1967.

11 Horlock, J. H., and Lakshminarayana, B., "Secondary Flows; Theory Experiment and Application in Turbomachinery Aerodynamics," *Annual Review of Fluid Mech.*, Vol. 5, 1973, pp. 247-279.

12 Horlock, J. H., and Perkins, J. H., "Annulus Wall Boundary Layers in Turbomachines," AGARD Monograph No. 185, 1974.

13 Hirsch, C., "Endwall Boundary Layers in Axial Compressors," ASME Paper No. 76-GT-72, 1976.

14 Hah, C., "A Navier-Stokes Analysis of Three-Dimensional Turbulent Flows Inside Turbine Blade Rows at Design and Off-Design Conditions," ASME Journal of Engineering for Power, Vol. 106, 1984, pp. 421-429.

15 Wadia, A. R., and Booth, T. C., "Rotor-Tip Leakage Part II – Design Optimization Through Viscous Analysis and Experiment," ASME Journal of Engineering for Power, Vol. 104, Jan. 1982, pp. 162-169.

16 Hah, C., "Turbulence Closure and Prediction of the Wake in a Rotating Wall Shear Layer," *AIAA Journal*, Vol. 20, Nov. 1982, pp. 1599-1605.

17 Lam, C. K. G., Bremhorst, K. A., "Modified Form of the k-ϵ-Model for Predicting Wall Turbulence," *J. Fluids Eng.*, Vol. 103, p. 456, 1981.

18 Rodi, W., Celik, I., Demuren, A. O., Scheuerer, G., Shirani, I., Leschziner, M. A., and Rastogi, A. K., *Proc., 1980-81 AFOSR-HTTM-Stanford Conference on Complex Turbulent Flows*, edited by S. J. Kline, B. J. Cantwell, and G. M. Lilley, Vol. III, 1982, p. 1495.

19 Leonard, B. P., "A Stable and Accurate Convective Modeling Procedure Based on Quadratic Upstream Interpolation," *Comp. Meth. In Appl. Mech. and Engng.*, Vol. 19, 1979, pp. 59-98.

20 Issa, R. I., "Solution of Implicitly Discretized Fluid Flow Equations by Operator-Splitting." Int. Rep., Dept. Min. Resources Engng., Imperial College, London, 1982.

B. Lakshminarayana

N. Sitaram

J. Zhang

Department of Aerospace Engineering,
The Pennsylvania State University,
University Park, PA 16802

End-Wall and Profile Losses in a Low-Speed Axial Flow Compressor Rotor

The blade-to-blade variation of relative stagnation pressure losses in the tip region inside the rotor of a single-stage, axial-flow compressor is presented and interpreted in this paper. The losses are measured at two flow coefficients (one at the design point and the other at the near peak pressure rise point) to discern the effect of blade loading on the end-wall losses. The tip clearance losses are found to increase with an increase in the pressure rise coefficient. The losses away from the tip region and near the hub regions are measured downstream. The losses are integrated and interpreted in this paper.

Introduction

The flow in the tip and hub regions of a rotor of an axial flow compressor is very complex, due to the interaction of various viscous phenomena such as three-dimensional end-wall and blade boundary layers, and tip clearance flows in the case of tip region flow. The losses arising from these phenomena are a major source of rotor inefficiency, reduced stall margin, and increased noise. The losses in an axial flow compressor rotor can be classified as follows:

1 Hub end-wall boundary-layer loss, including secondary flow.

2 Profile loss due to blade boundary layers, possibly including shock boundary-layer interaction.

3 Tip-region losses, including the secondary flow, tip clearance losses, and the annulus wall boundary-layer losses.

There has been considerable interest in recent years to investigate loss mechanisms in order to improve performance (e.g., energy-efficient engine) and to enable methods of incorporating the loss distribution (hub to tip) in compressor design codes. These losses not only influence the efficiency but also the velocity and pressure field characteristics within the blade row and at the exit. Hence, a knowledge of losses is also essential for the design of downstream blade rows.

There have been several survey papers [1, 2, 3] and reports of investigations of loss mechanisms [4-8] in axial flow compressors. Most of the loss (profile and end-wall loss) correlations available in the open literature are based on cascade data and may not be adequate to represent rotor losses. Even though the trends are predicted correctly, the magnitudes and the radial distributions are not. The correlations, especially those for end-wall losses, have been inadequate. Koch and Smith [6], in evaluating end-wall loss correlations, have pointed out that "the present model is based on assumptions and data that are of limited scope and, therefore, of questionable generality." This is true of most end-wall loss correlations derived from cascade experiments. One exception is the tip-clearance loss model proposed in [9], which was based on rotor data.

There are some data available for losses in axial flow compressors, but most of them were taken downstream of the rotor using a stationary probe. It has also been pointed out by many investigators that the losses are dependent on measuring stations and the magnitude depends on the mixing losses downstream. It is essential to distinguish between the losses inside the blade row and the losses due to the mixing of shear layers downstream. Such data enable generalized correlations to be developed for a rotor-blade row independent of the rotor-stator spacing. Rotor-stator spacing controls the mixing losses downstream of the blade row. In many situations where the wake or the leakage vortex have not decayed to an axisymmetric flow field, the results from a stationary probe may be subject to error due to the unsteady nature of the flow field. Thus, it becomes essential to carry out measurements in the rotating system. One example of such data at the exit of the blade row is Dring et al. [8]. Similar data do not exist for flow inside the rotor-blade row to evaluate the evolution of losses in the blade row.

Lakshminarayana et al. [10] measured the velocity and turbulence fields in the tip region inside the blade passage of a low-speed axial flow compressor at the design flow coefficient using a rotating three-sensor hot-wire probe. In order to understand the loss mechanisms involved, stagnation pressure measurements were taken in this region as well as in the blade wake region and the hub-wall region. Using this information, stagnation pressure losses were derived and correlated. Furthermore, the effect of tip-clearance flow on the peak pressure rise coefficient was also investigated. The experiments were repeated at two flow coefficients: one at the design flow coefficient and the other at the near peak pressure rise coefficient. The information derived in the tip region, hub region, and between the two end-walls was correlated and interpreted.

Contributed by the Gas Turbine Division of The American Society of Mechanical Engineers and presented at the 30th International Gas Turbine Conference and Exhibit, Houston, Texas, March 18-21, 1985. Manuscript received at ASME Headquarters, January 10, 1985. Paper No. 85-GT-174.

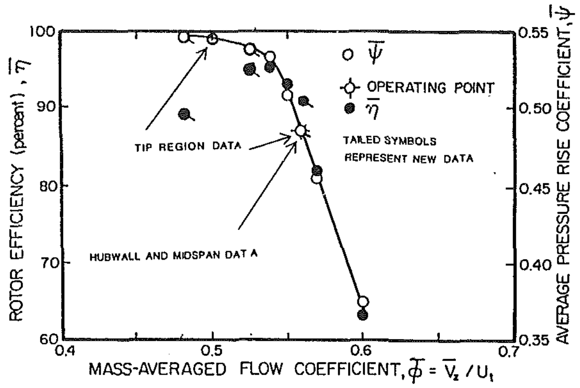

Fig. 1 Overall performance of the compressor rotor

Experimental Facility, Technique, and Program

The measurements reported in this paper were performed in the rotor of the axial flow compressor facility described in [11]. The compressor stage (designed by Smith [12]) is composed of an inlet guide vane (IGV) blade row, a rotor row, and a stator row. The IGV blade row consists of 43 blades, and the rotor of 21 blades. The distance between the IGV trailing edge and the rotor leading edge is 24.1 cm (or three chord lengths of the IGV blades) at midspan. The unsteadiness upstream of the rotor due to IGV wake was found to be very small. The hub/casing diameter ratio of the facility is constant at 0.5, with the diameter of the outer annulus wall equal to 0.932 m. The tip clearance varied from 0.2 cm to 0.25 cm from blade to blade. The performance curve for this compressor is shown in Fig. 1. The data are based on measurements taken far downstream of the rotor. It should be remarked here that the performance measurements were repeated subsequent to its first reporting in [11]. The only change in the data observed was in the region of peak pressure rise. The peak pressure rise was measured at $\bar{\phi} = 0.48$, and this data point is shown in Fig. 1. The tip region flow data was acquired at $\bar{\phi} = 0.50$ ($\bar{\psi} = 0.54$) and $\bar{\phi} = 0.56$ ($\bar{\psi} = 0.486$). The latter is the design condition at which all the earlier flow measurements were taken [10, 13–15]. The profile losses and hub end-wall loss were measured at the exit of the rotor at the design condition ($\bar{\psi} = 0.486$, $\bar{\phi} = 0.56$) only.

The facility is equipped with a rotating-probe mechanism that permits a circumferential traverse to be done while the rotor is rotating in motion. The main feature of the rotating-probe traverse gear mechanism is a SLO-SYN motor of 0.007 Nm torque driving shaft through a planetary reduction gear train. The circumferential stepping is 0.0166 deg/step; this represents 1032 steps per blade passage. Because of this fine step, the positioning of the probe can be done accurately with a maximum uncertainty of ±0.05 mm at the midspan location. The probe holder, stepping motor, and probe are mounted inside the rotating hub of the machine. The motor is powered and controlled by a stationary traverse indexing device.

All measurements were taken at a constant speed of 1050 rpm. The flow coefficient was varied using an aerodynamically design throttle. A United Sensor Kiel probe (Type KAA) was used to measure the relative stagnation pressure inside the rotor blade passage in the tip-wall region. Because of its small head size (1.65 mm), it introduced only small shear gradient and blockage errors. All the data were acquired in the rotating frame. The relative flow inside the rotor is found to be steady, since the IGV is located far upstream of the rotor. Further details of the experimental procedure and sources of errors in measurements can be found in [16]. The estimated experimental accuracies are as follows: axial position of the probe, 1.6 mm; radial and initial tangential positions of the probe, 0.8 mm; relative tangential position, 0.05 mm; rotor speed, ±rpm; stagnation pressure losses ±1% of dynamic head based on tip speed.

The Kiel probe was used to measure the relative stagnation pressure in the rotor-blade tip end-wall region at two flow coefficients ($\bar{\phi} = 0.56$, design flow coefficient and $\bar{\phi} = 0.50$, peak pressure rise flow coefficient), at 20–30 tangential locations at the following axial and radial stations: $Z = -0.20$, 0.25, 0.50, 0.75, 0.98, 1.3, and 1.9; $R = 0.9184$, 0.9456, 0.9592, 0.9728, 0.9796, and 0.9864. At $\bar{\phi} = 0.50$, measurements were also taken at $R = 0.8912$ at all axial locations except at $Z = 0.25$.

Nomenclature

C = blade chord
P_R = relative stagnation pressure
PS = pressure surface
p = static pressure
R = nondimensional radius, r/r_t
r = radius
S = blade spacing
SS = suction surface
T_z = turbulence intensity in the axial direction
T_θ = turbulence intensity in the tangential direction
U = blade speed
V_z, V_θ = axial and tangential velocity, absolute flow
W = relative velocity normalized by blade tip speed
W_S = velocity along the direction S. S is the coordinate along the stream wise direction at the midpassage
W_{S_0} = maximum value of W_S at a given R and Z
$\underline{W}_{\text{Sec}}$ = secondary velocity vector (resultant of spanwise and transverse velocity)
YS = tangential distance measured from blade surface (YS = 0 on pressure side and YS = 1 on suction side)
Z = axial distance from rotor leading edge normalized by rotor axial chord
θ_p = tangential station closest to pressure surface
θ_s = tangential station closest to suction surface
θ_{11} = momentum thickness based on streamwise velocity
ρ = air density
$\bar{\phi}$ = mass-averaged flow coefficient (normalized by blade-tip speed)
$\bar{\psi}$ = mass-averaged pressure rise coefficient (normalized by $\rho U_t^2/2$)
ψ_{loss} = relative stagnation pressure loss coefficient $(P_{R1} - P_{Rl})/(1/2)\rho U_t^2$
ψ_R = relative stagnation pressure coefficient $(P_{R1} - P_a)/(1/2)\rho U_t^2$
$\bar{\eta}$ = mass-averaged efficiency based on measured and Euler pressure rise

Subscripts and Superscripts

a = atmosphere
1 = rotor inlet
l = local
r, θ, z = radial, tangential, and axial component
t = blade tip
max = maximum value at any given axial location
$\bar{\ }$ = blade-to-blade mass averaged values
$\bar{\bar{\ }}$ = mass-averaged values for the passage at a given axial location (equation (1))

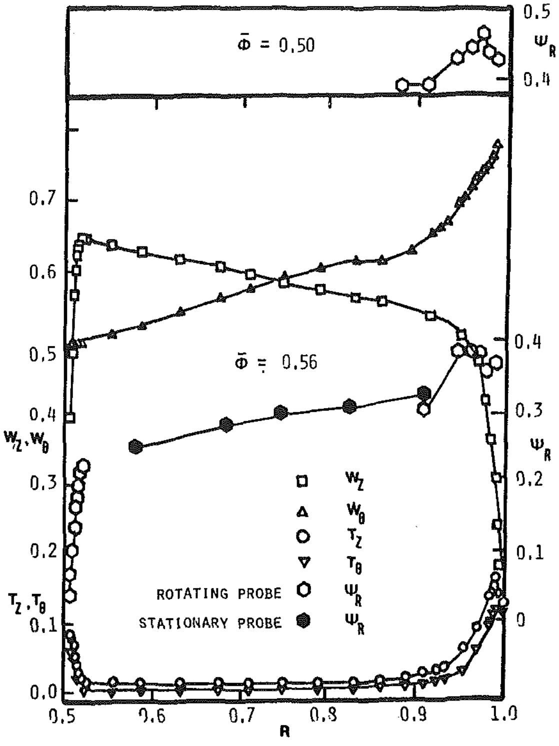

Fig. 2 Inlet distribution of W_θ, W_z, ψ_R, T_z, T_θ

A rotating five-hole probe was employed for the measurement of the exit flow in the hub-wall region and away from the tip wall region. The probe was of miniature type with a probe diameter of 1.65 mm. The probe was rotated with the rotor using the rotating probe traverse mechanism described earlier. The data were processed using the technique developed by Treaster and Yocum [17]. The hub-wall measurements were carried out at about 30 tangential locations across the passage at $R=0.507$, 0.513, 0.52, 0.527, 0.521, 0.554 at $Z=1.17$. These distances from the hub wall were 3.2 mm, 6.4 mm, 9.5 mm, 12.7 mm, 19.1 mm, 25.4 mm, respectively.

The passage flow away from the hub and tip was measured at $R=0.587$, 0.67, 0.75, 0.832, 0.918 at about forty tangential locations and the value of Z varied from 1.049 at $R=0.587$ to 1.085 at $R=0.918$. The details of the last set of measurements (especially the velocity field) can be found in [13].

It should be emphasized here that considerable amount of flow data inside the passage available is for this rotor. The mean velocity data in the tip wall region are reported in [10], the passage flow data in the inviscid region are given in [13], the blade boundary-layer data in [14], and all the velocity data are integrated in [15]. However, none of these references contain the information on stagnation pressures and losses reported in this paper.

Experimental Results and Interpretation

The axial and the tangential velocities as well as turbulence intensities (T_z, T_θ) were measured upstream of the rotor at $Z=-0.35$ using a two-sensor hot-wire probe traversed circumferentially to derive the blade-to-blade averages (Fig. 2). The tangential variation of velocities was found to be small.

The stagnation pressures near the tip and hub regions (shown marked in Fig. 2) were measured using a rotating Kiel probe at $Z=-0.2$. The stagnation pressures away from the hub and the tip regions ($R=0.587$–0.918) were measured using a five-hole probe at $Z=-0.35$. The values of ψ_R were derived from the five-hole probe data, since the velocity field is known. The radial velocities are found to be small in this region and the circumferential variation of flow properties was found to be negligible. All these data are shown plotted in Fig. 2. There is a small discrepancy between the rotating and the stationary probe data for ψ_R at $R=0.918$. The value of ψ_R derived from a stationary hole probe is found to be very sensitive to error in the measured yaw angle and the velocity. The ψ_R from the rotating Kiel probe is more accurate as it is a measured quantity (as opposed to a derived quantity) and the Kiel probe is insensitive to angle, reading the total pressure of the relative flow over a cone angle of 45 deg. A jump in ψ_R from $R=0.918$ to 0.9456 is caused by an increase in the relative tangential velocity.

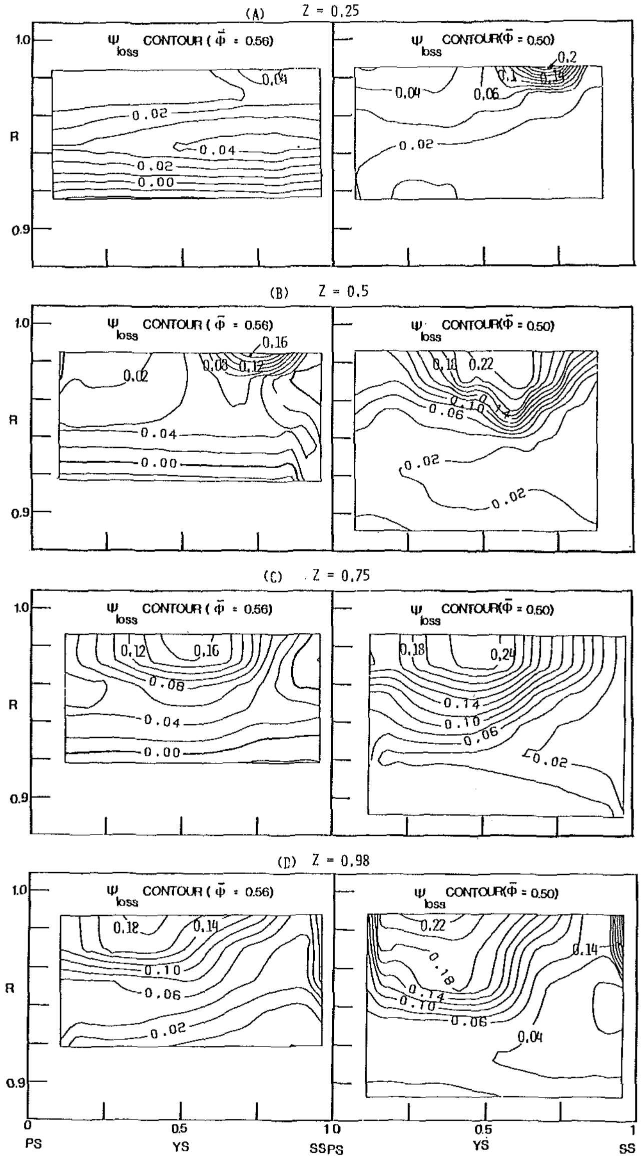

Fig. 3 Contours of ψ_{loss} at Z = 0.25, 0.50, 0.75, and 0.98; $\bar{\phi}=0.5$ and $\bar{\phi}=0.56$

The hub and the annulus wall boundary layers are found to be thin at the inlet, and the turbulence intensities in the annulus-wall boundary layer are generally higher.

Both the flow field and the pressure data inside the rotor passages are available at $\phi=0.56$ in the end-wall region, but only the stagnation pressure data inside the rotor are available in the end-wall region for $\bar{\phi}=0.5$.

Tip Region Flow Losses Inside the Passage. The relative stagnation pressure loss coefficients inside the rotor-blade

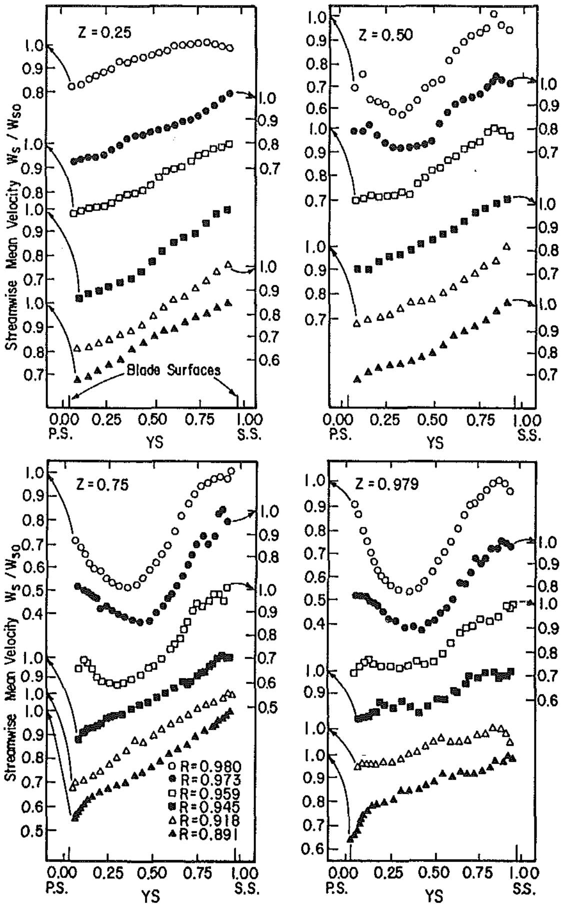

Fig. 4 Blade-to-blade distribution of streamwise velocity (W_S) at $Z = 0.25, 0.5, 0.75$, and 0.98; $\bar{\phi} = 0.56$

end-wall region are presented in contour form in Figs. 3(*a*–*d*) for flow coefficients, $\bar{\phi} = 0.56$ and $\bar{\phi} = 0.50$ and at $Z = 0.25$, 0.5, 0.75, and 0.98 respectively. Because of the mechanical limitations, the probe could not reach the blade surfaces and hence the blade profile losses are not measured in the end-wall region inside the passage. The loss coefficient is defined as follows:

$$\psi_{\text{loss}} = \frac{(P_{R1} - P_{Rl})}{\frac{1}{2}\rho U_t^2}$$

where P_{R1} is the relative stagnation pressure (see Fig. 2) at a particular radius, at $Z = -0.2$, where it is uniform across the blade passage, and P_{R2} is the relative stagnation pressure at the same radius, at the measuring station.

It should be recognized that the definition of the loss coefficient introduced here assumes that the stream surfaces are cylindrical. There is a radial transport of mass in this region and a logical definition would be to define losses along a streamline. This is almost an impossible task, and, hence, the losses are computed on a cylindrical surface. To this extent the losses should be viewed as qualitative, but the integrated end-wall losses (discussed later) eliminate this error since the radial velocities away from the tip region are small, except very near the blade surfaces.

In order to understand the loss mechanisms in the tip region, it is essential to examine the velocity field in this region. The three-sensor hot-wire data on the velocity field, discussed in [10], are reproduced in Fig. 4. In this figure, W_S is the relative velocity component along the S direction, where S is the projection of the resultant streamwise direction at midpassage onto a cylindrical surface. The secondary velocities derived from the hot-wire data are shown in vectorial form in Fig. 5. The secondary velocity vector is the

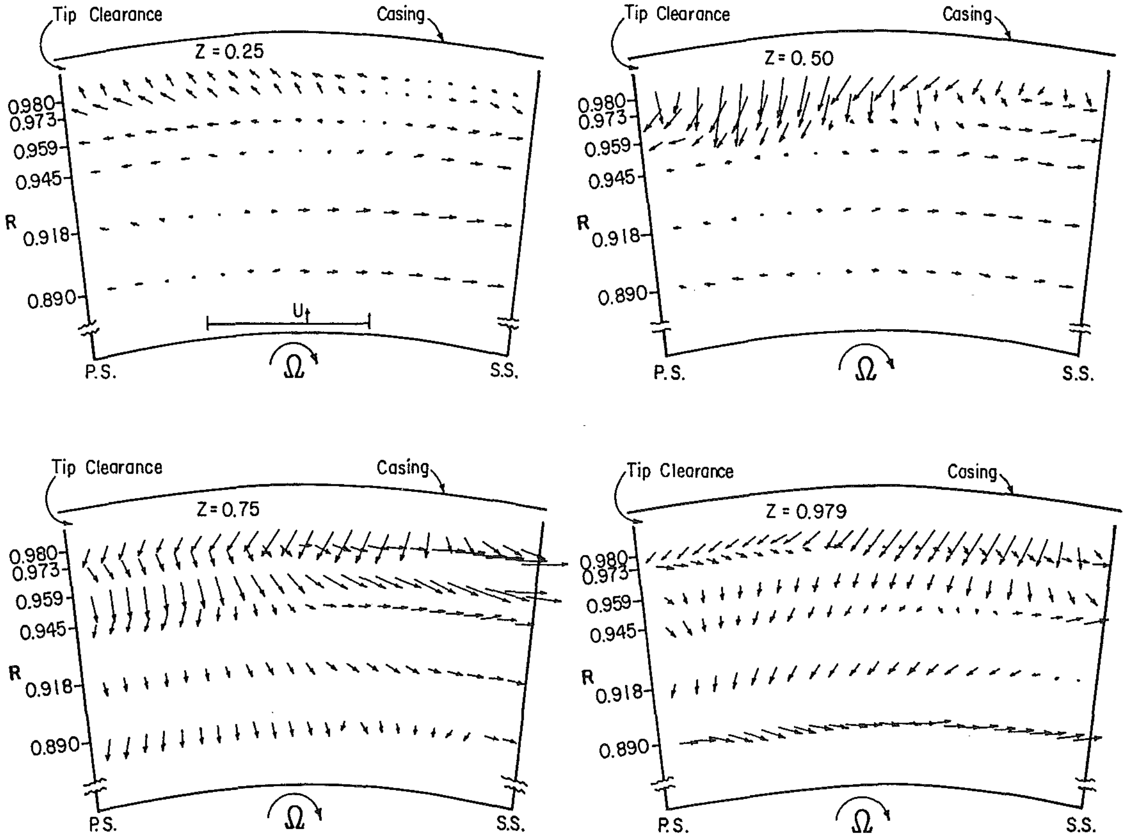

Fig. 5 Secondary velocity vectors ($\underline{W}_{\text{Sec}}$) at $\bar{\phi} = 0.56$

resultant of W_r, the radial velocity and W_n, the velocity component normal to the streamwise direction in the free stream, away from the annulus wall boundary-layer region. According to this definition $W_n = 0$ at $R = 0.891$ and YS = 0.5. In this figure, $\underline{W}_{\text{Sec}} = \sqrt{W_r^2 + W_n{}^2}$; this component represents the deviation of the flow field from its inviscid or design values.

The interpretation of the loss data will now be based on ψ_R distribution shown in Fig. 3, W_S distribution shown in Fig. 4, and $\underline{W}_{\text{Sec}}$ distribution shown in Fig. 5.

At $Z = 0.25$ and $\bar{\phi} = 0.56$ (Fig. 3), the losses are small and fairly uniform across the blade passage. At $\bar{\phi} = 0.50$, the losses are again small and fairly uniform across the passage up to $R = 0.970$. A concentrated region of high losses is seen above this radius. The center of this region is located at about a distance of 30% of blade spacing from the suction surface. This is attributed to the tip leakage flows. The tip leakage flow originated earlier along the chord at the peak pressure rise operating condition ($\bar{\phi} = 0.50$). This is due to a higher blade loading at $\bar{\phi} = 0.50$. Furthermore, the blade pressure distribution derived from an inviscid code indicated that the suction peak at $\bar{\phi} = 0.50$ occurred much closer to the blade leading edge, compared to that at $\bar{\phi} = 0.56$. Also the magnitude of suction peak at $\bar{\phi} = 0.50$ was found to be much larger than that for $\bar{\phi} = 0.56$. Hence, the pressure difference across the blade is large near the leading edge at $\bar{\phi} = 0.50$, resulting in higher tip-leakage flows at this location.

The distribution of $\underline{W}_{\text{Sec}}$ at $\bar{\phi} = 0.56$, shown in Fig. 5, indicates the presence of leakage flow at this location, even though its effect on W_S distribution is not dominant. The distribution of W_S (Fig. 4) from the pressure to the suction surface is almost linear and the gradient in W_S ($\partial W_S / \partial \theta$) is very small at $R = 0.980$, indicating the unloading of the blade in this region. This seems to suggest that even though the leakage flow exists in this region, its interaction with the main flow is not strong at this axial location. The influence of leakage flow is negligibly small for $R < 0.973$ (Figs. 4 and 5).

At $Z = 0.5$ (Fig. 3), the region of high loss increases both in the tangential and the radial directions at both the flow coefficients. While the tip-leakage flow and losses at $\bar{\phi} = 0.56$ are moderate, the losses at higher blade loading have increased substantially from $Z = 0.25$ to 0.5. The peak loss coefficient has increased about 30%, and the loss region now extends across most of the passage beyond $R = 0.94$ for $\bar{\phi} = 0.5$. The loss contours at the design condition ($\bar{\phi} = 0.56$) indicate that the leakage flow effects are confined to a smaller region (than at $\bar{\phi} = 0.50$) near the suction surface. It is the mixing of the leakage flow (with the mainstream) that originated earlier along the chord that is causing higher losses at $\bar{\phi} = 0.50$. The contours of ψ_{loss} for $\bar{\phi} = 0.50$ indicate that the leakage velocity in this case is larger and this enables the leakage flow to penetrate deeper into the passage.

The velocity data at $Z = 0.5$, for $\bar{\phi} = 0.56$, reveals the presence of a vortex type of distribution near the suction surface, marked by the flow toward the suction surface in regions away from the blade tip. The leakage flow observed at $Z = 0.25$, for $\phi = 0.56$, shows a tendency to move away from the suction surface and roll back to form a vortex at $Z = 0.5$. The presence of this roll up causes low pressures and velocities which is well known. This is clear from the ψ_{loss}, $\underline{W}_{\text{Sec}}$ data at $Z = 0.5$ near $YS = 0.75$. The relative stagnation pressures are low in this region which suggests the presence of a leakage vortex. The presence of considerable radial inward flow near the pressure surface ($Z = 0.5$, Fig. 5) may have been caused by the presence of a scraping vortex which induces a radial inward velocity near the pressure surface.

As the flow proceeds downstream to $Z = 0.75$ (Fig. 3), the high-loss region increases in both the radial and tangential extent for $\bar{\phi} = 0.56$. The losses are nearly uniform at lower radii, caused mainly by the presence of the annulus-wall boundary-layer growth. Even though the peak loss coefficient is nearly the same at $Z = 0.5$ and 0.75 for $\bar{\phi} = 0.56$, a substantial increase in losses at other radial and tangential locations indicates that the dominant influence of leakage flow occurs between these two axial locations. Increased leakage flow is evident. This seems to indicate that unloading of the blade due to leakage flow occurs farther down the leading edge for the design case, while most of the unloading for the off-design case ($\bar{\phi} = 0.50$) occurs before midchord. The extent of total loss regions for both flow coefficients is about the same, even though the magnitudes are much higher for the off-design case ($\bar{\phi} = 0.50$). The peak losses occur near midpassage for both flow coefficients. The development of leakage flow and losses between $Z = 0.5$ and $Z = 0.75$ is controlled mainly by diffusion and the transport, covering the entire passage (blade to blade) at $Z = 0.75$.

The velocity data at $Z = 0.75$ (Figs. 4 and 5) clearly reveal the increasing strength and extent of the vortex. The large defect in W_S near midpassage at $Z = 0.75$ from $R = 0.959$ to $R = 0.980$ is consistent with the size of the vortex observed in Fig. 4 and the extent of loss regions indicated in Fig. 3. The peak loss coefficient and the maximum defect in W_S occur at nearly the same passage location (near midpassage from $T = 0.959$ to 0.98). It is clear from Fig. 5 that the vortex strength, revealed by the magnitude of the transverse and radial velocities, is maximum near midpassage. The presence of the radial inward flow from the pressure surface to midpassage (Fig. 5) may be attributed to the influence of the leakage vortex (induced flow field) and the scraping vortex. The leakage flow through the tip clearance gap seems to have been reduced, as evidenced from the absence of flow towards the pressure surface near the blade tip. The blade loading is probably very small near the tip at this axial location. Even though the leakage flow is small at this axial location, the leakage vortex is stronger due to the past history of the flow and the entrainment process of the vortex.

As the flow proceeds from $Z = 0.75$ to 0.98 (very near the trailing edge), the losses spread out to a wider region, brought out mainly from the interaction and penetration of the leakage flow toward the inner radius (Fig. 3). The extent of region affected by the leakage flow is generally higher for $\bar{\phi} = 0.50$ and the losses are also higher. The relative velocities (W_S) generally decrease inside the passage from $R = 0.94$ to $R = 0.98$, resulting in large shear gradients in this region. The velocity data at this location show (Fig. 4) no major changes even though the leakage flow influence has spread inward to $R = 0.918$ (approximately 16% of the blade span from the tip). The loss distribution indicates that the leakage flow influences about 16-18% of the span from the blade tip. The secondary velocity distribution at this axial location, shown in Fig. 5, seems to indicate the diffusion of the vortex. The vortex spreads out to a larger spanwide and passage extent.

Tip Region Flow Losses at the Exit. The loss contours downstream of the trailing edge ($Z = 1.3$) are shown in Fig. 6. The loss distribution in the rotor wake as well as the passage regions can be clearly distinguished in this figure. The losses are generally higher than those observed at $Z = 0.98$ for $\bar{\phi} = 0.50$. This is an indication of the extent of diffusion and transport of the leakage flow. A similar trend, but to a lesser degree, is observed at $\bar{\phi} = 0.56$. The extent of the region affected by the leakage flow is higher for $\bar{\phi} = 0.50$. Approximately 16-20% of the blade span from the tip is affected by the leakage flow and the annulus-wall boundary-layer growth.

The loss contours far downstream of the blade trailing edge ($Z = 1.9$) are shown in Fig. 7 for $\bar{\phi} = 0.56$. The wake and the leakage vortex regions are clearly revealed here. The leakage flow tends to distort the wake in the region $R > 0.9$ and the

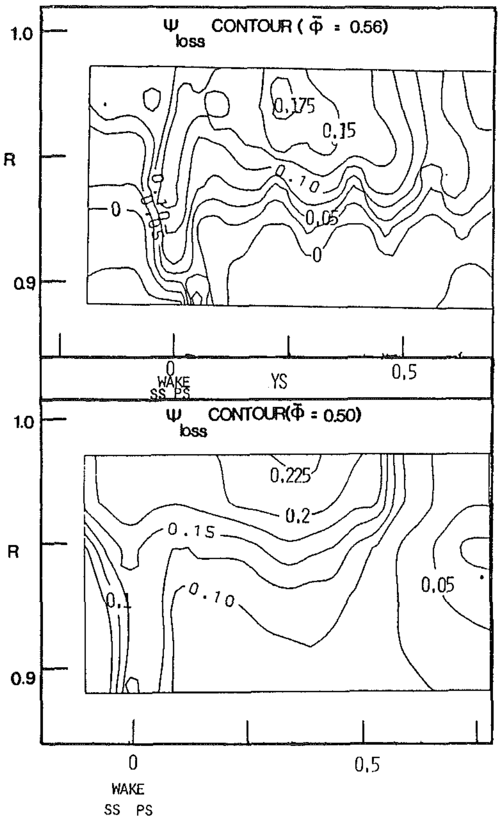

Fig. 6 Contours of $\bar{\psi}_{\text{loss}}$ at $Z = 1.3$, $\bar{\phi} = 0.56$, and $\bar{\phi} = 0.50$

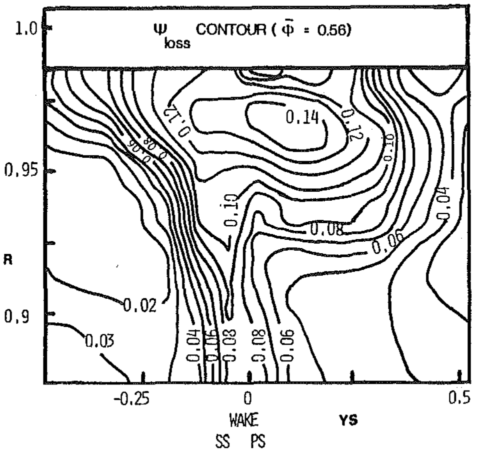

Fig. 7 Contours of $\bar{\psi}_{\text{loss}}$ at $Z = 1.9$ and $\bar{\phi} = 0.56$

leakage vortex is located closer to the pressure side. Even though the maximum loss coefficient has decreased from 0.175 to 0.14, between $Z = 1.3$ and 1.9, the loss in other regions, away from the core, has increased substantially. The leakage flow influence, as evidenced by the losses, has spread up to 20% of the blade span from the tip at this axial location.

Maximum and Mass-Averaged Loss Coefficient in the Tip Region. The maximum loss coefficient measured at each axial station, for both the flow coefficients, is presented in Fig. 8. The maximum loss at $\bar{\phi} = 0.50$ is much larger than that at $\bar{\phi} = 0.56$, up to $Z = 0.75$. Near and beyond the blade trailing edge, the maximum loss is about the same for both the flow coefficients. This clearly reveals the presence of stronger leakage flow and vortex at the peak pressure rise coefficient inside the passage.

The mass-averaged loss coefficient ($\bar{\bar{\psi}}_{\text{loss}}$) for the entire end-wall region at $\bar{\phi} = 0.56$ is shown in Fig. 9. The mass-averaged loss coefficient is defined as

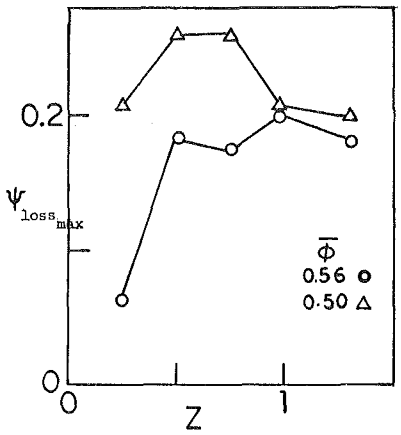

Fig. 8 Axial variation of maximum loss coefficient ($\bar{\phi} = 0.56$ and $\bar{\phi} = 0.50$)

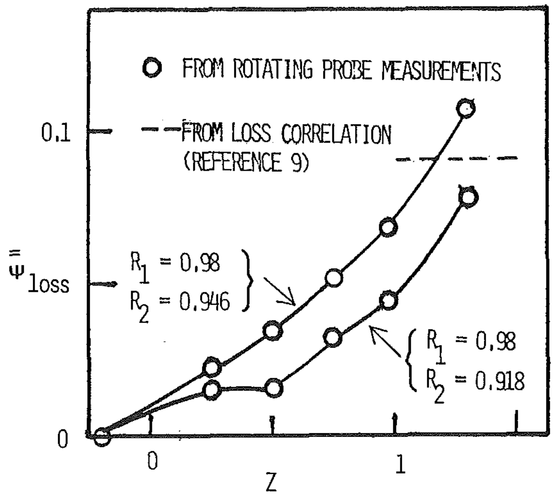

Fig. 9 Axial variation of $\bar{\bar{\psi}}_{\text{loss}}$ in the tip region at $\bar{\phi} = 0.56$ (values of $\bar{\bar{\psi}}_{\text{loss}}$ up to $Z = 0.98$ do not include blade profile losses)

$$\bar{\bar{\psi}}_{\text{loss}} = \int_{R_2}^{R_1}\left[\int_{\theta_s}^{\theta_p} \bar{\psi}_{\text{loss}} V_z R d\theta\right] dR \Big/ \int_{R_2}^{R_1}\left[\int_{\theta_s}^{\theta_p} V_z R d\theta\right] dR \qquad (1)$$

where R_1 is the highest radius where loss measurements were taken and θ_s and θ_p are tangential measurement positions closest to the suction and pressure surfaces, respectively. The lower limit R_2 was varied to determine the extent of end-wall losses. Its significance is explained below.

The emphasis of the paper is to understand the mechanisms causing losses, rather than to generalize the results. The integrated losses are sensitive to the extent of the region included in the integration in equation (1). It should be noted that the losses in the clearance region ($R = 0.98$ to 1.0), as well as the profile losses in the passage, were not measured.

Initially, the integration was carried out to about 16.4% of the blade span from the tip ($R_1 = 0.98$, $R_2 = 0.918$, the lowest radii for which loss data are available). This integration would thus include some inviscid regions, and, hence, the averaged losses would be lower. The results shown in Fig. 9 indicate that the losses for $\bar{\phi} = 0.56$ increase from $Z = -0.2$ (upstream of the rotor) to $Z = 0.25$. This may be caused by the leading edge and the blade-scraping effects. The losses are nearly constant from $Z = 0.25$ to 0.5, and increase beyond this axial location.

To evaluate the losses due to tip-clearance effects and the

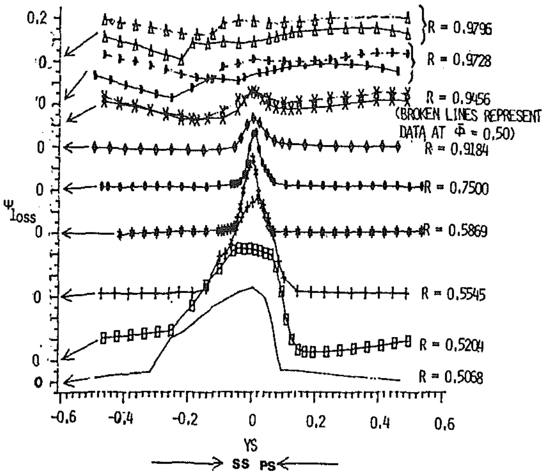

Fig. 10 Blade-to-blade variation of ψ_{loss} at various radii for $\bar{\phi} = 0.56$ at the exit

annulus-wall boundary layer, the integration was carried out from $R = 0.94$ to 0.98 as dominant effects of the leakage flow are confined to this region within the blade passage. The mass-averaged losses at various axial locations are shown in Fig. 9. The values of $\bar{\bar{\psi}}_{loss}$ from $Z = 0$ to $Z = 0.98$ do not include the blade-profile losses, while the data at $Z = 1.3$ do include all the losses in this region. Due to mechanical limitations, no measurement was carried out inside the blade boundary-layer region inside the passage, but the exit flow measurements include all the regions including the rotor wake. Hence, an appreciable increase in losses between $Z = 0.98$ and 1.3 is due to the profile loss. It should be mentioned here that these integrated losses do not include the losses inside the gap from $R = 0.98$ to 1.0 and thus the total losses should be somewhat higher.

On the basis of the contour plots provided earlier, it can be inferred that the main contribution to the total losses is from the leakage flow. The integrated losses increase almost linearly from the leading edge to the trailing edge.

Also shown in Fig. 9 is the loss coefficient calculated from the correlation presented [9]. This correlation includes only the tip-clearance losses. Considering that the data point at $Z = 0.98$ includes only the leakage losses and the annulus-wall boundary-layer losses, and the data point at $Z = 1.3$ includes additional losses due to the blade boundary layer and wake, the agreement is quite good. This also confirms the earlier conclusions that the leakage flow has a dominant influence on the end-wall losses. Since the tip clearance used here (about 1% of blade span) is typical of many compressors, the results are significant.

Blade Profile Losses. The stagnation pressure and flow properties from blade-to-blade were measured near the trailing edge of the rotor, away from the end walls using a rotating five-hole probe at $\bar{\phi} = 0.56$. These measurements were taken at about 5-10% of the chord from the trailing edge. All the flow data are presented and interpreted in [13]. The relative stagnation pressure data from [13] are used to calculate the losses and compare them with the correlations. The losses away from the hub and tip-wall regions are confined to the rotor-wake region. This is evident from Fig. 10, where the blade-to-blade distribution of loss coefficient $\bar{\psi}_{loss}$ is plotted at various radii. The local value of inlet stagnation pressure (shown in Fig. 2) was used in calculating these losses. As expected, the losses are appreciable in the wake region.

The mass-averaged (blade to blade) values of the loss coefficient were derived from the following expression

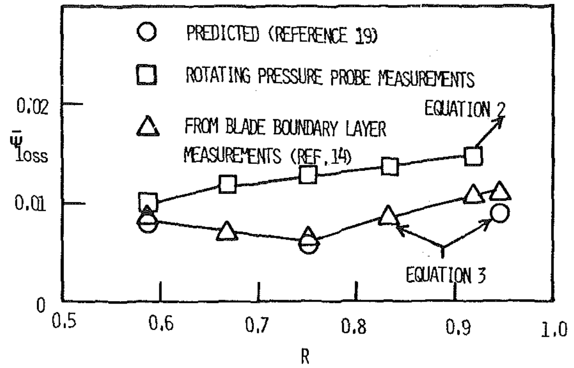

Fig. 11 Radial variation of profile loss coefficient ($\bar{\psi}_{loss}$) away from the hub and tip regions at the exit; $\bar{\phi} = 0.56$

$$\bar{\psi}_{loss} = \left[\int_{\theta_s}^{\theta_p} V_z \psi_{loss} r d\theta\right] \Big/ \int_{\theta_s}^{\theta_p} V_z r d\theta \qquad (2)$$

The radial variations of $\bar{\psi}_{loss}$ are shown plotted in Fig. 11. Also shown plotted in Fig. 11 are the losses derived from the rotor-blade boundary-layer measurements [14] and the formula by Speidel (18)

$$\bar{\psi}_{loss} = \frac{2[(\theta_{11})_{SS} + (\theta_{11})_{PS}]_{TE}}{\cos^3\beta_2 \cos^{-2}\beta_1} \frac{C}{S} \left(\frac{U_t}{W_1}\right)^2 \qquad (3)$$

where θ_{11} is the momentum thickness based on the streamwise velocity defect; β_1 and β_2 are inlet and outflow angles, respectively. The distribution of $\bar{\psi}_{loss}$ based on the measured values of θ_{11} as well as the predicted values of θ_{11} [19] are shown compared with the data from the pressure measurements. The agreement between the predicted and measured values of $\bar{\psi}_{loss}$, based on equation (3), is good; but the comparison with the present data is good near the lower radii, with substantial departure at the midspan region.

There are several possible reasons for the discrepancy between the losses derived from the pressure measurements and the losses based on the momentum thickness and equation (3).

1 The measured and the predicted values of θ_{11} are accurate and the evaluation of the loss coefficient ($\bar{\psi}_{loss}$) is based on the value of θ_{11} measured at 4-7% of chord upstream of the trailing edge. The pressure measurements were taken downstream of the trailing edge (0.049 to 0.085 chord lengths downstream). At this location, the momentum thickness is likely to be higher than the values measured upstream of the trailing edge.

2 As indicated in [20], considerable flow redistribution occurs downstream of the trailing edge. As the flow travels downstream, the momentum thickness decreases below the midspan, but increases in most other radial locations. Considerable loss redistribution takes place downstream of the trailing edge due to the radial transport of mass, momentum, and energy.

3 Equation (3), based on two-dimensional mixing analysis, may not adequately describe the losses in a rotor with three-dimensional blade boundary layers and three-dimensional mixing downstream of the passage. It is desirable to carry out an analysis (similar to Adkins and Smith [21]) and develop an equation similar to equation (3) valid for a rotor.

Hence the losses are likely to be higher than those derived from the values of θ_{11} measured upstream of the trailing edge. Furthermore, the mass-averaged loss coefficient based on the pressure data (Fig. 11) is consistent with the efficiencies shown in Fig. 1. This will be discussed later. In view of these comments, it is concluded that the losses derived from the pressure measurements downstream of the trailing edge (0.049 to 0.085 chord length downstream) are more accurate. It is

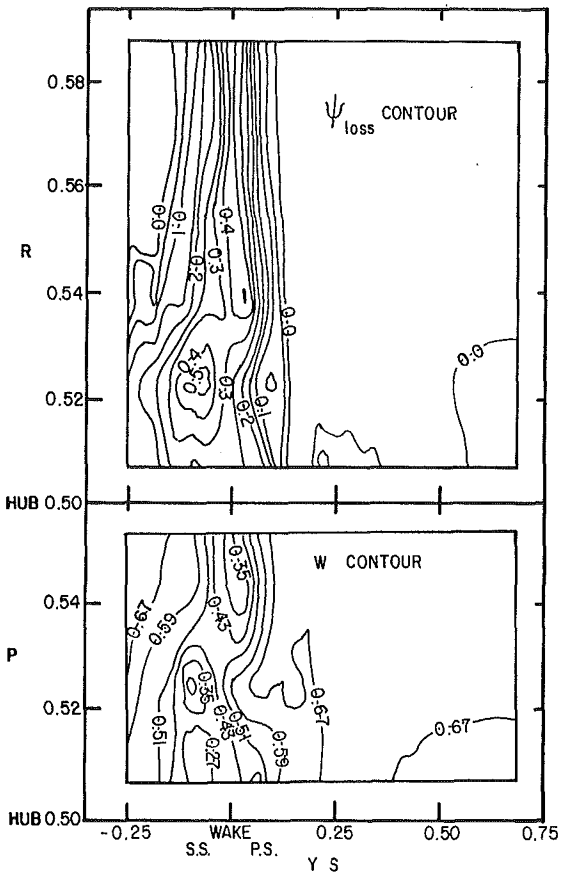

Fig. 12 Contours of ψ_{loss} and W in the hub region at the exit ($\bar{\phi} = 0.56$)

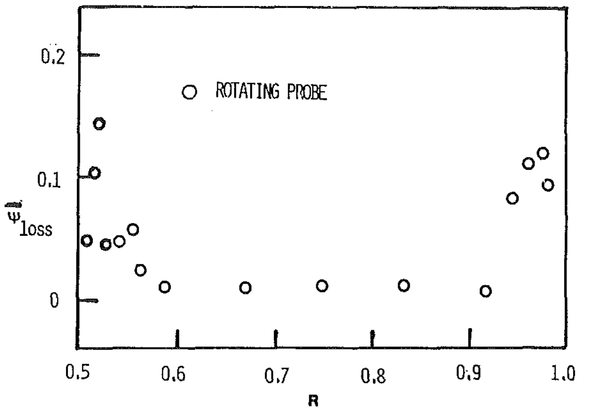

Fig. 13 Radial variation of mass-averaged loss coefficient ($\bar{\psi}_{loss}$) at the exit; $\bar{\phi} = 0.56$

also clear from Fig. 10 that the stagnation pressure losses at the radial locations shown in Fig. 10 are confined to only the rotor-wake region; hence, it represents the profile loss. It should be cautioned here that the loss coefficient presented here represents only the profile losses inside the blade row and the mixing losses in the immediate vicinity of the trailing edge. It does not include mixing losses downstream of the trailing edge.

Flow and Losses in the Hub-Wall Region. The flow near the hub-wall region was measured at $Z=1.17$ for $R=0.507$ ($R=0.5$ at hub), 0.513, 0.52, 0.527, 0.541, 0.554. The compressor was operated at the design flow coefficient. The contours of ψ_{loss} and W, are shown plotted in Fig. 12.

The hub-wall boundary layer is thin at the inlet (Fig. 2) and its growth in the rotor passage is small, except in the corner region formed by the suction surface and the hub wall. The first radial measuring station was 3.2 mm ($R=0.50$) from the hub wall. Hence the boundary-layer thickness in regions away from this corner is of the order 3.2 mm or less.

The hub-wall boundary layer becomes highly skewed at the inlet during its transition from the stationary hub to the rotating hub. The axial gap (which was very small in this case) between the rotating hub and the stationary hub does have an influence on the entry velocity profile. The skewed (or three-dimensional) boundary layer entering the rotor passage is subjected to centrifugal force in the transverse direction, thus developing a secondary flow from the pressure to the suction surface. This secondary flow has a tendency to transport the hub-wall boundary layer toward the suction surface corner, resulting in what is known as "corner stall." The presence of a corner-stall region is clearly evident from Fig. 12 indicated by high-loss and low-velocity regions away from the hub ($R \cong 0.515$) and away from the suction surface. The corner stall region is confined to $-0.25<YS<0$, and $0.5<R<0.53$. The region $R>0.54$ is clearly dominated by the rotor wake. The rotor wake in the hub-wall region is highly distorted due to the presence of the secondary flow.

The high-loss region occurs away from the hub, at $R=0.525$, near the suction surface (Fig. 12). In most cascade end-wall experiments, the corner-stall region and the secondary vortex were observed near the corner formed by the suction surface and the end wall. In a rotor, the effect of rotation is to transport the low-momentum fluid outward. This may be the reason for the location of a high-loss region away from the hub. The loss region is confined to about a third of the passage near the suction surface, and the losses are negligibly small elsewhere.

The mass-averaged loss coefficient derived from an expression similar to equation (2) is shown in Fig. 13. The value of $\bar{\psi}_{loss}$ increases from the hub wall to $R=0.52$. Another peak is observed at $R=0.55$. The presence of two peaks in the loss distribution is unusual and may represent the effect of the corner stall and the rotation on the hub-wall flow development.

Integrated end-wall losses were calculated from many of the loss correlations proposed on the basis of the cascade data (see [1, 3, 6, 7] for various correlations). None of these agree with the measured data, indicating the need for the development of end-wall loss correlations based on rotor data.

Radial Distribution of Loss for the Entire Rotor. The blade-to-blade variations of ψ_{loss} at the exit at various radii from hub to tip are shown plotted in Fig. 10. It is evident that the losses are localized near the hub in the wake region as well as in the corner region (formed by the suction surface and the hub-wall), while the losses away from the hub and the tip regions are confined to the rotor wake. It is interesting to note that losses in the tip region ($R=0.9456$ to $R=0.9796$) are spread across the entire passage. This is caused by the mixing of the leakage flow and the vortex with the mainstream.

Stagnation pressure loss contours at the rotor exit at the design flow coefficient are shown in Fig. 14. It should be noted that there are slight differences in the axial stations at which the hub end-wall flow, midspan flow, and tip-region flow measurements were undertaken. But a composite loss distribution, shown in Fig. 14, provides a valuable insight into loss mechanisms occurring in a rotor passage. The most interesting feature is that the wake structure is modified substantially by the hub end-wall and the tip-region flow. In the midspan region, the wake is thin. In the hub and casing end-wall regions, the end-wall flows broaden the wake. Furthermore, the tip-region losses are spread across the entire passage and the hub-wall losses are confined to a fraction of the passage near the suction surface.

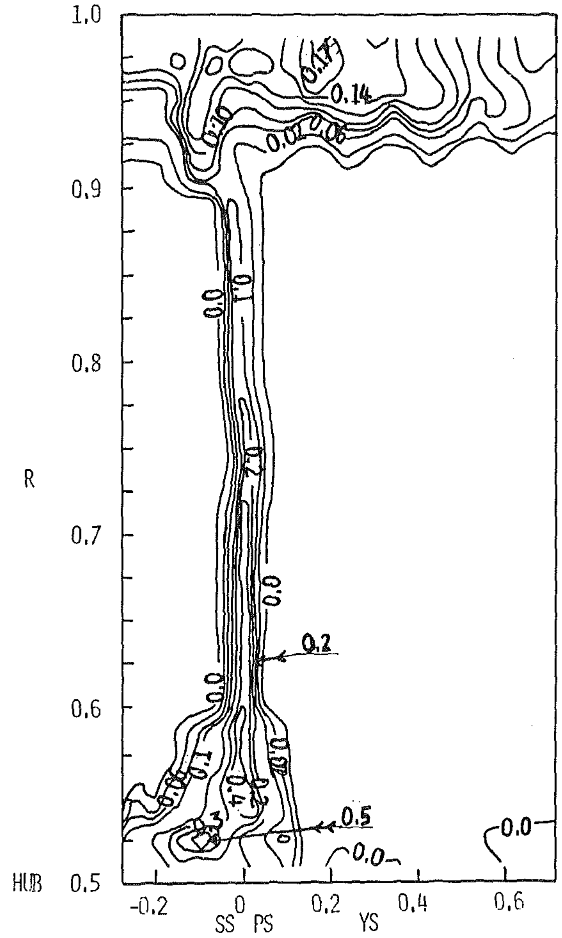

Fig. 14 Composite loss contours at the exit of the rotor, $\bar{\phi} = 0.56$

The passage-averaged stagnation pressure losses, $\bar{\psi}_{\text{loss}}$, at rotor exit are shown in Fig. 13. $\bar{\psi}_{\text{loss}}$ is defined as

$$\bar{\psi}_{\text{loss}} = \int_{\theta_s}^{\theta_p} V_z \psi_{\text{loss}} R d\theta \Big/ \int_{\theta_s}^{\theta_p} V_z R d\theta$$

where θ_s and θ_p are tangential stations closest to the pressure and suction surfaces respectively. As expected, the losses in the hub-wall and tip-wall regions are much larger than those in the midspan regions. The spanwise extent of the hub-wall and the tip-region losses are about the same. It should be cautioned here that the data shown in Fig. 13 are very close to the trailing edge (downstream of the blade row) and do not include the downstream mixing losses. Hence, the actual losses attributable to the rotor passage and downstream flow will be higher. The loss evaluation should be based on either far downstream measurement (where the mixing effects are complete) or the trailing edge location. We hope the present investigation will stimulate interest in resolving details of the mixing losses downstream of a compressor rotor.

It is instructive to compare whether the integrated losses in the rotor, measured by the rotating probes, are consistent with the efficiencies reported in Fig. 1. Furthermore, the sources and magnitude of these losses are also of interest. For this purpose, the span of the rotor blade was divided into three regions:

Region I	Hub region: $R = 0.507$ to 0.60
Region II	Profile loss region: $R = 0.60$ to 0.90
Region III	Tip region: $R = 0.90$ to 0.9864

The losses in these regions (Fig. 14) were integrated (mass averaged) to derive the inefficiency due to various sources. These were found to be 1.1%, 1.55%, and 1.44%, respectively, for regions I, II, and III, for an efficiency of 95.9%. It should be remarked here that the inefficiency due to viscous flow in regions $R = 0.5$ to 0.507, 0.98 to 1.00 are not included in this calculation. Hence the efficiencies should be lower than 95.9%. The efficiency calculated from the stationary probe measurement far downstream ($Z = 3.03$, where the flow has become axisymmetric) is 90.8% (Fig. 2). The difference between these two measurements is attributed to the blade row losses not accounted for in these measurements as well as the mixing losses downstream. It is interesting to note that Smith [12] reported an efficiency of 95% for the same rotor. The efficiency was derived from the measured energy addition to the flow and the shaft horsepower. The rotor-stator spacing employed by Smith was much closer (less than one axial chord of the rotor) than the present configuration (more than five axial chords of the rotor) and the flow measurement was taken about midway between the rotor trailing edge and the stator leading edge.

The loss data reported in this paper are thus consistent.

Conclusions

The relative stagnation pressure losses inside the rotor of a low-speed axial flow compressor are presented. The tip-region loss is presented at two flow coefficients to discern the effect of blade loading on the tip-region losses. From this investigation, the following major conclusions are drawn.

1 The tip-region losses originate earlier along the blade chord in the case of the peak pressure rise coefficient, but the extent of the loss region at the exit is not significantly different in both cases. Inside the passage, up to $Z = 0.5$, the extent of loss regions is much more significant at higher blade loading.

2 The tip-region loss core is located near midpassage, and its spanwise extent increases continuously from the leading to the trailing edge.

3 The tip leakage loss seems to dominate the end-wall regions; the losses due to the secondary flow and the annulus-wall boundary layer seem to be small. The agreement between the tip-leakage loss correlation and the measured data is good.

4 The hub-wall region is dominated by the corner stall and secondary flow. The effect of rotation is to transport the loss core away from the hub. The hub-wall boundary layer growth away from the corner region (about one-third passage width) is small. There are significant differences between the rotor hub-wall loss and the cascade end-wall loss. The loss correlations proposed for the end-wall flow in cascades do not agree with the rotor-loss data.

5 The blade profile losses away from the end-walls, calculated from the pressure data, are different from those calculated from the expression relating the losses to the momentum thickness. There is a need for a rotor-blade profile loss correlation based on experimental data from rotors.

Acknowledgments

This work was supported by the National Aeronautics and Space Administration through Grant No. NSG 3032, with Dr. P. M. Sockol as the Technical Monitor. The authors wish to thank Dr. M. Pouagare for some of the velocity data presented in this paper. Detailed comments and criticisms by reviewers enabled improved interpretation of the data.

References

1 Hirsch, Ch., and Denton, J. D. (Ed.), "Through Flow Calculations in Axial Turbomachines," AGARD A.R. 175, Oct. 1981.

2 Serovy, G. K., and Bry, P., "Loss Distributions in Axial Compressor Blade Rows," Iowa State University Report ERI 811144, Feb. 1981.

3 Lakshminarayana, B., "Loss Evaluation Methods in Axial Flow Compressors," *Proc. Workshop on Flow in Turbomachines*, M. H. Vavra et al., Naval Post-Graduate School Report NPS57VA71111A, Nov. 1971.

4 Lebot, V., Paulon, J., and Belaygue, P., "Theoretical and Experimental Determination of Pressure Losses in a Single Stage Axial-Flow Compressor," ASME JOURNAL OF ENGINEERING FOR POWER, Vol. 92, pp. 407-414, 1976.

5 Wisler, D. C., "Loss Reduction in Axial Flow Compressors Through Low Speed Testing," ASME Paper 84-GT-184.

6 Koch, C. C., and Smith, L. H., "Loss Sources and Magnitude in Axial Flow Compressors," ASME JOURNAL OF ENGINEERING FOR POWER, Vol. 98, No. 3, July 1976, p. 411.

7 Cyrus, V., "Secondary Losses in Axial Compressor," *Proc. 6th Conference on Fluid Machinery*, Budapest, Sept. 1979, pp. 260-269.

8 Dring, R. P., Joslyn, H. D., and Wagner, J. H., "Compressor Rotor Aerodynamics," AGARD CP 351, 1983.

9 Lakshminarayana, B., "Methods of Predicting the Tip Clearance Effects in Axial Flow Turbomachinery," ASME *Journal of Basic Engineering*, Vol. 92, No. 3, 1970, pp. 467-482.

10 Lakshminarayana, B., Pouagare, M., and Davino, R., "Three-Dimensional Flow Field in the Tip Region of a Compressor Rotor—Part I: Mean Velocity Profiles and Annulus Wall Boundary Layer and Part II: Turbulence Properties," ASME JOURNAL OF ENGINEERING FOR POWER, Vol. 104, No. 4, Oct. 1982, pp. 760-781.

11 Lakshminarayana, B., "An Axial Flow Compressor Facility with Instrumentation for Relative Flow Measurement," *J. Fluids Engineering*, Vol. 102, 1980.

12 Smith, L. H., "Three Dimensional Flow in Axial Flow Turbomachinery-Part I," Report I-14, Johns Hopkins University, Nov. 1953.

13 Pouagare, M., Murthy, K. N. S., and Lakshminarayana, B., "Three Dimensional Flow Field Inside the Passage of a Low-Speed Axial Flow Compressor," AIAA Paper 82-1006, 1982. (Synoptic, *AIAA Journal*, Vol. 21, Dec. 1983, p. 1679).

14 Pouagare, M., Galmes, J., and Lakshminarayana, B., "An Experimental Study of the Compressor Rotor Blade Boundary Layer," ASME JOURNAL OF ENGINEERING FOR GAS TURBINES AND POWER, Vol. 107, No. 2, Apr. 1985, pp. 364-373.

15 Pouagare, M., and Lakshminarayana, B., "Three-Dimensional Flow Field Data Inside a Low-Speed Axial Flow Compressor Rotor Passage," NASA CR (submitted for publication), 1985.

16 Sitaram, N., "Blade End Wall Flows in an Axial Flow Compressor Stage," Ph.D. Thesis, Dept. of Aerospace Engineering, The Pennsylvania State University, Dec. 1983.

17 Treaster, A. L., and Yocum, A., "The Calibration and Application of Five-Hole Probe," *Trans. Instrument Society of America*, Vol. 19, No. 3, 1979, pp. 23-24.

18 Speidel, L., "Berechrung der Stromungverluste Von Ungestaffelten Ebenen Schaufelgitter," *Ing. Arch.*, Vol. 22, 1954, p. 295.

19 Lakshminarayana, B., and Govindan, T. R., "Analysis of Turbulent Boundary Layers in Cascades and Rotor Blades of Turbomachinery," *AIAA Journal*, Vol. 19, No. 10, 1981, pp. 1333-1341.

20 Ravindranath, A., and Lakshminarayana, B., "Rotor Wake Mixing Effects Downstream of a Compressor Rotor," ASME JOURNAL OF ENGINEERING FOR POWER, Vol. 104, Jan. 1982, p. 202.

21 Adkins, G. G., Jr., and Smith, L. H. Jr., "Spanwise Mixing in Axial Flow Turbomachines," ASME JOURNAL OF ENGINEERING FOR POWER, Vol. 104, No. 1, Jan. 1982, p. 97.

Y. Senoo
Professor,
Research Institute of
Industrial Science,
Kyushu University,
Kasugashi, Fukuoka 816, Japan
Mem. ASME

M. Ishida
Professor,
Faculty of Engineering,
Nagasaki University,
Nagasaki, 852, Japan

Pressure Loss Due to the Tip Clearance of Impeller Blades in Centrifugal and Axial Blowers

The pressure loss based on the tip clearance of impeller blades consists of the pressure loss induced by the leakage flow through the clearance and the pressure loss for supporting fluid against the pressure gradient in the channels and in the thin annular clearance space between the shroud and the impeller. Equations to evaluate these losses are derived and the predicted efficiency drop is compared with experimental data for two types of centrifugal impellers. Furthermore, the equations are simplified for axial impellers as a special case, and the predicted efficiency drop is compared with the experimental data for seven cases in the literature. Fair agreement demonstrates plausibility of the present model.

Introduction

In many turbomachines impellers are not shrouded and the leakage flow through the tip clearance of blades is an unavoidable factor which deteriorates the performance. Therefore, the impeller geometry should be designed considering the tip clearance effects, but there is no rational method to evaluate the tip clearance loss. Loss equations have been derived from a few experimental data [1] or many assumptions on the loss mechanism [2]. There are several papers [3, 4, 5] which concern tip clearance, but they do not clarify the mechanism of pressure loss.

The leakage flow through the tip clearance of impeller blades modifies the flow pattern in the impeller. Considerable effort has been made to examine the details of the flow pattern [6, 7], but the results have not been utilized to evaluate the pressure loss due to the tip clearance of turbomachines.

Pressure Loss Due to Leakage Through the Clearance

One blade pitch of an impeller which is rotating counterclockwise is taken as a control volume as shown in Fig. 1(*a*). Between the blades the relative velocity is the maximum along the suction surface of the left side blade and it is decreased monotonically toward the pressure surface of the right side blade. If there is a clearance at the blade tip, fluid in the left channel leaks into the central channel through the tip clearance of the left blade. At the same time an equal amount of fluid with identical dynamic condition leaks away from the central channel. As a result it looks as if the tip leakage has no net effect on the flow in the central channel. However, in reality there is a drag due to the leakage.

Cases Where Blades Are Loaded by Curvature. In a case of ideal two-dimensional flow in a curved channel, the velocity w_p near the concave wall is smaller than the velocity w_s near the convex wall. If a small amount of fluid q is removed from the concave wall and an equal amount of fluid with identical total head is injected in at the convex wall in such a way that the tangential velocity is identical to w_s, there is no loss of total pressure, and the flow downstream in the curved channel is hardly modified by the disturbance due to the injection. That is, although the tangential velocity of the injected fluid at the convex surface is larger than the tangential velocity of the outgoing fluid at the concave surface the flow in the curved channel as a whole gets no net effect.

If the direction of injection at the convex surface is changed so that the tangential velocity component is equal to w_p instead of w_s, the flow in the curved channel suffers a drag force $q(w_s - w_p)$ because the tangential momentum of the injected fluid is smaller by $q(w_s - w_p)$ compared with the value of the last example.

The conditions of leakage through the tip clearance of blades, which are loaded by the curvature of streamlines, is identical to the second case in the above examples, and the drag due to leakage through the tip clearance is $q(w_s - w_p)$.

Cases Where Blades Are Loaded by Rotation of Impeller. If a fluid particle transverses a channel of an impeller which is loaded only by rotation of the impeller, the parallel component of velocity w of the fluid particle is decelerated by $-dw/dt = 2\Omega v dr/dm$ due to the Coriolis acceleration; meanwhile the fluid particle moves to a line which is parallel to the blade and at a circumferential distance of $ds = v dt/\sin\beta$ away from the blade. Since $-dw/ds = -(dw/dt)(dt/ds) = -2\Omega \sin\beta \, dr/dm$, the circumferential reduction rate of the relative velocity w is independent of the transverse velocity, and the reduction rate is identical to the velocity gradient of the main flow. That is, any fluid particle reduces the velocity component parallel to the blade by

---

Contributed by the Gas Turbine Division of THE AMERICAN SOCIETY OF MECHANICAL ENGINEERS and presented at the 30th International Gas Turbine Conference and Exhibit, Houston, Texas, March 18–21, 1985. Manuscript received at ASME Headquarters, January 16, 1985. Paper No. 85-GT-196.

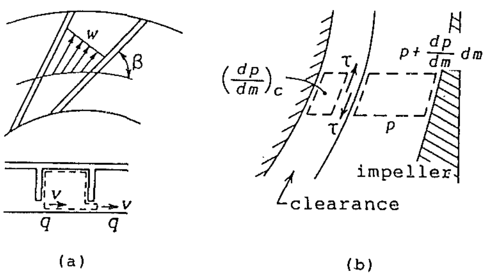

Fig. 1 Models of flow and forces at the clearance

$w_s - w_p$ while it transverses a channel from the suction surface of a blade to the pressure surface of the adjacent blade.

If a small amount of fluid q leaks away from the pressure surface of a channel and an equal amount of fluid leaks into the suction surface of the channel with a velocity component parallel to the blade which is equal to w_p instead of w_s, the drag due to the leakage is $q(w_s - w_p)$.

In general cases the blades of impellers are loaded by curvature of blades as well as rotation of the impeller. Since the drag due to leakage is expressed as $q(w_s - w_p)$ whether the blade is loaded by the Coriolis force or by the curvature of blades, the relation is applicable to any impellers where the blades are loaded by a combination of them.

Influence of Number of Blades. The angle between the two adjacent blades of an impeller is $(2\pi/Z)(dr/dm)$. Therefore, the leakage flow normal to the blade surface must change the momentum in the direction of blades by $qv(2\pi/Z)(dr/dm)$ keeping the momentum qv normal to the blades identical at the clearances of both blades. As a result the fluid in the channel of the impeller receives a negative drag.

Combining these three effects, the drag force D due to the leakage flow q is expressed as

$$D=q(w_s-w_p)-qv(2\pi/Z)(dr/dm)$$

Leakage Rate and Pressure Loss. The velocity of leakage flow normal to the blade is

$$v=\sqrt{2(p_p-p_s)/\rho}=\sqrt{2\bar{w}_0(w_s-w_p)}$$

where w_s, w_p, and $\bar{w}_0$ are the values of an ideal flow with $\sigma = 1.0$. Even when the effectiveness σ of the channel cross-sectional area is reduced by displacement thickness and the velocity $\bar{w}$ is large so that $\bar{w} = \bar{w}_0/\sigma$, as long as the blade loading remains constant the pressure difference across a blade hardly varies; therefore the foregoing equation should be generalized as follows

$$v=\sqrt{2(p_p-p_s)/\rho}=\sqrt{2\sigma\bar{w}(w_s-w_p)} \tag{1}$$

The leakage flow rate per blade length is

$$dq/dl=\alpha c\rho v$$

where α is the contraction factor of leakage flow.

The power loss P' based on the leakage drag force is the product of D and the main flow velocity $\bar{w}$ near the shroud in the impeller.

$$\frac{dP'}{dl}=\frac{dq}{dl}\,\bar{w}\left\{(w_s-w_p)-\frac{2\pi}{Z}\,v\frac{dr}{dm}\right\}$$

$$=\alpha c\rho v^2\left\{\frac{v}{2\sigma}-\frac{2\pi}{Z}\,\bar{w}\frac{dr}{dm}\right\}$$

The power loss is related to the entropy rise $\Delta s'$ (or pressure loss p_l' for the incompressible case) at the exit of the impeller as follows:

$$\rho QT\Delta s'\,(=Qp_l')=Z\int_{m_1}^{m_2}\alpha\rho cv^2\left(\frac{v}{2\sigma}-\frac{2\pi}{Z}\,\bar{w}\frac{dr}{dm}\right)\frac{dm}{\sin\beta_b}$$

where $dl = dm/\sin\beta_b$. Replacing $T\Delta s'\ (=p_l'/\rho) = \psi_l'\,U^2/2$, $Q = \varphi U2\pi r_2b_2$ and $c/b_2 = \lambda$,

$$\psi_l'\doteq\frac{Z}{\rho_2\pi r_2\varphi}\int_{m_1}^{m_2}\frac{\rho\alpha\lambda}{\sin\beta_b}\left(\frac{v}{U}\right)^2\left(\frac{v}{2\sigma U}-\frac{2\pi}{Z}\,\frac{\bar{w}}{U}\,\frac{dr}{dm}\right)dm \tag{2}$$

Clearance Loss Due to Pressure Gradient

In a bundle of stream tubes passing through a cross section, if there is a stream tube where the flow does not have enough velocity or momentum to support itself against the adverse pressure gradient, a shear force supports the flow in the stream tube to keep the steady state and a pressure loss results. There are similar problems regarding the flow in the tip clearance region of an impeller.

Annular Tip Clearance Space Along the Shoud. The meridional pressure gradient along the shroud induced by an impeller is usually larger than the centrifugal force of fluid in the impeller. If the fluid in the annular clearance space rotates with a circumferential velocity which is equal to that of the fluid in the impeller, the excess portion of the pressure

Nomenclature

b = blade height
c = clearance
D = drag force due to leakage flow
k = slip coefficient
l = distance along blade or chord
m = meridional distance along shroud
p = pressure
p_l = pressure loss of incompressible flow due to clearance
P = power loss per channel
q = leakage mass flow per blade
Q = volume flow rate of impeller
r = radial distance from the axis
$\tilde{r}$ = hub tip mean radius
s = pitch of blades or entropy
T = absolute temperature
u = circumferential component of velocity
U = peripheral speed of impeller outer diameter
v = component of leakage velocity normal to blade
w = velocity component parallel to blade
Z = number of blades
α = contraction factor of leakage flow
β = flow angle, from circumference
β_b = blade angle
δ = blockage multiplier due to tip clearance
ϵ = pressure recovery coefficient
η = efficiency
λ = tip clearance ratio c/b_2
ρ = density of fluid
σ = effectiveness of flow area in impeller, equation (4)
φ = flow coefficient at impeller exit
ψ $\doteq$ pressure coefficient of impeller
ψ_h = pressure loss coefficient due to causes other than tip clearance
ψ_i ≒ work input coefficient of impeller
ψ_l ≒ pressure loss coefficient due to tip clearance
Ω = angular velocity of impeller

Subscripts and Superscripts

e = experiment
m = mean value along blade length
p = pressure surface
s = suction surface
u = circumferential component
0 = values for zero clearance
1 = inlet
2 = exit
$'$ = due to leakage
$''$ = due to pressure gradient on annular clearance
$'''$ = due to pressure gradient on blockage in channel
$\bar{\ }$ = circumferential average value

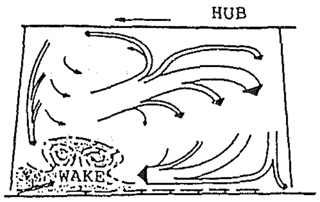

Fig. 2 Secondary flow pattern in the radial part of a centrifugal impeller

gradient exerted by the impeller must be balanced by the shear force along the surface of revolution of blade-edges as shown in Fig. 1(*b*).

If there is no pressure loss in the impeller,

$$\frac{-\kappa}{\kappa-1}\frac{p}{\rho}=\frac{w^2}{2}-\frac{r^2\Omega^2}{2}+\text{constant}$$

where κ is the specific heat ratio and it is infinity for incompressible flow. Differentiating the equation and considering the pressure loss due to deceleration,

$$\frac{1}{\rho}\frac{dp}{dm}=r\Omega^2\frac{dr}{dm}-\epsilon w\frac{dw}{dm}$$

for compressible as well as for incompressible flows.

If the circumferential velocity of fluid in the annular clearance space is equal to that in the impeller, the pressure gradient which can be supported by the centrifugal force in the annular space is

$$\frac{1}{\rho}\left(\frac{dp}{dm}\right)_c=\frac{1}{r}(r\Omega-w\cos\beta)^2\frac{dr}{dm}$$

The meridian component of the shear force along the surface of revolution is

$$\tau=c\left\{\frac{dp}{dm}-\left(\frac{dp}{dm}\right)_c\right\}$$

and the power loss P'' due to this drag force is

$$Z\frac{dP''}{dm}=\rho QT\frac{ds''}{dm}\left(=Q\frac{dp_l''}{dm}\right)=2\pi r\tau w\sin\beta$$

Integrating the foregoing equation along the shroud

$$\psi_l''=\frac{2}{r_2\varphi}\int_{m_1}^{m_2}\frac{\rho}{\rho_2}r\lambda\frac{w}{U}\sin\beta\left(-\epsilon\frac{w}{U^2}\frac{dw}{dm}+\frac{2\Omega w}{U^2}\cos\beta\frac{dr}{dm}-\frac{w^2}{U^2r}\cos^2\beta\frac{dr}{dm}\right)dm \qquad (3)$$

The region where the value in the parentheses is negative must be excluded in the integration.

Stagnant Flow Area in the Impeller Due to Clearance. The leakage flow through the tip clearance is intercepted by a secondary flow along the shroud which moves from the pressure side of a blade to the suction side of the adjacent blade, and the flow with low velocity component w near the shroud moves into the channel between blades as shown in Fig. 2. It is presumed that the flow area of an impeller $2\pi r(b+c)$ sin β_b is virtually reduced by the tip clearance, and the decrement of the effective flow area is expressed as $2\pi rc\,(1+\delta)$ sin β_b. That is, the effectiveness σ of the flow area is expressed as

$$\sigma=1-\delta\lambda(b_2/b) \qquad (4)$$

The power loss to support the stagnant flow area in the channel between blades due to the tip clearance is expressed as

$$ZP'''=\int_{l_1}^{l_2}-\frac{\rho}{\rho_2}2\pi rc\delta\sin\beta\epsilon w^2\frac{dw}{dm}dl=\rho QT\Delta s'''\;(=Qp_l''')$$

$$\psi_l'''=\frac{2}{r_2\varphi}\int_{m_1}^{m_2}\frac{\rho}{\rho_2}r\lambda\frac{w}{U}\sin\beta\left(-\epsilon\delta\frac{w}{U^2}\frac{dw}{dm}\right)dm \qquad (5)$$

Integration should be made excluding the region where the value in the parentheses is negative.

The pressure loss due to the tip clearance is the summation of the leakage loss and the pressure gradient losses

$$\psi_l=\psi_l'+\psi_l''+\psi_l''' \qquad (6)$$

Working Equations for Change of Performances

The effective flow area in the channel between blades is reduced due to the leakage through the clearance of blades and the velocity is increased. On the other hand, the velocity distribution in the impeller is usually estimated for the case without tip clearance. Therefore, the equations (1, 2, 3, 5) are expressed as follows using the relation $w=w_0/\sigma$, where w_0 is the value at $\sigma=1.0$

$$v=\sqrt{2\bar{w}_0(w_s-w_p)} \qquad (7)$$

$$\psi_l'=\frac{Z}{\pi r_2\varphi}\int_{m_1}^{m_2}\frac{\rho}{\rho_2}\frac{\alpha\lambda}{\sigma\sin\beta_b}\left(\frac{v}{U}\right)^2\left(\frac{v}{2U}-\frac{2\pi}{Z}\frac{\bar{w}_0}{U}\frac{dr}{dm}\right)dm \qquad (8)$$

$$\psi_l''+\psi_l'''=\frac{2}{r_2\varphi}\int_{m_1}^{m_2}\frac{\rho}{\rho_2}\frac{r\lambda\bar{w}_0}{\sigma^3U}\sin\beta\left\{-\epsilon(1+\delta)\frac{\bar{w}_0}{U^2}\frac{d\bar{w}_0}{dm}+\frac{2\sigma\Omega\bar{w}_0}{U^2}\cos\beta\frac{dr}{dm}-\frac{\bar{w}_0{}^2}{U^2r}\cos^2\beta\frac{dr}{dm}\right\}dm \qquad (9)$$

For integrating the foregoing equation δ must be assumed zero in the region where $d\bar{w}_0/dm>0$, and if there is a region where the value in the brackets is negative the region must be omitted from the range of integration.

Tip clearance not only induces a pressure loss but also reduces the Euler head of the impeller, and the decrement of the pressure rise due to tip clearance is the sum of the two effects. That is

$$\psi_0-\psi=\psi_{i0}-\psi_i-(\psi_{h0}-\psi_h)+\psi_l \qquad (10)$$

where ψ_h is the hydraulic pressure loss other than the tip clearance loss and subscript 0 indicates the values for the case of zero clearance.

Reduction of the efficiency due to the tip clearance is evaluated as the difference of the two equations

$$\eta_0=1-(\psi_{h0}/\psi_{i0}),\;\;\eta=1-(\psi_h+\psi_l)/\psi_i$$

$$\frac{\eta_0-\eta}{\lambda_2}=\frac{\psi_l}{\psi_i\lambda_2}-\frac{\psi_{h0}-\psi_h}{\psi_i\lambda_2}+(1-\eta_0)\frac{\psi_{i0}-\psi_i}{\psi_i\lambda_2} \qquad (11)$$

$\psi_{h0}-\psi_h$ is almost zero but it may be negative at off-design conditions.

Loading Equations for Centrifugal Impellers

The flow behavior in a centrifugal impeller without tip clearance can be evaluated by means of quasi-three-dimensional flow analysis assuming inviscid flow. In reality the viscous effect is not negligible, but it is known that the predicted work input of an impeller agrees well with the experiment. Therefore, it is expected that the distribution of p_p-p_s along the blade may be predicted well using an inviscid flow analysis. The pressure gradient along the shroud in the meridional plane is reduced by various kinds of pressure losses, and their effects may be expressed in equations (3) and (5) by properly choosing the recovery coefficient ϵ. That is, a quasi-three-dimensional flow analysis in an impeller supplies sufficient information to evaluate the pressure losses due to the tip clearance.

In many cases it is desired to evaluate the pressure losses based on the tip clearance without executing laborious flow analysis. If the meridian component of velocity along the shroud is evaluted by some relatively simple means, the blade loading may be roughly estimated in the following way.

It is assumed that the flow is axisymmetric, and on the surface of revolution along the shroud the direction of flow varies smoothly from the inlet relative flow angle to the blade angle at the throat of the impeller blades, and then it flows parallel to the blades up to a radius of about $(1-2k)r_2$. Near the exit of the impeller the flow deviates from the direction of blades so that it satisfies the slip coefficient k.

The blade loading of an impeller is related to the change of angular momentum of the flow as follows:

$$\begin{aligned}(p_p-p_s)rbZdm &= \rho\bar{w}_0(w_s-w_p)rbZdm \\ &= 2\pi rb\sigma\rho\bar{w}\sin\beta\frac{d}{dm}(r^2\Omega-r\bar{w}\cos\beta)\,dm\end{aligned}$$

Replacing $\bar{w} = \bar{w}_0/\sigma$, this equation becomes

$$\begin{aligned}w_s-w_p = \frac{2\pi r}{Z}\sin\beta\Big\{&2\Omega\frac{dr}{dm}+\frac{1}{\sigma^2}\bar{w}_0\cos\beta\frac{d\sigma}{dm} \\ &-\frac{1}{\sigma}\left(\frac{\bar{w}_0}{r}\cos\beta\frac{dr}{dm}+\cos\beta\frac{d\bar{w}_0}{dm}-\bar{w}_0\sin\beta\frac{d\beta}{dm}\right)\Big\}\end{aligned} \tag{12}$$

Comparison With Experiments of Centrifugal Impellers

Reliable experimental data on the tip clearance effects of centrifugal impellers are scarce in the literature. In [9] data of two impellers are presented where uncertainty of efficiency and head coefficient are 0.019 and 0.008 respectively.

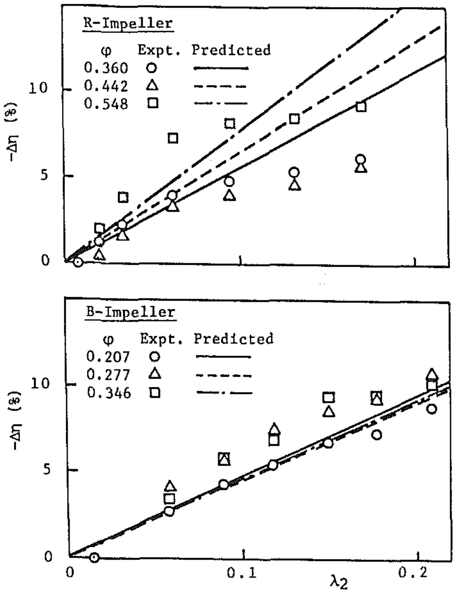

Fig. 3 Decrement of efficiency due to tip clearance ratio, centrifugal impellers

The tip clearance changes the head coefficient in two ways: one through input head ψ_i and the other through head loss. That is, in order to predict head coefficient, it is necessary to know variation of input head due to tip clearance, but the relation is not well known. Therefore, comparison of predicted head coefficient with experimental data is not possible. On the other hand, variation of efficiency is not much influenced by a little change of the input head. However, uncertainty of 0.019 is not satisfactory for the present purpose because the variation of efficiency is about 0.05 for a change of 0.1 in λ_2. Because of these reasons quantitative comparison between the prediction and experimental data is difficult unless accurate data with respect to efficiency are available. At the present stage only the order of magnitude of efficiency change should be compared between the prediction and the experiments.

According to [9] R-impeller is an impeller of 0.21m in diameter with 20 radial blades and 20 inducers and b_2/r_2 = 0.14. B-impeller is an impeller of 0.51m in diameter with 16 backward-leaning untwisted blades and b_2/r_2 is 0.067. The latter had originally a rotating shroud which was removed for the experiment. They were tested at 4000 and 2000 rpm respectively.

The tip clearances of these impellers were changed by moving the stationary shrouds axially relative to the impellers. In the case of B-impeller, the clearance is constant from the inlet to the exit of the impeller, while the clearance of R-impeller varies from the radial clearance at the inlet to the axial clearance at the exit and the distribution of clearance varies with the dimension of the exit clearance. The details are presented in [9].

The characteristic curves of these impellers demonstrate that the decrement of pressure due to tip clearance is large at the medium flow rate but it is rather small both at a large flow rate and at a small flow rate [9]. The pressure distributions along the wall demonstrate that at off-design conditions the leakage flow through the tip clearance relieves the pressure drop behind the leading edge and reduces the incidence loss, and the decrement of hydraulic loss $\psi_h - \psi_{h0} < 0$ in equation (10) considerably compensates the pressure loss due to the tip clearance c. Therefore, in this paper prediction is limited to three flow rates near the design point where the incidence loss is not significant even when the tip clearance is small.

Prediction and Comparison with Experiments. In the case of R-impeller the velocity distribution along the shroud was estimated based on an inviscid quasi-three-dimensional flow analysis at three different flow rates. In the case of B-impeller, the shroud profile is almost straight and the

Table 1 Comparison between experimental and predicted efficiency drops due to tip clearance, centrifugal impellers

	φ	ψ_{io}	$-\left(\frac{\Delta\psi_i}{\Delta\lambda_2}\right)_e$	η_o	$-\frac{\Delta\eta_e}{\Delta\lambda_2}$	$\frac{\Delta\psi_i}{\Delta\lambda_2}$	$\frac{\Delta\psi_L}{\Delta\lambda_2}$	$-\frac{(1-\eta_o)}{\psi_i}\left(\frac{\Delta\psi_i}{\Delta\lambda_2}\right)_e$	$-\frac{\Delta\eta}{\Delta\lambda_2}$	$\frac{-\frac{\Delta\eta_e}{\Delta\lambda_2}}{-\frac{\Delta\eta}{\Delta\lambda_2}}$
R-Impeller	0.360	1.76	0.39	0.91	0.55	0.637	0.940	0.020	0.554	0.98
	0.442	1.76	0.43	0.90	0.62	0.715	1.080	0.025	0.638	0.97
	0.548	1.76	0.40	0.90	0.87	0.825	1.300	0.022	0.761	1.14
B-Impeller	0.207	1.35	0.10	0.77	0.44	0.256	0.610	0.017	0.471	0.93
	0.277	1.21	0.04	0.81	0.52	0.172	0.540	0.005	0.454	1.15
	0.346	1.07	0.14	0.81	0.53	0.100	0.468	0.026	0.464	1.15
B'-Impeller	0.207	(1.35)	-	-	-	0.261	0.722	(0.017)	0.553	-
B"-Impeller	0.346	(1.21)	-	-	-	0.178	0.537	(0.005)	0.451	-

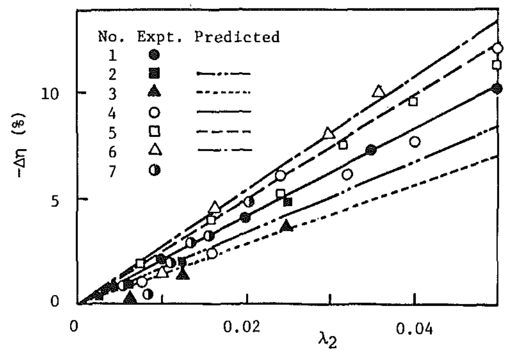

Fig. 4 Decrement of efficiency due to tip clearance ratio, seven axial impellers

meridian component of velocity along the shroud was simply estimated using the continuity equation. The distributions of the flow angle and the velocity were estimated at three flow rates following the simple method mentioned before. The decrement of efficiency due to the tip clearance was calculated for various values of tip clearance λ_2 at the impeller exit assuming that $\alpha = 0.8$, $\epsilon = 0.9$, and $\delta = 0.3$. The results show that the efficiency drops almost in proportion to the tip clearance. The experimental data of these impellers are plotted against the tip clearance λ_2 in Fig. 3. The relation is straight for B-impeller. In the case of R-impeller the relation is not straight, but in the range $0 < \lambda_2 < 0.10$ it is almost straight. The lines in Fig. 3 are the predicted lines.

In order to present the contribution of each term of equations (6) and (11) for the drop of the efficiency, the values of these terms are evaluated for $\lambda_2 = 0$ and $\lambda_2 = 0.10$ and the differences are divided by $\Delta\lambda_2 = 0.10$ to estimate the inclination. The results are presented in Table 1 together with the inclinations of experimental data which are decided by means of the least mean square method. Agreement between prediction and experimental data is fair and satisfactory considering the large uncertainty involved in the experimental data.

Influence of Impeller Geometry on Clearance Losses

Figure 3 and Table 1 clearly show that $-\Delta\eta/\Delta\lambda_2$ becomes larger as the flow rate φ is larger for R-impeller, while it becomes slightly smaller as the flow rate is larger for B-impeller. It is observed in Table 1 that the column $\Delta\psi_l'/\Delta\lambda_2$ or the leakage loss is the item which has opposite tendency for the two impellers. In the case of R-impeller with radial blades, the blade loading is proportional to the flow rate and the leakage loss is increased with the flow rate. In the case of B-impeller with backward leaning blades the blade loading is reduced as the flow rate becomes larger and the leakage loss is also reduced.

B′-impeller is proposed which has the blade geometry and the inlet and exit widths identical to those of B-impeller, but the blade width is narrower at the middle so that the minimum relative velocity does not occur at the middle. The predicted tip clearance loss of B′-impeller is considerably larger than that of B-impeller as listed in Table 1. That is, the tip clearance loss is influenced by the distribution of relative velocity in the impeller.

B″-impeller is designed so that it has the identical pressure rise and the flow rate as those of B-impeller at $\varphi = 0.277$, but the exit width b_2 of B″-impeller is 0.8 times the width of B-impeller. The prediction in Table 1 shows that the ratios $\Delta\psi_l/\Delta\lambda_2$ and $\Delta\eta/\Delta\lambda_2$ are almost equal to those of B-impeller. For the same tip clearance, the clearance ratio λ_2 of B″-impeller is 1.25 times the value of B-impeller; therefore, the clearance loss is also 1.25 times as large. In cases of low specific speed impellers where the tip clearance cannot be made very small, a better efficiency may be achieved by designing a wider impeller with many blades so that the clearance loss is reduced even though the fluid dynamic losses other than the clearance loss are larger.

Table 2 Comparison between experimental and predicted efficiency drops due to tip clearance, axial impellers

No.	Authors	φ	ψ_e	$\sin\beta_m$	$\frac{\Delta\psi_l'}{\psi_i\Delta\lambda}$	$\frac{\Delta\psi_L}{\psi_i\Delta\lambda} = -\frac{\Delta\eta}{\Delta\lambda}$	$-\frac{\Delta\eta_e}{\Delta\lambda}$	$\frac{-\frac{\Delta\eta_e}{\Delta\lambda}}{-\frac{\Delta\eta}{\Delta\lambda}}$
1	Jefferson & Turner	0.94	0.87	0.9	1.108	1.774	2.0	1.13
2	Williams	0.343	0.5	0.581	0.978	1.681	1.8	1.07
3	Williams	0.500	0.29	0.707	0.670	1.402	1.4	1.00
4	Ruden	0.388	0.225	0.46	0.991	2.086	2.0	0.96
5	Ruden	0.34	0.288	0.40	1.294	2.433	2.4	0.99
6	Koleshnikov	0.6	0.6	0.575	1.440	2.689	2.8	1.04
7	Spencer	0.21	0.26	0.246	1.603	2.572	2.3	0.89

Working Equations for Axial Impellers

The foregoing equations are derived for mixed flow impellers, which include axial impellers as a special case with $dr/dm = 0$. In cases of axial impellers, equations (2, 3, 5) are respectively

$$\psi_l' = \frac{Z}{\pi\tilde{r}\varphi}\int_{m_1}^{m_2}\frac{\rho}{\rho_2}\frac{\sqrt{2\sigma}\alpha\lambda}{\sin\beta_b}\left(\frac{\bar{w}}{U}\frac{w_s-w_p}{U}\right)^{1.5}dm \quad (13)$$

$$\psi_l'' + \psi_l''' = \frac{-2\epsilon}{\tilde{r}\varphi}\int_{m_1}^{m_2}\frac{\rho}{\rho_2}r\lambda(1+\delta)\sin\beta\,\frac{\bar{w}^2}{U^3}\frac{d\bar{w}}{dm}dm \quad (14)$$

where equation (1) is substituted for v, and the flow rate is expressed as $2\pi\tilde{r}b\varphi U = 2\pi r(\tilde{r}/r)b\varphi U$. That is, $(\tilde{r}/r)b$ is an equivalent blade length. Since $\sigma\bar{w}\sin\beta = \varphi U$ and $\rho/\rho_2 \cong 1$, equation (14) becomes

$$\psi_l'' + \psi_l''' = \frac{\epsilon\lambda(1+\delta_m)}{\tilde{r}/r}\frac{w_1{}^2 - w_2{}^2}{\sigma U^2} \quad (15)$$

If it is further assumed that the blade loading is uniform from the leading edge to the trailing edge, the lift force L of a blade is

$$L = \rho l w_m (w_s - w_p)_m$$

The work input of a blade is related to the theoretical head as $LU\sin\beta_m = (\rho\psi_i U^2/2)\,s\varphi U$. Substituting for L

$$\frac{w_m(w_s-w_p)_m}{U^2} = \frac{s\varphi\psi_i}{2l\sin\beta_m} \quad (16)$$

On the other hand

$$w_1^2 - w_2^2 = w_{1u}^2 - w_{2u}^2 = 2w_{mu}(w_{1u} - w_{2u})$$

and $U(w_{1u} - w_{2u}) = \psi_i U^2/2$. Therefore,

$$w_1^2 - w_2^2 = w_m\cos\beta_m\psi_i U = (\varphi/\sigma)\psi_i U^2/\tan\beta_m \quad (17)$$

Substituting equations (16) and (17) into equations (13) and (15)

$$\psi_l' \doteq \frac{\alpha\lambda\psi_i}{\tilde{r}/r}\sqrt{\frac{\sigma s}{l}\frac{\varphi\psi_i}{\sin^3\beta_m}} \quad (18)$$

$$\psi_l'' + \psi_l''' = \frac{\epsilon\lambda(1+\delta_m)}{(\tilde{r}/r)\sigma^2}\frac{\varphi\psi_i}{\tan\beta_m} \quad (19)$$

Equation (11) becomes

$$\frac{\eta_0 - \eta}{\lambda} = \frac{\alpha}{\tilde{r}/r}\sqrt{\frac{\sigma s\varphi\psi_i}{l\sin^3\beta_m}} + \frac{\epsilon(1+\delta_m)\varphi}{\sigma^2(\tilde{r}/r)\tan\beta_m}$$

$$- \frac{\psi_{h0} - \psi_h}{\psi_i \lambda} + \frac{1 - \eta_0}{\psi_i} \frac{\psi_{i0} - \psi_i}{\lambda} \qquad (20)$$

Comparison With Experiments of Axial Impellers

Seven experimental data out of eight data in [2] are compared with the predictions based on equation (20). One case is excluded because it is an experiment on a turbine rotor. Since the pitch chord ratio at the blade tip is not given in [2], it is simply assumed that $s/l = 1.0$. It is also assumed that the hub tip ratio is 0.6 or the ratio $\bar{r}/r = 0.8$ except the case No. 7, where it is assumed that $\bar{r}/r = 1.0$ because the aspect ratio of the blades is 0.47 and a large hub/tip ratio is expected.

The mean flow angle β_m of the original papers is quoted in [2] except two cases, No. 4 and No. 5. In [2] it is estimated that $\sin \beta_m = 0.46$ for the two cases. Since they are the data at two different flow rates of an impeller, $\sin \beta_m$ must vary with the flow rate. Here it is assumed that $\sin \beta_m = 0.46$ for No. 4 following [2], and $\sin \beta_m = 0.40$ is assumed for No. 5 so that they are proportional to the flow coefficients.

It is necessary to estimate a few coefficients in the equations. They are assumed $\alpha = 0.8$, $\epsilon = 0.9$ and $\delta = 0.3$, identical to those for centrifugal impellers in the last examples. Furthermore, the efficiency is assumed $\psi/\psi_i = 0.9$ and the last two terms in equation (20) are disregarded because of lack of relevant data and also because they are very small for axial impellers with $\lambda < 0.05$ and $0.985 < \sigma < 1.0$.

The decrements of efficiency due to the tip clearance at various values of λ_2 in the literature are reproduced in Fig. 4. These data show that the efficiency drop is proportional to λ_2. For comparison the predicted relationships for those impellers are indicated as lines. Good agreement with the experimental data is observed.

Regarding the data in Fig. 4, the conditions of flow in the impellers are presented in Table 2 together with the predicted efficiency drops and clearance losses which consist of the leakage loss and the loss due to the pressure gradient. Comparison with the experimental data is in the right end column. Fair agreement is observed.

Optimum Tip Clearance

According to the present theory there is no optimum dimension of the tip clearance, because all the losses related to the tip clearance are almost proportional to the tip clearance. In a cascade test, it is demonstrated [10] that the secondary flow along the endwall becomes weak by the leakage through the tip clearance and the overall pressure loss can be smaller as the tip clearance is larger.

Also there is a note [2] which experimentally recommends a tip clearance of ~1-1.5% of the blade span as the optimum, but in all seven cases in Table 2, the efficiency is continuously improved by reducing the tip clearance and in cases of No. 2 and No. 3 the minimum clearance was as small as 0.3% of the blade span. Judging from these data and above discussions, it is not easy to estimate the optimum tip clearance for respective cases, and even if it is determined, it is likely that the optimum clearance is too small to make in practice.

Conclusions

The pressure loss and the efficiency drop based on the tip clearance of impellers are examined and the following items are clarified.

1 The pressure loss due to the tip clearance of an impeller is induced by two types of drag forces: One is induced by the leakage flow through the tip clearance and the other is the force to support a layer of fluid against the pressure gradient.

2 Equations of pressure loss and of efficiency drop due to tip clearance are derived for axial impellers as well as for centrifugal impellers. They are not applicable to turbine rotors.

3 A few empirical coefficients are included in these equations. For the time being they were assumed based on the knowledge of conventional hydraulics. Some of them may be examined based on flow measurement at the exit of impellers.

4 The tip clearance loss and the efficiency drop are almost proportional to the tip clearance ratio at the exit of impellers for $\lambda_2 < 0.1$.

5 Prediction is less accurate at off-design conditions, because incidence loss varies with the tip clearance.

6 Tip clearance losses are predicted for three impellers which have identical specifications. The results clearly show that tip clearance ratio is the most important parameter but it is not the only factor which controls the tip clearance losses.

7 Experimental data with good accuracy are required for critical comparison and improvement of the present method.

8 In order to predict the change of discharge pressure due to tip clearance, a good prediction method regarding the change of Euler head due to tip clearance is required.

References

1 Mashimo, T., Watanabe, I., and Ariga, I., "Effect of Fluid Leakage on Performance of a Centrifugal Compressor," ASME JOURNAL OF ENGINEERING FOR POWER, Vol. 101, July 1979, p. 337.

2 Lakshminarayana, B., "Methods of Predicting the Tip Clearance Effects in Axial Flow Turbomachinery," ASME *Journal of Basic Engineering*, Vol. 92, Sept. 1970, p. 467.

3 Booth, T. C., and Dodge, D. G., "Rotor-Tip Leakage: Part I – Basic Methodology," ASME JOURNAL OF ENGINEERING FOR POWER, Vol. 104, Jan. 1982, p. 154.

4 Wadia, A. R., and Booth, T. C., "Rotor-Tip Leakage: Part II – Design Optimization Through Viscous Analysis and Experiment," ASME JOURNAL OF ENGINEERING FOR POWER, Vol. 104, Jan. 1982, p. 162.

5 Bettner, J. L., and Elrod, C., "The Influence of Tip Clearance, Stage Loading, and Wall Roughness on Compressor Casing Boundary Layer Development," ASME JOURNAL OF ENGINEERING FOR POWER, Vol. 105, Apr. 1983, p. 280.

6 Pandya, A., and Lakshminarayana, B., "Investigation of the Tip-Clearance Flow Inside and at the Exit of a Compressor Rotor Passage: Part I – Mean Velocity Field, Part II – Turbulence Properties," ASME JOURNAL OF ENGINEERING FOR POWER, Vol. 105, Jan. 1983, pp. 1, 13.

7 Lakshminarayana, B., and Pandya, A., "Tip Clearance Flow in a Compressor Rotor Passage at Design and Off-Design Conditions," ASME JOURNAL OF ENGINEERING FOR GAS TURBINES AND POWER, Vol. 106, July 1984, p. 570.

8 Eckardt, D., "Detailed Flow Investigations within a High-Speed Centrifugal Compressor Impeller," ASME *Journal of Fluids Engineering*, Vol. 98, Sept. 1976, p. 360.

9 Ishida, M., and Senoo, Y., "On the Pressure Losses due to the Tip Clearance of Centrifugal Blowers," ASME JOURNAL OF ENGINEERING FOR POWER, Vol. 103, Apr. 1981, p. 271.

10 Dean, R. C., "Influence of Tip Clearance on Boundary Layer Characteristics in a Rectilinear Cascade," *MIT Gas Turbine Lab. Report*, No. 27-3, 1954.

Investigation of a Tip Clearance Cascade in a Water Analogy Rig

J. A. H. Graham
Staff Aerodynamicist.
Pratt and Whitney Canada, Inc.,
Longueuil, Quebec, Canada J4K 4X9

The tip clearance flow region of high-pressure axial turbine blades for small gas turbine engines has been investigated in a water flow cascade. The blade model features variable clearance and variable endwall speeds. The cascade is scaled for Reynolds number and sized to give velocities suitable for visualization. Pressure profiles were measured on one blade, and correlated with the visualization. Unloading is found to be a major feature of the pressure field at both tip and midspan, and is intimately connected with scraping effects and the behavior of the clearance vortex. Some initial hot-film velocity measurements are also presented.

1.0 Introduction

Tip clearance flows are an important source of turbine energy losses. Major efforts have been expended in investigating these flows from an experimental and theoretical point of view, partly at least with the idea of inventing modifications to blades or shrouds to reduce energy losses. Our own efforts have hitherto concentrated on cold flow rig tests [1], in which efficiency could be measured against changes in hardware configuration.

Indeed the bulk of the research effort in this field has consisted of efficiency measurements on engine hardware. This is virtually as true today as in 1954 when Rains [2] noted the fact in his paper on clearance flow visualization in a rotating compressor water rig. Theoretical work has ranged from the geometric correlations of Ainley and Mathieson [3, 4] and others, through the body of theory based on the lifting line theory of Lakshiminarayana and Horlock [5, 6, 7], to detailed analysis of the clearance gap flow itself [8]. Detailed modeled experiments of the tip clearance flow have also appeared in the literature [9, 10].

Our investigations were prompted by certain baffling aspects of the cold flow turbine rig work, and by initial work on a detailed clearance gap flow analysis at P&WC that showed physical insight was lacking in certain areas. In particular the question of unloading toward the blade tip, and its dependence on clearance, needed quantification. Related to this is the effect of the clearance vortex on the suction surface pressure field, on the flow field in general, and on energy losses. There was also the question of frictional forces on the clearance flow itself. Although there is evidence in the literature [9, 10] that clearance flows at large but realistic clearances are substantially potential, there was still a need to investigate scraping and frictional effects, especially at tight clearances. Thus we decided to include relative motion of blade and endwall in the experimental design. We also desired that the experiments could extend to the design of blade tip and endwall devices to reduce clearance losses. Accordingly it was decided to press the then-new Water Flow Analogy Rig into service, using cascade models with water as the working substance, in order to take advantage of the relative ease of visualizing flows in water at low speed. At the same time it was decided to develop pressure and velocity measuring techniques to quantify the investigation.

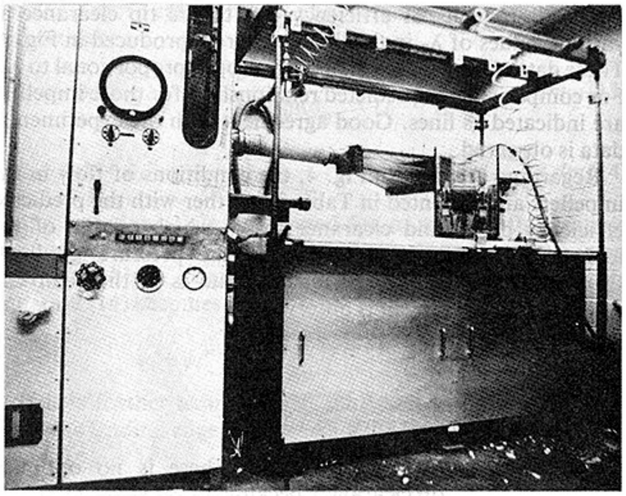

Fig. 1 Water flow analogy rig

The Water Flow Analogy rig had already been developed for investigating highly complex flows that are not amenable to purely analytical treatment. It was designed for Reynolds number modeling of gas flows on the scale of our own small gas-turbine engine parts and is intended both as a research tool and as a means for optimizing the design of hardware in which a fluid flow is of critical importance.

The first research job for the rig is the present investigation into the mechanics of tip leakage flow. It was decided that the working section should consist of transparent, quasi-two-dimensional plexiglass cascades having four channels separated by three blades with variable tip clearance. This cascade flow is analogous to the gas flow in the blade tip and outer shroud region in the engine. The wall of the test section which corresponds to the shroud in the engine consists of a moving belt which simulates the relative motion of blade tip and shroud. Different cascades, corresponding to different

---

Contributed by the Gas Turbine Division and presented at the 1985 Beijing International Gas Turbine Symposium and Exposition, Beijing, People's Republic of China, September 1-7, 1985. Manuscript received at ASME Headquarters May 31, 1985. Paper No. 85-IGT-65.

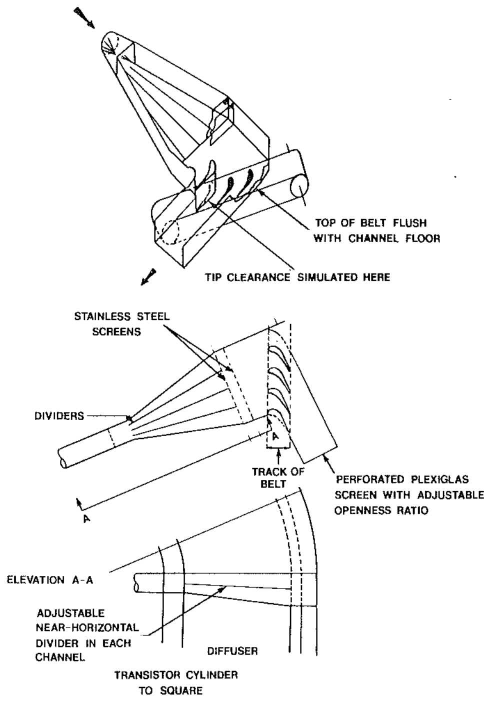

Fig. 2 Tip clearance model

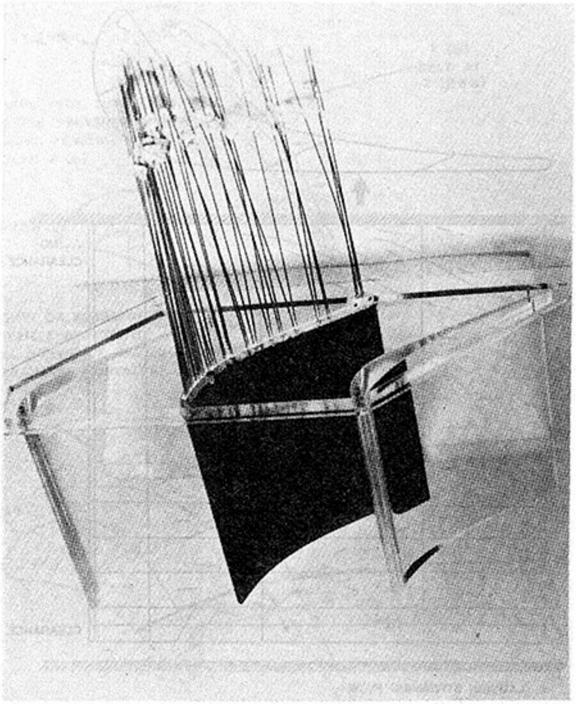

Fig. 3 Cascade with instrumented blade

blade designs, can be inserted in the test section, while the surface treatment of the belt can simulate various shroud liner geometries.

Investigations consist of visual observations on the blade tip and shroud region for blades of different tip profile; pressure measurements at tip and midsection on one instrumented blade; and mean velocity measurements with constant temperature anemometer using hot-film probes. Experiments with each cascade are shaken down with a stationary endwall and a clearance gap typical of engine practice. Configurations are then varied to include a variety of clearance gaps and endwall speeds, including the speed that correctly models the engine gas velocity triangles and blade speed.

2.0 Description of Rig

2.1 General Description. The water rig (Fig. 1) consists of a recirculating water system. Water is pumped from a storage tank (lower right) into a header tank (upper left) from which it runs through the test section (upper right) and returns to the storage tank. The photograph shows a blade cascade installed in the working area. In practice a wide variety of internal flow model or open water tables can be installed. Two pumps provide a maximum water flow of 260 gal/min delivered at the top of the auxiliary tank. A maximum head of 20 ft is available. All parts of the system in contact with water are made of plastic, fiberglass, or stainless steel, to avoid corrosion. The pumps are designed for slurry and can easily cope with polystyrene particles used for flow visualization.

A typical cascade (Fig. 2) consists of five plexiglass blades, each 6.5 in. long, having throughout their length a cross section modeled on a blade tip cross section. The blades are suspended vertically, with the simulated tip clearance at the floor of the cascade. The cascade duct, and the blades, are made of transparent plexiglass. Flush with the cascade floor, beneath the blades, runs the smooth rubber belt which simulates blade-shroud relative motion. This is stretched between pulleys which are driven by a compressed air motor with widely variable speed. The duct is operated full of water so that the flow in the blade channels has solid borders, and the secondary flows are in the correct direction. The scale of the model is eight times prototype, at the tip section. With full flow this gives a reasonable simulation of the engine Reynolds number, about 1×10^5, thus ensuring that dynamic effects are modeled. Compressibility effects are not modeled. This, with the partial two-dimensional nature of the model arrangement, is the main shortcoming of the model.

2.2 Observations and Measurements

2.2.1 Flow Visualization. Two principal observation techniques were used. Firstly, the flow was seeded with neutrally buoyant polystyrene balls, which were selectively illuminated with a planar beam of light in different directions. The planar beam of light was produced by a mercury vapor lamp, enclosed in a metal reflector box from which the ozone produced by the light was withdrawn to outdoors by an extractor fan. This airstream was designed also to cool the 1.0-kW lamp. The light that leaves the box passes through collimating slits and a cylindrical lens, thus creating a near parallel (but focusing) beam of light for up to 12 or 24 in. from the lens.

Secondly, details of the flow were highlighted with dye streaks, delivered to desired points in the flow by easily positioned flexible hypodermic tubing. Tufts of wool were also, at times, taped to wall surfaces.

2.2.2 Pressure Measurements. One of the blades (our R15) was instrumented with pressure tappings (Fig. 3). Ten tappings were made on each surface at both midspan and at 0.125 in. from the tip. The pressure tubes are made of hypodermic, molded into a blade made of Devcon, for which one of the plexiglass blades was master. The blade is carefully lacquered so that the tapping holes are correctly shaped. The 40 pressure lines are then connected, via swagelock connections and 1/16-in.-dia. nylon flexible tubing, to a 48 Channel Scanivalve system. Eight channels, used for checking, are spread among the other 40. A very sensitive transducer is necessary to measure the pressure differences generated by a water flow of only 1 to 2 ft/s. A Druck PDCR22 was chosen. It is completely compatible with water.

All the tubing is kept full of Merriam fluid, completely

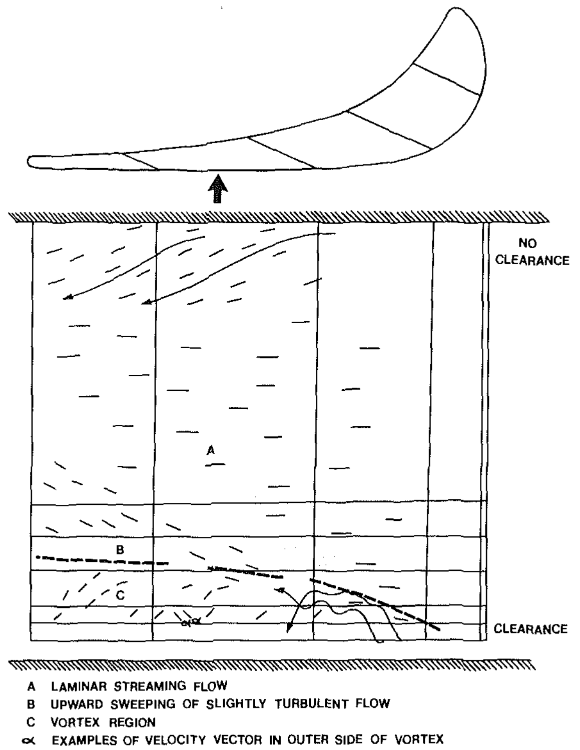

Fig. 4 Suction surface flow distribution with clearance of 2.5 percent at zero belt speed

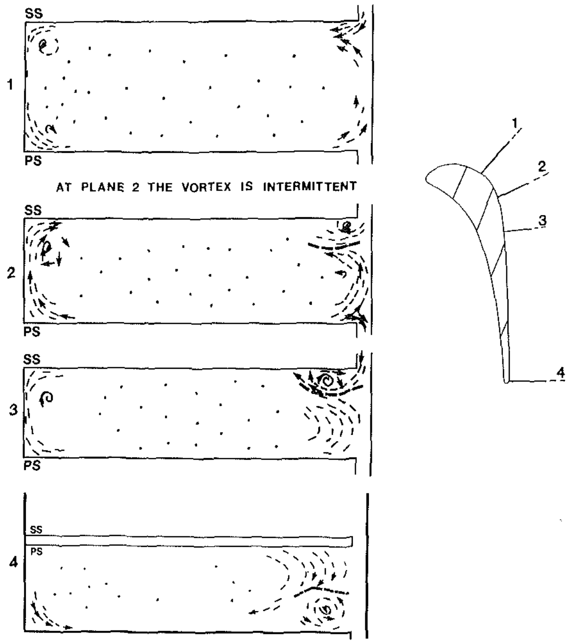

Fig. 5 Secondary flows in channel between blades with clearance of 2.5 percent at zero speed

bubble free, during measurements. This acts as a surfactant which prevents air bubbles from attaching themselves to tubing walls. The bleeding process is difficult and tedious. Much development time was spent in refining the system to make bleeding effective. Thicker, and opaque tubing was discarded, and a system was arrived at having constant tube cross section, and loose enough to allow bubble hunting through the system. It was found necessary to replace the fluid in the system about every two months in order to clear coagulants that form in Merriam fluid, imparting to the measuring system a most unwelcome hysteresis. There is a Merriam-fluid:water interface at the pressure tappings or in the tubing nearby when the system is running. Merriam escape into the general water system must be limited because its excessive presence causes air entrainment and bubbling, which prevents accurate pressure measurements, and is detrimental to hot-film velocimetry.

2.2.3 Hot-Film Anemometry. A simple system of hot-film anemometry was developed for mean velocity measurements in the cascade channels and in the clearance gap. The bridge anemometer is a DISA 56C01 (multichannel) rack system constant temperature anemometer with a 56N221 mean value unit, consisting of DVM, integrator, and filter. Signals are not linearized. Instead, calibration curves are set up by running the CTA in the calibration system described later. At the low velocities prevalent in our rig the calibration curves diverge somewhat from King's Law, and thus the normal linearizer, which assumes that King's Law is in operation, cannot be used. It is, in any case, unnecessary when analogue measurement of turbulent quantities is not being performed.

3.0 Flow Visualization

3.1 General. Two radically different types of tip section were investigated: two examples of the first, fairly thick blade ($t/c = 0.175$) and one of a "squealer" tip ($t/c = 0.042$). One of the thick blades was instrumented for pressure measurements, as will be reported later on. These radically different blade sections are considered to represent extremes in the range of possible shapes in tip sections, at least for our small gas turbine high-pressure blades.

In order to model Reynolds number (about 10^5, based on chord) the flow is run between 80 and 240 gpm, with an 8:1 enlargement of scale to keep velocities low enough for visualization. The test section is arranged with outer shroud and clearance gap at the floor, and the cascade suspended inside the duct. Thus the gravity-induced pressure distribution in the water model is in the same direction as the centrifugally induced pressure gradient in the engine, and is close to the right magnitude. As the model flow is incompressible, Re simulation cannot extend to all parts of the flow field; but a reasonably close approximation can be achieved.

3.2 Observations. With water flux set to simulate Re, the endwall was run at various speeds: stationary, for preliminary shakedown and to establish a "standard" case; the correct speed for engine velocity triangle simulation (EES); and also one faster speed, about double EES, and a slower one, about half EES.

3.2.1 Thick-Tipped Blade. Figure 4 shows the suction surface flow, and Fig. 5 the flows viewed in planes crossing the blade-to-blade channel. Endwall is stationary in each case. The short markings show local flow vectors, while the long arrowed lines are typical streamlines. The heavy broken line marks the vortex boundary.

The secondary flow is well developed in Fig. 4 and can be seen as a convergence in the flow direction along the suction surface at hub and tip. The vortex caused by the efflux of clearance gap flow into the channel is quite obvious near the tip of the blade, toward the trailing edge. The vortex begins about 1/3 of the way along the curve of the suction surface. The cross-sectional views (Fig. 5) show this vortex, with the secondary vortices, as they develop downstream. There is no vortex in the leading part of the suction surface, as a threshold strength appears to be necessary for the overshoot and rolling up process necessary to form it.

3.2.1.1 Variation of Clearance. Figures 6 and 7 form a digest of plan views of flow in the clearance gap at a variety of clearances up to 2.5 percent of equivalent blade span, which is the span that a three-dimensional model of the entire blade at 8:1 scale would have. This clearance equals 3.85 percent of the

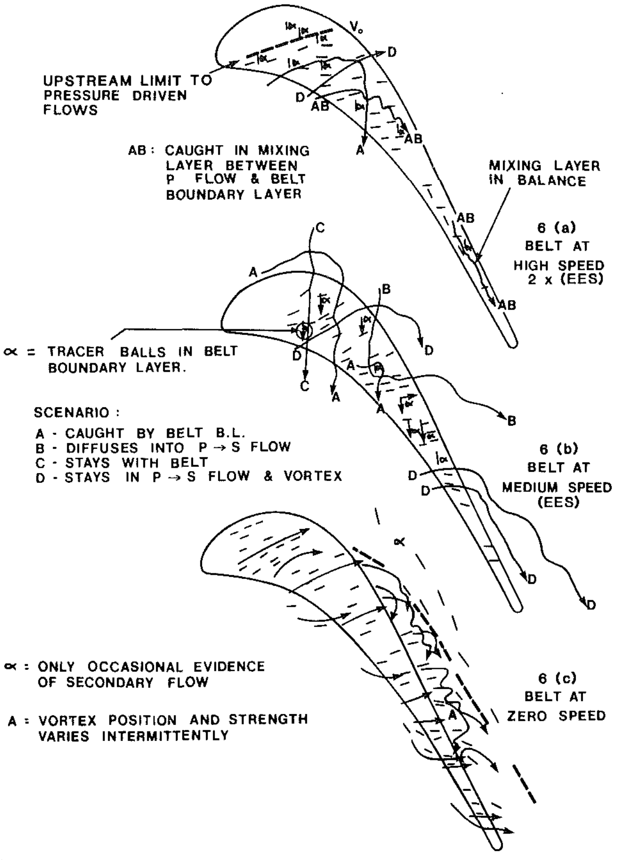

Fig. 6 Tip clearance flow comparison with maximum clearance of 2.5 percent at various speeds

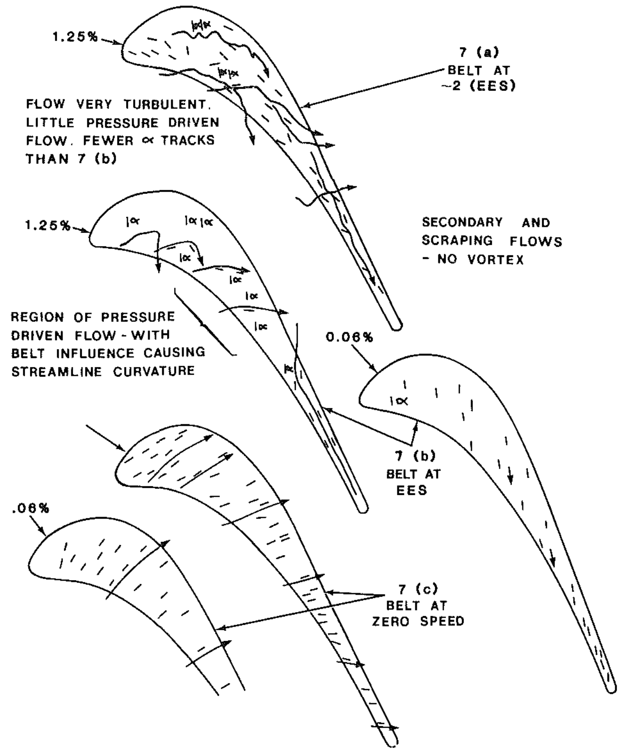

Fig. 7 Tip clearance flow comparison with clearance of 1.25 and 0.6 percent at various speeds

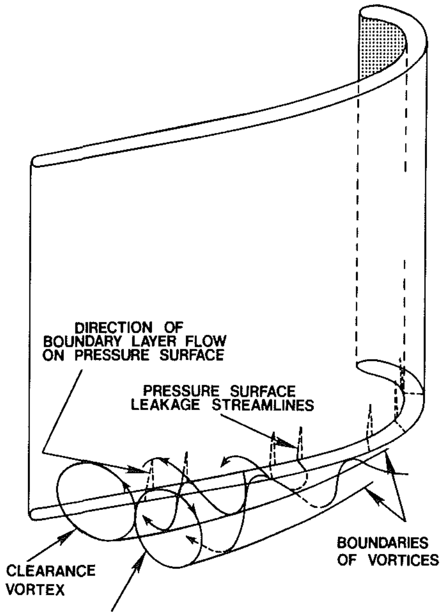

Fig. 8 Clearance and passage vortices

cascade blade span, and 3.45 percent of blade true chord at the tip. Clearance is given in terms of equivalent span throughout the paper. Speeds of endwall vary also. If we look through Figs. 6 and 7 we see that at zero endwall speed leakage flow tends toward the normal to the pressure surface, as clearance is reduced. Viscous domination of the flow increases, and the influence of the entry velocity to the gap reduces.

With the endwall in motion, leakage flow is reduced as clearance is reduced, and the belt boundary layer occupies a relatively increasing proportion of the gap space. The pressure-driven clearance flow is turned toward the (engine) axis and is eventually drawn almost parallel to the direction of the moving belt. At this separation (0.6 percent) there is no leakage flow. At 1.2 percent there is some leakage flow, but its vortex is very weak. At greater belt speeds vortex behavior is qualitatively similar, but equivalent phenomena occur at greater separation. At higher speed there is also more mixing between the two flow regions in the clearance space. Turbulence is more energetic. The reduction of clearance flow (at any belt speed) is nonlinear, and no simple formulation is likely.

At engine equivalent speed (EES) the vortex onset position moves downstream as clearance is reduced and disappears between 1.2 and 0.6 percent clearance. At these clearances, there is a region of reduced clearance flow in the trailing edge region. This increases in size as clearance is reduced. With belt at EES, and a clearance of 0.6 percent, there is no pressure-driven clearance flow at all.

3.2.1.2 Speed Variation. In the clearance gap we have observed, as outlined above, that the pressure-driven clearance flow and the endwall boundary layer act in opposition when the endwall is moving. At any given clearance increasing the belt speed reduces the clearance flow quantity, and at tight clearances (1.2 or 0.6 percent) leakage flow can be cut off by increasing the belt speed.

3.2.2 Implications. At tight clearances, increasing the speed has roughly the same effect as reducing tip clearance. It reduces or cuts out the leakage flow, by changing its direction and reducing the leakage layer thickness. This has implications in the desirable velocity triangle design at the tip section of a blade. It confirms the notion that reducing loading at the tip will reduce clearance losses, by making use

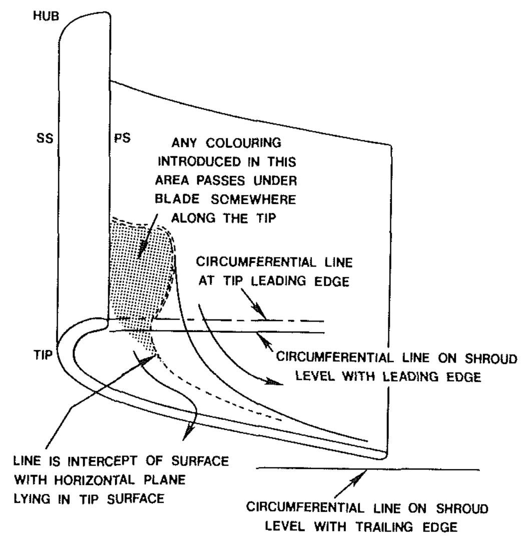

Fig. 9 Leakage line on PT6 blade

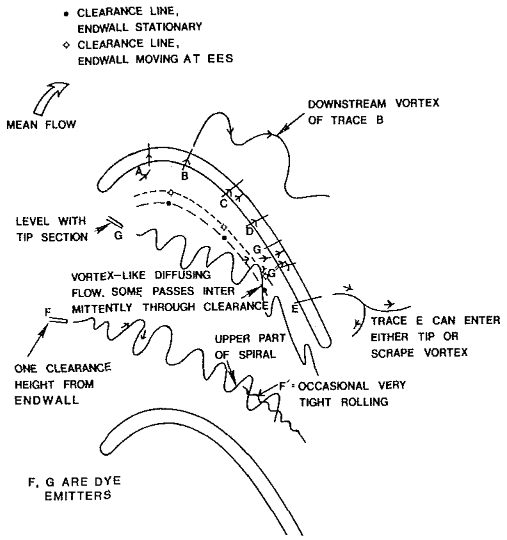

Fig. 10 Clearance gap flows for moving endwall, gap 2.5 percent span

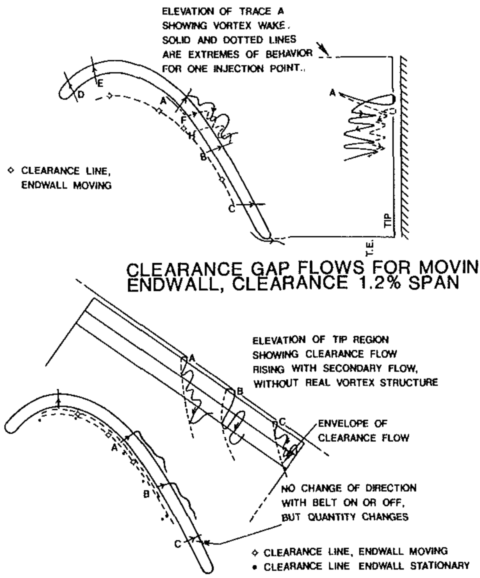

Fig. 11 Clearance gap flows for moving endwall, clearance 0.6 percent span

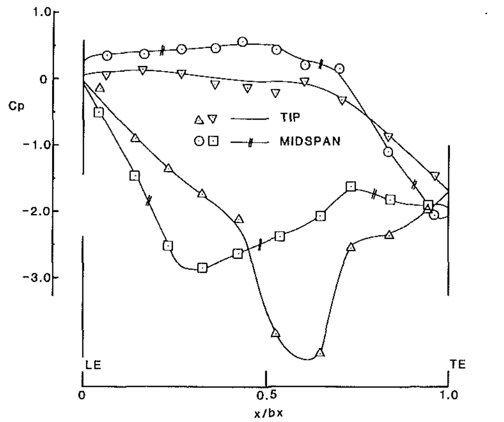

Fig. 12 Pressure profiles around blade, clearance 2.5 percent, endwall stationary

of the endwall scraping effect. We return to this point in section 4.3, after discussing the pressure measurements.

For purposes of leakage loss control, it appears that leakage reduction devices are needed only in the central part of the blade section, at least for the wide section type of blade we have here. Efforts should probably be focused on annulling the leakage vortex, for several reasons. The leakage vortex can cause separated flow on the suction surface near the tip, while its enhancement of pressure loading at the tip section increases leakage flow. It disrupts channel flow and delivers off-design flow to downstream engine stages. Leakage flows too weak to form a vortex would appear to cause disproportionately reduced losses.

3.2.2 Thin-Tipped Blade. Similar observations were performed on a thin-tipped blade cascade representing a PT6 high-pressure turbine blade tip section. The model blades were formed of curved plexiglass sheet of uniform thickness, with correctly rounded leading and trailing edges. Belt speed and clearance were varied as with the thick-tipped blade.

Figures 8 and 9 show the passage vortices schematically, and define the clearance lines for the thin blade. The broad patterns of channel flow resemble those outlined above; there are however marked differences in the tip leakage region. As Figs. 8-11 show, the blade tip is so thin that the leakage flow passes directly, in virtually straight lines, normal to the pressure surface. The short trajectory of pressure-driven flow in the clearance gap means that it is hardly influenced by the tip and endwall boundary effects, except very close to those boundaries.

3.2.2.1 With the Moving Belt. The thin blade design is a compromise design in which the contours are quite a departure from channel design requirements. The channel flow is expected to be less than ideal, and the cascade flow shows this in Fig. 10. Near the pressure surface, in the deeply concave section, there is stagnant flow on the verge of separation. Surface flow descends almost vertically (that is, almost radially outward in the engine situation) before entering the clearance gap. Midstream flow markers confirm the existence of the stagnation region.

Rolled up secondary flow vortices are made strikingly visible by the dye streak technique in this channel. These intermittently roll up and the vortex line stretching as the flow leaves the stagnation region produces exceptionally rapid, tightly rotating flow.

The straight, near normal to pressure surface, tip gap flows retain these characteristics from the leading edge for about 60 percent of the blade chord. After that there is a slowly increasing divergence from the normal toward the trailing edge, reaching perhaps 30 or 40 deg. These flow angles remain the

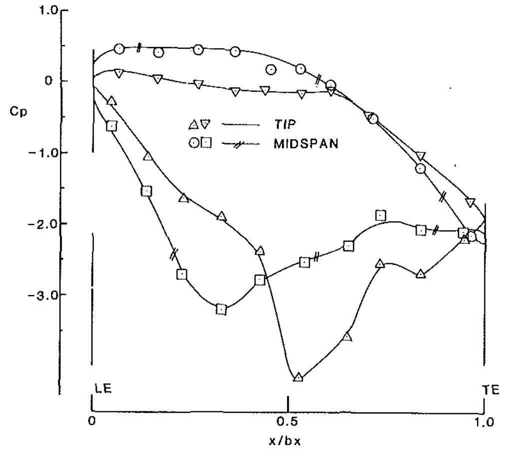

Fig. 13 Pressure profiles: clearance 1.8 percent, endwall stationary

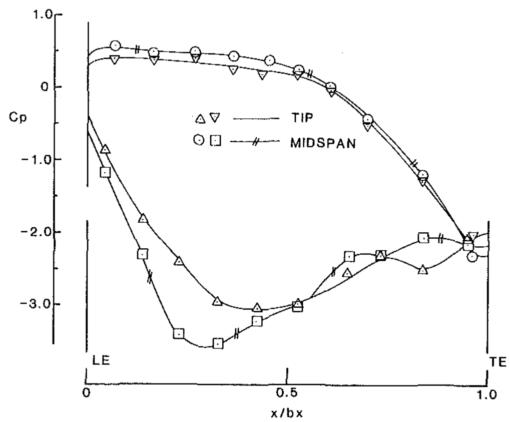

Fig. 15 Pressure profiles: clearance zero (unsealed), endwall stationary

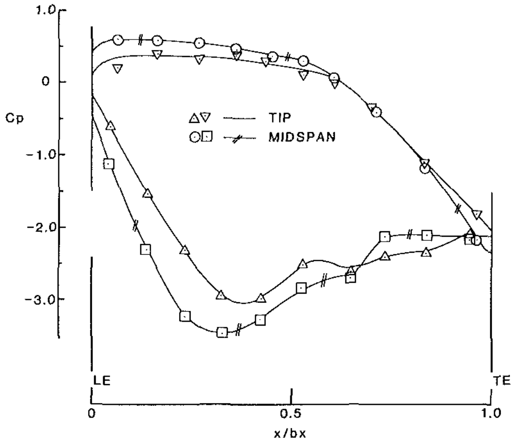

Fig. 14 Pressure profiles: clearance 0.6 percent, endwall stationary

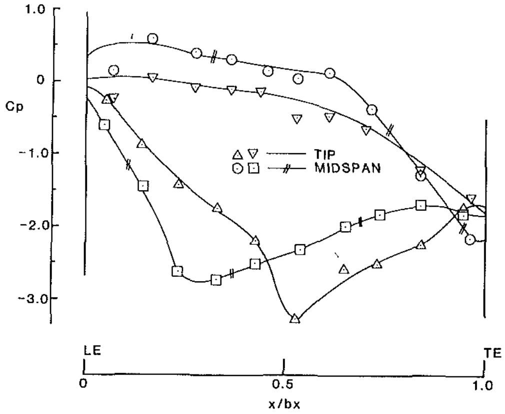

Fig. 16 Pressure profiles: clearance 2.5 percent, endwall at EES

same at all tip clearances, for both stationary and moving belts. Thus the pressure difference between the blade surface overwhelms all surface frictional effects, in the clearance range used here, for the main clearance flow. At the smallest clearance, 0.6 percent, the pressure-driven clearance flow is reduced. The leakage lines in Figs. 10 and 11 show how leakage flow is reduced as clearance is reduced. Pressure-driven clearance flow direction is not affected.

The foregoing suggests that the thin-tipped blade will be unresponsive to schemes that seek to reduce leakage flow by introducing additional drag to the clearance gap walls. This has already been observed in cold flow turbine rig efficiency measurements.

A thick R15 blade was instrumented with pressure tappings on both pressure and suction surfaces at blade tip and midspan. These 40 tappings are connected through the tubing system to the scanivalve and pressure transducer outlined in section 2.2.2. After a lengthy shakedown period excellent reproducibility of data was achieved. With air rigorously excluded from the system the scatter of any single piece of data is very close to Gaussian and dependable results can be obtained by averaging over a sufficiently large sample. While there is some damping of random pressure fluctuations in the approximately 1-m-long tubing, there is only a short integration time in the transducer-D.V.M. system. Averaging, then, is achieved by accumulating a large sample at each data point.

Data are taken sequentially, with the 40 pressure measuring points interspersed with eight constant "check" pressures. Thus any unexpected changes can be detected as they occur, and spoiled data edited out of the record. As many as 20 records at any given flow condition are collected, and some data points repeated at the end of an experiment to ensure there has been no drift.

As before, data are collected with the endwall stationary, at engine equivalent speed, and at a speed nearly twice this. Clearance gap is varied between zero and 2.5 percent of equivalent blade span. A selection of these pressure plots is presented in Figs. 12–18. In each the ordinate is pressure, while the abscissa is positioned along the direction of the engine axis. Four pressure contours are depicted: one each at midspan and at the tip on the pressure and suction surfaces.

4.1 Endwall Stationary. Let us first consider the cases with stationary endwall. Figure 12 has large clearance (2.5 percent). In the forward part of this blade the unloading is quite evident and appears to be as great as 50 percent. Perhaps surprising at first sight, the reversal of this unloading in the downstream part of the suction surface is attributable to the powerful vortex that sits off the suction surface at the tip. As the line of pressure tappings is imbedded in the vortex the pressure will be significantly lower than the channel flow alone would lead us to expect. Now consider Fig. 14. Here the clearance gap is 0.6 percent and the leakage flow, too weak to form a vortex, merely joins the secondary flow creeping up the suction surface away from the tip (section 3.2.1.1, Figs. 6 and 7). The vortex pressure signature on the suction surface is virtually absent. In the forward part of this blade unloading is reduced to about 25 to 30 percent, undoubtedly because of the severely restricted clearance flow. A view of Fig. 15 takes this one step further. Here there is no clearance gap, and the pressure surface profiles at tip and midspan are virtually coincident. There is still unloading on the suction surface which is associated with the secondary flow. An intermediate

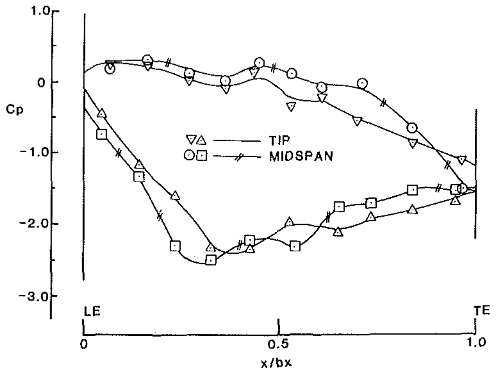

Fig. 17 Pressure profiles: clearance 2.5 percent, endwall at ~ x EES

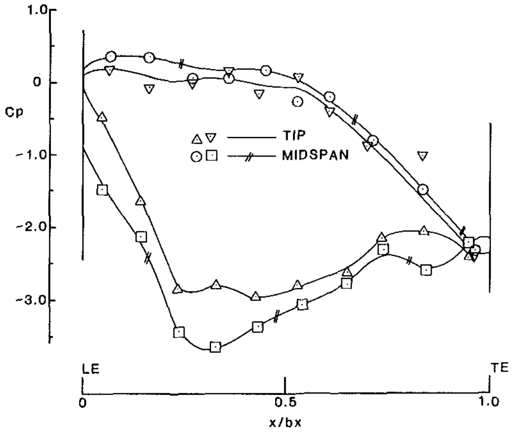

Fig. 18 Pressure profiles: clearance 0.6 percent, endwall at EES

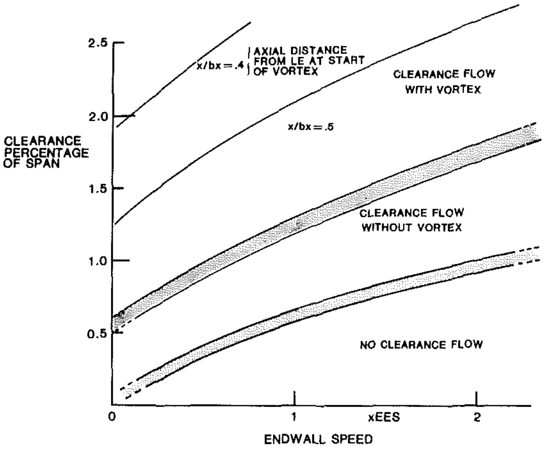

Fig. 19 Clearance vortex flow regimes

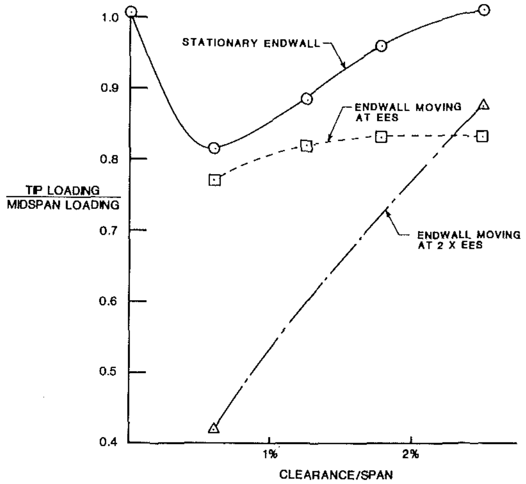

Fig. 20 Ratio of loading at tip to midspan

case – Fig. 13 – for 1.8 percent clearance is very similar to the 2.5 percent clearance case, though milder both in its unloading in the forward part of the blade and in the pressure drop caused by the clearance vortex.

An examination of the midspan pressure curves in Figs. 12–15 shows that unloading effects are apparent at midspan as clearance is increased. This is to be expected as midspan is less than half a blade chord from the tip.

4.2 Endwall in Motion. Movement of the endwall affects flow and pressure distributions most strongly at small separations (section 3.2.1.1). Thus in Fig. 16, which shows the endwall at engine equivalent speed, at 2.5 percent separation, the pressure distribution and unloading are basically similar to Fig. 12, where the endwall is stationary. There is however a significant reduction in the vortex strength, demonstrated by the reduced pressure effect at the tip, toward the trailing edge. Further increase of endwall speed, to nearly double engine equivalent, causes further, more striking change, as seen in Fig. 17. Now the foward unloading is reduced greatly, and the vortex strength is reduced to vanishing. This corroborates the visualization work, reported above. The reduction in overall loading, which is stronger at the midspan section, is probably due to the high scraping effects and the circulatory channel motion that it causes.

Engine equivalent speed at 0.6 percent clearance is demonstrated in Fig. 18. The difference to Fig. 14 is slight. Forward section unloading is reduced, and rear section unloading increased, at least on the suction surface. Visualization shows that at this separation, with endwall moving, there is no clearance flow at all. The secondary and scraping flows however tend to stagnate on the tip suction surface, thereby raising the pressure above the stationary wall case. A doubling of wall velocity causes significant change only in the suction surface tip pressures. These are raised to double or triple the differences at EES, due to the enhancement of the scraping effect.

4.3 A Summary of Clearance Flow Regimes. From the visualization work and the corroboration provided by a pressure profile data a somewhat speculative plot of clearance vortex flow regimes has been prepared (Fig. 19). Clearance and endwall speed are the variables. The boundaries between regimes of clearance vortex existence, and clearance flow without apparent vortex, are broad hatched regions to emphasize the fact that no sharp transitions of behavior are observed.

4.4 Tip Loading as a Function of Clearance and Endwall Speed. Figure 20 illustrates the dependence on clearance of the ratio of tip loading to midspan loading at different endwall speeds. For stationary endwall this ratio is lowest for a clearance of about 0.6 percent, where the tip loading effect of the clearance vortex is absent. As the vortex builds up in strength at higher clearances, tip unloading is reduced near the trailing edge until tip and midspan loading are equal at 2.5 percent clearance. At engine equivalent speed, the curve follows the same trend, but with lower values of the ratio of loading because the vortex is weaker at any given clearance. At double engine equivalent speed the extreme tip unloading caused by scraping effects gives a very low value (0.42) for the loading ratio at a tight, 0.6 percent clearance.

5.0 Velocity Measurements With Hot-Film Anemometer

Velocity measurements have so far been restricted to the

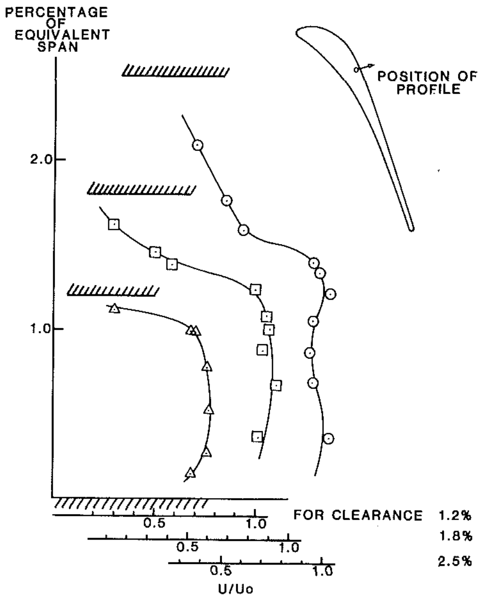

Fig. 21 Velocity in clearance gap

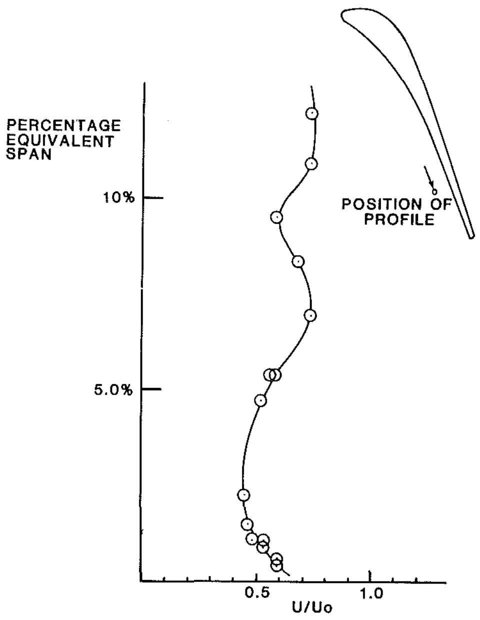

Fig. 22 Channel velocity near pressure surface

case of stationary endwall. Attention has been focused on making velocity profiles in the blade-to-blade channel and in the clearance gap itself. Central to the question of measuring velocity is the question of flow direction and orientation of the probe. In a parallel homogeneous flow, if the probe is aligned with the flow (that is, the sensitive element is normal to velocity direction), the anemometer registers maximum output voltage. Thus if the probe is oriented to give maximum output, we have found the flow direction. However, sensitivity to small deviations from flow direction is poor – far less than with a cosine law – and our cascade flow is highly nonhomogeneous. Thus we need the guidance of the visualization study to help setting up profile traverses. Although it is difficult to accurately determine direction with the anemometer probe alone, this does not adversely affect accuracy in the measurement of speed, because of the abovementioned insensitivity.

Calibration is carried out by running the probe and anemometer, with identical circuitry and overheat setting, in a small rig which consists of a 0.5-in. tube, 20.0 in. long, fed from the main test section, and discharging into a small rectangular reservoir with a weir. The probe is placed on the axis of the pipe at its exit into the reservoir. A turbulent velocity profile is assumed, as the pipe flow is turbulent over the range of operation, with a fine netting at its entry plane. The DISA anemometer is always set, for calibration and routine operation, at the same resistance, one that gives slightly more than 10 percent overheat for a water temperature of 70°F. The water temperature always rises slowly during operation, so a family of calibration curves was drawn up, each for a different water temperature. When operating, temperature is taken at the time each anemometer output is recorded. Frequent reference is made to standard velocity in the channel, to detect calibration drift from causes other than temperature change. Keeping the probe free of bubbles is sufficient to ensure calibration stability.

At the present time anemometry work has concentrated on clearance areas with stationary endwall. Figure 21 shows velocity profiles in the most active part of the clearance gap, close to the suction surface. Direction is as shown in the figure. At the greatest separation, there is a region of high velocity ($U/U_0 = 0.93$ to 1.06, where U_0 is average oncoming velocity) in the lower half of the channel, and an extensive upper area moving more slowly ($U/U_0 = 0.25$ to 0.65). This area is in the wake of the large entry bubble observed just inside the edge between the pressure surface and the tip surface. It is generally extensive enough at 2.5 percent separation to account for the size of this wakelike area. It should be noted that the channel flow in the clearance will be quite undeveloped, with very thin boundary layers on the bounding surfaces. These boundary layers are undoubtedly laminar, and in a typical fetch of 0.4 in. in the middle of the blade would have Re = 2000, and δ^*, based on a laminar profile, of about 0.01 in. The probe cannot reach this close to the wall because of its wedge-shaped substrate, so the boundary layer of the clearance flow cannot be detected with the present equipment.

As the clearance gap is reduced to 1.9 from 2.5 percent, the extent of the bubble-wake region is significantly reduced, from 1.0 to 0.5 percent of equivalent span, with little change to the speed or extent of the main potential flow region. At 1.2 percent separation the wake region is much reduced in extent, and the main region slightly reduced in speed.

A vertical profile in the blade-to-blade channel, in Fig. 22, gives a rather intriguing profile. In the two-dimensional cascade one might at first sight expect a constant velocity, near the floor; however, there is a marked reduction in velocity as the secondary flow sweeps the slow moving pressure surface flow into the position of the probe. This effect apparently abates before the wall boundary layer is felt.

6.0 Conclusions

Water model cascade tests have yielded, so far, much physical insight into tip clearance physics. Measurements of pressure and velocity in these same flows, at first doubtful because of the low water velocities, have proved successful, and capable of yielding detailed information about flow quantities, even in small-scale regions of the flow.

It is clear that unloading is a major feature of the pressure field at both tip and midspan and is strongly dependent on the clearance, especially when reduced below 1.5 percent span. The clearance vortex, because of its deleterious influence on the channel flow and on downstream engine stages, appears to be a major cause of clearance losses, at clearances greater than about 1.25 percent span.

We are now at the point of being able to correlate clearance flux with pressure loading and clearance height. This will have a major impact on our detailed clearance gap analysis.

The visualization work especially shows that tip or shroud treatments intended to reduce clearance losses for any given clearance gap height can be localized in the central region of the blade. If such a device is just adequate to annul the clearance vortex, without removing the clearance flow completely, the best tradeoff between weight and/or complexity of the device, and efficiency improvement, will probably have been obtained.

Such efficiency improvement is most likely to be obtained on rather thick blades, indicating that minishrouds (winglets) may be desirable, especially for thin blades.

Progress to date indicates that further research should be directed toward blades with minishrouds and recessed tips, and toward various types of shroud treatment.

Acknowledgments

It is a pleasure to acknowledge the guidance of Mr. Ulo Okapuu, who instigated tip clearance research and the application of water analogy experimentation to turbine technology at P&WC. Some of the flow observations were made by Nader Pezeshkzad, who developed the ink streak visualization system.

References

1 Patel, K. V., "Research on a High Work Axial Gas Generator Turbine," SAE Paper No. 800681, 1980.

2 Rains, D. A., "Tip Clearance Flows in Axial Flow Compressor and Pumps," Cal. Inst. Tech. Rept. 5, June 1954.

3 Ainley, D. G., and Mathieson, G. C. R., "An Examination of the Flow and Pressure Losses in Blade Rows of Axial Flow Turbines," R&M 2891, Mar. 1951.

4 Ainley, D. G., and Mathieson, G. C. R., "A Method of Performance Estimation for Axial Flow Turbines," R&M 2974, Dec. 1951.

5 Lakshminarayana, B., and Horlock, J. H., "Leakage and Secondary Flows in Compressor Cascades," Min. Tech. R&M 3483, 1965.

6 Lakshminarayana, B., and Horlock, J. H., "Tip Clearance Flow and Losses for an Isolated Compressor Blade," Min. Tech. R&M 3316.

7 Lakshminarayana, B., "Methods of Predicting the Tip Clearance Effects in Axial Flow Turbomachinery," ASME *Journal of Basic Engineering*, Vol. 92, 1970.

8 Wadia, A. R., "Numerical Calculations of Time Dependent Three-Dimensional Viscous Flows in a Blade Passage With Tip Clearance," AIAA Paper No. 83-1171.

9 Booth, T. C., Dodge, P. R., and Hepworth, H. K., "Rotor Tip Leakage: Part I—Basic Methodology," ASME JOURNAL OF ENGINEERING FOR POWER, Vol. 104, No. 1, pp. 154-161.

10 Wadia, A. R., and Booth, T. C., "Rotor Tip Leakage: Part II—Design Optimization Through Viscous Analysis and Experiment," ASME JOURNAL OF ENGINEERING FOR POWER, Vol. 104, No. 1, pp. 162-169.

F. Sugeng

K. Fiedler

Hochschule der Bundeswehr,
Hamburg

An Experimental Investigation Into Unsteady Blade Forces and Blade Losses in Axial Compressor Blade Cascade

The unsteady flow problem in the axial compressor has been simulated in windtunnels by means of high-speed rotating cylinders upstream of the blade row. To obtain the dynamic changes in the flow properties 20 high-response pressure transducers and 20 high-response hot-film, which are embedded at the surface of the selected blade, have been used in connection with a periodic sampling and averaging technique in digital data acquisition and reduction. The fluctuating forces and the fluctuating drags acting on the blade due to passing wakes shedding through the blade row are carried out.

1.0 Introduction

The unsteady nature of fluid flows in the stages of turbomachines has received considerable attention in recent years. As is well known, the unsteadiness in the flow is important with respect to:

- the excitation of blade vibrations
- noise generation
- stage efficiency and internal energy exchange.

The unsolved problems of the unsteady flow in the stages of turbomachines are partly due to the unsteady flow character caused by relative motion of rotor and stator blades of turbomachine. Actually, the unsteady flow in turbomachines can be broken down to the following effects:

1. The circulation effect arises because of the presence of circulation about the blade;
2. the blade thickness effect arises from the presence of the potential flow field about the blade;
3. the wake effect arises because of the wake shed by the upstream blade row.

The unsteady flow problem is extremely complicated and has not been solved up to now. Some theoretical studies have been published for the unsteady flow problems [1–4] and experimental studies have been done by some authors [5–8]. However, due to limiting assumptions in the theoretical analysis, more experimental data to validate the results and to improve the analytical models are needed.

The purpose of the present paper is to describe the results of the experimental work, in order to develop a better understanding of unsteady flow in turbomachines. As had been shown by previous investigations of some authors, the influence of the circulation effect becomes negligibly small compared with the wake effect, if the distance between the stator and the rotor grows over more than 10–20% of the blade width. In axial compressors, the axial distance is normally of the order of 10–15% of the blade width. Therefore, the influence of the wake effect is dominating in the turbomachines and it is the objective of this paper to study the wake effect of the unsteady flow in the axial compressor blade cascade in windtunnels, using the high-response transducers in connection with the averaging technique in the digital data acquisition and reduction.

2.0 Experimental Facilities

The experimental program was carried out in the high-speed windtunnel of the University Army College, Hamburg, which is shown schematically in Fig. 1. The test section of the windtunnel is 300 mm wide and 800 mm high. The windtunnel receives air through two centrifugal compressors of 1800 kW each. It was designed specially to generate large-scale, two-dimensional, incompressible flow and operated at a $Re = 0.6E+06$. The blade cascade at the exit of the test section windtunnel consists of 10 highly cambered NACA 65-series blades, each having a chord $s = 100$ mm and a span $l = 300$ mm. The blade gap-to-chord ratio is $t/s = 1.00$ and the stagger angle of the blade βs, measured between the tangent to the blade camber line at the leading edge and the leading edge locus line, is 60 deg. The blade inlet angle $\beta 1$ is measured between the inlet velocity C and the leading edge locus line. The high-speed rotating cylinders (rotor speed $U = 60$–100 m/s) in front of the blade were used in an attempt to simulate the effect of the rotor wakes upon the blade. The center of the cylinder-rotor with its drive mechanism was placed at the side of the channel, as shown schematically in Fig. 2. The axial gap between the cylinder-rotor and the leading edge of the blade is 40 mm. At this distance Adachi et al. [6] found that the level of the unsteadiness, which results from the circulation effect

---

Contributed by the Gas Turbine Division of THE AMERICAN SOCIETY OF MECHANICAL ENGINEERS and presented at the 30th International Gas Turbine Conference and Exhibit, Houston, Texas, March 18–21, 1985. Manuscript received at ASME Headquarters, January 7, 1985. Paper No. 85-GT-132.

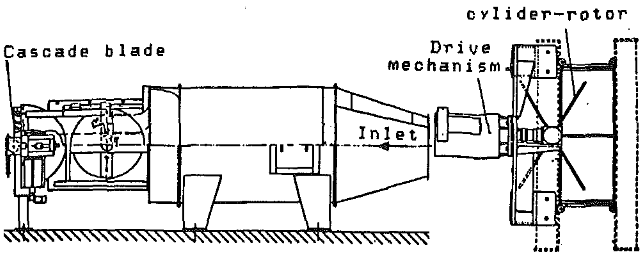

Fig. 1 The windtunnel of HSBw, Hamburg with the wake simulator

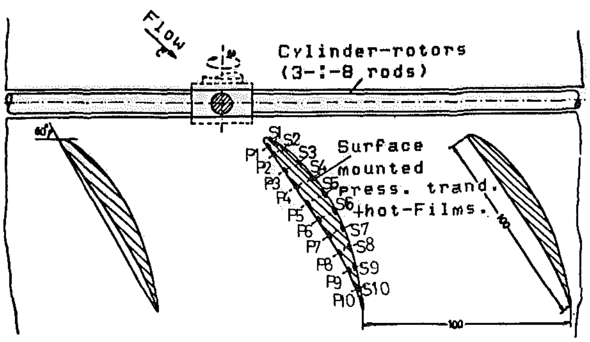

Fig. 2 Schematic of the wake simulator apparatus

and the interaction of the blade potential field, will be insignificant, when compared to the unsteadiness, which is caused by the wake effect.

In order to obtain measurements of the unsteady blade forces, the center blade was replaced by a special blade as the observed blade. There were two types of transducers, which were embedded on the suction side and the pressure side of the blade. First were the 20 miniature high-response pressure transducers, which are small enough to be embedded on the blade surface and have a frequency response in excess of 125 kHz. They were used to measure the unsteady surface pressure on the observed blade, which can be integrated to obtain the instantaneous blade forces. In addition, static orifices, coincident in chord position with each of the high-response transducers, provided a zero reference for each unsteady pressure. Next are 20 high-response surface mounted hot-film sensors. The films were attached directly to the observed blade surface for the direct measurement of the wall shear stress. The hot-films were placed at the same chordwise positions as the pressure transducers. The sensor consists of two nickel film gages on a thin plastic. The total thickness of the sensor is very small (0.025 mm thick) and was insufficient to disturb the boundary layer on the blade surface. The usual form of the calibration for the constant temperature, surface mounted hot-film is given by equation (1)

$$E^2/\Delta T = A + B(\tau w)^{1/3} \qquad (1)$$

where E = voltage, ΔT = temperature difference between the fluid and the film, and A and B are the calibration constants of the sensor.

2.1 Analysis of Unsteady Random Signals. Generally the flow field in a turbomachine is made up of two types of fluctuating flows, a periodic component and a random component. In order to obtain sufficient information from the instantaneous signal of the transducers, an averaging technique as described by Hirsch and Kool [9] was used. The technique is described schematically in Fig. 3. It can be shown that the instantaneous signal can be decomposed into the periodic signal $U_p(t)$ and the random signal $U_s(t)$.

$$U(t_i) = U_p(t_i) + U_s(t_i) \qquad (2)$$

$i = 1, 2, \ldots N$ (N = number of measurements)

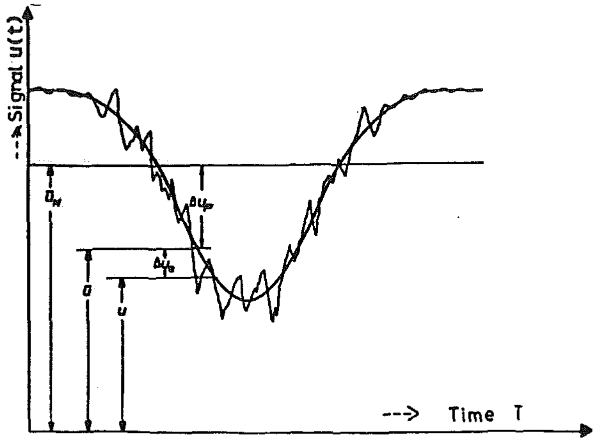

Fig. 3 Schematic of the periodic random signal

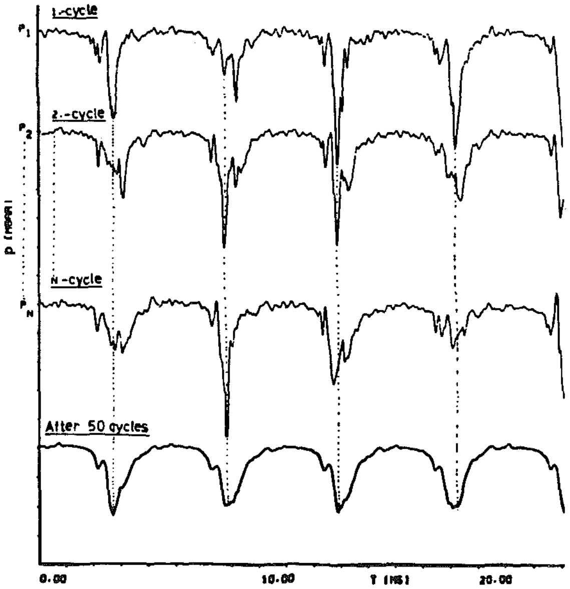

Fig. 4 Effect of periodic sampling

The instantaneous average signal $U(t_i)$ can be expressed as follows

$$U(t_i) = 1/N \sum_{k=1}^{K} U_p(t_i + k \cdot T) + 1/N \sum_{k=1}^{K} U_s(t_i + k \cdot T) \qquad (3)$$

If N is made large enough, the last term of equation (2) will be zero, because of its random character, and the periodic component $U_p(t)$ can be obtained from $U(t_i)$ by using a periodic sampling and the averaging technique. A periodic signal of the pressure transducer, as shown at the bottom of Fig. 4, was obtained by taking 4864 samples every cycle within 22 ms and averaging the signal over N = 50 cycles. To initiate the sampling, a timing reference was necessary. An electromagnetic sensor, producing a sharp electric signal, was used to synchronize the data processing device activity and the cylinder-rotor motion. Figure 5 shows the schematic of the data processing device with the PDP-11 computer controlled data-acquisition system. The signals of the high-response sensors were digitized by analog digital converters of the PDP-11 computer at a sampling rate of up to 200,000 samples per second and stored on the disc. A computer program was used, which initiated the sampling and averaged the results arithmetically.

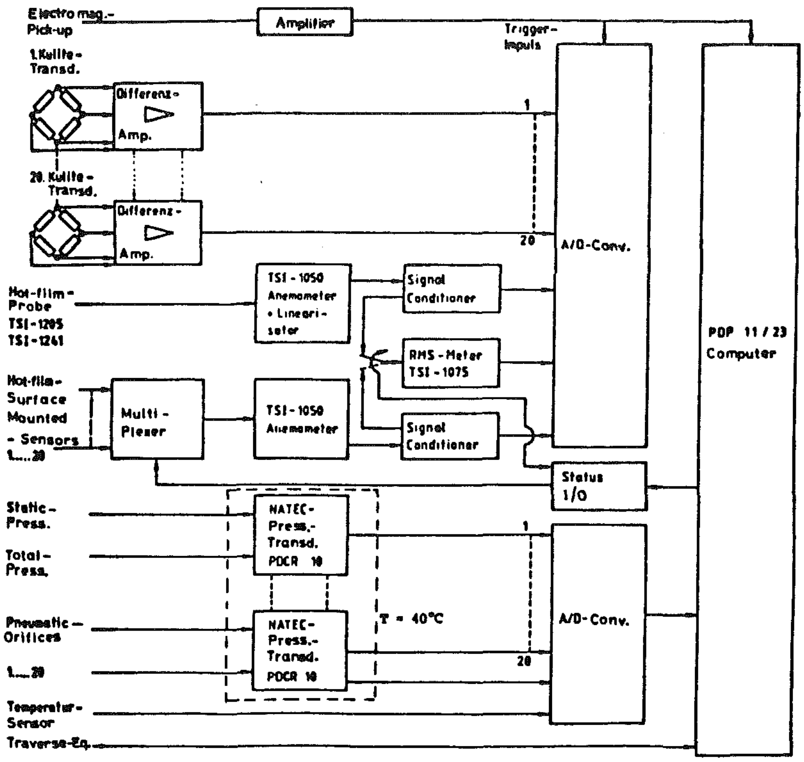

Fig. 5 Block diagram of the data-processing device

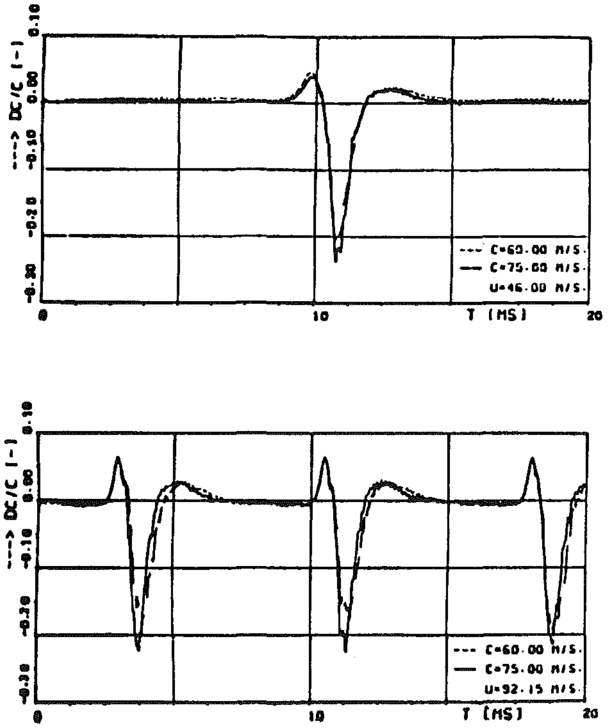

Fig. 6 Measured wakes behind the cylinder-rotor

3.0 Results

3.1 Cylinder-Rotor Wake Analysis. In order to obtain a qualitative picture of what proportion of the unsteady blade forces is due to the wake at the entrance of the blade, wake measurements of the instantaneous axial velocity C and the instantaneous flow angle were made behind the cylinder-rotor with the X-type cross-wire probe. For these measurements the observed blade was removed and the hot-wire probe was placed at the position of the leading edge of the blade (40 mm behind the cylinder-rotor). To enable accurate alignment in the probe direction as well as to reduce the position error, the probes are mounted on a precision traverse gear and its position is controlled on-line by the PDP-11 computer. The ensemble-averaging technique described previously was used and the ensemble-averaged velocities and the flow angle were taken to be the average over 100 cycles. Figure 6 shows the results of the periodic variations in the cylinder-rotor wake profiles as a function of the free-stream velocity C upstream of the cylinder-rotor and the rotor velocity U. The wakes at the entrance of the blade cascade have remarkable influence on the whole flow within the cascade. In the wake, there exists a relative velocity lower than the one in the free flow. As shown in Fig. 6, as each wake passes the probe, the velocity shows a defect in the velocity of at least 20%. Further, the periodic variations of the wake profiles show an interesting trend. As seen from Fig. 6 the profile shows an asymmetry variation that first rises slightly before the wake passes the probe, reaches a peak and then decreases continuously when the wake passes the probe. The asymmetry in the wake profile and the increase phenomena in the velocity before the wake passes the probe can be explained on the basis of the potential flow effect. As found by Adachi et al. [6] the level of the unsteadiness because of the potential flow effect may be small, amounting to between 12% and 25% of the level of the unsteadiness caused by the wake effect.

At a constant free-stream velocity to the cylinder-rotor, an increase in the cylinder-rotor speed can be seen from the figure, resulting in a small increase in the peak of the velocity deficit. As the free-stream velocity to the cylinder-rotor is increased, the wake decay at a constant rotor speed shows an insignificant influence in the wake profile.

The variations of the flow angle downstream of the cylinder-rotor in Fig. 7 are different from the variations of the velocity. The unsteady flow angle was found to have a peak-to-peak variation of between +5 deg and −8 deg. At a constant free-stream velocity to the cylinder-rotor, an increase

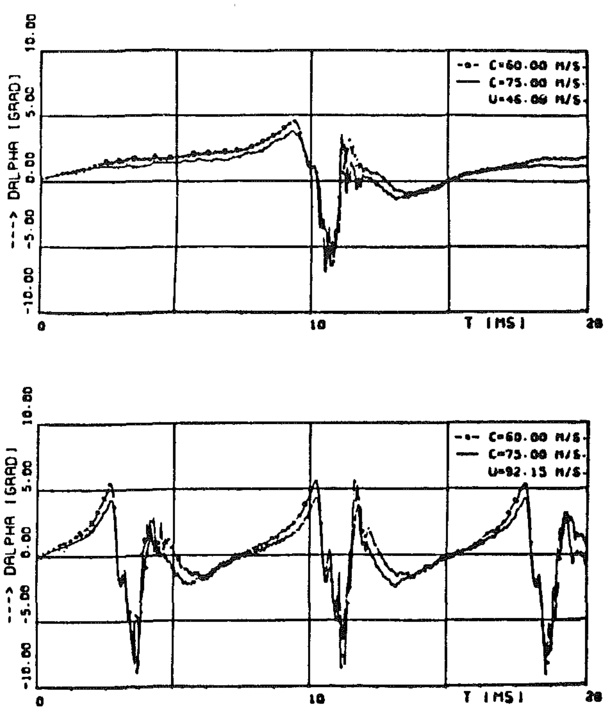

Fig. 7 Measured flow angle behind the cylinder-rotor

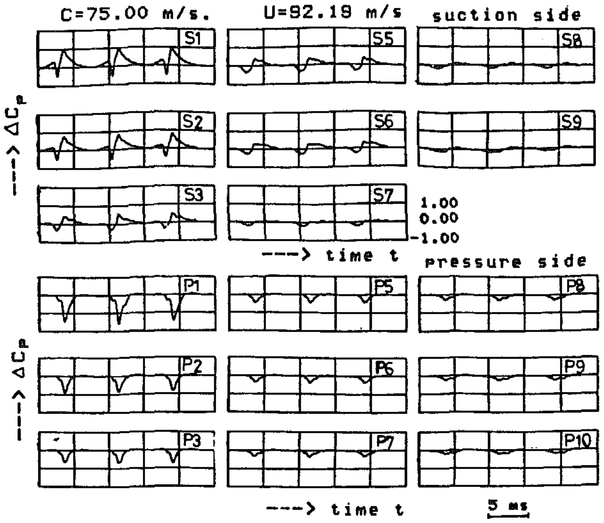

Fig. 8 Unsteady pressure distributions

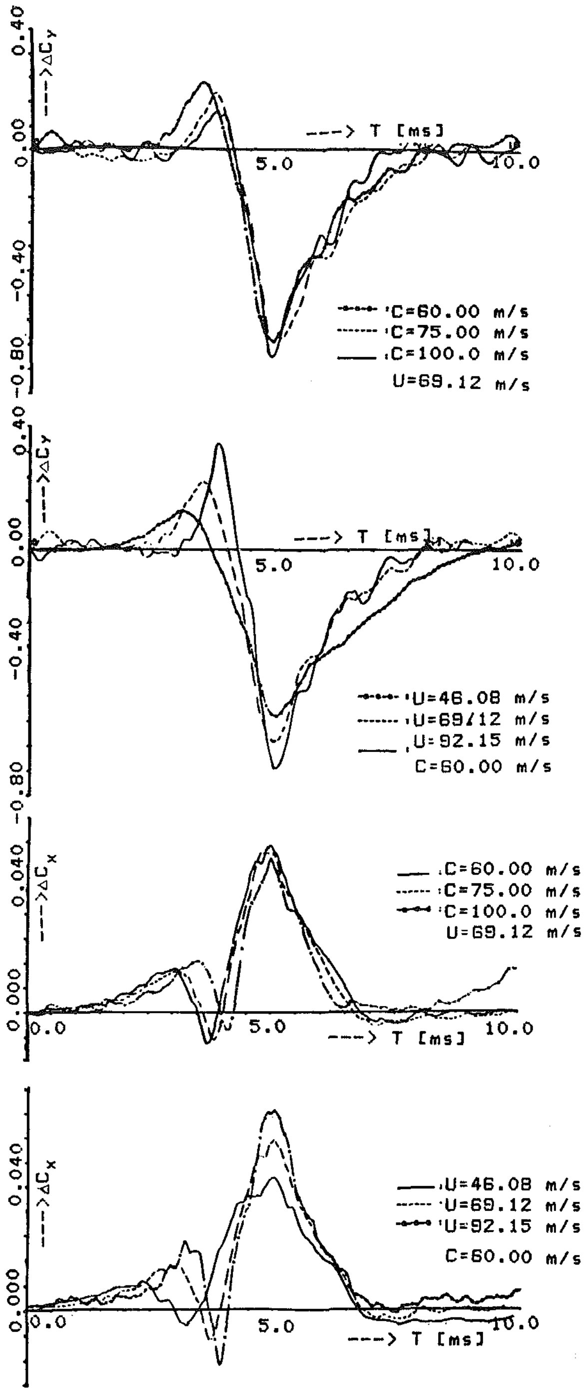

Fig. 9 Unsteady blade forces versus time

in the cylinder-rotor speed shows an increase in the flow angle variations, leading to higher unsteady variations of angle of attack into the blade cascade. An increase in the free-stream velocity to the cylinder-rotor has only a small influence on the peak of the unsteady flow angle variations.

3.2 Unsteady Pressure Measurement Results. Sample results of the unsteady pressure at any transducer position and at any instant of time that were obtained from the embedded high-response pressure transducers are shown in Fig. 8 for a cylinder-rotor speed $U=62$ m/s and the free-stream velocity to the cylinder-rotor $C=75$ m/s. The data in the figure represented the unsteady pressure fluctuations on the blade suction side and pressure side when the wakes of the cylinder-rotor pass the blade. The measured pressure fluctuations show a remarkable peak at the position of the first transducers $x=10$ mm near the leading edge of the blade. It becomes smaller in the downstream positions and shows a small fluctuation at the position of the last transducer $x=90$ mm near the trailing edge. Along the pressure side of the blade, the fluctuations show a momentary minimum in the blade pressure, when the wake meets the blade. The remarkable changes of the tendency of the fluctuations along the blade suction side are due to the fact that besides the wake effect additional fluctuation is still caused by another effect, such as the circulation effect, the potential flow effect, etc.

3.3 Unsteady Blade Forces. The unsteady blade forces were obtained by integrating the measured unsteady pressure difference $\Delta p(x,t)$ across the blade suction side and pressure side. The nondimensional coefficient form of the unsteady normal force ΔC_y and tangential force ΔC_x can be defined as

$$\Delta C_y(t)=\frac{\oint \Delta p(x,t)\,dx}{R/2\cdot C\cdot s} \qquad (4)$$

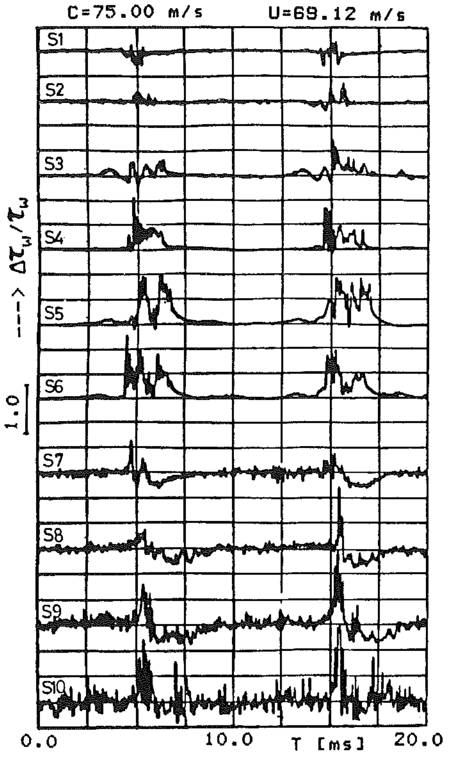

Fig. 10 Fluctuating hot-film signals on the blade surface side

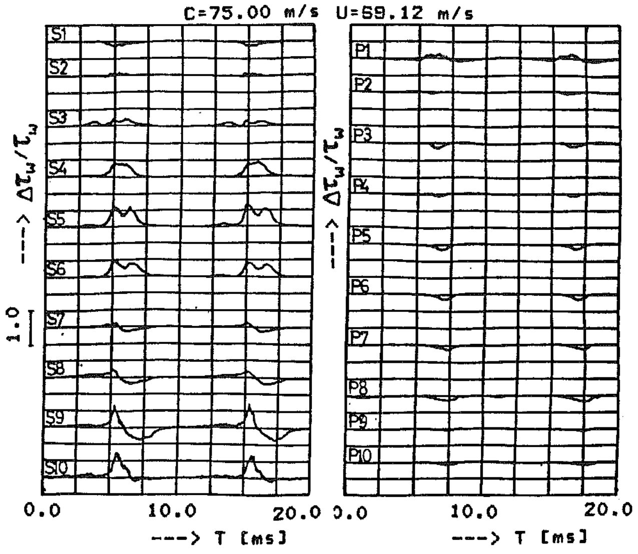

Fig. 11 Unsteady wall shear stress distribution

$$\Delta C_x(t) = \frac{\oint \Delta p(x,t)\,dy}{R/2\cdot C\cdot s} \qquad (5)$$

Figure 9 shows the unsteady normal force and tangential force coefficients ΔC_y and ΔC_x acting on the observed blade at different cylinder-rotor speed U and free-stream velocity C, when the wake passes the blade. The wake effect results in a remarkable decrease of the normal force coefficient ΔC_y and an increase of the tangential force coefficient ΔC_x momentarily. As seen from the measurement of the cylinder-rotor wakes, the effect of the wake is momentarily to change the velocity and the angle of attack with respect to the blade and thereby momentarily to change the force acting on the blade. The small influence of the potential flow effect can also be seen from the increase in the normal force coefficient and the decrease in the tangential force coefficient, just at the moment when the wake interacted with the blade.

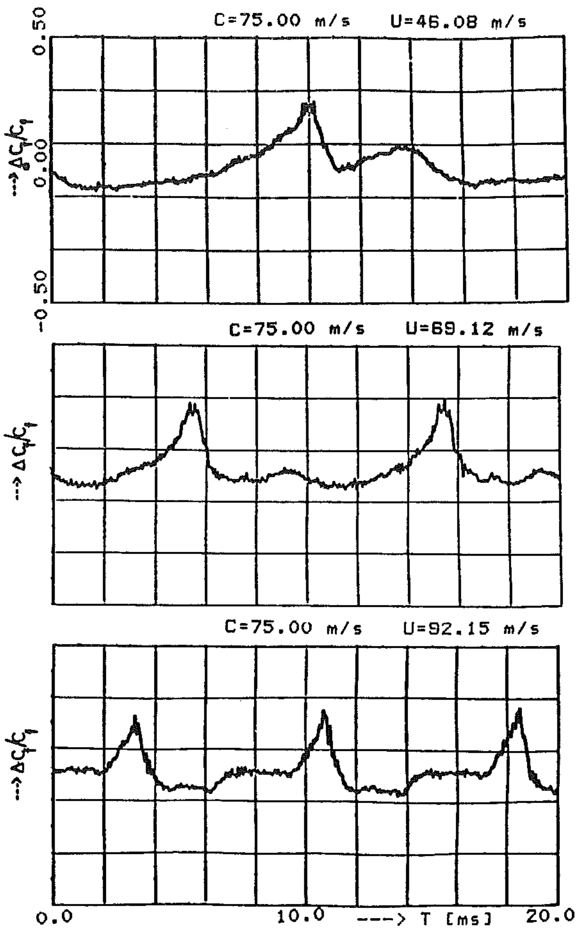

Fig. 12 Unsteady blade losses versus time

The results of the previous measurement of the cylinder-rotor wakes have shown that an increase in the cylinder-rotor speed results in an increase in the variations of the angle of attack to the blade. As seen from Fig. 9, it becomes obvious that the fluctuations of the blade force coefficients ΔC_y and ΔC_x rise progressively with increasing cylinder-rotor speed, while the changes in the free-stream velocity to the cylinder-rotor have only a small influence on the peak of the unsteady blade fluctuations.

3.4 Hot-Film Measurement Results. A knowledge of the unsteady wall shear stress is essential in understanding the characteristics of the blade losses. In order to investigate the unsteady blade losses, the unsteady wall shear stress was measured by means of the surface mounted hot-films. Typical measurement results with the hot-film are presented in Fig. 10 for the hot-films located on the suction side of the blade. All of the hot-film data in the figure represented a portion of data acquired over a single cylinder-rotor revolution. It was not averaged over 50 revolutions as in the averaging technique. The purpose was first to distinguish, as seen in the figure, the difference between the laminar and turbulent portions of the flow in the boundary layer of the blade. At the first six hot-film locations the boundary layer of the blade shows the laminar state, which can be seen by the small level of the signal fluctuations. Transition starts to occur between hot-film 6 and hot-film 7. The boundary layer of the blade is turbulent from hot-film 7 downstream to hot-film 10 near the trailing edge, which can be seen from the strong fluctuations in the hot-film signal. Further, as each cylinder-rotor wake passes the blade, the boundary layer on the blade suction side

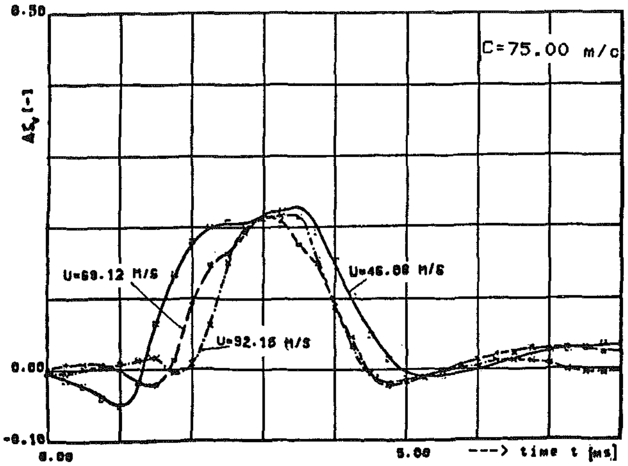

Fig. 13 Unsteady cascade losses versus time

oscillates between a characteristically laminar and turbulent state. This phenomenon in the boundary layer of the blade suction side was in agreement with similar observations made by Herbst [4].

The sample averaging technique results of the hot-film data over 50 cylinder-rotor revolutions are shown in Fig. 11 for each hot-film position at the blade suction side and pressure side. The data represent the unsteady wall shear stress at any hot-film position along the blade suction side and pressure side. The wall shear stress difference across the blade suction side and pressure side were then used to obtain the unsteady blade loss coefficient ΔC_f by the direct numerical integration

$$\Delta C_f = \frac{\oint \Delta \tau w(x,t)\,dx}{R/2 \bullet C \bullet s} \qquad (6)$$

The results of the unsteady blade losses in Fig. 12 show that the wake at the entrance of the blade results in a momentary increase of the unsteady blade losses of at least 20% of its steady-state value. Further, the cylinder-rotor speed variations have a negligibly small influence on the peak of the unsteady blade loss variations.

3.5 Unsteady Cascade Losses. Finally, the unsteady wake of the blade was measured at a distance of 40 mm behind the blade cascade by means of X-type cross-wire probe and using the averaging technique in the data acquisition. The unsteady cascade losses ζ_v were obtained by integrating the measured unsteady wake profile of the blade at any instant of time, as shown in Fig. 13. It was found that the cylinder-rotor wakes at the entrance of the blade influence the cascade losses remarkably. However, the measured unsteady cascade loss profile in Fig. 13 was influenced very strongly by the wake of the cylinder and the losses consist of the losses of the cylinder cascade and the losses of the blade cascade. An approximation of the unsteady cascade losses only can be obtained by extracting the losses caused by the cylinder cascade, which can be calculated by integrating the previously measured cylinder-rotor wakes. The mean level of the cascade losses was then found to increase momentarily from $\zeta_v = 0.02$ in the case without disturbance to $\zeta_v = 0.04$ in the case with disturbances at the entrance of the blade cascade.

4.0 Conclusions

In this paper, the experimental results were discussed describing the unsteady flow problem caused by the wake effect at the entrance of the blade cascade. The wake effect has been simulated in the windtunnel by means of high-speed rotating cylinders at the entrance of the blade cascade. As each wake passes the blade, the entrance velocity to the blade shows a defect of at least 20% and the angle of attack of the blade shows a peak-to-peak variation of between +5 deg and −8 deg. The influences of the wake on the blade forces, which were measured by means of the embedded miniature high response transducers, were then found to vary remarkably and an increase in the cylinder-rotor speed shows an increase in the peak of the unsteady blade force fluctuations, while an increase in the free-stream velocity to the cylinder-rotor have only a small influence on the peak of the fluctuations. The measured unsteady blade losses by means of the surface mounted hot-films shows a momentary increase in the unsteady blade losses of at least 20% due to the wake effect upstream of the blade. Finally, an increase was found in the mean level of the cascade losses from 0.02 in the case without disturbance to 0.04 with disturbance at the entrance of the blade.

5.0 References

1 Kemp, N. M., and Sears, W. R., "The Unsteady Forces Due to Viscous Wakes in Turbomachines," *J. of the Aero. Sc.*, Vol. 22, 1955, p. 478-483.

2 Naquib, M., "Theoretical Estimation of Dynamic Forces and Vibratory Stresses for Turbine Blade," *Mitt. Inst. Therm. Turbom. ETH Zurich 9, 1965.*

3 Henderson, R. E., "The Unsteady Response of an Axial Turbomachine to an Upstream Disturbance," Ph.D. thesis, University of Cambridge, 1972.

4 Herbst, R., and Pfeil, H., "Grenzschichtentwicklung bei instationaerer Zustroemung," VDI-Bericht 361, 1980.

5 Lefcord, M. D., "An Investigation Into Unsteady Blade Forces in Turbomachinery," JOURNAL OF ENGINEERING FOR POWER, Vol. 87, 1965, pp. 345-354.

6 Adachi, T., and Murakami, Y., "Unsteady Force on a Cambered Blade Passing Through an Oblique Wake," *Bull. of JSME*, Vol. 21, 1981, pp. 1543-1549.

7 Gallus, H. E., Lambertz, J., and Wallmann, T., "Blade-Row Interaction in an Axial-Flow Subsonic Compressor Stage," JOURNAL OF ENGINEERING FOR POWER, Vol. 102, 1980, pp. 169-176.

8 Lahm, G., "Experimentelle Bestimmung der Schaufel-Kraefte durch stationaere und instationaere Druckmessungen an interferierenden Doppelgittern," Diss. T. U. Munich, 1981.

9 Hirsch, C., and Kool, P., "Measurement of the Three-Dimensional Flow Field Behind an Axial Compressor Stage," JOURNAL OF ENGINEERING FOR POWER, Vol. 103, 1977, pp. 168-180.

Unsteady Pressure Measurements on a Biconvex Airfoil in a Transonic Oscillating Cascade

L. M. Shaw

D. R. Boldman

A. E. Buggele

National Aeronautics and
Space Administration,
Lewis Research Center,
Cleveland, OH

D. H. Buffum

Purdue University,
West Lafayette, IN

Flush-mounted dynamic pressure transducers were installed on the center airfoil of a transonic oscillating cascade to measure the unsteady aerodynamic response as nine airfoils were simultaneously driven to provide 1.2 deg of pitching motion about the midchord. Initial tests were performed at an incidence angle of 0.0 deg and a Mach number of 0.65 in order to obtain results in a shock-free compressible flow field. Subsequent tests were performed at an angle of attack of 7.0 deg and a Mach number of 0.80 in order to observe the surface pressure response with an oscillating shock near the leading edge of the airfoil. Results are presented for interblade phase angles of 90 and -90 deg and at blade oscillatory frequencies of 200 and 500 Hz (semichord reduced frequencies up to about 0.5 at a Mach number of 0.80). Results from the zero-incidence cascade are compared with a classical unsteady flat-plate analysis. Flow visualization results depicting the shock motion on the airfoils in the high-incidence cascade are discussed. The airfoil pressure data are tabulated.

Introduction

This paper addresses the need for aerodynamic data associated with transonic flutter in turbomachinery. Although considerable progress was made in the seventies [1], additional information is needed in order to support the development of contemporary analyses for the prediction of this type of flutter (e.g., [2]). One method of obtaining such information is through the use of a driven linear cascade of the type described in [3].

The previously reported study [3] emphasized the use of flow visualization methods to examine the shock-wave dynamics associated with transonic stall flutter. A simple flutter stability model was developed to assess the influence of the direct motion of the oscillating shock on cascade stability. The results in [3] revealed that the shock phase lag, which was measured over a range of reduced frequencies and interblade phase angles, was insufficient to imply instability in the cascade based on the simple shock motion model. The present paper represents an extension of the previous work with emphasis on the measurement of the airfoil dynamic surface pressures and subsequent estimates of the cascade stability.

The transonic oscillating cascade used in this investigation was capable of producing realistic reduced frequencies associated with observed transonic stall flutter in turbomachinery while operating at inlet Mach numbers sufficient to provide transonic effects. Driven cascades of this type are usually more complex than classical steady-state cascades because, in addition to meeting the blade-to-blade periodicity requirements in steady-state flow, periodicity must be achieved as the airfoils are driven in a controlled manner [4]. In general, the airfoils are oscillated by an external source to provide either a two-dimensional pitching or plunging motion to simulate a torsional or bending mode of flutter. By performing the experiments in this way, the aerodynamic aspects can be separated from the structural aspects of flutter. Various driven cascades are described in [4–6].

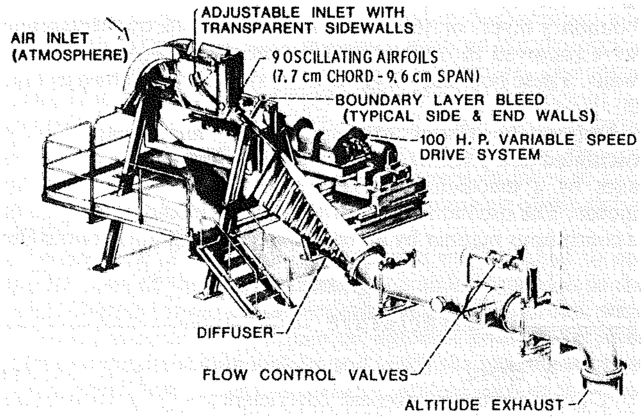

Fig. 1 Transonic oscillating cascade

This paper describes the results of a flutter experiment which was performed with nine driven biconvex airfoils operating in a linear cascade at free-stream Mach numbers of 0.65 and 0.80. During the flutter experiments, the airfoils were oscillated to provide a pitching motion of 1.2 deg about the midchord axis at nominal frequencies of 200 and 500 Hz. The reduced frequency based on the airfoil semichord was about 0.5 at the 500 Hz condition with a free-stream Mach number of 0.80. Results from flow visualization experiments

---

Contributed by the Gas Turbine Division of The American Society of Mechanical Engineers and presented at the 30th International Gas Turbine Conference and Exhibit, Houston, Texas, March 18–21, 1985. Manuscript received at ASME Headquarters, January 18, 1985. Paper No. 85-GT-212.

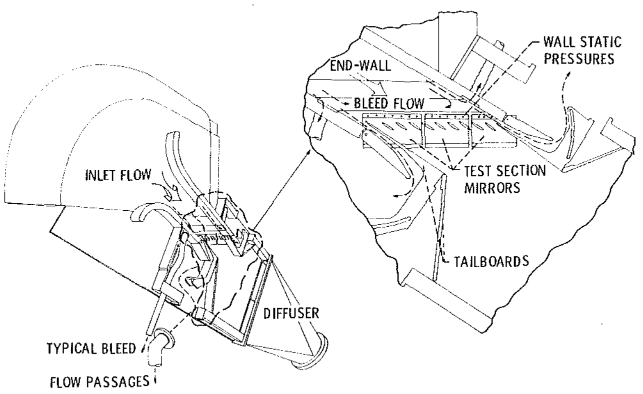

Fig. 2 Test section

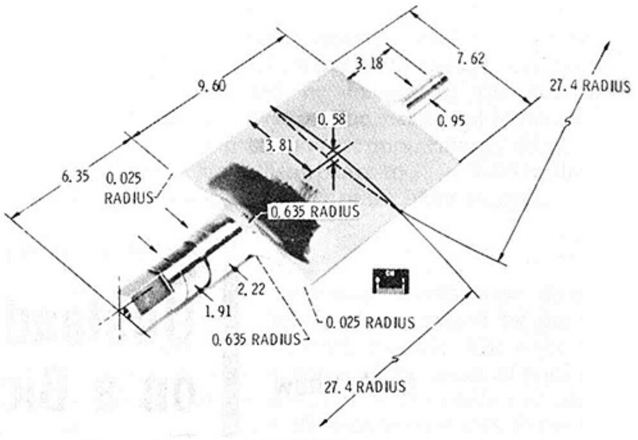

Fig. 3 Biconvex airfoil (all dimensions in centimeters)

are presented for interblade phase angles of ±90 deg. The above conditions are believed to be valid for the experimental modeling of the unsteady fluid dynamics associated with torsional stall flutter in fans and compressors.

Description of Cascade

Experimental Facility. An overall view of the transonic oscillating cascade is shown in Fig. 1. Room air entered the inlet contraction section and expanded through a 9.78-cm-wide by 29.21-cm-high test section into a diffuser and exhaust header having a nominal pressure of 3.0 N/cm. Flow rates were controlled by means of two valves located downstream of the diffuser. A partitioned (five section) end-wall boundary layer bleed system located two chord lengths upstream of the airfoils was used to remove the boundary layer on each end wall and provide steady-state blade-to-blade periodicity. The bleed passages consisted of perforated plates having an open area ratio of 22.5% and a hole diameter of 0.15 cm. The boundary layers on the upper and lower walls of the cascade were removed through slots between the tailboards and the walls. These boundary layer control systems are shown in Fig. 2.

During the flutter experiments the nine airfoils were oscillated in a pitching (torsional) motion about the midchord axes by a mechanical drive system powered by a 100 hp motor. The oscillatory or flutter frequency could be varied in a continuous manner by an eddy-current coupling between the motor and gearbox. The direction of rotation of the motor drive system was reversible so that the sign of the interblade phasing could readily be changed from positive to negative.

Airfoils. Nine two-dimensional, uncambered, biconvex airfoils with a chord of 7.62 cm and a span of 9.6 cm were installed as shown in Fig. 2. The airfoil radius of curvature was 27.4 cm, yielding a maximum thickness of 0.58 cm or a thickness-to-chord ratio of 0.076. This airfoil thickness provided the stiffness required to maintain a two-dimensional flutter mode at the highest frequency of 500 Hz. The airfoils were supported by two trunnions with the centerline located at the midchord as shown in Fig. 3. The larger trunnion which was used to oscillate the airfoil had a diameter of 1.91 cm whereas the freely supported shaft had a diameter of 0.95 cm. Each airfoil and its trunnions were machined from a single piece of titanium containing 6% aluminum and 4% vanadium.

Test Section. The airfoils were mounted between end walls containing three 0.64-cm-thick mirrors on one side and three optical quality glass windows on the other side (refer to Fig. 2). These mirrors and windows comprised part of a schlieren flow visualization system which was used to observe the flow field. Nonporous bronze alloy bushings containing two "O" rings and helical lubrication grooves were used to

Nomenclature

C = chord
C_M = unsteady moment coefficient per unit amplitude
C_{M_I} = imaginary part of the unsteady moment coefficient per unit amplitude
C_p = unsteady pressure coefficient per unit amplitude
$\bar{C}_p$ = amplitude of unsteady pressure coefficient
$\tilde{C}_p$ = time-averaged pressure coefficient, $(P-P_1)/q_1$
C_W = unsteady work done on the system per cycle of oscillation
f = oscillatory frequency
i = incidence angle
Im() = imaginary part of a complex number
M = Mach number
N = airfoil number
p = static pressure
q = dynamic head, $(\gamma/2)p\mathrm{M}^2$
Re() = real part of a complex number
S = airfoil spacing
t = time
V = velocity
x_c = coordinate in the chordwise direction
X = nondimensional chordwise direction, x_c/C
X_p = nondimensional position of pitching axis
α = angle of attack
$\bar{\alpha}$ = amplitude of airfoil pitching motion
α_0 = mean angle of attack
α_R = real part of unsteady pitching motion
β = flow angle
γ = stagger angle
κ = blade angle
ϕ_M = phase lead of unsteady moment coefficient toward motion
ϕ_p = phase lead of unsteady pressure coefficient toward motion
$\phi_{\Delta p}$ = phase lead of unsteady pressure difference coefficient toward motion
Ω = reduced frequency based on airfoil semichord
ω = angular frequency

Subscripts and Superscripts

1 = upstream condition
2 = downstream condition
U = upper or suction surface
L = lower or pressure surface
* = critical value

SENSOR NUMBER		$\frac{x_c}{C}$
ss	ps	
1	6	0.12
2	5	.25
3	4	.40
4	3	.60
5	2	.75
6	1	.88

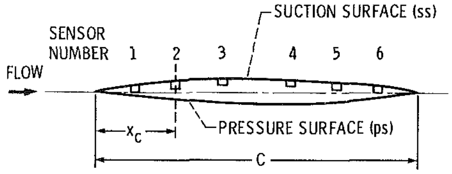

Fig. 4 Location of high-response pressure transducers, C = 7.62 cm

support the large trunnion. A similar bronze alloy bushing was lightly pressed into the glass window to provide support for the small trunnion.

The limitation in the region of flow visualization over the airfoil surface was governed by the large trunnion and the size of the corresponding hole in the mirror required to accommodate the small fillet at the airfoil-trunnion junction (Fig. 3). The diameter of this hole, which appears as a shadow in the schlieren images, was 2.3 cm.

Airfoil Drive System. A special high-speed mechanical drive system was used to oscillate the airfoils. This system, which represents a modification of the drive mechanism design described in [7], consists of a series of nine barrel cams attached to a common 50-cm diameter shaft. Each cam contained a six-cycle, 1.27-cm-wide by 0.762-cm-deep sinusoidal groove machined in the surface. A close-coupled 7.62-cm-long connecting arm and button follower transmitted six cycles of harmonic pitching motion for each revolution of the cam. The amplitude of the airfoil motion was 1.2 deg as dictated by the cam and follower geometry. Power from the motor drive system was transferred to the cam shaft by a 20.3-cm-wide endless belt consisting of layers of plastic-coated textile fabric, a polyester tension member, and a leather friction surface. The cams and followers were immersed in a multiviscosity 80W-140 high performance gear lubricant to minimize wear. With this system, each flutter test was arbitrarily limited to about 30 s with 15 to 20 s at the desired oscillatory frequency. In this operational mode, the cams and button followers incurred negligible wear.

Instrumentation

Steady-State. The instrumentation included 200 channels of pressures and temperatures from which the steady-state cascade performance was established and an additional 14 channels of high-response data for the flutter tests. The steady-state data were recorded through a system of microprocessors coupled to a dedicated minicomputer. The majority of pressures including end-wall and airfoil static pressures and boundary layer bleed passage pressures were connected to a scanivalve system containing three 48-channel units scanning in parallel at a rate of seven samples/second. The remainder of the pressures, used as reference values for the scanivalve system and for various traversing probes, were recorded with a system of signal conditioners and pressure transducers. CRT displays were used to expedite tuning of the cascade and provide on-line performance data. Off-line calculations of the detailed performance of the cascade were performed with an IBM 370 computer.

The temperatures in the cascade were essentially equal to the room temperature of 530 K. These temperatures were measured with chromel-alumel thermocouples.

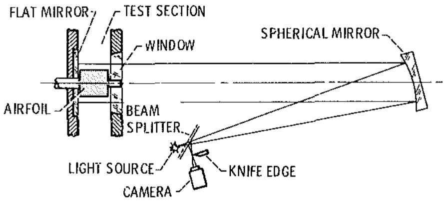

Fig. 5 Double-pass schlieren system

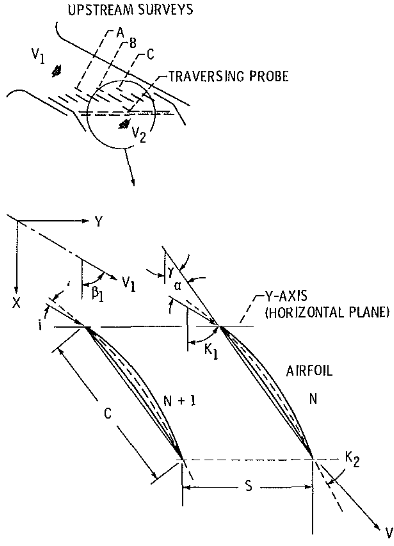

Fig. 6 Coordinate system and geometric parameters

High Response. The high-frequency response measurements included the displacement and frequency of the vibrating airfoils, strain gauge signals on the cam follower arms, and blade surface pressures. Airfoil displacement and oscillatory frequency were measured with an electro-optical displacement meter located outside the test section. This meter tracked a discontinuity of light reflected from the edge of the center airfoil and converted the optical image to an electron image. A servo loop controlled the position of the electron image in an aperture. The deflection current required to keep the image centered in the aperture was a measure of the airfoil angular displacement.

A network of two dual-strain gauges was attached to opposite sides of the arm connecting the airfoil trunnion to the cam. Signals from a conventional full-bridge circuit were recorded in order to determine the dynamic phase differences between the oscillating airfoils and verify the interblade phase angle which was preset by manually rotating each of the cams on the cam shaft.

The center airfoil in the cascade contained six commercial high-response strain-isolated pressure transducers which were mounted with the sensing elements aligned flush with the airfoil surface as shown in Fig. 4. The leads from the transducers were routed through the large trunnion by means of slots machined in the opposite surface of the airfoil. The transducers were a modified commercial type having a silicon diaphragm. The selection of the transducer and mounting arrangement was based on the results described in [8] in conjunction with in-house studies of various installation configurations designed to minimize the effects of strain-induced apparent pressure response. The transducer was a 69 kPa cylindrical type which was modified by reducing the overall length and mounted as shown in [8], configuration "E." The signals were amplified in the test cell close to the source followed by a second stage of amplification in the adjacent control room to achieve the maximum dynamic range compatible with the recording system.

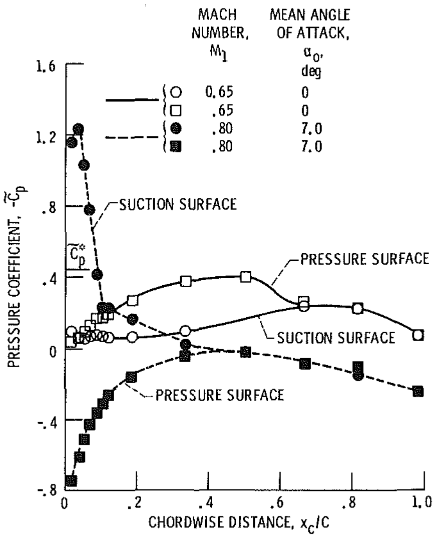

Fig. 7 Steady-state surface pressure distribution on center airfoil

All high-response measurements were recorded on a frequency modulated (FM) magnetic tape recorder with a frequency response to 10 kHz. The output from the taped signals was analyzed on a Fast Fourier Transform (FFT) analyzer.

Flow visualization was accomplished by means of a double-pass schlieren system, shown in Fig. 5. The schlieren images were photographed with a 16-mm-high speed motion picture camera operating at about 5000 frames/second (or about 10 frames/cycle of airfoil motion).

The periodicity in the cascade was determined by the uniformity of rows of upstream and downstream static pressures along the length of the cascade. The pressure taps were spaced 2.92 cm apart (1/2 of the blade spacing) and were one and two chord lengths upstream and downstream of the airfoils, respectively.

Flow angle probes were located at three tangential positions upstream of the airfoils for measuring the inlet flow angle and flow uniformity in the tangential direction. These measurements were obtained in the plane of the static pressure taps. The location of the upstream probes is shown schematically in Fig. 6.

Geometric Parameters

The coordinate system and geometric parameters for the cascade are shown in Fig. 6. All of the tests were performed at inlet flow angles, β_1, of 53 deg and 60 deg which provided angles of attack, α_0, of 0.0 deg and 7.0 deg, respectively. The blade stagger angle, γ, was fixed at 53 deg. The solidity or chord-to-spacing ratio, C/S, was 1.3. Since the biconvex airfoils were uncambered, $i=\alpha_0$ and $\gamma=\kappa_1=\kappa_2$.

Results

Details of the steady-state flow field have already been presented in [3] and, therefore, will not be repeated herein. The principal goal of this experiment was to measure and assess the airfoil unsteady surface pressures. Consequently, the pressure data will be discussed along with cascade stability results as determined from the integrated pressure distributions. The pressure data will be presented in tabular form in order to serve as a potential aid to the development of new computational methods for the prediction of flutter instability. Comparisons of the experimental results with predictions based on a flat-plate calculation method will be made as appropriate.

Table 1 Time-averaged surface pressures on center airfoil

(a) $M_1 = 0.65$, $\alpha_0 = 0°$,
$P_1 = 75.54$ kPa,
$q_1 = 22.04$ kPa

X_c/C	$\tilde{C}p_L$	$\tilde{C}p_U$
0.016	-0.026	-0.100
.033	-.064	-.044
.050	-.099	-.052
.067	-.139	-.073
.083	-.168	-.075
.100	-.178	-.064
.117	-.193	-.064
.183	-.270	-.069
.333	-.374	-.099
.500	-.389	------
.667	-.249	-.229
.817	-.219	-.215
.983	-.066	-.063

(b) $M_1 = 0.80$, $\alpha_0 = 7°$,
$P_1 = 64.09$ kPa,
$q_1 = 28.72$ kPa

0.016	0.761	-1.156
.033	.617	-1.233
.050	.522	-1.029
.067	.437	-.781
.083	.369	-.413
.100	.321	-.230
.177	.277	-.230
.183	.168	-.163
.333	.055	-.015
.500	.023	------
.667	.109	.097
.817	.105	.165
.983	.289	.260

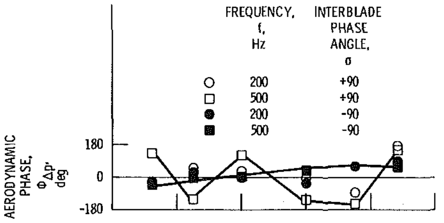

(a) Phase angle.

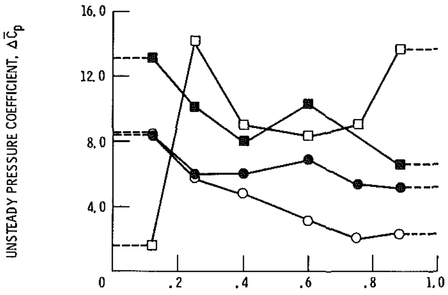

(b) Pressure coefficient.

Fig. 8 Distribution of unsteady aerodynamic phase angle and pressure coefficient showing assumed distribution for moment calculation; $M_1 = 0.65$, $\alpha_0 = 0$ deg

Steady-State Airfoil Pressure Distributions. The chordwise distributions of time-averaged pressure coefficient, $\tilde{C}_p$, on the center airfoil are shown in Fig. 7 for Mach numbers of 0.65 ($\alpha_0 = 0.0$ deg) and 0.80 ($\alpha_0 = 7.0$ deg) and are tabulated in Table 1. The results for $\alpha_0 = 0.0$ deg show an appreciable asymmetry in the distributions resulting from the influence of the staggered cascade. At a Mach number of 0.80 and corresponding angle of attack of 7.0 deg, the distributions reveal the presence of transonic flow (region above $\tilde{C}_p^*$) and the pronounced rise in pressure resulting from the formation of a lambda-type shock wave. This region of supersonic flow extends over a distance of about 10% of the chord as shown in Fig. 7.

Tests With Oscillating Airfoils. The airfoils were oscillated in simple harmonic motion to provide information on the phase between the unsteady moment and airfoil motion. This motion can be described by the following equation:

$$\alpha(t) = \alpha_0 - \bar{\alpha}\cos\omega t \tag{1}$$

Table 2 Unsteady surface pressures on center airfoil

(a) $M_1 = 0.65$, $\alpha_0 = 0°$, $f \approx 200$ Hz, $\sigma = 90°$, $p = 73.91$ kPa

	Suction surface			Pressure surface		
x_c/C	$\bar{C}_p$	$\mathrm{Re}C_p$	$\mathrm{Im}C_p$	$\bar{C}_p$	$\mathrm{Re}C_p$	$\mathrm{Im}C_p$
0.12	5.566	-5.565	-0.097	4.115	2.088	3.546
.25	3.730	-3.725	-.182	3.898	.292	3.887
.40	2.451	-2.276	.910	3.872	1.830	3.412
.60	3.698	-2.432	2.788	2.267	.640	2.175
.75	2.427	.212	2.418	.472	.247	.402
.88	2.984	-.073	2.983	3.934	-2.427	3.096

(b) $M_1 = 0.65$, $\alpha_0 = 0°$, $f \approx 500$ Hz, $\sigma = 90°$, $p = 74.19$ kPa

0.12	6.935	1.073	6.851	8.144	0.046	8.132
.25	5.220	3.842	3.533	8.977	-6.264	-6.430
.40	3.902	2.091	3.294	11.473	-2.111	11.277
.60	4.377	3.692	2.352	9.429	-.740	9.399
.75	7.298	4.652	5.623	3.270	-3.125	.962
.88	6.358	5.484	3.218	10.195	-7.876	6.423

(c) $M_1 = 0.65$, $\alpha_0 = 0°$, $f = 200$ Hz, $\sigma = -90°$, $p = 74.19$ kPa

0.12	4.929	-4.478	2.060	3.611	2.758	-2.331
.25	3.762	-3.753	-2.690	1.761	1.878	-.655
.40	3.447	-3.187	-1.316	3.176	2.842	-1.417
.60	5.601	-4.946	-2.630	1.031	1.181	-5.760
.75	5.532	-2.989	-4.655	.428	.290	-.314
.88	3.448	-.776	-3.360	1.828	.204	1.816

(d) $M_1 = 0.65$, $\alpha_0 = 0°$, $f = 500$ Hz, $\sigma = -90°$, $p = 74.17$ kPa

0.12	4.731	-2.847	3.778	7.186	7.974	-3.458
.25	5.253	-5.248	.220	5.432	5.429	.190
.40	1.611	-1.111	-1.167	6.961	6.868	-1.137
.60	7.355	-6.258	-3.865	2.977	2.687	1.282
.75	-----	------	------	2.224	2.220	-.136
.88	4.341	-1.463	-4.086	2.867	2.662	1.065

(e) $M_1 = 0.80$, $\alpha_0 = 7°$, $f \approx 200$ Hz, $\sigma = 90°$, $p = 64.29$ kPa

0.12	5.003	-4.888	1.066	5.824	4.906	3.138
.25	3.684	-3.449	1.296	4.445	2.904	3.365
.40	2.675	-2.053	1.716	3.450	1.588	3.063
.60	3.050	-1.998	2.306	2.418	.642	2.331
.75	3.368	-2.398	2.365	.571	.223	.526
.88	2.581	-1.853	1.796	3.326	1.326	3.050

(f) $M_1 = 0.80$, $\alpha_0 = 7°$, $f \approx 500$ Hz, $\sigma = 90°$, $p = 64.38$ kPa

0.12	6.473	-1.013	6.393	10.338	10.311	-.739
.25	4.847	-1.057	4.731	3.232	1.863	-2.641
.40	5.781	.914	5.708	1.062	9.439	4.872
.60	4.999	-2.704	4.992	8.030	5.456	5.892
.75	9.315	-.698	9.289	2.603	2.155	1.459
.88	5.597	-.283	5.590	3.300	-1.003	3.144

(g) $M_1 = 0.80$, $\alpha_0 = 7°$, $f = 200$ Hz, $\sigma = -90°$, $p = 64.56$ kPa

0.12	4.368	-3.356	2.796	5.744	4.173	-3.946
.25	3.835	-3.658	1.153	3.480	2.434	-2.486
.40	3.450	-3.432	-3.486	2.089	1.762	-1.122
.60	4.161	-4.050	-.957	.645	.556	-.329
.75	3.851	-3.694	-1.087	.237	.219	-.090
.88	2.247	-1.231	-1.881	3.626	2.287	-2.814

(h) $M_1 = 0.80$, $\alpha_0 = 7°$, $f = 500$ Hz, $\sigma = -90°$, $p = 64.61$ kPa

0.12	5.461	-4.666	2.837	8.853	5.583	-6.870
.25	5.869	-5.805	-.868	2.806	1.613	-2.296
.40	3.023	-2.369	-1.878	4.583	4.449	-1.101
.60	5.816	-4.436	-3.762	1.141	1.619	1.149
.75	5.753	-3.454	-4.600	1.385	1.385	-4.836
.88	3.123	.286	-3.160	4.716	-1.101	-4.585

where the amplitude, $\bar{\alpha}$, was 1.2 deg and the mean angle of attack, α_0, was either 0.0 deg or 7.0 deg. The airfoils were oscillated at 200 and 500 Hz which yielded reduced frequencies ranging from 0.18 to 0.46 at a Mach number of 0.80 where the reduced frequency is

$$\Omega = \frac{\omega C}{2V_1} \tag{2}$$

The results were obtained for interblade phase angles of 90 deg and -90 deg. Positive interblade phase angle is defined such that airfoil N leads airfoil $N+1$, etc. (refer to Fig. 6). Positive interblade phase angles would correspond to a wave moving in the direction of rotor rotation.

In order to measure the pressures on the suction and pressure surfaces, it was necessary to rotate the center airfoil 180 deg and perform the tests in two steps. The symmetry of the biconvex airfoil permitted this type of data acquisition at the expense of doubling the number of tests relative to an experiment in which both surfaces of the airfoil are instrumented with pressure transducers (or two airfoils are instrumented to acquire the measurements in a single blade passage). The pressure data were reduced by the procedure given in the Appendix to yield local values of the moment coefficient. Subsequent integration of the chordwise distribution of moment coefficient yielded the aerodynamic damping, Ξ, where

$$\Xi = -C_{M_I} \tag{3}$$

Therefore for negative values of the imaginary part of the

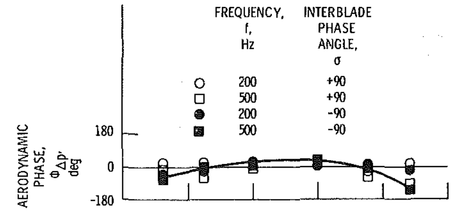

(a) Phase angle.

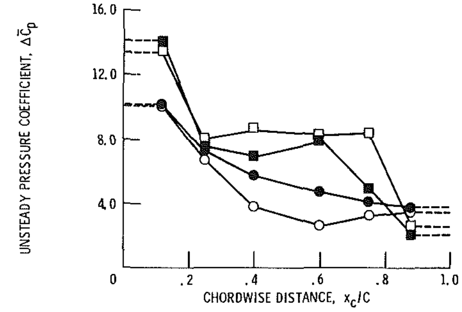

(b) Pressure coefficient.

Fig. 9 Distribution of unsteady aerodynamic phase angle and pressure coefficient showing assumed distribution for moment calculation; $M_1 = 0.80$, $\alpha_0 = 7$ deg

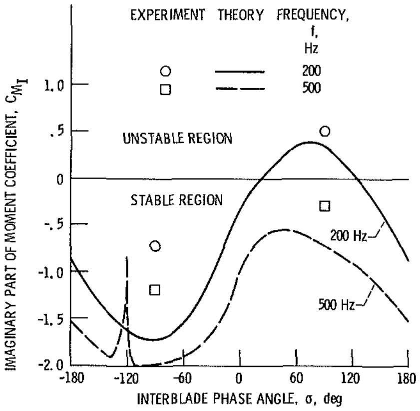

Fig. 10 Comparison of cascade stability results with flat-plate code (9); $M_1 = 0.65$, $\alpha_0 = 0$ deg

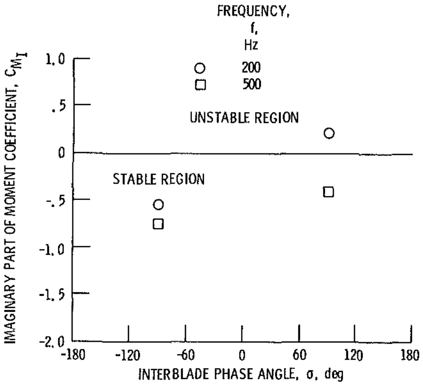

Fig. 11 Experimental stability results; $M_1 = 0.80$, $\alpha_0 = 7$ deg

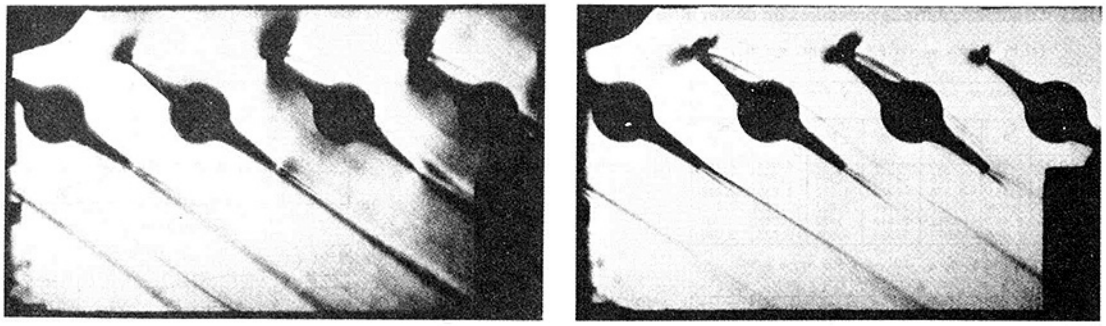

(a) f = 200 Hz, σ = +90 deg.　　(b) f = 200 Hz, σ = -90 deg.

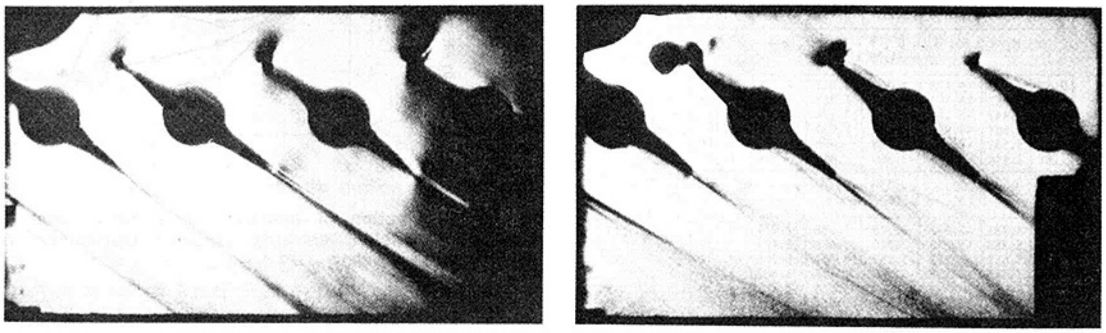

(c) f = 500 Hz, σ = +90 deg.　　(d) f = 500 Hz, σ = -90 deg.

Fig. 12 Schlieren images of oscillating airfoils at two interblade phase angles and two oscillatory frequencies $M_1 = 0.80$, $\alpha_0 = 7$ deg

moment coefficient, the aerodynamic damping is positive, i.e., the cascade is stable.

Unsteady Aerodynamic Response. Chordwise distributions of aerodynamic phase angle, $\phi_{\Delta p}$, and pressure difference coefficient, $\Delta\bar{C}_p$, are presented in Fig. 8 for a Mach number of 0.65 and an angle of attack of 0.0 deg. In general, the phase angle shows a gradual increase from a negative to a positive angle across the chord. The major exception occurs at 500 Hz at +90 deg interblade phase angle where the aerodynamic phase fluctuates between positive and negative angles along the chord.

The pressure distributions shown in Fig. 8(*b*) are generally well behaved with the exception of the 500 Hz results at an interblade phase angle of 90 deg, which as noted above, exhibited much higher values of aerodynamic phase lag than observed at the other conditions. Here the pressure difference coefficient increased appreciably over the first 25% of the airfoil and then attained a level over the midchord region that was similar to the 500 Hz data with an interblade phase angle of −90 deg.

The unsteady response data for each surface of the airfoil from which the results in Fig. 8 were derived are tabulated in Tables 2(*a*) to 2(*d*).

The response data for a Mach number of 0.80 and an angle of attack of 7.0 deg are presented in Fig. 9. In general, the phase angle near midchord is more positive than at the leading and trailing edges. However, the aerodynamic phase angle at 200 Hz and +90 deg phase angle is nearly constant over the entire chord.

The distributions of unsteady pressure difference coefficients are presented in Fig. 9(*b*). The results are well organized and similar to the results in Fig. 8 which were obtained at a Mach number of 0.65 and at an angle of attack of 0.0 deg. The presence of the shock wave near the leading edge of the suction surface did not manifest itself in an obvious way through differences in the local values of $\Delta\bar{C}_p$.

The unsteady response data for each surface of the airfoil from which the results in Fig. 9 were derived are tabulated in Tables 2(*e*) to 2(*h*).

Cascade Stability. The stability of the cascade was determined by computing the imaginary part of the moment coefficient C_{M_I} (equation (3)) from the pressure difference distributions shown in Figs. 8 and 9. The distributions were closed at the leading and trailing edges of the airfoil by assuming a constant level of $\Delta\bar{C}_p$ as in [5].

The results for $M_1 = 0.65$ and $\alpha_0 = 0.0$ deg are shown in Fig. 10. Instability occurred at one of the four experimental conditions; namely, at an interblade phase angle of 90 deg and a frequency of 200 Hz ($\Omega = 0.221$). These results are consistent with predictions based on a flat-plate analysis [9] although the observed levels of C_{M_I} are somewhat higher than flat-plate theory.

The results for $M_1 = 0.80$ and $\alpha_0 = 7.0$ deg are shown in Fig. 11. As in the previous case, instability was observed at an interblade phase angle of 90 deg and at a frequency of 200 Hz ($\Omega = 0.185$). All of the other experimental cases exhibited stability.

Flow Visualization. Individual frames from the high-speed movies of schlieren images of the flow were reproduced in a 35-mm format and are shown in Fig. 12. These pictures represent one state of the flow during a cycle of oscillation at a Mach number of 0.80. The most pronounced feature is a total separation of the flow downstream of the shock as the blade pitches upward toward the maximum angle of attack of 8.2 deg. This separation was not evident while operating at steady-state conditions and was not evident in the previous study [3] at the same conditions. It is believed that this total separation became apparent in these latest tests because of an improved optical system which permitted a better cutoff at the knife edge in the schlieren system (Fig. 5). The separation was repeatable from blade to blade within the visible flow field which encompassed approximately the three central airfoils.

Discussion

Results of unsteady aerodynamic response have been presented for two cascade conditions; namely, a 0 deg angle of attack cascade operating at an inlet Mach number of 0.65 and the same cascade operating at an angle of attack of 7.0 deg and a corresponding inlet Mach number of 0.80. In the latter case, a lambda-type shock wave was present near the leading edge of the suction surface of the airfoils. The tests were performed at interblade phase angles of ±90 deg in order to explore conditions which might yield high levels of stability and instability. These conditions were selected on the basis of results from a flat-plate analysis. The unsteady aerodynamic data were obtained from six high-response pressure transducers mounted flush with the surface of the center airfoil.

It was anticipated that the cascade stability results at the zero angle of attack condition and a Mach number of 0.65 would be in reasonable agreement with flat-plate theory since the surface pressure gradients on the biconvex airfoils were low. The stability results indeed corroborated this hypothesis. However it was somewhat surprising to discover that the results for the more ambitious case in which the angle of attack was 7.0 deg and the inlet Mach number was 0.80 were quite similar to the flat-plate results. It is recognized that the uncertainty in the stability results for the transonic flow experiment is greater than for the subsonic flow experiment because of a limitation in the number of transducers used to acquire the pressure data. The six chordwise transducers, which were considered to be the maximum allowable number for structural reasons, would not be expected to present problems at the zero angle of attack flow condition but could be marginal at an angle of attack of 7.0 deg where the local pressure gradient would be large due to the presence of a shock wave near the leading edge. This factor should be considered in interpreting the stability results for the high Mach number cascade flow. Because of the limitations in chordwise resolution of the unsteady pressures, especially at the high Mach number condition, the pressure data are presented in tabular form. Consequently, comparisons of theory with experiment can be made on the basis of both the individual pressures and the calculated stability.

References

1 Sisto, F., "Overview: NASA/AF/NAVY Symposium on Aeroelasticity of Turbine Engines," ME-RT-81003, Stevens Institute of Technology, Hoboken, N.J., Oct. 1980.

2 Verdon, J. M., and Caspar, J. R., "A Linear Aerodynamic Analysis for Unsteady Transonic Cascades," NASA CR-3833, 1984.

3 Boldman, D. R., Buggele, A. E., and Michalson, G. M., "Stall Flutter Experiment in a Transonic Oscillating Linear Cascade," NASA TM-82655, 1981.

4 Carta, F. O., "An Experimental Investigation of Gapwise Periodicity and Unsteady Aerodynamic Response in an Oscillating Cascade, Part I: Experimental and Theoretical Results," NASA CR-3513, 1982.

5 Riffel, R. E., and Rothrock, M. D., "Experimental Determination of Unsteady Blade Element Aerodynamics in Cascades, Vol. 1: Torsional Mode Cascade," EDR-10119-Vol. 1, Detroit Diesel Allison, Indianapolis, IN, June 1980 (NASA CR-159831).

6 Szchenyi, E., and Finas, R., "Aeroelasticity Testing in a Straight Cascade Wind Tunnel," *Aeroelasticity in Turbomachines*, Office National d'Etudes et de Recherches Aerospatiales (ONERA), Lausanne, Switzerland, 1980.

7 Boldman, D. R., and Buggele, A. E., "Wind Tunnel Tests of a Blade Subjected to Midchord Torsional Oscillation at High Subsonic Stall Flutter Conditions," NASA TM-78998, 1978.

8 Grant, H. P., and Lanati, G. A., "Instrumentation for Measuring the Dynamic Pressure on Rotating Compressor Blades," PWA-5558-12, United Technologies Corporation, East Hartford, CT, Sept. 1978 (NASA CR-159466).

9 Smith, S. N., "Discrete Frequency Sound Generation in Axial Flow Turbomachines," ARC-R/M-3709, Aeronautical Research Council, London, England, 1973.

APPENDIX

Calculation of Cascade Stability From Unsteady Surface Pressure Measurements

Signals from the high-response pressure transducers on the center airfoil were tape recorded and analyzed on a Fast-Fourier Transform analyzer to provide the amplitude of the first harmonic component of pressure and its phase relative to the blade motion signal. The pressure signals were converted to coefficient form as in [4] such that

$$C_p(X,t) = \frac{p(X,t)}{q_1 \bar{\alpha}} = \bar{C}_p(X)\, e^{i(\omega t + \phi_p)} \qquad \text{(A1)}$$

where ϕ_p is the phase by which the pressure leads the airfoil motion and $X = x_c / C$.

The airfoil motion can be expressed as

$$\alpha(t) = \alpha_0 + \bar{\alpha} e^{i\omega t} \qquad \text{(A2)}$$

where α_0 is either 0.0 deg or 7.0 deg and $\bar{\alpha}$ is 1.2 deg. The pressure difference across the airfoil is defined in coefficient form as

$$\begin{aligned} \Delta C_p(X,t) &= C_{p_L}(X,t) - C_{p_U}(X,t) \\ &= \Delta \bar{C}_p(X)\, e^{i(\omega t + \phi_{\Delta p})} \qquad \text{(A3)} \end{aligned}$$

The unsteady moment is

$$C_M(t) = \int_0^1 (X_p - X) \Delta C_p(X,t) dX = \bar{C}_M e^{i(\omega t + \phi_M)} \qquad \text{(A4)}$$

where X_p is the nondimensional position of the pitching axis from the leading edge of the airfoil. The value of X_p in this study was 0.5.

The unsteady work per cycle is defined as

$$C_W = \oint \mathrm{Re}\{\bar{\alpha} C_M(t)\} d\alpha_R \qquad \text{(A5)}$$

Upon substituting from equations (A2) and (A4) and integrating equation (A5), the unsteady work per cycle can be expressed as

$$C_W = \pi \bar{\alpha}^2 \overline{C_M} \sin \phi_M = \pi \bar{\alpha}^2 C_{M_I} \qquad \text{(A6)}$$

A positive value of C_W implies the airstream is doing work on the airfoil, i.e., negative damping takes place and the airfoil is unstable. The aerodynamic damping is given by

$$\Xi = -\frac{C_W}{\pi \bar{\alpha}^2} = -C_{M_I} \qquad \text{(A7)}$$

The stability results in the present paper are presented in terms of C_{M_I}; therefore positive values of C_{M_I} imply negative damping or instability.

Aerodynamic Detuning Analysis of an Unstalled Supersonic Turbofan Cascade

D. Hoyniak
Aerospace Engineer.
NASA-Lewis Research Center,
Cleveland, OH

S. Fleeter
Professor,
School of Mechanical Engineering.
Director, Thermal Sciences and
Propulsion Center.
School of Mechanical Engineering,
Purdue University,
West Lafayette, IN

A new, and as yet unexplored, approach to passive flutter control is aerodynamic detuning, defined as designed passage-to-passage differences in the unsteady aerodynamic flow field of a rotor blade row. Thus, aerodynamic detuning directly affects the fundamental driving mechanism for flutter, i.e., the unsteady aerodynamic forces and moments acting on individual rotor blades. In this paper, a model to demonstrate the enhanced supersonic unstalled aeroelastic stability associated with aerodynamic detuning is developed. The stability of an aerodynamically detuned cascade operating in a supersonic inlet flow field with a subsonic leading edge locus is analyzed, with the aerodynamic detuning accomplished by means of nonuniform circumferential spacing of adjacent rotor blades. The unsteady aerodynamic forces and moments on the blading are defined in terms of influence coefficients in a manner that permits the stability of both a conventional uniformly spaced rotor configuration as well as the detuned nonuniform circumferentially spaced rotor to be determined. With Verdon's uniformly spaced Cascade B as a baseline, this analysis is then utilized to demonstrate the potential enhanced aeroelastic stability associated with this particular type of aerodynamic detuning.

Introduction

Structural detuning is defined as blade-to-blade differences in the natural frequencies of a blade row resulting from variations in the individual blade structural properties. Mathematical models have been developed which demonstrate that even the small amounts of blade-to-blade structural detuning associated with manufacturing tolerances can have a beneficial effect on the flutter characteristics of rotor assemblies [1-5]. Furthermore, these models indicate that the aeroelastic stability of a rotor can be controlled by the deliberate introduction of increased levels of blade-to-blade structural detuning of the rotor design.

However, blade-to-blade structural detuning is not a universally accepted potential mechanism to eliminate flutter from the operating range of a fan or compressor stage. This is because of the associated manufacturing, material, inventory, engine maintenance, control, and cost problems.

A new, and as yet unexplored, approach to passive flutter control is aerodynamic detuning, defined as designed passage-to-passage differences in the unsteady aerodynamic flow field of a rotor blade row. Thus, aerodynamic detuning results in blade-to-blade differences in the unsteady aerodynamic forces and moments acting on a blade row. This results in the blading not responding in a classical traveling wave mode typical of the flutter behavior of a conventional aerodynamically tuned rotor. Thus, aerodynamic detuning directly affects the fundamental driving mechanism for flutter, the unsteady aerodynamic forces and moments acting on individual rotor blades.

Supersonic unstalled flutter is a significant problem in the development of advanced gas-turbine fans and compressors because it restricts the high-speed operating range of the engine. Hence, the objective of this research program is to develop a model for aerodynamic detuning applicable to supersonic unstalled flutter. In particular, a mathematical model is developed to analyze the stability of an aerodynamically detuned rotor operating in a supersonic inlet flow field with a subsonic leading edge locus, with the aerodynamic detuning accomplished by means of nonuniform circumferential spacing of adjacent rotor blades. This method of aerodynamic detuning was selected because small solidity variations do not have a dominant effect on the steady-state aerodynamic performance of a rotor. In this model, the unsteady aerodynamic forces and moments acting on the blading are defined in terms of influence coefficients in a manner that permits the stability of both a conventional aerodynamically tuned rotor configuration as well as the detuned nonuniform circumferentially spaced rotor to be determined.

Unsteady Aerodynamic Model

Current aeroelastic stability analyses of conventional aerodynamically tuned and structurally detuned rotors utilize two-dimensional aerodynamic models applied in a strip theory technique. Hence, a two-dimensional, uniformly

---

Contributed by the Gas Turbine Division of The American Society of Mechanical Engineers and presented at the 30th International Gas Turbine Conference and Exhibit, Houston, Texas, March 18-21, 1985. Manuscript received at ASME Headquarters, January 16, 1985. Paper No. 85-GT-192.

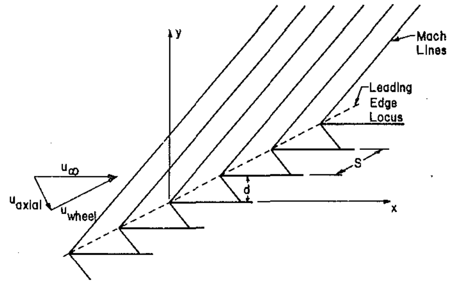

Fig. 1 Flat-plate airfoil cascade in a supersonic inlet flow with a subsonic leading edge locus

spaced, airfoil cascade is used to represent a typical rotor blade section. These models then analyze the unsteady aerodynamics associated with the airfoil cascade executing harmonic oscillations in a classical traveling wave mode, i.e, with a constant interblade phase angle β between adjacent airfoils.

For supersonic unstalled flutter, a flat-plate airfoil cascade embedded in a supersonic inlet flow field with a subsonic leading edge locus (Fig. 1) undergoing torsion mode harmonic oscillation is considered. The fluid is assumed to be an inviscid, perfect gas with the flow isentropic, adiabatic, and irrotational. The unsteady continuity and Euler equations are linearized by assuming that the unsteady perturbations are small as compared to the uniform throughflow. Thus, the boundary conditions, which require the unsteady flow to be tangent to the blade and the normal velocity to be continuous across the wake, are applied on the mean positions of the oscillating airfoils.

Unsteady cascade aerodynamics and, in particular, the unsteady forces and moments acting on the uniformly spaced airfoils are then predicted using various techniques, for example, [6-14]. Of particular interest are the analyses of Verdon [6], Brix and Platzer [9], and Caruthers [10]. These analyses utilize a finite cascade representation of the semi-infinite cascade. The cascade periodicity condition is enforced by stacking sufficient numbers of uniformly spaced, single airfoils until convergence in the unsteady flow field is achieved.

For the aerodynamically detuned, alternate nonuniform circumferentially spaced rotor, an analogous unsteady aerodynamic model is utilized. In particular, the unsteady aerodynamics associated with the small perturbation torsion mode harmonic oscillations of a nonuniformly spaced two-dimensional flat plate airfoil cascade embedded in an inviscid, supersonic inlet flow field with a subsonic leading edge locus is considered.

The analysis of this type of configuration is most easily accomplished utilizing a finite cascade representation of the semi-infinite cascade (Fig. 2). As seen, there are two distinct flow passages: a reduced spacing or increased solidity passage and an increased spacing or reduced solidity passage. Also, the detuned cascade is composed of two separate sets of airfoils. For convenience, these are termed the set of even-numbered airfoils and the set of odd-numbered airfoils. Thus, two-passage periodicity is required for this detuned cascade, i.e., the periodic cascade unsteady flow field is achieved by stacking sufficient numbers of two nonuniform flow passages or two airfoils, one from each set.

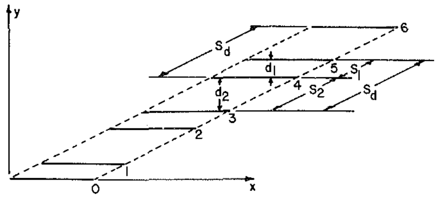

Fig. 2 Finite cascade representation for alternate nonuniform circumferential spacing

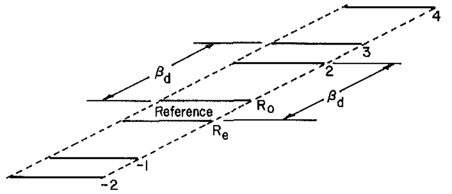

Fig. 3 Reference airfoil passage for nonuniformly spaced cascade

For the alternate nonuniform airfoil spacing aerodynamic detuning technique being considered, the spacing, S_d, of the two sets of airfoils is equal (Fig. 2). Thus, the individual sets of odd- and even-numbered airfoils can be considered as cascades of uniformly spaced airfoils each with twice the spacing of the associated baseline uniformly spaced cascade. This enables an interblade phase angle for this aerodynamically detuned cascade configuration to be defined. In particular, each set of airfoils is assumed to be executing harmonic torsional oscillations with a constant interblade phase angle, β_d, between adjacent airfoils. Thus, this detuned cascade interblade phase angle is twice that for the corresponding baseline uniformly spaced cascade. The interblade phase angle for the motion between the sets of even-numbered and odd-numbered airfoils is determined from the flutter mode which is obtained by specifying the detuned cascade phase angle, β_d, and the level of aerodynamic detuning, ϵ, which defines the nonuniform airfoil spacing.

$$S_{1,2} = (1 \mp \epsilon) S \qquad (1)$$

Nomenclature

c = airfoil chord
i = $-1^{1/2}$
k = reduced frequency, $k = \omega c / u_\infty$
u_∞ = cascade inlet velocity
y_s = mean airfoil position
C = perturbation sonic velocity
$C_{\alpha\alpha}$ = unsteady aerodynamic moment coefficient
C_M^n = influence coefficient of airfoil n
$C_p = \dfrac{P}{1/2 \rho u_\infty^2}$
$\Delta C_p = \dfrac{\Delta \rho}{1/2 \rho u_\infty^2}$
M = dimensionless unsteady aerodynamic moment
M_∞ = cascade inlet Mach number
P = perturbation pressure
ΔP = perturbation pressure difference
S = uniform airfoil spacing
S_d = nonuniform airfoil spacing
U = perturbation chordwise velocity
V = perturbation normal velocity
α = amplitude of oscillation
$\bar{\alpha}$ = complex oscillatory amplitude
β = interblade phase angle
ϵ = level of aerodynamic detuning
ρ = fluid density
ω = oscillatory frequency
ζ = cascade stagger angle
[ ] = matrix

Subscripts

d = detuned cascade
n = airfoil number
R = reference airfoil uniformly spaced cascade
R_e = reference for set of even-numbered airfoils of detuned cascade
R_o = reference for set of odd-numbered airfoils of detuned cascade

where S is the spacing of the baseline uniformly spaced cascade and S_1 and S_2 denote the spacing of the reduced and increased-flow passages of the detuned cascade.

The formulation of the linearized differential equations describing the unsteady perturbation quantities for the finite aerodynamically detuned cascade is based on the method of characteristic analysis of the finite uniformly spaced airfoil cascade developed by Brix and Platzer [9]. In particular the dependent variables are the nondimensional chordwise, normal, and sonic perturbation velocities, U, V, and C, respectively. The independent variables are the dimensionless chordwise and normal coordinates, x and y as defined in Figs. 1 and 2, and time t. Assuming harmonic motion at a frequency ω, the resulting set of differential equations which describes the unsteady perturbation flow field is specified in equation (2).

$$\frac{\partial U}{\partial x}+\sqrt{M_\infty^2-1}\,\frac{\partial V}{\partial y}+\frac{\partial C}{\partial x}+ikM_\infty^2C=0 \tag{2a}$$

$$\frac{\partial U}{\partial x}+\frac{\partial C}{\partial y}+ikU=0 \tag{2b}$$

$$\frac{\partial U}{\partial y}-\sqrt{M_\infty^2-1}\,\frac{\partial V}{\partial x}=0 \tag{2c}$$

Solutions to this system of equations are obtained by the method of characteristics. The compatibility equations are specified in equation (3).

$$\left(\frac{dU}{dx}\right)_\xi-\left(\frac{dV}{dx}\right)_\xi+\frac{ikM_\infty^2}{M_\infty^2-1}(U-C)=0 \tag{3a}$$

$$\left(\frac{dU}{dx}\right)_\eta+\left(\frac{dV}{dx}\right)_\eta+\frac{ikM_\infty^2}{M_\infty^2-1}(U-C)=0 \tag{3b}$$

$$\left(\frac{dU}{dx}\right)_{\text{str}}+\left(\frac{dC}{dx}\right)_{\text{str}}+ikU=0 \tag{3c}$$

where the subscripts ξ, η, and str indicate that the relation is valid along the left or right running characteristic and the characteristic in the streamline direction, respectively.

The flow tangency boundary condition requires that the normal perturbation velocity component, V, be equal to the normal velocity of the airfoil surfaces on the mean position of the oscillating airfoils. For an aerodynamically detuned airfoil cascade executing harmonic torsional motions about an elastic axis located at x_o as measured from the leading edge, the dimensionless normal perturbation velocity component on the nth airfoil is specified in equation (4).

$$V_n(x,y_s,t)=-\alpha_o(1+(x-x_o)ik)e^{i(kt+n\beta_d)} \tag{4}$$

where y_s denotes the mean position of the airfoils, k is the reduced frequency, β_d is the interblade phase angle, and α_o denotes the amplitude of oscillation of the oth airfoil.

These boundary conditions are applied on the mean positions of the oscillating cascaded airfoils. For the uniformly spaced cascade depicted in Fig. 1, the mean position of the nth airfoil is given in equation (5).

$$nd\tan\zeta\le x\le nd\tan\zeta+1 \tag{5a}$$

$$y_s=nd \tag{5b}$$

$$n=0,\pm1,\pm2,\ \ldots$$

where d is the perpendicular distance between adjacent airfoils, as indicated in Fig. 1.

For the nonuniformly spaced airfoil cascade depicted in Fig. 2, the mean position of the nth even-numbered airfoil is specified in equation (6).

$$d_1+d_2=D \tag{6a}$$

$$\left(\frac{n}{2}\right)D\tan\zeta\le x\le\left(\frac{n}{2}\right)D\tan\zeta+1 \tag{6b}$$

$$y_s=\left(\frac{n}{2}\right)D \tag{6c}$$

The mean positions of the set of odd-numbered airfoils can be expressed in an analogous manner.

Thus, the formulation of the mathematical problem for the unsteady aerodynamic model of the alternate nonuniform circumferentially spaced detuned cascade is complete. At the intersection points of the characteristics, equation (3) represents a system of three differential equations in three unknowns, with the appropriate boundary conditions specified in equations (4, 6). The unknown chordwise, normal, and sonic dimensionless perturbation velocities, U, V, and C, in each of the two periodic flow passages of the semi-infinite cascade are then determined by means of the two-airfoil passage-stacking technique in conjunction with the finite difference scheme developed by Brix and Platzer for the tuned cascade configuration.

The dimensionless unsteady perturbation pressure distributions on the surfaces of a reference airfoil from each set in the periodic detuned cascade are defined by these perturbation velocities. In particular, these perturbation unsteady surface pressure distributions are determined by means of the linearized unsteady Bernoulli equation. The nondimensional unsteady aerodynamic moment acting on the reference airfoil, M_R, and the standard torsion mode unsteady aerodynamic moment coefficient, $C_{\alpha\alpha}$, are then calculated by integrating the unsteady surface perturbation pressure difference across the chordline per equation (7),

$$M_R=\int_0^1\Delta P(x,y_s,t)(x-x_o)dx=C_{\alpha\alpha}\alpha_Re^{i\omega t} \tag{7}$$

where α_R is the amplitude of oscillation of the reference airfoil.

Influence Coefficient Technique

The boundary conditions specified in equations (4, 6) require that the nonuniformly spaced airfoils oscillate with equal amplitudes, a situation not appropriate for the detuned airfoil cascade. In addition, the application of this analysis is unnecessarily costly because the complete periodic perturbation flow field must be recalculated, not only for every new cascade geometry and flow condition, but also for each interblade phase angle value considered for a particular cascade and flow condition. These limitations are easily rectified by calculating the unsteady aerodynamic moment coefficients, $C_{\alpha\alpha}$, by means of influence coefficients. This influence coefficient technique will first be developed for a cascade of uniformly spaced airfoils and then extended for the aerodynamically detuned nonuniformly spaced cascade.

For an aerodynamically tuned cascade with N uniformly spaced airfoils, the total unsteady aerodynamic moment acting on an arbitrary reference airfoil, M_R, can be expressed in terms of influence coefficients per equation (8).

$$M_R=\hat\alpha_0(C_M^0)_R+\hat\alpha_1(C_M^1)_R+\ .\ .\ .\ +\hat\alpha_R(C_M^R)_R$$
$$+\ .\ .\ .\ +\hat\alpha_N(C_M^N)_R \tag{8}$$

Here, $(C_M^n)_R$ denotes the influence coefficient on the reference airfoil, R, associated with the motion of airfoil number n. Physically it represents the unsteady aerodynamic moment acting on the fixed reference airfoil, R, due to a unit amplitude torsional oscillation of airfoil number n. When n corresponds to R, the influence coefficient $(C_M^R)_R$ is the unsteady moment acting on airfoil R due to its own motion, with all other airfoils fixed.

For the detuned nonuniformly spaced cascade, a reference flow passage bounded by two reference airfoils must be considered. This is because the detuned cascade is made up of two distinct sets of airfoils, termed the odd-numbered and the

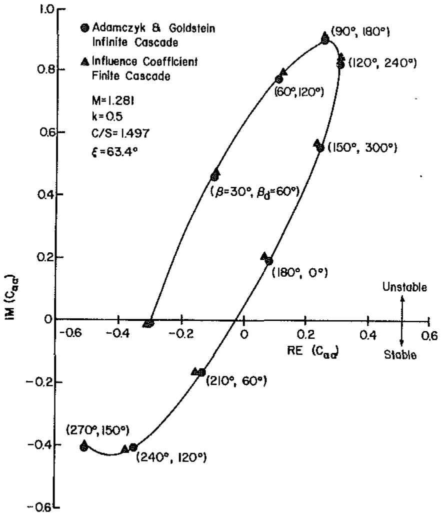

Fig. 4 Comparison of finite cascade influence coefficient model with infinite cascade conventional tuned cascade analysis

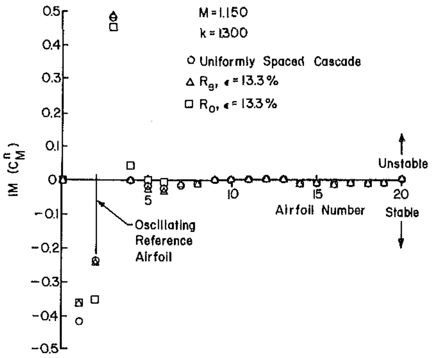

Fig. 5 Influence coefficients for uniform and nonuniform circumferentially spaced cascades

even-numbered airfoils, and two distinct flow passages. Each of these flow passages is bounded by one airfoil from each airfoil set, per Fig. 3.

A reduced spacing flow passage is taken as the reference. The reference airfoil for the lower boundary of the reference flow passage and for the set of even-numbered airfoils is denoted by R_e. The reference airfoil for the upper boundary of the reference flow passage and for the set of odd-numbered airfoils is denoted by R_o. Thus, the unsteady aerodynamic moment acting on these two reference airfoils can each be written in terms of the influence of the sets of odd and even-numbered airfoils as follows.

$$\begin{aligned} M_{R_o},R_e = {} & \{\hat{\alpha}_1(C_M^1)_{R_o,R_e} + \hat{\alpha}_3(C_M^3)_{R_o,R_e} + \ldots \\ & + \hat{\alpha}_{R_o}(C_M^{R_o})_{R_o,R_e} + \ldots + \hat{\alpha}_N(C_M^N)_{R_o,R_e}\} \\ & + \{\hat{\alpha}_0(C_M^0)_{R_o,R_e} + \hat{\alpha}_2(C_M^2)_{R_o,R_e} + \ldots \\ & + \hat{\alpha}_{R_e}(C_M^{R_e})_{R_o,R_e} + \ldots + \hat{\alpha}_{N-1}(C_M^{N-1})_{R_o,R_e}\} \end{aligned} \tag{9}$$

The two groups of bracketed terms are associated with the motion of the sets of odd-numbered and even-numbered airfoils, respectively. Also, to assure that there are an equal number of reduced spacing and increased spacing flow passages in the cascade, i.e., that periodicity is achieved by stacking two airfoil pasages at a time, equation (9) has been developed assuming that the cascade is made up of an odd number of airfoils, thereby resulting in an even number of airfoil passages.

The amplitude of the harmonic oscillations of the set of odd-numbered airfoils is denoted by $\hat{\alpha}_{R_o}\exp(in\beta_d)$, with β_d defining the constant interblade phase angle between sequentially odd-numbered airfoils. The set of even-numbered airfoils is assumed to oscillate with a complex amplitude $\hat{\alpha}_{R_e}\exp(in\beta_d)$, with the same constant interblade phase angle. The amplitude and phase difference between the motions of the sets of odd- and even-numbered airfoils is accounted for by considering the amplitudes of oscillation, $\hat{\alpha}_{R_o}$ and $\hat{\alpha}_{R_e}$, to be complex quantities. Because the interblade phase angles are referenced to the reference airfoils, R_o and R_e, the dimensionless unsteady aerodynamic moments (equation (10)), are rewritten in terms of the amplitudes of oscillation of the two reference airfoils as follows.

$$\begin{aligned} M_{R_o,R_e} = {} & \hat{\alpha}_{R_o}\Big\{(C_M^{R_o})_{R_o,R_e} + e^{i\beta_d}(C_M^3)_{R_o,R_e} \\ & + \ldots + e^{i\left(\frac{N-1}{2}\right)\beta_d}(C_M^N)_{R_o,R_e}\Big\} \\ & + \hat{\alpha}_{R_e}\Big\{(C_M^{R_e})_{R_o,R_e} + e^{i\beta_d}(C_M^2)_{R_o,R_e} + \ldots \\ & + e^{i\left(\frac{N-3}{2}\right)\beta_d}(C_M^{N-1})_{R_o,R_e}\Big\} \end{aligned} \tag{10}$$

where the subscripts R_o, R_e refer to the individual reference airfoils.

These two reference airfoil unsteady aerodynamic moments can be shown to be a standard eigenvalue problem, expressed in matrix form as follows.

$$\begin{aligned} \begin{bmatrix} M_{R_o} \\ M_{R_e} \end{bmatrix} &= C_{\alpha\alpha} \begin{bmatrix} \hat{\alpha}_{R_o} \\ \hat{\alpha}_{R_e} \end{bmatrix} \\ &= \begin{bmatrix} (CM^1)_{R_o} & (CM^2)_{R_o} \\ (CM^1)_{R_e} & (CM^2)_{R_e} \end{bmatrix} \begin{bmatrix} \hat{\alpha}_{R_o} \\ \hat{\alpha}_{R_e} \end{bmatrix} \end{aligned} \tag{11}$$

where:

$$\begin{aligned} (\mathrm{CM}^1)_{R_o,R_e} &= (C_M^{R_o})_{R_o,R_e} + e^{i\beta_d}(C_M^3)_{R_o,R_e} + \ldots \\ &\quad + e^{i\left(\frac{N-1}{2}\right)\beta_d}(C_M^N)_{R_o,R_e} \\ (CM^2)_{R_o,R_e} &= (C_M^{R_e})_{R_o,R_e} + e^{i\beta_d}(C_M^4)_{R_o,R_e} + \ldots \\ &\quad + e^{i\left(\frac{N-3}{2}\right)\beta_d}(C_M^{N-1})_{R_o,R_e} \end{aligned}$$

The terms $(CM^1)_{R_o,R_e}$ describe the influence that the set of odd-numbered airfoils has on the unsteady moment developed on reference airfoils R_o and R_e respectively. $(CM^2)_{R_o,R_e}$ represents the effect that the set of even-numbered airfoils has on these two reference airfoils.

Equation (11) denotes a standard eigenvalue problem. The unsteady aerodynamic moment coefficient, $C_{\alpha\alpha}$, is the eigenvalue of the influence coefficient matrix, (CM), with the associated eigenvector defining the flutter mode for the nonuniformly spaced cascade, i.e., the relationship between the motions of the sets of odd-numbered and even-numbered airfoils. In the limit wherein this aerodynamically detuned cascade becomes uniformly spaced, the eigenvalue problem of equation (11) reduces exactly to that considered by Bendiksen [4], for a tuned airfoil cascade.

The influence coefficients $(C_M^n)_{R_o,R_e}$ are determined from a modification of the unsteady aerodynamic model previously described. For example, to determine $(C_M^n)_{R_o}$, airfoil n is harmonically oscillated while all of the other nonuniformly spaced cascaded airfoils are kept fixed and the effect on reference airfoil R_o calculated. With all of the influence coefficients determined in this manner, $(CM^1)_{R_o,R_e}$ and

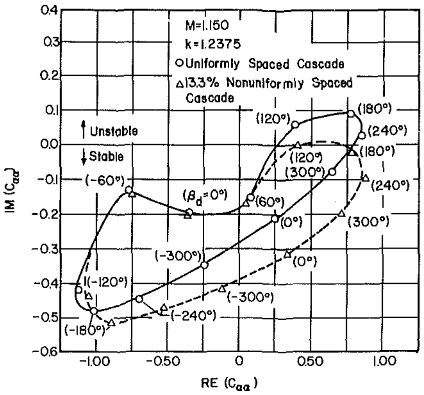

Fig. 6 Effect of aerodynamic detuning on the unsteady aerodynamic moment coefficients

$(CM^2)_{R_o,R_e}$ are calculated by vector addition of the appropriate influence coefficients after multiplication by the specified complex interblade phase angle term. To analyze a different interblade phase angle, it is only necessary to perform the vector addition in terms of this new phase angle. The influence coefficients calculated from the unsteady aerodynamic model do not have to be recalculated.

Thus, this matrix formulation of the eigenvalue problem, equation (11), is utilized herein in conjunction with the influence coefficient technique to efficiently determine the standard dimensionless torsion mode unsteady aerodynamic moment coefficients, $C_{\alpha\alpha}$, for specified aerodynamically tuned and detuned nonuniformly spaced cascade configurations.

Model Verification

To verify the formulation of this aerodynamically detuned finite cascade model, the limiting case of a uniformly spaced cascade configuration is considered. In particular, both this detuned finite cascade analysis based on an influence coefficient technique and the uniformly spaced infinite cascade analysis of Adamczyk and Goldstein [11] are applied to Verdon's uniformly spaced Cascade B configuration [14].

The real and imaginary parts of the unsteady aerodynamic moment coefficient, $C_{\alpha\alpha}$, predicted with these two models are presented in Fig. 4, with the interblade phase angle β as a parameter. Two interblade phase angles are associated with each point shown in Fig. 4. β_d refers to the interblade phase angle utilized in equation (10) and β is the interblade phase angle calculated from the eigenvectors of equation (11). Because the cascaded airfoils are executing single degree of freedom torsion mode oscillations, the stability of the cascade is specified by the sign of the imaginary part of this moment coefficient, with positive values corresponding to an unstable configuration. As seen, there is excellent agreement between these two analyses for all interblade phase angles.

Results

To demonstrate this nonuniform airfoil spacing technique for aerodynamic detuning, the Cascade B geometry is utilized as a baseline with a midchord elastic axis location.

The influence coefficients, (C_M^n), for both the uniformly spaced baseline cascade and a 13.3% nonuniformly spaced cascade are presented in Fig. 5. As seen, the airfoils from 0 to $-\infty$ have no influence because of the law of forbidden signals. For the detuned cascade, the reference airfoils R_o and R_e are oscillated. For comparison purposes, the results are shifted so that the results presented in this figure correspond to airfoil No. 2 being the oscillating reference airfoil in all cases. These influence coefficients are displayed in a manner corresponding to airfoil No. 2 harmonically oscillating with all other airfoils in the cascade fixed. As seen, the oscillating airfoil has a significant effect only on the unsteady moments developed on the airfoils in its immediate vicinity. Also, the influence of the oscillating airfoil itself on the total unsteady moment coefficient, $C_{\alpha\alpha}$, is stabilizing. The stabilizing or destabilizing influence of the other airfoils in the cascade can not be determined from these influence coefficients alone. This is because the total unsteady moment coefficient is determined from these influence coefficients by performing the vector addition indicated in equation (11) for a specified interblade phase angle value referenced to the oscillating airfoil.

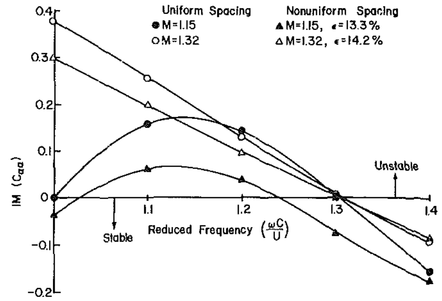

Fig. 7 Effect of inlet Mach number on the stability of the uniform and aerodynamically detuned cascades

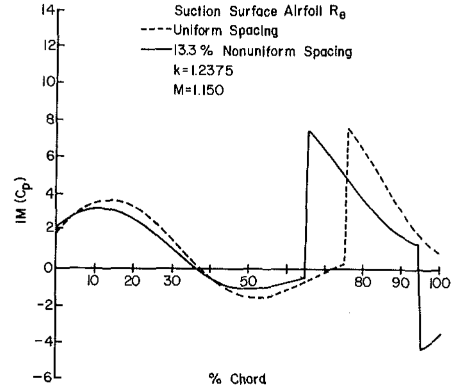

Fig. 8 Airfoil R_e suction surface imaginary unsteady pressure distributions for stable uniform cascade and neutrally stable detuned cascade

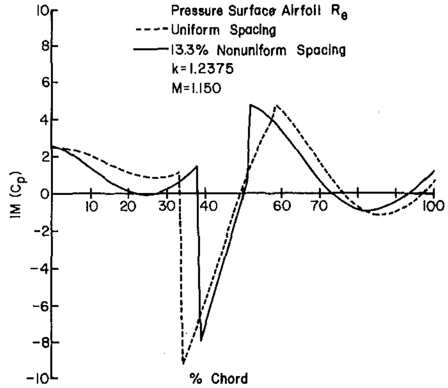

Fig. 9 Airfoil R_e pressure surface imaginary unsteady pressure distributions for stable uniform cascade and neutrally stable detuned cascade

The variation of $C_{\alpha\alpha}$ with interblade phase angle for both the 13.3% nonuniformly spaced detuned cascade and the baseline, determined from the influence coefficients of Fig. 5, is presented in Fig. 6. For conditions considered, the baseline cascade exhibits an instability, i.e., the imaginary part of $C_{\alpha\alpha}$

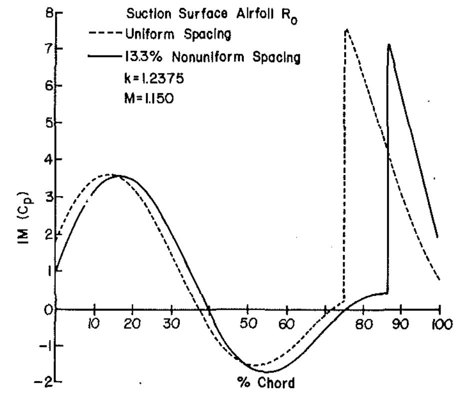

Fig. 10 Airfoil R_0 suction surface imaginary unsteady pressure distributions for stable uniform cascade and neutrally stable detuned cascade

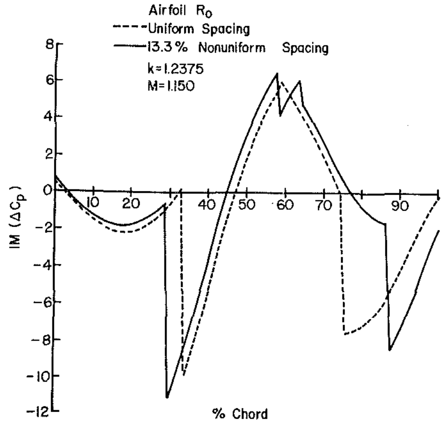

Fig. 13 Airfoil R_0 imaginary pressure difference distributions for stable uniform cascade and neutrally stable detuned cascade

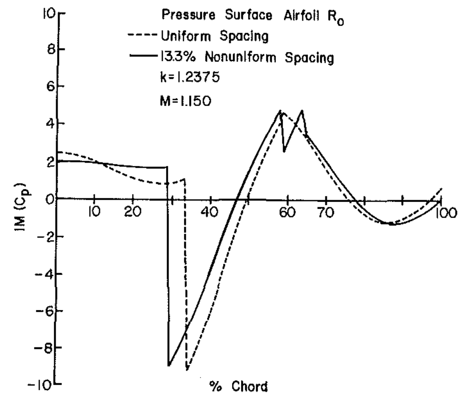

Fig. 11 Airfoil R_0 pressure surface imaginary unsteady pressure distributions for stable uniform cascade and neutrally stable detuned cascade

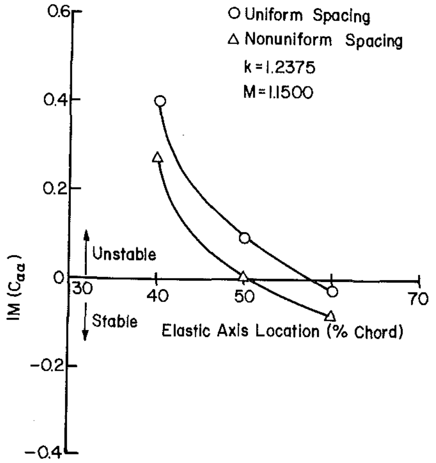

Fig. 14 The effect of elastic axis location on the stability of the uniform and aerodynamically detuned cascades

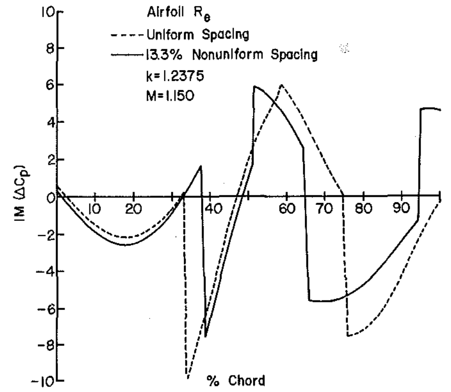

Fig. 12 Airfoil R_e imaginary pressure difference distributions for stable uniform cascade and neutrally stable detuned cascade

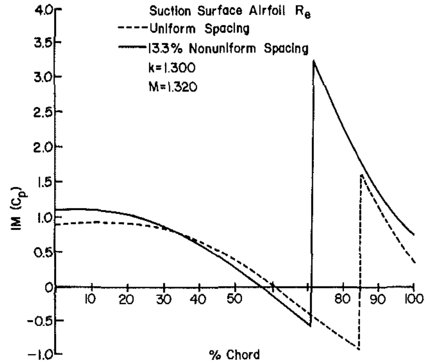

Fig. 15 Airfoil R_e suction surface imaginary pressure distributions for neutrally stable uniform and aerodynamically detuned cascades

has a positive value. However, the aerodynamic detuning associated with this nonuniform spacing results in a neutrally stable or stable configuration for all interblade phase angle values. Also, the nonuniform airfoil spacing generally exhibits a beneficial effect on stability in that this aerodynamic detuning results in the imaginary part of the moment coefficients for the detuned cascade becoming more negative than the corresponding baseline values. This beneficial effect is particularly evident for interblade phase angle values corresponding to forward-traveling waves, being somewhat less pronounced for backward traveling waves.

Figure 7 shows the effect of inlet Mach number on the variation with reduced frequency of the imaginary part of $C_{\alpha\alpha}$ for the least stable interblade phase angle value. For a constant Mach number value, the stability of the uniformly spaced baseline configuration is generally enhanced by the nonuniform airfoil spacing, with the larger effects associated with the lower Mach numbers. Also, as the Mach number increases, there is a decreased effect of aerodynamic detuning on the critical reduced frequency, defined as the reduced frequency resulting in neutral stability and characterized by a value of zero for the imaginary part of $C_{\alpha\alpha}$.

To demonstrate the fundamental mechanism for the enhanced stability of the detuned cascade, the reduced frequency and Mach number at which the detuned configuration is neutrally stable but the baseline cascade is un-

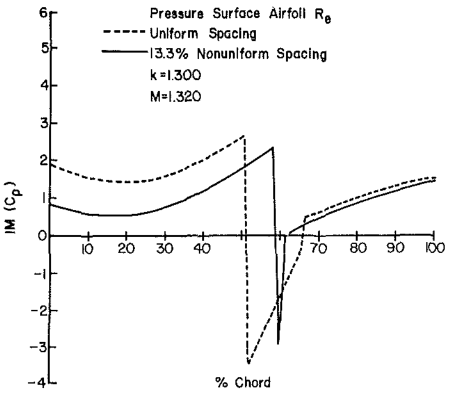

Fig. 16 Airfoil R_e pressure surface imaginary pressure distributions for neutrally stable uniform and aerodynamically detuned cascades

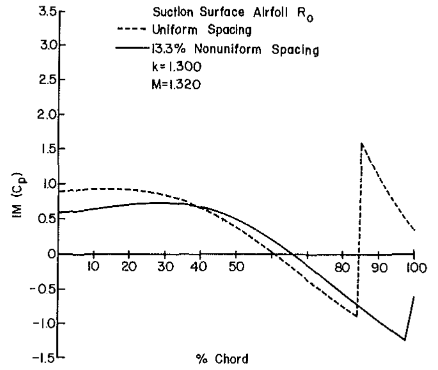

Fig. 17 Airfoil R_0 suction surface imaginary pressure distributions for neutrally stable uniform and aerodynamically detuned cascades

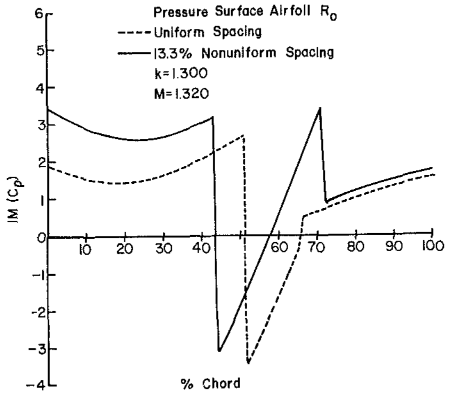

Fig. 18 Airfoil R_0 pressure surface imaginary pressure distributions for neutrally stable uniform and aerodynamically detuned cascades

stable is considered: $R=1.2375$ and $M=1.15$, per Fig. 7. The chordwise variation of the imaginary part of the dimensionless surface pressure and pressure differences on the reference airfoils for the detuned and baseline configurations are presented in Figs. 8-13. As seen, the aerodynamic detuning affects the imaginary part of the unsteady surface pressure distributions over the complete airfoil chord, including the surface intersection locations of the Mach waves and their reflections (Fig. 8-11). However, there is only a relatively small effect on the chordwise distributions of the unsteady pressure differences in front of the first Mach wave-airfoil intersection location as a result of this aerodynamic detuning (Figs. 12, 13). The effects of aerodynamic detuning

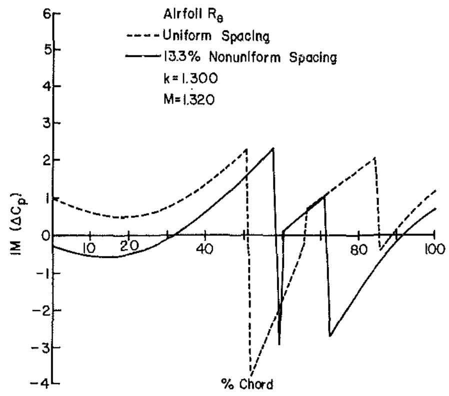

Fig. 19 Airfoil R_e imaginary pressure difference distributions for neutrally stable uniform and aerodynamically detuned cascades

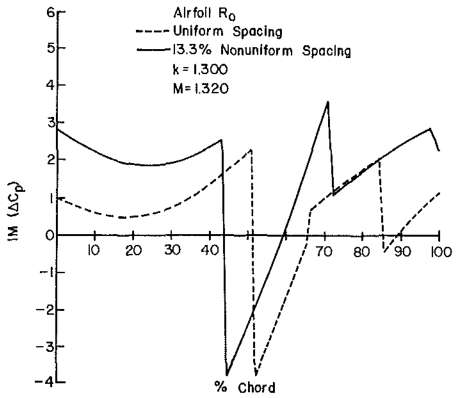

Fig. 20 Airfoil R_0 imaginary pressure difference distributions for neutrally stable uniform and aerodynamically detuned cascades

on these unsteady pressure difference distributions are associated with the Mach wave-airfoil intersection locations and the chordwise distributions aft of the first intersection.

Because the nonuniform airfoil spacing at these conditions primarily affects the pressure difference distribution over the mid and aft chord portions of the airfoil surfaces, the elastic axis location should have a significant effect on the detuning stability enhancement. This is demonstrated in Fig. 14 which considers the effect of elastic axis location on the stability of the baseline and detuned cascades of these conditions. As seen, as the elastic axis is moved forward of midchord, the improvement in stability due to aerodynamic detuning is increased as compared to a movement of the elastic axis aft of midchord.

It is interesting to consider the fundamental differences between the two cascade configurations at the conditions for which both are neutrally stable, $M=1.32$ and $k=1.3$ per Fig. 7. The chordwise variation of the imaginary part of the surface pressures and the pressure differences are presented in Figs. 15-20. As seen, the detuning primarily affects the chordwise distributions of the unsteady pressures on the pressure surfaces of the two reference airfoils (Figs. 15-18). However, the chordwise distributions of the unsteady pressure difference for the baseline and the detuned cascade configurations are significantly different (Figs. 19 and 20) even though their integrated values are equal, i.e., the imaginary part of $C_{\alpha\alpha}$ for each of these configurations is zero. Thus, although the aerodynamic detuning has greatly affected the unsteady aerodynamic loading distributions, the aeroelastic stability has not been affected.

Summary and Conclusions

A model for aerodynamic detuning to achieve enhanced supersonic unstalled aeroelastic stability has been developed. This model analyzes the stability of an aerodynamically detuned rotor operating in a supersonic inlet flow field with a subsonic leading edge locus, with the aerodynamic detuning accomplished by means of nonuniform circumferential spacing of adjacent rotor blades. The unsteady aerodynamic forces and moments acting on the blading are defined in terms of influence coefficients in a manner that permits the stability of both a conventional uniformly spaced rotor configuration as well as the detuned nonuniform circumferentially spaced rotor to be determined.

The effect of this aerodynamic detuning on the fundamental unsteady aerodynamics and aeroelastic stability were considered utilizing Verdon's Cascade B as a baseline configuration. This study demonstrated the potential enhanced stability associated with this type of aerodynamic detuning. The aerodynamic detuning significantly affected the chordwise distributions of the unsteady surface pressures. However, aerodynamic detuning did not always affect the unsteady pressure distributions over the complete airfoil chord. For conditions such that the baseline configuration was unstable but the detuned cascade neutrally stable, the effect of aerodynamic detuning on the unsteady pressure differences was shown to be associated with the Mach wave-airfoil intersection locations and the chordwise distributions aft of the first intersectioon. For these conditions, it was then demonstrated that a forward position, as opposed to an aft position, for the elastic axis was associated with increased stability enhancement. It was also shown that for one particular set of conditions, both the uniformly spaced and the aerodynamically detuned cascade configurations were neutrally stable but the associated unsteady surface pressure and pressure difference chordwise distributions were significantly different, i.e., detuning significantly affected the surface pressure distributions but did not enhance the cascade stability.

Acknowledgments

The NASA-Lewis Research Center and, in particular, Donald Boldman and Calvin Ball, are most gratefully acknowledged for their encouragement, discussions, and support.

References

1 Whitehead, D. S., "Effect of Mistuning on the Vibration of Turbomachine Blades Induced by Wakes," *Journal of Mechanical Engineering Science*, Vol. 8, No. 1, Mar. 1966.

2 Kaza, K. R. V., and Kielb, R. E., "Effect of Mistuning on Bending-Torsion Flutter and Response of a Cascade in Incompressible Flow," *AIAA Journal*, Vol. 20, No. 8, Aug. 1982.

3 Kielb, R. E., and Kaza, K. R. V., "Aeroelastic Characteristics of Mistuned Blades in Subsonic and Supersonic Flows," *Journal of Vibration, Stress, and Reliability in Design*, Vol. 105, Oct. 1983.

4 Bendiksen, O. O., "Flutter of Mistuned Turbomachinery Rotors," ASME JOURNAL OF ENGINEERING FOR GAS TURBINES AND POWER, Vol. 106, No. 1, Jan. 1984, pp. 25-33.

5 Crawley, E. F., and Hall, K. C., "Optimization and Mechanisms of Mistuning in Cascades," ASME JOURNAL OF ENGINEERING FOR GAS TURBINES AND POWER, Vol. 107, 1985, pp. 418-426.

6 Verdon, J. M., "The Unsteady Aerodynamics of a Finite Supersonic Cascade with Subsonic Axial Flow," *Journal of Applied Mechanics*, Vol. 40, Sept. 1973.

7 Kurosaka, M., "On the Unsteady Supersonic Cascade with a Subsonic Leading Edge—An Exact First Order Theory: Parts 1 and 2," ASME JOURNAL OF ENGINEERING FOR POWER, Vol. 96, No. 1, Jan. 1974.

8 Verdon, J. M., and McCune, J. E., "The Unsteady Supersonic Cascade in Subsonic Axial Flow," *AIAA Journal*, Vol. 13, Feb. 1975.

9 Brix, C. W., and Platzer, M. F., "Theoretical Investigation of Supersonic Flow Past Oscillating Cascades with Subsonic Leading Edge Locus," AIAA Paper No. 74-14, Jan. 1974.

10 Caruthers, J. E., and Riffel, R. E., "Aerodynamic Analysis of a Supersonic Cascade Vibrating in a Complex Mode," *Journal of Sound and Vibration*, Vol. 71, 1980.

11 Adamczyk, J. J., and Goldstein, M. E., "Unsteady Flow in a Supersonic Cascade with Subsonic Leading Edge Locus," *AIAA Journal*, Vol. 16, No. 12, Dec. 1979.

12 Yates, J. E., "Analysis of Supersonic Unsteady Cascades with the Method of Characteristics," AFFDL-TR-75-159, 1975.

13 Ni, R. H., and Sisto, F., "Numerical Computation of Non-stationary Aerodynamics of Flat Plate Cascades in Compressible Flow," ASME JOURNAL OF ENGINEERING FOR POWER, Vol. 98, No. 2, Apr. 1976.

14 Verdon, J. M., "Further Developments in the Aerodynamic Analysis of Unsteady Supersonic Cascades, Parts 1 and 2," ASME Papers 77-GT-44 and 77-GT-45, Mar. 1977.

F. K. Moore
Cornell University,
Ithaca, NY

E. M. Greitzer
Massachusetts Institute of Technology,
Cambridge, MA

A Theory of Post-Stall Transients in Axial Compression Systems: Part I—Development of Equations

An approximate theory is presented for post-stall transients in multistage axial compression systems. The theory leads to a set of three simultaneous nonlinear third-order partial differential equations for pressure rise, and average and disturbed values of flow coefficient, as functions of time and angle around the compressor. By a Galerkin procedure, angular dependence is averaged, and the equations become first order in time. These final equations are capable of describing the growth and possible decay of a rotating-stall cell during a compressor mass-flow transient. It is shown how rotating-stall-like and surgelike motions are coupled through these equations, and also how the instantaneous compressor pumping characteristic changes during the transient stall process.

Introduction

Background. Problems of compressor instability have been of concern to aircraft engine designers for a number of years, and the provision of sufficient stall margin is an important consideration in any compressor design. In addition to problems associated with the inception of stall, however, another aspect of this general topic has been of increasing import in recent years. This is the behavior of the compression system subsequent to the onset of stall, i.e., subsequent to the onset of compressor or compression system instability.

The reason for this increased interest in post-stall behavior has to do with the phenomenon of nonrecoverable stall (or stall "stagnation"). If the engine enters this condition, described in [1], the only remedy may be to shut the engine down and restart it.

Clearly, therefore, it is important to gain the ability to predict post-stall behavior, as a basis for rational design of stagnation-resistant compressors. This is true not only for quasi-steady operation but also for the unsteady features of the compression system response. In the first instance, one may be able to consider the compressor in isolation, without coupling it to the system. This is essentially the pure rotating-stall problem treated by Day, Greitzer, and Cumpsty [2] semi-empirically and, more recently, by Moore [3] in a more fundamental manner. To understand engine behavior more generally, however, one must deal with the unsteady behavior of the compression system during the mass flow oscillations that characterize post-stall transients. Thus, one must describe the possible formation and growth in the compressor of a rotating-stall cell during a transient process when the compressor is interacting dynamically with other components of the system, as, for example, in a surge cycle.

It is to be stressed from the outset that this task cannot today be carried out by exact or numerical solution of the basic partial differential equations of fluid motion. The prediction of even steady-state rotating-stall performance has not yet been carried out on this level. However, many of the salient features of rotating stall have recently been predicted [3,4] using certain simplifying assumptions, and we have found that an effective model for general transients of compressor operation can be formulated on the basis of these same assumptions. We believe that the resulting general theory, to be described in this paper (Part I) and its companion (Part II) will prove helpful for general physical insight, give guidance to experimental studies, and also will help to unravel and assess the various interactive effects of many important design parameters.

Before plunging into the theoretical development, it seems appropriate to outline certain expectations, based on past studies [5,6] and a consideration of relevant time scales. First, we expect that a general theory of transients should show rotating stall [2,3,4] developing and ultimately predominating in some circumstances, and surge [5,6] ultimately predominating in others. Those two types of oscillation differ fundamentally in that pure rotating stall is steady (in the proper rotating frame of reference) but not axisymmetric. Pure surge, on the other hand, we will define to be axisymmetric but unsteady. We will assume that a transient is initiated by some disturbance which is generally both unsteady and nonaxisymmetric; thus, we expect surgelike and rotating-stall-like features to be coupled in the transient as it develops.

As discussed in [7], in many practical compression systems the time needed to form a rotating-stall cell and the time for mass flow to change (as in surge) are comparable. Therefore, rotating stall will not have time to fully form during a typical transient. This has significant implications for the modeling of post-stall transients, because during the transient, the compressor is not performing in a quasi-steady manner.

Contributed by the Gas Turbine Division of THE AMERICAN SOCIETY OF MECHANICAL ENGINEERS and presented at the 30th International Gas Turbine Conference and Exhibit, Houston, Texas, March 18–21, 1985. Manuscript received at ASME Headquarters, January 10, 1985. Paper No. 85-GT-171.

Therefore, information obtained from a steady-state compressor test with the machine operating in rotating stall will generally not represent performance during a rapid post-stall transient. This being so, it is imperative that the theory developed herein should predict how the growth or decay of rotating stall affects the instantaneous compressor pumping characteristic.

We may also note that the expected asymmetric flow patterns will have length scales on the order of compressor diameter. They will therefore change on a time scale which is typically very much longer than that associated with the unsteady response of a single-blade passage. Thus, the precise modeling of the unsteady aerodynamic performance of the blades would not be expected to be important for a successful theory of stall-cell growth [7].

In this paper, we will first derive a set of coupled nonlinear equations which describe the time-dependent state of the assumed compression system. These equations will be simplified by use of an approximate (Galerkin) procedure, and then specialized by introduction of a particular compressor performance curve. The general nature of the resulting equations will be briefly discussed, concluding the present paper (Part I). In the companion paper (Part II—Application), some general features of the solutions will be analyzed, and numerical solutions will be presented which indicate the effects of certain parameters of practical interest. Part II will conclude with comments about future avenues of research, both theoretical and experimental, that are thought to be needed to extend and exploit the theory.

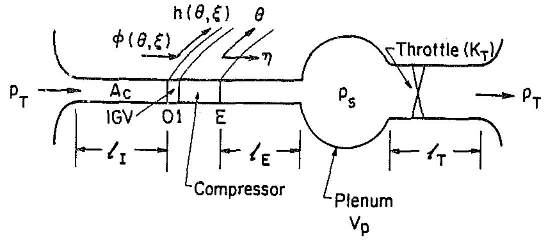

Fig. 1 Schematic of compressor and compression system geometry showing nondimensional lengths

Fluid Dynamic Model

The basic compression system to be analyzed is shown in Fig. 1. It consists of a compressor operating in a duct and discharging to a downstream plenum. The plenum dimensions are large compared to those of the compressor and its ducts, so that the velocities and fluid accelerations in the plenum can be considered negligible. Hence the pressure in the plenum can be considered to be uniform spatially, although possibly varying in time. The flow through the system is controlled by a throttle at the plenum exit.

The systems that we consider will have overall pressure rises, atmosphere to plenum, that are small compared to the ambient level. If, also, we assume Mach numbers to be small, and oscillations to have frequencies well below those of acoustic resonance, then we can assume incompressible flow in the compressor itself. The gas in the plenum must be

Nomenclature

A = amplitude function of first-harmonic angular disturbance, equation (53)
A_c = compressor duct area
a = reciprocal time-lag parameter of blade passage, equation (6)
a_s = sound speed
B = $(U/2a_s)\sqrt{V_p/A_cL_c}$
F = pressure-rise coefficient in blade passage, equation (2)
F_T = throttle characteristic function, equation (39); inverse is $F_T^{-1}(\Psi)$
f = nondimensional speed coefficient, relative to propagation of laboratory, of angular disturbance
f_0 = value of f for single harmonic disturbance, equation (57)
g = disturbance of axial flow coefficient
H = semi-height of cubic axisymmetric characteristic, Fig. 3
h = circumferential velocity coefficient
J = square of amplitude of angular disturbance of axial-flow coefficient, equation (58); J_e for pure rotating stall
K_G = loss coefficient at IGV entrance, equation (10)
K_T = throttle coefficient, equation (39)
l_c = total aerodynamic length (L_c/R) of compressor and ducts, in wheel radii, equation (24)
l_E, l_I, l_T = length of exit, entrance, and throttle ducts, in wheel radii, Fig. 1
m = compressor-duct flow parameter, equation (20)
N = number of stages of core compressor
P = pressure coefficient, equation (17)
p_0 = static pressure at entrance to IGV, Fig. 1
p_1, p_E = static pressures at entrance and exit of core compressor, Fig. 1
p_S = static pressure at end of exit (diffuser) duct, and pressure in the plenum, Fig. 1
p_T = total pressure ahead of entrance and following the throttle duct, Fig. 1
R = mean wheel radius
r = time-dependent phase angle, equation (53)
t = time
U = wheel speed at mean diameter
V_p = volume of plenum, Fig. 1
K_T = throttle coefficient, equation (39)
W = semi-width of cubic characteristic, Fig. 3
Y = disturbance potential at compressor entrance, equation (31)
η = axial distance measured in wheel radii, Fig. 1
θ = angular coordinate around wheel, Fig. 1
θ^* = angular coordinate around wheel, measured relative to a rotating-stall cell, equation (46)
λ = rotating-stall parameter, equation (47)
ξ = time, referred to time for wheel to rotate one radian
ρ = density
τ = coefficient of pressure-rise lag, equation (2)
Φ = axial flow coefficient in compressor, annulus averaged; axial velocity divided by wheel speed
Φ_T = flow coefficient of throttle duct, referred to entrance-duct area, Fig. 1
ϕ = local axial flow coefficient, a function of θ and ξ
$\tilde{\phi}$ = velocity potential in entrance duct, equation (11)
$\tilde{\phi}'$ = disturbance velocity potential, equation (14)
Ψ = total-to-static pressure-rise coefficient, equation (22)
ψ_c = axisymmetric pressure-rise coefficient, equation (23)
ψ_{c_0} = shut-off value of axisymmetric characteristic, Fig. 3

Subscripts

0 = at the entrance to the compressor
E = at the exit of the compressor

considered compressible, however, because it acts dynamically as a gas spring.

This basic compression system model has been used in many investigations of surge. Where we will depart from previous practice in analysis of compression system transients, however, is in the coupling of an analysis of the two-dimensional unsteady flow in the compressor with the lumped-parameter system model. We therefore begin by describing our representation of the compressor.

Flow Disturbance in the Compressor. The basic compressor model is that of [3]. The compressor is considered to have a high hub-to-tip radius ratio, so that a two-dimensional description can be used. The compressor duct is modeled as an inlet contraction followed by a constant-area section upsteam of the compressor. The annulus immediately downstream of the compressor also has constant area. These restrictions simplify the present analysis, but could be removed in a more general treatment.

The following nomenclature will be used (see Fig. 1 and the list provided at the beginning of this paper). All distances will be nondimensionalized by the mean compressor radius (R). The nondimensional circumferential coordinate is then simply the wheel angle θ, while the axial coordinate, also referred to R, will be denoted by η. Time will be denoted by radians of wheel travel:

$$\xi = Ut/R \tag{1}$$

As discussed in [3], the basic model we adopt for the unsteady performance of a compressor blade row is that the pressure rise across a single row is given by

$$\frac{\Delta P}{\frac{1}{2}\rho U^2} = F(\phi) - \tau \frac{d\phi}{dt} \tag{2}$$

where $\phi(= C_x/U)$ is the local, unsteady axial velocity coefficient at the compressor. The quantity $F(\phi)$ represents the axisymmetric steady performance of the blade row, and τ can be viewed as a "time constant" associated with the internal lags in the compressor. In [3], it was shown that a reasonable value for τ can be based on the inertia of fluid in the passage.

The unsteadiness of the flow through a stator passage reflects the accelerations associated with transient effects. For a rotor, however, there is also unsteadiness due to the rotor blades moving (with velocity U) through a circumferentially nonuniform flow. Therefore, using equation (1),

$$\left(\frac{d\phi}{dt}\right)_{\text{stator}} = \frac{U}{R}\frac{\partial\phi}{\partial\xi} \tag{3}$$

$$\left(\frac{d\phi}{dt}\right)_{\text{rotor}} = \frac{U}{R}\left(\frac{\partial\phi}{\partial\xi} + \frac{\partial\phi}{\partial\theta}\right) \tag{4}$$

We note that in the present situation, because of the possibility of growth or decay of velocity nonuniformities, there is not necessarily a Galilean equivalence between the changes in time and the spatial derivatives, as there was for the pure traveling wave analyzed in [3].

Applying these ideas to a compressor of N stages, we record the pressure rise across a compressor (not including the inlet and exit guide vanes which we will discuss subsequently) comprising N rotor–stator pairs:

$$\frac{p_E - p_1}{\rho U^2} = NF(\phi) - \frac{1}{2a}\left(2\frac{\partial\phi}{\partial\xi} + \frac{\partial\phi}{\partial\theta}\right) \tag{5}$$

where we refer to Fig. 1 to identify the pressures p_E and p_1, and, for convenience, we define

$$a \equiv R/(N\tau U). \tag{6}$$

Returning to the overall sketch provided in Fig. 1, an irrotational, inviscid flow is imagined to proceed from an upstream (atmospheric) reservoir at stagnation pressure p_T through an entrance duct to the IGV entrance at 0. We note that ϕ, the axial flow coefficient at 0, can depend on both angle θ around the wheel and time ξ, even though the reservoir pressure is constant. As a result of the flow process in the approach duct, if ϕ varies with θ, then we will find that a circumferential coefficient $h(\xi,\theta)$ must also appear at the IGV entrance. It should be noted that the present coordinate system is fixed in the laboratory, whereas in [3, 4], the system traveled with a supposed permanent rotating-stall pattern.

We define an average of ϕ around the wheel

$$\frac{1}{2\pi}\int_0^{2\pi} \phi(\xi,\theta)\,d\theta \equiv \Phi(\xi) \tag{7}$$

Proceeding just as in [3, 4], we suppose that any circumferential nonuniformity of axial velocity within the compressor must, by a continuity argument and by evidence cited in [2], go straight through the machine. That is, we write

$$\phi = \Phi(\xi) + g(\xi,\theta); \quad h = h(\xi,\theta) \tag{8}$$

and note that, by definition, the angle average of g must vanish. Also, because under the stated assumptions no circulation can arise in the entrance duct, h must have vanishing average as well. Thus,

$$\int_0^{2\pi} g(\xi,\theta)\,d\theta = 0; \quad \int_0^{2\pi} h(\xi,\theta)\,d\theta = 0 \tag{9}$$

We could now introduce equation (8) into equation (5) to describe pressure rise in terms of Φ and g. We defer this step until after entrance and exit duct pressure changes have also been found.

Flow Disturbance in the Entrance Duct and Guide Vanes. The overall pressure rise from compressor inlet to exit will include the pressure difference associated with the circumferential velocity component just ahead of the inlet guide vanes. The pressure difference from station 0 to station 1 (where the flow is axial) can be written as:

$$\frac{p_1 - p_0}{\rho U^2} = \frac{1}{2}K_G h^2 \tag{10}$$

If the IGV entrance is lossless, the entrance recovery coefficient K_G is unity, but if a loss does occur there, then $K_G < 1$.

In the entrance duct upstream of the IGV, we assume irrotational flow, so that a velocity potential exists which, though unsteady, will satisfy Laplace's equation. Specifically, we define a velocity potential $\tilde{\phi}$ the gradient of which will give axial and circumferential velocity coefficients everywhere in the entrance duct; that is,

$$\tilde{\phi}_\eta = v/U; \quad \tilde{\phi}_\theta = u/U \tag{11}$$

Henceforward, we will use subscripts to denote partial differentiation. Accordingly, at the IGV entrance (point 0 on Fig. 1, where v and u are described in terms of g and h),

$$(\tilde{\phi}_\eta)_0 = \Phi(\xi) + g(\xi,\theta); \quad (\tilde{\phi}_\theta)_0 = h(\xi,\theta) \tag{12}$$

Far upstream, in the reservoir, we take $\tilde{\phi}$ itself to be zero because the flow is at rest.

As a general matter, we must solve Laplace's equation for $\tilde{\phi}$ and then apply Bernouilli's equation to evaluate pressure at the point 0. For unsteady flow, with our particular definitions of variables, the result is

$$\frac{P_T - P_0}{\rho U^2} = \frac{1}{2}(\phi^2 + h^2) + (\tilde{\phi}_\xi)_0 \tag{13}$$

The unsteady contribution, $(\tilde{\phi}_\xi)_0$, is due to unsteadiness in both Φ and g. The complexity of this term is reduced if we consider a straight inlet duct, preceded by a much shorter contracting passage, as sketched in Fig. 1. In such a duct, of dimensionless length l_I, the angle-averaged coefficient $\Phi(\xi)$ will be constant along the duct, and, in view of equation (11), the velocity potential may be immediately written as

$$\tilde{\phi} = (\eta + l_I)\Phi(\xi) + \tilde{\phi}'(\xi,\eta) \qquad (14)$$

where $\tilde{\phi}'$ is a disturbance velocity potential vanishing at $\eta = -l_I$, and giving g and h at point 0:

$$(\tilde{\phi}'_\eta)_0 = g(\xi,\theta); \quad (\tilde{\phi}'_\theta)_0 = h(\xi,\theta) \qquad (15)$$

The term needed for equation (13) is simply

$$(\tilde{\phi}_\xi)_0 = l_I \frac{d\Phi}{d\xi} + (\tilde{\phi}'_\xi)_0 \qquad (16)$$

Flow Disturbance in the Exit Duct and Guide Vanes. In the exit duct, a complicated rotational flow appears even with axial OGV's, when axial flow varies with θ. We will use an approximation, somewhat generalized, developed in [3]. We consider the function P, defined below, to be sufficiently small that it satisfies Laplace's equation.

$$P \equiv \frac{p_s(\xi) - p}{\rho U^2}; \quad \nabla^2 P = 0 \qquad (17)$$

That is, pressure in the exit duct is assumed to differ (owing to circumferential flow nonuniformities) only slightly from static pressure at discharge (p_s); and in such a case, one may show from the Euler equations that it then satisfies Laplace's equation. Now, the axial Euler equation, evaluated at the compressor discharge (point E of Fig. 1), gives exactly

$$(P_\eta)_E = (\tilde{\phi}_{\eta\xi})_0 = \frac{d\Phi}{d\xi} + (\tilde{\phi}'_{\eta\xi})_0 \qquad (18)$$

Thus, the potential problem for P is the same as the one already mentioned for $-\tilde{\phi}'_\xi$; the minus sign is necessary because, in the exit duct, η increases away from the compressor face, whereas in the entrance duct, η increases toward the compressor face. Choosing a constant to make $P = 0$ at the duct exit, $\eta = l_E$, we find

$$P = (\eta - l_E)\frac{d\Phi}{d\xi} - \tilde{\phi}'_\xi \qquad (19)$$

The foregoing simplified analysis assumes that l_E is not smaller than the distance (conservatively, l_I) at which the entrance flow disturbance potential vanishes. If it were much shorter, presumably the second term of equation (19) should be omitted. Therefore, just as in [3], we introduce a parameter m in the final result for exit pressure change

$$\frac{p_S - p_E}{\rho U^2} = (P)_E = -l_E \frac{d\Phi}{d\xi} - (m-1)(\tilde{\phi}'_\xi)_0 \qquad (20)$$

where $m = 2$ would refer to a "long enough" exit duct, and $m = 1$ would refer to a very short one.

Net Pressure Rise to End of Compressor Exit Duct. Between the upstream reservoir (p_T) and the discharge from the exit duct (p_S) is the zone where circumferential pressure variations may arise. Further downstream are the plenum and throttle, which we assume to contain only axisymmetric disturbances. We can now form the net pressure rise in the zone of possible angular variations by combining equations (5, 10, 13, and 19). After introducing equations (8, 16), the result may be written

$$\frac{p_S - p_T}{\rho U^2} = \left(NF - \frac{1}{2}\phi^2\right) - \left(l_I + \frac{1}{a} + l_E\right)\frac{d\Phi}{d\xi} - m(\tilde{\phi}'_\xi)_0$$
$$- \frac{1}{2a}(2\tilde{\phi}'_{\xi\eta} + \tilde{\phi}'_{\theta\eta})_0 - \frac{1}{2}(1 - K_G)h^2 \qquad (21)$$

In effect, this is the integral of the axial momentum equation from the upstream reservoir to the plenum.

Following [3], we identify the left side, which is the total-to-static pressure rise coefficient, as $\Psi(\xi)$, and the first parenthesis on the right as the quasisteady, axisymmetric compressor characteristic, also familiar from [3]; we notice that for steady flow with no disturbance, all other terms on the right vanish, leaving the obvious identity $\Psi = \psi_c$. The foregoing definitions are

$$\Psi(\xi) \equiv \frac{p_S - p_T}{\rho U^2} \qquad (22)$$

$$\psi_c(\phi) \equiv NF(\phi) - \frac{1}{2}\phi^2 \qquad (23)$$

It should be emphasized that the "axisymmetric characteristic," ψ_c, is the compressor performance that would be realized if no angle or time dependence were permitted, even in a stalled condition.

The second parenthesis on the right of equation (21) is the effective flow-passage length through the compressor and its ducts, measured in radii of the compressor wheel. This we denote as l_c

$$l_c \equiv l_I + \frac{1}{a} + l_E \qquad (24)$$

As explained in [3], if the compressor lag τ is considered to be purely inertial, one could write

$$\frac{1}{a} = (2NL_R)\left(\frac{1}{R}\right)\frac{k}{\cos^2\gamma} \qquad (25)$$

The first factor in parentheses is simply the axial length of the compressor, L_R being the axial length of a row; the factor $1/R$ puts the distance into wheel radians; k is a factor which could account for interrow spacing and possible unsteady losses; and $\cos^2\gamma$ accounts for the tortuous flow path through the compressor, γ being the effective stagger angle of the blades. Thus, the effective (inertial) path length for the system is longer than the axial length.

The last term of equation (21) will be neglected in the present treatment, in effect assuming that the recovery coefficient K_G at the IGV entrance is 1. Finally, therefore, we may write equation (21) in the form

$$\Psi(\xi) = \psi_c(\Phi + (\tilde{\phi}'_\eta)_0) - l_c \frac{d\Phi}{d\xi} - m(\tilde{\phi}'_\xi)_0 - \frac{1}{2a}(2\tilde{\phi}'_{\xi\eta} + \tilde{\phi}'_{\theta\eta})_0 \qquad (26)$$

In this we have used equations (8, 15) to express the argument of ψ_c in terms of $\tilde{\phi}'$:

$$\phi = \Phi + (\tilde{\phi}'_\eta)_0 \qquad (27)$$

The next step will be to place equation (26) in the context of the complete compression system, with plenum and throttle, as sketched in Fig. 1. Before doing so, we simplify equation (26) by introducing a generalization of an approximation used in the previous study of pure rotating stall [3].

A Simplifying Approximation of the $dh/d\theta = -g$ Type. The upstream disturbance potential $\tilde{\phi}'$ introduced by equation (14) satisfies Laplace's equation

$$\tilde{\phi}'_{\theta\theta} + \tilde{\phi}'_{\eta\eta} = 0 \qquad (28)$$

Its value and normal derivative ϕ'_η at the compressor entrance are needed, which implies that equation (28) must be solved as part of our analysis. We would like to avoid the difficulties of such a procedure, if possible.

We know that g is a periodic function of θ, and, by definition, must have a vanishing average over 2π. Therefore, it has a Fourier series and the solution of equation (28), vanishing at $\eta = -\infty$, is

$$\tilde{\phi}' = \sum_{n=1}^{\infty} \frac{1}{n} e^{n\eta}(a_n \sin n\theta + b_n \cos n\theta); \ \eta \le 0 \qquad (29)$$

If, as approximation, we were to keep only the first term of equation (29), we would infer that

$$(\tilde{\phi}'_\eta)_0 = -(\tilde{\phi}'_{\theta\theta})_0 \tag{30}$$

In view of equation (15), this is precisely the relation $dh/d\theta = -g$ introduced and discussed in [3].

Thus, it will be expedient to use the value of $\tilde{\phi}'$ at $\eta = 0$ as dependent variable, using the notation Y for simplicity. Equation (30) becomes

$$(\tilde{\phi}')_0 \equiv Y(\xi,\theta) ; (\tilde{\phi}'_\eta)_0 = -Y_{\theta\theta} \tag{31}$$

Equation (31) gives the pressure-rise equation (26) the form

$$\Psi(\xi) = \psi_c(\Phi - Y_{\theta\theta}) - l_c \frac{d\Phi}{d\xi} - mY_\xi + \frac{1}{2a}(2Y_{\xi\theta\theta} + Y_{\theta\theta\theta}) \tag{32}$$

This equation is far easier to apply than equation (26), because only derivatives in time and angle (ξ,θ) are involved, whereas equation (26) requires solution in the axial coordinate (η) as well.

Equations (12) and (31) imply that

$$h = Y_\theta ; g = -Y_{\theta\theta} \tag{33}$$

Therefore, if Y is simply required to be periodic in θ, as it obviously must be to describe a physical quantity in the compressor,

$$Y(\xi, \theta + 2\pi) = Y(\xi,\theta) \tag{34}$$

then the cyclic integrals of g and h vanish, as equation (9) requires. It is also obvious from the general solution of equation (29) that the cyclic integral of ϕ' itself must vanish, so we know that Y should have the property

$$\int_0^{2\pi} Y(\xi,\theta)\, d\theta = 0 \tag{35}$$

In summary, we have formulated the approximate governing equation (32) to describe the dynamic pressure rise of our system, subject to equations (34) and (35) as requirements on the unknown $Y(\xi,\theta)$.

An idea described in Appendix A of [4], to improve the accuracy of the $dh/d\theta = -g$ approximation for rotating stall, could be adapted for the present more general case. We will omit this possible refinement, because recent numerical studies have shown that the present approximation (equation (33)) is quite accurate over a wide range of circumstances.

Overall Pressure Balance of the Compression System. We now return to Fig. 1 and account for dynamic pressure changes downstream of the compressor exit, in the plenum and across the throttle, following closely ideas used in previous studies of pure surge [5].

As we have already mentioned, the plenum will eliminate any spatial variations. It will receive mass at a rate $\rho U A_c \Phi(\xi)$, and discharge mass at a generally different rate $\rho U A_c \Phi_T(\xi)$. Duct areas at entrance and discharge of the plenum would both presumably be different from the compressor area A_c; the difference is accounted for in the definition of Φ_T as in [5]. If Φ and Φ_T are different, then mass must accumulate in the plenum, changing the density there. As discussed in [5], we can take this change to be isentropic for the situations under consideration, and the plenum will act as a gas spring.

We assume that the compressor exit discharges as a free jet into the plenum, so that its pressure is $p_S(\xi)$. The isentropic relation between density and pressure then provides that the rate of density change in the plenum is the ratio of dp_S/dt to the square of sound speed, a_S. The rate of increase of stored mass in the plenum volume (V_p) is thus proportional to the dimensionless time derivative of the pressure-rise coefficient $\Psi(\xi)$, defined in equation (22). After some manipulation, the balance of entering, leaving, and stored mass of the plenum can then be written in the following convenient form:

$$l_c \frac{d\Psi}{d\xi} = \frac{1}{4B^2}[\Phi(\xi) - \Phi_T(\xi)] \tag{36}$$

in which the familiar "B-parameter" [5] appears

$$B \equiv \frac{U}{2a_S}\sqrt{\frac{V_p}{A_c L_c}} \tag{37}$$

The throttle then discharges to an infinite reservoir which, in the present study, we take to be at the same pressure p_T as the system inlet (Fig. 1).

Therefore, the pressure difference $p_S - p_T$ balances the throttle loss, and also provides any acceleration of the mass in the throttle duct. In coefficient form,

$$\Psi(\xi) = F_T(\Phi_T) + l_T \frac{d\Phi_T}{d\xi} \tag{38}$$

In the present paper, we will take the throttle duct to be short enough to justify neglecting l_T. This is generally quite a good assumption for realistic throttle ducts. A realistic throttle characteristic might be parabolic in form:

$$F_T = \frac{1}{2} K_T \Phi_T^2 \tag{39}$$

with K_T being a constant throttle coefficient. In any case, we write that Φ_T is simply the inversion of F_T, according to equation (39):

$$\Phi_T = F_T^{-1}(\Psi) \tag{40}$$

In principle, equations (36, 40) complete our system of equations for disturbances of the compression system. We imagine that Φ_T may be eliminated between these two equations, and the resulting equation connecting Ψ and Φ can be combined in some way with equation (32). However, there are only two equations, so far, for the three unknowns $\Psi(\xi)$, $\Phi(\xi)$, and $Y(\xi,\theta)$. The third equation comes from realizing that equation (32) involves terms which are functions only of time. If that equation is integrated over a cycle of θ, and equations (34) and (35) are applied, one finds

$$\Psi(\xi) + l_c \frac{d\Phi}{d\xi} = \frac{1}{2\pi}\int_0^{2\pi} \Psi_c(\Phi - Y_{\theta\theta})\, d\theta \tag{41}$$

which will serve as the needed third equation. In fact, equation (41) is the annulus average of the axial momentum equation.

Equations of a General Disturbance. For convenience, we assemble below the three pressure-balance equations we have just derived and will use in subsequent analysis, giving them new numbers.

$$\Psi(\xi) + l_c \frac{d\Phi}{d\xi} = \psi_c(\Phi - Y_{\theta\theta}) - mY_\xi + \frac{1}{2a}(2Y_{\xi\theta\theta} + Y_{\theta\theta\theta}) \tag{42}$$

$$\Psi(\xi) + l_c \frac{d\Phi}{d\xi} = \frac{1}{2\pi}\int_0^{2\pi} \psi_c(\Phi - Y_{\theta\theta})\, d\theta \tag{43}$$

$$l_c \frac{d\Psi}{d\xi} = \frac{1}{4B^2}[\Phi(\xi) - F_T^{-1}(\Psi)] \tag{44}$$

The first of these is the local (in θ) momentum balance of the system; the second is annulus-averaged momentum balance; and the third is the mass balance of the plenum. Our task is to find suitable solutions for Φ, Ψ, and Y under the influences of the various system parameters appearing in the equations.

Pure Rotating Stall and Pure Surge as Special Cases

Before attempting any general application of equations (42–44), we will find it instructive to see how those equations describe the special cases of pure rotating stall and pure surge, which have already been analyzed [3, 5]. Surge is the simplest;

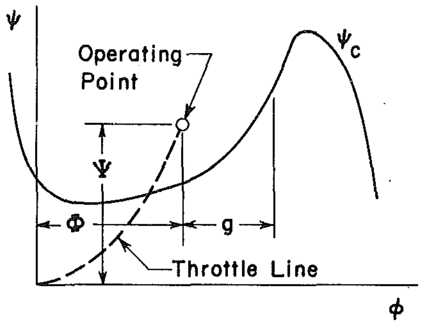

Fig. 2 Notation used for compressor performance characteristics; total-to-static pressure rise (ψ_c) versus flow coefficient (ϕ) in absence of rotating stall or surge; operating point lies on throttle line if $\Phi = \Phi_T$

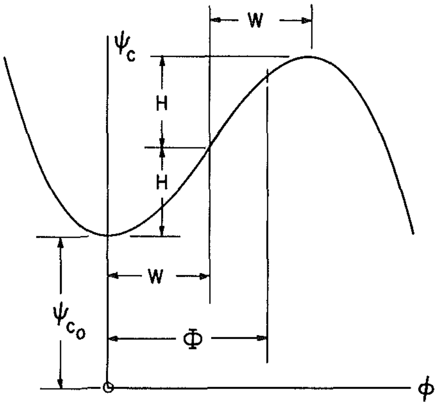

Fig. 3 Notation used in definition of cubic axisymmetric compressor characteristic

in that case there is no θ variation, and $Y(\xi, \theta)$ may therefore be set equal to zero. Equations (42) and (43) then become the same equation, namely

$$\Psi(\xi) + l_c \frac{d\Phi}{d\xi} = \psi_c(\Phi) \tag{45}$$

This equation, together with equation (45), defines the surge problem according to the analysis of [5].

In contrast, for pure rotating stall, the plenum pressure and the angle-averaged through flow are constant with time; therefore, $d\Psi/d\xi$ and $d\Phi/d\xi$ both vanish. Equation (44) then reduces to a statement that $\Phi = \Phi_T$, or that the operating point must lie on the throttle characteristic. It now becomes possible to represent Y as a wave traveling at some constant speed f; that is, as a function of a single variable:

$$Y(\xi, \theta) \equiv Y(\theta^*), \text{ where } \theta^* \equiv \theta - f\xi \tag{46}$$

The variable θ^* is then an angle measured relative to the disturbance. After making a convenient definition,

$$\lambda \equiv \frac{1}{a}\left(\frac{1}{2} - f\right) \tag{47}$$

equations (42) and (43) become

$$\mu \frac{d^3 Y}{d\theta^{*3}} + mf \frac{dY}{d\theta^*} - \left[\Psi - \psi_c\left(\Phi - \frac{d^2 Y}{d\theta^{*2}}\right)\right] = 0 \tag{48}$$

$$\Psi = \frac{1}{2\pi}\int_0^{2\pi} \psi_c\left(\Phi - \frac{d^2 Y}{d\theta^{*2}}\right) d\theta^* \tag{49}$$

Next, we recall equation (33) and see that, now,

$$\frac{dY}{d\theta^*} = h; \quad \frac{d^2 Y}{d\theta^{*2}} = -g \tag{50}$$

These last equations convert equation (48) precisely into the governing equation of pure rotating stall to be found in [3].

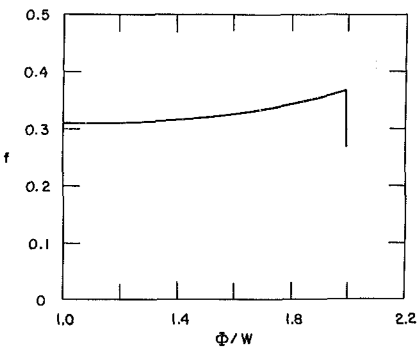

Fig. 4 Nondimensional stall cell speed (f) versus normalized throttle setting (Φ/W), calculated numerically for cubic characteristic with H/W = 0.72; pure rotating stall

After g is found, equation (49) would give the performance effect of rotating stall [3], a matter discussed more fully below.

A Cubic Characteristic

In order to pursue our line of analysis further, we need first to specify the axisymmetric characteristic function $\psi_c(\phi)$ for use in equations (42–44), and then we need to devise a method of solution. First, we will introduce a particular characteristic function, and show its effect for pure rotating stall.

In our general theory, we are making a necessary distinction between Ψ, the actual pressure rise, and ψ_c, the axisymmetric, steady characteristic that would hypothetically be measured for a compressor with rotating stall and surge absent. Figure 2 schematically shows the difference. At a given flow coefficient ϕ, the value of Ψ may differ from ψ_c even if, as is true in pure rotating stall, Ψ is constant at an operating point fixed by a given throttle setting. This is a nonlinear consequence of rotating stall [3], should it occur.

It is to be emphasized that it is $\psi_c(\phi)$ which we must choose, because it is an inherent feature of the compressor, independent of any disturbance motions. In [8] and [9] it is argued that the axisymmetric characteristic is typically a smooth S-shaped curve. (In those references, the axisymmetric curve is estimated for a three-stage compressor using a procedure based on corrections to transient data.) If this idea is correct, a physically realistic choice could be a simple cubic, as shown in Fig. 3. We expect that the rotating-stall or transient characteristic calculated using this cubic will be a good representation of that calculated using an exact, but as yet unknown, axisymmetric diagram.

The formula for the curve shown in Fig. 3 is

$$\psi_c(\phi) = \psi_{c_0} + H\left[1 + \frac{3}{2}\left(\frac{\phi}{W} - 1\right) - \frac{1}{2}\left(\frac{\phi}{W} - 1\right)^3\right] \tag{51}$$

where ψ_{c_0}, H, and W are parameters. We locate a throttle point at the angle-averaged flow coefficient, Φ. The local flow coefficient to be used in equation (51) includes departures (g or $-Y_{\theta\theta}$) from that value. Thus, for use in equation (51), we set

$$\phi = \Phi - Y_{\theta\theta} \tag{52}$$

The resulting expressions for $\psi_c(\phi)$ will be used in equations (42, 43) or (48), as appropriate.

To show the effect of the cubic characteristic in pure rotating stall, Chue has carried out calculations for a particular cubic using a numerical procedure [8, 9] for solving equation (48). The value used for m was 1.75. H and W were chosen so that the cubic would have the the same peak and valley points as a measured curve; their values were 0.18 and 0.25 respectively. Rather than equation (47), a somewhat more elaborate relation between λ and f was used, in which

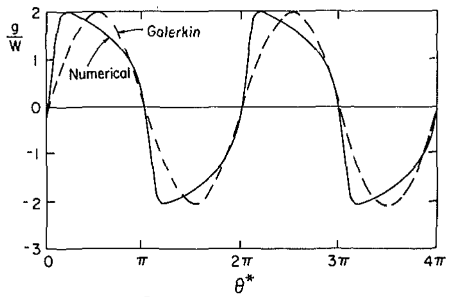

(a) Throttle at Φ/W = 1

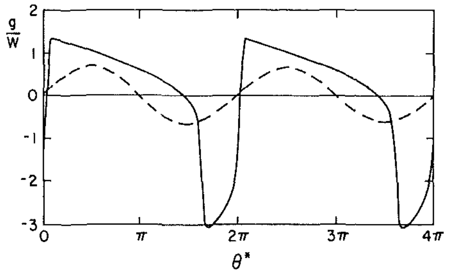

(b) Throttle at Φ/W = 1.92

Fig. 5 Comparison between numerical calculation (solid line) and single harmonic Galerkin representation (dashed line) of circumferential variation of axial velocity coefficient for cubic characteristic, $H/W = 0.72$, and pure rotating stall

guide-vane effects were included, following [9]. Numerically, the relation was, in effect,

$$\lambda = 4.34(0.38 - f)$$

Figure 4 shows how the rotating-stall propagation speed f increases when the throttle is opened (i.e., as Φ is increased), as was predicted in [3]. Figures 5(*a*, *b*) show how the axial velocity disturbance $g(\theta^*)$ changes as the throttle is opened. When $\Phi = W$, the symmetry features shown in Fig. 5(*a*) must appear because of the symmetry assumed for ψ_c, and we also note that $g(\theta^*)$ swings between extremes which lie on the unstalled and reverse-flow legs of the characteristic. As Φ increases, these extrema remain nearly the same, but more time is spent unstalled, so to speak. Figure 5(*b*) shows the result for $\Phi = 0.48$. There is no solution beyond $\Phi = 0.50$, which corresponds to the peak point of the curve. The dashed lines on Figs. 5(*a*, *b*) will be discussed later.

The most interesting result is shown in Fig. 6. There, the cubic axisymmetric characteristic is shown with the calculated Ψ (equation (49)) superposed as a solid line to form a prediction of how the actual in-stall pressure rise varies with throttle setting (Φ). Again, the dashed line will be discussed later.

This graph dramatically illustrates the idea of [8], that the usually observed sudden break in performance at the stall point, and subsequent drop as the throttle is closed, can be the result of an appearance of rotating stall, rather than a direct effect of the inherent axisymmetric characteristic of the compressor. The latter might, in fact, be quite smooth and gradual, with no break at all. The reasonableness of these results gives us confidence to adopt the cubic characteristic for use in the theoretical development to follow.

A Galerkin Procedure

To treat a general transient disturbance which may have both angular variation like rotating stall and time-dependent mean flow like surge will require solution of the complete system of equations (42–44), which include derivatives which are third order in angle, but only first order in time. Therefore, at this initial stage of investigation, we would like to devise a simple method of solution which effectively reduces the order of the equations in angle θ.

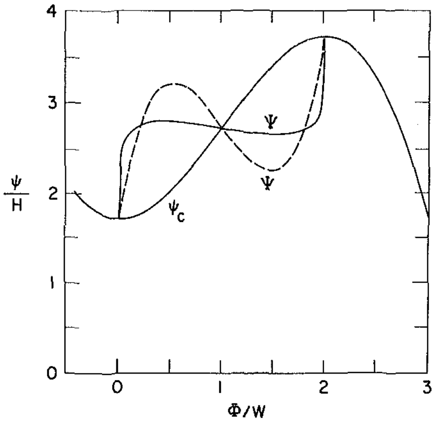

Fig. 6 Numerical (solid) and single-harmonic Galerkin (dashed) solutions for compressor performance (Ψ) in pure rotating stall, for a given axisymmetric characteristic (ψ_c) with $H/W = 0.72$ and $\psi_{c_0}/H = 1.67$

If the function $\psi_c(\phi)$ is smooth, the Galerkin method of nonlinear mechanics [10] will perhaps serve this purpose. In fact, this method has been used successfully for the van der Pol problem, which is just the symmetric case ($\Phi = W$) in the present theory of pure rotating stall with cubic ψ_c.

In a Galerkin procedure, the solution to the differential equation is represented by a suitable sequence of basic functions. If the functions are well chosen, and enough terms in the sequence are taken, the "true" solution can be represented very accurately. Fourier series or spectral methods are examples of this procedure. For present purposes, we are seeking the simplest possible wave representation, capable of describing the transient phenomena. Accordingly we have chosen a single harmonic wave to serve as our representational function. The sequence is truncated at one term, in effect.

For the present exploratory purposes, this approximation will prove to be reasonable. However, it is very important to recognize the limitations of this approximation. The single-term Galerkin procedure is most reliably accurate for weakly nonlinear systems. The present set of equations is strongly nonlinear. Thus, although we shall see that the amplitudes of axial velocity disturbance (g) calculated by the single-term Galerkin method for pure rotating stall are in reasonable agreement with exact calculations, as are the corresponding pressure-rise curves, which are averaged functions of g, the method does not give a good description of the derivatives of g. This is to be expected, because as the Figs. 5(*a*, *b*) show, the exact solutions are not of harmonic shape.

In this study, we wish to emphasize the amplitudes of disturbances and the integrated effects on performance. Thus, the information that is of most interest at present is just that information which should be least sensitive to the higher harmonics of the stall-cell description. We proceed, then, to develop a single-term Galerkin method for our general transient equations (42–44), and we will note the simple results obtained in the special case of pure rotating stall.

We begin by representing Y by a single harmonic function, of unknown amplitude A

$$Y = WA(\xi)\sin(\theta - r(\xi)) \tag{53}$$

We include an unknown phase angle $r(\xi)$ in this equation, because we must not expect nodes of the disturbance always to reamin in the same angular location. We note that the question of validity of the "$h' = -g$" assumption (equation (33)) does not arise when our Galerkin method is used; for a single harmonic wave, equation (33) may be shown to be exact.

We substitute equation (53) into equation (42), to formulate a residual (which would vanish if the solution were exact). We then set various moments of that residual equal to 0. First its integral must vanish; this accounts directly for one of the basic equations, equation (43):

$$\frac{1}{2\pi}\int_0^{2\pi} \psi_c(\Phi + WA\sin\zeta)\,d\zeta = \Psi + l_c\,\frac{d\Phi}{d\xi} \tag{54}$$

The $\sin(\theta - r)$ moment of the residual gives

$$\frac{1}{\pi W}\int_0^{2\pi} \sin\zeta\,\psi_c(\Phi + WA\sin\zeta)\,d\zeta = \left(m + \frac{1}{a}\right)\frac{dA}{d\xi} \tag{55}$$

and the $\cos(\theta - r)$ moment gives

$$\frac{1}{\pi W}\int_0^{2\pi} \cos\,\psi_c(\Phi + WA\sin\zeta)\,d\zeta = -\left[\left(m + \frac{1}{a}\right)\frac{dr}{d\xi} - \frac{1}{2a}\right]A \tag{56}$$

Even before specifying the characteristic function ψ_c, we see that if it is a regular function of its argument, the integral on the left of equation (56) must vanish when carried out over a complete cycle. Thus, very generally, it is clear that $dr/d\xi$ must be a particular constant if A is not to be zero. Calling that constant f_0,

$$r = \xi f_0;\quad f_0 \equiv \frac{1/2}{1 + ma} \tag{57}$$

In fact, f_0 is identical to the propagation speed found in [3] for small-disturbance rotating stall (which is a simple harmonic wave). We conclude that, even though the amplitude A varies with time, the one-term approximation provides that nodes of the circumferential disturbance will travel at a constant speed comparable to that of pure rotating stall. This is a result of the Galerkin method we are using; Fig. 4 tells us that propagation speed is actually a rising function of Φ, in rotating stall.

We are left with equations (44, 54, 55) which contain the unknown functions of time, Ψ, Φ, and A. These equations apply for any characteristic function ψ_c.

Final Simplified Equations. In the foregoing equations, it remains only to specify the axisymmetric characteristic; we adopt the cubic function defined in equation (51). It is obvious that if ψ_c can be expressed as a sum of powers of ϕ, only even powers of $A\ \sin\zeta$ will contribute to the integral in equation (54), and only odd powers in equation (55). Inspection of those equations then shows that A must enter as the square, no matter what the particular form of ψ_c. For convenience, therefore, we define a new variable J to replace A:

$$J(\xi) \equiv A^2(\xi) \tag{58}$$

and we note that J must always be positive.

Carrying out the indicated integrals, we find the final governing equations to be

$$\frac{d\Psi}{d\xi} = \frac{W/H}{4B^2}\left[\frac{\Phi}{W} - \frac{1}{W}F_T{}^{-1}(\Psi)\right]\frac{H}{l_c} \tag{59}$$

$$\frac{d\Phi}{d\xi} = \left[-\frac{\Psi - \psi_{c0}}{H} + 1 + \frac{3}{2}\left(\frac{\Phi}{W} - 1\right)\left(1 - \frac{1}{2}J\right) - \frac{1}{2}\left(\frac{\Phi}{W} - 1\right)^3\right]\frac{H}{l_c} \tag{60}$$

$$\frac{dJ}{d\xi} = J\left[1 - \left(\frac{\Phi}{W} - 1\right)^2 - \frac{1}{4}J\right]\frac{3aH}{(1 + ma)\,W} \tag{61}$$

These are our final equations for instantaneous values of circumferentially averaged flow coefficient (Φ), total-to-static pressure rise (Ψ), and squared amplitude of angular variation (J), all as functions of time (ξ). Compressor and system parameters which will govern the solutions are diagram steepness (H/W), shut-off head (ψ_{c_0}/H), compressor duct length (l_c) and slope (m), internal compressor lag (a), plenum volume and compressor annulus area (B), and the throttle pressure characteristic function $F_T\ (\Phi)$.

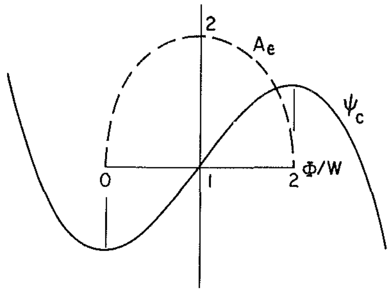

Fig. 7 Amplitude (A_e) of single harmonic Galerkin solution for pure rotating stall as a function of Φ/W; the cubic axisymmetric compressor characteristic (ψ_c) is also shown for reference

Galerkin Solution for Pure Rotating Stall. For rotating stall, time derivatives in equations (59-61) must vanish. Equation (61) then requires that J either vanish or have the constant "equilibrium" value

$$J_e = 4\left[1 - \left(\frac{\Phi}{W} - 1\right)^2\right] \tag{62}$$

Figure 7 displays this result (in terms of $A = \sqrt{J}$), which quite reasonably shows the rotating-stall amplitude to vanish at the neutral-stability points $\Phi = 0,\ 2W$, and have its maximum at the midvalue $\Phi = W$. These features are essentially correct, according to the exact calculations displayed in Fig. 5(a, b).

Equations (33, 46, 53, and 58) combine to give a representation of $g(\theta)$, for rotating stall; it appears as the dashed harmonic waves on Figs. 5(a, b), for two values of Φ. As we expect, these Galerkin results correctly suggest the trend of amplitude with Φ, but are incapable of representing the exact wave shape. Obviously, the simple harmonic wave cannot represent the sudden drop into, and recovery from, reversed flow which occurs when Φ is near $2W$.

When J_e from equation (62) is substituted into the right side of equation (60), which must vanish for rotating stall, one finds the steady performance Ψ:

$$\Psi = \psi_{c_0} + H\left[1 - \frac{3}{2}\left(\frac{\Phi}{W} - 1\right) + \frac{5}{2}\left(\frac{\Phi}{W} - 1\right)^3\right] \tag{63}$$

which may be compared with equation (51) to infer the performance effect of rotating stall. Indeed, equation (63) is shown in Fig. 6 as the dashed line, which may be compared with the exact (solid line) result. Although the two curves do not agree numerically, it is remarkable that the qualitative features of the performance effect are well predicted by the simple, first-harmonic Galerkin theory, especially the steep rise near $\Phi = 2W$, and the equally steep drop near $\Phi = 0$.

This examination of the special case of rotating stall gives us confidence that the single harmonic Galerkin method will prove to be a useful approximation for the general transients contemplated in the final equations (59-61). It correctly forbids any solution beyond the stability limits of the compressor characteristic, and it gives a qualitatively correct picture of the nonlinear effect of rotating stall on performance. However, it cannot accurately represent wave shape of the relaxation type of transition which arises in fully developed rotating stall, nor can it show effects of extreme diagram steepness, as in [3].

Discussion of Simplified Equations

Pure Modes and Their Growth. Our intention is to use the foregoing equations (59–61) to compute the consequences of an initial disturbance of a compression system. Before doing that, we should examine these equations to discover what we can about their general features.

First, we have already observed how these equations describe pure surge or rotating stall. In the case of pure surge, $J = 0$ and equation (60) becomes simply equation (49) with cubic ψ_c (equation (51)). In pure rotating stall, amplitude J is constant at an "equilibrium" level defined by J_e (equation (62)).

Our equations thus appear to permit the existence of pure modes; that is, either surge or rotating stall without the other. However, we should question whether such modes could evolve from initially infinitesimal disturbances. Clearly, such a process is possible for pure surge; if J is zero it will remain zero forever, according to equation (61), and the other two equations will deal with the evolution of pure surge disturbances, as described in [5, 6].

It appears to be impossible, however, for rotating stall to evolve without producing at least some disturbance of Φ or ψ; if J changes, then equation (60) says the Ψ or Φ must also change. A disturbance of Φ induced in this way might of course be a noncyclic transient, not to be identified as "surge." Further comments on these points are given in Part II.

Nature of the Coupling Process. We have seen that equation (61) describes how angular-disturbance amplitude J grows at a rate which initially depends only on the disturbance itself, but then tries to approach an equilibrium condition defined by equation (62). In general, the flow coefficient and therefore J_e will change with time. Therefore, during a coupled oscillation, $J_e(\xi)$ will be a moving target, so to speak, for J. Whether J actually achieves and stays on that target, which is quasi-steady equilibrium with $\Phi(\xi)$, will be known only from simultaneous solution of the equations, that is, a trajectory in the three-dimensional space Ψ, Φ, J. This behavior may remind one of the relaxation of an internal degree of freedom in physical gas dynamics.

Inspection of equation (61) also shows that excursions of Φ away from the central point $\Phi = W$ will diminish the rate of change of J. Thus, for a throttle setting of $\Phi = W$, the presence of surgelike variations of Φ will tend to suppress circumferential variations. Furthermore, if B is small, equation (59) implies that swings of Φ will tend to be small, which, relatively, would encourage circumferential variation, according to equation (61). This is in accordance with our expectation [5, 6] that small B will favor rotating stall.

Turning to equation (60), we see that the presence of a circumferential angular variation in velocity will diminish the term in which J appears (recalling that J must always be positive). That term describes the central slope of the characteristic, at the midpoint of Fig. 3, thus reducing the basic amplifying effect of the characteristic in the stall region. We can conclude that this variation (i.e., the presence of a rotating-stall-like disturbance) would tend to inhibit surgelike disturbances of Φ.

The foregoing arguments, which are certainly in qualitative agreement with the many experimental observations that have been made of these phenomena, only suggest how surgelike and rotating-stall-like disturbances are coupled through equations (60) and (61). The coupling is mediated by equation (59), and one must carry out trajectory calculations to discover the actual consequences of a given initial disturbance.

Conclusions

We are now ready to trace the evolution of disturbances in an axial compression system, in order to predict when pure surge or pure rotating stall, or perhaps some composite motion, prevails. Calculations can proceed using equations which have a known basis in the differential equations of fluid mechanics; while assumptions have been made, all assumptions are identified, and, ultimately, can be evaluated. In this sense, the present theory is a "first-principle" one, as distinct from a "model" which proceeds from commonly observed features of the phenomena themselves.

The equations show that pure modes of surge (time variation) or rotating stall (angle variation) each can exist without the other. However, in general, time and angle fluctuations are coupled. Angular variations must grow toward an equilibrium, or target value; this target depends on the strength of any time variation in progress. Conversely, the damping rate of any time variation of flow coefficient depends on the strength of any angular variation in progress.

The equations presented here account, approximately, for many important compression-system features, including system volumes, inlet and diffuser shapes, axisymmetric compressor characteristic, throttle characteristic, system hysteresis (because the actual system pressure rise depends on the existence of rotating stall), compressor geometry and speed, and internal lag processes in the compressor. Some important effects have not yet been included; in this category are inlet distortion, compressibility, and combustor phenomena.

In the companion paper to this one, Part II, we will further study the nature of the general transient equations, show the results of illustrative calculations, and discuss needs for future research.

Acknowledgments

We acknowledge the support of NASA, through Lewis Research Center, for this research. Especially, we thank Mr. C. L. Ball of NASA for arranging for us to work together at Lewis in the summer of 1983, when the present research was carried out. We also acknowledge the contribution of Mr. R. Chue of MIT, who carried out certain calculations here and in Part II.

References

1 Stetson, H. D., "Designing for Stability in Advanced Turbine Engines," in: AGARD CP3424, *Engine Handling*, Oct. 1982.

2 Day, I. J., Greitzer, E. M., and Cumpsty, N. A., "Prediction of Compressor Performance in Rotating Stall," ASME JOURNAL OF ENGINEERING FOR POWER, Vol. 100, No. 1, Jan. 1978, pp. 1–14.

3 Moore, F. K., "A Theory of Rotating Stall of Multistage Compressors, Part I, II, III," ASME JOURNAL OF ENGINEERING FOR POWER, Vol. 106, No. 2, Apr. 1984, pp. 313–336.

4 Moore, F. K., "A Theory of Rotating Stall of Multistage Compressors," NASA Contractor Report 3685, July 1983.

5 Greitzer, E. M., "Surge and Rotating Stall in Axial Flow Compressors, Parts I, II," ASME JOURNAL OF ENGINEERING FOR POWER, Vol. 98, No. 2, Apr. 1976, pp. 190–217.

6 Greitzer, E. M., "The Stability of Pumping Systems—the 1980 Freeman Scholar Lecture," *ASME J. Fluids Eng.*, Vol. 103, June 1981, pp. 193–243.

7 Moore, F. K., and Greitzer, E. M., "A Theory of Post-Stall Transients in Multistage Axial Compression Systems," NASA Contractor Report 3878, Mar. 1985.

8 Koff, S. G., and Greitzer, E. M., "Stalled Flow Performance for Axial Compressors—I: Axisymmetric Characteristics," ASME Paper No. 84-GT-93, 1984.

9 Koff, S. G., "Stalled Flow Characteristics for Axial Compressors," S. M. Thesis, Massachusetts Institute of Technology, Department of Mechanical Engineering, 1983.

10 Magnus, K., *Vibrations*, Chap. 3, Blackie and Sons, London, 1965.

Dynamic Response of a Centrifugal Blower to Periodic Flow Fluctuations

A. N. Abdel-Hamid
Professor of Mechanical Engineering.
The American University in Cairo,
Cairo, Egypt

Experimental investigation of the dynamic response of a centrifugal blower to periodic flow rate modulations was carried out at different blower operating conditions. For modulation frequencies in the range of 0.0085–0.085 of the shaft rotation frequency, the fluctuating pressures at inlet, discharge, and across a flow orifice were simultaneously measured and analyzed in the time and frequency domains. Measurements of the amplitude and phase of the transfer function between the blower static pressure rise and the discharge flow rate fluctuations indicated that the quasi-steady approximation should be limited to frequencies lower than 0.02 of the shaft rotation frequency. For the same average flow rate, the static pressure rise progressively lagged the discharge flow rate fluctuations as the frequency was increased. The trend was similar to that of the inertia effects of a fluctuating flow in a pipe. For the same frequency these inertia effects increased as the average flow rate through the blower was decreased. Applications of the results to on-line measurements of the slope of the characteristic curve and improved dynamic modeling of centrifugal compressors and blowers are discussed.

Introduction

Unsteady response of a compression system to transients in flow rate and pressure levels is governed by the dynamic characteristics of each component of the system. Models for the dynamic behavior of such components as intake and discharge pipes, storage volumes, nozzles, and valves have been suggested in the past and can be found in classical textbooks [1]. Dynamic modeling of the compressor or blower is still however a subject of continued investigation. Traditionally the compressor or blower is assumed to behave in a quasi-steady manner and transient changes in the pressure rise and flow rate are related to each other by the slope of the steady-state characteristic curve.

Motivated by the need to provide a better understanding of the behavior of compression systems during rotating stall and surge, a number of theoretical and experimental results on the transient response of axial flow compressors have recently been published [2–9]. Very few results on the other hand are available on the overall dynamic characteristics of centrifugal compressors, although some of the compressor elements, such as the inducer and the vaneless radial diffuser, have recently received considerable attention [10–14]. Very recently a detailed model for the dynamic behavior of a centrifugal compressor has been presented [15]. This latest model however also used the quasi-steady approximation for the evaluation of the force and energy input from the compressor.

Incentive for the present investigation started during an experimental program on surge control for centrifugal water chillers [16]. During the program different techniques were attempted to predict the occurrence of surge in the centrifugal chiller. One of these techniques was to measure the slope of the compressor characteristic curve at the different operating points to ensure that the peak of the curve has not been reached.

Following a preliminary experimental investigation of the response of the centrifugal compressor to steplike transients, in which the compressor response deviated from the quasi-steady behavior, the present detailed study was carried out under controlled laboratory conditions. The objective of the study was experimental determination of the dynamic relationship between the blower static pressure rise and flow rate fluctuations at different frequencies and operating conditions. The use of periodic flow fluctuations was preferred over aperiodic transients because of the relative ease of measurements using the cross-spectral averaging technique.

The study confirmed the preliminary findings of the previous investigations [16], and showed that deviations from the quasi-steady behavior existed even for the low-frequency range considered here. Analysis of the experimental results showed dominance of an inertia-like effect which tends to cause a phase lag between the static pressure rise and the flow rate fluctuations.

Experimental Facility and Test Procedure

A schematic diagram of the experimental test facility is shown in Fig. 1. The centrifugal blower from Buffalo Forge was a type 4RE standard unit. The impeller inlet and outlet

---

Contributed by the Gas Turbine Division of THE AMERICAN SOCIETY OF MECHANICAL ENGINEERS and presented at the 30th International Gas Turbine Conference and Exhibit, Houston, Texas, March 18–21, 1985. Manuscript received at ASME Headquarters, January 16, 1985. Paper No. 85-GT-195.

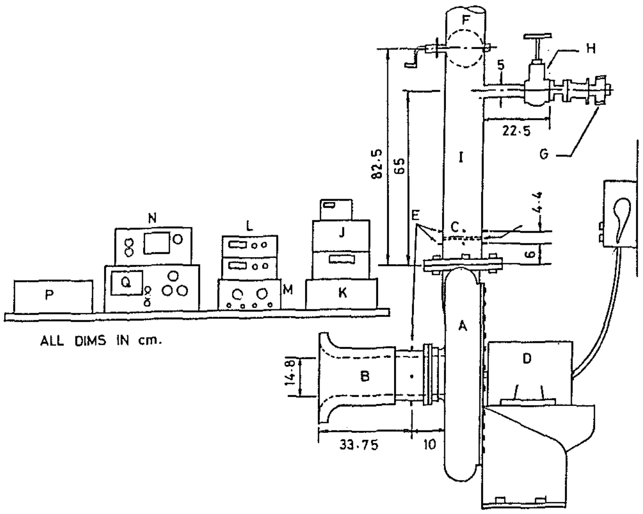

A	Blower
B	Bellmouth
C	Flow Orifice
D	Motor
E	3 mm Static Pressure Holes
F	Main Butterfly Valve
G	Motorized Modulating Valve
H	Gate Valve
I	Discharge Pipe
J	Transducer's Power Supply
K	Signal Conditioner
L	RMS Voltmeters
M	Dual Channel Filter
N	Digital Storage Oscilloscope
P	X-Y Plotter
Q	Dual Channel Spectrum Analyzer

Fig. 1 Schematic diagram of the experimental test facility

diameters were 150 mm and 660 mm, respectively. The rotational speed was constant at 3550 rpm which resulted in an impeller tip Mach number of 0.36 using ambient air as a working medium. The blower was driven by a 15 hp electric motor.

For the purpose of the present study the blower was fitted at the inlet with a bellmouth and at the discharge with a flow orifice. The static pressures at the blower inlet, discharge, and the flow orifice were determined using the instantaneous average of six pressure values measured around the circumference of the flow perimeter at each location. The flow orifice characteristics were measured during the steady-state operation of the blower using the bellmouth as a flow meter.

The flow rate through the blower was adjusted using two valves located downstream of the flow orifice. The main butterfly valve was used to set the time average flow rate while the side modulating valve was used to generate periodic flow rate modulations around the average flow rate. The flow modulations were accomplished through the relative rotation of two perforated disks within the body of the modulating valve. The maximum flow area of the modulating valve was only 5% of the area of the discharge pipe. A gate valve was installed on the side branch upstream of the modulating valve to control the amplitude of the flow rate modulations. The frequency of the flow modulations was adjusted in the range 0.0085–0.085 of the shaft rotation frequency by varying the speed of rotation of the moving perforated disk. The instantaneous flow rates at the blower inlet and discharge during flow modulations were measured using the bellmouth and the flow orifice respectively assuming quasi-steady response of these two components.

Dynamic signals proportional to the static pressure rise across the blower, the pressure drop across the flow orifice, and the bellmouth static pressure were generated using calibrated pressure transducers. The pressure signals were manipulated using a dual channel digital storage oscilloscope and a dual channel spectrum analyzer to evaluate their simultaneous characteristics in the time and frequency domains.

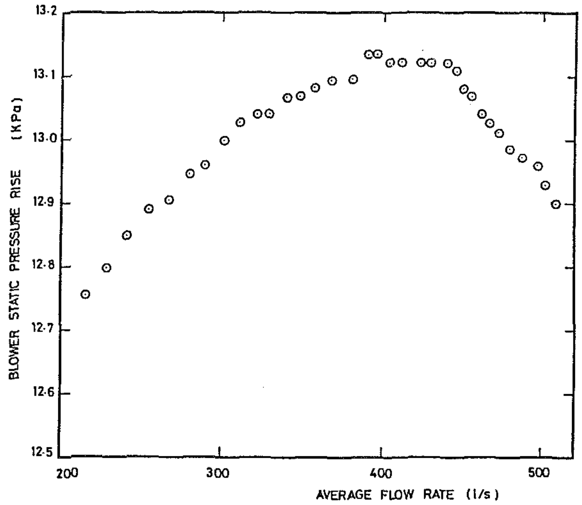

Fig. 2 Blower steady-state characteristics

Test Procedure. The blower was initially operated under steady-state conditions and its pressure rise flow characteristics were determined. For a number of representative blower operating points, covering the entire flow range, the flow through the blower was modulated at frequencies in the range 0.5–5.0 Hz which corresponded to 0.0085–0.085 of the shaft rotation frequency. For every dynamic run the following quantities were measured:

1 The time domain fluctuations of the blower static pressure rise, the static pressure drop across the flow orifice, and the static pressure just downstream of the bellmouth.

2 The amplitudes of the fluctuations of the blower static pressure rise, the flow orifice static pressure drop, and the bellmouth static pressure as obtained from their autospectra.

3 The amplitude and phase of the transfer function between the blower static pressure rise and the orifice static-pressure drop. These were obtained from the averaged cross and autospectra of the two fluctuating signals.

4 The amplitude and phase of the transfer function between the bellmouth static pressure and the orifice static pressure drop. These were also evaluated from the cross and autospectra of the respective signals.

Values of the pressure drop across the flow orifice and the bellmouth were manipulated to yield the instantaneous flow rates at inlet and discharge and are presented as such in the results.

All frequency domain quantities were measured at the fundamental frequency of flow modulation. The number of averages used for the cross and autospectra was typically 32. This number was sufficient to yield the required accuracy for the levels of flow modulations used and the random flow fluctuations present in the flow.

A total of 117 dynamic runs were carried out during the test program.

Results and Discussions

1 Steady Characteristics of the Blower. Figure 2 shows the variation of the blower static pressure rise with flow rate for the range of conditions investigated in the present study. The data indicate some irregular changes in the slope of the characteristics at a number of points before and after the peak of the characteristics curve. Examination of the static pressure autospectra at blower inlet and discharge however did not reveal any evidence of occurrence of a self-excited flow oscillations in the blower. Furthermore, although the slope of the characteristic curve changed from negative to positive as the flow rate was gradually decreased, the blower system did not surge at any operating conditions tested in the present study.

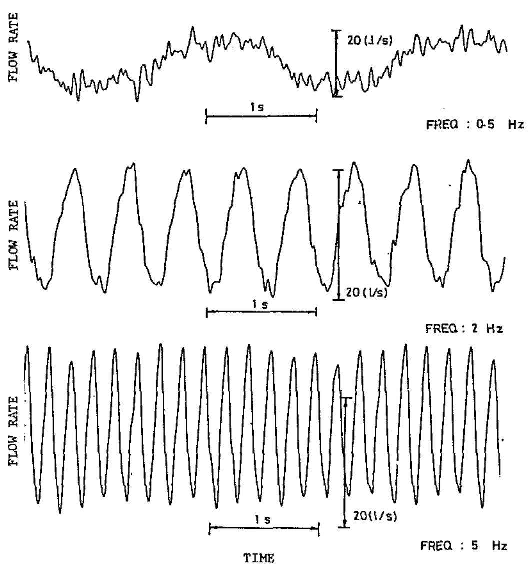

Fig. 3 Effect of frequency on the waveform of the flow rate fluctuations; gate valve opening; 100% open

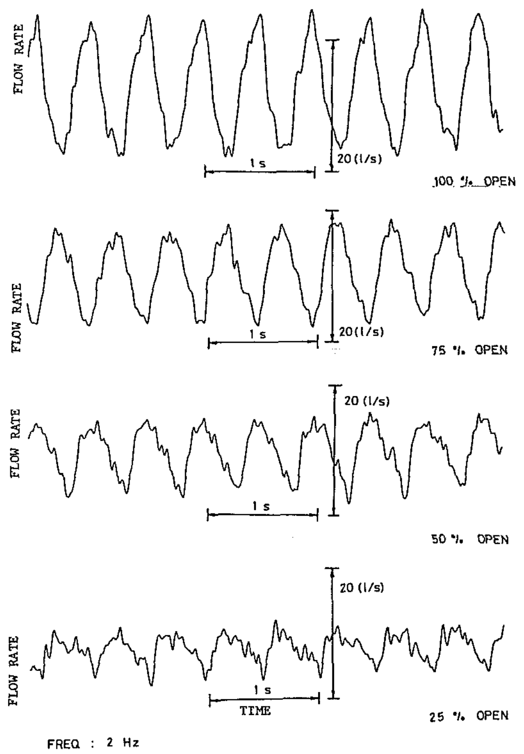

Fig. 4 Effect of amplitude on the waveform of the flow rate fluctuations

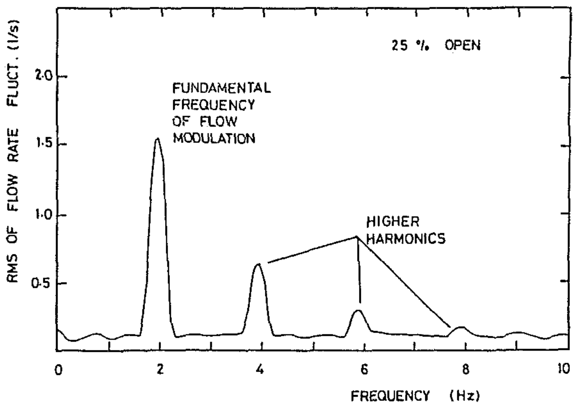

Fig. 5 Typical autospectrum of the flow rate fluctuation

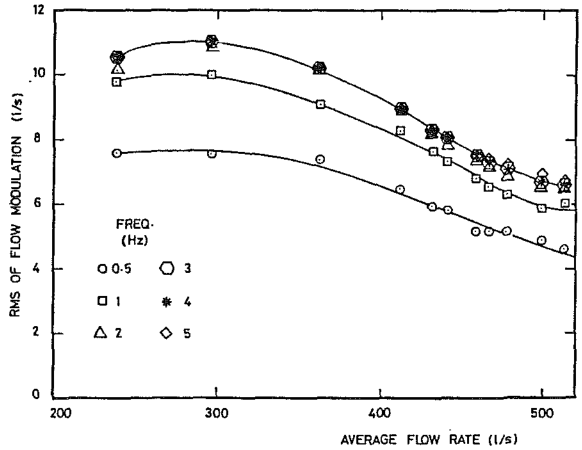

Fig. 6 Variation of the magnitude of flow rate fluctuations with average flow rate for different frequencies

2 Blower Response to Operation of the Flow Modulation Valve. Although the main thrust of this paper is to determine the dynamic transfer properties of the blower at different operating conditions the variations of each of the measured quantities with test conditions are presented first to give an indication of their relative magnitudes. Blower transfer properties are then presented with emphasis on practical applications.

2.1 Effect of the Modulation Frequency on the Magnitude of the Flow Fluctuations at Blower Discharge. Figure 3 shows the variation of the discharge flow rate with time for modulating frequencies of 0.5, 2.0, and 5.0 Hz. The average flow rate through the blower was 500 L/s and the gate valve upstream of the modulating valve was fully opened. The periodic modulations are superimposed on random fluctuations associated with the random pressure fluctuations across the flow orifice. The random component of the signal from the flow orifice pressure transducer has the effect of masking the accurate definition of the waveform of the periodic component especially at low modulation frequencies.

The effect of partial closure of the gate valve upstream of the modulating valve on the waveform of the flow rate fluctuations is shown in Fig. 4 for a frequency of 2 Hz and an average flow rate of 500 L/s. Although the existence of the periodic fluctuations can still be detected from these traces even at a gate valve opening of 25%, uncertainties regarding the amplitude and phase values can be excessive if evaluated from the time-domain traces.

The magnitudes of the periodic fluctuating quantities were determined in this study from the autospectra of their respective time-domain signals. A typical autospectrum of the signal corresponding to the discharge flow rate is shown in Fig. 5 for a modulation frequency of 2 Hz, and gate valve opening of 25%. The average flow rate was 500 L/s. The spectrum clearly shows the magnitudes of the flow rate fluctuations at the fundamental frequency and a number of its harmonics. The existence of these harmonics indicates the deviation of the flow rate fluctuations from the pure sinusoidal waveform and the necessity for evaluating the dynamic quantities from their spectral components. Attention was focused in this study on the magnitudes of the fluctuating quantities at the fundamental frequency of modulation.

Figure 6 shows the effect of the blower average operating point on the magnitude of the flow rate fluctuations at blower

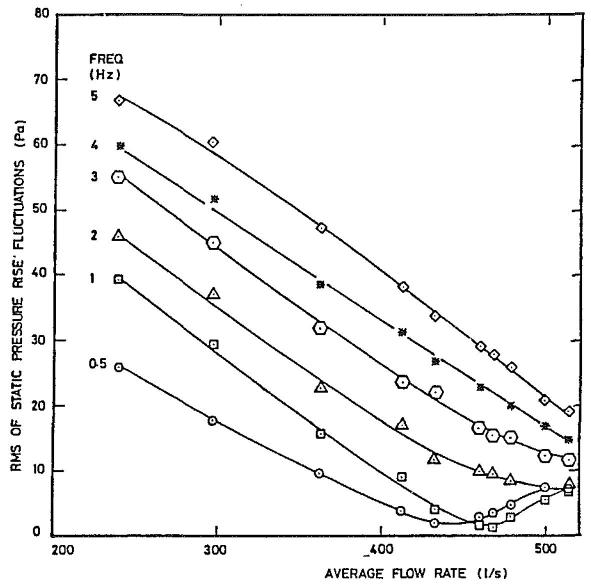

Fig. 7 Variation of the magnitude of the static pressure rise fluctuations with average flow rate for different frequencies

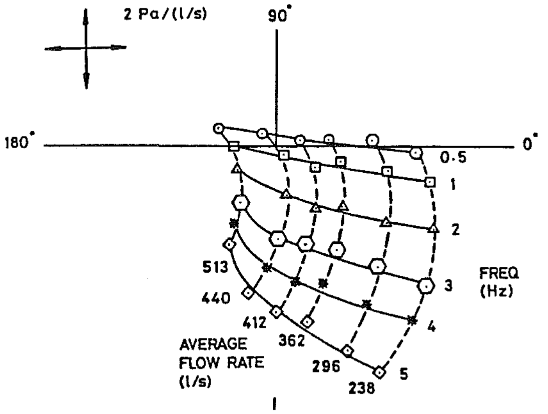

Fig. 8 Polar plot of the transfer function between the static pressure rise and flow rate fluctuations for different average flow rates

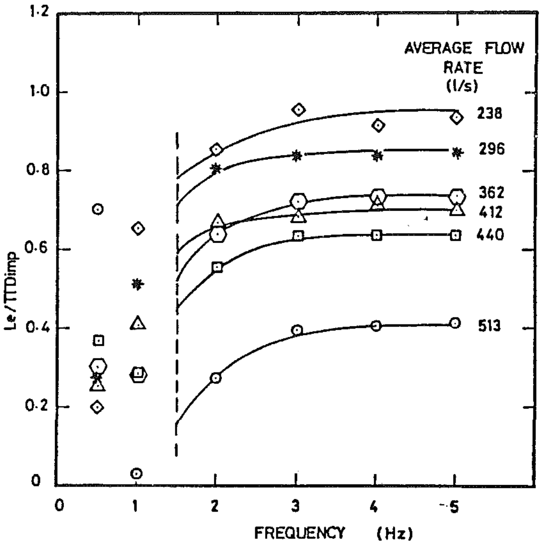

Fig. 9 Variation of the effective dynamic length of the flow with frequency for different average flow rates

discharge for different frequencies. The gate valve was fully opened. For a constant average flow rate and discharge pressure the measured magnitude of the flow fluctuations varied with frequency. This can be attributed to the interaction between the frequency dependent dynamic responses of the components of the blower system. For a fixed frequency of modulation the magnitude of the flow fluctuations initially increased and then tapered off to an almost constant value as the flow rate was gradually decreased.

At the highest average flow rate the flow fluctuation was less than 1.4% of the average flow rate. The flow rate fluctuations increased to 4.5% at the lowest average flow rate. At reduced values of gate valve opening the flow fluctuations were proportionately reduced. Dynamic properties of the flow rate fluctuations were still measurable with a high level of confidence using the technique of averaged spectra even when the flow rate fluctuations were only 0.5% of the average flow rate.

2.2 Effect of Modulation Frequency on Blower Static Pressure Rise Fluctuations. The magnitude of the blower static pressure rise fluctuations also varied with flow modulation frequency and average operating point as shown in Fig. 7. At low frequencies, 0.5–1.0 Hz, the magnitude of the fluctuations exhibited minimum values at average flow rates near the peak of the blower characteristics curve. At higher frequencies the magnitude of the blower static pressure rise fluctuations increased monotonically as the average flow rate was decreased. At 2 and 3 Hz, however, the effect of the peak region of the characteristic curve on the pressure rise fluctuations was still evident. At the highest flow rate the magnitude of the static pressure rise fluctuations was 0.15% of the average pressure rise while at the lowest average flow rate the pressure rise fluctuations increased to 0.55% for a fully opened gate valve.

2.3 Dynamic Relationship Between the Blower Static Pressure Rise and the Discharge Flow Rate. The transfer function between the periodic fluctuations in the blower static pressure rise and the discharge flow rate was evaluated for all dynamic operating conditions. Figure 8 shows a polar plot of the transfer function for different average flow rates. The trends exhibited by these results are the main findings of this paper and are discussed in detail.

For a constant flow rate a gradual increase in the modulation frequency from 0.5–5.0 Hz resulted mainly in a change in the "quad-component," along the 90–270 deg axis, of the transfer function while the "co-component," along the 0–180 deg axis, is slightly affected.

The variation of the quad-component of the transfer function with frequency is similar to that due to the inertia effects of a fluctuating flow in a pipe: the longer the pipe, the larger the mass of the oscillating fluid and consequently the larger the quad-component of the transfer function. The data shown in Fig. 8 therefore suggest that the lower the average flow rate the larger the inertia effects, or alternatively, the lower the average flow rate the longer the effective length of the flow path in the blower.

Further support for this idea is given in Fig. 9 which shows the variation of the effective length of the flow with frequency for different average flow rates. The data were calculated from the "quad-component" of the transfer function data shown in Fig. 8 and is nondimensionalized with respect to the circumference of the impeller. For the relatively high frequency range (3–5 Hz) the nondimensional effective flow length is fairly constant for each average flow rate. The constant values varied from 0.41 at the highest flow rate to 0.94 at the lowest flow rate. At much lower frequencies the inertia effects are not dominant and the effective length values are scattered due to other unsteady flow effects in the impeller and the scroll.

The co-component of the transfer function at low frequencies is related to the quasi-steady response of the

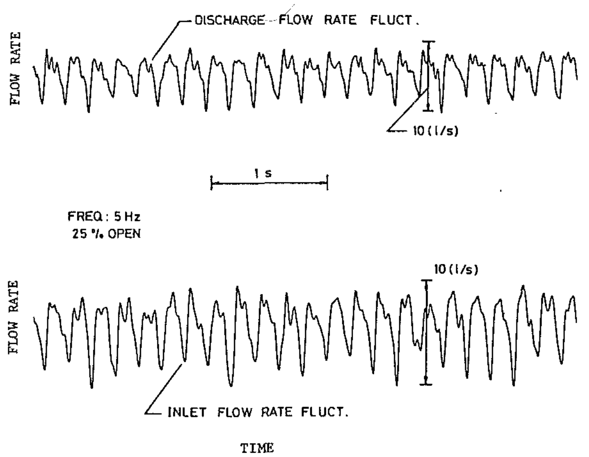

Fig. 10 **Flow rate fluctuations at inlet and discharge**

blower to flow modulation. Values of the co-component were negative when the average flow rate was larger than that corresponding to the peak of the characteristics curve, and positive for smaller average flow rates.

Other properties of the transfer function should also be noted. For a constant flow rate the co-component had a maximum between 1 and 3 Hz. Furthermore, at very low frequencies and high average flow rates, the quad-component of the transfer function was positive but the magnitude was small. The transfer function must of course approach the quasi-steady response, on the 0–180 deg axis, as the frequency of modulations approaches zero. Although these two properties do not seem to be significant for the blower tested here they could be important for other blowers and compressors of different designs.

2.4 Relation Between Flow Rate Fluctuations at Blower Inlet and Discharge. Figure 10 shows the time-domain fluctuations of the inlet and discharge flow rates for a modulation frequency of 5 Hz and gate valve opening of 25%. The average flow rate was 521 L/s. The magnitude and phase of the transfer function between the blower flow rate fluctuations at inlet and discharge are shown in Figs. 11 and 12 respectively. The discharge flow rate was used as a reference. As shown in Fig. 11 the flow rate transfer function increased with frequency but the magnitude varied only between 0.93 and 1.18. At low frequencies the flow rate fluctuations were nearly in phase but as the frequency was increased the bellmouth flow fluctuations lead the discharge flow fluctuations. The magnitude of the phase lead increased with frequency and reached 18 deg at 5 Hz for an average flow rate of 430 L/s.

A number of reasons can be responsible for the instantaneous difference between the flow rate at inlet and discharge as measured in the present study. The static pressure holes downstream of the bellmouth, which were used in the measurements of the inlet flow rate fluctuations, were 340 mm downstream of the bellmouth inlet. This could lead to the introduction of small amplitude and phase factors in the measured inlet flow rate fluctuations for the range of frequencies considered. Alternatively, the instantaneous mass inside the volume of the blower could fluctuate as the frequency of flow modulations was increased. The instantaneous inlet and discharge mass flow rates under these conditions need not be identical.

Because of the apparent linear change of the phase angle with frequency the first reason is thought to be the main cause of the measured small deviations between the flow rate fluctuations at inlet and discharge. All results presented in this paper were based on the discharge flow rate fluctuations which were considered to be fairly accurate for the range of conditions of the present study.

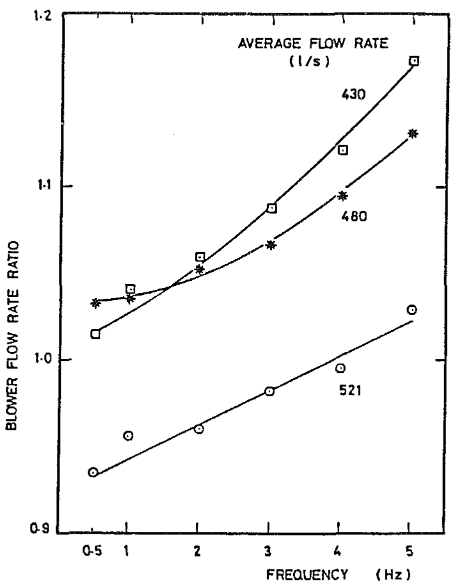

Fig. 11 **Variation of the magnitude of the transfer function between the inlet and discharge flow rates with frequency for different average flow rates**

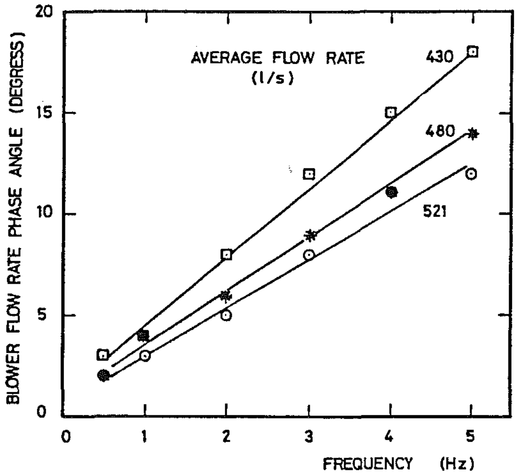

Fig. 12 **Variation of the phase angle between the inlet and discharge flow rates with frequency for different average flow rates**

Possible Practical Applications of the Results

1 One-Line Determination of the Slope of the Characteristic Curve. In applications where the flow rate requirement from a compressor or a blower is variable, the operating point of the compressor or blower may approach the peak of the characteristic curve and possibly result in the occurrence of system surge. To avoid such a situation the flow rate through the machine must be controlled such that the blower or compressor does not operate in the region of positive slope of the characteristic curve.

Because of the inevitable gradual change of machine performance with time after installation, effective utilization of the machine in the whole of its stable range can only be achieved if the slope of the characteristic curve is continuously evaluated and used as an input to the flow rate controller.

The method presented in this paper can be used for such a purpose. Flow modulation of the order of 0.5% of the average flow rate would be sufficient to produce a detectable signal. The frequency of modulation should be in the range of 0.02 of the shaft rotation frequency in order to avoid significant dynamic effects. At high flow rate the co-component of the transfer function between the pressure rise and the flow rate should be negative and its magnitude should be equal to the magnitude of the slope of the characteristic line at the average operating point. As the average flow rate is decreased the co-component of the transfer function should gradually decrease in magnitude until it becomes equal to zero at the peak of the characteristic curve. Absolute limits on the magnitude can be selected to set the minimum average flow rate.

2 Transient Response of Blower and Compressor Systems. In classical transient analyses of centrifugal compression systems the compressor or blower element is usually assumed to respond in a quasi-steady manner. The data presented here clearly demonstrate the limitations of such an assumption. A better model of a centrifugal machine of a design similar to the one investigated here is obtained if an inertia element of an effective length in the range of 0.4 impeller circumference is added downstream of the "quasi-steady" compressor or blower. The length of the inertia element should be increased as the average flow rate through the machine is decreased. Other adjustments may still be needed to account for the variation of the co-component of the transfer function with frequency.

Conclusions

1 Periodic flow modulation of a very small magnitude can be used to determine the unsteady characteristics of a blower or a compressor. The use of spectral averaging techniques was found to be very effective in eliminating the masking effects of random fluctuations of the flow quantities even at very low flow modulation amplitudes.

2 For the centrifugal blower and the frequency range investigated here the deviation of the blower dynamic behavior from the quasi-steady response was dominated by an inertia-like effect which resulted in a progressive phase lag between the static pressure rise and the discharge flow rate fluctuations with modulation frequency.

3 On-line measurements of the slope of the characteristics curve can be carried out by evaluating the co-component of the transfer function between the static pressure rise and the flow rate fluctuations at low modulation frequencies. Negative and positive values would indicate corresponding negative and positive slopes of the characteristics curve.

Acknowledgment

This research was partially supported by the Natural Sciences and Engineering Research Council of Canada under Grant Number A7451 and the American University in Cairo.

References

1 Thompson, P. A., *Compressible-Fluid Dynamics*, McGraw-Hill, New York, 1972.

2 Kuhlberg, J. F., Sheppard, D. E., King, E. O., and Baker, J. R., "The Dynamic Simulation of Turbine Engine Compressors," *AIAA 5th Propulsion Specialists Conference*, Paper No. 69-486, June 1969.

3 Corbett, A. G., and Elder, R. L., "Mathematical Modelling of Compressor Stability in Steady and Unsteady Flow Conditions," *AGARD Conference Proceedings No. 177*, Paper 12, Sept. 1973.

4 Greitzer, E. M., "Surge and Rotating Stall in Axial Flow Compressors, Part I and Part II," ASME JOURNAL OF ENGINEERING FOR POWER, Apr. 1976, p. 190.

5 Day, I. J., Greitzer, E. M., and Cumpsty, N. A., "Prediction of Compressor Performance in Rotating Stall," ASME JOURNAL OF ENGINEERING FOR POWER, Vol. 100, Jan. 1978, pp. 1-14.

6 Peacock, R. E., and Das, D. K., "Compressor Response to Pulsed Transients," *AIAA/SAE/ASME 16th Joint Propulsion Conference*, June 1980, Hartford, CT, AIAA Paper No. 80-1080.

7 Greitzer, E. M., "Review-Axial Compressors Stall Phenomena," ASME *Journal of Fluids Engineering*, Vol. 102, June 1980, pp. 134-151.

8 Moore, F. K., "A Theory of Rotating Stall of Multi-Stage Axial Compressors. Part I: Small Disturbances," ASME JOURNAL OF ENGINEERING FOR GAS TURBINES AND POWER, Vol. 106, No. 2, Apr. 1984, pp. 313-320; Paper No. 83-GT-44.

9 Paulon, J., "Theoretical and Experimental Determination of the Transfer Function of a Compressor," ASME Paper No. 84-GT-283.

10 Abdel Hamid, A. N., Colwill, W. H., and Barrows, J. F., "Experimental Investigation of Unsteady Phenomena in Vaneless Radial Diffusers," ASME JOURNAL OF ENGINEERING FOR POWER, Vol. 101, No. 1, 1979, pp. 52-60.

11 Abdel-Hamid, A. N., "Analysis of Rotating Stall in Vaneless Diffusers of Centrifugal Compressors," ASME Paper No. 80-GT-184.

12 Frigne, P., and Van den Braembussche, R., "A Theoretical Model for Rotating Stall in the Vaneless Diffusers of a Centrifugal Compressor," ASME Paper No. 84-GT-204.

13 Toyama, K., Runstadler, P. W., Jr., and Dean, R. C., Jr., "An Experimental Study of Surge in Centrifugal Compressors," ASME *Journal of Fluids Engineering*, Mar. 1977, pp. 115-131.

14 Jansen, W., Carter, A. F., and Swarden, M. C., "Improvements in Surge Margin for Centrifugal Compressors," *AGARD Conference Proceedings*, No. 282, Paper No. 19, 1980.

15 Elder, R. L., and Gill, M. E., "A Discussion of the Factors Affecting Surge in Centrifugal Compessors," ASME Paper 84-GT-194.

16 Abdel-Hamid, A. N., "Surge Detection and Alleviation in Centrifugal Water Chillers," Borg-Warner Research Center, Report 4293, Feb. 1982.

APPENDIX

Calculation of the Effective Length of the Blower

Consider the unsteady flow of an incompressible non-viscous fluid of density ρ in a pipe of a constant area A and length L. The difference between the pressure at exit and inlet of the pipe, Δp, is related to the flow rate fluctuations with time (dQ/dt) by the equation

$$\Delta p = -(\rho L/A)\,(dQ/dt)$$

For sinusoidal flow fluctuations at a frequency ω, the preceding equation becomes $\Delta p_0 = -(\rho L/A)\ (i\omega \Delta Q_0)$ where Δp_0 and ΔQ_0 are the amplitudes of the pressure and flow rate fluctuations respectively and $i = \sqrt{-1}$.

The pressure fluctuations therefore lag the flow fluctuations by 90 deg and the ratio between the amplitudes of the pressure and flow fluctuations is $(\rho L \omega / A)$.

For the blower under investigation here the ratio between the amplitudes of the pressure and flow fluctuations has a co-component X_0 and a quad-component X_q. If the quad-component is assumed to be due to the inertia effects associated with the flow path inside the blower the effective length of the flow can be calculated from $L_e = X_q\,(A/\rho\omega)$.

The inlet and exit areas of the blower were almost equal and the discharge area was used in the calculation of the effective length.

A Distinction Between Different Types of Stall in a Centrifugal Compressor Stage

N. Kämmer

M. Rautenberg

Institute for Turbomachinery
and Gas Dynamics,
Universität Hannover,
Hannover, West Germany

The flow at the stall line of a centrifugal compressor with vaneless diffuser was investigated at different speeds. A distinction between three kinds of stall phenomena could be made. One type of stall with regurgitation of fluid at the impeller inlet was of a nonperiodic character, whereas two different types of periodic stall appeared at higher speeds. The rotating nature of these two types of stall was verified from a comparison of signals of peripherally spaced pressure transducers. The low-frequency rotating stall exhibited features of diffuser generated stall and a lobe number of three was measured. From a detailed investigation of the high-frequency rotating stall, which included unsteady probe measurements upstream and downstream of the impeller, it can be shown that this type of rotating stall is generated in the impeller by a periodic breakdown of energy transfer from the rotor to the flow. This conclusion is supported by the distribution of shroud static pressures.

Introduction

Stalled flow in centrifugal compressors limits the operating range, deteriorates the performance, and may cause the compressor to surge. The mechanical hazards of operation during rotating stall or surge conditions force the compressor manufacturer to use pessimistic assumptions when certifying the operating range of a compressor. Compressor operation with stalled flow may involve severe financial losses for the operator and the manufacturer due to poor efficiency. It is therefore necessary to gain further insight into the flow mechanism that triggers the inception of stall in order to find stall criteria and to improve existing theoretical models for the prediction of compressor stall.

For a centrifugal compressor stage with an unvaned diffuser, impeller stall [1, 2, 3, 4, 5] as well as diffuser stall [6, 7, 8, 9, 10] have been reported. Some authors relate diffuser stall to the effects of boundary-layer separation while others explain it by a hydrodynamic instability of the diffuser core flow [6, 7, 11]. Stall phenomena may be of a steady or of a propagating and therefore rotating nature. Stall of different nature and origin may appear in one stage depending upon rotor speed and aerodynamic parameters [5, 10]. Thus, several parameters must be considered as criteria for the inception of stall.

The stall behavior of the compressor under investigation was suspected to be influenced by more than one type of stall [12]. The questions to be answered were what kind of flow phenomena were involved along the stall line at different speeds, how could the origin of the different types of stall be identified, and what parameters appeared most useful as stall criteria. Detailed flow measurements throughout the compressor were employed using steady and unsteady transducers in order to analyze the flow through the compressor stage at the stall line.

Table 1 Geometric and aerodynamic parameters of tested compressor

Impeller exit diameter	d_2	$= 0.4$ m
Inlet diameter ratio	$d_{1,a}/d_2$	$= 0.7$
Hub-to-trip ratio	$d_{1,i}/d_2$	$= 0.225$
Impeller exit width ratio	b_{2}/d_2	$= 0.065$
Inlet blade angle	$\beta_{1,a}$	$= 27$ deg
Exit blade angle	β_{200}	$= 90$ deg
Diffuser radius ratio	d_3/d_2	$= 2.0$
Number of impeller blades (14 splitter blades)	Z	$= 28$
Diffuser area distribution	$d \cdot b$	= const
Circumferential Mach number	M_u	$= 0.86^*$
Compressor Reynolds number	Re_d	$= 1.0 \cdot 10^{7*}$

* at $n_{\mathrm{red}} = 14{,}000$ rpm

Experimental Apparatus and Measurement Technique

The compressor used for this investigation is a single-stage machine with an unshrouded impeller and a vaneless constant area diffuser. The geometric and aerodynamic parameters are listed in Table 1. The test rig was operated as an open loop, the air supply was through a short axial suction pipe from a settling chamber, and the compressed air was delivered from the diffuser to an annular collection chamber. The throttle valve is installed in the pressure pipe. In a modification of the diffuser, a ring was installed in the diffuser at half the diffuser's radial extent in order to simulate a diffuser with a radius ratio of $\lambda_3 = 1.5$. This ring reduced the diffuser axial width to 50% of its original value at that location.

Contributed by the Gas Turbine Division of THE AMERICAN SOCIETY OF MECHANICAL ENGINEERS and presented at the 30th International Gas Turbine Conference and Exhibit, Houston, Texas, March 18–21, 1985. Manuscript received at ASME Headquarters, January 16, 1985. Paper No. 85-GT-194.

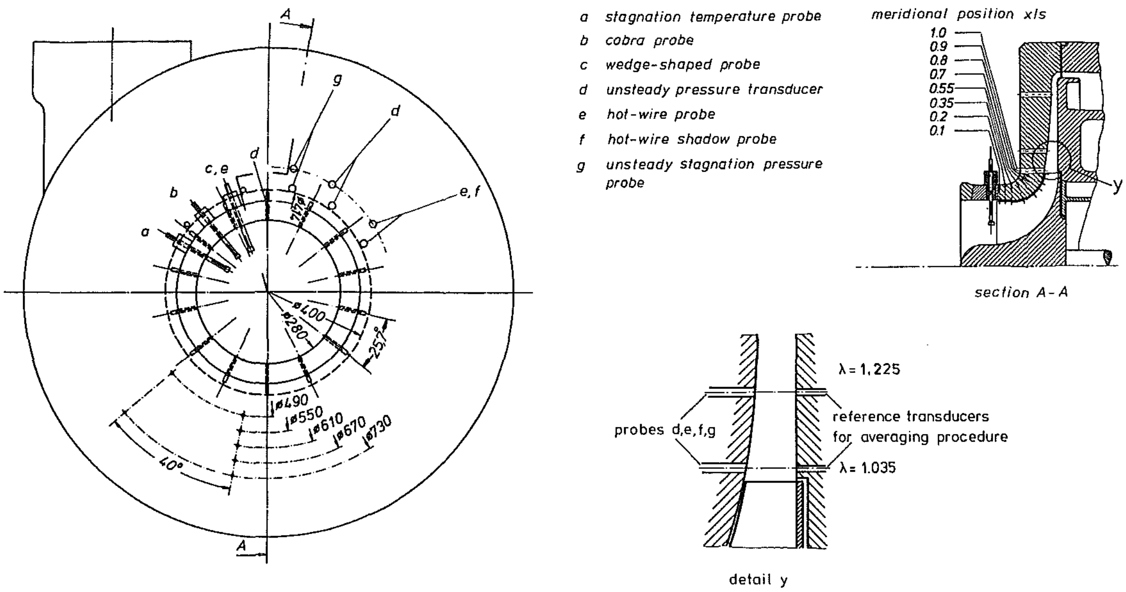

Fig. 1 Sketch of test compressor

Conventional pressure and temperature probes were used to determine the overall compressor performance. A scanning of the flow in the suction pipe immediately upstream of the impeller was performed to determine the velocity and temperature profiles of the flow approaching the impeller. The impeller exit flow field was also traversed with stagnation pressure, stagnation temperature, and with cobra probes. High-frequency semiconductor pressure transducers were used to investigate the unsteady flow in the impeller and in the diffuser. In the first configuration they were positioned meridionally along the shroud line to determine the pressure field between the blades and in the second configuration they were arranged on the circumference to measure the peripheral distribution of the rotating stall pattern. Furthermore, an unsteady stagnation pressure probe, a hot-wire probe, and a hot-wire shadow probe were traversed shortly behind the impeller exit to study the unsteady flow field across the diffuser width. The traversing positions were at identical radial but different peripheral positions.

In order to obtain the stagnation temperature the hot-wire signal as well as the instantaneous static and stagnation pressures had to be combined using a heat transfer analysis of the hot-wire. This procedure is described in [13]. For the purpose of determining the unsteady stagnation temperature and the unsteady Mach number in a periodically fluctuating flow using peripherally spaced transducers an averaging

Nomenclature

a_K = sonic speed in inlet plenum
b = diffuser width
b_i = average impeller width
c = absolute velocity
d = diameter
D_f = diffusion factor [5],

$$D_f = 1 - \frac{\bar{w}_2}{W_{1\mathrm{rms}}} + \frac{\pi r_2 \mu u_2}{Z s w_{1\mathrm{rms}}} + 0.1 \frac{b_i}{r_s} \cdot \left(1 + \frac{\bar{w}_2}{w_{1\mathrm{rms}}}\right)$$

m = lobe number
$\dot{m}$ = mass flow rate
M = Mach number
M_u = circumferential Mach number, $\mathrm{M}_u = u_2/a_K$
n = rotor speed
p = pressure
q = relative dynamic heat, $1/2\ \rho w^2$
r = radius
r_s = mean radius of curvature
Re_d = compressor Reynolds number,

$$\mathrm{Re}_d = \frac{u_2 d_2}{\nu_2}$$

s = blade length at tip
t = time
T = temperature
T = time period
u = peripheral velocity
w = relative velocity
x = distance from inducer inlet at blade tip
z = axial distance
Z = number of impeller blades
α = absolute flow angle from tangential
β = relative flow angle from tangential
$\beta_{2\infty}$ = blade angle at impeller exit
$\Delta\beta_{st}$ = incidence angle
γ^2 = coherence
η_i = adiabatic efficiency of stage
η_L = adiabatic efficiency of impeller
λ = radius ratio, $\lambda = r/r_2$
μ = slip factor
ν = viscosity
π = pressure ratio
ρ = density
φ^* = flow coefficient,

$$\varphi^* = \frac{4 \cdot \dot{m}_{\mathrm{red}}}{\rho_K \pi D_2^2 u_2}$$

φ = peripheral angle
τ = temperature ratio, $\tau = T/T_K$

Subscripts and Superscripts

a = shroud side
c = calculated
i = hub side
K = inlet plenum
r = relative
red = reduced to reference conditions $T_K = 288.15\ K$, $p_K = 1.01325$ bar
rms = value taken at mean area radius
rot = rotor
RS = rotating stall
st = stall
th = inducer throat
tot = stagnation
1 = inducer inlet
2 = impeller exit
3 = diffuser outlet/collector inlet
$\hat{}$ = amplitude
$\bar{}$ = averaged value
$\tilde{}$ = instantaneous value
$\tilde{}$ = including incidence loss correlation

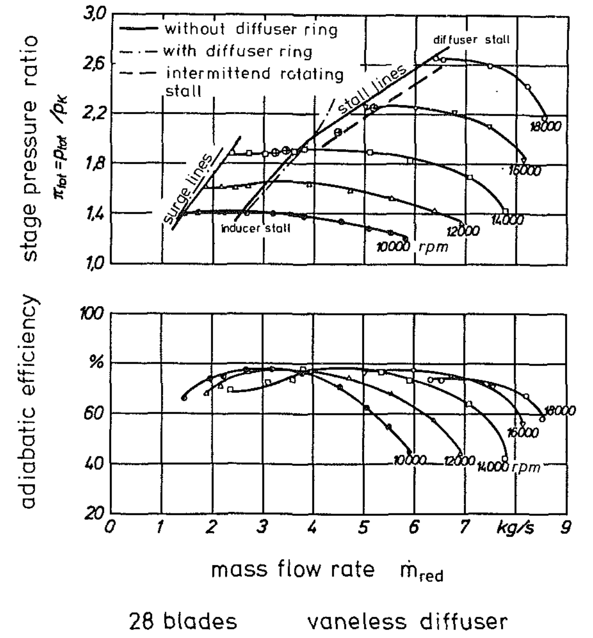

Fig. 2 Compressor map

procedure was employed to give a mean signal trace over one period for each of the transducer signals. Each probe was accompanied by a reference pressure transducer mounted flush with the diffuser wall facing the probe position. Since the signals from the unsteady probes and from the reference pressure transducers were highly periodic in the rotating flow region the reference signals were used to perform the averaging process of each probe signal and the phase relationship between the averaged probe signals was determined from the averaged reference signals. This averaging process may be termed conditional ensemble averaging. A sketch of the tested compressor and the measurement positions is given in Fig. 1.

Discussion of Results

The compressor map is shown in Fig. 2. The stall line was determined from the steady probe readings mounted upstream of the impeller and from an inspection of the flush-mounted unsteady pressure transducers at the shroud. Stall was encountered in the lower speed range when a self-induced prerotation was indicated by the probes, and at the higher speeds the inception of stall became apparent by a characteristic change of the unsteady pressure signals. This indicated a periodic breakdown of the pressure gradient from suction to pressure side. The rotating stall did not always appear in a quasi-steady fashion. Only at $n = 14{,}000$ rpm did a rotating stall occur suddenly and disappear only when the throttle setting was changed again. At higher speeds the compressor periodically ran into rotating stall and then recovered. Further throttling of mass flow eventually caused the compressor to exhibit continuous rotating stall allowing a steady operation with rotating stall. The first appearance of this periodic operation with and without rotating stall is termed the intermittent stall line and the continuous appearance termed stall line in the compressor map of Fig. 2.

At lower speeds operation of the compressor was possible over a certain flow range with self-induced prerotation before the compressor ran into surge. However, the surge line was not experimentally determined at the higher speeds due to safety considerations. It is noted that the stall line exhibits a kink at $n = 14{,}000$ rpm showing that different flow phenomena are responsible for the appearance of stall at the higher and the lower speeds.

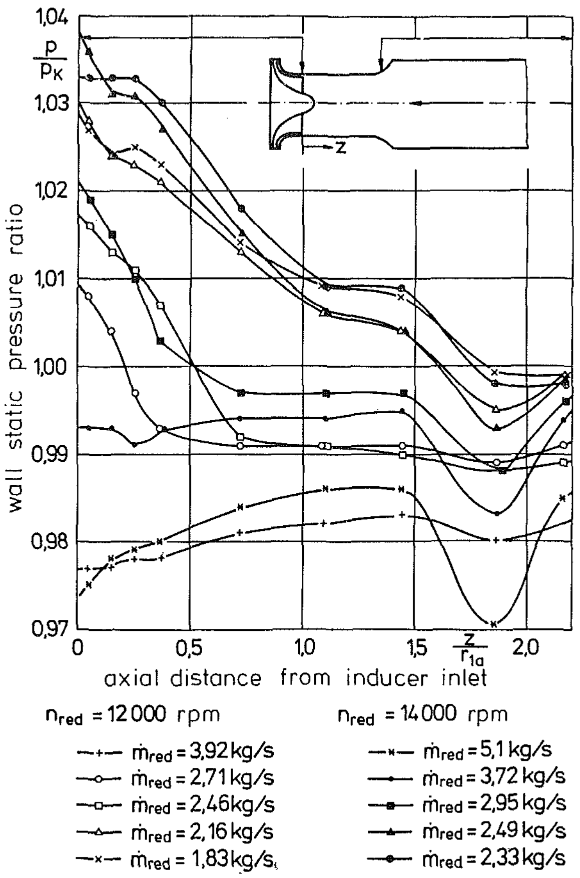

Fig. 3 Static pressure upstream of impeller

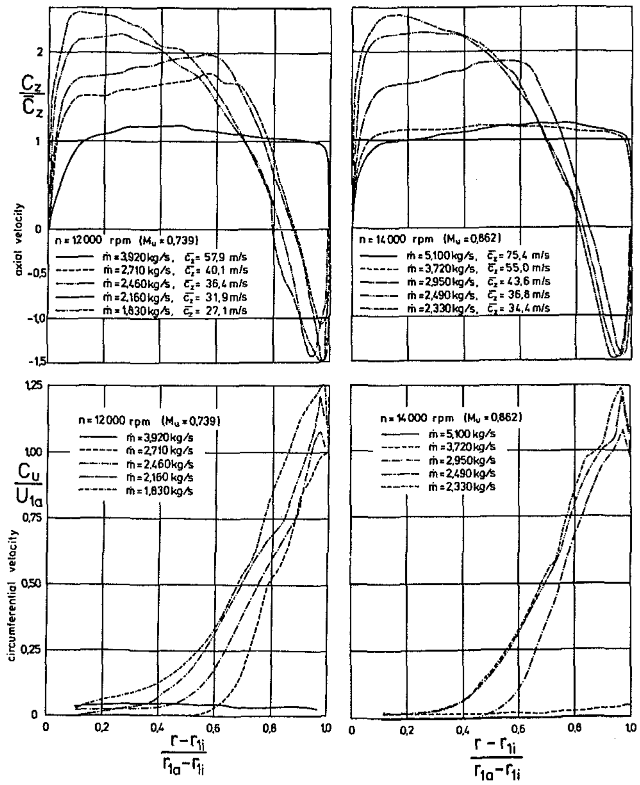

Fig. 4 Velocity distribution upstream of impeller

Inducer Stall

The scanning of the flow upstream of the impeller was intended to determine the velocity profiles and the amount of

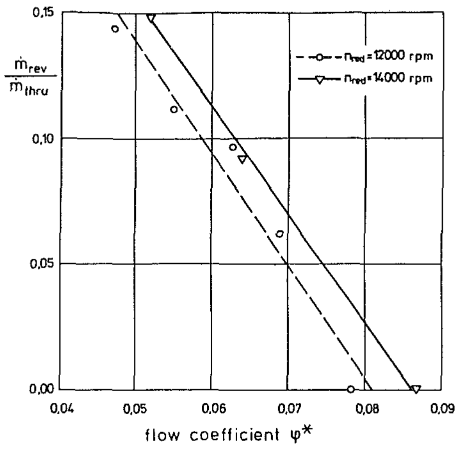

$\dot{m}_{rev}$ - reverse flow rate
$\dot{m}_{thru}$ - net through flow rate

Fig. 5 Strength of flow reversal at impeller inlet

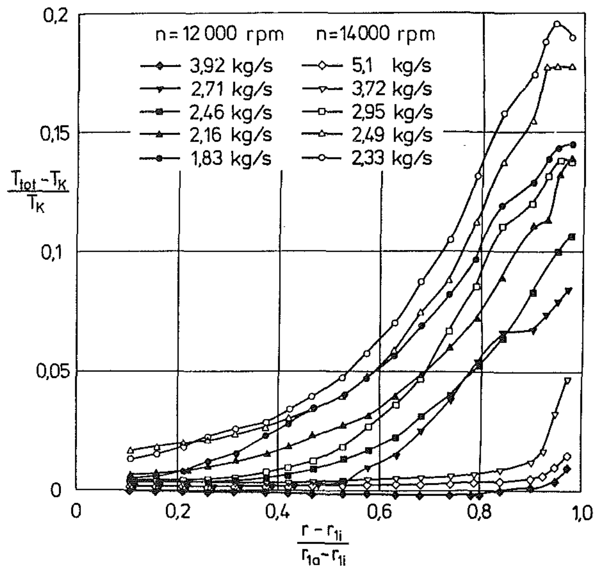

Fig. 6 Stagnation temperature upstream of impeller

self-induced swirl and the magnitude of the flow regurgitation from the impeller. The distribution of wall static pressures upstream of the impeller shown in Fig. 3 clearly gives evidence of a circumferential velocity component and of the axial extent of this swirling flow regime. A comparison of the pressure distributions with the compressor map reveals that only the operating points to the left of the stall line exhibit upstream wall static pressures in excess of the plenum pressure p_K. The axial extend of this region is limited by the position where the inlet suction pipe diameter is reduced to that of the impeller eye diameter.

Figure 4 gives the results of the probe measurements. The reverse flow zone close to the wall increases in radial extent with a further reduction of mass flow and requires axial velocities in the core flow that are higher than twice the area-averaged axial velocity. The swirling component can only be introduced in the reverse flow zone but is carried over into the core of the approaching flow by way of mixing effects. This induced swirl in the core flow reduces the energy transfer in the impeller and therefore must eventually cause the compressor to surge. A simple relation between the magnitude of reverse flow and flow coefficient φ^* is evident from Fig. 5 where the fraction of reverse flow to through flow is plotted against flow coefficient φ^*. Once reverse flow occurs its magnitude increases almost linearly with flow reduction, and one may assume that the inducer can tolerate only a certain fraction of reverse flow before a complete breakdown of energy transfer occurs, thus triggering surge. Figure 5 shows that for both speeds investigated, the magnitude of reverse flow reached 15% of the net through-flow at the operating point closest to the surge line.

Since energy is transferred to the fluid in the reverse flow zone, the enthalpy rise can be measured as a higher stagnation temperature. The stagnation temperature profiles are shown in Fig. 6. If flow reversal appears an increase in stagnation temperature is experienced almost along the entire blade height. A stronger reverse flow with a higher swirl component also produces a stronger increase in stagnation temperature. Calculation of the relative flow angle distribution in the reverse flow zone from the data in Fig. 4 shows that the flow follows the direction of the blades more closely with flow reduction, thus producing a higher circumferential velocity component and therefore an increasing stagnation temperature in the reverse-flow zone. This accords with the results found by Kämmer et al. [14] for the steady reverse flow through a complete centrifugal stage, where an increase in energy transfer with rising back-flow rate was measured. The mixing of the stagnation temperature across the inlet plane and the rising temperature with flow reduction further contribute to the deterioration of energy transfer in the impeller.

An insight into the flow through the impeller before the appearance of stall and after the development of a steady reverse-flow zone may be obtained from the averaged shroud pressure contours presented in Fig. 7 for different flow rates. At flow rates to the right of the stall line the pressure contours in the inducer part indicate a continuous pressure rise from blade suction to pressure side and no separation due to a high incidence angle is present. There is a region of small pressure differences upstream of the leading edge of the splitter blades, which is a typical feature of this type of impeller with a fairly large axial extent of the inducer. However, from the flow field measurements by Mizuki [2] inside an impeller it is known that low-energy material accumulates in this region and therefore contributes to build up a region of very low energy transfer to the fluid. Once the flow reversal appears, no energy transfer is achieved in the inducer. A noticeable pressure gradient appears downstream of the splitter blade leading edge and is more pronounced in the left blade channel. It should be mentioned that the degree of unsteadiness is highest at the flow rate close to surge and the given pressure contours represent an average state of the flow. However, Fig. 7 clearly shows that the energy transfer to the fluid is well developed in the radial impeller section when the rotor operates with continuous inducer stall. This is why even in this type of operation the compressor characteristic decreases continuously, enabling steady operation over a certain flow range between the inception of stall and the initiation of surge.

Stall Criterion Parameters

Parameters suited as stall criteria are plotted in Fig. 8 against Mach number. For inducer stall these parameters are the measured incidence angle $\Delta\beta_{st}$, deceleration ratio $\tilde{w}_{th}/w_1$, and relative pressure rise $\Delta\tilde{p}_{st}/q$. While w_1 is the measured relative velocity upstream of the inducer, w_{th} is the calculated relative velocity in the inducer throat, assuming flow direction parallel to the blades. $\Delta\tilde{p}_{st}$ is the corresponding static pressure rise and q is the relative dynamic head. The superscript ~ indicates that an incidence loss correlation was incorporated into the calculation of $\Delta\tilde{p}_{st}$ and $\tilde{w}_{th}$. For the entire impeller the velocity ratio $w_2/w_{1\text{rms}}$ and the diffusion factor D_f [3] are used as stall criterion parameters and for the diffuser this is the absolute flow angle α_2 at impeller exit. All averaged flow

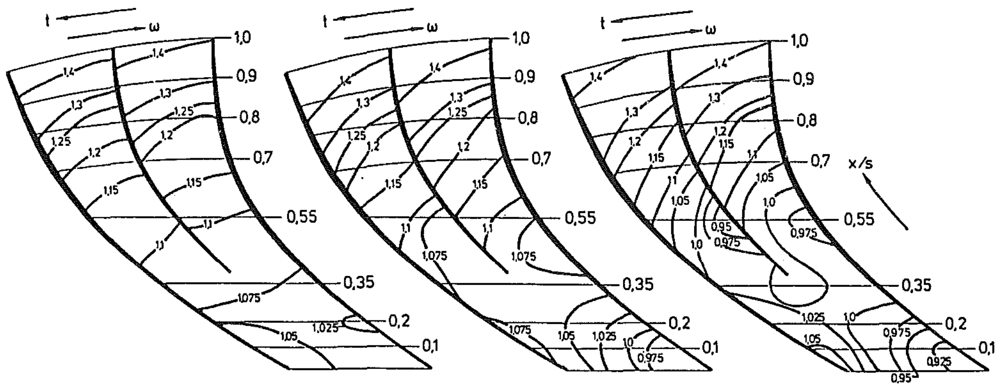

$\dot{m}_{red} = 2{,}33$ kg/s $\dot{m}_{red} = 3{,}83$ kg/s $\dot{m}_{red} = 5{,}1$ kg/s

$n_{red} = 14000$ rpm

Fig. 7 Shroud pressure contours

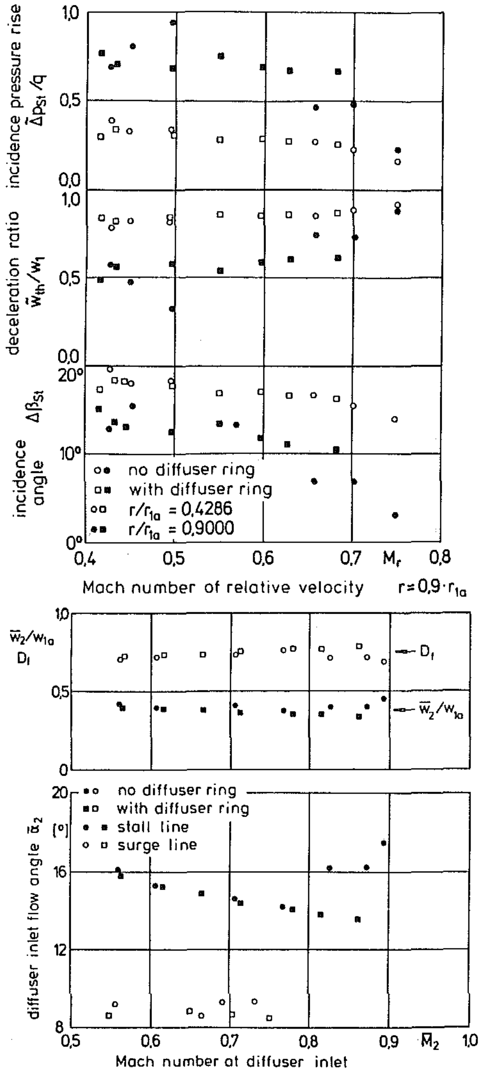

Fig. 8 Stall criterion parameters

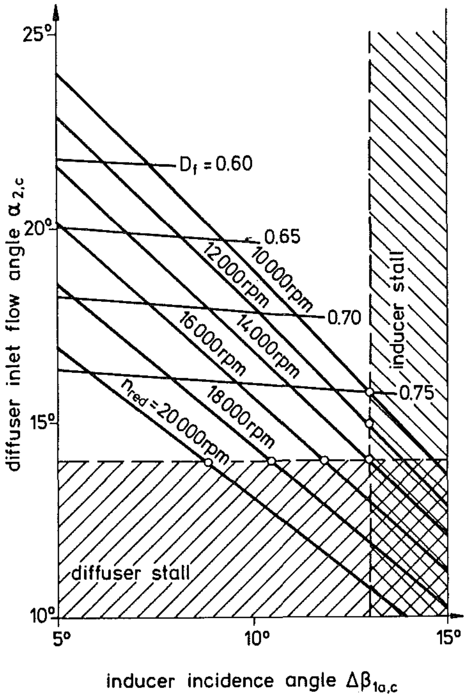

Fig. 9 Influence of rotor speed on critical stage element

properties are obtained from the probe measurements at impeller exit.

The measured incidence angles show that $\Delta\beta_{st}$ is larger at the hub than at the blade tip. There is more scatter among the data points for the tip than for the hub, because the tip flow angle close to the stall line is very sensitive to flow rate variations. However, both incidence angles at hub and tip exhibit the general trends of decreasing values at the stall line with increasing Mach number and hence increasing rotor speed. This is in agreement with the incidence angle correlation at stall given by Senoo [4]. However, at the blade tip there is a higher loading than at the hub because of the smaller blade angles at the tip and the smaller blade blockage. This is reflected in the velocity deceleration ratio and the incidence pressure rise. At relative Mach numbers greater than $M_{1r} = 0.6$, all three inducer load parameters show a distinctly lower blade loading at the stall line. This, however, is due to the fact that the stall line is no longer determined by the inducer blade loading. The impeller loading as reflected by the diffusion factor is fairly constant along the stall line or increases slightly if the deceleration ratio w_2/w_{1rms} is considered. The loading of the diffuser increases constantly since the flow angle at diffuser inlet α_2 decreases continuously. At Mach numbers greater than $M_2 = 0.8$ α_2 rises sharply for the diffuser version without throttle ring, because these data points were measured at speeds where the stall line was defined by the appearance of intermittent rotating stall. If no

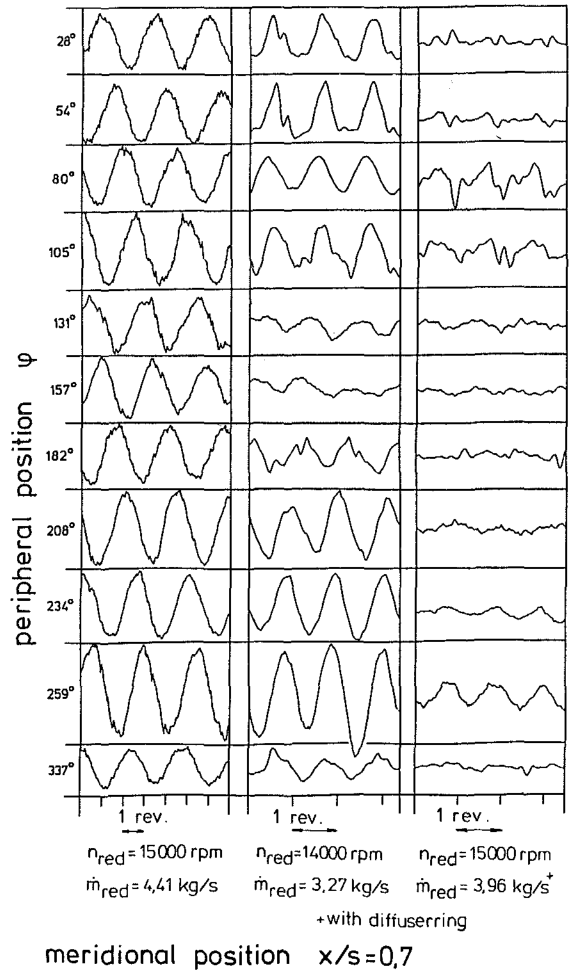

Fig. 10 Wall pressure with rotating stall

intermittent rotating stall is experienced as is the case with the diffuser throttle ring, much smaller values of α_2 may be achieved at the stall line. Figure 8 suggests that while at lower speeds the stall limit is determined by the inducer, the loading of the diffuser is constantly increasing with speed and eventually the diffuser loading is high enough to render this the critical stage element.

This concept is illustrated by the results of a very simple impeller flow calculation. In Fig. 9 the diffuser inlet flow angle $\alpha_{2,c}$ is plotted against impeller incidence angle $\Delta\beta_{1a,c}$ at the shroud for different speeds. Constant axial velocity at the impeller eye and averaged flow properties at diffuser inlet are assumed in the calculation. Assuming the incidence angle at impeller tip and the diffuser inlet flow angle as stalling criteria, taking reasonable values from Fig. 8, Fig. 9 shows that the inducer stall criterion is violated at lower speeds, while at higher speeds the diffuser stall criterion is violated prior to inducer stall. Furthermore, there is a speed line at which inducer and diffuser loading is critical at the same mass flow, and one may expect that at this point the mutual influence of impeller and diffuser flow will be particularly strong once the compressor runs into stall. Even though Fig. 9 is based on very simple calculations it corroborates the idea that impeller and diffuser stall phenomena are involved in the compressor investigated.

Rotating Stall

Evidence of the rotating stall flow is given in Fig. 10, where the recordings of the circumferentially spaced pressure transducers are presented. At 15,000 rpm the pressure recordings were taken in the intermittent rotating stall region

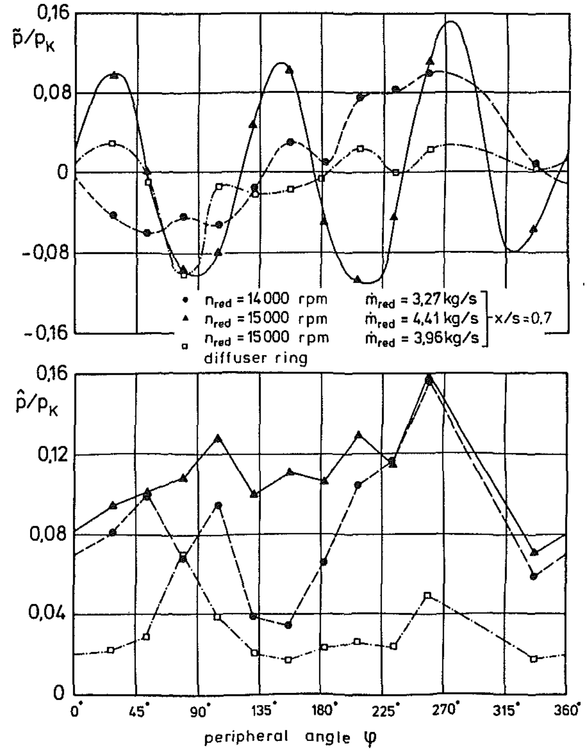

Fig. 11 Instantaneous peripheral pressure distribution

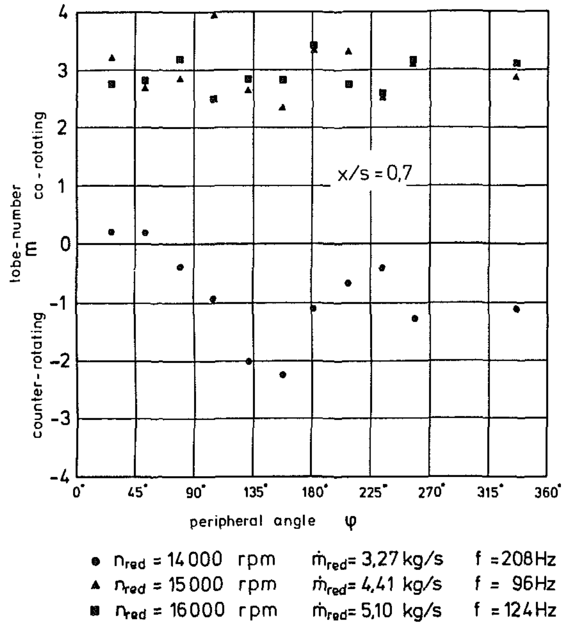

Fig. 12 Peripheral distribution of lobe number

of the map when the compressor operated with stall. The blade passing frequency was removed before plotting the data. While the rotating nature of the pressure disturbances is clearly evident at 15,000 rpm over the entire circumference, the self-induced oscillations are also found at 14,000 rpm, but with strong circumferential variation. With the diffuser ring installed, pressure oscillations are induced at a lower flow rate and in a rather incoherent manner with a much smaller amplitude. A plot of the instantaneous pressure distribution and of the magnitude of oscillations over the periphery is given in Fig. 11. At 15,000 rpm the rotating stall pattern is almost sinusoidal with a lobe number of three, while at 14,000 rpm the instantaneous pressure distribution has one maximum and one minimum. However, though the propagating nature of the stall pattern at 15,000 rpm becomes obvious if the pressure distributions at small time intervals are plotted, the picture is much more complicated at a speed of 14,000 rpm. Although the pressure amplitudes undergo some variation along the circumference for 15,000 rpm, this variation is much stronger at 14,000 rpm. If the diffuser ring is installed there is a circumferential distribution of a stall pattern but its amplitude is much smaller than that of the other two oscillations.

The peripheral phase relations are determined with an HP 3582A spectrum analyzer. The number of lobes of the rotating pressure pattern can be calculated from the signal phase shift and the known geometrical angle between the two transducer positions taking only circumferential propagation into account. The ambiguity in this calculation is avoided assuming that no complete lobe fits between the transducers. The results are presented in Fig. 12 for three speeds. At the two higher speeds the results for the lobe numbers are clustered around three lobes. In the absolute frame of reference the pattern is propagated in the same direction as the impeller. This accords with the observation from Fig. 10, whereby the scatter may be introduced in the instrumentation, by the limited accuracy of the phase shift determination, and a variation of the meridional propagation component. At 14,000 rpm the picture is competely different. The lobe number is not constant over the periphery and most of the results show a propagation contrary to the impeller rotation. However, the stall frequency is highest at this speed corresponding to 89% of impeller speed. It can only be speculated that one reason for the large difference in lobe numbers over the circumference may be a strong variation in the meridional propagation of the stall pattern. The dramatic change in "indicated" lobe number may also be the result of the superposition of inducer and diffuser stall. However, the results for $n = 14{,}000$ rpm remain very puzzling, while for the two higher speeds the propagating speed of the stall pattern, 12.8% and 15.5% of impeller speed, respectively, agree well with the data reported in the literature [6, 7, 10].

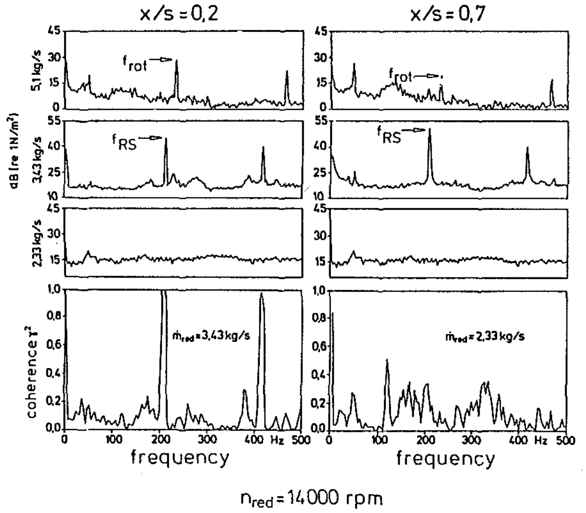

Fig. 13 Frequency spectra and coherence

Figure 13 is provided to clarify the difference between the rotating stall and the inducer stall phenomena experienced at 14,000 rpm. This figure contains pressure frequency spectra for two transducer locations at three flow rates, and in the lower section the coherence γ^2 between these two signals is given for the flow rate $\dot{m} = 3.43$ kg/s with rotating stall and $\dot{m} = 2.33$ kg/s with inducer stall. At the highest flow rate a frequency peak appears at the frequency of impeller rotation f_{rot} as well as at its first harmonic. The rotor frequency in the pressure signal originates from imperfect symmetry of the flow distribution in the impeller. The spikes at a flow rate of $\dot{m} = 3.43$ kg/s are clearly distinguished from the rotor frequency f_{rot}. Here the fundamental stall frequency is at $f_{\mathrm{RS}} = 208$ Hz and its first harmonic at 416 Hz. The spikes at the fundamental stall frequency f_{RS} exceed the spikes at the rotor frequency f_{rot} by 16.3 dB in the inducer section ($x/s = 0.2$) and by 21.1 dB in the radial impeller section ($x/s = 0.7$). Further throttling causes the rotating stall to disappear, and the spectra up to 500 Hz are of a noise type without distinct frequencies. The coherence plots reveal that this noise did not mask any distinct freqencies as it was reported by Abdelhamid [7] and the inducer stall is of a nonperiodic though unsteady nature. The rotating stall, on the other hand, is highly coherent through the impeller with coherence values equal to unity at the stall frequency.

The difference in flow rates with rotating stall at the 14,000 rpm speed line from $\dot{m} = 3.27$ kg/s in Fig. 10 to Fig. 12 and $\dot{m}$

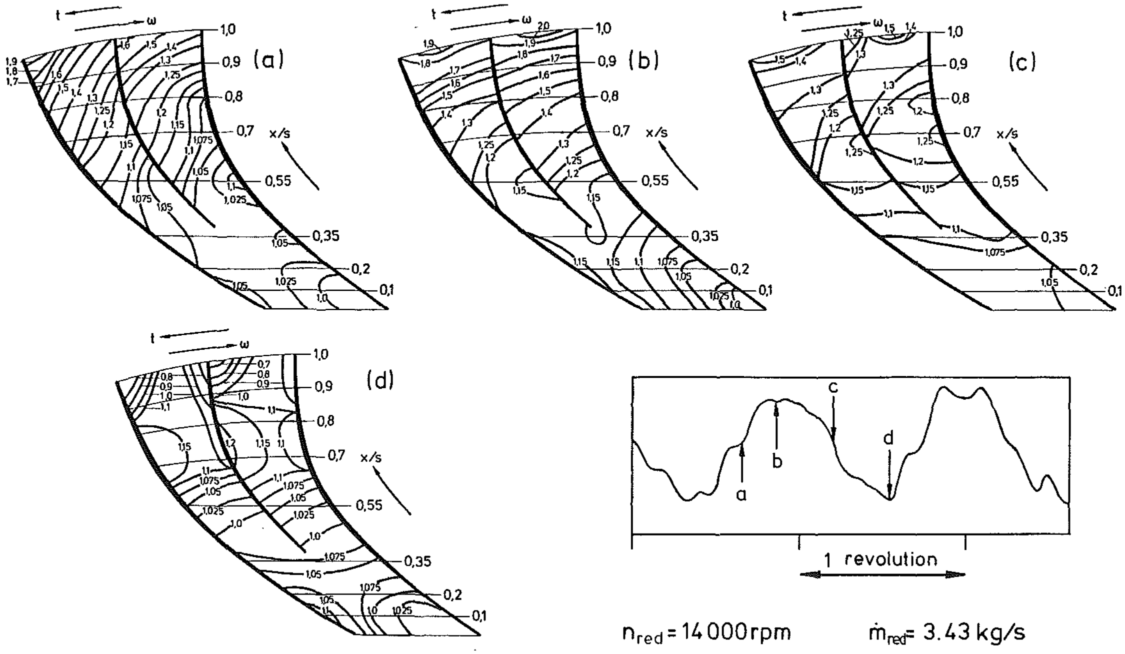

Fig. 14 Instantaneous shroud pressure contours with rotating stall

= 3.43 kg/s in the following figures gives the range over which a pronounced rotating stall occurred at that speed.

Probe Measurements During Rotating Stall. The probe measurements during rotating stall were performed only on the 14,000 rpm speed line. Before discussing their results it is illustrative to look at the instantaneous shroud pressure contours in Fig. 14. The four pressure distributions are plotted at selected moments during one stall period, referring to the low pass filtered pressure signal in the lower section of Fig. 14. These selected moments were during pressure increase (*a*), maximum pressure (*b*), pressure decrease (*c*), and minimum pressure (*d*). Pressure patterns (*a*) and (*b*) are similar to the ones shown in Fig. 7 to the right of the stall line where large blade-to-blade pressure differences indicate a high mass flow rate. This pressure gradient decreases in the radial part from (*a*) to (*b*), whereas in the inducer section this gradient increases. With falling average pressure ratio (*c*) there is virtually no blade-to-blade gradient up to $x/s = 0.55$ and even in the radial section of the impeller the constant pressure contours indicate normal flow conditions only between $x/s = 0.7$ and $x/s = 0.9$. A completely distorted pressure pattern is found at minimum average pressure (*d*) in the radial section, while in the inducer the isobars are already well organized again. The different pressure patterns show that both the inducer and the radial part of the impeller participate in the stalling flow and a strong motion normal to the compressor shroud is indicated in (*c*) and (*d*) where only local energy transfer from the impeller to the flow may be detected.

The measurements with the hot wire probe are presented in Fig 15 to show the radial extend of rotating stall along the inducer blade height. The probe was inserted with the wire position in the radial direction so that the signal was insensitive to flow angle. Though the frequency of rotating stall is present in the voltage signal for at least more than half the blade height it is more pronounced in the other radii. The pressure signals upstream of the inducer and in the diffuser are given for reasons of comparison. It may be concluded that the radial extent of the rotating stall flow indicated by the hot-wire signals is much larger than the radial extent of the stationary reverse flow zone shown in Fig. 4. This again emphasizes the different nature of these stall phenomena.

The results of the probe measurements at the impeller exit are given in Fig. 16 together with the wall static pressures. There is a strong variation in stagnation pressure ratio π_{tot} as well as in temperature ratio τ_{tot} over one stall period. This means a periodically changing energy transfer to the flow and can only be caused by impeller stalling, since the energy transfer must be independent of flow rate for an impeller with an exit blade angle of $\beta_{2\infty} = 90$ deg. The temperature ratio changes in particular reveal that the stall originates in the impeller, since exit stagnation temperature is directly linked with energy transfer to the flow. Thus, this rotating stall flow is caused by a periodic breakdown of energy transfer in the impeller. The stagnation pressure and temperature ratio fluctuations seems to be more pronounced at the shroud side of the open impeller, whereas static pressures are fairly constant across the diffuser width, inferred from the linear interpolation of the static pressures. The instantaneous pressure and temperatures are basically in phase across impeller exit and diffuser width. During convection through the diffuser, the static pressure and the stagnation temperature

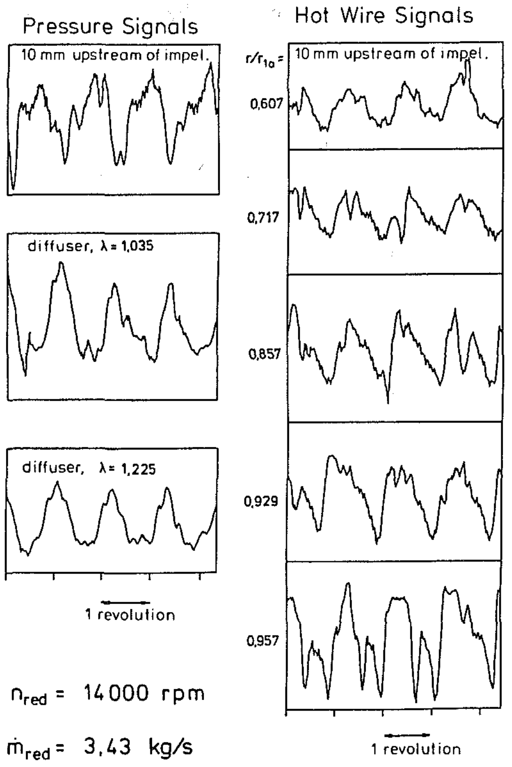

Fig. 15 Hot wire signals upstream of impeller

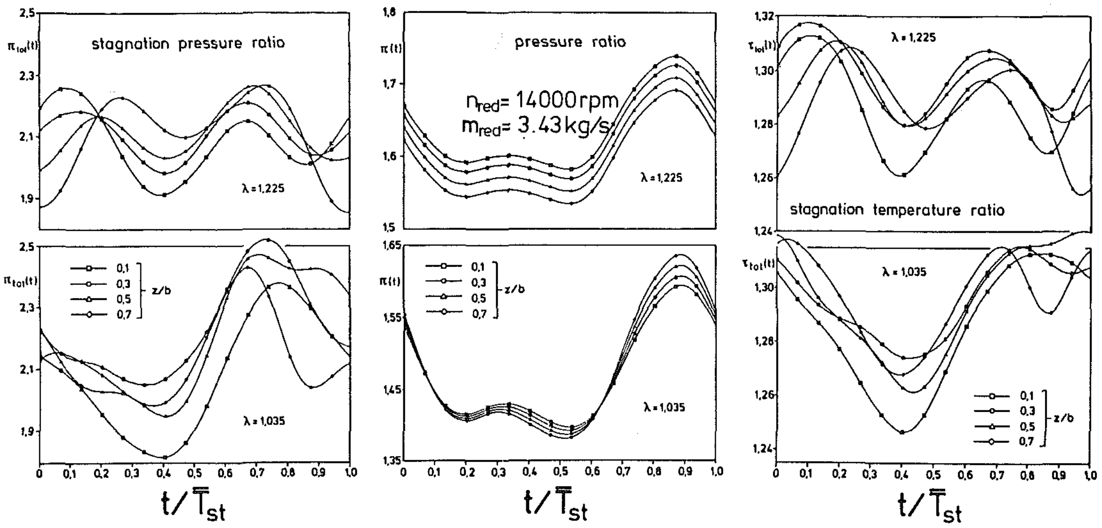

Fig. 16 Rotating stall flow properties over one stall period

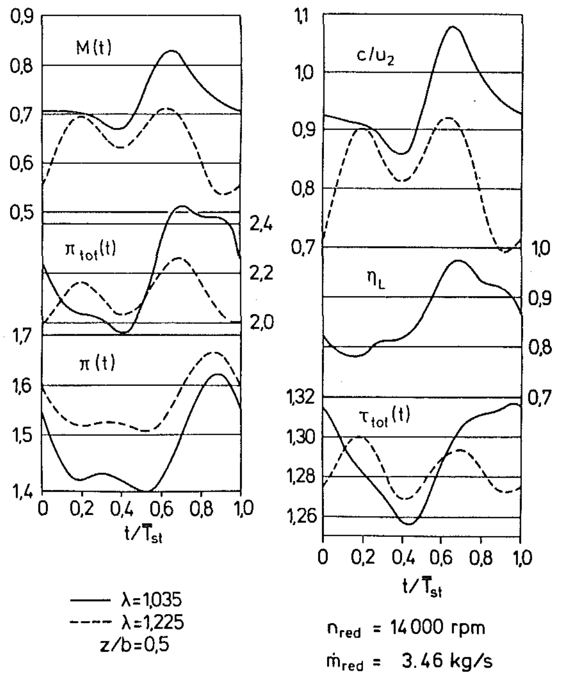

Fig. 17 Rotating stall flow properties over one stall period

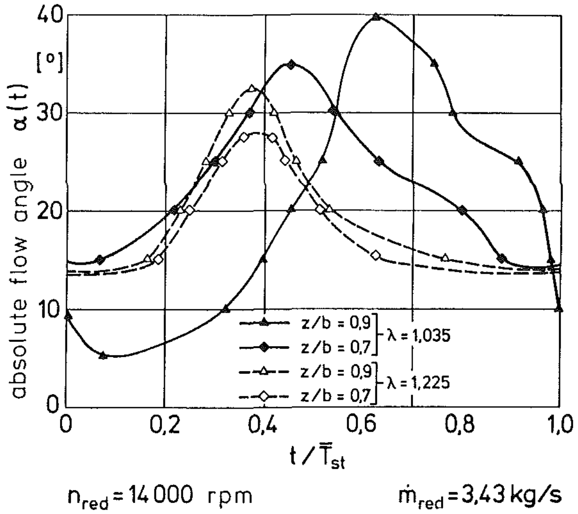

Fig. 18 Flow angle distribution over one stall period

fluctuations decrease slightly and the stagnation pressure fluctuations are noticeably reduced.

An idea of the flow features under rotating stall conditions can be obtained from Fig. 17 where pressures, temperatures, absolute velocity, Mach number, and instantaneous impeller efficiency are presented in one diagram. A complete stall period may be subdivided into three distinctly different phases: the phase of breakdown of energy transfer, the phase of recovery, and the phase of healthy operation. The breakdown of energy transfer begins with a rapid decline of stagnation pressure ratio π_{tot} and stagnation temperature ratio τ_{tot}. Since the static pressure ratio also decreases in this phase, the variation of Mach number M and absolute velocity c is not as drastic. The recovery of energy transfer is indicated by the sharp rise of stagnation pressure and temperature ratios. This phase is shorter than the phase of breakdown of energy transfer and it is accompanied by a considerable increase in Mach number M and velocity c, thus producing an increasing throughflow. The end of this second phase is marked by the maximum stagnation pressure ratio π_{tot} while the stagnation temperature ratio τ_{tot} now increases only slightly. At this moment maximum impeller efficiency η_L is reached. Since the static pressure ratio π also increases during the period of healthy operation, Mach number and absolute velocity and therefore the flow rate decrease while the impeller efficiency falls due to the rising stagnation temperature and declining stagnation pressure ratio. Thus, the impeller energy transfer deteriorates slowly and eventually triggers the beginning of the next stall cycle, presumably when the flow rate has fallen below a critical value.

The periodic fluctuation of flow angle is shown in Fig. 18 where the instantaneous flow angle is plotted over one stall period. The time scale of this averaged flow angle distribution is synchronous with those from Fig. 17. Only the width positions $z/b = 0.7$ and $z/b = 0.9$ could be evaluated, because the blade-to-blade flow angle variation masked the rotating stall flow angle fuctuation at the positions closer to the shroud side.

The largest angle fluctuations are found close to the rear side of the diffuser, which corresponds to the impeller hub side, and they diminish when passing through the diffuser. At impeller exit the largest flow angle is found at $z/b = 0.9$ when stagnation pressure and absolute velocity are maximum and a rather steep decrease coincides with the appearance of stall seen in the stagnation pressure and temperature distributions in Fig. 17. However, nowhere does the flow angle exhibit negative values which would mean a back-flow of fluid from the diffuser into the impeller.

Conclusions

Three types of stall were found at different speeds in a centrifugal compressor stage operating with a vaneless diffuser. At low speeds inducer stall determines the stall line of the stage causing a stationary and unperiodic reverse flow zone in the impeller eye with a strong self-induced swirl component. Further throttling increases the extent and magnitude of this reverse flow and reduces the energy transfer in the impeller so that it eventually stimulates compressor surge. Inducer stall correlates with high values of tip blade incidence angles. At higher shaft speeds a rotating stall appears. This is of a rapidly rotating type at 14,000 rpm and of a slowly rotating type at higher speed lines. The rotating nature of the latter type was revealed from circumferential phase relations. The speed of the pressure pattern and the lobe number are well in accordance with the data published in the literature for diffuser generated rotating stall. The insertion of a ring into the diffuser shifted the stall line and suppressed to a high degree the appearance of rotating stall giving further evidence for the generation of this type of stall in the diffuser. The fast-rotating stall could be attributed to a periodic breakdown of energy transfer in the impeller inferred from probe measurements downstream of the impeller. A simple impeller flow calculation supported the conclusion drawn from the comparison of impeller and diffuser stall criteria that an increasing speed changes the load from the inducer to the unvaned diffuser. Thus, at lower speeds the impeller is likely to cause the stage to stall while at higher speeds it is the unvaned diffuser.

Acknowledgments

This investigation was partly carried out under a grant from the Deutsche Forschungsgemeinschaft. The contribution of Mr. Tanneberg when operating the test rig and performing the measurements is gratefully acknowledged.

References

1 Lennemann, E., and Howard, J. H. G., "Unsteady Flow Phenomena in Rotating Centrifugal Impeller Passages," ASME JOURNAL OF ENGINEERING FOR POWER, Vol. 92, Jan. 1970.

2 Mizuki, S., et al., "Reversed Flow Phenomena Within Centrifugal Compressor Channels at Lower Flow Rate," ASME Paper No. 76-GT-86, 1976.

3 Rodgers, C., "A Diffusion Factor Correlation for Centrifugal Impeller Stalling," ASME JOURNAL OF ENGINEERING FOR POWER, Vol. 99, 1977.

4 Senoo, Y., et al., "Experimental Study on Flow in a Supersonic Centrifugal Impeller," ASME JOURNAL OF ENGINEERING FOR POWER, Vol. 101, 1979.

5 Kosuge, H., Ito, T., and Nakanishi, K., "A Consideration Concerning Stall and Surge Limitations within Centrifugal Compressors," ASME JOURNAL OF ENGINEERING FOR POWER, Vol. 104, 1982.

6 Abdelhamid, A. N., and Bertrand, J., "Distinctions between Two Types of Self-Excited Gas Oscillations in Vaneless Radial Diffusers," ASME Paper No. 79-GT-58, 1979.

7 Abdelhamid, A. N., "Effects of Vaneless Diffuser Geometry on Flow Instability in Centrifugal Compression Systems," ASME Paper No. 81-GT-10, 1981.

8 Senoo, Y., and Kinoshita, Y., "Limits of Rotating Stall and Stall in Vaneless Diffuser of Centrifugal Compressors," ASME Paper No. 78-GT-19, 1978.

9 Ligrani, P. M., van der Braembussche, R., and Roustan, M., "Rotating Stall Measurements in the Vaneless Diffuser of a Radial Flow Compressor," ASME Paper No. 82-GT-254, 1982.

10 Frigne, P., and van den Braembussche, R., "Distinction Between Different Types of Impeller and Diffuser Rotating Stall in a Centrifugal Compressor With Vaneless Diffuser," ASME JOURNAL OF ENGINEERING FOR GAS TURBINES AND POWER, Vol. 106, Apr. 1984.

11 Abdelhamid, A. N., "Analysis of Rotating Stall in Vaneless Diffusers of Centrifugal Compressors," ASME Paper No. 80-GT-184, 1980.

12 Kämmer, N., Rautenberg, M., "An Experimental Investigation of Rotating Stall Flow in a Centrifugal Compressor Impeller," ASME Paper No. 82-GT-82, London, 1982.

13 Bammert, K., et al., "Untersuchung der Laufradströmung in hochbelasteten Radialverdichterrädern," *Forschungsberichte Verbrennungskraftmaschinen*, Heft 155, 1974.

14 Kämmer, N., Mobarak, A., and Rautenberg, M., "Performance Measurements of Small Centrifugal Compressors Including Negative Mass Flow Rates," *Fourth International Conference for Mechanical Power Engineering*, Cairo, Egypt, 1982.

B. C. Weinberg

R.-J. Yang*

H. McDonald

S. J. Shamroth

Scientific Research Associates, Inc.,
Glastonbury, CT 06033

Calculations of Two and Three-Dimensional Transonic Cascade Flow Fields Using the Navier-Stokes Equations

The multidimensional, ensemble-averaged, compressible, time-dependent Navier-Stokes equations have been used to study the turbulent flow field in two and three-dimensional turbine cascades. The viscous regions of the flow were resolved and no-slip boundary conditions were utilized on solid surfaces. The calculations were performed in a constructive 'O'-type grid which allows representation of the blade rounded trailing edge. Converged solutions were obtained in relatively few time steps (~ 80-150) and comparisons for both surface pressure and heat transfer showed good agreement with data. The three-dimensional turbine cascade calculation showed many of the expected flow-field features.

Introduction

A current major problem in turbomachinery focuses upon the prediction of turbulent viscous flow in compressor and turbine passages. These may be either basically steady or unsteady and in some instances may contain important three-dimensional effects. A general method for accurately calculating the flow in these passages which would include turbulence viscous effects with minimum approximations would provide a major tool for both the research and the design engineer to improve compressor and turbine performance and durability. This motivation has led to a major effort in developing cascade flow analyses of various degrees of sophistication.

Nearly all of the analyses to date have considered two-dimensional flow. Although two-dimensional flow does represent a simplification, two-dimensional analyses can give significant insight and design information. Futher, the two-dimensional analyses obviously represent a necessary step in developing a three-dimensional analysis. Among the analyses being pursued are inviscid analyses (e.g., [1, 2]), inviscid analyses with boundary layer corrections (e.g., [3]), and Navier-Stokes analyses (e.g., [4, 5]). Each of these approaches is viable under certain circumstances. Inviscid analyses can give good predictions of the blade-pressure distribution for conditions where the effect of viscous phenomena upon the blade-pressure distribution remains small. However, inviscid analyses require some method of assuming airfoil circulation to obtain a unique flow solution. In general, this specification is straightforward for sharp trailing edged blades in steady flow where the Kutta-Joukowski condition serves to specify circulation. However, in cases where the trailing edge is rounded or the flow is unsteady or trailing-edge separation occurs, specification of a proper circulation condition is ambiguous. In addition, since inviscid methods are devoid of viscous effects by definition, they obviously by themselves cannot give either heat-transfer or viscous-loss information.

If an inviscid analysis is combined with a boundary-layer analysis in either a strong interaction or weak interaction mode, some of these limitations may be relieved. In cases where the viscous displacement effect has an insignificant or only small effect on the actual blade pressure distribution, an inviscid calculation can be used to obtain the pressure distribution and a boundary-layer calculation then made to obtain heat transfer and loss effects. However, in many cases, such as when boundary layers thicken significantly or separate (stall), the viscous-displacement effect may alter the pressure distribution. This may be a particular problem in transonic flow where the local pressure distribution and shock location become very sensitive to small changes in the effective passage area. In these cases a strong interaction solution is required to account for the mutual effects of the viscous boundary layer and the nominally inviscid core flow. Although the strong interaction approach does include viscous effects, its generality is still limited.

The final procedure currently available is the solution of the full ensemble-averaged, Navier-Stokes equations. Analyses of this type have been developed for steady flow by Hah [4], and for both steady and time-dependent mean flows by Shamroth, McDonald, and Briley [5]. The use of the full Navier-Stokes equations for the cascade problem allows use of a single set of equations for the entire flow field and thus

---

*Current affiliation Rocketdyne Division, Rockwell International Corp.

Contributed by the Gas Turbine Division of THE AMERICAN SOCIETY OF MECHANICAL ENGINEERS and presented at the 30th International Gas Turbine Conference and Exhibit, Houston, Texas, March 18-21, 1985. Manuscript received at ASME Headquarters, December 21, 1984. Paper No. 85-GT-66.

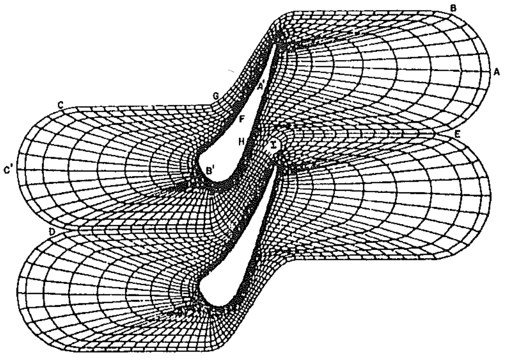

Fig. 1 O-type grid coordinate system for C3X cascade

removes the need for an interaction analysis to couple different equation descriptions for different flow regions. The analysis simultaneously predicts both the blade pressure distribution and, if the appropriate length scales are resolved, viscous and heat-transfer effects.

Hah's analysis [4] is restricted for steady mean flow and uses wall functions to replace the governing fluid mechanics equations in the immediate vicinity of the wall. In the present work, in view of the heat-transfer interest, wall functions are not employed. The analysis is also based upon the use of the unsteady formulation and hence the approach can be applied to problems where either steady or time-dependent phenomena (in a mean sense) are of interest. In the case of steady solutions, matrix preconditioning techniques such as those discussed in [6, 7] are used to obtain converged solutions in a relatively small number of time steps (~ 70). Although when utilized these matrix preconditioning techniques preclude transient accuracy, they represent a very efficient method for obtaining converged solutions of the steady-state equations. If a time-dependent solution is sought, the time-dependent equations can be solved without matrix preconditioning techniques, and transients can then be followed in an accurate manner. To date, most of the Navier–Stokes cascade analyses have concentrated upon the prediction of steady-state flow fields. The predicted flows have included the turbine cascades of Turner [8] and Hylton, Mihelc, Turner, Nealy, and York [9], the compressor cascades of Stephens and Hobbs [10] and Hobbs, Wagner, Dannenhoffer, and Dring [11] and the compressor rotor cascade of Dring, Joslyn, and Harden [12]. Since most experimental data were limited to surface-pressure data, the comparisons were made primarily between calculated and measured surface pressure distributions. Here comparisons are also made between predicted and measured surface heat-transfer rates together with illustrative calculations for a turbine stator. In general, the comparisons are quite favorable and indicate the Navier–Stokes approach to be a viable and practical technique for predicting cascade flow fields which does not contain the possible inadequacies of approximate approaches. Details of the analysis are now given.

Approach

The present approach extends a two-dimensional Navier–Stokes analysis [5] employing the time-dependent linearized block implicit scheme (LBI) of Briley and McDonald [13] to two-dimensional and three-dimensional transonic viscous cascade flows. In general, the geometrical configuration of the turbine blade affects both the grid-construction procedure and the implementation of the numerical algorithm. Since modern turbine blades of interest, e.g., *the Allison C3X turbine cascade shown in Fig. 1*, are characterized by very blunt leading edges, rounded trailing edges and high stagger angles, a robust grid construction procedure is required that can accommodate the severe body shape while resolving regions of large flow gradients. In the previous work reported in [5], cusped trailing edges were considered and a C-type constructive coordinate system used. For the present work a constructive O-type grid generation technique, suitable for cascades with rounded trailing edges, has been developed and used to construct the C3X turbine cascade coordinate grid shown in Fig. 1. The C3X was selected in view of the extensive heat-transfer measurement program being undertaken on this airfoil by Allison as part of the HOST program and reported in [9].

Another aspect of the numerical algorithm addressed here and in [5] is the setting of boundary conditions on the body, upstream and downstream boundaries and the periodic surfaces. Particularly in the transonic regime, where the pressure on the blade is sensitive to the upstream and downstream conditions, proper boundary condition specification is crucial in obtaining accurate predictions. In the present work modification of the coordinate system used in [5] was undertaken and the downstream region reflected in an S-shaped manner to be roughly parallel to the inlet region. This had the effect of moving the downstream boundary further from the cascade and thus reducing the influence of the exit boundary condition on the flow solution. Two-dimensional calculations were performed employing the Navier–Stokes procedure for the C3X turbine cascade, and the predicted pressure coefficients and heat-transfer rates were compared with the experimental data generated under the HOST program by Hylton et al. [9]. In addition, the corresponding three-dimensional rectilinear C3X turbine cascade was considered in which blade–endwall effects are present.

Coordinate System

The coordinate system used in the analysis should satisfy conditions of (*a*) generality, (*b*) smoothness, (*c*) resolvability, and (*d*) allow easy application of boundary conditions. Obviously, a coordinate system must be sufficiently general to allow application to a wide class of problems of interest if it is to be practical. The metric data associated with the coordinate system must be sufficiently smooth so that the variation from grid point to grid point does not lead to a numerical solution dominated by metric coefficient truncation error. It should be noted that this requirement differs from the requirement of the existence of a specified number of transformation derivatives. The coordinate system must resolve flow regions where rapid flow-field changes occur. Finally, the coordinate system should allow accurate implementation of boundary conditions; for the cascade this requirement is equivalent to the requirement that the metric coefficients be continuous across the periodic lines where periodic boundary conditions are to be applied. Unfortunately most of these criteria are qualitative in nature. Coordinate system generation has not yet progressed to the point where quantitative criteria of grid quality can be given.

To date, several types of coordinate systems are available. These include (*a*) solutions based upon a conformal transformation, (*b*) solutions based upon solution of a Poisson equation (e.g., [14]), and constructive systems. The present approach uses a constructive system based originally upon the approach of Eiseman [15]. Shamroth et al. [5] have applied the constructive techniques to generate 'C'-type grids which may require an approximation of the actual trailing edge geometry. The effect of trailing edge approximation will depend upon the type of cascade being considered. In compressor-type cascades, the trailing edge radius is small and the viscous boundary layers are subjected to large adverse pressure gradients. Under these conditions, the blade viscous displacement effects are expected to dominate any trailing edge geometry approximations and consequently the cusped approximation should not have a major influence upon the results for subsonic compressor blades. However, turbine blades can have a large trailing edge radius and their boundary layers are subjected to strong favorable pressure gradients.

In transonic flow the pressure distribution and the shock location are very sensitive to small changes in the blade shape or the effective blade shape due to viscous effects. In these cases the potential for inaccuracies resulting from trailing edge geometry approximations required by the C-grid is high. Therefore, as a first step in the present effort an O-grid capability was developed.

In brief, the coordinate system consists of two families of curves: the $\xi=$constant curves such as lines FG in Fig. 1 and the η = constant curves such as outer loop $ABCDEA$ or inner loop $A'FB'HA'$ in Fig. 1. The coordinate system is constructed by first forming the inner loop $A'FB'HA'$ which includes the blade, then the outer loop $ABCDEA$.

Following the construction and selection of the grid point locations for the inner and outer loops, two intermediate loops are constructed as shown in Fig. 2. The first intermediate loop is constructed around the blade surface with a normal distance, h_1, from the inner loop. A similar loop is constructed inside the outer loop with a normal distance, h_2, from the outer loop. Points on these intermediate loops must then be associated with a loop parameter s, $0 \le s \le 1$, where s is the distance along the curve. This is accomplished as shown in Fig. 2 by setting $s_A{}' = s_A$ and $s_B{}' = s_B$. These four loops allow the construction of the pseudo-radial lines such as GF of Fig. 1 via the multiloop method originally developed by Eiseman [15].

The multiloop method requires introduction of a position vector $\mathbf{P}(r, s)$ with components (x, y) which will represent the coordinate location of grid points. Based upon the four-loop construction process, vectors $\mathbf{P}_i(s)$ are defined with $i=1, 2, 3, 4$. Each P_i has coordinates (x_i, y_i) associated with it as specific values of s through the previously described construction process. A radial parameter, r_i, is then introduced. This parameter is defined as the distance from the loop in question to the inner loop, normalized by the distance from the outer loop to the inner loop, h_3. Thus, $r_1 = 0, r_2 = h_1/h_3,\ r_3 = (h_3-h_2)/h_3,\ r_4 = 1$. With the definition of these quantities, the general position vector $\mathbf{P}(r, s)$ is related to the loop position vectors $\mathbf{P}_1(s)$, $\mathbf{P}_2(s)$, $\mathbf{P}_3(s)$, and $\mathbf{P}_4(s)$ via

$$\mathbf{P}(r,s)=(1-r)^2(1-a_1r)\mathbf{P}_1(s)+(a_1+2)(1-r)^2r\mathbf{P}_2(s) + r^2[1-a_2(1-r)]\mathbf{P}_4(s)+(a_2+2)r^2(1-r)\mathbf{P}_3(s) \tag{1}$$

where

$$\begin{aligned} a_1 &= \frac{2}{3r_2-1} \\ a_2 &= \frac{2}{3(1-r_2)-1} \end{aligned} \tag{2}$$

It should be noted that at $r = 0$, $\mathbf{P}(0, s) = P_1(s)$ and at $r = 1$, $\mathbf{P}(1, s) = \mathbf{P}_4(s)$. Further, since at $r = 0$,

$$\frac{\partial P}{\partial r}(0,s)=[\mathbf{P}_2(s)-\mathbf{P}_1(s)](a_1+2) \tag{3}$$

and at $r = 1$

$$\frac{\partial P}{\partial r}(1,s)=[\mathbf{P}_4(s)-\mathbf{P}_3(s)](a_2+2) \tag{4}$$

Specification of the derivatives at the inner and outer boundaries is determined by the parametric representation of intermediate loops 2 and 3. Thus, the four-loop method allows specification of the boundary-point locations and coordinate angles at these boundaries. The present method of construction assures that the grid is orthogonal at the inner and outer loop boundaries.

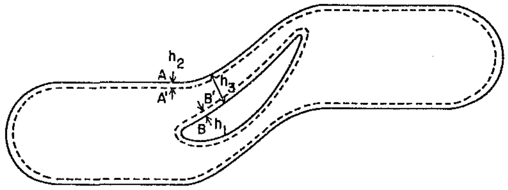

Fig. 2 Constructive coordinate system – four basic loops

After loops 2 and 3 are constructed to satisfy the coordinate angle at the boundary points, the grid is constructed as follows. If the grid is to contain M pseudo-radial lines (such as line FG of Fig. 1) and N pseudo-azimuthal lines (such as line $ABCDEA$), the values of the pseudo-radial coordinate are

$$r(i)=i/(N-1) \quad i=0, 1, 2, \ldots, N-1$$

and the values of pseudo-azimuthal coordinates are

$$s(j)=j/(M-1) \quad j=0, 1, 2, \ldots, M-1$$

Then the position vector, i.e., the grid locations x, y, for each point in the grid is given by equation (1).

The preceding has assumed a uniform spacing in the radial direction. If radial grid-point concentration is desired, it is simply necessary to assume a radial distribution function. The present analysis assumed a distribution function

$$R=\left[1-\frac{\tanh D(1-r)}{\tanh D}\right] \tag{5}$$

which concentrates points in the wall region. Grid points are then chosen at $r(i) = (i)/(N-1)$ and the analysis proceeds as outlined.

Governing Equations

The equations used are the ensemble-averaged, time-dependent Navier–Stokes equations which can be written in vector form as

Continuity

$$\frac{\partial\rho}{\partial t}+\nabla\cdot\rho\mathbf{U}=0 \tag{6}$$

Momentum

$$\frac{\partial\rho\mathbf{U}}{\partial t}+\nabla\cdot(\rho\mathbf{UU})=-\nabla P+\nabla\cdot(\bar{\bar{\pi}}+\pi^T) \tag{7}$$

Energy

$$\frac{\partial\rho h}{\partial t}+\nabla\cdot(\rho\mathbf{U}h)=-\nabla\cdot(\mathbf{Q}+\mathbf{Q}^T)+\frac{DP}{Dt}+\Phi+\rho\epsilon \tag{8}$$

where ρ is density, $\mathbf{U}$ is velocity, P is pressure, $\bar{\bar{\pi}}$ is the molecular stress tensor, π^T is the turbulent stress tensor, h is enthalpy, $\mathbf{Q}$ is the mean heat flux vector, $\mathbf{Q}^T$ is the turbulent heat flux vector, Φ is the mean flow dissipation rate and ϵ is the turbulence energy dissipation rate. If the flow is assumed as having a constant total temperature, the energy equation is replaced by

$$T_t=T+\frac{q^2}{2C_p}=\text{constant} \tag{9}$$

where T_t is the stagnation temperature, q is the magnitude of the velocity, and C_p is the specific heat at constant pressure. In a number of cases considered in this work, the total temperature has been assumed constant. This assumption was made to reduce computer run time when the constant T_t assumption was warranted. Cases in which this substitution has been made are identified in the text describing results. A number of terms appearing in equations (6–8) require definition. The stress tensor appearing in equation (7) is defined as

$$\bar{\bar{\pi}} = 2\mu\mathbf{D} - \left(\frac{2}{3}\mu - K_B\right)\nabla\cdot\mathbf{U}I \tag{10}$$

where K_B is the bulk viscosity coefficient, I is the identity tensor, and $\mathbf{D}$ is the deformation tensor, defined by:

$$\mathbf{D} = \frac{1}{2}\left((\nabla\mathbf{U}) + (\nabla\mathbf{U})^T\right) \tag{11}$$

In addition, the turbulent stress tensor has been modeled using an isotropic eddy viscosity such that:

$$\pi^T = -\rho\overline{\mathbf{u}'\mathbf{u}'} = 2\mu_T\mathbf{D} - \frac{2}{3}(\mu_T\nabla\cdot\mathbf{U} + \rho K)I \tag{12}$$

where k is the turbulent kinetic energy and μ_T, the turbulent viscosity, is determined by a suitable turbulence model. Turbulence modelling is described in the next section.

Equation (8) contains a mean heat flux vector defined as follows:

$$\mathbf{Q} = -\kappa\nabla T \tag{13}$$

and a turbulent heat flux vector defined as:

$$\mathbf{Q}^T = -\kappa^T\nabla T \tag{14}$$

where κ and κ^T are the mean and turbulent thermal conductivities, respectively.

Also appearing in equation (8) is the mean flow dissipation term Φ.

$$\Phi = 2\mu\mathbf{D}:\mathbf{D} - \left(\frac{2}{3}\mu - K_B\right)(\nabla\cdot\mathbf{U})^2 \tag{15}$$

The equation of state for a perfect gas

$$P = \rho RT \tag{16}$$

where R is the gas constant, the caloric equation of state

$$e = C_v T \tag{17}$$

and the definition of static enthalpy

$$h = C_p T \tag{18}$$

supplement the equations of motion.

Finally, the flow properties μ, κ, and K_B are determined using the following constitutive relations.

The variation with temperature of the molecular viscosity μ is determined using Sutherland's law:

$$\frac{\mu}{\mu_0} = \left(\frac{T}{T_0}\right)^{3/2}\frac{T_0 + S_1}{T + S_1} \tag{19}$$

where $S_1 = 100\text{K}$ for air.

The bulk viscosity is assumed to be zero

$$K_B = 0 \tag{20}$$

and the variation with temperature of the thermal conductivity is determined by use of a relation similar to Sutherland's law, viz.,

$$\frac{\kappa}{\kappa_0} = \left(\frac{T}{T_0}\right)^{3/2}\frac{T_0 + S_2}{T + S_2} \tag{21}$$

where $S_2 = 194\text{K}$ for air.

Dependent Variables and Coordinate Transformation

The governing equations, equations (6–8), are written in general vector form and prior to their application to specific problems it is necessary to decide upon both a set of dependent variables and a proper coordinate transformation. Based upon previous investigations (e.g., [5]) the specific scalar momentum equations to be solved are the x, y, and z Cartesian momentum equations. The dependent variables chosen are the physical Cartesian velocities u, v, w and the density ρ. If the energy equation is solved, enthalpy is added to the set of dependent variables.

The equations are then transformed to a general coordinate system in which the general coordinates, y^j, are related to the Cartesian coordinates, x_1, x_2, and x_3, by

$$\begin{aligned} y^j &= y^j(x_1, x_2, x_3, t);\ j = 1, 2, 3 \\ \tau &= t \end{aligned} \tag{22}$$

As implied by equation (22) the general coordinate y^j may be a function of both the Cartesian coordinates and time. This coordinate time dependence will have an implication insofar as the choice of governing equation form is concerned.

The governing equations can be expressed in terms of the new independent variables y^j as

$$\begin{aligned} &\frac{\partial W}{\partial \tau} + \xi_t\frac{\partial W}{\partial \xi} + \xi_x\frac{\partial F}{\partial \xi} + \xi_y\frac{\partial G}{\partial \xi} + \xi_z\frac{\partial H}{\partial \xi} \\ &\quad + \eta_t\frac{\partial W}{\partial \eta} + \eta_x\frac{\partial F}{\partial \eta} + \eta_y\frac{\partial G}{\partial \eta} + \eta_z\frac{\partial H}{\partial \eta} \\ &\quad + \zeta_t\frac{\partial W}{\partial \zeta} + \zeta_x\frac{\partial F}{\partial \zeta} + \zeta_y\frac{\partial G}{\partial \zeta} + \zeta_z\frac{\partial H}{\partial \zeta} \\ &= \frac{1}{\text{Re}}\left[\xi_x\frac{\partial F_1}{\partial \xi} + \eta_x\frac{\partial F_1}{\partial \eta} + \zeta_x\frac{\partial F_1}{\partial \zeta} + \xi_y\frac{\partial G_1}{\partial \xi} + \eta_y\frac{\partial G_1}{\partial \eta}\right. \\ &\quad \left. + \zeta_y\frac{\partial G_1}{\partial \zeta} + \xi_z\frac{\partial H_1}{\partial \xi} + \eta_z\frac{\partial H_1}{\partial \eta} + \zeta_z\frac{\partial H_1}{\partial \zeta}\right] \end{aligned} \tag{23}$$

through a straightforward application of chain rule differentiation. In equation (23)

$$\xi = y^1 \quad \eta = y^2 \quad \zeta = y^3$$

and

$$W = \begin{bmatrix} \rho \\ \rho u \\ \rho v \\ \rho w \end{bmatrix},\quad F = \begin{bmatrix} \rho u \\ \rho u^2 + p \\ \rho uv \\ \rho uw \end{bmatrix},\quad G = \begin{bmatrix} \rho v \\ \rho uv \\ \rho v^2 + p \\ \rho vw \end{bmatrix}, \tag{24}$$

$$H = \begin{bmatrix} \rho w \\ \rho uw \\ \rho vw \\ \rho w^2 + p \end{bmatrix},\quad F_1 = \begin{bmatrix} 0 \\ \tau_{xx} \\ \tau_{xy} \\ \tau_{xz} \end{bmatrix},\quad G_1 = \begin{bmatrix} 0 \\ \tau_{xy} \\ \tau_{yy} \\ \tau_{yz} \end{bmatrix},$$

$$H_1 = \begin{bmatrix} 0 \\ \tau_{xz} \\ \tau_{yz} \\ \tau_{zz} \end{bmatrix}$$

Notice that the metric coefficients $(\xi, \eta)_{x_i}$ appear outside the derivatives. Experience of [5] shows the results obtained via the so-called "semi-strong" conservation form given above are less sensitive to the method used to evaluate the metric coefficients than are results obtained via the so-called "strong" conservation form, since less differentiation of the metric occurs with the semi-strong form. Both forms can return uniform flow in a nonuniform mesh, but to achieve this the strong form requires that a further "conservation" condition on the metric coefficients be satisfied. This additional condition can be automatically satisfied if the metric coefficients are differenced using the same difference operators as the fluids. With a coarse mesh the lack of complete conservation of mass energy or momentum inherent with the semi-strong form of the equations may not be acceptable, but this did not appear to be a factor in the present calculations.

Turbulence Modeling

Several alternative turbulence models have been considered in the course of the present work. The models are described in detail in [22]. The most general model considered, the two-equation model, is described here. Although the zero-equation and one-equation approaches do have the advantage of relative simplicity they still require specification of a length scale. The κ-ϵ, two-equation turbulence model [16] in which both the turbulence kinetic energy κ and the turbulence dissipation rate are governed by transport equations represents a more general model. In this approach, ϵ is given by the following transport equation:

$$\frac{\partial \rho\epsilon}{\partial t}+\nabla\bullet(\rho\mathbf{U}\epsilon)=\nabla\bullet\left(\frac{\mu_T}{\sigma_\epsilon}\nabla\epsilon\right)+C_1(2\mu_T\mathbf{D}{:}\mathbf{D})\frac{\epsilon}{\kappa}+2\mu\mu_T(\nabla^2U)^2-C_2\rho\frac{\epsilon^2}{\kappa} \tag{25}$$

However, attempts to solve equation (25) without modification present problems because an appropriate boundary condition for ϵ at a solid boundary is difficult to prescribe such that equation (25) is satisfied. Following the suggestion of Jones and Launder [16], the turbulence-dissipation equation has been modified by the inclusion of the term:

$$-2\mu\mu_T(\nabla^2U)^2$$

in the energy dissipation equation, equation (25), and by the inclusion of the term:

$$-2\rho\nu(\nabla K^{1/2})^2$$

in the turbulence energy equation which becomes

$$\frac{\partial \rho\kappa}{\partial t}+\nabla\bullet(\rho\mathbf{U}\kappa)=\nabla\bullet\left(\frac{\mu_T}{\sigma_K}\nabla\kappa\right)+2\mu_T(\mathbf{D}{:}\mathbf{D})-\rho\epsilon-2\rho\nu(\nabla\kappa^{1/2})^2 \tag{26}$$

These additional terms allow an $\epsilon=0$ wall-boundary condition to be applied and appear to model the near-wall region in a reasonable manner. Following Jones and Launder [16], the following empirical relations are used:

$$\sigma_\epsilon=1.3\quad \sigma_k=1.0\quad C_1=1.43$$

$$C_\mu=0.09\exp\left[-2.5/(1+R_\tau/50)\right]$$

$$C_2=1.92[1.0-0.3\exp(-R_\tau^2)]$$

and R_τ is defined as:

$$R_\tau=\frac{\rho k^2}{\mu\epsilon}$$

The turbulent eddy viscosity is evaluated by the Prandtl–Kolmogorov relationship

$$-\overline{\rho u_i'u_j'}=\mu_T\frac{\partial U_j}{\partial x_i}\qquad \mu_T=C_\mu\frac{\rho\kappa^2}{\epsilon}$$

Boundary Conditions

The authors' experience in solving Navier–Stokes equations has indicated the important role boundary conditions play in determining accurate solutions and rapid numerical convergence. The boundary conditions used in the present calculations follow the suggestion of Briley and McDonald [13] which specifies upstream total pressure and downstream static pressure conditions. For the two-dimensional cascade system shown in Fig. 2, *BC* and *ED* are periodic boundaries and periodic conditions are set here.

Specification of upstream and downstream conditions is somewhat more difficult. For an isolated cascade, boundary conditions for the differential equations may be known at both upstream infinity and downstream infinity. However, since computation economics argues for placing grid points in the vicinity of the cascade and minimizing the number of grid points far from the cascade, the upstream and downstream computational boundaries should be set as close to the cascade as is practical. In addition, with the particular body-fitted coordinates used, as the upstream boundary moves further upstream, the angle between pseudo-radial and pseudo-azimuthal coordinate lines becomes smaller. Decreasing the coordinate angle causes the coordinate system to become less well conditioned, increases truncation error, and increases the role of cross-derivative terms in the equations. All of these characteristics could be detrimental to the present numerical procedure and, therefore, they also argue for placing the upstream boundary as close to the cascade as possible. However, when the upstream boundary is placed close to the cascade, most flow-function conditions on the boundary will not be known, since these will have been changed from values at infinity by the presence of the cascade.

In the present approach, the suggestion of [13] is followed which sets total pressure on boundary *CC′D* (see Fig. 1). Unless boundary *CC′D* is very far upstream, the flow velocity along this boundary will not be equal to the velocity at upstream infinity since some inviscid deceleration will have occurred. However, as long as the boundary is upstream of the region of any significant viscous or shock phenomena, the total pressure on this boundary will be equal to the total pressure at upstream infinity. Hence, total pressure is an appropriate boundary condition realistically modeling the desired flow condition. In addition to specifying upstream total pressure, it is necessary to specify the inlet flow angle. In the present calculation, a value was assumed constant on the upstream boundary at a specified value. This assumption concerning the inflow angle is a potential source of significant error which should be examined at some point in the future. If found deficient it is possible to conceive of using the inflow angle obtained from a potential flow calculation where the boundary conditions can be enforced at infinity. The third condition set on the upstream boundary concerns the density and a zero-density derivative at this boundary was specified as a numerical treatment of the boundary.

The downstream boundary *EAB* is considered to be far away from blade surface. Notice that a small portion of the boundary may contain inlet flow depending upon the turning of the passage flow. For this inlet-flow portion, the flow variables were set equal to those at the end of the periodic line, e.g., at point *E* in Fig. 1. For outflow portion, the boundary was treated by setting a constant static pressure as a boundary condition, and by extrapolating (first derivatives) both velocity components along exit flow direction at this location. In the present application, a constant static pressure was set at downstream infinity and hence it is assumed that the downstream boundary is located in a region where the static pressure is uniform.

Both the upstream and downstream boundaries have boundary conditions associated with them which are nonlinear functions of the dependent variables. These are the specifications of total pressure on the upstream boundary and static pressure on the downstream boundary. These nonlinear boundary conditions are linearized in the same manner as the governing equations (via a Taylor expansion of the dependent variables in time), and then solved implicitly along with the interior point equations. No-slip conditions (except film-cooling option) together with zero pressure gradient were set at solid walls. If film cooling is applied on the blade surface, a wall velocity is specified via input for that portion of the surface.

For a three-dimensional rectilinear cascade configuration, which consists of a turbine cascade situated in the azimuthal-radial plane and bounded in the transverse direction by an endwall and a symmetry plane, the incoming flow at the upstream boundary is of boundary-layer form due to the endwall and not a uniform stream as in the two-dimensional unbounded cascade. A two-layer velocity profile condition was set at the upstream boundary in place of a uniform velocity profile. The so-called two-layer model used at the inflow boundary is essentially a total pressure boundary condition applied to the core flow with a specified boundary-layer profile shape for the wall region. Matching the static pressure at the edge, defined by the first computational point from the wall at which $|u|/|u|_{max}$ was greater than or equal to 0.99 on the previous time step, enables calculation of $|u|$ at this point. This provides the required normalizing value for the prespecified boundary-layer profile shape. Overall, the method provides a mechanism for drawing mass flow in order to satisfy the downstream pressure, given an upstream core total pressure, while maintaining a given inlet endwall boundary-layer shape. This specification corresponds to the usual wind-tunnel experiment where stagnation conditions are set in an upstream reservoir and static pressure is set at some downstream location. No-slip conditions in conjunction with zero pressure gradient were set on the endwall. Symmetry boundary conditions were applied on the symmetry plane. The other necessary boundary conditions were the same as those for the two-dimensional case.

It should be noted that the present formulation contains several important advantages over alternative formulations. Specification of upstream total pressure and downstream static pressure allows the flow to develop in a natural manner with no need to specify the velocity magnitude on the upstream boundary. Proper specification of velocity magnitude on the upstream boundary may be difficult for two-dimensional cases and is very difficult in transonic cascades and/or three-dimensional cascades. In addition, specification of no-slip condition at solid surfaces eliminates the problem of developing a satisfactory three-dimensional wall function. Although wall functions may be appropriate for relatively simple two-dimensional flow, their use becomes questionable for two-dimensional separated flows. In three-dimensional flows near-wall flows are not well described by such universal laws and consequently their use in these cases does not seem appropriate, particularly if heat transfer or loss information is required. It should be noted that use of the no-slip condition along with proper resolution of the boundary layer does not hinder convergence properties of the present numerical method.

Numerical Procedure

The numerical procedure used to solve the governing equations is a consistently split linearized block implicit (LBI) scheme originally developed by Briley and McDonald [13]. A conceptually similar scheme has been developed for two-dimensional MHD problems by Lindemuth and Killeen [17]. The procedure is discussed in detail in [5, 13]. The method can be briefly outlined as follows: The governing equations are replaced by an implicit time difference approximation, optionally a backward difference or Crank-Nicolson scheme. Terms involving nonlinearities at the implicit time level are linearized by Taylor expansion in time about the solution at the known time level, and spatial difference approximations are introduced. The result is a system of multidimensional coupled (but linear) difference equations for the dependent variables at the unknown or implicit time level. To solve these difference equations, the Douglas-Gunn [18] procedure for generating alternating-direction implicit (ADI) schemes as perturbations of fundamental implicit difference schemes is introduced in its natural extension to systems of partial differential equations. This technique leads to systems of coupled linear difference equations having narrow block-banded matrix structures which can be solved efficiently by standard block-elimination methods.

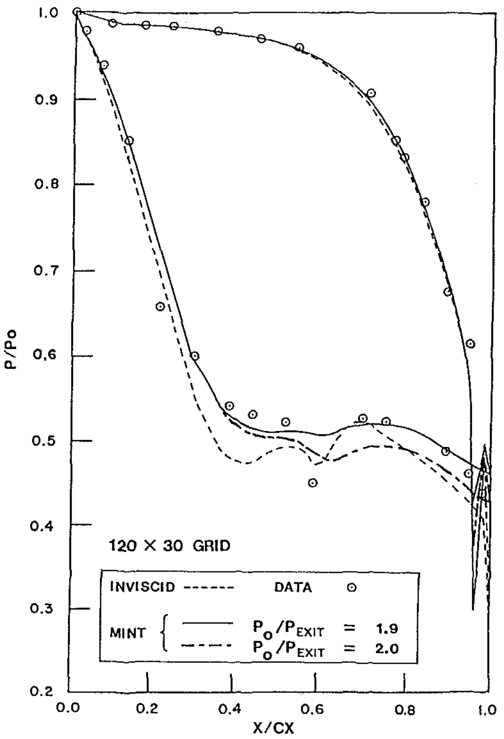

Fig. 3 Comparison between measured and calculated pressure distributions, C3X cascade

The method centers around the use of a formal linearization technique adapted for the integration of initial-value problems. The linearization technique, which requires an implicit solution procedure, permits the solution of coupled nonlinear equations in one space dimension (to the requisite degree of accuracy) by a one-step noniterative scheme. Since no iteration is required to compute the solution for a single time step, and since only moderate effort is required for solution of the implicit difference equations, the method is computationally efficient; this efficiency is retained for multidimensional problems by using what might be termed block ADI techniques. The method is also economical in terms of computer storage, in its present form requiring only two time levels of storage for each dependent variable. Furthermore, the block ADI technique reduces multidimensional problems to sequences of calculations which are one-dimensional in the sense that easily solved block-banded matrices associated with narrow one-dimensional rows of grid points are produced. A more detailed discussion of the solution algorithm is given in [19, 20].

Test Cases and Results

Several test cases were run under the present effort to demonstrate and assess the computer code for the Navier-

Stokes analysis. The first case examined the two-dimensional (2-D) Turner turbine cascade [8]. The second case examined the 2-D low solidity Allison C3X turbine cascade [9]. The final case considered is a three-dimensional (3-D) rectilinear C3X cascade.

In order to assess the impact of the new O-type grid upon the calculated turbine cascade flow fields a series of Navier–Stokes computations was run for the Turner cascade with a rounded trailing edge. These results were compared with earlier results obtained using a C-grid. Results of both calculations agree very well over the entire airfoil and both agree with the data over most of the surface except very near the trailing edge. In view of the excellent agreement between the two calculations, the conclusion to be drawn is that the discrepancy between the measured data and C-grid calculations originally noted in [21] is not due to the approximated trailing edge geometry in the C-grid calculation and no obvious reason for the discrepancy is evident. In the interest of brevity these and related calculations are to be found in [22].

The coordinate system for the C3X turbine cascade is shown in Fig. 1. This O-type grid consists of 30 points in the pseudo-radial direction and 120 points in the pseudo-azimuthal direction. In keeping with the objectives of the construction procedure, the minimum coordinate intersection angle is 20 deg, and the upstream boundary is placed at 2.25 axial chords upstream of the leading edge and the downstream boundary is placed at 2.65 axial chords downstream of the trailing edge. High radial resolution is obtained near the surface of the blade, with the first coordinate line located at a distance of 1.0×10^{-6} axial chords from the surface. In addition, high pseudo-azimuthal resolution is obtained in both leading and trailing-edge regions. The C3X cascade geometry is given in detail in [9]. The geometric inlet angle is approximately 0 deg and the geometric exit angle is approximately 72 deg. The vane spacing to axial chord ratio is approximately 1.5. The true chord to axial chord ratio is approximately 1.85.

The first flow examined corresponds to case 143 in [9] in which inlet Mach number $M_i = 0.17$, exit Mach number $M_{\text{exit}} = 1.05$, inlet Reynolds number based on true chord $Re_i = 0.63 \times 10^6$, and the estimated ratio of inlet total to exit static pressure $P_o/P_{\text{exit}} = 2.0$. It is noted that the "exit" data given in [9], i.e., the "average Mach number" downstream of the trailing edge, is not suitable for specifying boundary conditions at the downstream boundary of the computational domain as required by the Navier–Stokes procedure (2.65 axial chords downstream of the trailing edge). In the present computational domain the flow is subsonic at the rear cap; thus, a static exit pressure can be specified. However, a sensitivity study of the effect of P_o/P_{exit} on surface pressure distribution was undertaken, where P_o is the upstream stagnation pressure, and P_{exit} is the static pressure at the downstream boundary of the computational domain. Two values of P_o/P_{exit} were chosen, 1.9 and 2.0. Constant total temperature was assumed in the present calculation. The computed pressure distribution is shown in Fig. 3, and is compared with the DDA experimental data [9] and the inviscid predictions [2] according to Delaney.

Figure 3 indicates that the pressure distributions on the pressure side of the turbine blade and the forward portion of the suction side are relatively insensitive to P_o/P_{exit}. However, the pressure distribution on the aft portion of the suction side is sensitive to the pressure ratio, in that a 5% change in P_o/P_{exit} results in a commensurate pressure variation on the blade's surface. Such behavior is not totally unexpected since the flow through the cascade is in the transonic regime and, furthermore, indicates a need for definitive specification of boundary conditions if a data comparison is to be made.

Mixing length and two-equation k-ϵ turbulence modeling were employed in the calculation, and very little difference in the prediction of the pressure coefficient resulted. Consequently, these calculations are not shown.

The second flow considered is case 144 in [9]. Here heat-transfer effects are included in the calculation. The flow conditions are inlet Mach number $M_i = 0.16$, inlet total temperature $T_t = 815$K, exit Mach number $M_{\text{exit}} = 0.9$, exit Reynolds number based on true chord $Re_{\text{exit}} = 2.43 \times 10^6$, the estimated $P_o/P_{\text{exit}} = 1.66$, and the free-stream turbulence intensity Tu = 6.5%. The surface-temperature distribution of the turbine blade is given in [9]. The boundary conditions for the energy equation, i.e., equation (8), are specified as follows: (*a*) total temperature is held constant at upstream inlet, (*b*) surface temperature distribution is specified through input, (*c*) conditions on periodic and downstream boundaries are treated similarly to other variables at the same boundaries. The present calculations were compared with the Allison experimental pressure data and inviscid predictions where excellent agreement was obtained. It was expected that the inviscid pressure calculations would show close agreement with the present computed Navier–Stokes results since this is

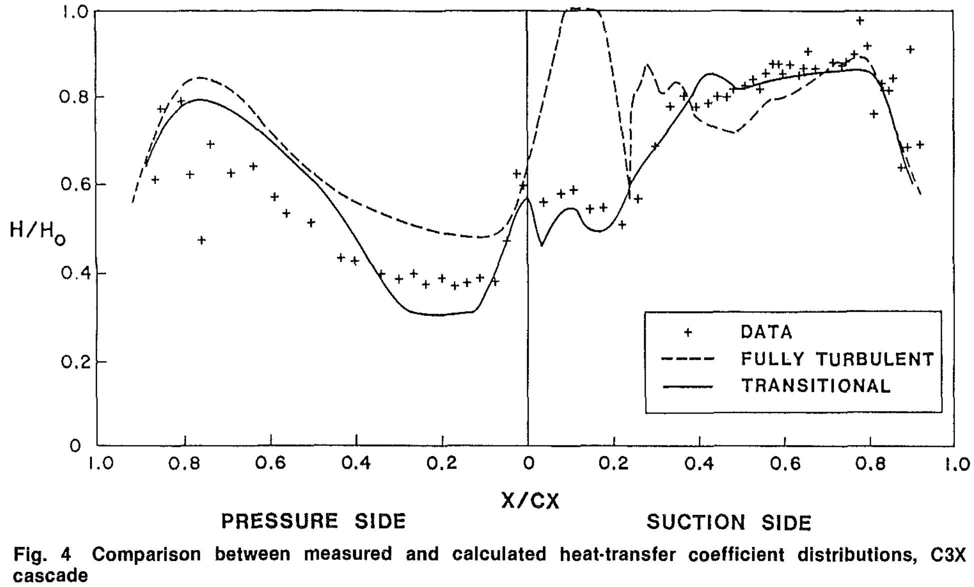

Fig. 4 Comparison between measured and calculated heat-transfer coefficient distributions, C3X cascade

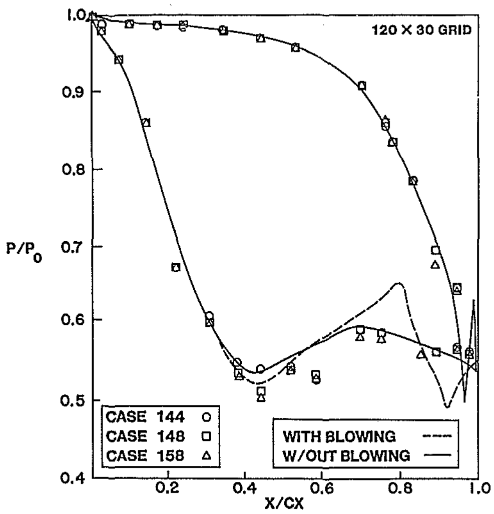

Fig. 5 Effect of film cooling on pressure coefficient distribution

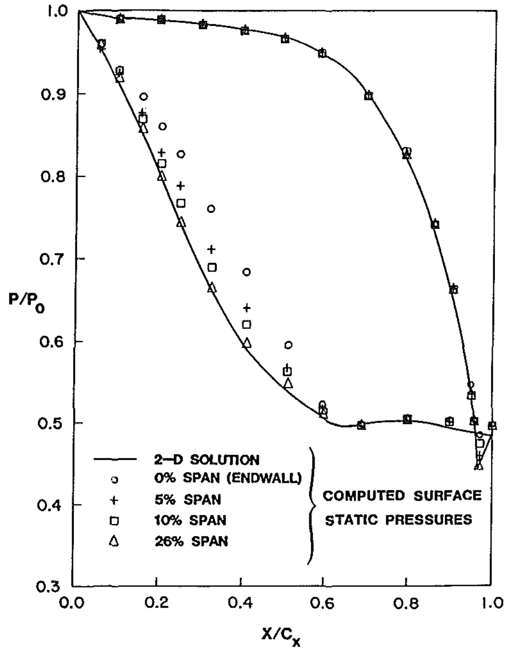

Fig. 6 C3X 3-D rectilinear cascade-pressure coefficient distribution

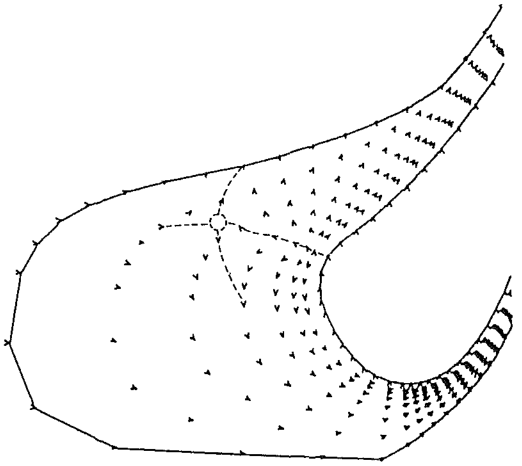

Fig. 7(*a*) Leading edge vector plot on 0.135% spanwise plane

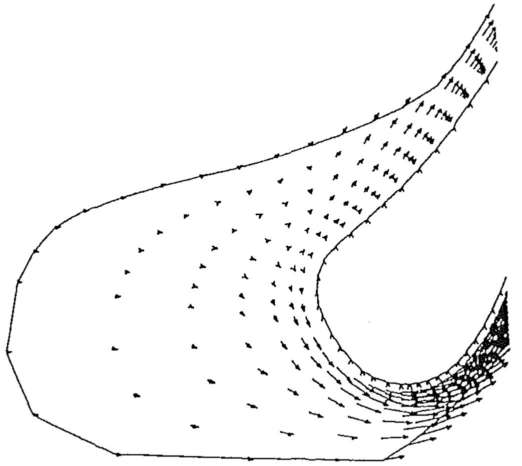

Fig. 7(*b*) Leading edge vector plot on 2.95% spanwise plane

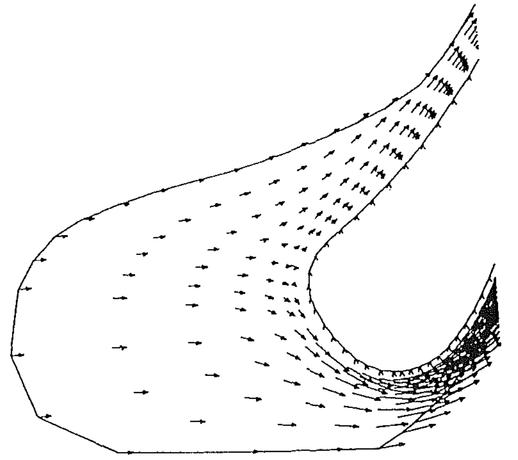

Fig. 7(c) Leading edge vector plot on midspan plane

an on-design case in which viscous displacement effects are expected to be small. Significant discrepancies would be expected at off-design conditions. Three turbulence models were employed; these were a mixing length model, a k-l one-equation model, and a k-ϵ two-equation model. Computed results based upon these three models show very little difference in the pressure distribution. It should be noticed that the flow turning (i.e., the exit angle) is predicted by the analysis rather than being an input item.

The energy equation was coupled with the momentum equations during this calculation. In these calculations, the laminar Prandtl number, Pr, was set to 0.73 and the effective turbulent Prandtl number, Pr_t, was set to 0.9. Addition of the energy equation to the governing set made little difference to the calculated pressure distribution; however, it allows the calculation of the surface heat-transfer coefficient. In this regard, it should be noted that surface heat-transfer prediction on a turbine blade represents a stringent test due to the flow-field character. The turbine passage flow field starts from laminar at upstream and then undergoes transition and becomes fully turbulent. The calculation of the transitional behavior represents a most difficult factor in the prediction for heat-transfer coefficient. Two cases were considered in employing a mixing-length turbulence model: fully turbulent flow and transitional flow in the stagnation region. As can be seen in Fig. 4, the fully turbulent flow case overpredicts the heat-transfer coefficient, particularly in the stagnation zone. Use of a fully turbulent mixing length in the immediate vicinity of the leading edge, particularly on the suction surface with its large favorable pressure gradient, is clearly unrealistic and the predictions should be given little weight in this region. Note that over the rear of the airfoil fully turbulent flow is much more probable and here the predicted heat-transfer levels approach the measured values. In view of this behavior, a transition model was incorporated in order to investigate the effects on heat transfer. Laminar flow was assumed in the region $X/C_x < 0.2$, followed by a transitional zone based upon the correlation of Dhawan and Narasimha [23], and thereafter by fully turbulent flow. The predictions obtained with this simple model compare well with the experimental data, as can be seen from Fig. 4.

The final two-dimensional flow considered is case 144 with the film-cooling option. In this case, air was injected at 30° to the suction side over $0.8 < x/C_x < 0.9$ at a velocity of 7% of free stream and the local surface temperature of the blade was kept fixed at the same value as the nonblowing option. A mixing-length turbulence model in conjunction with the transition model used in the non-film-cooling option for case 144 was employed in the calculation. As expected, the heat-transfer rate drops to nearly zero from the onset of the injection to the trailing edge. However, since no data were available for comparison these heat-transfer predictions are not shown. The observed behavior is a consequence of the buffer region of constant-temperature cool gas which protects the blade surface from the hotter fluid in the cascade passage. The comparison of the pressure distributions for both film-cooling and non-film-cooling options is shown in Fig. 5. The predicted effect of transpiration on the pressure distribution is clearly evident. The adverse pressure gradient that is generated, the resulting upstream influence, and the subsequent favorable pressure gradient that follows it can also be seen in this figure. The effect of cooling on the pressure field is a challenge to predict using non-Navier–Stokes analysis.

The final case considered is a three-dimensional demonstration calculation assuming laminar flow. The configuration consisted of a C3X cascade situated in the azimuthal-radial plane, and bounded in the transverse direction by an endwall and a symmetry plane. The three-dimensionality was introduced by stacking similar planes parallel to each other in the direction normal to a fixed endwall. For the three-dimensional calculation, a grid was constructed consisting of 100 × 25 × 15 grid points in the pseudo-azimuthal, pseudo-radial, and transverse directions, respectively. The height of the blade above the endwall (to the symmetry plane, midspan) was set to be one axial chord, while the inlet boundary-layer thickness was 20% of that value.

The calculation was initiated with an initial condition which consisted of a 2-D solution with a simple boundary-layer correction applied in the vicinity of the endwall. The corresponding 2-D solution was obtained with 100 × 25 grid points, inlet Mach number $M_i = 0.15$, inlet Reynolds number based on inlet freestream conditions and chord $Re_i = 730$, and the ratio of inlet total to downstream exit static pressure $P_o/P_{\text{exit}} = 1.95$. Total temperature was assumed to be constant. With this initial condition, a converged solution was obtained in fewer than 60 time steps.

The computed pressure distributions at different heights above the endwall are shown in Fig. 6. The pressure side is minimally affected by the endwall, remaining at or near the two-dimensional value run on the same spanwise cross-sectional grid, while the suction side, which shows as much as a 15% change over the two-dimensional value near the 30% axial chord location, approaches the two-dimensional value at 26% span above the endwall. Thus, near the endwall the suction side of the blade is more lightly loaded compared to the value of the midspan. These differences from the two-dimensional value are due to the effects of secondary flow generated by horseshoe and passage vortices. The effect of endwall on the pressure distributions is clearly shown. In Fig. 7 the velocity vector plots are presented for the forward portion of the C3X cascade at three different planes above the endwall. Very near the endwall (within 2.95% spanwise plane) a saddle point exists as indicated in the picture. This saddle point moves toward the leading edge and disappears beyond the 2.95% spanwise plane. A stagnation point forms on the nose of the blade surface beyond the 2.95% spanwise plane. These features are consistent with those expected.

Concluding Remarks

The work described in this report has focused upon the application of the time-dependent ensemble-averaged Navier–Stokes equations to transonic turbine cascade flow fields. In particular, efforts have focused upon an assessment of the procedure in conjunction with a suitable turbulence model to calculate steady turbine flow fields using an O-type coordinate system. Three cascade configurations have been considered: These are the two-dimensional turbine cascade of Turner [8], the two-dimensional C3X turbine cascade of Hylton et al. [9], and the three-dimensional C3X rectilinear turbine cascade. The calculations were carried out in nonorthogonal body-fitted coordinate systems, while grid points were orthogonal near body surfaces where viscous flow gradients were suitably resolved. Stagnation pressure inflow–static pressure outflow boundary conditions were employed together with no-slip on the solid surfaces. In general, converged solutions were obtained within 80-150 time steps. For example, it took 80 time steps to reach the steady-state solution for a two-dimensional laminar Turner turbine cascade flow on a 100 × 30 computational grid starting with a uniform velocity (except for a near-wall no-slip correction) and a uniform pressure field. The solution was obtained in approximately 570 CPU secs of unvectorized CRAY-1 system. However, the code used to implement the algorithm is still a research code with a large amount of overhead computation. Recent efforts show the run time can be reduced by 50% with simple code restructuring. In addition code vectorization has been undertaken and initial results have indicated that in conjunction with some other code restructuring, two-dimensional solutions may be obtained in less than one minute of Cray I CPU time.

Comparisons were made between the predicted and measured surface-pressure and heat-transfer distributions wherever available. In general, the pressure predictions were in good agreement with data. The computed heat-transfer results also showed good agreement with data when an empirical transition model was used; however, further work on the development of laminar-turbulent transitional models is indicated. The calculations showed most of the known features associated with turbine cascade flow fields. The flow turning, leading edge stagnation region, boundary-layer development, wake development, film-cooling effects, and three-dimensional boundary-layer separation were all clearly observed. These results indicate the ability of the present Navier–Stokes analysis to predict the surface-pressure distribution, heat-transfer rates, and viscous flow development for practical turbine cascades operating at realistic flow conditions in reasonable amounts of computation time with a suitable turbulence model, and very plausible boundary conditions.

For the particular turbine flows examined there was little effect of the choice of turbulence model upon the predicted pressure distributions, which were by and large in good agreement with both data and inviscid flow predictions. In either a compressor or a small turbine where the effects of the hubs and shroud boundary layers could start to become important these conclusions might change drastically. In any event the potential for simultaneously predicting the heat transfer and loss level around cascades with rounded trailing edges in two and three dimensions has been demonstrated.

Acknowledgments

The work presented in this paper was supported by NASA Lewis Research Center through a subcontract issued by Allison Gas Turbine Operations. The NASA prime contract was NAS3-23695.

References

1 Casper, J. R., Hobbs, D. E., and Davis, R. L., "The Calculation of Two-Dimensional Compressible Potential Flow in Cascades Using Finite Area Techniques," *AIAA Journal*, Vol. 18, No. 1, Jan. 1980.

2 Delaney, R. A., "Time Marching Analysis of Steady Transonic Flow in Turbomachinery Cascades Using the Hopscotch Method," ASME JOURNAL OF ENGINEERING FOR POWER, Vol. 105, No. 2, Apr. 1983, pp. 272–279; Paper No. 82-GT-152, 1982.

3 Hansen, E. C., Serovy, G. K., and Sockol, P. M., "Axial Flow Compressor Turning Angle and Loss by Inviscid-Viscous Interaction Blade-to-Blade Computations," ASME JOURNAL OF ENGINEERING FOR POWER, Vol. 102, 1980.

4 Hah, C., "A Navier-Stokes Analysis of Three-Dimensional Turbulent Flows Inside Turbine Blade Rows at Design and Off Design Conditions," ASME JOURNAL OF ENGINEERING FOR GAS TURBINES AND POWER, Vol. 106, No. 2, Apr. 1984, pp. 421–429; Paper No. 83-GT-40.

5 Shamroth, S. J., McDonald, H., and Briley, W. R., "Prediction of Cascade Flow Fields Using the Averaged Navier-Stokes Equations," ASME JOURNAL OF ENGINEERING FOR GAS TURBINES AND POWER, Vol. 106, No. 2, Apr. 1984, pp. 383–390.

6 Briley, W. R., McDonald, H., and Shamroth, S. J., "A Low Mach Number Euler Formulation and Application to Time Iterative LBI Schemes," *AIAA Journal*, Vol. 21, 1983.

7 Briley, W. R., and McDonald, H., "Computational Fluid Dynamic Aspects of Internal Flow," AIAA Paper No. 79-1455, 1979.

8 Turner, A. B., "Local Heat Transfer Measurements on a Gas Turbine Blade," *Journal of Mechanical Engineering Sciences*, Vol. 13, 1971.

9 Hylton, L. D., Mihelc, M. S., Turner, E. R., Nealy, D. A., and York, R. E., "Analytical and Experimental Evaluation of the Heat Transfer Distribution Over the Surface of Turbine Vanes," NASA-CR-168015, May 1983.

10 Stephens, H. E., and Hobbs, D. E., "Design and Performance of Supercritical Airfoils for Axial Flow Compressors," Pratt and Whitney Aircraft Report FR11455, 1979; Final Report for NASC Contract N00019-77-C-0546.

11 Hobbs, D. E., Wagner, J. H., Dannenhoffer, J. F., and Dring, R. P., "Wake Experiment and Modelling for Fore and Aft-Loaded Compressor Cascade," Pratt and Whitney Aircraft Report FR13514, 1980.

12 Dring, R. P., Joslyn, H. D., and Hardin, L. W., "An Investigation of Axial Compressor Rotor Aerodynamics," ASME JOURNAL OF ENGINEERING FOR POWER, Vol. 104, 1982.

13 Briley, W. R., and McDonald, H., "Solution of the Multidimensional Compressible Navier-Stokes Equations by a Generalized Implicit Method," *Journal of Computational Physics*, Vol. 24, 1977, pp. 372–397.

14 Thompson, J. F., Thames, F. C., and Mastin, C. W., "Boundary Fitted Curvilinear Coordinate Systems for Solution of Partial Differential Equations on Fields Containing Any Number of Arbitrary Two-Dimensional Bodies," NASA CR-2729, July 1977.

15 Eiseman, P. R., "A Coordinate System for a Viscous Transonic Cascade Analysis," *Journal of Computational Physics*, Vol. 26, Mar. 1978, pp. 307–338.

16 Jones, W. P., and Launder, B. E., "The Prediction of Laminarization with a Two-Equation Model of Turbulence," *Int. J. of Heat and Mass Transfer*, Vol. 15, 1972.

17 Lindemuth, I., and Killeen, J., "Alternating Direction Implicit Techniques for Two-Dimensional Magnetohydrodynamic Calculations," *Journal of Computational Physics*, Vol. 13, 1973.

18 Douglas, J., and Gunn, J. E., "A General Formulation of Alternating Direction Methods," *Numerische Math.*, Vol. 6, pp. 428–453, 1964.

19 McDonald, H., Shamroth, S. J., and Briley, W. R., "Transonic Flows with Viscous Effects," *Transonic Shock and Multi-Dimensional Flows: Advances in Scientific Computing*, Academic Press, New York, 1982.

20 McDonald, H., and Briley, W. R., "Some Observations on Numerical Solutions of the Three-Dimensional Navier-Stokes Equations," *Numerical and Physical Aspects of Aerodynamic Flows*, Ed. T. Cebeci, Springer-Verlag, 1982 (CPI).

21 Shamroth, S. J., and McDonald, H., "An Assessment of an Ensemble-Averaged Navier-Stokes Calculation Procedure for Cascade Flow Fields," SRA Report R82-920011-F, 1982.

22 Yang, R.-J., Weinberg, B. C., Shamroth, S. J., and McDonald, H., "Numerical Solutions of the Navier-Stokes Equations for Two- and Three-Dimensional Turbine Cascades with Heat Transfer," Final Report, July 1984, NAS3-23695.

23 Dhawan, S., and Narasimha, R., "Some Properties of Boundary Layer Flow During Transition from Laminar to Turbulent Motion," *J. Fluid Mechanics*, Vol. 3, 1958, pp. 418–436.

O. Schäfer
Research Engineer.

H.-H. Frühauf
Head Turbomachinery Aerodynamics Group.

B. Bauer
Research Assistant.

M. Guggolz
Research Engineer.

Universität Stuttgart,
D-7000 Stuttgart 80

Application of a Navier-Stokes Analysis to Flows Through Plane Cascades

A newly developed method is used to compute a variety of laminar/turbulent, attached/separated flows through plane turbine or compressor cascades. The thin-layer or full Navier-Stokes equations are solved in a 2-D or quasi-2-D/quasi-3-D form taking into account variable axial velocity density ratio/cascade aspect ratio. The turbulence is modeled by the Baldwin-Lomax algebraic two-layer eddy viscosity approach. Improved mesh generation and discretization techniques are introduced. A fully implicit formulation of the flow problem is developed which ensures high stability and convergence. Numerous quantitative comparisons of viscous solutions with experiments and other existing solutions are performed to validate the method. First results on the applicability of the thin-layer assumption are included.

Introduction

The real flow through straight cascades is:

(*a*) turbulent with strong interaction between boundary-layer flow and core flow;
(*b*) often characterized by separation zones; and
(*c*) three-dimensional due to non-parallel sidewalls and significant sidewall boundary layer effects.

Therefore the numerical simulation of this flow requires:

(*a*) a mathematical model which describes all of the physical effects mentioned above;
(*b*) a fast implicit algorithm for solving the basic equations;
(*c*) a computational grid which resolves all important physical features of the flow field; and
(*d*) boundary conditions which are consistent with the mathematical model and which are introduced implicitly in the numerical algorithm.

The current work (see [1]) is mainly concerned with:

(*a*) a new quasi-three-dimensional (Q-3-D) formulation of the basic equations;
(*b*) the fully implicit formulation of all cascade boundary conditions;
(*c*) an accurate discretization of the basic equations; and
(*d*) a validation of the code for subsonic cascade flows.

Other Navier-Stokes cascade solvers based upon implicit ADI schemes are described in [2, 3].

It is demonstrated that the high stability of the applied Beam-Warming ADI algorithm is maintained if all boundary conditions are introduced implicitly. Higher accuracy of the numerical solution, especially near singular points, is obtained by a so-called finite-volume discretization. Numerous computations of viscous flows have been performed to validate the numerical method. The results also show that the Q-3-D equations, which describe the flow through plane cascades with strongly divergent/convergent sidewalls, are sufficiently accurate.

Grids

The cascade computations were restricted to profiles with round leading edges and wedge-type trailing edges. C-grids are best suited for flow fields around such profiles. The main disadvantage of those grids, however, is their artificial boundary which emanates from the trailing edge and leads to the downstream boundary. Overlapping C-type grids were introduced which allow to compute the flow near the branch cut in the wake region and near the periodic boundaries like the flow in interior points. In this way, the accuracy of the solution in the wake region and the convergence rate could be increased significantly. An elliptic generation system similar to that of [4] is used to generate two-dimensional C-type, H-type and combined meshes. A method was designed to precisely control the profile point distribution in arc length increments. The grid aspect ratio and grid cell skewness are controlled at the boundaries. Thus, the grid points can be easily concentrated in the regions of the leading and trailing edges, as well as closer to the blade and its wake. The character of the mesh is determined by the nonhomogeneous terms in the Poisson equations.

Basic Equation

The complexity of real, separated cascade flows requires simplified or full Navier-Stokes equations as a mathematical model. Simplifications based on boundary layer theory are often impossible for several reasons:

(*a*) It is impossible to subdivide the flow field in a viscid

---

Contributed by the Gas Turbine Division of THE AMERICAN SOCIETY OF MECHANICAL ENGINEERS and presented at the 30th International Gas Turbine Conference and Exhibit, Houston, Texas, March 18–21, 1985. Manuscript received at ASME Headquarters, December 21, 1984. Paper No. 85-GT-56.

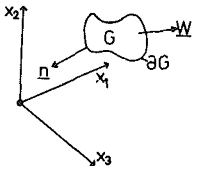

Fig. 1 Notation

boundary-layer flow and in an inviscid core flow; a global approach is necessary;

(*b*) the boundary layer equations are parabolic and therefore cannot describe flows with separation zones.

For high Reynolds number flows, the only simplification possible is to neglect viscous terms in the streamwise direction. This leads to the so-called thin-layer equations [5], which are more closely related to the Navier–Stokes equations than to the boundary-layer equations, and which permit the computation of cascade flows with small separation zones.

The integral form of the basic equation is (see Fig. 1)

$$\int_G \partial_t(\mathbf{q})dV+\int_{\partial G}(\mathbf{q}\ \mathbf{w}^T+\mathbf{K})\mathbf{n}\ dF = \frac{1}{\mathrm{Re}}\int_{\partial G}\mathbf{R}\ \mathbf{n}\ dF \qquad (1)$$

and the differential form is

$$\partial_t(\mathbf{q})+(\mathbf{q}\ \mathbf{w}^T+\mathbf{K})\nabla = \frac{1}{\mathrm{Re}}\mathbf{R}\ \nabla \qquad (2)$$

with

$$\mathbf{q}=\left|\begin{matrix}\rho\\ \rho\ \mathbf{w}\\ e\end{matrix}\right|;\quad \mathbf{K}=\left|\begin{matrix}0\\ p\ \mathbf{I}\\ p\ \mathbf{w}^T\end{matrix}\right|;\quad \mathbf{R}=\left|\begin{matrix}0\\ \tau\\ \mathbf{w}^T\tau-\dfrac{1}{\mathrm{Pr}}\dfrac{1}{\kappa-1}\mathbf{J}^T\end{matrix}\right|$$

$$\tau=\mu[(\mathbf{w}\nabla^{\ T})+(\mathbf{w}\nabla^{\ T})^{\ T}]-\frac{2}{3}\mu\ \nabla^{\ T}\mathbf{w}\mathbf{I};\quad \mathbf{J}=-\lambda\ \nabla\ \theta$$

where μ = molecular viscosity, θ = temperature,
λ = heat conduction coefficient.

The integration over the surface ∂G and the differentiation with the Nabla operator ∇ are performed with the identical matrix $(\mathbf{q}\ \mathbf{w}^T+\mathbf{K})$. The differential form in curvilinear coordinates

$$\partial_t(d\ \mathbf{q})+\sum\partial_{\xi_i}[d(\mathbf{q}\ \mathbf{w}^T+\mathbf{K})\nabla\ \xi_i] = \frac{1}{\mathrm{Re}}\sum[\partial_{\xi_i}(d\ \mathbf{R}\ \nabla\ \xi_i)] \qquad (3)$$

can be derived from equation (2), using the relation

$$\nabla^T\mathbf{x}=\frac{1}{d}\sum_i\partial_{\xi_i}(d\ \mathbf{x}^T\nabla\ \xi_i),\ \mathbf{x}\text{ arbitrary vector}$$

with $\mathbf{T}^T = (x_1,\ldots,x_n)$, $\xi_i = \xi_i\ (x_1,\ldots,x_n)$, $d=\det[\partial_{\xi_i}T]$

The quasi-two-dimensional (Q-2-D) equations are derived for the flow through plane cascades with arbitrary nonparallel symmetrical sidewalls (see Fig. 2). In this Q-2-D flow model (or Q-2-D stream sheet model) the viscous forces are confined to the symmetry plane. The inviscid part of the Q-2-D equations is derived from the 3-D Euler equations, which follow from equation (3), wherein the viscous terms are omitted.

$$\begin{aligned}\partial_t(d\ \mathbf{q})&+\partial_\xi[d(\mathbf{q}\ \mathbf{w}^T+\mathbf{K})\nabla\ \xi]\\ &+\partial_\eta[d(\mathbf{q}\ \mathbf{w}^T+\mathbf{K})\nabla\ \eta]\\ &+\partial_\zeta[d(\mathbf{q}\ \mathbf{w}^T+\mathbf{K})\nabla\ \zeta]=0\end{aligned} \qquad (4)$$

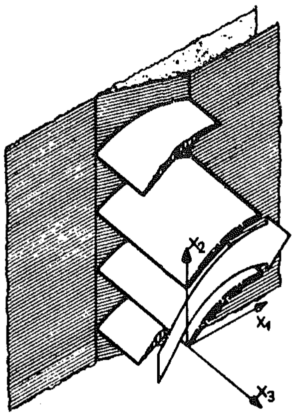

Fig. 2 Plane cascade with nonparallel sidewalls

where $\xi_1 = \xi;\ \xi_2 = \eta;\ \xi_3 = \zeta$.

In the stream sheet model the ζ = constant surfaces are assumed to be known stream surfaces. The symmetry stream surface $\zeta = x_3 = 0$ is assumed to be a plane. ξ and η are curvilinear coordinates in the symmetry plane; ζ is normal to the symmetry plane (see Fig. 2). The following assumptions then hold:

$$\begin{aligned}&\mathbf{w}^T\nabla\ \zeta=0 && \text{in the whole 3-D domain}\\ &\partial_\zeta p=0 && \\ & &&\text{at the symmetry plane}\\ &\mathbf{w}^T=(u,v,0) &&\end{aligned} \qquad (5)$$

With the above model assumptions, the 3-D Euler equation is reduced at the symmetry plane to

$$\begin{aligned}\partial_t(\tilde d\ \mathbf{q})&+\partial_\xi[\tilde d(\mathbf{q}\ \mathbf{w}^T+\mathbf{K})\ \tilde\nabla\ \xi]\\ &+\partial_\eta[\tilde d(\mathbf{q}\ \mathbf{w}^T+\mathbf{K})\ \tilde\nabla\ \eta]\\ &+p\partial_\zeta[\mathbf{E}\ \tilde d\ \tilde\nabla\ \zeta]=0;\end{aligned}\qquad \mathbf{E}=\left|\begin{matrix}0\\ \mathbf{I}\\ 0\end{matrix}\right| \qquad (6)$$

where $\tilde d$, $\tilde\nabla\ \xi$, $\tilde\nabla\ \eta$, $\tilde\nabla\ \zeta$ are 3-D metric terms in the symmetry plane. These terms can be expressed as follows by the 2-D metric terms d, $\nabla\ \xi$, $\nabla\ \eta$ in the symmetry plane (see [1])

$$\tilde d=|T_\zeta|d;\quad \tilde\nabla\ \xi=\nabla\ \xi;\quad \tilde\nabla\ \eta=\nabla\ \eta \qquad (7)$$

The only difference between the 2-D and 3-D metric terms is the differential stream-sheet thickness $|T_\zeta|$. The term $\partial_\zeta(\tilde d\ \tilde\nabla\ \zeta)$ in equation (6) can be expressed as (see [1]):

$$\partial_\zeta(\tilde d\ \tilde\nabla\ \zeta)=-[\partial_\xi(\tilde d\ \tilde\nabla\ \xi)+\partial_\eta(\tilde d\ \tilde\nabla\ \eta)] \qquad (8)$$

Inserting equations (7) and (8) in equation (6), and approximating the differential stream-sheet thickness by the finite thickness of the flow channel, the Q-2-D equations

$$\begin{aligned}\partial_t(\tilde d\ \mathbf{q})&+\partial_\xi[\tilde d(\mathbf{q}\ \mathbf{w}^T+\mathbf{K})\ \tilde\nabla\ \xi]-\frac{1}{\mathrm{Re}}\{\partial_\xi[\tilde d\ \mathbf{R}\ \tilde\nabla\ \xi]\}\\ &+\partial_\eta[\tilde d(\mathbf{q}\ \mathbf{w}^T+\mathbf{K})\ \tilde\nabla\ \eta]-\frac{1}{\mathrm{Re}}\{\partial_\eta[\tilde d\ \mathbf{R}\ \tilde\nabla\ \eta]\}\\ &-p\{\partial_\xi[\tilde d\ \mathbf{E}\ \tilde\nabla\ \xi]+\partial_\eta[\tilde d\ \mathbf{E}\ \tilde\nabla\ \eta]\}=0\end{aligned} \qquad (9)$$

are obtained (the viscous terms in the symmetry plane have been added again). If this Q-2-D equation is compared with the well-known 2-D equation, the only two differences existing are: *i*) the modified transformation Jacobian $\tilde d = |T_\xi|\ d$ and *ii*) the pressure term, as follows:

$$-p\{\partial_\xi[\tilde d\ \mathbf{E}\ \tilde\nabla\ \xi]+\partial_\eta[\tilde d\ \mathbf{E}\ \tilde\nabla\ \eta]\}.$$

This pressure term represents the sidewall force in the symmetry plane. The stream-sheet thickness enters into all conservation equations. Note that these terms have been obtained formally by reducing the 3-D equations to the Q-2-D equations. As already mentioned, in the Q-2-D model the

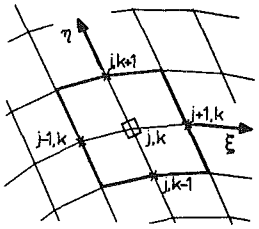

Fig. 3 Central spatial discretization for an interior point

midspan differential stream-sheet thickness is approximated by the finite height of the flow channel. If the finite-flow channel height changes rapidly in the streamwise direction, this approximation is too inaccurate. In this case, the midspan differential stream-sheet thickness can be computed more accurately by solving the 2-D Euler equations (2-D flow model) in the blade-free flow channel and by applying the mass conservation equation at the symmetry line

$$|T_\xi| = \frac{(\rho u)_1}{\rho u}, \qquad \text{subscript } 1 = \text{inflow boundary}.$$

The combined 2-D/Q-2-D model is the so-called quasi-three-dimensional (Q-3-D) model which allows quite accurate computation of flows through straight cascades with strongly converging/diverging sidewalls.

Numerical Algorithm

The Q-2-D equations (9) are solved with a modified Beam–Warming scheme. The modification of the Beam–Warming scheme is performed with the aim of implementing a correct computation of the fluxes at singular mesh points. This will be achieved by a combined finite-difference/finite-volume discretization. With the exception of the singular mesh points, all cascade boundary conditions will be introduced implicitly in the viscous equations to enhance the stability of the solution method.

Equivalent Finite-Difference/Finite-Volume Discretization. Using the 2-D Euler equations as an example, it will be shown that the central spatial finite-difference discretization, which is originally used in the Beam-Warming scheme, is equivalent to a distinct discretization in equation (1). This equivalence will be used in designing the modified finite-difference/finite-volume scheme. The 2-D differential Euler equations

$$\partial_t(d\,\mathbf{q}) + \partial_\xi[(\mathbf{q}\,\mathbf{w}^T + \mathbf{K})\nabla\,\xi] + \partial_\eta[(\mathbf{q}\,\mathbf{w}^T + \mathbf{K})\nabla\,\eta] = 0 \tag{10}$$

are obtained from equation (3) with $\xi_1 = \xi$; $\xi_2 = \eta$ and zero right-hand side. Introducing the relations

$$d\,\nabla\,\xi = \alpha\,\mathbf{T}_\eta;$$
$$\mathbf{d}\,\nabla\,\eta = -\alpha\,\mathbf{T}_\xi; \quad \alpha = \begin{vmatrix} 0 & 1 \\ -1 & 0 \end{vmatrix}; \quad \mathbf{T}^T = (x_1, x_2)$$

and discretizing the spatial derivatives centrally for the point (j, k), equation (10) becomes (see Fig. 3)

$$\begin{aligned}(d\partial_t\mathbf{q})_{j,k} &+ \\ [(\mathbf{q}\,\mathbf{w}^T+\mathbf{K})\quad \alpha\,\mathbf{T}_\eta]_{j+1,k} &- [(\mathbf{q}\,\mathbf{w}^T+\mathbf{K})\quad \alpha\,\mathbf{T}_\eta]_{j-1,k} \\ + [(\mathbf{q}\,\mathbf{w}^T+\mathbf{K})(-\alpha)\mathbf{T}_\xi]_{j,k+1} &- [(\mathbf{q}\,\mathbf{w}^T+\mathbf{K})(-\alpha)\mathbf{T}_\xi]_{j,k-1} \\ = 0.\end{aligned} \tag{11}$$

Since d approximates the volume of the flux cell, $(d\partial_t\mathbf{q})_{j,k}$ is a spatial approximation of ${}_G\int\partial_t\;\mathbf{q}\,dV$ in the integral equation (1). $\alpha\,\mathbf{T}_\eta$, $-\alpha\mathbf{T}_\xi$ are vectors normal to, and of the same length as, the flux-cell surface, and therefore approximate $\mathbf{n}\,dF$ in equation (1).

The scalar products $[(\mathbf{q}^T\mathbf{w} + \mathbf{K})\ldots]$ are evaluated at the four sides of the flux cell and summed. This sum therefore approximates the surface integral

$$\int_{\partial G} (\mathbf{q}\,\mathbf{w}^T + \mathbf{K})\mathbf{n}\,dF \qquad \text{in equation (1).}$$

Thus the same discretization, equation (11), is obtained for the spatially discretized differential and integral equations at regular mesh points.

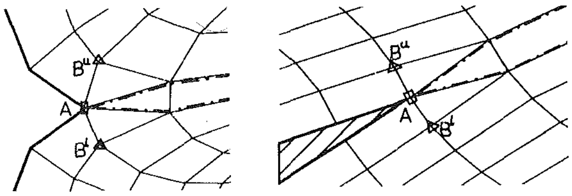

Fig. 4 Singular points of overlapping C-type meshes

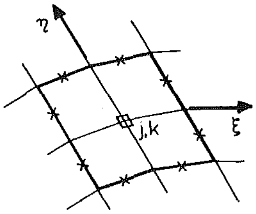

Fig. 5 Modified finite-volume discretization for interior points

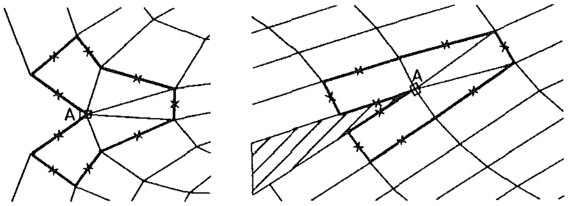

Fig. 6 Special singular point flux boxes

Modified Finite-Volume Discretization. In the case of overlapping C-type cascade meshes, singular mesh points exist at a wedge-type trailing edge and at the conjunction of two neighboring inflow boundaries (see Fig. 4). Here, singular mesh points are defined as points which separate different boundaries from one another. At a singular mesh point (point A), and at neighboring points (point B^u, B^l), the above spatial discretization leads to inaccuracies.

For the flux cells with the centers B^u and B^l, the above discretization is not correct on surfaces where the boundary type changes, since it does not distinguish between different boundary types. Therefore a new spatial discretization is introduced, which separates one boundary type from the other. In this discretization, the surface integral in equation (1) is approximated by a sum of eight (instead of four) scalar products (see Fig. 5).

Using this modified finite-volume discretization, the fluxes can be computed correctly for the cells B^u and B^l. A special closed flux cell (see Fig. 6) is used for correct computation of the single-valued flow quantities at the singular point A by means of the modified spatial finite-volume discretization and an explicit time discretization.

Applying this technique, accurate trailing-edge solutions can be obtained. This can be seen in Figs. 12 and 13 for inviscid flows past cusp and wedge-type trailing edges. Computing viscous flows with trailing edge separations, the shape of the separation zones at the trailing edges can be predicted more accurately.

Modified Beam–Warming Scheme. The Beam–Warming scheme [4] (implicit linear one-time step differencing method in a factored delta form):

$$
\begin{aligned}
&\xi\text{-sweep}:[\mathbf{I}+\Delta t\delta_\xi(\mathbf{A}+\mathbf{L})]\Delta(\tilde{d}\,\mathbf{q})^* &&= \mathbf{R\,H\,S}\\
&\eta\text{-sweep}:[\mathbf{I}+\Delta t\delta_\eta(\mathbf{B}+\mathbf{M})]\Delta(\tilde{d}\,\mathbf{q}) &&= \Delta(\tilde{d}\,\mathbf{q})^*\\
&\qquad\qquad\qquad\qquad\qquad\qquad \tilde{d}\,\mathbf{q}^{n+1} &&= \tilde{d}\,\mathbf{q}^n+\Delta(\tilde{d}\,\mathbf{q})
\end{aligned}
$$

$$
\begin{aligned}
\mathbf{R\,H\,S}=-\Delta t\{&\hat{\delta}_\xi[\tilde{d}(\mathbf{q}\,\mathbf{w}^T+\mathbf{K})\,\tilde{\nabla}_\xi]-\frac{1}{\mathrm{Re}}\hat{\delta}_\xi[\tilde{d}\,\mathbf{R}\,\tilde{\nabla}\,\xi]\\
&+\hat{\delta}_\eta[\tilde{d}(\mathbf{q}\,\mathbf{w}^T+\mathbf{K})\,\tilde{\nabla}_\eta]-\frac{1}{\mathrm{Re}}\hat{\delta}_\eta[\tilde{d}\,\mathbf{R}\,\tilde{\nabla}\,\eta] \qquad (12)\\
&-p\,[\hat{\delta}_\xi(\tilde{d}\,\mathbf{E}\,\tilde{\nabla}\xi)+\hat{\delta}_\eta(\tilde{d}\,\mathbf{E}\,\tilde{\nabla}\eta)]\}+\mathbf{AV}
\end{aligned}
$$

$$\mathbf{AV}=-\beta\tilde{d}\,\Delta t(\delta_{\xi\xi\xi\xi}+\delta_{\eta\eta\eta\eta})\mathbf{q}$$

$$\mathbf{A}\ =\partial_{\tilde{d}\ \mathbf{q}}[\tilde{d}(\mathbf{q}\,\mathbf{w}^T+\mathbf{K})\,\tilde{\nabla}\ \xi]\quad \mathbf{L}=\partial_{\tilde{d}}\ \mathbf{q}[\tilde{d}\,\mathbf{R}\ \tilde{\nabla}\ \xi]$$

$$\mathbf{B}\ =\partial_{\tilde{d}\ \mathbf{q}}[\tilde{d}(\mathbf{q}\,\mathbf{w}^T+\mathbf{K})\tilde{\nabla}\ \eta]\quad \mathbf{M}=\partial_{\tilde{d}\ \mathbf{q}}[\tilde{d}\,\mathbf{R}\ \tilde{\nabla}\ \eta]$$

$\hat{}$ = FV discretization in the whole flowfield

is used to integrate the quasi-two-dimensional equation (9). The ADI algorithm used ensures that the converged steady-state solution is independent of the time step. Also, for converged steady-state calculations, only the right-hand side differencing determines the solution. Thus different spatial discretizations can be used on the left and right-hand sides of the Beam-Warming scheme, equation (12). Integrating the Q-2-D equations, the modified spatial finite-volume discretization is used on the right-hand side, while the original spatial finite-difference discretization (which allows the factorization) is retained on the left-hand side. The artificial viscosity **AV** is introduced as in [7]. The thin-layer equations (**L** = 0) and the full Navier-Stokes equations (**L** ≠ 0) can be solved in the quasi-two-dimensional form. The complete, steady, viscous Q-2-D equations are implemented on the right-hand side only [see equation (12)].

Boundary Conditions

The cascade flow boundary conditions are derived from physical considerations and are consistent with the mathematical model. The boundary conditions are the inflow/outflow boundary conditions, the rigid-wall boundary condition and the periodicity condition. These must be introduced implicitly to maintain the high stability of the ADI code, as will be seen in the section "Accuracy/Convergence." Here the boundary conditions and the so-called numerical boundary conditions have to be linearized temporally.

Inflow/Outflow Boundary Conditions. At the in- and outflow boundaries flow angle, stagnation values, and static pressure are prescribed, respectively. Numerical boundary conditions for the in- and outflow boundaries are the continuity equation, and the continuity and momentum equations, respectively. The linearization of the boundary conditions leads to the form

$$\mathbf{C}\,\Delta\,\mathbf{q}=\mathbf{R\,H\,S}_{BC}$$

with

$$
\mathbf{C}=\left|\begin{array}{c|c|c}
\multicolumn{3}{c}{\text{continuity equation}}\\
\hline
\dfrac{1}{\kappa-1}\rho^{\kappa-1}-\dfrac{1}{2}\mathbf{w}^T\mathbf{w} & \mathbf{w}^T & -1\\
\hline
0 & \mathbf{T}^T & 0\\
\hline
\dfrac{1}{(\kappa-1)^2}-\dfrac{1}{2}\mathbf{w}^T\mathbf{w} & \mathbf{w}^T & -\dfrac{\kappa}{\kappa-1}
\end{array}\right|
$$

with $\mathbf{T}^T$ = (tan α, -1), α = flow angle at the inflow boundary and

$$
\mathbf{C}=\left|\begin{array}{c|c|c}
\multicolumn{3}{c}{\text{continuity equation}}\\
\hline
\multicolumn{3}{c}{\xi\text{-momentum}\quad\text{equation}}\\
\hline
\multicolumn{3}{c}{\eta\text{-momentum}\quad\text{equation}}\\
\hline
-\dfrac{1}{2}\mathbf{w}^T\mathbf{w} & \mathbf{w}^T & -1
\end{array}\right|
$$

at the outflow boundary.

Rigid Wall Boundary Condition. The boundary conditions at the solid wall are:

Euler equations:
physical boundary condition
tangency condition: $\mathbf{w}^T\nabla\ \eta=0$
numerical boundary conditions
extrapolation of ρ
extrapolation of $\mathbf{w}^T\nabla\ \xi$
solution of the normal momentum equation

Navier-Stokes equations:
physical boundary conditions
no slip condition: $\mathbf{w}=0$
adiabatic wall condition: $\partial_\eta\theta=0$
numerical boundary condition:
$\partial_\eta p=0$ deduced from boundary layer theory.

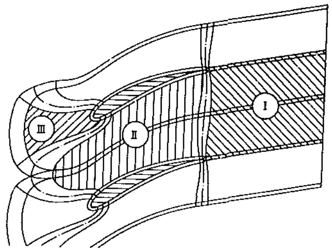

Fig. 7 Implicit implementation of the periodicity condition

Periodicity Condition. Special modifications of the ADI scheme are necessary for an implicit implementation of the periodicity condition on C-grids (see Fig. 7).

The ξ and η-sweeps are performed over different domains. *i*) The ξ-sweep over the upper C-type domain. After this sweep $\Delta(\tilde{d}\,\mathbf{q})^*$ is known at all interior points of this domain. Then $\Delta(\tilde{d}\,\mathbf{q})^*$ is restored to the domains I, II. *ii*) The η-sweep over

domain I:	coupling two periodic boundaries
domain II:	coupling two rigid wall boundaries
domain III:	coupling the upstream boundary with the rigid wall boundary.

Accuracy/Convergence

A high convergence rate is very important for an economical computation, especially of high Reynolds number cascade flows. An increase in the convergence rate was achieved on single grids with constant time-stepping, primarily using a fully implicit formulation of the cascade code which includes an implicit formulation of all boundary conditions. For steady-state calculations, only the right-hand side differencing determines the solution [see equation (12)]. Converged solutions satisfy the finite-volume approximation of the steady governing equations. The numerical approximation includes second-order-accurate central discretization of the fluxes and fourth-order artificial dissipation terms which influence stability and convergence. The residual (right-hand side) is selected as one convergence

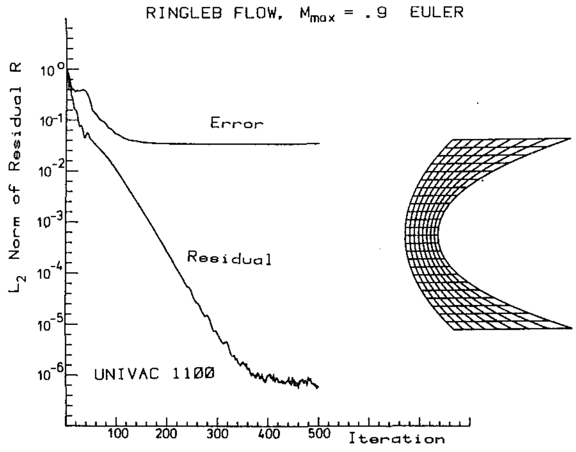

Fig. 8 RINGLEB/convergence

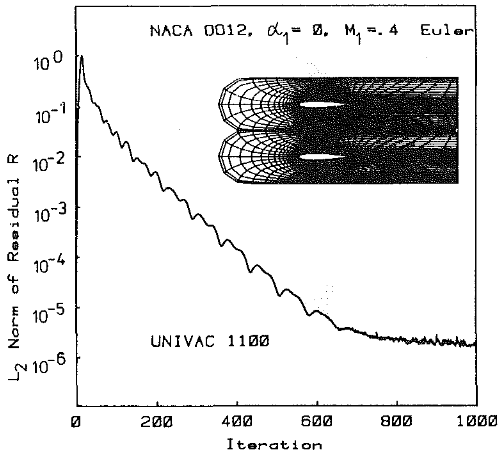

Fig. 9 NACA 0012/convergence

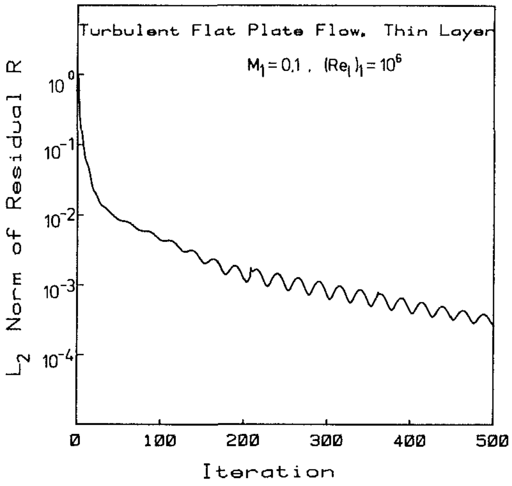

Fig. 10 Flat plate/convergence

criterion. Other criteria used were pressure coefficient, skin friction coefficient, and velocity profile convergence. The maximum possible constant time-step size is used as a mesh-independent measure for the stability of the fully implicit method. The implicit implementation of all boundary conditions generally leads to a nearly mesh-independent time-step size, which is typically 3 to 100 times greater than that in the case of explicit boundary conditions (in the latter case the maximum possible time-step size is clearly mesh-dependent). In the fully implicit formulations, the dimensionless time-step size, close to 0.1 (reference quantities: chord, upstream local speed of sound) proved to be nearly mesh-independent and roughly "problem-independent": i.e., turbulent flows inviscid up to high Reynolds numbers could be computed with the above (nearly optimal) time-step size. The residual convergence rate, however, proved to be mesh-dependent (and hence CFL number dependent). This dependency of the residual convergence rate seems to be partly caused by the factorization error of the ADI scheme. A decrease of the residual by one order of magnitude typically affords 60 to 100/100 to 600 iterations for subsonic inviscid/high Reynolds number turbulent cascade flows. In all cascade solutions the residual converged to the machine accuracy (about 1×10^{-6}), except in high Reynolds number flow cases, where the computation was stopped when the residual converged to about 1×10^{-4}. The convergence rate is not essentially affected by computing flows at high incidence or flows through highly staggered and deflecting cascades. The convergence properties are demonstrated in the following, for three selected flow problems.

The subsonic RINGLEB flow is computed with a fully implicit quasi-linear Euler code [8] using the Beam-Warming ADI scheme and characteristic concepts in the boundary condition implementation. A (rather coarse) 9 × 25 H-type mesh is used to compute the subsonic flow with a maximum Mach number of 0.9. A smooth 60% pressure disturbance initial condition distribution was selected. The residual convergence is shown in Fig. 8. The residual convergence rate is about 1.66×10^{-2}. Maximum contour pressure error convergence is achieved after 160 iterations.

A subsonic flow was computed through a cascade with unstaggered NACA 0012 profiles and with the solidity 1 (inflow Mach number 0.4, inflow angle 0 deg). An overlapping 51 × 21 C-type mesh is used. The conservative Euler code is used with an explicit solid boundary condition implementation. All other boundary conditions are introduced implicitly. An undisturbed inflow initial distribution was chosen. The residual convergence is shown in Fig. 9 (time step 0.15). Profile pressure coefficient convergence is achieved after 200 iterations.

A turbulent zero pressure gradient, flat plate flow (Reynolds number 10^6, Mach number 0.1) was computed with the fully implicit thin-layer code prescribing density and velocity vector/pressure at the in/outflow boundaries. No artificial viscosity was used in the computations. A 37 × 81 Cartesian H-type mesh is used, which is adapted to the boundary-layer edge at midchord. The streamwise mesh spacing is 0.025 l and the smallest transverse spacing is 0.000035 l. The laminar sublayer/turbulent layer contains 3/26 points. A constant 1/7 power law distribution was selected as initial velocity distribution. With the constant time step 0.075, a residual convergence rate of 2.25×10^{-3} was obtained (see Fig. 10) and velocity profile and local wall skin friction coefficient convergence were achieved after 250 iterations.

Cascade Results

Numerous cascade-flow computations are performed to demonstrate the accuracy of the method and its capability to compute complex cascade flows. In turbulent flow cases, only "small" separation zones are computed with regard to the limitations of the algebraic turbulence model used.

Gostelow Cascade. The low Mach number flow through the Gostelow cascade [9] is computed using the 2-D Euler method and compared with the incompressible flow, as computed by Gostelow using an inverse conformal mapping method. The flow was calculated for an inflow angle of 53.5 deg and an isentropic downstream Mach number of 0.2. The point distribution on the profile was selected close to that of Gostelow, with 90 points on the profile. A periodic

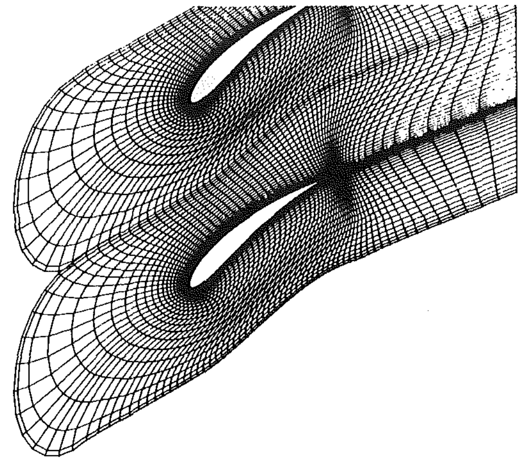

Fig. 11 Gostelow 127 × 25 C-mesh

overlapping 127 × 25 C-type mesh was used in the computation shown in Fig. 11.

In Fig. 12 the compressible computed pressure coefficient is compared with the pressure coefficient of the incompressible Gostelow flow. The agreement is good, the small difference being due to compressibility effects. The compressible, computed exit flow angle of 30.10 deg is very close to the incompressible angle of 30.025 deg. The computed pressure coefficient at the stagnation point is 1.001, while the exact value is 1.023. The entropy errors are smaller than -0.003 on the pressure and suction side, except near the leading edge, where values of -0.001 and -0.006 were computed at the stagnation point and at the point of minimal pressure coefficient. The computed flow angle at the trailing edge is very close to the geometrical trailing-edge angle.

VKI-1 Cascade. The subsonic flow through the highly deflecting VKI-1 cascade is computed with the 2-D Euler method and compared with the measurements of Lehthaus [10]. The flow was calculated for an inflow angle of 30 deg and an isentropic downstream Mach number of 0.6. A wedge-type trailing edge was used instead of the originally blunt one (see Fig. 13). A periodic overlapping 127 × 25 C-type mesh was selected for the computation. In Fig. 13 the computed and the measured critical pressure coefficients are compared. The Euler solution agrees favorably with the high Reynolds number experiment. Due to the correct treatment of the singular trailing-edge point, the typical Euler wedge-type trailing-edge pressure distribution is obtained.

Turbulent Attached Cascade Flow. The attached turbulent flow through a plane turbine cascade is computed in the thin-layer approximation and with the full Navier-Stokes equations. The results are compared to cascade measurements which were performed by Scholz in the low Mach number regime [11]. Nearly two-dimensional flow conditions were attempted by means of side wall suction. The viscous flow solution for a NACA 8410 cascade blade was obtained for an inflow angle of -15 deg, a Reynolds number based upon the chord and the downstream velocity of 6 × 10^5, a stagger angle of -30 deg, and a solidity of 1.33. The experimental downstream Mach number was 0.12. A periodic overlapping 133 × 37 C-mesh was used in the computations with 3 points in the laminar sublayer and 17 points in the outer layer. The first point off the surface was placed 0.000064 chords from the surface. The distance between grid points along the blade surface in the vicinity of the stagnation point has the value of 0.005 chords. In addition, the grid was extended four chords downstream of the airfoil trailing edge. Figure 14 shows the 2-D Euler, the 2-D thin-layer, and the full Navier-Stokes pressure coefficients together with the experimental pressure coefficient.

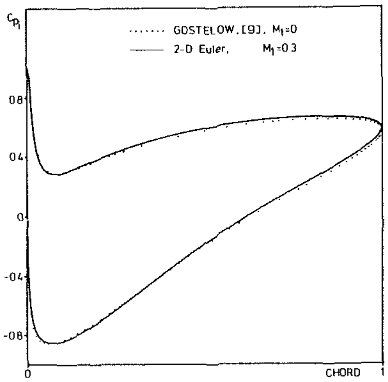

Fig. 12 Gostelow/pressure coefficient

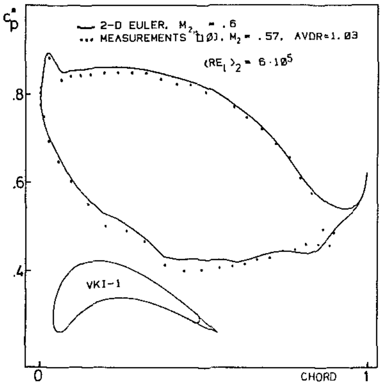

Fig. 13 VKI-1 pressure coefficient

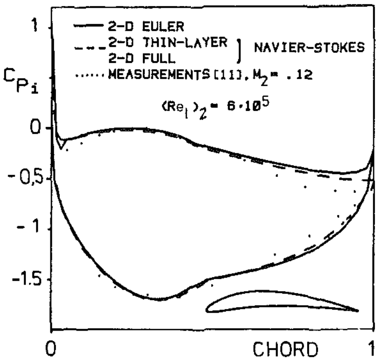

Fig. 14 NACA 8410 pressure coefficient

No compressibility correction was applied to the nearly incompressible experimental pressure coefficient. The differences in the inviscid and viscous surface pressure distributions are consistent with the inclusion of the boundary-layer development in the viscous solution. In Fig. 15 the eddy viscosity contours (normalized by the molecular viscosity coefficient) are plotted in the trailing edge region (full Navier-Stokes solution).

The suction side trailing edge flow is close to separation, leading to the observable boundary-layer thickness increase at the trailing edge. The thin-layer and full Navier-Stokes equations have been computed on the same mesh. The streamwise profile mesh spacing at midchord and at the trailing edge is about the size of the trailing edge boundary-layer thickness. The streamwise resolution may be too coarse to resolve the streamwise diffusion terms in the full Navier-Stokes equation. Nevertheless, the thin-layer and the full Navier-Stokes pressure coefficients closely agree, as expected, for the turbulent attached flow. The Navier-Stokes pressure coefficient is slightly smaller than the thin-layer

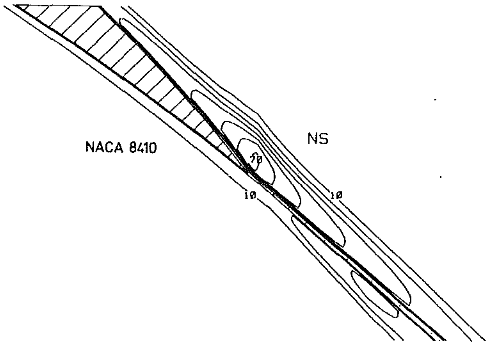

Fig. 15 NACA 8410 eddy viscosity contours

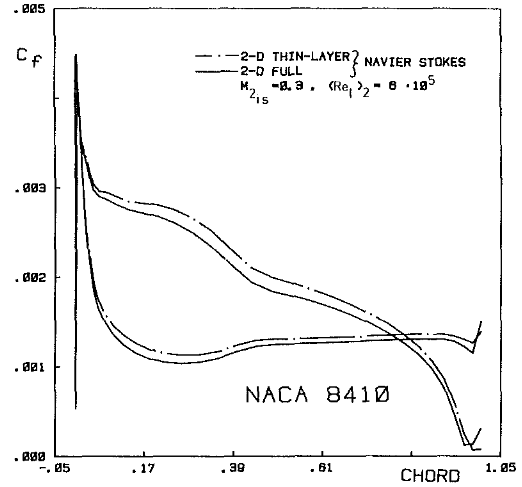

Fig. 16 NACA 8410 skin friction coefficient

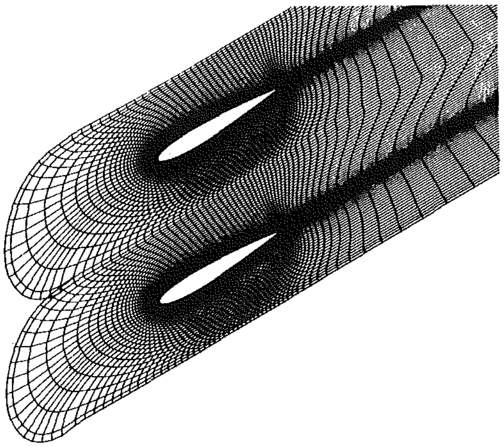

Fig. 17 133 × 33 C-mesh

coefficient, indicating a thicker boundary layer as computed with the full equations. Consistent with this, the Navier-Stokes local friction coefficient is smaller than that of the thin-layer computation (see Fig. 16).

Laminar Separated Cascade Flow. A separated, laminar cascade flow is computed with the compressible thin-layer and full Navier-Stokes equations and compared with the incompressible solution of the steady, full Navier-Stokes equations in a vorticity stream function formulation, given by Rosenfeld and Wolfshtein [12]. Similar to the preceding chapter, the applicability of the thin-layer approximation is now investigated for a separated, medium Reynolds number, laminar cascade flow. Errors in the turbulence modeling of

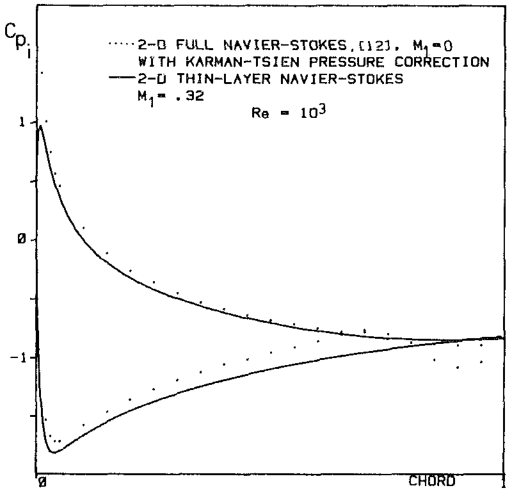

Fig. 18 Pressure coefficient

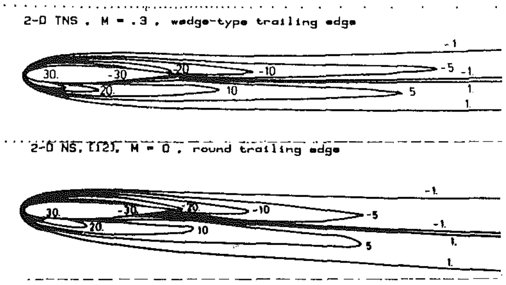

Fig. 19 Vorticity contours

separated flows do not enter these investigations. Again the thin-layer and full Navier-Stokes equations are solved using the same grid. No effort has been made to increase the streamwise mesh resolution in the case of the full Navier-Stokes equation. The laminar flow is computed through a cascade of symmetrical NACA 0012 airfoils with a solidity of 1, and a stagger angle of 30 deg. Wedge-type and round trailing edges are computed in the compressible and the incompressible solutions, respectively. The inflow angle is 20 deg (−10 deg = angle of attack), and the Reynolds number 1000 (based upon chord and axial inflow velocity). A periodic overlapping C-type mesh was used in the compressible thin-layer and full Navier-Stokes computations, while an O-type mesh was applied in the incompressible full Navier-Stokes solution. The C-type mesh used (see Fig. 17) has 17 points in the boundary layer. The first point off the surface was placed 0.0056 chords from the surface. The distances between grid points along the blade surface at the leading and trailing edges have the value of 0.005. The pressure coefficient distributions are given in Fig. 18 for the compressible thin-layer and the incompressible full Navier-Stokes solutions. A compressibility correction was applied to the incompressible solution. In the incompressible full Navier-Stokes solution, a separation is formed at the suction side near the round trailing edge and a second small separation bubble is created at approximately one-half chord distance from the leading edge. The thin-layer solution predicts a separation at the wedge-type trailing edge as well (separation point at 85% chord). The vorticity contours of the thin-layer and incompressible full Navier-Stokes solutions are plotted in Fig. 19. The compressible thin-layer and full Navier-Stokes pressure coefficients do not deviate significantly from each other (see Fig. 20). The extension of the separation zones, however, is very different in the thin-layer and full Navier-Stokes solutions (see Fig. 21). Obviously, the compressible and incompressible full Navier-Stokes solutions do agree to a better extent. These

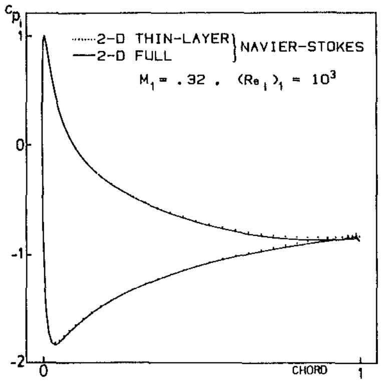

Fig. 20 Pressure coefficient

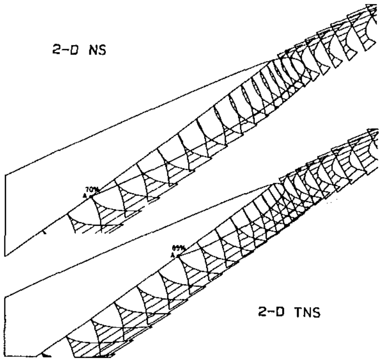

Fig. 21 Separation zones

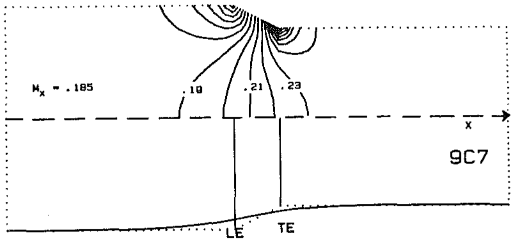

Fig. 22 9C7 blade-free channel

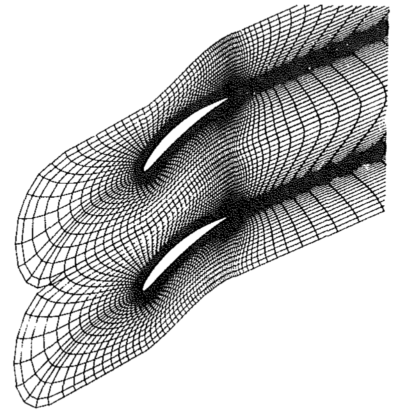

Fig. 23 9C7-133 × 37 C-mesh

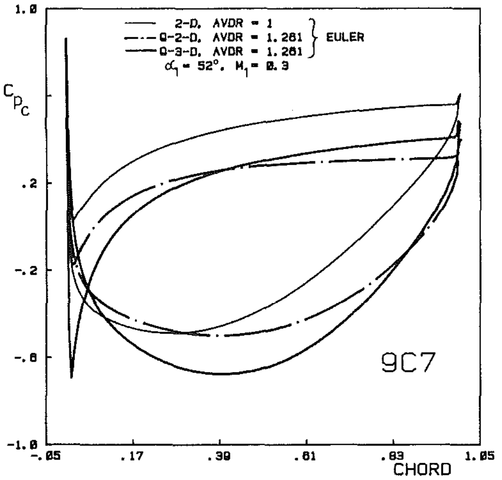

Fig. 24 9C7 inviscid pressure coefficients

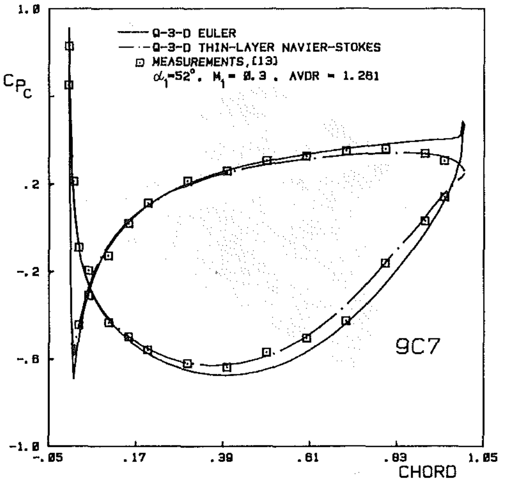

Fig. 25 9C7 pressure coefficient

preliminary Navier–Stokes results indicate limitations of the thin-layer approximation in an accurate prediction of separated, medium Reynolds number flows.

Cascade Flow With Strong Sidewall Contraction. In many rectilinear compressor cascade experiments, the flow is remarkably three-dimensional, leading to significant streamwise changes in the axial velocity density ratio. An accurate prediction of the flow quantities in the cascade symmetry plane would be provided by a three-dimensional viscous method. A rather accurate prediction of the midspan flow quantities would be possible with a Q-2-D method, if a measured field distribution of the midspan axial velocity density ratio or the midspan stream-sheet thickness ratio were used. Since these difficult and expensive measurements are usually not available, a Q-3-D flow model is proposed, which more accurately predicts plane cascade flows with significant symmetrical sidewall divergence/convergence. A simple sidewall boundary layer displacement thickness model is used. The subsonic flow is computed through a 9C7 compressor cascade with strong sidewall contraction and compared to cascade measurements which were performed by Stark and Hoheisel [13]. Quasi-two-dimensional and quasi-three-dimensional forms of the governing equations are used to predict this three-dimensional cascade flow more accurately. The solidity of the cascade is one, the stagger angle 40 deg, the aspect ratio 3.75, and the geometrical contraction ratio 1.2. Linear contracting sidewalls are used within the blading. The experiment with the inflow Mach number of 0.3, the inflow angle 52 deg, and a Reynolds number based on inlet velocity of 4 × 10^5 was selected as test case. In the computations, the displacement thickness of the sidewall boundary layer was assumed to vary linearly within the cascade (zero thickness at the inlet) and to be constant downstream of the cascade. The measured far-field axial velocity density ratio of 1.261 was used in the Q-2-D/Q-3-D computations. Consistent 2-D, Q-2-D, and Q-3-D Euler computations were performed for the inflow Mach number 0.3, and the inflow angle of 52 deg. An overlapping 127 × 25 C-type Euler mesh was used with a rather coarse leading edge resolution. Uncertainties in predicting viscous effects were excluded in these inviscid computations. The sidewall geometry, with the superimposed sidewall boundary-layer displacement thickness, is shown in Fig. 22 together with the midspan differential stream-sheet thickness ratio used in the Q-3-D model, which was computed from the flow through the blade-free cascade.

The up/downstream influence of the contracted flow channel can be clearly seen. The Mach number contours indicate the significant three-dimensionality of this cascade flow. In the Q-2-D model the differential stream-sheet thickness ratio is approximated by the finite-flow channel height, which is corrected using the sidewall boundary displacement thickness. Due to the heavily contracted sidewalls, the 2-D and Q-2-D profile pressure coefficient distributions deviate significantly (see Fig. 24).

Note that the leading-edge flow structure is similar in the 2-D and the Q-2-D cases. The Q-2-D and the Q-3-D profile pressure coefficient distributions are also compared in Fig. 24. Consistent with the great differences in the Q-2-D/Q-3-D stream-sheet thickness ratio distributions, the Q-3-D profile pressure coefficient distribution departs significantly from that of the Q-2-D. This is especially true in the leading edge region where the experimentally verified suction peak is predicted by the Q-3-D solution only. Important for boundary-layer computation is the fact that the Q-2-D/Q-3-D streamwise profile pressure gradients are different. In Fig. 25 the Q-3-D Euler solution is finally compared to the experiment. Although there are still simplifications in the Q-3-D Euler model, it predicts the 3-D cascade flow quite well. The difference in the profile pressure coefficient distribution is consistent with the inclusion of the profile boundary-layer displacement thickness, which is not taken into account in the Q-3-D Euler solution. Finally, the Q-3-D thin-layer equations are solved for this turbulent cascade flow. The viscous pressure coefficient is also plotted in Fig. 25. The Q-3-D thin-layer pressure coefficient agrees favorably with that of the experiment. A trailing-edge separation is computed with the thin-layer equations. The separation point is located at 86% chord. The thin-layer solution also predicts a very small reverse flow zone at the leading edge, which is caused by the Q-3-D suction peak. Note that this leading edge flow structure would not have been obtained in a Q-2-D solution.

Conclusions

A new straight cascade code was developed, which solves the two/quasi-two/quasi-three-dimensional forms of the Euler equation, the thin-layer Navier-Stokes equation, and the full Navier-Stokes equation. A modified implicit ADI scheme with a spatial finite-difference/finite-volume discretization is used which ensures an accurate treatment of singular mesh points. With the exception of singular mesh points, all boundary conditions are implemented implicitly. The code was successfully validated through numerous quantitative comparisons of computed inviscid and viscous subsonic solutions with experiments and other existing solutions.

(*a*) A good convergence rate is obtained on single grids with constant time-stepping due to the fully implicit implementation of the cascade code;

(*b*) Using the applied fine meshes with a suitable point distribution inviscid up to high Reynolds number attached and separated flows could be predicted at least within engineering accuracy;

(*c*) Still finer meshes seem to be necessary for a more accurate prediction of the local skin friction coefficient and the cascade loss coefficient. This is especially true for separated flows where a higher streamwise resolution seems to be necessary;

(*d*) Preliminary results indicate that the thin-layer assumption seems to be inadequate for accurate computations of separated medium Reynolds number flows; and

(*e*) It was demonstrated that the use of the quasi-two/quasi-three-dimensional forms of the governing equations is important for an accurate prediction of the midspan flow through plane cascades with significant sidewall effects.

Acknowledgments

The authors gratefully acknowledge the contributions of U. Küster, W. Gross, and Ch. Föhl to this paper. The results presented originate from research projects, which are funded by DEUTSCHE FORSCHUNGSGEMEINSCHAFT.

References

1 Schäfer, O., "A Fully Implicit ADI Scheme for Inviscid and Viscous Quasi-Three-Dimensional Flows Through Plane Cascades" (in press).

2 Norton, R. J. G., Thompkins, Jr., and Haimes, R., "Implicit Finite Difference Schemes with Non-Simply Connected Grids—A Noval Approach," AIAA Paper No. 84-0003, 1984.

3 Shamroth, S. J., "Calculation of Steady and Oscillating Airfoil Flow Fields Via the Navier-Stokes Equations," AIAA Paper No. 84-0525, 1984.

4 Sorenson, R. L., and Steger, J. L., "Numerical Generation of Two-Dimensional Grids by the Use of Poisson Equations with Grid Control at Boundaries," NASA Conf. Pub. 2166, 1980, pp. 449-461.

5 Baldwin, B. S., and Lomax, H., "Thin-Layer Approximation and Algebraic Model for Separated Turbulent Flows," AIAA Paper No. 78-257, 1978.

6 Beam, R. M., and Warming, R. F., "An Implicit Factored Scheme for the Compressible Navier-Stokes Equations," *AIAA J.*, Vol. 16, No. 4, 1978, pp. 393-402.

7 Steger, J. L., "Implicit Finite Difference Simulation of Flow About Arbitrary Geometries with Application to Airfoils," AIAA Paper No. 77-665, 1977.

8 Küster, U., "Boundary Procedures for the Euler Equations," *Conf. Proc. 6th GAMM-Conference on Numerical Methods in Fluid Mechanics*, Göttingen, Sept. 25-27, 1985.

9 Gostelow, J. P., "Potential Flow Through Cascades—A Comparison Between Exact and Approximate Solutions," ARC CP 807, 1965.

10 Lehthaus, F., "Berechnung der transsonischen Strömung durch ebene Turbinengitter nach dem Zeitschrittverfahren," Dissertation TU Braunschweig, 1977.

11 Schlichting, H., "Berechnung der reibungslosen inkompressiblen Strömung für ein vorgegebenes ebenes Schaufelgitter," VDI-Forschungsheft 447, 1955.

12 Rosenfeld, M., and Wolfshtein, M., "Numerical Solution of Viscous Flow Around Arbitrary Airfoils in a Straight Cascade," *8th Int. Conf. on Numerical Methods in Fluid Dynamics, Lecture Notes in Physics*, Springer, New York, 1982, pp. 433-439.

13 Stark, U., and Hoheisel, H., "The Combined Effect of Axial Velocity Density Ratio and Aspect Ratio on Compressor Cascade Performance," ASME Paper No. 80-GT-138, 1980.

Zhang Jialin
Institute of Engineering Thermophysics,
Chinese Academy of Sciences,
Beijing, China

3D Transonic Potential Flow Computation in an Axial-Flow Compressor Rotor by an Approximate Factorization Scheme

A conservative full-potential equation of 3D transonic flow in a turbomachine has been derived with the tensor method and expressed with respect to nonorthogonal curvilinear coordinates, and a fully implicit approximate factorization scheme to calculate the flow field has been developed in this paper. The new algorithm has been used to compute the 3D transonic flow field within an axial-flow single-stage compressor rotor tested by DFVLR. Comparisons between the computed flow field and the DFVLR data have been made. Results demonstrate that fast convergence can be achieved by the presented algorithm and that the agreement with the measurements obtained with an advanced laser velocimeter is quite good.

Introduction

In current transonic axial-flow compressors, the rotor inlet relative Mach numbers range from subsonic at the rotor hub to supersonic over the outer parts of the rotor span. In the supersonic regions, 3D shocks are formed causing a complicated 3D transonic flow field. In order to understand the complicated 3D transonic flow field, both advanced experimental techniques and fast and accurate 3D computation methods are needed.

There are two main categories of 3D computation methods: (*a*) the quasi-3D and fully 3D computation methods which employ iterations between solutions on two kinds of relative streamsurface, S_1 and S_2, and (*b*) the fully 3D computation methods which solve 3D governing equations. Both categories of 3D computation methods were discussed in Wu's classical theory [1] and can yield accurate results due to the strong coupling between sections of the flow field (see [2] and [3]).

Recently, there has been marked progress in fully 3D computation methods by solving 3D governing equations, especially those which solve 3D Euler equations [3, 4]. The Euler methods are able to predict the main features of the 3D transonic flow field in turbomachines, but, in general, take long run times which hinder their application to real engineering problems.

It is well known that when only weak shock waves occur, a full-potential method may be a good substitute for an Euler method [5–16]. Since the full-potential method has only a single unknown variable, it should be computationally more efficient than the Euler methods. In fact, in [5] both an Euler method and a finite-volume full-potential method have been used to compute identical turbomachine stator 3D transonic flow fields. The comparisons demonstrate that both methods predict the major 3D effects on the flow correctly.

In the present study, a fully implicit approximate factorization (AF) scheme for solving the mixed elliptic-hyperbolic 3D full-potential equation, derived with the tensor method and expressed with respect to nonorthogonal curvilinear coordinates, is presented and used to compute the 3D transonic flow field within the axial-flow single-stage compressor rotor tested by DFVLR [17].

The AF scheme was early presented in [7]; [8–11] have extended it to the computation of 2D and 3D full-potential equations describing the flows over wings and wing/body combinations, and [12] has extended it to an algorithm solving the S_1 streamsurface transonic flow field in turbomachines. All of these have shown that the AF scheme is a reliable and effective technique for improving the convergence of transonic potential flow computations.

The AF scheme presented in this paper is a modified and extended version of the AF2 scheme developed in [9]. In this scheme the artificial densities, $\tilde{\rho}$, $\bar{\rho}$, $\hat{\rho}$, defined and used in [9] are replaced by a new artificial density, $\tilde{\rho}$, defined in this paper for the whole 3D transonic flow field. The new artificial density, $\tilde{\rho}$, is only dependent on the directions and magnitude of the relative velocity and not on the selected coordinates.

Basic Aero-Thermodynamic Equations

For the present study, it is assumed that the absolute flow in a turbomachine is isentropic and irrotational. The basic aero-thermodynamic equations governing the steady relative flow of an inviscid gas in the turbomachine can be written in the following forms:

Contributed by the Gas Turbine Division of THE AMERICAN SOCIETY OF MECHANICAL ENGINEERS and presented at the 30th International Gas Turbine Conference and Exhibit, Houston, Texas, March 18–21, 1985. Manuscript received at ASME Headquarters, December 17, 1984. Paper No. 85-GT-16.

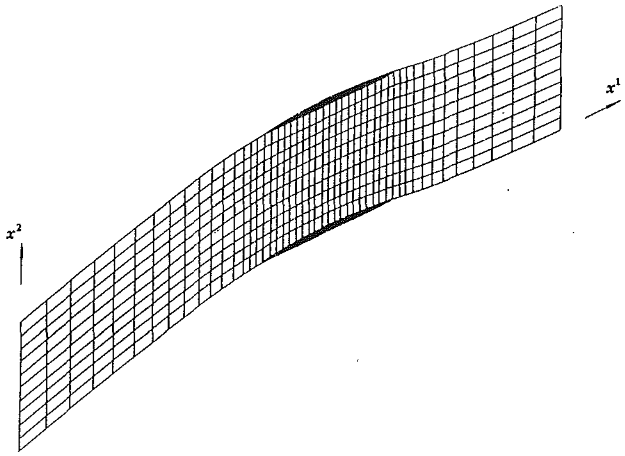

Fig. 1(*a*) S_1 surface

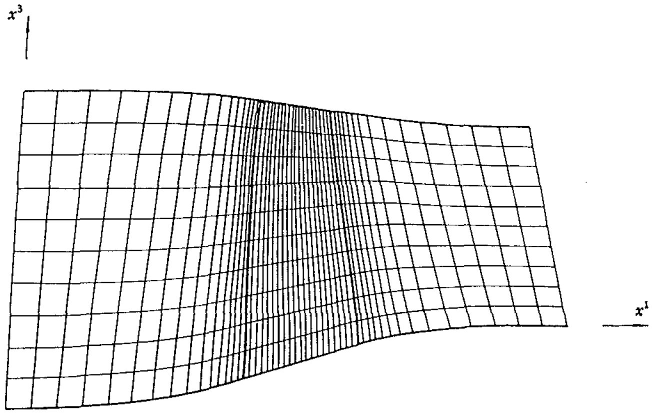

Fig. 1(*b*) S_2 surface

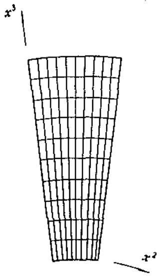

Fig. 1(*c*) S_3 surface

Fig. 1 Coordinate surfaces and computational mesh

Continuity

$$\nabla \cdot (\rho \mathbf{W}) = 0 \tag{1}$$

Irrotationality

$$\nabla \times \mathbf{V} = 0 \tag{2}$$

First law of thermodynamics

$$\frac{dI}{dt} = 0 \tag{3}$$

Second law of thermodynamics

$$\frac{ds}{dt} = 0 \tag{4}$$

Nonorthogonal Curvilinear Coordinate System and Computational Mesh

Let (x^1, x^2, x^3) be the nonorthogonal curvilinear coordinate system selected in the relative frame rotating with the rotor, in which the x^1-lines are in the directions of the quasi-streamlines, the x^2-lines are in the direction of the circumference, and the x^3-lines are in the directions of the quasi-radius, as shown in Fig. 1. Let (S_3, S_2, S_1) be the coordinate surfaces of the selected nonorthogonal curvilinear coordinate system, in which the S_1 surfaces are a family of quasi-streamsurfaces equally spaced between the hub and tip, the S_2 surfaces are a family of quasi-streamsurfaces equally spaced between the blade pressure and suction surfaces, and the S_3 surfaces are a family of surfaces axially spaced between the inlet and exit surfaces. The computational mesh is formed by intersections of the three families of different coordinate surfaces and also shown in Fig. 1.

Computation of Grid Parameters

Let (y^1, y^2, y^3) be the usual orthogonal curvilinear coordinates of a point, P, and (x^1, x^2, x^3) be its nonorthogonal curvilinear coordinates with its base vector [18]:

$$\mathbf{e}_i = \frac{\partial \mathbf{R}}{\partial x^i} \tag{5}$$

where **R** is the radius vector from origin. The reciprocal vector, $\mathbf{e}^i$, is given by

$$\mathbf{e}^i = \frac{\mathbf{e}_j \times \mathbf{e}_\kappa}{\sqrt{g}} \tag{6}$$

or by

$$\mathbf{e}_i \cdot \mathbf{e}^j = \delta_i^j \tag{7}$$

The unit vector of $\mathbf{e}_i$, $\mathbf{u}_i$, is defined by

$$\mathbf{u}_i = \mathbf{e}_i \div \sqrt{g_{ii}} \tag{8}$$

The covariant metric tensor, g_{ij}, is

$$g_{ij} = \frac{\partial y^k}{\partial x^i} \cdot \frac{\partial y^k}{\partial x^j} = \mathbf{e}_i \cdot \mathbf{e}_j = g_{ji} \tag{9}$$

The contravariant metric tensor, g^{ij}, can be given by

$$g^{ij} = \mathbf{e}^i \cdot \mathbf{e}^j = g^{ji} \tag{10}$$

or by

$$g_{i\kappa} g^{j\kappa} = \delta_i^j \tag{11}$$

Nonorthogonal Velocity Components

With tensor analysis and relationships between the relative

Nomenclature

C_p = pressure coefficients: $C_p = P/P_{\text{in}}$
M = relative flow Mach number
I = $h + (W)^2/2 - (U)^2/2$
s = entropy per unit mass of gas
t = time
U = blade velocity at radius r
V = absolute velocity of gas
v^i, v_i, V^i = contravariant, covariant, and physical component of **V**, respectively
W = relative velocity of gas
w^i, w_i, W^i = contravariant, covariant, and physical component of **W**, respectively
ω = angular velocity of blade

flow and absolute flow in a turbomachine, the nonorthogonal velocity components are derived and given as follows:

$$\mathbf{W} = w^i \mathbf{e}_i = w_i \mathbf{e}^i = W^i \mathbf{u}_i \tag{12}$$

$$\mathbf{V} = v^i \mathbf{e}_i = v_i \mathbf{e}^i = V^i \mathbf{u}_i \tag{13}$$

$$\mathbf{V} = \mathbf{W} + \mathbf{U} = \mathbf{W} + \omega \times \mathbf{r} \tag{14}$$

$$w_i = g_{ij} w^i, \quad W^i = \sqrt{g_{ii}}\, w^i \tag{15}$$

$$v_i = g_{ij} v^i, \quad V^i = \sqrt{g_{ii}}\, v^i \tag{16}$$

For the nonorthogonal curvilinear coordinates selected in the present study, equation (14) can be written in the following forms:

$$W^1 = V^1, \; W^2 = V^2 - \omega r, \quad W^3 = V^3 \tag{17}$$

Full-Potential Equation for Flow Within a Compressor Rotor

For irrotational absolute flow within a compressor rotor, the following equation is obtained:

$$\mathbf{V} = \nabla \Phi = \Phi_{x^i} \mathbf{e}^i \tag{18}$$

By using equations (12-18), the contravariant component of $\mathbf{W}$, w^i, can be expressed as follows:

$$w^1 = \sum_{i=1}^{3} g^{1i} \Phi_{x^i}, \quad w^2 = \sum_{i=1}^{3} g^{2i} \Phi_{x^i} - \omega r/\sqrt{g_{22}},$$

$$w^3 = \sum_{i=1}^{3} g^{3i} \Phi_{x^i} \tag{19}$$

The continuity equation (1) can be written in the following form:

$$\sum_{i=1}^{3} (\sqrt{g}\, \rho\, w^i)_{x^i} = 0 \tag{20}$$

Substituting equation (19) into equation (20) results in

$$\left[\sqrt{g}\, \rho \sum_{i=1}^{3} g^{1i} \Phi_{x^i}\right]_{x^1} + \left[\sqrt{g}\, \rho \left(\sum_{i=1}^{3} g^{2i} \Phi_{x^i} - \omega r/\sqrt{g_{22}}\right)\right]_{x^2}$$

$$+ \left[\sqrt{g}\, \rho \sum_{i=1}^{3} g^{3i} \Phi_{x^i}\right]_{x^3} = 0 \tag{21}$$

where

$$\rho = \left[1 - \frac{(W)^2 - (U)^2}{2I}\right]^{\frac{1}{\kappa - 1}} \tag{22}$$

Equation (21) is the conservative 3D full-potential equation describing the rotational relative flow in the compressor rotor. It can be shown that equation (21) is a mixed elliptic-hyperbolic equation, which is elliptic in subsonic regions and hyperbolic in supersonic regions.

Difference Equation

In order to discretize the mixed elliptic-hyperbolic full-potential equation (21) in a transonic flow field, the artificial compressibility technique [12, 14] has been used. The artificial density, $\tilde{\rho}$, is defined in the present study as follows:

$$\tilde{\rho} = \rho - \mu \left(\frac{|W^1|}{W} \rho_{\overleftrightarrow{x}^1} \Delta x^1 + \frac{|W^2|}{W} \rho_{\overleftrightarrow{x}^2} \Delta x^2 + \frac{|W^3|}{W} \rho_{\overleftrightarrow{x}^3} \Delta x^3 \right. \tag{23}$$

Here, the double arrow in the subscript $\overleftrightarrow{x}^i$ means that when $W^i > 0$ the $\rho_{\overleftarrow{x}^i}$ is selected, and when $W^i < 0$ the $\rho_{\overleftarrow{x}^i}$ is selected. The artificial viscosity coefficient, μ, is defined by

$$\mu = \min\{\max[(\mathrm{M}^2 - 1)D, 0], 1\} \tag{24}$$

where D is a user-specified constant. In the present computation, $D = 0.3$. Introducing the artificial density, $\tilde{\rho}$, into equation (21) and differencing it according to the conservative central-difference scheme over the whole 3D transonic flow field results in

$$L\Phi^n_{\alpha,\beta,\gamma} = \overleftarrow{\delta}_{x^1} \left[\sqrt{g}\, \tilde{\rho} \sum_{i=1}^{3} g^{1i} \delta_{x^i} \Phi\right]_{\alpha+\frac{1}{2},\beta,\gamma}$$

$$+ \overleftarrow{\delta}_{x^2} \left[\sqrt{g}\, \tilde{\rho} \left(\sum_{i=1}^{3} g^{2i} \delta_{x^i} \Phi - \omega r/\sqrt{g_{22}}\right)\right]_{\alpha,\beta+\frac{1}{2},\gamma}$$

$$+ \overleftarrow{\delta}_{x^3} \left[\sqrt{g}\, \tilde{\rho} \sum_{i=1}^{3} g^{3i} \delta_{x^i} \Phi\right]_{\alpha,\beta,\gamma+\frac{1}{2}} \tag{25}$$

where the subscripts α, β, γ are grid stations along x^1, x^2, x^3, respectively, $\overleftarrow{\delta}_{x^i}$ is the backward difference operator, and the operator δ_{x^i} is the central-difference operator.

AF2 Iteration Scheme

In the present study the AF2 fully implicit scheme presented by Holst in reference [9] has been modified and extended to the computation of 3D transonic flow in turbomachines to accelerate the convergence of the iteration process. The new scheme developed in this paper can be expressed as follows:

$$N\, C^n_{\alpha,\beta,\gamma} + \sigma L \Phi^n_{\alpha,\beta,\gamma} = 0 \tag{26}$$

where

$$C^n_{\alpha,\beta,\gamma} = \Phi^{n+1}_{\alpha,\beta,\gamma} - \Phi^n_{\alpha,\beta,\gamma} \tag{27}$$

$$N = -\frac{1}{\xi} \left[\left(\xi - \frac{1}{A_\alpha} \overrightarrow{\delta}_{x^2} A_\beta \overleftarrow{\delta}_{x^2}\right) \left(A_\alpha - \frac{1}{\xi} \overrightarrow{\delta}_{x^3} A_\gamma \overleftarrow{\delta}_{x^3}\right) - \xi\, E^{+1}_{x^1} A_\alpha \right] (\xi + \overleftarrow{\delta}_{x^1}) \tag{28}$$

in which

$$A_\alpha = (\sqrt{g}\, g^{11} \tilde{\rho})^n_{\alpha-\frac{1}{2},\beta,\gamma},$$

$$A_\beta = (\sqrt{g}\, g^{22} \tilde{\rho})^n_{\alpha,\beta-\frac{1}{2},\gamma},$$

$$A_\gamma = (\sqrt{g}\, g^{33} \tilde{\rho})^n_{\alpha,\beta,\gamma-\frac{1}{2}} \tag{29}$$

In the preceding equations, $L\Phi^n_{\alpha,\beta,\gamma}$ is the residual, which is a measure of how well the finite-difference equation (25) is satisfied by the n-th level velocity-potential solution, σ is a relaxation factor, $E^{+1}_{x^1}$ is a shift operator given by

$$E^{+1}_{x^1}(\qquad)_{\alpha,\beta,\gamma} = (\qquad)_{\alpha+1,\beta,\gamma} \tag{30}$$

and ξ is a sequence of

$$\xi_k = \xi_h (\xi_l/\xi_h)^{\frac{k-1}{m-1}} \tag{31}$$

where

$$k = 1, 2, 3, \ldots, m$$

and m, ξ_h, ξ_l are all user-specified constants. Implementation of the AF iteration scheme is achieved by writing equation (26) in a three-step form as follows:

$$\left(\xi - \frac{1}{A_\alpha} \overrightarrow{\delta}_{x^2} A_\beta \overleftarrow{\delta}_{x^2}\right) F^n_{\beta,\gamma} = \xi \sigma L \Phi^n_{\alpha,\beta,\gamma} + \xi A_{\alpha+1} B^n_{\alpha+1,\beta,\gamma},$$

$$\left(A_\alpha - \frac{1}{\xi} \overrightarrow{\delta}_{x^3} A_\gamma \overleftarrow{\delta}_{x^3}\right) B^n_{\alpha,\beta,\gamma} = F^n_{\beta,\gamma},$$

$$(\xi + \overleftarrow{\delta}_{x^1}) C^n_{\alpha,\beta,\gamma} = B^n_{\alpha,\beta,\gamma} \tag{32}$$

Here, $F^n_{\beta,\gamma}$, $B^n_{\alpha,\beta,\gamma}$ are the intermediate results, which have no physical meaning.

Boundary Conditions

In the present study, the necessary upstream and downstream boundary conditions to yield a unique and stable converged solution are given by experiment data. At the inlet grid surface, the flow is assumed to be axisymmetric, the radial velocity component to be zero, and I and s are assumed to be uniform ($\nabla I = \nabla s = 0$). At the exit grid surface, the flow is also assumed to be axisymmetric, and the radial velocity component to be zero. At the inlet grid surface the total conditions and mass flow are specified, and at the exit grid surface the radial distribution of total temperature and relative flow angle at hub or another radius are specified. Other boundary conditions used in the present study include periodicity up and downstream of the blade row, and tangency on the hub, shroud, and blade surfaces. Note that since the exit relative flow angle at hub or other radius is specified, no Kutta condition is used in the code.

Computed Results

The new algorithm presented in this paper has been coded and used to compute the 3D transonic flow field within an axial-flow single-stage compressor rotor tested by DFVLR. The compressor is designed for a total pressure ratio of 1.51 and a mass flow of 17.3 kg/s at 20,260 rpm. The rotor consists of 28 blades with inlet tip diameter of 399 mm and a hub-to-tip radius ratio of 0.5. The rotor blades are composed of MCA-profiles. The comparison between the computed flow field and the DFVLR data is made at the 100% design speed, maximum-efficiency condition. The computation was made on an HP-1000 computer and used a grid system of 50 × 11 × 11. If a drop of the maximal residual, $L\phi^{n}_{\max}$, by three orders of magnitude is taken to be the convergence criterion,

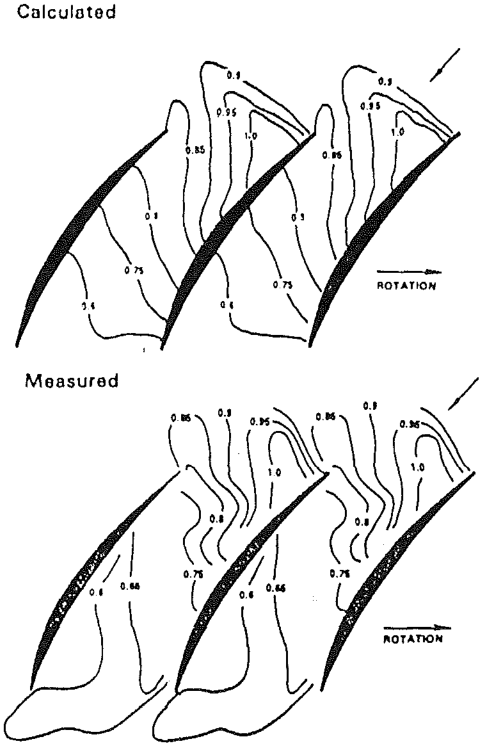

Fig. 2(a) 18% span

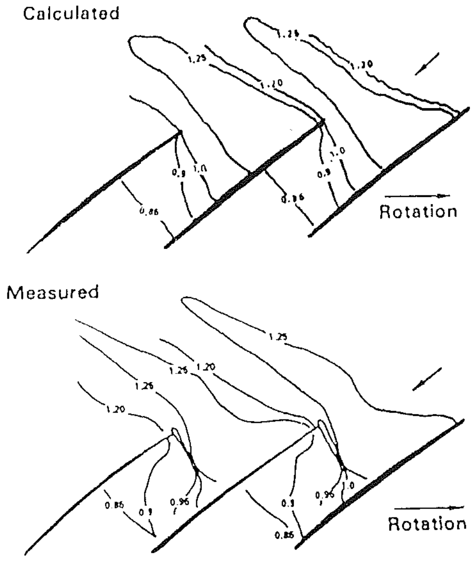

Fig. 2(c) 68% span

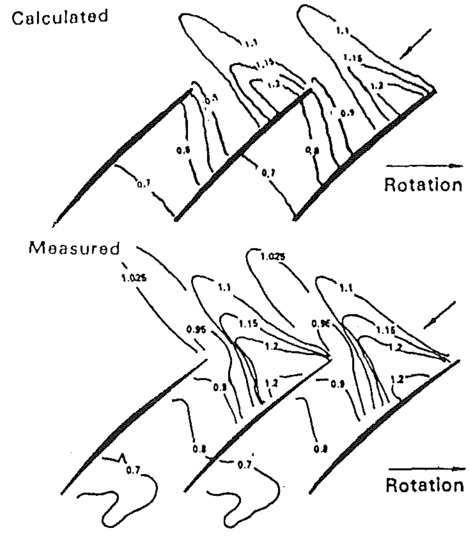

Fig. 2(b) 45% span

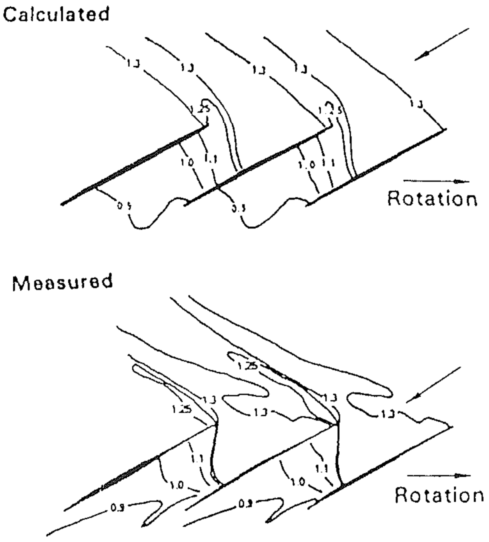

Fig. 2(d) 89% span

Fig. 2 Comparisons of computed relative Mach number contours and DFVLR data

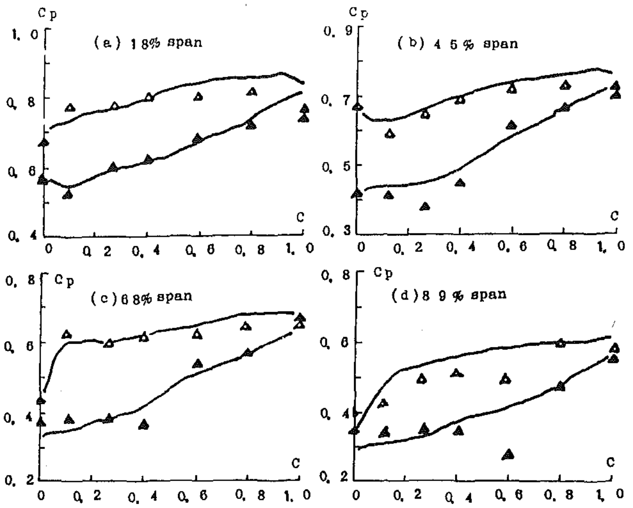

Fig. 3 Distributions of pressure coefficients (△ ▲ experiment data, —— computed results)

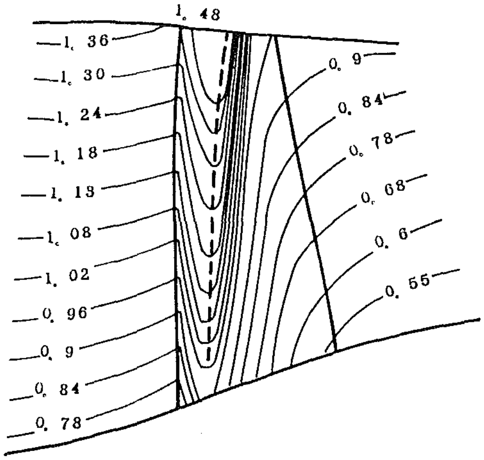

Fig. 4(a) Suction surface

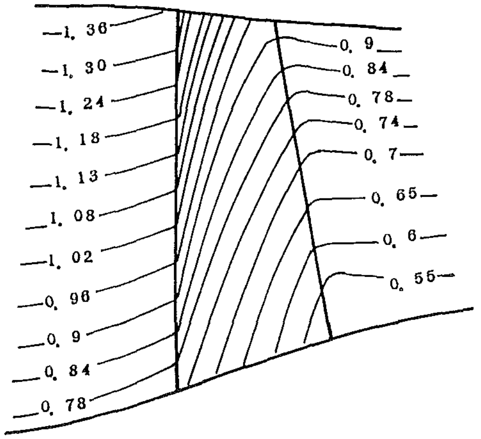

Fig. 4(b) Pressure surface

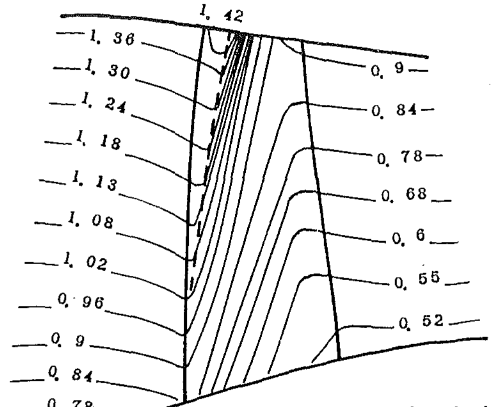

present method

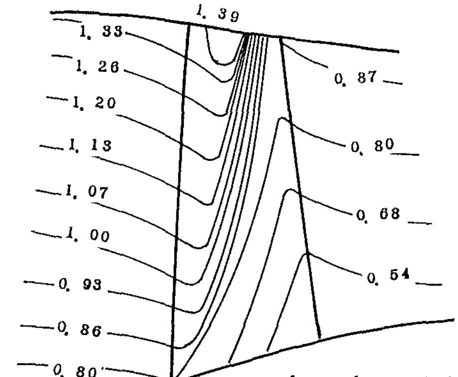

from reference (15)

Fig. 4(c) S_{2m} surface

Fig. 4 Computed relative Mach number contours on S_2 surface

convergence, in this case, is achieved in approximately 7 h of CPU time (or in approximately 160 iterations).

The computed results are shown in Figs. 2–4. Figures 2(*a–d*) show a comparison between the computed and measured relative Mach number contours at 18, 45, 68, and 89% span, respectively. The comparisons show that at the 18, 45, and 68% span the computed results are in good agreement with DFVLR data, but at the 89% span the discrepancy has become obvious. This phenomenon can also be seen in Figs. 3(*a–d*). Figures 3(*a–d*) show the comparisons between the computed and measured distributions of surface pressure coefficient at the 18, 45, 68, and 89% span, respectively. The discrepancy between the computed flow field and the measurements has increased with the radius.

Figure 4(*a*) shows the computed relative Mach number contours on the S_2 quasi-streamsurface coincident with the blade suction surface. In the figure the computed 3D shock is shown by a dashed line. Figure 4(*b*) shows the computed relative Mach number contours on the S_2 quasi-streamsurface coincident with the blade pressure surface. In Fig. 4(*c*), the former figure shows the relative Mach number contours computed by the presented algorithm on the center S_2 quasi-streamsurface, and the latter figure shows the computed result from [15] on the identical S_2 surface.

Conclusion

In the present study, a conservative full-potential equation of 3D transonic flow in compressor rotors has been derived with the tensor method and expressed with respect to nonorthogonal curvilinear coordinates, and an implicit AF scheme has been developed to compute the 3D transonic flow field in axial-flow compressor rotors. In the modified AF iteration scheme, the artificial density, $\tilde{\rho}$, is substituted for the $\bar{\rho}$, $\hat{\rho}$, $\hat{\rho}$ used in [9]. The modification has reduced computer storage and improved the stability of computation in 3D transonic flow field. The computations made for the DFVLR axial-flow compressor rotor demonstrate that the new algorithm is fast and stable. The comparisons made in the previous section indicate that the presented algorithm can predict the main features of 3D transonic flow in compressor rotors. Obviously, the algorithm is also capable of computing the 3D transonic flow field in turbomachine stators where the angular velocity of blade, ω, is equal to zero. The algorithm is applicable to real engineering problems for its stability, effectiveness, and lower cost.

Acknowledgments

The author wishes to thank Professor Wu Chung-Hua for his directive help and support.

References

1 Wu Chung-Hua, "A General Theory of Three-Dimensional Flow in Subsonic or Supersonic Turbomachines of Axial Radial and Mixed Flow Types," ASME Paper No. 50-A-79, 1950 (Trans. ASME Nov. 1952); NACA TN 2604, 1952.

2 McDonald, P. W., Bolt, C. R., Dunker, R. J., and Weyer, H. B., "A Comparison Between Measured and Computed Flow Fields in a Transonic Compressor Rotor," ASME JOURNAL OF ENGINEERING FOR POWER, Vol. 102, No. 4, Oct. 1980, pp. 883-891.

3 Sarathy, K. P., "Computation of Three-Dimensional Flow Field Through Rotating Blade Rows and Comparison with Experiment," ASME Paper No. 81-GT-121, 1981.

4 Denton, J. D., and Singh, U. K., "Time Marching Methods for Turbomachinery Flow Calculations, Part I: Basic Principles and 2-D Applications, Part II: Three-Dimensional Flows," in: *Application of Numerical Methods to Flow Calculations in Turbomachines*, Von Karman Institute for Fluid Dynamics Lecture Series, April 23-27, 1979.

5 Camus, J. J., "An Experimental and Computational Study of Transonic Three-Dimensional Flow in a Turbine Cascade," ASME Paper No. 83-GT-12, 1983.

6 Caspar, J. R., Hobbs, D. E., and Davis, R. L., "Calculation of Two-Dimensional Potential Cascade Flow Using Finite Area Methods," *AIAA Journal*, Vol. 18, No. 1, Jan. 1980, pp. 103-109.

7 Ballhaus, W. F., Jameson, A., and Albert, J., "Implicit Approximate Factorization Schemes for the Efficient Solution of Steady Transonic Flow Problems," *AIAA Journal*, Vol. 18, No. 6, 1978, pp. 573-579.

8 Holst, T. L., "An Implicit Algorithm for the Conservative Transonic Full Potential Equation Using an Arbitrary Mesh," AIAA Paper No. 78-1113, July 1978.

9 Holst, T. L., "Fast, Conservative Algorithm for Solving the Transonic Full-Potential Equation," *AIAA Journal*, Vol. 18, No. 12, 1980, pp. 1431-1439.

10 Baker, T. J., "A Fast Implicit Algorithm for the Nonconservative Potential Equation," Open Forum Presentation at AIAA 4th Computational Fluid Dynamics Conference, Williamsburg, VA, July 1979.

11 Baker, T. J., and Forgey, C. R., "A Fast Algorithm for the Calculation of Transonic Flow Over Wing/Body Combinations," AIAA Paper No. 81-1015, 1981.

12 Zhang Jialin and Wu Chung-Hua, "A Fast Algorithm for Solving the Conservative Transonic S_1 Full-Potential Equation Employing Non-orthogonal Curvilinear Coordinates and Non-orthogonal Velocity Components," *Computational Methods in Turbomachinery*, I. Mech. E. Conference Publications 1984.

13 Jameson, A., "Transonic Potential Flow Calculations Using Conservative Form," *AIAA Second Computational Fluid Dynamic Conference Proceedings*, June 1975, pp. 148-155.

14 Hafez, M. M., Marman, E. M., and South, J. C., "Artificial Compressibility Methods for Numerical Solution of Transonic Full Potential Equation," AIAA Paper No. 78-1148, July 1978.

15 Lu Panming and Wu Chung-Hua, "Computation of Potential Flow on *S* Stream Surface for a Transonic Axial-Flow Compressor Rotor," ASME Paper No. 84-GT-30, 1984.

16 Deconinck, H., and Hirsch, Ch., "Finite Element Methods for Transonic Blade-to-Blade Calculation in Turbomachines," ASME JOURNAL OF ENGINEERING FOR POWER, Vol. 103, No. 4, Oct. 1981, pp. 665-677.

17 Dunker, R. J., Strinning, P. E., and Weyer, H. B., "Experimental Study of the Flow Field within a Transonic Axial Compressor Rotor by Laser Velocimetry and Comparison with Through-Flow Calculations," ASME Paper No. 77-GT-28, 1977.

18 Wu Chung-Hua, "Basic Equations of Three-Dimensional Flow in Turbomachines Expressed with Respect to Non-orthogonal Curvilinear Coordinates and Non-orthogonal Velocity Components and Its Methods of Solution," *Lecture Notes*, China University of Science and Technology, 1975; 3rd ISABE, 1976.

L. F. Schumann
Propulsion Laboratory,
AVSCOM Research and Technology
Laboratories,
Lewis Research Center,
Cleveland, OH

A Three-Dimensional Axisymmetric Calculation Procedure for Turbulent Flows in a Radial Vaneless Diffuser

An analytical model is proposed to calculate the three-dimensional axisymmetric turbulent flowfield in a radial vaneless diffuser. The model assumes that the radial and tangential boundary layer profiles can be approximated by power-law profiles. Then, using the integrated radial and tangential momentum and continuity equations for the boundary layer and corresponding inviscid equations for the core flow, there result six ordinary differential equations in six unknowns which can easily be solved using a Runge-Kutta technique. A model is also proposed for fully developed flow. The results using this technique have been compared with the results from a three-dimensional viscous, axisymmetric duct code and with experimental data and good quantitative agreement was obtained.

Introduction

The flowfield in the radial vaneless diffuser of a centrifugal compressor is extremely complex since the flow is turbulent, unsteady, viscous, and three-dimensional. Also, depending on the initial state of the end-wall boundary layers and the diffuser length, the flow may become fully developed (i.e., the end-wall boundary layers may merge in the center of the channel) or may separate off one of the walls. One of the earliest attempts to calculate this flowfield was due to Stanitz [1]. Other investigators have used a similar approach to calculate the frictional losses in the vaneless diffuser [2, 3]. In Stanitz' model, the flow is assumed to be one-dimensional with the losses accounted for by using a shear force term proportional to an assigned friction factor in the radial and tangential momentum equations. This approach has several weaknesses. First of all, the development of the end-wall boundary layers is not accounted for except through the inclusion of an effective channel height term. This generally leads to an overprediction of the static pressure rise unless an unrealistically high friction factor is used. Secondly, the method gives no information about the velocity profiles and flow angle distribution at the exit of the vaneless diffuser. This information would be helpful in the design of the leading edge of the diffuser vanes. Finally, the choice of an appropriate friction factor and the effective passage height distribution are totally arbitrary and will often vary from one machine to another.

More recently, several investigators [4-6] have attempted to calculate the three-dimensional boundary layers in vaneless diffusers. The major drawback of these methods is the empiricism used in the specification of the velocity profiles. This affects the calculation of the boundary layer shape factor and therefore also the skin friction and the location of possible separation points.

Currently, there are computer codes [7] which can calculate the three-dimensional flow fields in annular ducts. These codes can also be used for calculating the flow field in a radial vaneless diffuser but their running times and complexity preclude their use as design tools. Also, in the case of the ADD code [7], there are stringent Mach number and Reynolds number limitations.

In the present paper, a three-dimensional axisymmetric calculation procedure for turbulent flows in a radial vaneless diffuser is presented. The method is a noniterative integral method and is therefore much faster than finite difference methods. The primary assumption made is that both the axial and tangential boundary layer velocity profiles can be described by power laws; however, the exponents in these power laws are allowed to vary with radius as prescribed by the equations of motion. Compressibility is accounted for in the radial direction but not in the direction normal to the end walls. Turbulent flow is assumed everywhere using the semi-empirical Ludwieg-Tillman relation for skin friction. A method for calculating fully developed flows is also presented. Comparisons are made to results from the ADD code for both the boundary-layer analysis and for the fully developed flow analysis. Comparisons are also made with experimental data in the literature. In all cases, good agreement is demonstrated.

Analysis

The type of vaneless diffuser geometry considered by this method of analysis is shown in Fig. 1. Typical velocity

---

Contributed by the Gas Turbine Division of THE AMERICAN SOCIETY OF MECHANICAL ENGINEERS and presented at the 30th International Gas Turbine Conference and Exhibit, Houston, Texas, March 18-21, 1985. Manuscript received at ASME Headquarters, January 7, 1985. Paper No. 85-GT-133.

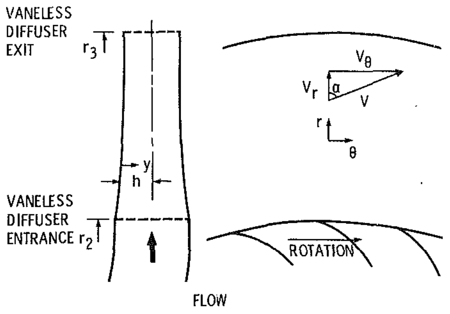

Fig. 1 Vaneless diffuser geometry

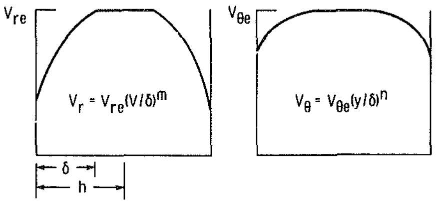

(a) Boundary layer flow.

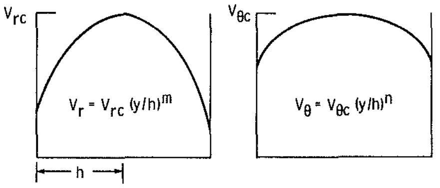

(b) Fully developed flow.

Fig. 2 Typical velocity profiles

profiles for the cases of boundary layer flow and fully developed flow are shown in Figs. 2(*a*) and 2(*b*).

Boundary Layer Flow. The following assumptions are made for this analysis:

1 The flow is steady and turbulent everywhere.
2 The fluid is a perfect gas.
3 The flow is axisymmetric.
4 The end walls of the vaneless diffuser are adiabatic.
5 There is no density variation in the direction normal to the vaneless diffuser end walls although the density is allowed to vary in the radial direction, i.e., $\rho = \rho(r)$.
6 The vaneless diffuser geometry and flow are symmetric about the diffuser centerline.
7 The boundary layer velocity profiles in the radial and tangential directions may be described by the power-law equations

$$\frac{v_r}{v_{re}} = \left(\frac{y}{\delta}\right)^m ; \frac{v_\theta}{v_{\theta e}} = \left(\frac{y}{\delta}\right)^n \tag{1}$$

where v_{re}, $v_{\theta e}$, δ, m, and n are functions of radius only.

The boundary layer equations of motion in cylindrical coordinates for axisymmetric turbulent flow are as follows:

Continuity

$$\frac{\partial(\rho v_r)}{\partial r} + \frac{\rho v_r}{r} + \frac{\partial(\rho v_y)}{\partial y} = 0 \tag{2}$$

Radial momentum

$$v_r \frac{\partial v_r}{\partial r} - \frac{v_\theta^2}{r} + v_y \frac{\partial v_r}{\partial y} = -\frac{1}{\rho}\frac{\partial p}{\partial r} + \frac{1}{\rho}\frac{\partial \tau_r}{\partial y} \tag{3}$$

Tangential momentum

$$v_r \frac{\partial v_\theta}{\partial r} + \frac{v_r v_\theta}{r} + v_y \frac{\partial v_\theta}{\partial y} = \frac{1}{\rho}\frac{\partial \tau_\theta}{\partial y} \tag{4}$$

y-momentum

$$\frac{\partial p}{\partial y} = 0 \tag{5}$$

If the power-law profiles of equation (1) are assumed, the problem reduces to that of determining the free-stream velocity components v_{re} and $v_{\theta e}$; the boundary layer thickness, δ; the boundary layer profile exponents, m and n;

Nomenclature

a = speed of sound
A = area
c_f = skin friction coefficient
c_p = specific heat ratio at constant pressure
c_{pr} = pressure coefficient, $\dfrac{p-p_2}{p'_{2e}-p_2}$
F = entrainment function
h = diffuser half-width
H_1 = shape factor, $\dfrac{\delta-\delta_1}{\delta_2}$
H_2 = shape factor, $\dfrac{\delta_1}{\delta_2}$
m = exponent in radial velocity profile
$\dot{m}$ = mass flow
M = Mach number
n = exponent in tangential velocity profile
p = pressure
p_{STD} = standard pressure, 101,325 N/m
r = radius
R = dimensionless radial distance, $\dfrac{r-r_2}{r_3-r_2}$
R_g = gas constant
Re = Reynolds number
S = entropy
s = streamline distance
T = temperature
T_{STD} = standard temperature, 288.2K
v = velocity
y = coordinate normal to the wall
Y = dimensionless *y*-distance, y/h
α = flow angle from radial direction
γ = specific heat ratio
δ = boundary layer thickness
δ_{1r} = displacement thickness, $\displaystyle\int_0^\delta \left(1-\frac{v_r}{v_{re}}\right)dy$
δ_{1s} = displacement thickness, $\displaystyle\int_0^\delta \left(1-\frac{v}{v_e}\right)dy$
δ_{2r} = momentum thickness, $\displaystyle\int_0^\delta \frac{v_r}{v_{re}}\left(1-\frac{v_r}{v_{re}}\right)dy$
δ_{2s} = momentum thickness, $\displaystyle\int_0^\delta \frac{v}{v_e}\left(1-\frac{v}{v_e}\right)dy$
μ = coefficient of viscosity
ρ = density
τ = shear stress
ϕ = entropy function, $\displaystyle\int c_p \frac{dT}{T}$

Subscripts and Superscripts

c = centerline
cr = critical
e = edge of boundary layer
r = radial direction
R = reference condition
s = streamwise direction
w = wall
y = direction normal to the wall
θ = tangential direction
1 = compressor inlet
2 = vaneless diffuser inlet
3 = vaneless diffuser exit
$'$ = total conditions
$(\bar{\ })$ = mass-averaged conditions

and the free-stream thermodynamic properties, p, ρ, and T_e. Thus eight equations are required to completely solve the flow field. Three of these equations are obtained by integrating equations (2–4) through the boundary layer which results in the following

$$\int_0^\delta \frac{\partial(\rho v_r)}{\partial r}dy+\frac{1}{r}\int_0^\delta \rho v_r dy+\int_0^\delta \frac{\partial(\rho v_y)}{\partial y}dy=0 \tag{6}$$

$$\int_0^\delta \frac{\partial(\rho v_r v_y)}{\partial y}+\int_0^\delta \frac{\partial(\rho v_r^2)}{\partial r}dy-\frac{1}{r}\int_0^\delta \rho(v_\theta^2-v_r^2)dy$$
$$=-\delta\frac{\partial p}{\partial r}-\tau_{rw} \tag{7}$$

$$\int_0^\delta \frac{\partial(\rho v_r v_\theta)}{\partial r}dy+\int_0^\delta \frac{\partial(\rho v_y v_\theta)}{\partial y}dy$$
$$+\int_0^\delta \frac{2\rho v_r v_\theta}{r}dy=-\tau_{\theta w} \tag{8}$$

Equations (3, 4) can also be evaluated for the isentropic core flow. This results in the following two equations

$$\frac{dp}{dr}=-\rho v_{re}\frac{dv_{re}}{dr}+\rho\frac{v_{\theta e}^2}{r} \tag{9}$$

$$\frac{dv_{\theta e}}{dr}=-\frac{v_{\theta e}}{r} \tag{10}$$

From the boundary layer assumption, which is inherent in equation (5), the static pressure is constant across the channel and thus is a function of radius only.

The remaining three equations are obtained from channel continuity, the energy equation, and the equation of state. Channel continuity can be written

$$\dot{m}=2\rho v_{re}(2\pi r)(h-\delta_{1r}) \tag{11}$$

where for a power-law profile

$$\delta_{1r}=\frac{m}{1+m}\delta$$

Differentiating equation (11) with respect to the radius yields an expression for dv_{re}/dr. If the total temperature is assumed to be constant in the vaneless diffuser, which is true if there are no inlet normal gradients of total temperature, the energy equation for the core flow can be written

$$T_e=T'-\frac{v_e^2}{2c_p} \tag{12}$$

The final equation which completes the system is the equation of state for the core flow which is

$$p=\rho R_g T_e \tag{13}$$

One additional equation is needed to solve this system since an additional unknown is added in the integration of equations (2–4), i.e., the normal velocity at the edge of the boundary layer, v_{ye}. This can be modelled using Head's entrainment relation which empirically predicts the rate at which fluid from the free stream is entrained into the boundary layer. Head showed that the entrainment rate can be modelled as a function only of a boundary layer shape factor. Sumner and Shanebrook [8] extended the definition to three-dimensional compressible flow as follows

$$F=\frac{1}{v_e}\left(v_e\frac{d\delta}{ds}-v_{ye}\right)=0.0306(H_1-3)^{-0.653} \tag{14}$$

Finally, expressions for the wall shearing stresses can be given by

$$\tau_{rw}=\frac{\rho v_{re}^2}{\cos\alpha_e}\frac{c_f}{2} \tag{15}$$

$$\tau_{\theta w}=\frac{\rho v_{re}^2}{\cos\alpha_e}\tan\alpha_e\frac{c_f}{2} \tag{16}$$

where c_f is given by the Ludwieg–Tillman relation which is

$$c_f=0.246\,Re_{\delta 2r}^{-0.268}\left(\frac{T}{T^*}\right)e^{-1.561\,H_2} \tag{17}$$

Using the velocity profiles from equation (1) and performing the indicated differentiations and integrations, equations (6–8) and (11) can be combined to yield the following equations

$$\left[\left(1-\mathrm{M}_{re}^2\right)+2m(1+2m)\frac{\delta}{h}\right]\frac{1}{v_{re}}\frac{dv_{re}}{dr}$$
$$=-\frac{\mathrm{M}_{\theta e}^2+1}{r}-\frac{1}{h}\frac{dh}{dr}$$
$$+2m(1+2m)\frac{\delta}{h}\left[\frac{n(1+2m)}{m(1+2n)}\frac{\tan^2\alpha_e}{r}+\frac{c_f(1+2m)}{4m\delta\cos\alpha_e}\right]$$
$$-2m^2\frac{F}{h\cos\alpha_e} \tag{18}$$

$$\frac{dm}{dr}=m(1+m)(1+2m)\left[-\frac{2}{v_{re}}\frac{dv_{re}}{dr}\right.$$
$$+\frac{2n(1+2m)}{m(1+2n)}\frac{\tan^2\alpha_e}{r}$$
$$\left.+\frac{c_f(1+2m)}{2m\delta\cos\alpha_e}-\frac{F}{\cos\alpha_e}\right] \tag{19}$$

$$\frac{d\delta}{dr}=-\delta\left[(1-\mathrm{M}_{re}^2)\frac{1}{v_{re}}\frac{dv_{re}}{dr}+\frac{\mathrm{M}_{\theta e}^2+1}{r}\right]$$
$$+\frac{\delta}{1+m}\frac{dm}{dr}+\frac{(1+m)F}{\cos\alpha_e} \tag{20}$$

$$\frac{dn}{dr}=\frac{n}{1+m}\frac{dm}{dr}+\frac{(1+m+n)^2}{\delta\cos\alpha_e}\left[\frac{c_f}{2}-\frac{nF}{(1+m+n)}\right] \tag{21}$$

Equations (9), (10), and (18–21) can then be solved sequentially for the six unknowns (v_{re}, m, δ, n, p, and $v_{\theta e}$) using a fourth-order Runge–Kutta technique such as that described in [9]. Equation (18) is good only for symmetric vaneless diffusers with moderate wall curvatures and uniform core flows. However, equations (9), (10), and (19–21) are good for nonuniform core conditions and could be solved together with the equations describing the core flow as an interactive boundary layer problem. The above system of equations is also good for incompressible flow if the Mach numbers, M_{re} and $\mathrm{M}_{\theta e}$, are set equal to zero in equations (18) and (20).

A complete derivation of the final form of the continuity equation is described in the Appendix. The radial and tangential momentum equations are derived similarly.

Fully Developed Flow. The system of equations described in the previous section for boundary layer flow breaks down when the boundary layers on the two end walls meet in the center of the channel, i.e., when $\delta \geq h$. In this case, the flow is said to be fully developed and the velocity profiles are assumed to be as shown in Fig. 2(*b*).

The following assumptions are made for fully developed flow in addition to those already made for boundary layer flow:

1 The boundary layer equations (2–5) remain valid for fully developed flow;

2 the velocity profiles can be described by the power-law equations

$$\frac{v_r}{v_{rc}}=\left(\frac{y}{h}\right)^m;\ \frac{v_\theta}{v_{\theta c}}=\left(\frac{y}{h}\right)^n \tag{22}$$

where v_{rc}, $v_{\theta c}$, h, m, and n are functions of radius only;

3 analogous to fully developed, turbulent, pipe flow theory [10], the shear stress is assumed to vary linearly across the channel.

For fully developed flow, an isentropic core flow no longer exists. Therefore equations (9) and (10) are no longer valid. However, with the assumption of a linear variation of shear stress across the channel, equations (3) and (4) can be evaluated along the channel centerline which yields the equations

$$\frac{dp}{dr}=-\rho v_{rc}\frac{dv_{rc}}{dr}+\frac{\rho v_{\theta c}^2}{r}-\frac{\tau_{rw}}{h} \tag{23}$$

$$\frac{dv_{\theta c}}{dr}=-\frac{v_{\theta c}}{r}-\frac{1}{\rho v_{rc}}\frac{\tau_{\theta w}}{h} \tag{24}$$

where τ_{rw} and $\tau_{\theta w}$ are given by equations (15) and (16) and c_f is given by equation (17) with

$$\delta_{2r}=\frac{H_2-1}{H_2(H_2+1)}h$$

If the continuity equation is integrated across the vaneless diffuser half-width, the following equation results

$$\frac{d}{dr}\int_0^h \rho r v_r dy=0 \tag{25}$$

For the power-law profiles of equation (22), this becomes

$$\frac{1}{r}+\frac{1}{\rho}\frac{d\rho}{dr}+\frac{1}{v_{rc}}\frac{dv_{rc}}{dr}+\frac{1}{h}\frac{dh}{dr}-\frac{1}{1+m}\frac{dm}{dr}=0 \tag{26}$$

The radial momentum equation (3) can also be integrated across the diffuser half-width. This becomes, after using the results from equations (23) and (26) and the velocity profiles from equation (22)

$$\frac{dm}{dr}=-2m(1+m)(1+2m)\left[\frac{1}{v_{rc}}\frac{dv_{rc}}{dr}\right.$$
$$\left.-\frac{n(1+2m)}{m(1+2n)}\frac{\tan^2\alpha_c}{r}\right] \tag{27}$$

When the tangential momentum equation is integrated across the diffuser half-width, the following equation results

$$\frac{dn}{dr}=\frac{n}{1+m}\frac{dm}{dr}+\frac{(m+n)(1+m+n)}{\cos\alpha_c}\frac{c_f}{2h} \tag{28}$$

The density variation in the throughflow direction can be obtained from a combination of the equation of state and the energy equation. Then, using the above relations, the following equation for the variation of the centerline radial velocity component results.

$$\left[(1-M_{rc}^2)+2m(1+2m)\right]\frac{1}{v_{rc}}\frac{dv_{rc}}{dr}=\frac{-(M_{\theta c}^2+1)}{r}-\frac{1}{h}\frac{dh}{dr}$$
$$+\frac{2n(1+2m)^2}{1+2n}\frac{\tan^2\alpha_c}{r}+\left[(\gamma-1)\mathrm{M}_{\theta c}^2+\gamma\mathrm{M}_{rc}^2\right]\frac{c_f}{2h\cos\alpha_c} \tag{29}$$

Equation (29) together with equations (23), (24), (27), and (28) then forms a system of five ordinary differential equations in five unknowns (v_{rc}, $v_{\theta c}$, m, n, and p) which can be solved using a fourth-order Runge-Kutta technique.

Separated Flow. By examining equations (19) and (27), it can be seen that the radial velocity profile exponent, m, and therefore also the shape factor, H_2, will increase rapidly if there is a large rate of deceleration or if the flow angle becomes large. This usually means that flow separation is imminent. A large deceleration rate is caused by a rapid increase in flow area. A large flow angle can be the result of the impeller design but will more often be the result of a low mass flow rate through the compressor. In the latter case, a large flow separation may occur in the vaneless space which could precipitate compressor stall and subsequent surge of the system.

The methods outlined in the previous two sections for boundary layer flow and fully developed flow could be used to calculate through a separated region of the flow. However, if this were done, large values of the velocity profile exponent, m, would be calculated which would result in unrealistic velocity profiles. A possible way of treating this problem would be to assume a constant value for the exponent, m, after separation. Separation could be determined by examining the shape factor, H_2, or the skin friction coefficient, c_f. The problem could then be treated in the inverse mode using either equation (19) for boundary layer flow or equation (27) for fully developed flow to determine the variation of free-stream radial velocity. However, since power-law profiles cannot describe negative velocities which occur when the flow separates, it would probably be necessary to use some other formulation for the separated flow problem.

Initial Conditions. In order to solve equations (9), (10), and (18-21) for boundary layer flow, initial values for the six variables (p, δ, v_{re}, $v_{\theta e}$, m, and n) must be specified. The value of the static pressure can be obtained from experimental data or from an analysis of the impeller flowfield. In the latter case, the pressure could be obtained from the equation

$$p=p_1 e^{\frac{\phi-\phi_1-\Delta S}{R_g}} \tag{30}$$

The entropy rise, ΔS, in equation (30) should include the entropy rise due to the mixing of the impeller blade surface boundary layers, wakes, and any other losses which are assumed to affect the impeller core flow.

The values of δ and m can only be obtained from an analysis of the impeller end-wall boundary layers. Ordinarily the value of m should be on the order of 0.2 or 0.3 if there is no great deceleration of the meridional velocity component in the impeller. However, δ will probably be a significant portion of the impeller exit half-width.

If the compressor mass flow is specified, the core flow radial velocity component can then be calculated from equation (11). However, the core flow tangential velocity component and corresponding velocity profile exponent are more difficult to determine. A boundary layer analysis of the impeller would give values for the relative tangential velocity component and its corresponding exponent. However, as the fluid moves from the relative frame of reference of the impeller (assuming a shrouded impeller) to the absolute frame of the vaneless diffuser, a large shear occurs on the fluid as it attempts to decelerate from a velocity near the wheel speed to zero near the end walls. Thus, it is impossible to model the velocity profile in this region by a power law. Experimental data do show, however, that a velocity profile that can be approximated by a power law is quickly established. Experimental data also show [4] that an exponent of $n = 0.1$ adequately describes the tangential boundary layer at the vaneless diffuser inlet. The core flow tangential velocity component can then be obtained from a conservation of tangential momentum analysis. In any event, the initial values of the exponents, m and n, do not have a large effect on the final solution.

For the case of fully developed flow entering the vaneless diffuser, the same variables must be specified as for the boundary layer case with the exception of the boundary layer

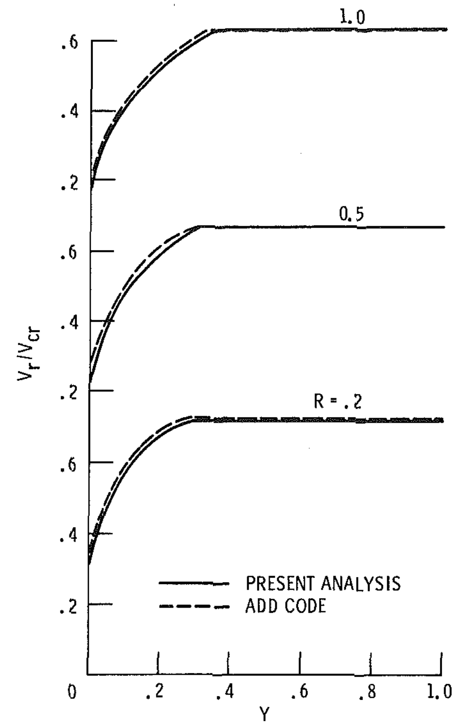

Fig. 3(a) Case I: boundary layer flow; α_{2e} = 0 deg

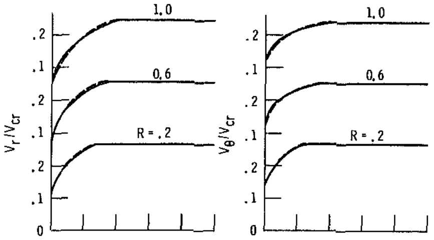

Fig. 3(b) Case II: boundary layer flow; α_{2e} = 45 deg

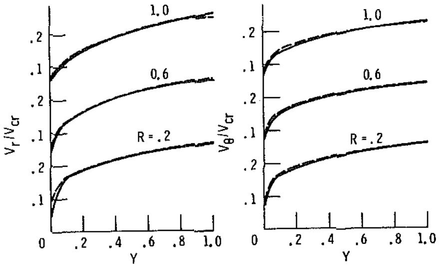

Fig. 3(c) Case III: fully developed flow; α_{2e} = 45 deg

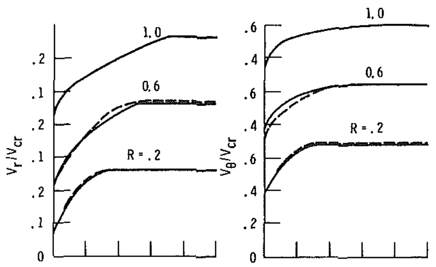

Fig. 3(d) Case IV: boundary layer flow; α_{2e} = 70 deg

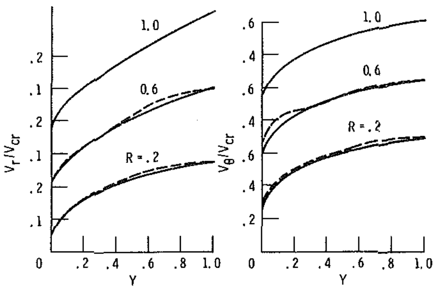

Fig. 3(e) Case V: fully developed flow; α_{2e} = 70 deg

Fig. 3 Velocity profile comparisons with results from ADD code

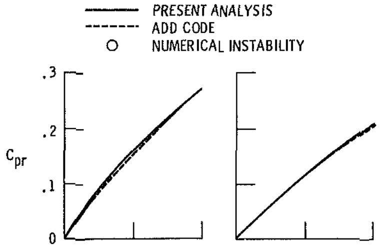

(a) Case I. (b) Case II.

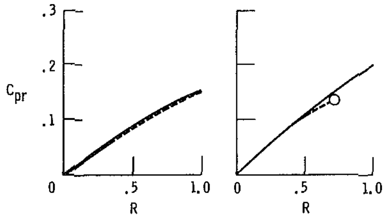

(c) Case III. (d) Case IV.

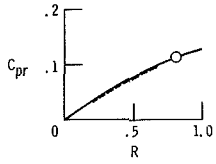

(e) Case V.

Fig. 4 Static pressure coefficient comparison with ADD code

thickness (which is equal to the diffuser half-width, h). For this case, the value of ΔS in equation (30) should also include the additional core flow loss due to a nonzero shear stress gradient at the centerline. The values of the other variables are then calculated in the same way as for boundary layer flow.

Loss Calculation. The loss in a vaneless diffuser can be expressed most easily and most rigorously by an increase in the mass-averaged entropy of the fluid. The mass-averaged entropy at a specified radius in the vaneless diffuser can be expressed

$$\overline{(S-S_{2e})}=\frac{2\rho\int_0^\delta (S-S_{2e})v_r(2\pi r)\,dy}{\dot m} \qquad (31)$$

where the local entropy is given by

$$S-S_{2e}=c_p\ln\frac{\dfrac{T}{T_{2e}}}{\left(\dfrac{p}{p_2}\right)^{\frac{\gamma-1}{\gamma}}} \qquad (32)$$

The entropy rise through the diffuser can then be expressed

$$\overline{(S_3-S_2)}=\overline{(S-S_{2e})}_3-\overline{(S-S_{2e})}_2 \qquad (33)$$

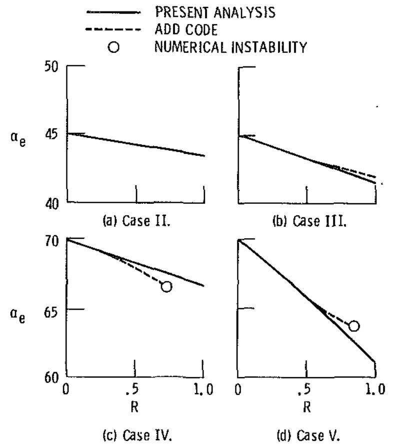

Fig. 5 Centerline flow angle comparison with ADD code

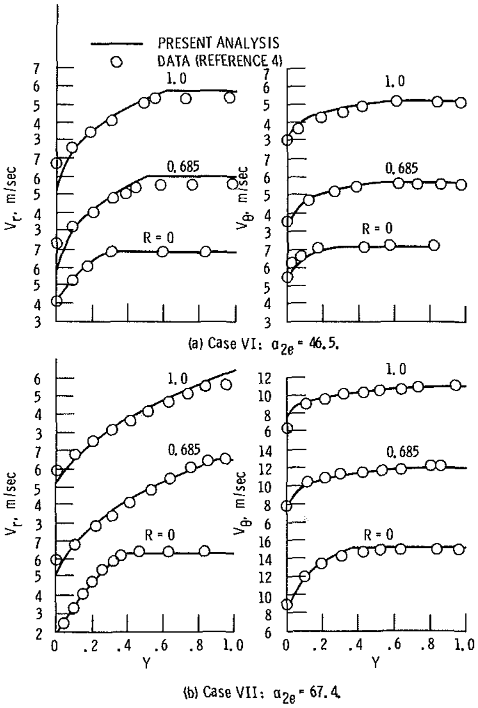

Fig. 6 Velocity profile comparisons with data from [4]

where the values of $(S - S_{2e})_2$ and $(S - S_{2e})_3$ are obtained by a numerical integration of equation (32) across the boundary layer. Since the total temperature in the vaneless diffuser is assumed to be constant everywhere, the mass-averaged total pressure ratio can be expressed

$$\frac{\overline{p_3'}}{\overline{p_2'}} = e^{-\frac{\overline{(s_3 - s_2)}}{R_g}} \tag{34}$$

Comparison With Results From a Three-Dimensional Viscous Diffuser Duct Code

The results from this analysis have been compared to the results from a three-dimensional viscous diffuser duct code (the ADD code, [7]) and are shown in Figs. 3-5 for the five test cases listed in Table 1. The ADD code solves the three-dimensional equations of motion for an axisymmetric duct. The equations are parabolized by making the boundary layer assumption, i.e., that the velocities in the normal direction are small compared to those in the throughflow direction.

Figure 3(*a*-*e*) shows comparisons between the velocity profiles predicted by the ADD code and those predicted by the above analysis for a parallel wall diffuser with varying inlet conditions. In all cases, the agreement is good. The largest discrepancies are near the edge of the boundary layer where there is a discontinuity in the slope of the profiles predicted by the present analysis due to the power-law assumption. It should also be noted that the agreement between the centerline velocity components, boundary layer thicknesses, and profile shapes (i.e., profile exponents) is good in all cases.

Table 1 **Five tests cases for comparison of analysis to results from the ADD code (parallel wall diffusers—$r_2 = 8.049$ cm, $r_3/r_2 = 1.1605$, $h/r_2 = 0.03329$, $T'/T_{STD} = 1$)**

Inlet conditions							
Case	δ/h	m	n	p/p_{STD}	v_{re}/v_{cr}	$v_{\theta e}/v_{cr}$	α_e
I	0.2400	0.2	0.2	0.7087	0.7498	0	0
II	.2400	.2	.2	.9172	.2705	0.2705	45
III	.9556	.2	.2	.9172	.2705	.2705	45
IV	.2400	.2	.2	.7009	.2603	.7151	70
V	.9556	.2	.2	.7009	.2603	.7151	70

Table 2 **Two test cases for comparison with data from [4] (parallel wall diffusers – $r_2 = 17.64$ cm, $r_3/r_2 = 1.377$, $h/r_2 = 0.0605$, $T'/T_{STD} = 1$)**

Inlet conditions							
Case	δ/h	m	n	p/p_{STD}	v_{re}, m/sec	$v_{\theta e}$, m/sec	α_e
VI	0.288	0.2	0.1	1	6.83	7.19	46.5
VII	.360	.5	.2	1	6.35	15.24	67.4

In Figs. 3(*d*) and 3(*e*), the velocity profiles at $R = 1$ are not displayed for the ADD code calculation. The reason for this is that, in both cases, a numerical instability occurred in the ADD code at a value of $R \approx 0.8$ which caused the calculation to stop at that point.

Figure 4 shows a comparison of the static pressure coefficient variation with radius for the five cases listed in Table 1. Figure 5 shows a comparison of the centerline flow angle variation with radius for cases II-V. For both the static pressure coefficient and centerline flow angle variations, the agreement is good in both magnitude and distribution.

Comparison With Experimental Data

The results from this analysis have been compared to the experimental data of Jansen [4]. Figures 6(*a*) and 6(*b*) show a comparison of the velocity profiles predicted by the present analysis with the measured profiles of Jansen for two essentially incompressible flow cases with differing swirl angles. The inlet conditions for these two cases are shown in Table 2. In both cases, the agreement with experiment is good. No data could be found in the literature which could be used to check the method at transonic Mach numbers.

Conclusion

An analytical method is proposed to calculate the three-dimensional axisymmetric turbulent flow field in a radial, vaneless diffuser. Results using the method show good agreement with the results from a more complex three-dimensional viscous parabolic marching code (ADD code) and with experimental data. The results show good agreement.

Although the present analysis is only valid for symmetric vaneless diffusers with uniform core flows, the method can easily be extended to asymmetric flows if each end-wall boundary layer is treated separately and the problem is treated as an interative boundary layer problem. Also, although compressibility is accounted for only in the radial direction, the fully compressible case could be accounted for approximately by including additional terms for the density variation in the direction normal to the throughflow direction.

Since the method is a noniterative integral method, it is very fast compared to more complex finite difference methods.

Thus, it can be easily adapted for use in preliminary design or off-design codes.

References

1 Stanitz, J. D., "One-Dimensional Compressible Flow in Vaneless Diffusers of Radial and Mixed-Flow Centrifugal Compressors, Including Effects of Friction, Heat Transfer, and Area Change," NACA TN-2610, 1952.

2 Dean, R. C., Jr., and Senoo, Y., "Rotating Wakes in Vaneless Diffusers," *Journal of Basic Engineering*, Vol. 82, No. 3, Sept. 1960, pp. 563-574.

3 Johnston, J. P., and Dean, R. C., Jr., "Losses in Vaneless Diffusers of Centrifugal Compressors and Pumps," ASME JOURNAL OF ENGINEERING FOR POWER, Vol. 88, No. 1, Jan. 1966, pp. 49-62.

4 Jansen, W., "Steady Fluid Flow in a Radial Vaneless Diffuser," *Journal of Basic Engineering*, Vol. 86, No. 3, Sept. 1964, pp. 607-619.

5 Senoo, Y., Kinoshita, Y., and Ishida, M., "Asymmetric Flow in Vaneless Diffusers of Centrifugal Blowers," *Journal of Fluids Engineering*, Vol. 99, No. 1, Mar. 1977, pp. 104-114.

6 Davis, W. R., "Three-Dimensional Boundary-Layer Computation on the Stationary End-Walls of Centrifugal Turbomachinery," *Journal of Fluids Engineering*, Vol. 98, No. 3, Sept. 1976, pp. 431-442.

7 Anderson, O. L., Hankins, G. B., and Edwards, D. E., "User's Manual for Axisymmetric Diffuser Duct (ADD) Code, Vols. I-III," UTRC81-65-Vol-1;-Vol-2;-Vol-3, United Technologies Corp., East Hartford, CT, Feb. 1982 (NASA CR-165598).

8 Sumner, W. J., and Shanebrook, J. R., "Entrainment Equation for Three-Dimensional, Compressible, Turbulent Boundary Layers," *AIAA Journal*, Vol. 10, No. 5, May 1972, pp. 693-694.

9 White, F. M., *Viscous Fluid Flow*, McGraw-Hill, 1974.

10 Schlicting, H., *Boundary-Layer Theory*, 6th ed., McGraw-Hill, 1968.

11 De Ruyck, J., and Hirsch, C., "Investigations of an Axial Compressor End-Wall Boundary Layer Prediction Method," ASME JOURNAL OF ENGINEERING FOR POWER, Vol. 103, No. 1, Jan. 1981, pp. 20-33.

APPENDIX

Detailed Derivation of the Final Form of the Continuity Equation. In order to be able to calculate the vaneless diffuser flow field, equations (6-8) must be recast as ordinary differential equations. The continuity equation will serve as an example of how this is done. Also, the continuity equation shows how the entrainment function is used in the derivation. If Leibnitz' rule is used to interchange differentiation and integration, equation (6) becomes

$$\frac{1}{\rho v_{re}}\frac{d}{dr}\int_0^{\delta}\rho v_r dy+\frac{1}{r}\int_0^{\delta}\frac{v_r}{v_{re}}dy=\frac{1}{v_{re}}\left(v_{re}\frac{d\delta}{dr}-v_{ye}\right) \qquad (35)$$

The term on the right-hand side of equation (35) is Head's entrainment function, F, and will be evaluated later. Since the density is assumed to be a function of radius only, it comes out of the integral and the integrals can be evaluated for the power-law profiles of equation (1) which results in the following equation

$$\frac{1}{\delta}\frac{d\delta}{dr}+\frac{1}{v_{re}}\frac{dv_{re}}{dr}+\frac{1}{\rho}\frac{d\rho}{dr}+\frac{1}{r}-\frac{1}{1+m}\frac{dm}{dr}=\frac{F(1+m)}{\cos\alpha_e} \qquad (36)$$

This is the form desired except for the density term. The density variation can be expressed in terms of the pressure variation for the isentropic core flow as follows

$$\frac{d\rho}{dr}=\frac{1}{a^2}\frac{dp}{dr} \qquad (37)$$

Combining this with equation (9) then yields

$$\frac{1}{\rho}\frac{d\rho}{dr}=-\frac{\mathrm{M}_{re}^2}{v_{re}}\frac{dv_{re}}{dr}+\frac{\mathrm{M}_{\theta e}^2}{r} \qquad (38)$$

The final form of the continuity equation then becomes

$$\frac{1}{\delta}\frac{d\delta}{dr}+\frac{(1+\mathrm{M}_{re}^2)}{v_{re}}\frac{dv_{re}}{dr}+\frac{1+\mathrm{M}_{\theta e}^2}{r}-\frac{1}{1+m}\frac{dm}{dr}=\frac{1+m}{\delta}\frac{F}{\cos\alpha_e} \qquad (39)$$

Using similar techniques, the radial and tangential momentum equations can also be reduced to ordinary differential equations.

The entrainment function, F, is given by equation (14). The shape factor, H_1, is defined by the expression

$$H_1=\frac{\delta-\delta_{1S}}{\delta_{2S}} \qquad (40)$$

De Ruyck and Hirsch [11] approximated this using the radial velocity components in the definitions of δ_1 and δ_2, thus

$$H_1=\frac{\delta-\delta_{1r}}{\delta_{2r}} \qquad (41)$$

Although DeRuyck and Hirsch stated that equation (41) is good only for small angles, α, Davis [6] shows that the radial thicknesses, δ_{1r} and δ_{2r}, are the proper thicknesses to use in the definition of H_1 for use in the entrainment function. Using the power-law profiles of equation (1) in the definition of δ_{1r} and δ_{2r}, the shape factor, H_1, then becomes

$$H_1=\frac{1+2m}{m} \qquad (42)$$

and finally the entrainment function, F, becomes

$$F=0.0306\left(\frac{m}{1-m}\right)^{0.653} \qquad (43)$$

J. Ishii
Gas Turbine Design Section,
Toshiba Corporation,
Tsurumi, Yokohama, 230
Japan

S. Honami
Mem. ASME
Mechanical Engineering Department,
Science University of Tokyo,
Shinjuku, Tokyo, 162
Japan

A Three-Dimensional Turbulent Detached Flow With a Horseshoe Vortex

Static and dynamic mechanisms in a three-dimensional, turbulent, detached flow with a horseshoe vortex, which is encountered in turbomachinery, are clarified experimentally. Flow directional intermittency is obtained by a thermal tuft probe and wall pressure fluctuation survey is performed. Flow visualization is also made by the oil film and smoke wire technique. Four types of vortices exist in the detached region. These vortices are generated by the different process. The detached region is divided into two parts: the region I and II. The flow in the region II, including the detachment point, has dynamic characteristics with low-frequency fluctuation. A new flow model in the detached region is proposed.

Introduction

An important problem that arises in the design of modern gas turbines and in the advancement of their performance is to understand the nature and flow mechanism of secondary flow in gas turbine passages. Currently used design methods for the passage are mostly based on a two-dimensional flow analysis. However, these methods have the limit of their use, since the flow is three-dimensional and complex in a turbomachine. In practice, inevitable drop in aerodynamic performance due to the secondary flow in a turbine blade cascade with a low aspect ratio was demonstrated by Langston et al. [1]. A compressor performance in a turbofan engine is deteriorated by a so-called horseshoe vortex, which occurs around the base of a strut. Moreover, it has been shown by many workers that it is necessary to investigate the secondary flow in detail in order to further improve the performance of turbomachinery [2-4]. Information about the secondary flow loss is provided, and the difference between the actual flow and the two-dimensional flow often assumed in the blade design is discussed. However, these investigations are not sufficient to cover every aspect of the flow mechanisms of the secondary flow, i.e., a horseshoe vortex and a passage vortex, which cause the losses. Furthermore, a cooling system at a blade-endwall junction has become an important subject in connection with an inlet temperature rise in a modern gas turbine, because a very high rate of heat transfer was encountered at the junction [5, 6].

The horseshoe vortex and the passage vortex at the junction between the endwall and the blade or the strut are known as the unavoidable secondary flow in turbomachinery as shown in Fig. 1. Understanding flow mechanism and characteristics of the three-dimensional turbulent detached region associated with the horseshoe vortex is very important in order to suppress the secondary flow by means of restraint and control of the vortex movement. The design technique which makes a gas turbine performance high should be established by the advanced understanding of the secondary flow behavior. However, mechanisms of the flow field previously mentioned have not been investigated often [7, 8]. Both the structure of the three-dimensional turbulent detached flow with the horseshoe vortex and the process of the vortex generation are not yet clear in detail.

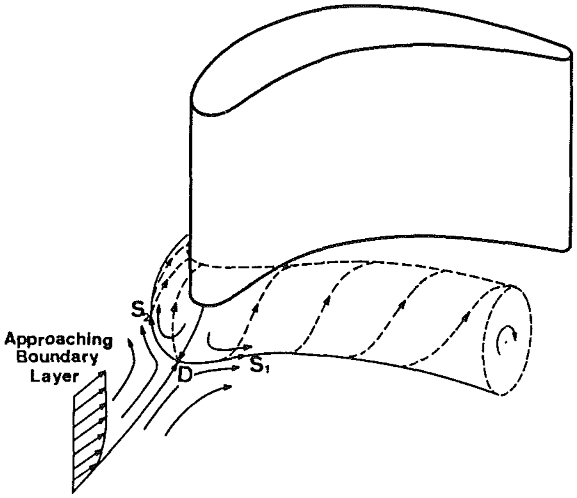

Fig. 1 Horseshoe vortex and passage vortex in turbomachinery: D, singular detachment point; S_1-S_2, separation line

The objective of the present paper is to clarify experimentally the static and dynamic mechanisms in a three-dimensional turbulent detached flow with a horseshoe vortex that is encountered at the leading edges of turbomachinery blades as an example.

Contributed by the Gas Turbine Division of THE AMERICAN SOCIETY OF MECHANICAL ENGINEERS and presented at the 30th International Gas Turbine Conference and Exhibit, Houston, Texas, March 18-21, 1985. Manuscript received at ASME Headquarters, December 21, 1984. Paper No. 85-GT-70.

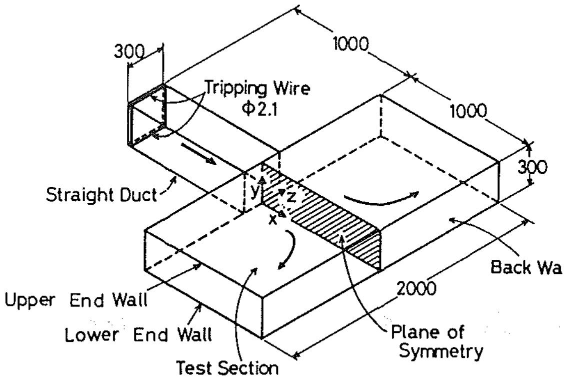

Fig. 2 Experimental apparatus (dimensions in mm)

Table 1 Boundary layer integral parameters at reference point

Boundary layer thickness, δ_{99}	20.30	mm
Momentum thickness, θ	2.25	mm
Shape factor, $H_{12} = \delta^*/\theta$	1.40	
Skin friction coefficient, $Cf/2$	0.00173	

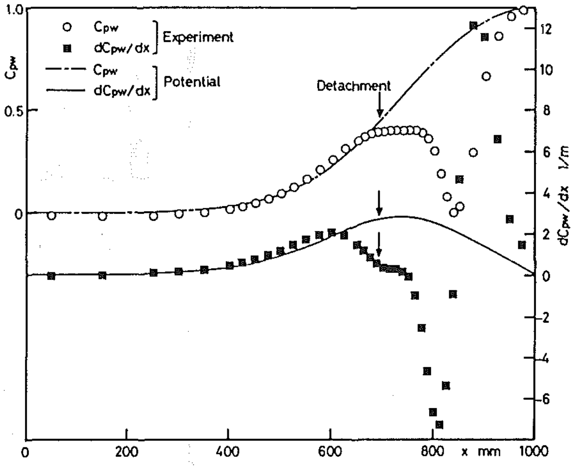

Fig. 3 Wall static pressure parameters: pressure coefficient and pressure gradient

Experimental Apparatus and Technique

Figure 2 shows an experimental test rig. The simple shape of the test rig was chosen to simulate the three-dimensional detached flow on the endwall near the leading edge as shown in Fig. 1. The test rig arrangement provides the same type of the flow field at the junction of the endwall and the blade leading edge in a turbomachine. As a result, three-dimensional detachment with a horseshoe vortex can be understood easily by using a plane back wall with zero curvature as a leading edge, though surface curvature of the actual blade at the leading edge has a finite value.

The new test rig with a large scale is the same shape as the old one reported by Ishii and Honami [8], but is newly designed to improve space resolution in measurements and reduce an interference of horseshoe vortices on the upper and lower endwalls which occur in detached regions ahead of a back wall. It consists of a test section and a straight duct with a square cross section. The inlet free-stream velocity at a reference point ($x = -100$ mm, $z = 0$ mm) was 20 m/s (± 1 percent) with the turbulence intensity of 0.2 percent. The momentum thickness Reynolds number of the boundary layer for the test was 2900. The boundary layer integral parameters at the reference point are shown in Table 1. A natural frequency of the lower wall at the test section was 33.9 Hz from a free oscillation measurement using an acceleration pickup sensor, when the flow was turned off.

The flow proceeds as a confined jet between the upper and lower endwalls and impinges on the back wall. The back wall causes the jet to diverge symmetrically with respect to the plane of symmetry which corresponds to a hatched portion in Fig. 2. A three-dimensional turbulent boundary layer develops on the endwall and is detached ahead of the back wall. The horseshoe vortex formed downstream of the detachment point trails toward the spanwise z-direction. This flow situation is clearly the case of surface mounted obstacles in boundary layers which introduce the horseshoe vortex.

The oil film and smoke wire techniques for flow visualization were used in the present experiment. Wall static pressure fluctuations were measured by use of a diffusion type of a semiconductor pressure transducer (Toyoda Machine Works Ltd., Model PD-104K-0.1F). The resolution in pressure is 1.0 Pa. The fraction of the time γ_p that the flow is in the downstream direction and flow reversal fluctuations were obtained by a wall thermal tuft probe [9] whose sensor was fixed at 1 mm from the lower endwall. But a newly devised circuit of the thermal tuft probe was used to improve the drift and noise characteristics [10]. Both the pressure transducer and the thermal tuft probe were flush-mounted on the lower endwall. The data except for flow visualization by the oil film technique were confined to measurements on the plane of symmetry.

Results and Discussions

Wall Static Pressure Parameters. Figure 3 shows mean wall static pressure coefficient *Cpw* and the pressure gradient *dCpw/dx* by using a cubic spline, data-smoothing program. The results of the potential flow analysis are also shown in the figure. *Cpw* and *dCpw/dx* show the similar distributions to those of the potential flow analysis upstream of the detachment point, which was decided by the thermal tuft measurement that will be discussed later in detail. The flow upstream of the detachment point is governed by an adverse pressure gradient ($dCpw/dx > 0$). The characteristics of *Cpw* downstream of the detachment point show a maximum and a minimum. In a flow around a cylinder mounted on a flat plate given by Baker [7] and a blade-endwall junction reported by Dechow [11], the distributions of the static pressure coef-

Nomenclature

Cpw = wall static pressure coefficient $(p - p_{\text{ref}})/(\rho/2)\, U_{\text{ref}}^2$
f = frequency
G = power spectrum density
p = wall static pressure
Tr = flow reversing time
t = time
t_s = delay time in smoke wire technique
U = free-stream velocity
x,y,z = coordinate direction, Fig. 2
x_w = smoke wire location
γ_p = fraction of the time that flow is in the downstream direction
ρ = density
ρ^* = cross-correlation coefficient

Subscripts

d = detachment
ref = reference point

Superscripts

$'$ = instantaneous value

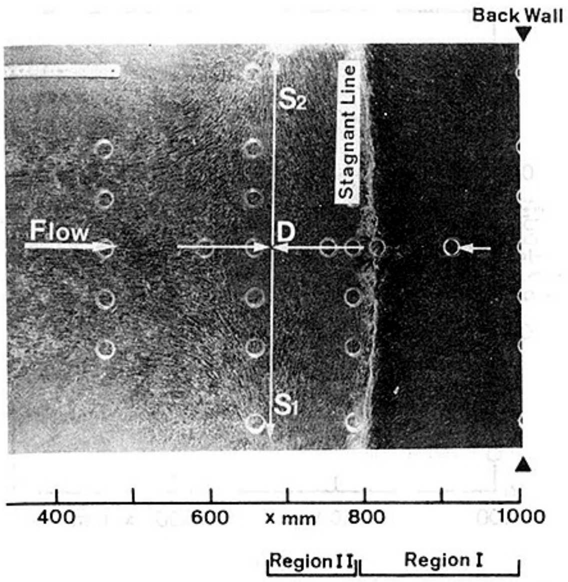

Fig. 4 Flow visualization of lower endwall surface by oil film technique

ficient have the same tendency. Therefore, the present flow feature has the same characteristics of the three-dimensional detached flow with the horseshoe vortex. The *Cpw* distribution, however, has a considerably large dip after detachment and is different from the other studies. This difference is introduced by curvature of the impinging back wall. Because curvature of the back wall is zero in the present study, the divergence rate of the flow with respect to a plane of symmetry, i.e., three-dimensional effect, is larger than that in the other studies. The pressure gradient $dCpw/dx$ exhibits a maximum value before the detachment and decays rapidly thereafter indicating a very small negative minimum value. The minimum value of the pressure gradient is caused by the very small minimum value of *Cpw*.

Flow Visualization. Figure 4 shows the flow visualization result on the lower endwall by the oil film technique. Since the three-dimensional effect of the flow is directly related to the pressure gradient, the skewness of the flow is generated downstream of the point where the pressure gradient starts to rise. According to the comparison of the result by the oil film technique with the wall static pressure distributions shown in Fig. 3, the aforementioned flow situation is clearly observed.

It can be determined by the oil film pattern that the singular detachment point on the plane of symmetry is located near $x = 675$ mm ± 10 mm (shown as a point D in the figure). The separation line is traced along the spanwise z-direction and across the singular detachment point (line S_1–S_2). The detachment point D and the separation line S_1–S_2 in Fig. 4 correspond to those at the leading edge in Fig. 1. The reverse flow occurs downstream of the separation line and the oil near $x = 815$ mm seems stagnant at a width of 10 mm hereafter named "a stagnant line" as shown in Fig. 4. The oil moves slightly in the negative x-direction at the region between the separation line and the stagnant line. On the other hand, the oil is swept away from the back wall to the stagnant line. It suggests that the negative wall shear stress is quite large. According to the foregoing results and the other results indicated later, it is obvious that the detached region can be divided into two parts (as the flow behavior varies at the stagnant line): the region from the stagnant line to the back wall and the region between the singular detachment point and the stagnant line. The former is defined as the region I and the latter as the region II in the present paper.

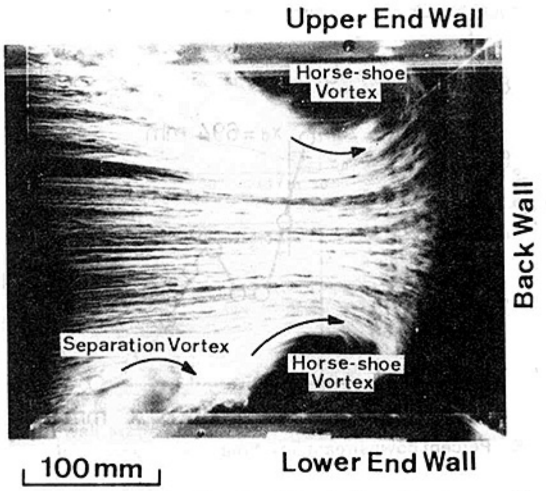

Fig. 5(*a*) Flow visualization in detached region by smoke wire technique (side view): smoke wire location $x_w = 650$ mm; delay time $t_s = 12.4$ ms (arrow indicates the direction of vortex rotation)

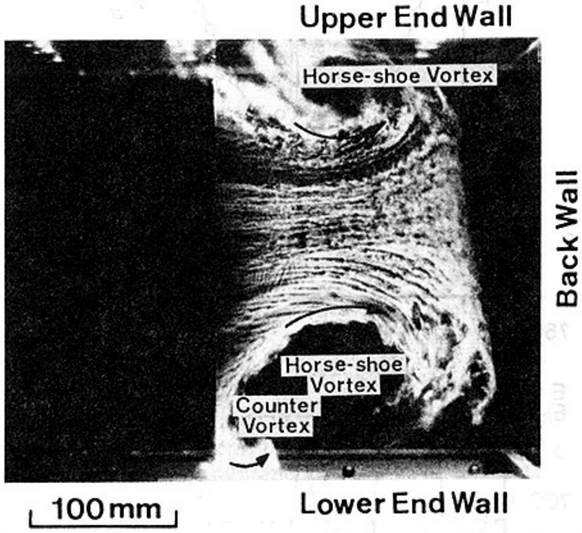

Fig. 5(*b*) Flow visualization in detached region by smoke wire technique (side view): smoke wire location $x_w = 775$ mm; delay time $t_s = 10.0$ ms (arrow indicates the direction of vortex rotation)

The typical photos in the detached region by the smoke wire technique are illustrated in Fig. 5. The existence of two types of vortices reported by Ishii and Honami [8], i.e., horseshoe vortex and the separation vortex, is confirmed in Fig. 5(*a*). The horseshoe vortex with a large scale can be observed as a primary vortex just ahead of the back wall. On the other hand, the separation vortex is formed by a roll-up of the wall shear layer. It is also verified by the oil film flow pictures that these two types of vortices have the different characteristics. Moreover, since a free-stream region clearly exists, no interference between the horseshoe vortices on the upper and lower endwalls occurs. After examining a large number of photos, the horseshoe vortex changes location in x-direction and the variation in size is not so remarkable. The separation vortex moves only within a narrow region in x-direction. The vortex centers of the horseshoe vortex and the separation vortex exist at $x = 850$ mm and 750 mm, respectively. Because of no interference of the vortices on the upper and lower endwalls, the dynamic behavior of the present flow field indicates the essential feature of the three-dimensional turbulent detachment with the horseshoe vortex.

It is worthwhile to notice that both the interaction of the horseshoe vortex and the separation vortex and the existence of a relatively small counterrotating vortex to the horseshoe

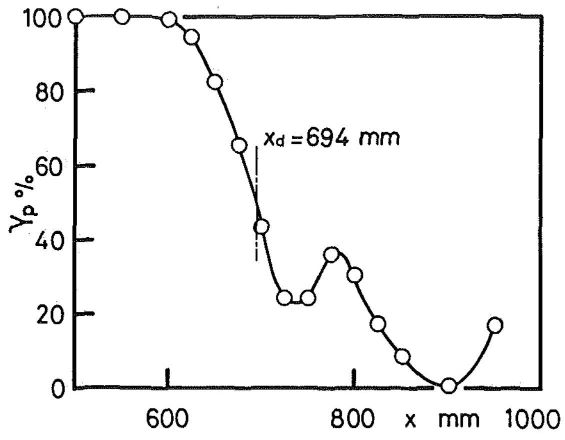

Fig. 6 Percent downstream flow time γ_p on the plane of symmetry

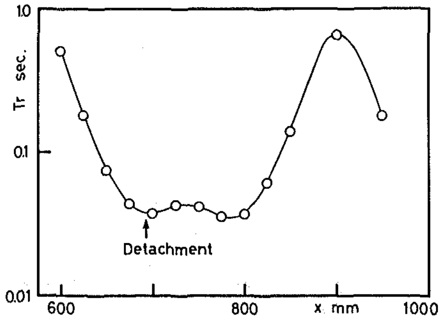

Fig. 7 Flow reversing time Tr on the plane of symmetry

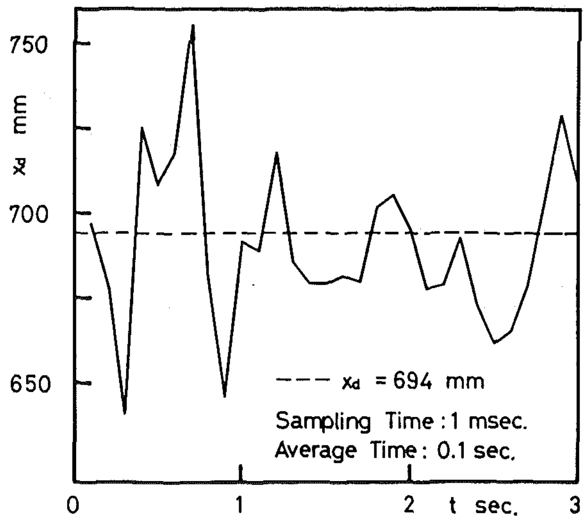

Fig. 8 Shift of the short-time average (0.1 s) detachment point

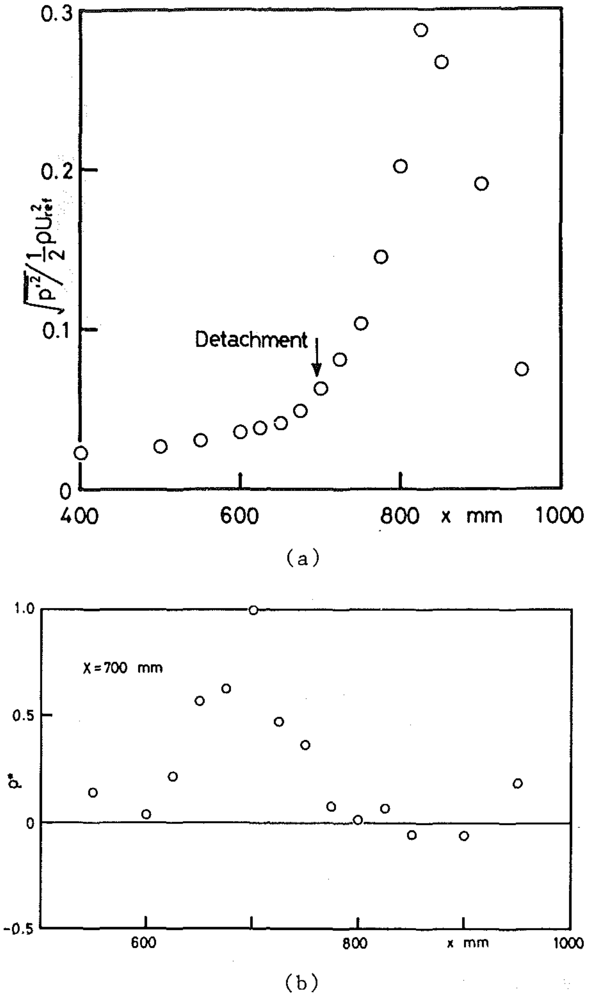

Fig. 9 Wall static pressure fluctuations: (*a*) RMS values; (*b*) cross-correlation coefficient

vortex and the separation vortex are confirmed in Fig. 5(*b*). The counter vortex is formed by the horseshoe vortex. However, the counter vortex is not always observed in a large number of flow visualization photographs and iterates generation and disappearance.

The Percent Downstream Flow Time and the Flow Direction Fluctuations. Figure 6 shows the distributions of the fraction of the time γ_p that the flow is in the downstream direction measured at $y = 1.0$ mm from the lower endwall by the thermal tuft probe. The averaging time of the output signal was 128 s. A time mean detachment point in the two-dimensional flow can be defined as a location where γ_p is 50 percent [9, 12]. Even in the case of three-dimensional turbulent detachment, the singular detachment point may be decided by extension of the two-dimensional flow definition [13]. Accordingly, the present singular detachment point on the plane of symmetry is located at $x = 694$ mm. The change of γ_p near the singular detachment point is abrupt. It indicates that the present three-dimensional turbulent detached flow has a more rapid detachment process than the two-dimensional cases.

The local increase of γ_p near $x = 775$ mm reconfirms the existence of a counter vortex indicated by the smoke wire photo. Moreover, γ_p is almost zero at $x = 900$ mm in the region I. It shows that the steady reverse flow of the horseshoe vortex exists in this region. Farther downstream, increase at $x = 950$ mm is caused by a corner vortex at the corner of the back wall and endwall. The existence of the corner vortex is also confirmed by the smoke wire photo in Fig. 5(*b*), which shows no smoke at the corner. Thus the distribution of γ_p of this type of flow is very complex and different from those of the two-dimensional detached flow where it decreases monotonously [14, 15]. It is obvious that the flow field of the three-dimensional detached region has not a simple structure of a single separation bubble but a multiple structure with the plural vortices.

Figure 7 shows the time mean flow reversing time Tr evaluated from the output signals of the thermal tuft probe. Tr decreases rapidly near the detachment point and shows a minimum value at the detachment point. In region II, Tr increases somewhat from the detachment point to the separation vortex at $x = 750$ mm and decreases again in-

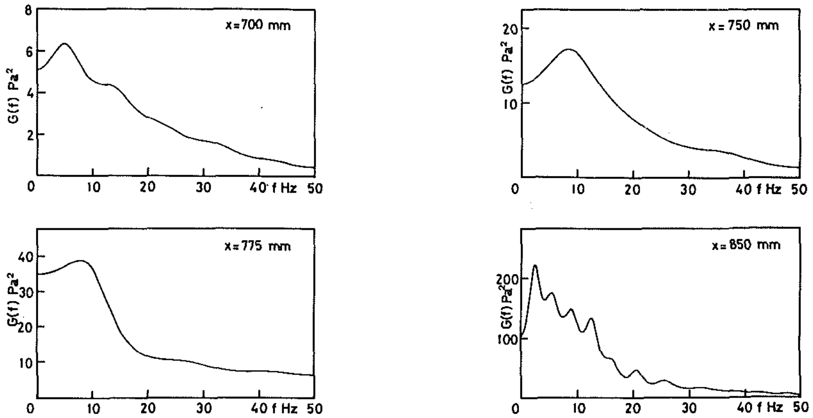

Fig. 10 Power spectrum density distributions of wall static pressure fluctuations in detached region

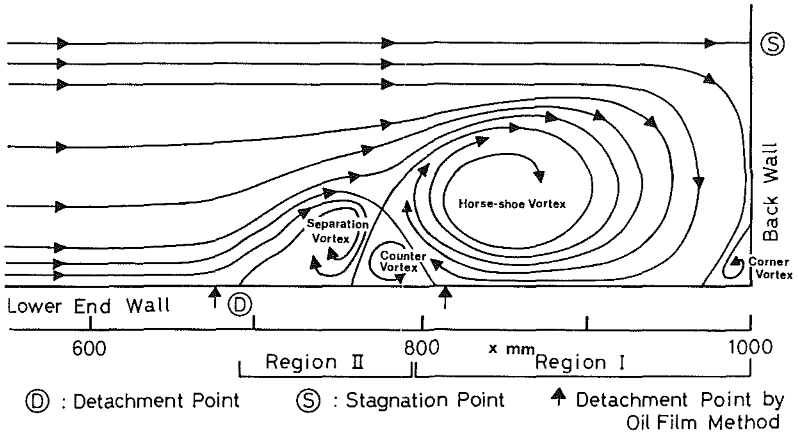

Fig. 11 New flow model of three-dimensional turbulent detached region on the plane of symmetry

dicating a little smaller value than that at the detachment point. This drop corresponds to the local increase of γ_p in Fig. 6. It is conceivable that Tr shows inherently a minimum at the detachment point. However, Tr at $x = 775$ mm and 800 mm indicates an almost equal value to that of the detachment point, nevertheless γ_p is 30 or 40 percent there. It shows that the counter vortex might not stay continuously but iterates generation and disappearance. The value of Tr is a maximum at $x = 900$ mm in the region I, where γ_p indicates almost zero. Farther downstream, decrease at $x = 950$ mm is caused by the corner vortex at the corner of the back and endwall.

Short-time averages of thermal tuft data were employed to clarify the dynamic behaviors of the detachment point, i.e., the unsteady movement. Shifts of a short-time averaged detachment point were obtained by use of three thermal tuft probes. The experimental procedure is similar to the previous measurements on the reattachment point in a two-dimensional backward-facing step flow [9], except a sample rate of 1 ms and a short-time average of 0.1 s interval is used. One of the records is shown in Fig. 8. The short-time averaged detachment point varies from about 640 mm to 760 mm around the time mean detachment point at $x = 694$ mm. Detachment point movement in up-and-downstream directions are introduced by a very complicated mechanism. The record of Fig. 8 and the other records show that the detachment point seems to move around the time mean detachment point for a relatively long period and shift intermittently by a large scale motion.

Wall Static Pressure Fluctuations. Figure 9(*a*) shows the distributions of the RMS values of the wall static pressure fluctuations. The RMS value in an attached boundary layer, where γ_p equals 100 percent, is almost constant. Downstream of 600 mm with the instantaneous flow reversal, the RMS value increases gradually. The value exhibits a noticeable increase in the region I and a peak in the horseshoe vortex.

The wall static pressure fluctuations are amplified by the increase in turbulence near the endwall in the region II, which is caused by the roll-up of the wall shear layer and the entrainment of the fluid outside the shear layer. On the other hand, the RMS value has a maximum in the region I, nevertheless *Cpw* changes very rapidly and the horseshoe vortex does not vary remarkably in size and location.

The cross-correlation coefficient ρ^* of the wall static pressure fluctuations between two different points is evaluated to clarify the space correlation of pressure fluctuations in the detached region. Figure 9(*b*) shows the distributions of the cross-correlation coefficients to the detachment point. In the region where the flow reversal is generated upstream of the detachment point, i.e., the region downstream of 625 mm, a strong positive correlation exists. Farther upstream, ρ^* is nearly equal to 0.1. On the other hand, it is more than 0.4 and the correlation is strong in the region from the detachment point to the separation vortex. The correlation is very weak downstream of the counter vortex in the region II, as ρ^* is less than 0.1. In the horseshoe vortex, no correlation exists because ρ^* is -0.05. Since it shows a steep peak in a narrow region, it is conceivable that the flow mechanism of the region I, which involves the horseshoe vortex and corner vortex, is different from that of the region II, which contains the detachment point and the separation vortex. Therefore, it is reasonable that the detached region is divided into two parts.

The Periodicity of the Detached Region. Figure 10 shows the power spectrum density distributions of wall static pressure fluctuations in the detached region. The power spectrum density was reduced by the one-dimensional, autoregressive program [16]. Stations at $x=700$, 750, and 775 mm correspond to the detachment point, the separation vortex, and the counter vortex in the region II, respectively. A station at $x=850$ mm corresponds to the horseshoe vortex in region I. Pressure fluctuations in each station are introduced by the unsteady movements of the vortices and the detachment point mentioned above.

The higher values of power spectrum density in region I, which are an order of magnitude larger than the values in the region II, are obtained, as expected from the results of RMS values in Fig. 9(*a*). The results at the detachment point, the separation vortex and counter vortex have an obvious peak less than 10 Hz. The dominant frequency of the power spectrum density at $x=700$, 750, and 775 mm is 4.9, 8.4, and 7.8 Hz, respectively. No discriminative peak is observed in the horseshoe vortex at $x=850$ mm, even though there is a wide frequency range of the power spectrum less than 20 Hz.

The separation vortex fluctuates in a shorter period than in the detachment point. As new vortices are generated by a roll-up of the wall shear layer with the separation vortex, the period of the pressure fluctuations is shortened. Because the movement of the detachment point causes the flow reversals and the wall pressure fluctuations near the detachment point, the detachment point moves in a low frequency. It is obvious from Fig. 9(*b*) that the movement of the detachment point affects the flow in the region II. Therefore, the flow in the region II fluctuates in a low frequency.

On the other hand, the power spectrum density distribution of the wall pressure fluctuations has no peak in the horseshoe vortex of the region I. Since no interference of the horseshoe vortices on the upper and lower endwalls as clarified by flow visualization exists, the horseshoe vortex has low-frequency components (less than 20 Hz) but essentially has random fluctuations.

Since the flow in the detached region has two different dynamic features, it is also reasonable that the detached region can be divided into two parts as proposed before; region I contains the horseshoe vortex and corner vortex, while region II involves the detachment point, the separation vortex, and counter vortex.

A New Flow Model in the Detached Region. Figure 11 shows a new flow model proposed by aforementioned results. Although such a flow model has been demonstrated, it was based simply on the qualitative measurements like the oil film or smoke wire method. Four types of vortices exist in the detached region that are generated through the different process. The detached region is divided into two parts: region I and II. Furthermore, these two parts have different flow mechanisms. The flow field in the detached region on the plane of symmetry can be reasonably explained by this flow model. Such a flow occurs at the leading edges of the turbomachinery blades. A contribution to the turbomachinery design will be obtained after providing the new flow model, since the methods of restraint and control of the horseshoe vortex might be easily found.

Conclusions

According to flow visualization and the data analysis for the wall pressure fluctuations and the flow direction fluctuations by the thermal tuft in the three-dimensional turbulent detached region on the plane of symmetry with a horseshoe vortex, the following conclusions are obtained:

1 It is confirmed that four types of vortices exist in the detached region, which are generated by the different process. Also, the detachment point and the vortices move unsteadily.

2 The detached region is divided into two parts: region I and II. Region I includes the horseshoe vortex and corner vortex. Region II contains the detachment point, the separation and counter vortex.

3 The flow in region II has dynamic characteristics with the low-frequency fluctuation. The fluctuations in region I are essentially random.

4 A new flow model on the flow field of the detached region is proposed.

Acknowledgment

The authors wish to thank Messrs. H. Asano, H. Naono, Y. Kishi, and K. Tabei, who assisted in data acquisition. The present project was supported by the Japanese Ministry of Education under the Grant-in-Aid for Scientific Research.

References

1 Langston, L. S., Nice, M. L., and Hooper, R. M., "Three-Dimensional Flow within a Turbine Cascade Passage," ASME JOURNAL OF ENGINEERING FOR POWER, Vol. 99, No. 1, Jan. 1977, pp. 21–28.

2 Dunham, J., "A Review of Cascade Data on Secondary Losses in Turbines," *Journal Mechanical Engineering Science*, Vol. 12, No. 1, 1970, pp. 48–59.

3 Hunter, I. H., "Endwall Boundary Layer Flows and Losses in an Axial Turbine Stage," ASME JOURNAL OF ENGINEERING FOR POWER, Vol. 104, No. 1, Jan. 1982, pp. 184–193.

4 Moore, J., and Ransmayr, A., "Flow in a Turbine Cascade: Part 1—Losses and Leading-Edge Effects," ASME JOURNAL OF ENGINEERING FOR GAS TURBINES AND POWER, Vol. 106, No. 2, Apr. 1984, pp. 400–408.

5 Graziani, R. A., et al., "An Experimental Study of Endwall and Airfoil Surface Heat Transfer in a Large Scale Turbine Blade Cascade," ASME JOURNAL OF ENGINEERING FOR POWER, Vol. 102, No. 2, Apr. 1980, pp. 257–267.

6 Gaugler, R. E., and Russell, L. M., "Comparison of Visualized Turbine Endwall Secondary Flows and Measured Heat Transfer Patterns," ASME JOURNAL OF ENGINEERING FOR GAS TURBINES AND POWER, Vol. 106, No. 1, Jan. 1984, pp. 168–172.

7 Baker, C. J., "The Turbulent Horseshoe Vortex," *Journal of Wind Engineering and Industrial Aerodynamics*, Vol. 6, 1980, pp. 9–23.

8 Ishii, J., and Honami, S., "Unsteady Structures of a Separated Three-Dimensional Turbulent Boundary Layer," *Three-Dimensional Turbulent Boundary Layers*, Springer-Verlag, New York, 1982, pp. 106–116.

9 Eaton, J. K., and Johnston, J. P., "Turbulent Flow Reattachment: An Experimental Study of the Flow and Structure Behind a Backward-Facing Step," Stanford University Report MD-39, 1980.

10 Saitoh, S., and Honami, S., "Backward Facing Step in a Curved Channel" (in Japanese), *Turbomachinery*, Vol. 10, No. 10, 1982, pp. 589–597.

11 Dechow, R., "Mittlere Geschwindigkeit Und Reynoldsscher Spannungstensor In Der Dreidimensionalen Turbulenten Wandgrenzschicht Vor Einen Stehenden Zilinder," Ph.D. dissertation, University of Karlsruhe, 1977.

12 Westphal, R. V., Eaton, J. K., and Johnston, J. P., "A New Probe for Measurement of Velocity and Wall Shear Stress in Unsteady, Reversing Flow," ASME *Journal of Fluids Engineering*, Vol. 103, No. 3, Sept. 1981, pp. 478–482.

13 Johnston, J. P., "The Turbulent Boundary Layer at a Plane of Symmetry in a Three-Dimensional Flow," ASME *Journal of Basic Engineering*, Vol. 82, No. 3, Sept. 1960, pp. 622–628.

14 Simpson, R. L., Strickland, J. H., and Barr, P. W., "Features of a Separating Turbulent Boundary Layer in the Vicinity of Separation," *Journal of Fluid Mechanics*, Vol. 79, 1977, pp. 553–594.

15 Ashjaee, J., Johnston, J. P., and Kline, S. J., "Subsonic Turbulent Flow in Plane-Wall Diffusers: Peak Pressure Recovery and Transitory Stall," Stanford University Report PD-21, 1980.

16 Akaike, H., "Statistical Predictor Identification," *Ann. Inst. Statist. Math.*, Vol. 22, 1970, pp. 203–217.

W. B. Roberts
Flow Application Research,
Fremont, CA

G. K. Serovy
Mechanical Engineering Department,
Iowa State University,
Ames, IA

D. M. Sandercock
National Aeronautics and
Space Administration,
Lewis Research Center,
Cleveland, OH

Modeling the 3-D Flow Effects on Deviation Angle for Axial Compressor Middle Stages

A model of the spanwise variation of the 3-D flow effects on deviation is proposed for middle-stage rotors and stators. This variation is taken as the difference above or below that predicted by blade element theory at any spanwise location. It was found that the stator variation is strongly affected by the end-wall boundary-layer thickness as well as camber, solidity, and blade channel aspect ratio. Rotor variation was found to depend on end-wall boundary layer thickness and tip clearance normalized by blade span. If these parameters are known or can be calculated, the models provide a reasonable approximation to the spanwise variation of deviation for middle compressor stages operating at low to high subsonic inlet Mach numbers.

Introduction

Turbomachinery flow fields are extremely complicated in that they contain inviscid, viscous, compressible, unsteady, three-dimensional, and rotational effects. As such they are not amenable to theoretical solution and it will be some time before computers and numerical techniques are sufficiently advanced to predict these flow fields. Furthermore, when analysis codes are available for such flows, there will remain the problem of initial design to produce the configuration to be analyzed. For these reasons it is necessary to formulate semi-empirical models that allow reasonable estimates of various three-dimensional (3-D) viscous effects. One such is the effect of the annulus end wall on the flow deflection of axial compressor blading.

Presently there are simple data correlations and some computational techniques to predict deviation, the angle between the downstream flow and trailing-edge camber line direction, for two-dimensional (2-D) flows. However, when bladings are used in axial compressors, the interaction with the end-walls causes a divergence from 2-D predictions. The objective of the effort described herein is to provide a simple model that can be used with the 2-D predictors to give an estimate of deviation across the entire blade span. It is assumed that a model for the spanwise distribution of deviation can be composed of two parts: the prediction of (1) primary or two-dimensional blade element deviation, and (2) secondary flow or end-wall induced deviation. This paper describes an approach to obtain part (2): a simple semi-empirical model for 3-D flow effects on deviation angle for axial compressor middle stages.

Data Base and Approach

A model for estimating blade row spanwise secondary flow induced deviation is based primarily on NASA data [1] from twelve (12) subsonic, middle-stage configurations covering a wide range of design parameters. All data considered were from operation at the design tip speed of 244 m/s and near maximum efficiency.

A two-dimensional (2-D) flow deviation angle (δ_{2D}) was calculated from a form of Carter's Rule [2] modified to account for the effects of radius and axial velocity changes across the blade row [3]. The radius and axial velocity changes were the experimentally measured values. These calculated δ_{2D} values were subtracted from the measured deviation angles (δ) and the remaining deviation assumed to be due to 3-D or secondary flow effects. Summary plots of these data for rotors and stators are shown in Figs. 1(*a*) and 1(*b*), respectively.

The plots of Fig. 1 do not indicate an obvious division for the 2-D and 3-D flow effects on deviation angle. This may be due to the need to further refine the δ_{2D} models, the lack of a purely 2-D flow region along the span, or measurement errors. Some combination of all these effects probably applies. However, for both the rotors and stators, a rather consistent spanwise distribution of the 3-D flow effects on deviation ($\delta - \delta_{2D}$) is apparent. The following approach is used to isolate the 3-D flow effects. It is assumed that, for each rotor or stator, a 2-D flow exists at the midspan (50%) streamline so that $(\delta - \delta_{2D})_{50} \equiv 0$. Then a replot of the data of Fig. 1 with the measured midpsan value of $(\delta - \delta_{2D})_{50}$ set at zero would give the estimated spanwise variation of deviation due to secondary flow or 3-D effects. The results of this procedure are presented in Fig. 2.

Figures 2(*a*) and 2(*b*) show the difference between rotor and stator spanwise variation of deviation, respectively.

It can be seen that the rotor has overturning at the hub and underturning at the tip with little variation between. This is probably due to the effect of rotation on the fluid in the blade

---

Contributed by the Gas Turbine Division of THE AMERICAN SOCIETY OF MECHANICAL ENGINEERS and presented at the 30th International Gas Turbine Conference and Exhibit, Houston, Texas, March 18–21, 1985. Manuscript received at ASME Headquarters, January 7, 1985. Paper No. 85-GT-189.

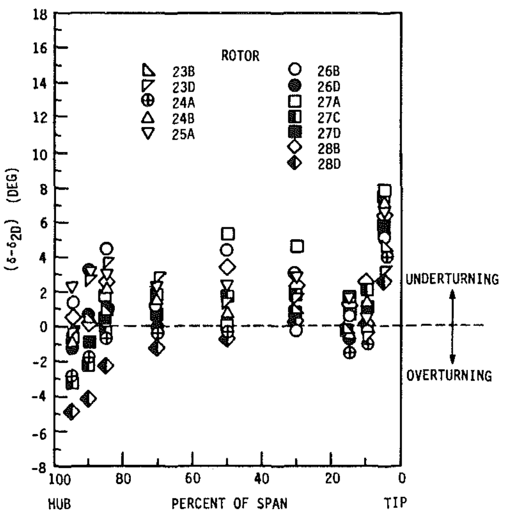

Fig. 1(*a*) Spanwise deviation performance of NASA middle-stage rotors operating near maximum efficiency

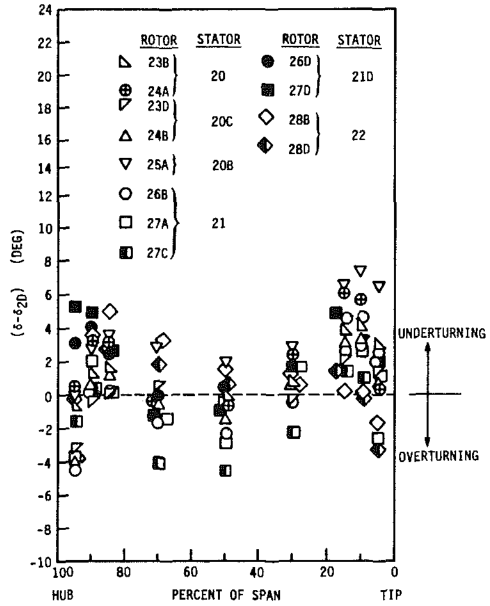

Fig. 1(*b*) Spanwise deviation performance of NASA stators in combination with various rotors at maximum efficiency operation

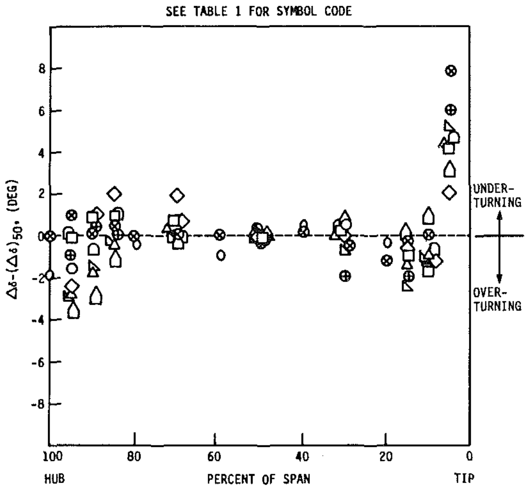

Fig. 2(*a*) Spanwise deviation performance of NASA middle-stage rotors with $(\Delta\delta)_{50}$ set to zero

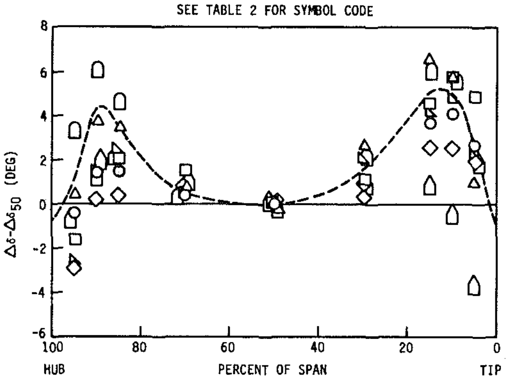

Fig. 2(*b*) Spanwise deviation performance of NASA stators in combination with various rotors with $(\Delta\delta)_{50}$ set to zero

wake. This fluid is centrifuged to the tip region. The gap at the tip would further increase the underturning due to the accumulation of low energy fluid at the tip (see Fig. 3(*a*)).

For stators with no end-wall gaps, there are two distinct maxima of underturning that occur near the end-walls as seen in Fig. 2. These maxima are caused by the "rolling up" of the two major secondary, viscous corner vortices that form because of the passage pressure gradient [4, 5]. The wall side

Nomenclature

AR = aspect ratio, $\frac{h}{c}$
AR_c = channel aspect ratio, $\frac{h}{s}$
c = blade chord, mm
h = span or mean blade height, mm
$\bar{h}_h$ = fraction of span near the hub where overturning starts for rotors
$\bar{h}_m$ = fraction of the span to the location of maximum underturning from the tip for stators
$\bar{h}_{mo}$ = fraction of the span to the location of maximum overturning in the tip region of rotors

s = blade spacing, mm
TC_s = static tip clearance, mm
$\overline{TC}_s$ = static tip clearance normalized by blade span or height, TC_s/h
x = distance along the span, mm
δ = deviation angle, deg
δ^* = boundary-layer displacement thickness, mm
$\bar{\delta}^*$ = boundary-layer displacement thickness normalized by blade span or height, δ^*/h
$\bar{\Delta}$ = difference in deviation, $(\delta - \delta_{2D}) - (\delta - \delta_{2D})_{50}$, deg
$\Delta\delta$ = $(\delta - \delta_{2D})$, deg
σ = blade solidity
φ = blade camber, deg

Subscripts

1 = inlet
5 = 5% of span from tip
15 = 15% of span from tip
50 = 50% of span from tip (midspan)
85 = 85% of span from tip
95 = 95% of span from tip
2D = equivalent two-dimensional conditions
h = hub
max = maximum
mo = maximum overturning
s = static
t = tip
w = wall (endwall)

Table 1 Parameters for spanwise deviation models for subsonic middle stage rotors

Rotor	$\bar{\Delta}_5$	$\bar{\Delta}_{mo}$	$\bar{\Delta}_5 - \bar{\Delta}_{mo}$	$\bar{h}_{mo}$	$\bar{h}_h$	δ_t^*	TC_s	φ_t	$(AR_c)_t$	h	σ_t	$\bar{\Delta}_{95}$	Symbol
	deg	deg	deg			mm	mm	deg		mm		deg	
NASA 23B	4.2	-0.3	4.5	0.10	.90	0.762	0.36	9.90	1.60	50.8	1.60	-1.5	○
NASA 23D	2.2	-1.5	3.7	0.10	.90	0.762	0.39	9.90	2.00	50.8	2.00	-2.3	◇
NASA 24A	4.2	-1.5	5.7	0.15	.85	0.610	0.55	9.30	1.07	50.8	1.60	-2.9	△
NASA 24B	5.2	-2.4	7.6	0.15	.85	0.813	0.55	9.90	1.34	50.8	2.00	-2.9	◺
NASA 25A	4.2	-1.9	6.1	0.15	.95	0.813	0.42	11.20	2.40	50.8	1.20	-0.1	□
NASA 27C	5.0	-1.1	6.1	0.15	.85	0.940	0.48	13.80	0.95	50.8	1.35	-2.5	⌓
NASA 28D	3.0	0	3.0	0.15	.80	0.610	0.45	18.95	1.44	50.8	1.36	-3.8	⌂
PSU-AFCF[1]	10.0	-1.0	11.0	0.15	.90	9.000	2.30	33.00	1.65	233.1	1.09	-1.5	0
GE-LSRC #9[2]	8.0	-1.8	9.8	0.15	.85	2.260	6.53	23.10	2.50	228.6	0.90	1.0	⊗
UTRC-LSRR[3]	5.0	-1.0	6.0	0.20	.90	2.210	1.52	49.40	0.90	152.0	0.90	-1.0	⊕

[1] Pennsylvania State University Axial Flow Compressor Facility

[2] General Electric Large Scale Research Compressor, #9 Configuration

[3] United Technologies Research Center Large Scale Rotating Rig

Table 2 Parameters for spanwise deviation models for NASA subsonic middle stage stators

Stator	AR_c	AR	φ_t (deg)	φ_h (deg)	σ_t	σ_h	$\bar{\Delta}_{max,t}$ (deg)	$\bar{\Delta}_{w,t}$ (deg)	$\bar{h}_{m,t}$	$\bar{h}_{m,h}$	$\bar{\Delta}_{max,h}$ (deg)	$\delta_{t_1}^*$ (mm)	Symbol
20 (Rotor 23B)	1.90	1.04	55.40	60.50	1.60	2.00	4.10	0	0.100	0.15	1.5	0.508	○
20 (Rotor 24A)	1.90	1.04	55.40	60.50	1.60	2.00	6.50	-2.5	0.150	0.10	3.7	0.686	△
20B (Rotor 25A)	1.42	1.04	55.40	60.50	1.20	1.50	5.60	-3.0	0.100	0.20	2.0	0.559	□
20C (Rotor 23D)	2.34	1.04	55.40	60.50	2.00	2.50	2.40	0.5	0.125	0.30	0.8	0.457	◇
20C (Rotor 24B)	2.34	1.04	55.40	60.50	2.00	2.50	4.60	-2.0	0.100	0.10	2.3	0.813	◺
21 (Rotor 27C)	2.48	1.24	68.50	72.40	1.80	2.25	6.00	-1.5	0.150	0.15	6.0	0.686	⌓
22 (Rotor 28D)	1.63	0.82	82.50	83.90	1.80	2.25	1.20	-4.8	0.200	0.15	2.0	0.254	⌂

Note: Blade span for all stators = 50.8 mm.

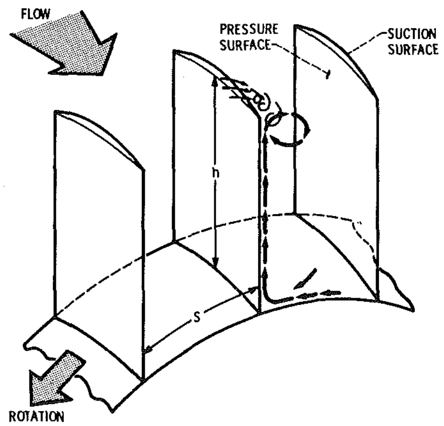

Fig. 3(*a*) Rotor spanwise flow phenomenon

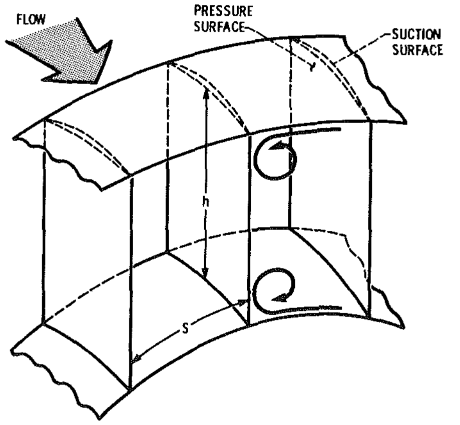

Fig. 3(*b*) Schematic of viscous end-wall vortices for stators

of the vortex enhances overturning and the midpassage side underturning due to the direction of rotation (see Fig. 3(*b*)).

The physical parameters that studies have indicated to affect rotor and stator spanwise distribution of deviation are blade camber, φ, blade aspect ratio, AR, blade channel aspect ratio, AR_c, solidity, σ, tip clearance, TC, end-wall boundary layer thickness at the inlet, represented by the inlet boundary layer displacement thickness, δ_1^*, and perhaps hub/tip radius

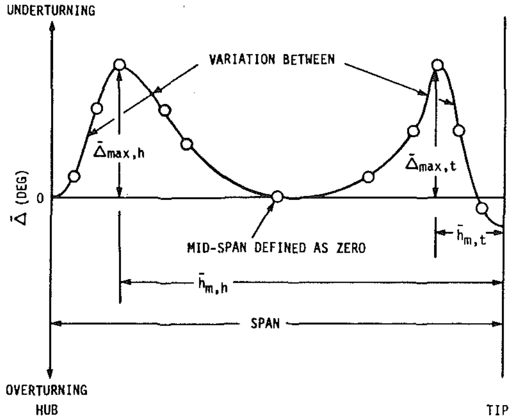

Fig. 4 Model for the variation of secondary flow-induced deviation for stators

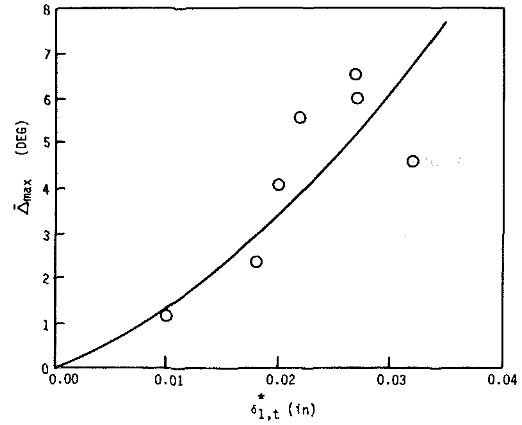

Fig. 5 Maximum underturning versus inlet tip displacement thickness for NASA stators

ratio. All of the above parameters, except displacement thickness, are available for all the rotor/stator combinations used in this study. However, [6] gives experimentally determined values of δ_1^* for seven of the rotor/stator pairs. A list of these combinations, along with pertinent physical parameters, is given in Tables 1 and 2 for rotors and stators, respectively.

Stator Deviation Model

The development of a spanwise deviation model for stators was done before the rotor model because the effects of rotation and end-wall gap did not have to be considered. A perusal of the data plots shows that, for most stators, there is a maximum underturning that occurs within 10–20% of the end-walls with an unsymmetrical exponential type variation between either the endwall or midspan. Therefore, the variation of secondary flow-induced deviation has been modeled in four parts: (1) the magnitude of the maximum underturning, (2) the location of the maximum underturning, (3) the value of underturning or overturning at the endwall, and (4) the variation between. A schematic of this model is shown in Fig. 4.

The Magnitude of Maximum Underturning. Based on a study of a series of 14 physical models for maximum underturning, it was determined that the significant parameters are end-wall boundary-layer thickness (i.e., displacement thickness or blockage), and camber, solidity, and blade channel aspect ratio. The criterion adopted for an acceptable model is the ability to correlate $\bar{\Delta}_{max}$ within ±1°. This value was chosen because that is the estimated uncertainty of the data [1].

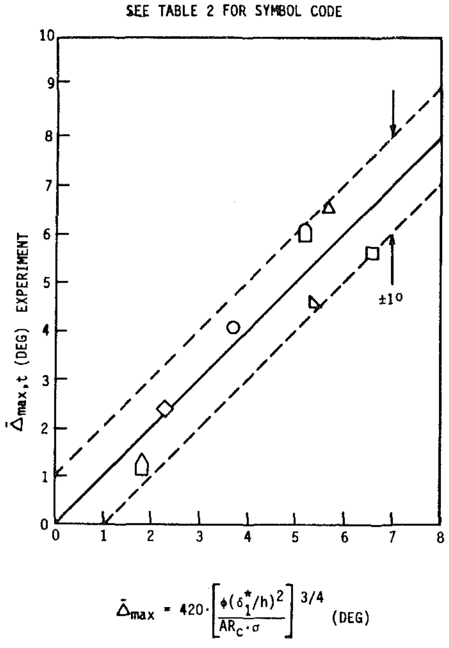

Fig. 6 Correlation of maximum underturning for stators

It should be emphasized that the end-wall boundary layers have a significant effect on secondary loss and fluid deflection in cascades and rotors [4, 5, 7]. The stators of Table 2 are those for which the boundary layer properties were available at the tip. Inlet displacement thickness was chosen as the parameter to represent the boundary-layer effect. Figure 5 shows the variation of $\bar{\Delta}_{max}$ with δ_1^*. As can be seen, the correlation is significant. It is unfortunate that the stators of Table 2 are the only ones known to the authors for which end-wall boundary-layer properties were defined.

The nondimensional linear model for maximum underturning is given below and shown in Fig. 6 with the constant of proportionality adjusted to reflect the inlet displacement thickness normalized by mean blade height or span, δ_1^*/h:

$$\bar{\Delta}_{max} = 420\left[\frac{\varphi(\delta_1^*/h)^2}{AR_c\bullet\sigma}\right]^{3/4} \text{(deg)} \qquad (1)$$

Equation (1) is a specific relationship derived from limited data. However, the model should be applicable to similar subsonic compressor stages since it covers significant ranges of most important variables. Therefore equation (1) is presented in a general form. It is physically logical to normalize the displacement thickness by the mean blade height. If an inlet boundary layer is large compared to the blade height, the effect on spanwise deviation should be large and vice versa. A drawback in this case is that the data used to make up the model all had the same blade height of 5.08 cm and there are no acceptable data available with a different height. Therefore, the model is uncalibrated for different blade heights.

Location of Maximum Underturning. Table 2 lists the location of maximum underturning for seven NASA rotor/stator combinations. A review of these data shows that the maximum underturning location clusters between 10–20% of span from the hub or tip. Data from five additional NASA middle-stage stators [1] as well as that from United Technologies Research Center (UTRC) [8] and General Electric (GE) [7, 9] confirms this trend. A careful study of all the available data indicates that there is no combination of

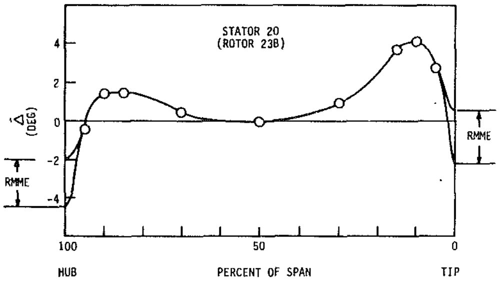

RMME-REGION OF MAXIMUM TO MINIMUM EXTRAPOLATION

Fig. 7 Illustration of reasonable region of maximum to minimum extrapolation for end-wall value of deviation difference

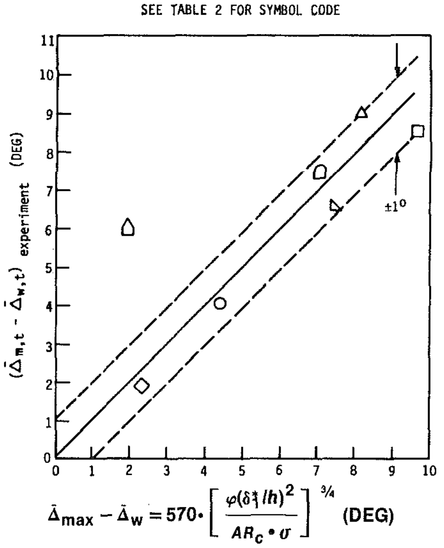

Fig. 8 Correlation for difference in underturning between maximum and the wall for stators

parameters that model this result. All the NASA and UTRC data are from test stages with a hub/tip radius ratio of 0.8, so this could be a correlating factor, although the GE stator has a radius ratio of 0.7 and it clusters with the NASA data. When the final model was compared to the data it was found that the best fit occurred when the location of maximum underturning, $\bar{\Delta}_{\max}$, was taken as 12.5% of the blade span (i.e., height) from the end wall. This agrees well with the average of the locations given in Table 2. Therefore, until additional data are available, the location of maximum underturning will be taken between 10–20% of span from the hub or tip with an arbitrary value of 12.5%, i.e.,

$$\bar{h}_{m-t} = 0.125$$
$$\bar{h}_{m-h} = 0.875 \qquad (2)$$

End-Wall Values. To completely model the spanwise variation of deviation, the value of under or overturning, $\bar{\Delta}_w$, must be estimated at the wall. This can be done by extrapolating the data of Fig. 2(*b*). The method used was to fit a curve through the 15%, 10%, and 5% span data points and onto the wall. This is illustrated in Fig. 7, where it can be seen that there is a region of "reasonable" maximum to minimum extrapolation.

Since the value of deviation difference at the wall is the result of the same corner vortex that causes maximum underturning, and the strength of this vortex will be proportional to the difference between $\bar{\Delta}_{\max}$ and the value at the wall, the same parameters that modeled $\bar{\Delta}_{\max}$ should model the difference.

Table 2 shows the appropriate parameters, with values of $\bar{\Delta}_w$ adjusted within the region of maximum to minimum extrapolation to best fit the model. Figure 8 shows that with the exception of one data point there is a linear relation between deviation difference and the vortex parameter:

$$\bar{\Delta}_{\max} - \bar{\Delta}_w = 570\left[\frac{\varphi(\delta_1^*/h)^2}{AR_c \cdot \sigma}\right]^{3/4} \text{(deg)} \qquad (3)$$

Once $\bar{\Delta}_{\max}$ is known, $\bar{\Delta}_w$ can be calculated using equation (3).

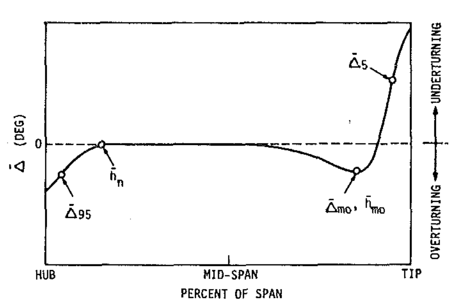

Fig. 9 Model for the variation of secondary flow-induced deviation for rotors

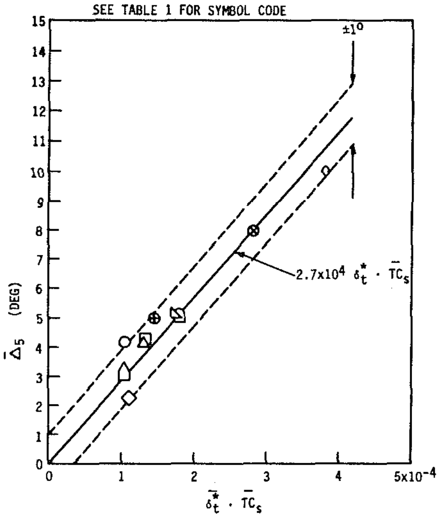

Fig. 10 Correlation for underturning at the 5% span location for rotors

Stator Spanwise Variation. The spanwise variation between the location of maximum underturning and the wall, and maximum underturning and the midspan was modeled by a fitted curve [10] with constants adjusted to reflect the values at the wall, maximum underturning, and the midspan location ($\bar{\Delta} = 0$ at midspan).

Spanwise Variation of Rotor Deviation

As was done for the stators, the rotor model considers the secondary flow or end-wall induced deviation and like the stators the data base for this model is the 12 NASA middle-stage rotor/stator combinations. However, unlike the stator model, there are additional data in the literature for rotors to assist the modeling. This consists of tests on three rotors reported in [7, 8, 9, 11].

The physical parameters that can affect rotor spanwise variation of deviation are the same as for stators with the addition of tip clearance (*TC*).

A study of Fig. 2(a) indicates that for rotors there is a maximum underturning located at the tip. The variation then goes to a small negative value near 15% of span (from the tip) and back to zero near midspan. It stays near zero until the hub region where, at approximately 85% span, the variation again goes negative (i.e., toward overturning). A schematic of this

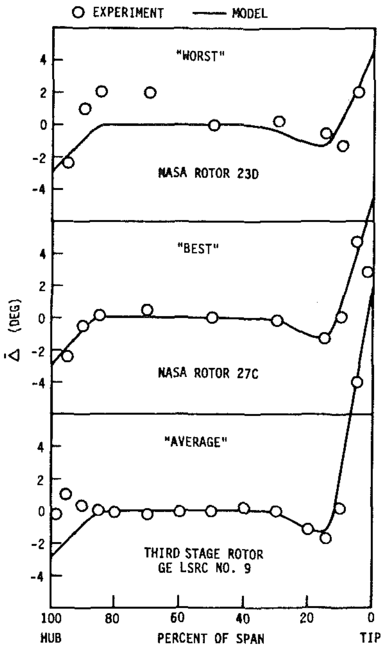

Fig. 11 Comparison of rotor spanwise deviation model with experiment

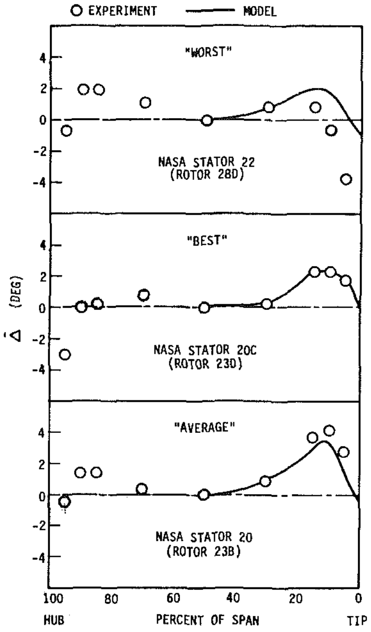

Fig. 12 Comparison of stator spanwise deviation model with experiment in the tip region

variation is shown in Fig. 9. As was stated previously, this variation is caused by centrifugation of hub end wall and blade boundary-layer and wake fluid to the tip region where it accumulates and, together with the flow induced by the pressure differences across the tip gap, causes the vortex roll-up shown in Fig. 3(*a*).

To model this variation one must be able to predict (1) the value of underturning at the tip, (2) the value of overturning in the tip region, (3) the value of overturning in the hub region, (4) the location of the start of tip region overturning, (5) the location where the hub overturning starts, and (6) the variation between.

Of the NASA rotors, only seven had sufficiently detailed data to be used in the modeling effort. Therefore, data from ten rotors was available for modeling: seven NASA middle-stage rotors and one each from General Electric [7, 9], United Technologies Research Center [8], and Pennsylvania State University (PSU) [11].

Underturning at the Tip. Eight models were proposed and tested. The first was the simplest and most successful. Figure 10 shows the effect of tip end-wall boundary-layer displacement thickness and tip clearance, both normalized by blade span or height, on the magnitude of underturning at 5% of span, $\bar{\Delta}_5$[1]. All ten rotors correlated within ±1 deg, which was the uncertainty of the data. More "complete" models, those including blade camber, aspect ratio, and solidity, did not correlate as well as Fig. 10. Therefore the relationship shown on Fig. 10 has been used to predict maximum underturning:

$$\bar{\Delta}_5 \simeq 2.7 \times 10^4 (\bar{\delta}^*_{1t} \cdot \overline{TC}_S) \tag{4}$$

Overturning Near the Tip. The data of Table 1 indicate that the location and value of maximum overturning near the tip can be approximated by two constants:

$$\bar{\Delta}_{mo} \simeq -1.25 \text{ deg} \tag{5}$$

$$\bar{h}_{mo} \simeq 0.15 \tag{6}$$

These relations are supported by other rotor data not presented in Table 1 [1, 7, 8, 9, 11] which agree within ±1.5° and 5% of span for most cases.

Overturning Near the Hub. Further study of Table 1 indicates that the value of hub overturning at 95% span and the location where hub overturning starts can be approximated by two constants

$$\bar{\Delta}_{95} \simeq -2.0 \text{ deg} \tag{7}$$

$$\bar{h}_h \simeq 0.85 \tag{8}$$

where $\bar{h}_h$ is the normalized span location at which hub overturning starts. Equations (7) and (8) are confirmed by other data not given in the table [1, 7, 8, 9, 11] and are accurate within ± 1.5 deg and 5% of span for most cases.

Rotor Spanwise Variation. Using equations (4) through (8), the spanwise variation of rotor deviation above or below 2-D can be estimated using a fitted curve [10] between the tip and midspan that goes through the predicted values of $\bar{\Delta}_5$ and $\bar{\Delta}_{mo}$. From there to the start of hub overturning the variation is zero. The variation is completed with a smooth curve from $\bar{h}_h$ through Δ_{95} and onto the wall.

Results and Discussion

Figures 11 and 12 show the rotor and stator models compared with the data for the best, average, and worst agreement. It can be seen that, except for the worst case, the models predict the spanwise variation of deviation to a good approximation.

Unfortunately there are very few independent data to validate these models. What there are lack sufficient detail, i.e., usually the specification of the end-wall boundary layers. Presently the one exception is a recent UTRC rotor test that provided detailed results with a screen-generated inlet velocity profile [12]. The rotor model given by equation (4) did not fit these data for the tip region underturning value, $\bar{\Delta}_5$. Variation away from the tip fit within tolerance.

It has been postulated that end-wall flows are very sensitive to the boundary-layer velocity gradients rather than thickness [13]. If this were the case, it could explain the lack of agreement for this data, since all previous data had thin end-wall boundary layers with steep gradients, while the UTRC data had relatively mild gradients. Therefore, until further

---

[1] For this NASA data, the measurements taken closest to the annulus walls were at 5% and 95% of span.

data are available, caution is required in applying these models to cases with unusual inlet velocity profiles.

Considering the importance of end-wall displacement thickness (or blockage) to the calculation of spanwise effects, it is essential to be able to estimate its varation through a compressor. This distribution might be obtained from direct measurement or a calculating procedure for estimating blockage [14].

The simple, design-point spanwise models for subsonic rotors and stators presented herein can be used to estimate the variation from blade element (2-D) deviation prediction. The models might be especially useful in design situations for which there is no prior experience available to guide the estimation of 3-D effects on deviation.

Conclusion

Design-point models for the spanwise variation of the effects of secondary flow on deviation angle for subsonic, axial compressor middle stages have been proposed. 3-D effects on rotor deviation can be estimated using a five-equation model that accounts for a nonsymmetric variation from tip to hub. A three-equation model suffices for stators since their variation is symmetrical in nature. With these simple models designers and analysts can quickly estimate the fluid deviation angle from hub to tip if 2-D deviation angle is known for each blade element.

These models were derived from a limited data base and, although present results are encouraging, further verification is needed over a greater range of design and flow parameters.

Acknowledgments

The work reported herein was supported under NASA Grant NAG 3-521. The authors thank the Lewis Research Center for this sponsorship.

References

1 Britsch, W. R., et al., "Effects of Diffusion Factor, Aspect Ratio, and Solidity on Overall Performance of 14 Compressor Middle Stages," NASA Technical Paper 1523, Sept. 1979.

2 Carter, A. D. S., and Hughes, H. P., "A Theoretical Investigation Into the Effect of Profile Shape on the Performance of Airfoils in Cascade," R. & M. 2384, British ARC, Mar. 1946.

3 Seyler, D., and Smith, L. H., Jr., "Single Stage Experimental Evaluation of High Mach Number Compressor Rotor Blading. Part 1—Design of Rotor Blading," NASA CR-54581, Apr. 1967, pp. 26-28.

4 Salvage, J. W., "A Review of the Current Concept of Cascade Secondary Flow Effects," VKI Tech. Note 95, Mar. 1984.

5 Griepentrog, H., "Secondary Flow Losses in Axial Compressors," AGARD LS-39, May 1970.

6 Roberts, W. B., et al., "Boundary Layer Development Through the Tip Regions of Core Compressor Stages," Final Scientific Report, NASA Grant NAS 3133, Aug. 1978.

7 Adkins, G. G., Jr., and Smith, L. H., Jr., "Spanwise Mixing in Axial-Flow Turbomachines, ASME JOURNAL OF ENGINEERING FOR POWER, Vol. 104, No. 1, Jan. 1982, pp. 97-110; Paper No. 81-GT-57.

8 Dring, R. P., et al., "An Investigation of Axial Compressor Rotor Aerodynamics," ASME JOURNAL OF ENGINEERING FOR POWER, Vol. 104, No. 1, Jan. 1982, pp. 84-96; Paper No. 81-GT-56.

9 Smith, L. J., Jr., "Casing Boundary Layers in Multistage Axial-Flow Compressors," in: *Flow Research on Blading*, L. S. Dzung, ed., Elsevier, Amsterdam, 1970, p. 275.

10 Roberts, W. B., and Sandercock, D. M., "Secondary Flow Spanwise Deviation Model for the Stators of NASA Middle Compressor Stages," Final Scientific Report, NASA Grant NAG 3-212, Feb. 1984.

11 Sitaram, N., and Lakshminarayana, B., "End Wall Flow Characteristics and Overall Performance of an Axial Flow Compressor Stage," NASA CR 3671, Feb. 1983.

12 Wagner, J. H., et al., "Inlet Boundary Layer Effects in an Axial Compressor Rotor, Part 1," ASME JOURNAL OF ENGINEERING FOR GAS TURBINES AND POWER, Vol. 107, 1985, pp. 374-380; Paper No. 84-GT-84.

13 Lakshminarayana's Discussion Comment (p. 24-15) on the paper by Dring et al., "Compressor Rotor Aerodynamics," AGARD Conference Proceedings No. 351: *Viscous Effects in Turbomachines*, 1983.

14 Stratford, B. S., "The Use of Boundary Layer Technique to Calculate Blockage From the Annulus Boundary Layers in a Compressor," ASME Paper No. 67-WA/GT-7, Nov. 1967.

Stream Function Solution of Transonic Flow Along S_2 Streamsurface of Axial Turbomachines

Zhao Xiaolu
Institute of Engineering Thermophysics,
Academy Sinica,
Beijing, China

Based on Wu's general equations of 3-D turbomachine flow, expressed with respect to nonorthogonal curvilinear coordinates, the conservative stream-function formulations of transonic flow along S_2 *streamsurface have been discussed. The problem of mixed flow can be solved by the use of the artificial compressibility method, and the passage shock on the* S_2 *streamsurface can be captured. The distribution of the fluid velocity from hub to shroud can be obtained directly by integrating the velocity gradient equation, after the principal equation has been solved, so that the difficulty of the nonuniqueness of density-mass flux relation is avoided. The density is determined after the velocity has been obtained. Two computer programs have been coded; one can be used to compute the hybrid or design problems, the other is suitable to compute the analysis problem. The former has been used to compute the transonic flow field along a mean* S_2 *streamsurface in the DFLVR compressor rotor at design speed. The numerical results agree well with L2F measurement data.*

1 Introduction

In the early 1950s, a general theory of three-dimensional compressible flow in turbomachines was presented in [1]. It suggested that the three-dimensional flow in a turbomachine may be determined by iterative calculation of the two-dimensional flows along the blade-to-blade S_1 streamsurfaces and hub-to-shroud S_2 streamsurfaces. This theory has been widely used for the computation of three-dimensional subsonic flow, analysis or design problems. Recently, it has also been used to solve the design [2] or analysis [3] problems of transonic turbomachines.

In the iterative calculation, a number of analysis methods for transonic flow along the S_1 streamsurface have been developed, for example, the Euler equation method [4, 5], the potential solution [6, 7] and stream-function solution [8, 9, 10], in which the shock jump can be captured automatically. But there is a lack of analysis methods for computing transonic flow with a passage shock on the S_2 streamsurface, and the through-flow method, in which the passage shock on the S_2 streamsurface is usually free, has been used for transonic iterative calculation [3]. A potential solution of transonic flow on the S_2 streamsurface was proposed recently [11]. By the use of artificial density, the full potential equation can be solved, and the passage shock on the S_2 surface can be captured.

In the potential solution, however, the irrotational assumption is not valid when the entropy is nonuniform downstream of a strong shock. Without the need to assume uniform entropy or irrotational flow, the stream-function equation is more suitable to compute the transonic flow. The stream-function solution was first used to compute the external transonic flow [12], and soon afterward was extended to the internal flow [8]. By the use of nonorthogonal curvilinear coordinates [13] the Dirichlet boundary condition can be satisfied easily in the stream-function equation, and it is particularly suitable for the complex geometries of turbomachines. The main difficulty of the stream-function method is the nonuniqueness of the density–mass flux relation. This can be overcome by integrating the velocity gradient equation. The distribution of the fluid velocity can be obtained from hub to shroud by the integrating procedure; after the principal equation has been solved, the density can be updated in terms of the speed.

Similar to the potential equation [14], the artificial compressibility technique was used to solve the conservative stream-function equation governing the transonic flow along the S_2 relative streamsurface. The conservative difference schemes were used in order to capture the passage shock correctly.

Traditionally, the geometry of the S_2 streamsurface shape and the thickness of stream sheet are to be dated from the last cycle calculation on S_1 streamsurface family, in the iterative calculation. However, for the beginning of cycle computation, or the computation of the hub-to-shroud two-dimensional flow field, they can be estimated from the geometry of the blade element. For the latter case, a

---

Contributed by the Gas Turbine Division of THE AMERICAN SOCIETY OF MECHANICAL ENGINEERS and presented at the 30th International Gas Turbine Conference and Exhibit, Houston, Texas, March 18–21, 1985. Manuscript received at ASME Headquarters, December 10, 1984. Paper No. 85-GT-2.

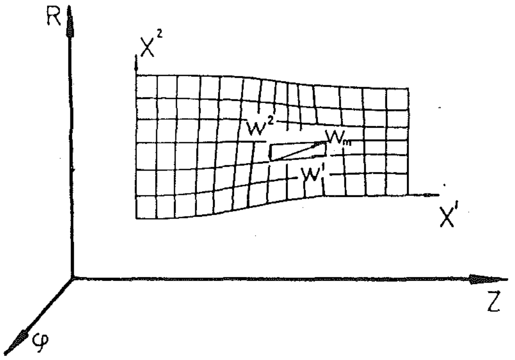

Fig. 1 Meridional coordinate system used for S_2 surface

meridional coordinate system was used. A Ψ-ρ-$V_\theta r$ iteration procedure was proposed to solve this hybrid problem. For the former case, a coordinate system set up on the streamsurface is more suitable for the analysis problem.

In the following, the stream-function formulations based on the two curvilinear coordinate systems are discussed, the details of the computer procedure are given, and the numerical results, in which the transonic flow along the mean S_2 surface in the DFVLR [3] and the ETP-1 [2] single-stage axial transonic compressor rotors was calculated, are presented.

2 Coordinate System and Stream Function Formulations

In this paper, the flow on the hub-to-shroud S_2 relative streamsurface can be considered as relative, steady, and nonviscous:

$$\text{continuity equation} \quad \nabla \cdot (\rho W) = 0 \qquad (1)$$

$$\text{equation of motion} \quad W \times (\nabla \times V) = \nabla I - T \nabla s \qquad (2)$$

$$\text{energy equation} \quad dI/dt = 0 \qquad (3)$$

In terms of the nonorthogonal curvilinear coordinate systems, the different kinds of the stream-function equations governing the flow along S_2 streamsurface can be obtained from these basic equations.

A meridional coordinate system (x^1, x^2, x^3) can be set up as follows: x^1 and x^2 lie in the meridional plane, $x^3 = \varphi$ (see Fig. 1). As described in [11], the relative velocity can be expressed with respect to the nonorthogonal velocity components:

$$W = w^i e_i = w_i e^i = W^i u_i = W_i u^i$$

and the tensor elements are:

$$a_{ii} = \left(\frac{\partial z}{\partial x^i}\right)^2 + \left(\frac{\partial r}{\partial x^i}\right)^2 \quad (i = 1,2)$$

$$a_{12} = \sqrt{a_{11}}\sqrt{a_{22}}\cos\theta_{12}$$

$$a_{13} = a_{31} = a_{23} = a_{32} = 0$$

The continuity equation and a component of motion equation can be written as:

$$\frac{\bar{\partial}}{\partial x^1}(\rho\tau\sqrt{a_{22}}\sin\theta_{12} W^1) + \frac{\bar{\partial}}{\partial x^2}(\rho\tau\sqrt{a_{11}}\sin\theta_{12} W^2) = 0 \qquad (4)$$

$$\frac{\bar{\partial}}{\partial x^2}[(W^1 + W^2\cos\theta_{12})\sqrt{a_{11}}] - \frac{\bar{\partial}}{\partial x^1}[(W^2 + W^1\cos\theta_{12})\sqrt{a_{22}}]$$
$$= \frac{\sqrt{a_{11}}}{W^1}\left[-\frac{W_\varphi}{r}\frac{\bar{\partial}}{\partial x^2}(V_\theta r) + \frac{\bar{\partial} I}{\partial x^2} - T\frac{\bar{\partial} s}{\partial x^2} - f_2\right] \qquad (5)$$

where $\tau = r\,B$.

The principal stream-function equation can be obtained from these equations:

$$\frac{\bar{\partial}}{\partial x^2}\left(A_1 \frac{1}{\rho}\frac{\bar{\partial}\Psi}{\partial x^2} - A_2 \frac{1}{\rho}\frac{\bar{\partial}\Psi}{\partial x^1}\right)$$
$$- \frac{\bar{\partial}}{\partial x^1}\left(A_2 \frac{1}{\rho}\frac{\bar{\partial}\Psi}{\partial x^2} - A_3 \frac{1}{\rho}\frac{\bar{\partial}\Psi}{\partial x^1}\right) = A_4 \qquad (6)$$

where

$$A_1 = \sqrt{a_{11}}/(\sqrt{a_{22}}\sin\theta_{12}\tau) \quad A_2 = \cos\theta_{12}/(\sin\theta_{12}\tau)$$

$$A_3 = \sqrt{a_{22}}/(\sqrt{a_{11}}\sin\theta_{21}\tau)$$

$$A_4 = \frac{\sqrt{a_{11}}}{W^1}\left[-\frac{W_\varphi}{r}\frac{\bar{\partial}}{\partial x^2}(V_\theta r) + \frac{\bar{\partial} I}{\partial x^2} - T\frac{\bar{\partial} s}{\partial x^2} - f_2\right]$$

and the stream function Ψ is defined such that:

$$\tau\rho\sqrt{a_{11}}\sin\theta_{12} W^2 = -\frac{\bar{\partial}\Psi}{\partial x^1};$$

$$\tau\rho\sqrt{a_{22}}\sin\theta_{12} W^1 = \frac{\bar{\partial}\Psi}{\partial x^2} \qquad (7)$$

The barred partial derivative sign is used to denote the partial derivative of a quantity following the motion along S_2 streamsurface with respect to x^1 or x^2 lines on the meridional plane. The f_2 is a component of a fictitious body force per unit mass of fluid in the direction of the x^2 line, which can be written as:

$$f_2 = \frac{\bar{\partial}\varphi}{\partial x^2}\frac{d(V_\theta r)}{dt}$$

It should be pointed out that the right-hand side of the

Nomenclature

A_{ij} = basic metric tensor of two-dimensional coordinate system
B = angular thickness of S_2 stream sheet
C = artificial compressibility coefficient
e_i, e^i = x^i coordinate base vector and reciprocal vector
g_{ij} = basic metric tensor of three-dimensional coordinate system
H = stagnation enthalpy per unit mass, $h + v^2/2$
I = relative stagnation rothalpy per unit mass, $h + w^2/2 - u^2/2$
n = unit normal vector of S_2 surface
$\frac{P}{P-t}$ = channel area ratio
(r, φ, z) = relative cylindrical coordinates
S = entropy per unit mass
T = absolute temperature, K
u_i, u^i = x^i coordinate unit base vector and reciprocal vector
W = relative velocity
W^i = physical component of W tangent to x^i
w^i = contravariant component of W
w_i = covariant component of W
κ = ratio of specific heats
θ_{12} = angle included by the coordinate lines
μ = switching function
ρ = fluid density
τ = thickness of S_2 stream sheet
Ψ = stream function
ω = angular velocity of blade

Subscripts

i = inlet

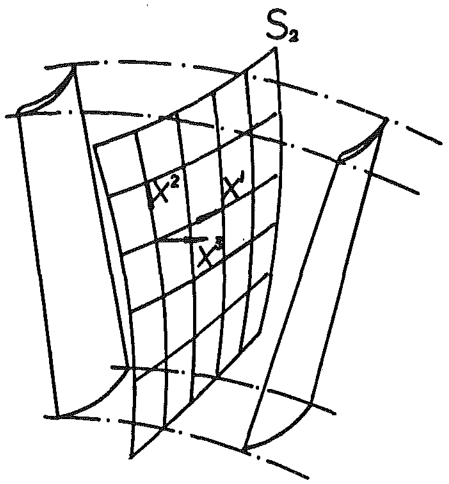

Fig. 2 Streamsurface coordinate system used for S_2 surface

equation contains the $V_\theta r$ term. For the case with $V_\theta r$ given, equation (6) is hyperbolic if the meridional velocity W_m, $W_m{}^2 = (W^1)^2 + (W^2)^2 + 2W^1W^2\cos\theta_{12}$, is greater than the speed of sound; it can be described as a design problem as in [15]. In the analysis problem, the $V_\theta r$ is unknown and equation (6) is always locally hyperbolic when the relative speed W, rather than the meridional speed W_m, is supersonic. This is true because the unit vector normal to the S_2 streamsurface is, of course, perpendicular to the relative velocity ($n \cdot W = 0$); the useful expression can be obtained:

$$W_\varphi = (r/\sqrt{a_{11}})(\partial\varphi/\partial x^1)W^1 + (r/\sqrt{a_{22}})(\partial\varphi/\partial x^2)W^2 \tag{8}$$

The $V_\theta r$ can be defined in terms of the components of meridional velocity:

$$V_\theta r = (\omega r + W_\varphi)r \tag{9}$$

Now, this principal equation can be used to solve the analysis, hybrid, and design problems of the flow along the hub-to-shroud S_2 relative streamsurface.

Similar to [12], the conservative stream equation may be used to solve the design problem. The flowpath, the streamsheet thickness, and the distribution of $V_\theta r$ on the S_2 streamsurface are described by the designer. The shock jump condition is completely determined in terms of the abrupt changes in $V_\theta r$.

It can also be used to solve the analysis problem. For the case with $V_\theta r$ unknown, but the shape of S_2 streamsurface $\varphi(x^1, x^2)$ and thickness are given from last cycle S_1 calculations. When the meridional velocity is known, the value of $V_\theta r$ can be updated by the use of equation (9), but it lags behind. In order to make the iterative calculation stabilized, the new value of $V_\theta r$ should be damped, otherwise it makes the iteration procedure (Ψ-ρ-$V_\theta r$) somewhat inefficient.

A more convenient set of conservative stream-function equations can be obtained, in which the unknown $V_\theta r$ term vanishes, by using a streamsurface coordinate system. This will be described in the following.

Equation (6) is more suitable for calculating the hub-to-shroud two-dimensional flow field; in this case only the flow along an S_2 mean (central) streamsurface, properly at the middle part of flow passage, is calculated. This is a typical hybrid problem. In the region upstream and downstream of the blade row, the distribution of $V_\theta r$ is known. For example, $V_\theta r$ is not changed along a streamline on the S_{2m} surface, but in the region of the blade row $V_\theta r$ is obtained by the iterative calculation described above. The shape of the S_2 streamsurface and thickness of the corresponding stream sheet within the blade row can be estimated from the geometry of the blade element. This calculation can also be used as the first step of the iterative calculation between two families of streamsurfaces.

For the analysis problem, it is convenient to use a streamsurface coordinate system: A coordinate surface coincides with the S_2 streamsurface, x^1, x^2 lie in this surface, and x^3 is perpendicular to it (see Fig. 2). The relative velocity W can be expressed with only two components W^1 and W^2 with the third component W^3 always being equal to zero ($W^3 = 0$). The tensor elements of three-dimensional coordinate system can be obtained as follows: If $dx^3 = 1$, then $\sqrt{g_{33}} = \tau_n$ $\sqrt{g^{33}} = 1/\tau_n$, where $\tau_n = r\,B\cos(n, \varphi)$ and

$$g_{11} = \left(\frac{\partial z}{\partial x^1}\right)^2 + \left(\frac{\partial r}{\partial x^1}\right)^2 + \left(r\frac{\partial\varphi}{\partial x^1}\right)^2$$

$$g_{22} = \left(\frac{\partial z}{\partial x^2}\right)^2 + \left(\frac{\partial r}{\partial x^2}\right)^2 + \left(r\frac{\partial\varphi}{\partial x^2}\right)^2$$

$$g_{13} = g_{31} = g_{23} = g_{32} = 0$$

$$g_{12} = \sqrt{g_{11}}\sqrt{g_{22}}\cos\theta_{12}$$

where θ_{12} is the angle included by the coordinate lines x^1 and x^2,

$$g = g_{11}g_{22}g_{33}\sin^2\theta_{12} = \tau_n^2 g_{11}g_{22}\sin^2\theta_{12}$$

With this coordinate system, a set of equations can be obtained:

$$\frac{\partial}{\partial x^1}(\rho\tau_n\sqrt{g_{22}}\sin\theta_{12}W^1) + \frac{\partial}{\partial x^2}(\rho\tau_n\sqrt{g_{11}}\sin\theta_{12}W^2) = 0 \tag{10}$$

$$\frac{\partial}{\partial x^2}[(W^1 + W^2\cos\theta_{12})\sqrt{g_{11}}] - \frac{\partial}{\partial x^1}[(W^2 + W^1\cos\theta_{12})\sqrt{g_{22}}]$$

$$= 2\sqrt{g_{11}}\sqrt{g_{22}}\,\omega^3\sin\theta_{12} + \frac{\sqrt{g_{11}}}{W^1}\left(\frac{\partial I}{\partial x^2} - T\frac{\partial s}{\partial x^2}\right) \tag{11}$$

where $\omega^3 = \omega\cos(n, z)/\tau_n$.

From equation (10) a stream function Ψ can be introduced:

$$\tau_n\rho\sqrt{g_{11}}\sin\theta_{12}W^2 = -\frac{\partial\Psi}{\partial x^1}; \quad \tau_n\rho\sqrt{g_{22}}\sin\theta_{12}W^1 = \frac{\partial\Psi}{\partial x^2} \tag{12}$$

Substituting equation (12) into equation (11), the principal equation in simpler form than equation (6) was obtained:

$$\frac{\partial}{\partial x^2}\left(C_1\frac{1}{\rho}\,\frac{\partial\Psi}{\partial x^2} - C_2\frac{1}{\rho}\,\frac{\partial\Psi}{\partial x^3}\right)$$

$$-\frac{\partial}{\partial x^3}\left(C_2\frac{1}{\rho}\,\frac{\partial\Psi}{\partial x^2} - C_3\frac{1}{\rho}\,\frac{\partial\Psi}{\partial x^3}\right) = C_4 \tag{13}$$

where

$C_1 = \sqrt{g_{11}}/(\sqrt{g_{22}}\sin\theta_{21}\tau_n)$

$C_3 = \sqrt{g_{22}}/(\sqrt{g_{11}}\sin\theta_{21}\tau_n)$

$C_2 = \cos\theta_{21}/(\sin\theta_{21}\tau_n)$

$C_4 = 2\sqrt{g_{11}}\sqrt{g_{22}}\,\omega^3\sin\theta_{12} + \dfrac{\sqrt{g_{11}}}{W^1}\left(\dfrac{\partial I}{\partial x^2} - T\dfrac{\partial s}{\partial x^2}\right)$

It is seen that this equation contains only two unknowns: Ψ and ρ. A traditional Ψ-ρ iteration procedure should be applied. The convergence rate of iteration seems to be faster than the preceding Ψ-ρ-$V_\theta r$ iterative procedure.

3 The Artificial Compressibility Method and Discretized Procedure

Similar to the potential solution [14], the stream-function equation in conservative form has been used, and the artificial compressibility method has been applied to solve the mixed equation governing the transonic flow along the S_2 streamsurface. This method consists of modifying the density so as to introduce numerical dissipation necessary in the supersonic region. The modified density $\tilde{\rho}$ is obtained as follows:

$$\tilde{\rho}=\rho-\mu\rho_s\Delta s;\quad \mu=\max\left[0,\ c\left(1-\frac{1}{M^2}\right)\right] \tag{14}$$

Standard finite differences are used in discretizing equation (6), leading to a large system of nonlinear algebraic equations in the unknown stream-function values at the grid points. The finite difference approximation of equation (6) at grid point (i,j) reads:

$$\begin{aligned}&\left[\left(A_1\frac{1}{\tilde{\rho}}\frac{\bar{\partial}\Psi}{\partial x^2}-A_2\frac{1}{\tilde{\rho}}\frac{\bar{\partial}\Psi}{\partial x^1}\right)_{i+\frac{1}{2},j}\right.\\&\quad\left.-\left(A_2\frac{1}{\tilde{\rho}}\frac{\bar{\partial}\Psi}{\partial x^2}-A_3\frac{1}{\tilde{\rho}}\frac{\bar{\partial}\Psi}{\partial x^1}\right)_{i-\frac{1}{2},j}\right]/\Delta x^1\\&\qquad-\left[\left(A_1\frac{1}{\tilde{\rho}}\frac{\bar{\partial}\Psi}{\partial x^2}-A_2\frac{1}{\tilde{\rho}}\frac{\bar{\partial}\Psi}{\partial x^1}\right)_{i,j+\frac{1}{2}}\right.\\&\quad\left.-\left(A_2\frac{1}{\tilde{\rho}}\frac{\bar{\partial}\Psi}{\partial x^2}-A_3\frac{1}{\tilde{\rho}}\frac{\bar{\partial}\Psi}{\partial x^1}\right)_{i,j-\frac{1}{2}}\right]/\Delta x^2=A_4\end{aligned} \tag{15}$$

where

$$\left(\frac{\bar{\partial}\Psi}{\partial x^1}\right)_{i+\frac{1}{2},j}=[\Psi_{i+1,j}-\Psi_{i,j}]/\Delta x^1$$

$$\begin{aligned}\left(\frac{\bar{\partial}\Psi}{\partial x^1}\right)_{i,j+\frac{1}{2}}&=\frac{1}{4}\left[\Psi_{i+1,j+1}+\Psi_{i+1,j}\right.\\&\quad\left.-\Psi_{i-1,j+1}-\Psi_{i-1,j}\right]/\Delta x^1\end{aligned}$$

The value at half points

$$\left(\frac{A_1}{\tilde{\rho}}\right)_{i,j+\frac{1}{2}}=\frac{1}{2}\left[\left(\frac{A_1}{\tilde{\rho}}\right)_{i,j+1}+\left(\frac{A_1}{\tilde{\rho}}\right)_{i,j}\right]$$

etc.

Equation (13) can be discretized in a similar way, only the barred partial derivative signs are replaced with the ordinary partial derivative signs, and also the coefficients A_1-A_4 are turned into C_1-C_4.

Upwind differencing is only used in evaluating $(\rho_s\Delta s)$; for equation (5) it can be written as:

$$(\rho_s\Delta s)_{i,j}=\frac{W^1}{W_m}\delta_{x^1}\rho\Delta x^1+\frac{W^2}{W_m}\delta_{x^2}\rho\Delta x^2$$

where

$$\delta_{x^1}\rho\Delta x^1=\rho_{i,j}-\rho_{i-1,j}$$

$$\delta_{x^2}\rho\Delta x^2=\rho_{i,j}-\rho_{i,j-1}\qquad W^2>0$$

$$\delta_{x^2}\rho\Delta x^2=\rho_{i,j+1}-\rho_{i,j}\qquad W^2<0$$

The boundary conditions of flow along the S_2 streamsurface should be specified. The stagnation pressure, stagnation temperature, and mass flow rate G_0 are given. At the solid walls, the stream function value should be equal to zero (at hub), or G_0 (at shroud). At inlet or exit boundaries, the radial velocity is considered to be zero, so that the condition $\partial\Psi/\partial x^1 = 0$ should be set up at the inlet and exit boundaries. Together with the discretized boundary condition, the formulation of discrete problem is complete, and the SIP, SLVOR methods are utilized here to solve the nonlinear algebraic equations. An appropriate $\Psi_{x't}$ term, necessary for stability, is added in the supersonic regions.

4 Determination of Density

The density is not a unique function of the mass flux, and traditionally for subsonic flow the density is updated by using this relation:

$$\frac{\rho}{\rho_{T_i}}=\left(\frac{I+\frac{1}{2}\omega^2r^2-\frac{1}{2}(W)^2}{H_i}\right)^{\frac{1}{\kappa-1}}e^{\frac{S-S_{T_i}}{R}} \tag{16}$$

As in [15], the speed was usually calculated in terms of the current values of stream function and the previous value of the density. This iteration procedure can be written as:

$$\frac{\rho^{n+1}}{\rho_{T_i}}=\left(\frac{I+\frac{1}{2}\omega^2r^2-\frac{1}{2}W_\varphi^2-\frac{1}{2}(\rho W_m/\rho^n)^2}{H_i}\right)^{\frac{1}{\kappa-1}}\cdot e^{\frac{S-S_{T_i}}{R}} \tag{17}$$

But for mixed flow this iteration procedure failed. A Σ-Φ plot can be used to describe the density-mass flux relation, which was described clearly for different cases in equation (146) of [1]. This plot has two branches: One is used to describe the hyperbolic flow, the other elliptic. When the mass flow is less than the maximum attainable value, there are two values of density for it.

Equation (6) can be rewritten as a velocity gradient equation:

$$\begin{aligned}\frac{\bar{\partial}}{\partial x^1}(\sqrt{a_{11}}W^1)&=\frac{\bar{\partial}}{\partial x^1}[(W^2+W^1\cos\theta_{12})\sqrt{a_{22}}]\\&\quad-(W^2\cos\theta_{12}\sqrt{a_{11}})\\&\quad+\frac{\sqrt{a_{11}}}{W^1}\left[-\frac{W_\varphi}{r}\frac{\bar{\partial}}{\partial x^2}(V_\theta r)+\frac{\bar{\partial}I}{\partial x^2}-T\frac{\bar{\partial}s}{\partial x^2}-f_2\right]\end{aligned} \tag{18}$$

The terms on the right-hand side are updated consistently with the main calculation of Ψ. The distribution of W^1 from hub to shroud may be determined by integrating equation (18) along x^2 coordinate lines after knowing the stream pattern. The integration procedure proceeds from an assumed value of W^1 on an initial data curve. Because the supersonic flow region does not extend to the hub in the rotor for most transonic fan and compressor, the initial data curve, along which the flow is subsonic, can be selected near or at the hub; then the distribution of ρ and W^1 along the corresponding curve may be obtained in terms of equation (17) as in subsonic flow. Then W^2 is updated from

$$W^2/W^1=-(\sqrt{a_{11}}\partial\Psi/\partial x^1)/(\sqrt{a_{22}}\partial\Psi/\partial x^2)$$

Knowing W^1 and W^2, W can be determined as:

$$(W)^2=(W^1)^2+(W^2)^2+2W^1W^2\cos\theta_{12}+W_\varphi^2$$

where W_φ is obtained from equation (8). The density ρ can then be obtained from equation (16). If the streamsurface coordinate system is used, the distribution of velocity and density can be obtained in a similar manner.

Two computer programs based on the abovementioned principal equations have been coded. One is for hybrid problems, the other for analysis problems. Two computational examples are presented in the next section: One belongs to the former, the other to the latter.

5 Numerical Results and Discussion

The two-dimensional hub-to-shroud flow field of the DFVLR rotor passage [3] has been calculated and compared with the experimental data. In this case only the flow on a mean S_2 streamsurface is calculated. The flow field in the DFVLR single-stage axial transonic compressor rotor was measured by an L2F instrument.

Figure 3 shows the projection of S_{2m} and the computing

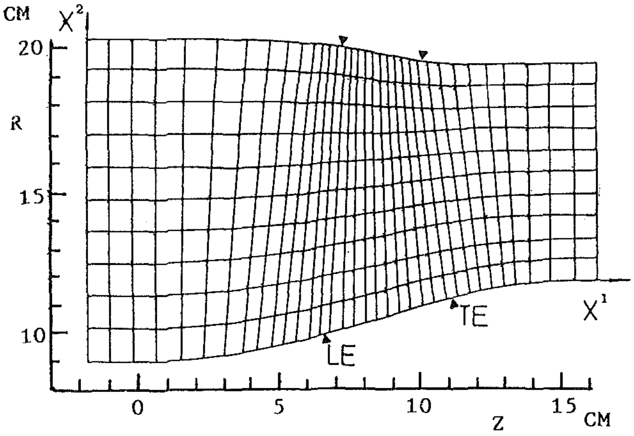

Fig. 3 Flowpath and computing network of DFVLR rotor

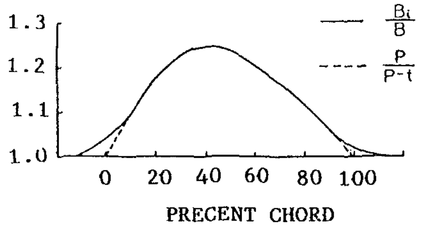

Fig. 4 Variation of thickness of S_2 stream sheet and channel area ratio

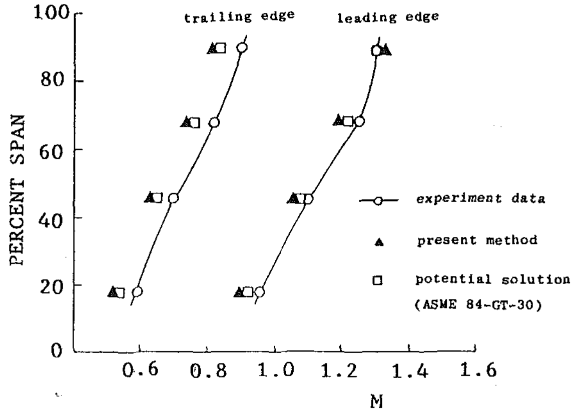

Fig. 5 Radial variation of computed Mach number for DFVLR compressor rotor

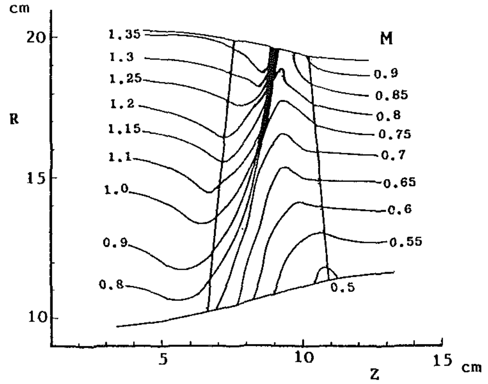

Fig. 6 Projection of computed relative Mach number contours of S_{2m} streamsurface on meridional plane of DFVLR rotor

network on the meridional plane. The computation conditions have been defined: Mass flow rate = 17.3 kg/s, rotational speed of rotor = 20,260 rpm, inlet stagnation temperature = 288.2 K, stagnation density = 1.203 kg/m^3. At exit boundary, the distribution of $V_\theta r$ was calculated from the measurement data. The thickness of the S_{2m} stream sheet was assumed to be proportional to the circumferential arc length of the flow passage. Some alterations were made so that the abrupt changes in thickness at the leading and trailing edges can be avoided (Fig. 4). The middle arc surface of the blade element was considered as one part of S_{2m} streamsurface. The abrupt changes in the shape and thickness of S_2 across the shock will be taken into account in the iterative calculation of three-dimensional transonic flow.

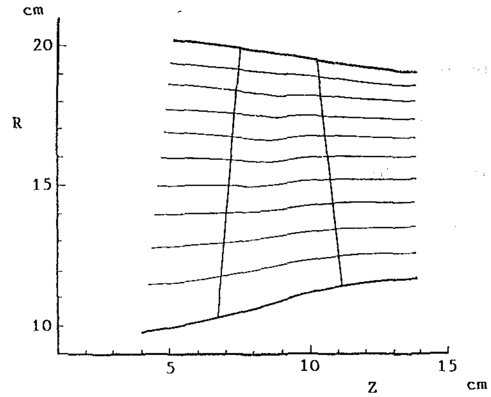

Fig. 7 Projection of streamlines of S_{2m} streamsurface on meridional plane for DFVLR rotor

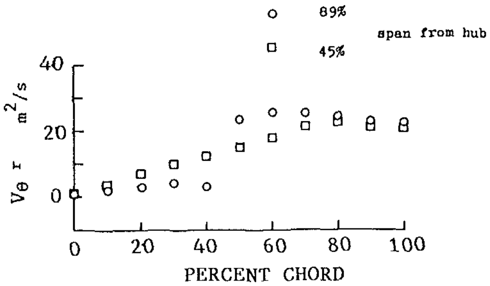

Fig. 8 Distribution of computed $V_\theta r$ on S_{2m} streamsurface of DFVLR compressor rotor

A comparison of calculated Mach number at the leading and trailing edges with the experiment and potential solution is shown in Fig. 5. At the leading edge the agreement is very good. If the blockage due to the boundary layer was taken into account, the discrepancy of Mach number between computed results and measured data could be expected to be reduced at the trailing edge. The projection of calculated Mach number contours of the relative flow on the mean S_2 streamsurface is plotted in Fig. 6. The projection of S_2 streamline shows the remarkable changes across the shock, which are more marked at a distance from the casing wall than in the region near casing (Fig.7). It seems that the constraining effect of the casing wall delays the radical changes, i.e., reduces streamline deflection.

The variations of the computed angular movement $V_\theta r$ are illustrated in Fig. 8. From this figure the abrupt changes across the shock can be seen clearly. The Mach number distribution on the hub and shroud is plotted in Fig. 9. It shows that some overshoot occurs across the shock, and probably makes the shock more sharp. Perhaps some improvements should be made in reducing the overshoots with the methods proposed in [4 and 16].

To demonstrate the applicability of the second computer code based on equation (13), an analysis problem of transonic flow on the S_{2m} streamsurface in the ETP-1 axial transonic compressor rotor has been solved. The geometry of the S_{2m} streamsurface shape and the thickness of stream sheet have been dated from the computed results of a design problem [2].

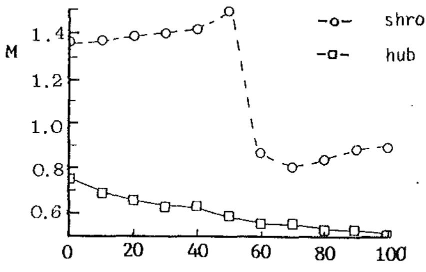

Fig. 9 Distribution of computed relative Mach number on S_{2m} streamsurface for DFVLR rotor

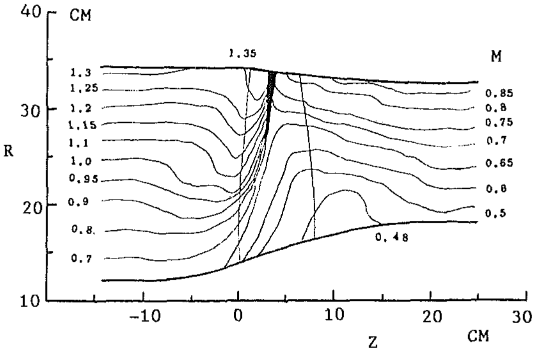

Fig. 10 Projection of computed relative Mach number contours of S_{2m} streamsurface on meridional plane for ETP-1 compressor rotor

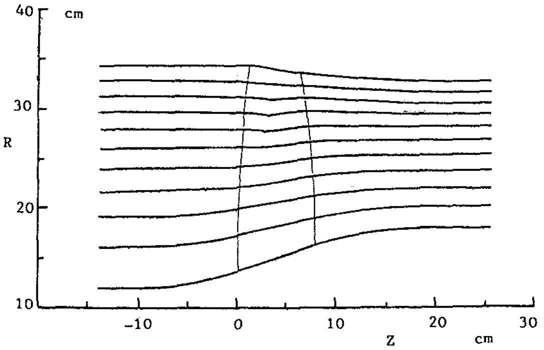

Fig. 11 Projection of streamline of S_{2m} streamsurface on meridional plane for ETP-1 compressor rotor

Figures 10 and 11 show the computed Mach number contours and the streamline pattern on the S_{2m} streamsurface in the ETP-1 transonic rotor, respectively.

6 Concluding Remarks

The stream function solution [9, 10], which has been heretofore used to analyze the transonic flow field along S_1 streamsurface, has been extended to compute the transonic flow along the hub-to-shroud S_2 streamsurface in this paper. With respect to two nonorthogonal curvilinear coordinate systems, two principal equations have been obtained, which are suitable to solve the analysis, hybrid, or design problems respectively.

The necessary numerical dissipation for the calculation of mixed flow with shocks is introduced by the artificial compressibility method, and the nonuniqueness of the problem of density is solved by the velocity gradient integration method.

A computer program was used to calculate the transonic flow along the mean S_2 streamsurface of the DFVLR transonic rotor. The computed results were compared with the L2F measurement data, and the agreement was good. The other computer code was used to solve an analysis problem; the transonic flow on a given S_2 stream surface has been calculated. However, more precise computation of the flow along the S_2 streamsurface should be carried out in the iterative calculation of two stream families, so that the abrupt changes in the shape and thickness of S_2 streamsurface will not be neglected.

Acknowledgments

The work reported herein was performed under the direct supervision of Professor Wu Chung-Hua. The author is greatly indebted to him for his encouragement and guidance.

References

1 Wu Chung-Hua, "A General Theory of Three-Dimensional Flow in Subsonic or Supersonic Turbomachines of Axial Radial and Mixed Flow Types," ASME Paper No. 50-A-79, ASME Trans., Nov. 1952; NACA TN 2604, 1952.

2 Academia Sinica and Shengyang Aeroengine Company, "Theory, Methods, and Application of Three-Dimensional Flow Design of Transonic Axial-Flow Compressor," *Journal of Engineering Thermophysics*, Vol. 1, No. 1, 1980, pp. 44–54.

3 McDonald, P. W., et al., "A Comparison Between Measured and Computed Flow Field in a Transonic Compressor Rotor," ASME JOURNAL OF ENGINEERING FOR POWER, No. 4, Oct. 1980.

4 Denton, J. D., "A Time Marching Method for Two and Three-Dimensional Blade to Blade Flow," Aer. Res. Co. R & M. 3775, 1975.

5 Lu Wenqian and Chen Xuming, "An Improved Time-Dependent Method for Transonic Flow Calculation on S_1 Surface of Revolution," in: Computational Methods in Turbomachinery, The University of Birmingham, Apr. 1984, pp. 191–198.

6 Deconinck, H., and Hirsch, Ch., "Finite Element Methods for Transonic Blade-to-Blade Calculation in Turbomachines," ASME JOURNAL OF ENGINEERING FOR POWER, Vol. 103, No. 4, 1981, pp. 665–667.

7 Zhang Jialin and Wu Chung-Hua, "Fast Algorithm for Solving the Conservative Transonic S_1 Full-Potential Equation Employing Nonorthogonal Curvilinear Coordinates and Nonorthogonal Velocity Components," in: Computational Methods in Turbomachinery, The University of Birmingham, Apr. 1984, pp. 247–254.

8 Habashi, W. G., and Hafez, M. M., "Finite Element Stream Function Solutions for Transonic Turbomachines Flow," AIAA-82-1268, 1982.

9 Zhao, X., "Solution of Transonic Flow Along S_1 Stream Surface Employing Nonorthogonal Curvilinear Coordinates and Corresponding Nonorthogonal Velocity Components," in: Computational Methods in Turbomachinery, The University of Birmingham, Apr. 1984, pp. 183–190.

10 Wang, Z., "Solution of Transonic S_1 Surface Flow by Successively Reversing the Direction of Integration of the Stream Function Equation," ASME Paper No. 84-GT-23, 1984.

11 Lu Panming and Wu Chung-Hua, "Computation of Potential Flow on S_2 Stream Surface for a Transonic Axial-Flow Compressor Rotor," ASME Paper No. 84-GT-30, 1984.

12 Hafez, M. M., and Lovell, D., "Numerical Solution of Transonic Stream Function Equation," *J. AIAA*, Vol. 21, 1983, pp. 327–335.

13 Wu Chung-Hua, "Three-Dimensional Turbomachine Flow Equations Expressed With Respect to Nonorthogonal Curvilinear Coordinates and Methods of Solution," Lecture Notes, China University of Science and Technology, 1975; *Proceedings of the 3rd ISABE*, 1976, pp. 233–252.

14 Hafez, M. M., Murman, E. M., and South, J. C., "Artificial Compressibility Methods for Numerical Solution of Transonic Full Potential Equation," *J. AIAA*, Vol. 17, 1979, pp. 838–884.

15 Zhu Rongguo, "Flow-Field Line-Relaxation Solution for Inverse Problem of Flow Along S_2 Relative Stream Surface Employing Nonorthogonal Curvilinear Coordinates and Corresponding Nonorthogonal Velocity Components," *Journal of Engineering Thermophysics*, Vol. 1, 1980, pp. 28–35.

16 Habashi, W. G., and Hafez, M. M., "Finite Element Solutions of Transonic Flow Problems," *J. AIAA*, Vol. 20, 1982, pp. 1368–1376.

Computation of Off-Design Flows in a Transonic Compressor Rotor

W. N. Dawes
Senior Assistant in Research.
Whittle Laboratory,
University Engineering Department,
Cambridge

Recent years have seen increasing efforts to develop efficient solvers for the compressible Navier-Stokes equations. For maximum benefit to be derived from this effort, these Navier-Stokes solvers must be capable of dealing with off-design flows as readily and accurately as the on-design cases. The current paper outlines an efficient implicit algorithm developed recently by the author for solving the compressible Navier-Stokes equations in turbomachinery blade-blade flows. The Navier-Stokes solver is applied to the study of a transonic compressor rotor with supersonic inlet velocities for three cases, one on-design and two off-design. The results are compared with experimental measurements and with the predictions of a viscous-inviscid interactive method.

Introduction

The complex flowfield in a transonic axial compressor rotor represents a considerable challenge for flow prediction methods. Typically the relative inlet Mach number varies from about 0.8 at the hub to around 1.4 near the tip. Strong shock waves may be present, particularly toward the tip, with peak suction surface Mach numbers as high as 1.5. The blade suction surface boundary layers are usually very thick and represent a considerable blockage. The shock-boundary layer interaction may lead to separation, even at the design point.

The strong coupling between the boundary layer flow and the core flow and the strong probability of boundary layer separation have led to two main approaches to the flow prediction problem. The first is the viscous-inviscid interactive method (e.g., [1, 2]) in which the boundary layer displacement effects are iteratively coupled to the main inviscid body of the flow. This is achieved either by computing and adding the boundary layer displacement thickness to the blade geometry [1] or by employing a time-dependent boundary layer calculation and representing the displacement effects by transpiration of mass through blade surfaces [2]. While the latter technique seems to be stable even through boundary layer separation, the former must be applied via a mixed-mode technique. In this, the inviscid calculation determines the blade pressure distribution and the boundary layer calculation modifies the effective blade shape (forward mode) as long as the boundary layers remain attached. Once separation occurs the inviscid calculation determines the effective blade shape (and hence boundary layer displacement thickness) and the boundary layer calculation estimates the blade pressure distribution corresponding to the specified displacement thickness (inverse mode).

The second approach to the flow prediction problem is the solution of the full compressible Navier-Stokes equations. This is an attractive option since there are no problems matching viscous and inviscid regions and no coupling problems, and since features like boundary layer separation and shock-boundary layer interaction can be captured automatically. However, a Navier-Stokes solver is complicated to code and must be efficiently structured and use efficient algorithms to avoid being too expensive for use in a design environment. Currently, much effort is being expended on the development of suitable Navier-Stokes solvers (for example [3, 4, and 5]).

The current paper outlines an efficient implicit algorithm developed recently by the author for solving the compressible Navier-Stokes equations in turbomachinery blade-blade flows. The algorithm is a development of that presented in [3]. The algorithm is based on the technique of "deferred correction" wherein a low-accuracy discretization of the flow equations is employed during the iterative time-marching and appropriate correction terms are added as the iteration proceeds so the asymptotic steady solution has the desired spatial accuracy. The discretization of the flow equations can thus be chosen to enhance iterative robustness. This is not a new technique and it has been used in the past in the context of an explicit Euler solver [6]. However, deferred correction does not yet seem to have been exploited with the compressible Navier-Stokes equations.

The Navier-Stokes solver is applied to the study of a transonic compressor rotor for three cases, one on-design and two off-design (positive and negative incidence). The blade has a multiple circular arc profile and has a design inlet Mach number of 1.09 and deflection of 12.5 deg. In the design and positive incidence cases the blade bow shock is detached; in the negative incidence case the shock is swallowed. The results are compared with experimental measurements and with the predictions of a viscous-inviscid interactive method [1].

Equations of Motion

The flowfield is described by the two-dimensional isenthalpic time-dependent equations of motion written in integral form as [7]

Contributed by the Gas Turbine Division of The American Society of Mechanical Engineers and presented at the 30th International Gas Turbine Conference and Exhibit, Houston, Texas, March 18-21, 1985. Manuscript received at ASME Headquarters, December 10, 1984. Paper No. 85-GT-1.

$$\frac{\partial}{\partial t}\oint_{\text{VOL}} \bar{U} d(\text{VOL}) = \oint_{\text{AREA}} \bar{H}\cdot d(\overline{\text{AREA}}) \qquad (1)$$

where

$$\bar{U} = \begin{bmatrix} \rho \\ \rho u \\ \rho v \end{bmatrix} \quad \bar{H} = \begin{bmatrix} \rho\bar{q} \\ \rho u\bar{q} + \bar{\bar{\tau}}\,\hat{i}_X \\ \rho v\bar{q} + \bar{\bar{\tau}}\,\hat{i}_Y \end{bmatrix}$$

with

$$\bar{q} = u\hat{i}_X + v\hat{i}_Y$$
$$\bar{\bar{\tau}} = \sigma_X\hat{i}_X\hat{i}_X + \tau_{XY}\hat{i}_X\hat{i}_Y + \tau_{YX}\hat{i}_Y\hat{i}_X + \sigma_Y\hat{i}_Y\hat{i}_Y$$

and $\hat{i}_X$ and $\hat{i}_Y$ are unit vectors. The stress tensor, $\bar{\bar{\tau}}$, has components

$$\sigma_X = p - \mu\left(\frac{4}{3}\frac{\partial u}{\partial X} - \frac{2}{3}\frac{\partial v}{\partial Y}\right)$$
$$\sigma_Y = p - \mu\left(\frac{4}{3}\frac{\partial v}{\partial Y} - \frac{2}{3}\frac{\partial u}{\partial X}\right) \qquad (2)$$
$$\tau_{XY} = -\tau_{YX} = \mu\left(\frac{\partial u}{\partial Y} + \frac{\partial v}{\partial X}\right)$$

where $\mu = (1+\mu_T)/\text{Re}$. Isenthalpic flow is assumed to reduce the computational work. The equation of state is:

$$p = \frac{\gamma - 1}{\gamma}\rho\left(h_0 - \frac{u^2+v^2}{2}\right)$$

with h_0 the constant stagnation enthalpy. The equations are expressed in nondimensional form with Re an appropriate Reynolds number.

Turbulence is modelled by an eddy viscosity concept and introduced via the coefficient μ_T. For expediency the eddy viscosity is described by a simple two-layer mixing length model patterned after that of Baldwin and Lomax [8].

Finite Volume Corrected Defect Algorithm

The flowfield is divided into a large number of arbitrary, nonorthogonal finite volume computational cells, as indicated in Fig. 1. Quadrilateral cells are used to maintain an efficient narrow-banded matrix structure in the differenced flow equations but any other convenient shape could be adopted. The cells are constructed such that cell faces lie along the blade surfaces to facilitate application of boundary conditions. Provision is made for variable streamsheet thickness.

The integral equations of motion (1) are discretized on this finite volume cell structure with the flow variables stored at cell centers (ij). The spatial flux integral is replaced by a summation of fluxes around the quadrilateral cell and the time differential replaced by a simple difference,

$$\frac{\Delta\bar{U}}{\Delta t}\Delta\text{VOL} = \sum_{\text{CELL}} \bar{H}\cdot(\Delta A_X\hat{i}_X + \Delta A_Y\hat{i}_Y) = \bar{L}_H(\bar{U}) \qquad (3)$$

where $\Delta\bar{U} = \bar{U}^{n+1} - \bar{U}^n$, L_H represents the spatial flux operator, and ΔA_X and ΔA_Y represent the projected areas of the cell faces. To compute the values of the flow variables on cell faces it is assumed that they vary linearly between cell centers. The result is that the spatial flux integral is represented by a second-order accurate approximate, $\bar{L}_H(\bar{U})$, analogous to a central difference operator in finite difference terms.

Velocity derivatives, and hence the viscous stresses, are evaluated on cell faces using a local nonorthogonal coordinate system (ξ,η). A typical derivative is given by

$$\frac{\partial u}{\partial Y} = \frac{\partial u}{\partial \xi}\cdot\frac{\partial \xi}{\partial Y} + \frac{\partial u}{\partial \eta}\cdot\frac{\partial \eta}{\partial Y} \qquad (4)$$

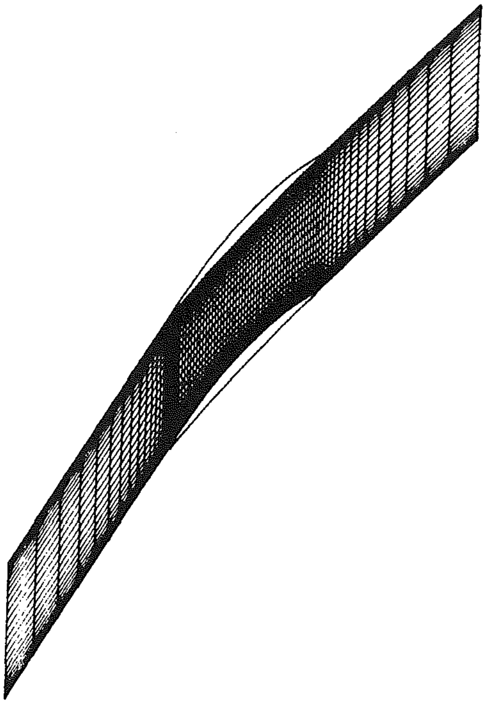

Fig. 1 The 86 × 31 finite volume mesh

where, for example,

$$(\partial u/\partial\eta)_{ij-1/2} = (u_{ij} - u_{ij-1})$$

The metrics $(\partial\eta/\partial Y$, etc.) are derived from the relationship between the (ξ,η) and (X,Y) mesh systems in the normal way [9]. The full stress tensor is retained in the difference equations.

In the present effort the asymptotic time-steady solution to the equations of motion is sought and so the algorithm used to time-march equation (3) forward to a solution is designed to be as economical and robust as possible with the time evolution treated purely as an iterative relaxation-type strategy.

Equation (3) is written implicitly as

$$\Delta\bar{U} = \frac{\Delta t}{\Delta\text{VOL}}\bar{L}_H^{n+1} \qquad (5)$$

where n is the time stepping index. The nonlinear spatial flux operators are linearized in the conventional way as

$$\bar{L}_H^{n+1} = \bar{L}_H^n + \bar{\bar{A}}\Delta\bar{U} \qquad (6)$$

simply by replacing ρ^{n+1} by $\rho^n + \Delta\rho$, $u^{n+1} = u^n - (u/\rho)\Delta\rho + (1/\rho)\cdot\Delta\rho u$ and so on. The algorithm now takes on the conventional Beam–Warming [9] form,

$$\left[\bar{\bar{I}} - \frac{\Delta t}{\Delta\text{VOL}}\bar{\bar{A}}\right]\Delta\bar{U} = \frac{\Delta t}{\Delta\text{VOL}}\bar{L}_H^n \qquad (7)$$

with the exception that all the operators are defined and manipulated from a finite volume standpoint.

To enhance the robustness, iterative stability, and convergence rate of equation (7), a defect operator, $D_1(U)$, is added to the flux operator. This defect operator is constructed to be essentially the difference between an upwinded discretization of the flux operator (i.e., first-order accurate but monotonic) and a centered discretization (i.e., second-order accurate but prone to oscillatory behavior). For example, for the simple scalar model equation,

$$\frac{\partial u}{\partial t} + A\frac{\partial u}{\partial X} = 0 \qquad (8)$$

the flux operator is $A\partial u/\partial X$. A second-order accurate centered approximation is:

$$A\delta_x^0 u = \frac{A}{2\Delta X}(u_{i+1} - u_{i-1}) \tag{9}$$

and a first-order accurate upwind approximation is ($A > 0$):

$$A\delta_x^u u = \frac{A}{\Delta X}(u_i - u_{i-1}) \tag{10}$$

In this context an appropriate defect operator would be:

$$D_1(u) = \frac{1}{2}\,|A|\,\Delta X \delta_{xx}^2 u \tag{11}$$

Adding this defect operator to an implicit centered discretization of the model equation (8)

$$\frac{\partial u}{\partial t} + A\delta_x^0 u^{n+1} = D_1(u)^{n+1} \tag{12}$$

produces a more robust set of difference equations, but effectively with the low accuracy associated with upwind differencing. Nevertheless, the diagonal dominance of difference equation (12) is guaranteed and it has the monotonic property. To force a higher order accuracy steady solution the defect operator must be somehow removed. This is achieved by adding a "defect correction," CF, to the difference equation (12) at the known time level. CF could be chosen in many ways; here it is chosen as

$$CF^n = (1-w)CF^{n-1} - wD_1{}^n \tag{13}$$

where w is a relaxation parameter. Thus the model difference equation is now:

$$\frac{\partial u}{\partial t} + A\delta_x^0 u^{n+1} = D_1{}^{n+1} + CF^n \tag{14}$$

The defect correction is built up recursively during the time marching and it is clear that in the converged steady state, $CF = -D_1$ and so the higher accuracy solution $A\delta_x^0 u = 0$ is recovered. The initial value of CF is taken as zero and in the present calculations the relaxation factor, w, was always taken as 0.1.

In the context of the full coupled set of flow equations (1) and their finite volume discretization, equation (7), an appropriate defect operator is defined by

$$\bar{D}_1(\bar{U}) = \partial_\xi(\rho_I \partial_\xi \bar{U}) + \partial_\eta(\rho_J \partial_\eta \bar{U}) \tag{15}$$

where $\bar{U} = (\rho,\ \rho u,\ \rho v)$ and $(\xi,\ \eta)$ is a local nonorthogonal coordinate system. The coefficients ρ_I and ρ_J are the spectral radii of the linearizing Jacobian matrices associated with the i-wise (ξ-wise) and j-wise (η-wise) parts of the flux operator respectively. These coefficients are given by

$$\rho_I = \hat{u}\left(\frac{\gamma+1}{2\gamma}\right) + \left\{\left(\frac{\gamma-1}{2\gamma}\right)^2 \hat{u}^2 + \frac{p}{\rho}\left(\frac{\partial Y^2}{\partial \eta} + \frac{\partial X^2}{\partial \eta}\right)\right\}^{1/2}$$

$$\rho_J = \hat{v}\left(\frac{\gamma+1}{2\gamma}\right) + \left\{\left(\frac{\gamma-1}{2\gamma}\right)^2 \hat{v}^2 + \frac{p}{\rho}\left(\frac{\partial X^2}{\partial \xi} + \frac{\partial Y^2}{\partial \xi}\right)\right\}^{1/2} \tag{16}$$

with $\hat{u} = u\partial Y/\partial\eta - v\partial X/\partial\eta$, $\hat{v} = v\partial X/\partial\xi - u\partial Y/\partial\xi$. The exact form of the defect D_1 is not important because the defect correction CF removes it as a converged steady solution is reached. The form defined in equation (15) was chosen to mimic the result for the simple model equation (11) and has the advantage of computational simplicity. The use of spectral radii ensures appropriate scaling of the defect relative to the convective fluxes in the flux operator.

Adding this defect operator with an associated defect correction to the basic finite volume discretization, equation (7), gives the algorithm in its final form:

$$\left[\bar{\bar{I}} - \frac{\Delta t}{\Delta \mathrm{VOL}}\{\bar{\bar{A}} + \bar{\bar{B}}\}\right]\Delta\bar{U} = \frac{\Delta t}{\Delta \mathrm{VOL}}\{\bar{L}_H + \bar{D}_1 + \bar{C}F + \bar{D}_2\}^n \tag{17}$$

Here, $\bar{\bar{B}}$ results from linearizing the defect operator, $D_1{}^{n+1} = D_1{}^n + \bar{\bar{B}}\Delta\bar{U}$, the defect correction is:

$$CF^n = (1-w)CF^{n-1} - wD_1^n, \text{ with } CF^0 = 0, w = 0.1,$$

and D_2 is an additional smoothing operator designed to remain after D_1 has been removed by the defect correction. In a converged steady solution $\Delta U = 0$ and $CF = -D_1$ so the algorithm, equation (17), converges to $\{L_H + D_2\} = 0$. Thus, while the defect D_1 is added for robustness and to enhance convergence rate, D_2 represents the residual steady-state artificial smoothing.

D_2 is added in a carefully monitored way to control the nonlinear instabilities associated with the resolution of shock waves and to limit the cell Reynolds numbers to those which can realistically be supported on the chosen mesh. The former is achieved by a numerical filter patterned after that used by Rizzi [10], whose effect is negligible everywhere except in the immediate vicinity of shock waves. The latter is achieved by a smoothing operator recommended by Shamroth et al. [5] which mimics the physical viscous terms, but which is set to zero locally if the local cell Reynolds number is less than a specified value (typically 10–100); otherwise just sufficient smoothing is introduced to reduce the cell Reynolds number to the specified value. By way of illustration, if the flux operator $L_H = -A\partial u/\partial x + \nu\partial^2 u/\partial x^2$ then

$$D_2 = \left[\nu\cdot\mathrm{MAX}\left\{\left(\frac{R_\Delta}{R_\Delta{}^*} - 1\right), 0\right\} + \Delta X\,\frac{|A|}{2}\,\theta\right]\frac{\partial^2 u}{\partial x^2}$$

where $R_\Delta = A\Delta X/\nu$, the cell Reynolds number, $R_\Delta{}^*$ is the specified cell Reynolds number limit and θ is a nonlinear switch of $0(1)$ in shocks and $0(\Delta X^2)$ elsewhere. For the present calculations $R_\Delta{}^*$ was set to 100 for the streamwise diffusion terms and 10 for the blade-normal diffusion terms. The switch θ was taken as $|p_{i+1} - 2p_i + p_{i-1}|/4p_i$. In practice, of course, as fine a mesh as can be afforded is used so that regions dominated by physical viscous effects are adequately resolved and the residual smoothing operator D_2 set to zero.

The algorithm, equation (17), is applied with spatially varying time steps, the local time step being set to typically 10 times the local explicit CFL limit. This is a simple way to improve the conditioning of the LHS matrix and speed up convergence [11].

The time marching of equation (17) proceeds by repeated inversion of the LHS matrix. This matrix is essentially block five-diagonal since a five-point difference molecule is used and each block is 3 × 3 (for ρ, ρu, and ρv). Currently, the matrix is factored into two block-tridiagonal operators and standard inversion techniques used (e.g., [12]) but other inversion strategies have been studied in the past (for example, Stone's strongly implicit procedure and the Jameson–Turkel LU factorization).

Boundary Conditions

Several types of boundary conditions have been used in the present study.

Periodic boundaries were treated just as if they were interior points.

At the outflow boundary, the static pressure is held constant and the other flow variables extrapolated from interior points.

At inflow boundaries, the total pressure is held constant and the flow angle fixed. This is quite appropriate for two of the three flows computed here (the zero and positive incidence cases) since the blade bow shocks are detached and so the inflow retains its physical dependence on the blade exit conditions (i.e., "unique incidence" does not apply). However, for the third case presented here, the negative incidence case, the shock is swallowed and so it is strictly preferable to fix the inlet swirl velocity and allow the inlet angle to emerge from the unique incidence condition. Nevertheless, no numerical difficulties were encountered.

The boundary conditions on the blade surfaces are those

Table 1

Cascade geometric data:			
Chord, *c*	90 mm		
Pitch/chord, *s/c*	0.621		
Stagger angle	48.5 deg		
Thickness/chord, *t/c*	0.05		
Cascade aerodynamic data:			
Reynolds number (based on chord)	1.6×10^6		
	Measured operating points		
	Case A	Case B	Case C
Inlet rel. Mach number	1.08	1.0	1.02
Inlet rel. flow angle	58.5 deg	63.0 deg	56.8 deg
Streamtube height ratio (inlet/exit)	1.18	1.23	1.08
Static pressure ratio (exit/inlet)	1.45	1.36	1.34
Flow incidence angle	0	+4.5 deg	−1.7 deg

appropriate to high Reynolds number flow with no slip. As mentioned earlier, cell faces rather than centers lie along blade surfaces so fluxes of mass and momentum across these faces are explicitly set to zero. The blade surface pressure is simply extrapolated from interior points and the blade surface shear stress is found from simple near-universal wall functions.

Turbulent flow over a solid surface is characterized by a very thin viscous sublayer in contact with the wall and a very rapid variation of velocity over a thin region near this wall. The number of mesh cells required to resolve this rapid variation is very large, especially at high Reynolds numbers, and leads to a very stiff system of equations to solve. It is found experimentally that turbulent flow near a wall can be represented by a number of near-universal laws and these may be used to reduce the need for severe mesh refinement near the wall. For the present study the simplest form of wall-function was selected [13]

$$u_p^+ = y_p^+ \text{ if } y_p^+ \leq 11.225 \qquad (18.1)$$

$$u_p^+ = \frac{1}{k} \log (E y_p^+) \text{ if } y_p^+ > 11.225 \qquad (18.2)$$

where:

$$u^+ = u/\sqrt{\tau_w/\rho},\ y^+ = \frac{\rho y}{\mu}\sqrt{\frac{\tau_w}{\rho}}$$

y is the distance normal to the wall
u is the velocity parallel to the wall
$E = 9.793$, $k = 0.4187$

and P is the center of the cell adjacent to the wall. Equation (18.1) represents a laminar wall function and is invoked if the mesh is refined enough locally for the cell adjacent to the wall to lie within the laminar sublayer. Equation (18.2) represents the logarithmic law of the wall mean velocity profile. Strictly equation (18) is only valid for incompressible flow, but more complicated versions are available (14) and will be used in the next version of the code. Essentially, equation (18) is used to deduce the wall shear stress from the local velocity field.

Typically, the finite volume mesh is designed so that y_p^+ is less than around 30–50 [8]. This means that as well as relieving the stiffness of the system of equations somewhat, fewer mesh cells are required to resolve the flowfield, reducing the computational work required to advance the flow by one time step.

However, it should be made clear that when the boundary layer becomes relatively thick, and particularly when separation occurs, y_p^+ will be less than 11, the laminar wall function invoked, and the boundary layer effectively resolved down to laminar sublayer scale.

All the boundary conditions are linearized and coupled into the implicit side of the algorithm. Although this restricts the generality of the algorithm, it is believed that implicit boundary conditions enhance iterative stability (see [11], for example). The full nonlinear boundary conditions are applied explicitly at the end of each time step.

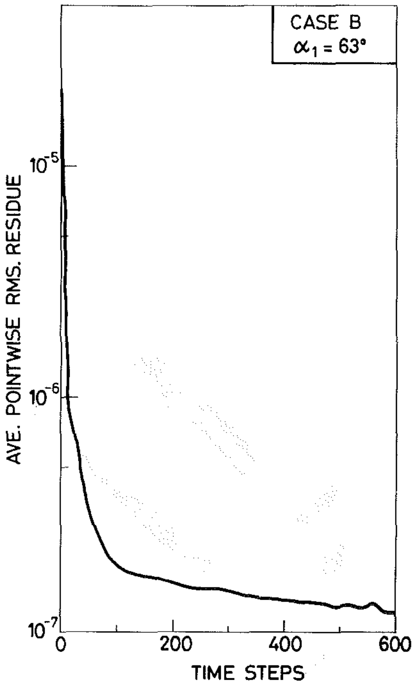

Fig. 2 Convergence history: Case B, positive incidence

Application to the Compressor Rotor

The subject of the present study is a cascade of blades derived from 45% height of the rotor of a DFVLR transonic compressor stage. Full details of the geometry and the experimental measurements were made available in [15]. The blade has a multiple circular arc profile and design inlet Mach number and deflection of 1.09 and 12.5 deg, respectively. The cascade was tested at a range of operating points, three of which were chosen for the present study. Table 1 gives the main geometric and aerodynamic parameters. Case A represents the "design" zero incidence case, Case B the positive incidence, and Case C the negative incidence. In all cases, the streamtube height ratio is substantial and while the present Navier–Stokes solver has provision for variable streamsheet thickness, there is no information about how this variation should be distributed; this is a key weakness of the so-called quasi-3D approach. For the present study, the streamsheet thickness was assumed constant up and downstream of the cascade with a linear variation between blade leading and trailing edges.

The Navier–Stokes solutions were obtained on the (86 × 31) finite volume mesh shown in Fig. 1. For expediency an "H-mesh" was used with mesh lines exponentially refined toward blade surfaces so as to resolve adequately the boundary layers. The mesh is refined near the leading edge to resolve the leading edge radius (the local streamwise mesh

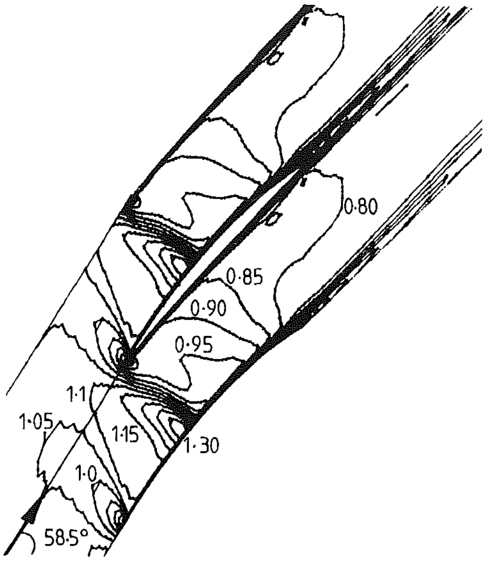

Fig. 3 Mach number contours predicted by the Navier-Stokes solver: Case A, design incidence (0 deg)

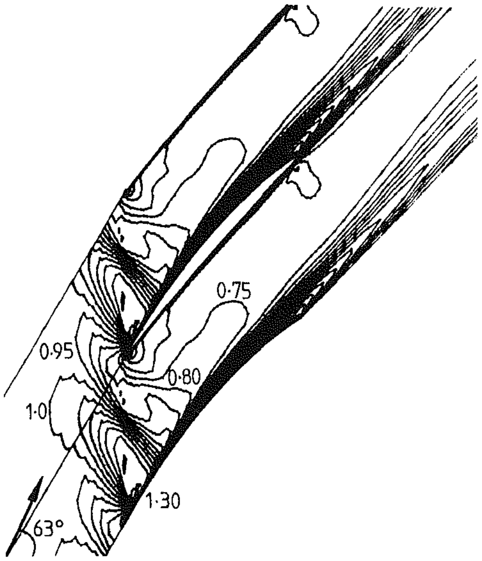

Fig. 4 Mach number contours predicted by the Navier-Stokes solver: Case B, positive incidence (+4.5 deg)

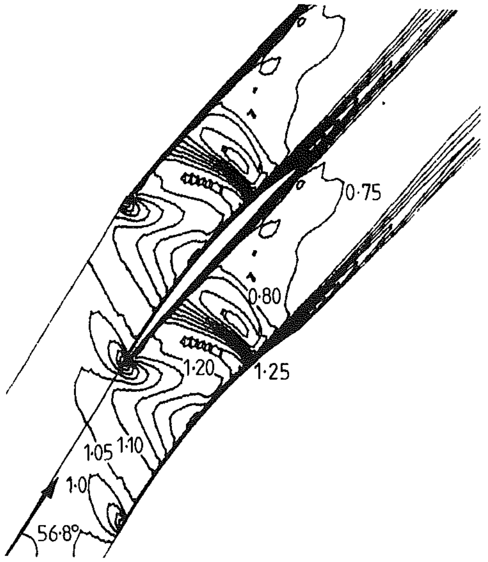

Fig. 5 Mach number contours predicted by the Navier-Stokes solver: Case C, negative incidence (−1.7 deg)

spacing is around 50% of the leading edge radius). No attempt was made to resolve the trailing edge radius since the exit flow is subsonic. Between 400 and 600 time steps were required to achieve an adequately converged solution on this mesh. Convergence was judged by monitoring not only the solution residues and their rate of change with time but also by following the development of global parameters like inlet and exit flow angle, inlet, exit, and peak Mach numbers and the ratio of inlet to exit mass flow. Figure 2 shows a convergence history in the form of the variation of average pointwise root mean square residue (i.e. rms (L_H)/number of points) with time step. Computations were performed on a Perkin-Elmer 3230 mini system, using 32 bit arithmetic, and required around 5 CPU h (equivalent to 30 CPU min on an IBM 3081 for example).

Discussion of Results

Contours of Mach number predicted by the Navier-Stokes solver are shown in Figs. 3, 4, and 5 for Cases A, B, and C respectively. The contours span the full range in the flow with an interval of 0.05. The predictions for Case A, design, show a well-defined, sharply captured shock, detached from the leading edge. The peak Mach number, just upstream of the interaction between the shock and the suction surface boundary layer, is around 1.34. The interaction leaves the boundary layer visibly thickened, but separation is not predicted to occur.

By contrast, the predictions for the positive incidence Case B show a rather stronger shock (peak Mach number about 1.45) positioned much further upstream. The interaction of this shock with the suction surface boundary layer causes a dramatic thickening of the boundary layer with a substantially increased blockage effect affecting the entire blade passage flowfield. Separation is predicted at the shock foot, with reattachment near midchord. It is interesting to note that most of the pressure surface experiences very little pressure gradient. At this operating point the flow "spilling" from one blade passage to the next is very large.

The predictions for the negative incidence Case C show the shock has been swallowed and terminates a supersonic expansion within the blade passage itself (peak Mach number of about 1.25). The shock is nearly normal to the flow and visibly thickens both the suction surface and the pressure surface boundary layers.

The blade surface isentropic Mach numbers predicted by the present Navier-Stokes solver have been compared with experimental measurements and the predictions of the viscous-inviscid interactive solver developed by Calvert [1]. Figures 6, 7, and 8 show Cases A, B, and C respectively. Calvert's method consists of an inviscid time-marching method (based on Denton [6]) coupled iteratively with an integral boundary layer method which estimates laminar boundary layer development, transition point and then turbulent boundary layer development. The boundary layer displacement thickness is added to the blade geometry via a mixed mode technique (forward mode for attached boundary layers and inverse mode for separated boundary layers) as described in the Introduction. Second-order boundary layer effects (like the variation of static pressure transverse to the boundary layer) are neglected. A typical solution on a 100 × 21 mesh requires 2 CPU min on a VAX 11/780 + 10 CPU min on an FPS 164 attached processor (this is roughly equivalent to 60–80 min on a Perkin Elmer 3230 system). For the design Case A the two predictions are in good agreement with each other and with the measurements except for slightly overpredicted peak Mach numbers.

Case B, the positive incidence case, is more interesting. The Navier-Stokes solution is in much better agreement with the measured surface pressure distribution than the viscous-

Table 2 The overall performance of the cascade (loss coefficient $\bar{\omega} = (p_{01} - p_{02})/(p_{01} - p_1)$)

Case A

	Measurement	Navier-Stokes solution	Viscous-inviscid interactive solution
α_1	58.5 deg	58.5 deg	58.6 deg
M_1	1.08	1.05	1.08
p_2/p_1	1.45	1.40	1.48
$\bar{\omega}$	8.3%	3.1%	5.2%
α_2	45.4 deg	46.7 deg	45.8 deg

Case B

	Measurement	Navier-Stokes solution	Viscous-inviscid interactive solution
α_1	63 deg	63 deg	62.2 deg
M_1	1.0	0.99	1.01
p_2/p_1	1.36	1.35	1.42
$\bar{\omega}$	14%	6.9%	8.7%
α_2	45.5 deg	48.5 deg	45.2 deg

Case C

	Measurement	Navier-Stokes solution	Viscous-inviscid interactive solution
α_1	56.8 deg	56.8 deg	57 deg
M_1	1.02	0.98	1.02
p_2/p_1	1.34	1.28	1.33
$\bar{\omega}$	9.1%	6.7%	6.9%
α_2	47.3 deg	48.1 deg	48.6 deg

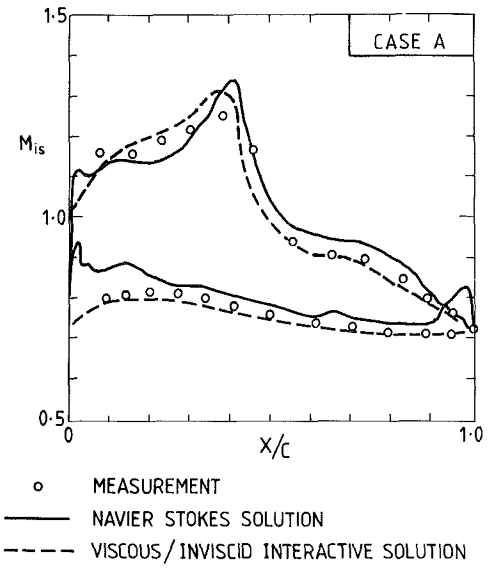

Fig. 6 Comparison between predicted and measured blade surface isentropic Mach numbers: Case A, design

inviscid interactive solution. This is particularly so along the pressure surface. The better agreement seems largely to be due to the Navier-Stokes solver modelling much more accurately the dramatically increased suction surface boundary layer blockage downstream of the shock interaction. The viscous-inviscid interactive solver underestimates this blockage and thus the predicted surface Mach numbers are much too low over most of the pressure surface and the aft half of the suction surface. There may be several reasons for this. Firstly, the Navier-Stokes solutions were produced assuming transition occurs at the leading edge whereas the viscous-inviscid interactive solver predicted transition at around 15% chord. It seems more reasonable for this case to assume transition at the leading edge because the large flow spillage leads to high local incidences onto the blade with the strong possibility of a leading edge separation bubble followed by a reattached turbulent boundary layer. Secondly, of course, this strongly coupled flowfield with its strong shock-boundary layer in-

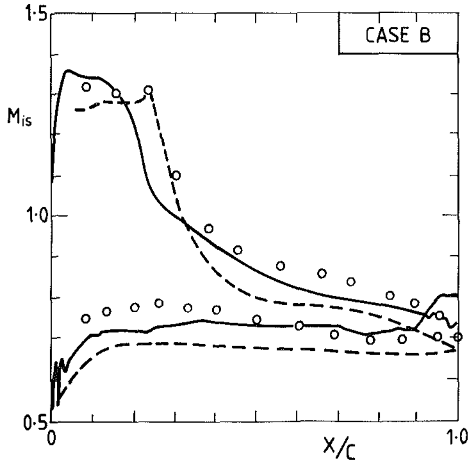

Fig. 7 Comparison between predicted and measured blade surface isentropic Mach numbers: Case B, positive incidence. Key as for Fig. 6.

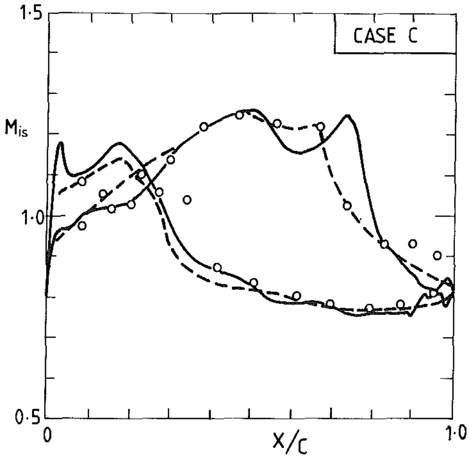

Fig. 8 Comparison between predicted and measured blade surface isentropic Mach numbers: Case C, negative incidence. Key as for Fig. 6.

teraction may be more appropriately handled by a Navier–Stokes solver which retains terms like the boundary layer transverse pressure gradient.

One point concerning the shock locations in Fig. 7 should be noted. The viscous-interactive solver is coded so that the shock location can be an input boundary condition and the exit static pressure is then iteratively adjusted to meet this boundary condition. Consequently, the shock location matches the measurements, even though the boundary layer blockage is not well predicted. By contrast, the Navier–Stokes solver simply fixes the exit static pressure and accepts whatever solution emerges. The predicted shock location is around 5% chord upstream of that measured.

In Case C, the negative incidence case, the Navier–Stokes solution and the viscous-inviscid interactive solution are again in good agreement with each other and with the measurements. The main discrepancies seem to be in shock locations with both solvers predicting the shock about 5% chord upstream of the measurements on the pressure surface and the Navier–Stokes solver predicting the shock about 5% chord downstream of the measurements on the suction surface.

For the design and negative incidences cases (A and C) the comparisons of blade isentropic Mach numbers show good agreement between the Navier–Stokes solutions, the viscous-inviscid interactive solutions, and the measurements. It is only for the more severe off-design case, the near-stall positive incidence Case B, that the Navier–Stokes solver is able to demonstrate better peformance than the viscous-inviscid solver by maintaining good agreement with the measured flow.

The predicted and measured overall performance of the cascade for each of the three cases is compared in Table 2. Among the interesting points this comparison reveals are that both prediction methods underestimate the loss compared to the measurements.

Concluding Remarks

The Navier–Stokes solver outlined in the current paper successfully simulated the off-design flow in the transonic compressor rotor. The predictions agree well with experimental measurements and the predictions of a viscous-inviscid interactive method. More work is needed on turbulence modelling, particularly transition modelling.

References

1 Calvert, W. J., "Application of an Inviscid-Viscous Interaction Method to Transonic Compressor Cascades," NGTE Report R 83001, Mar. 1983.

2 Freeman, C., "A Viscous Inviscid Interaction Method for Calculating the Flow in Transonic Fan Blade Passages by the Use of a Time-Dependent Free Stream Calculation and a Time-Dependent Boundary Layer Calculation," *I. Mech. E. Conf.*, Computational Methods in Turbomachinery, Birmingham, U.K., Apr. 1984.

3 Dawes, W. N., "An Efficient Implicit Algorithm for the Equations of 2D Viscous Compressible Flow," *Int. J. of Heat and Fluid Flow*, Vol. 4, No. 1, 1983.

4 Steger, J. L., Pulliam, T. H., and Chima, R. V., "An Implicit Finite Difference Code for Inviscid and Viscous Cascade Flow," AIAA Paper No. 80-1427, July 1980.

5 Shamroth, S. J., McDonald, H., and Briley, R. W., "Application of a Navier-Stokes Analysis to Transonic Cascade Flow Fields," ASME Paper No. 82-GT-235, 1982.

6 Denton, J. D., "An Improved Time Marching Method for Turbomachinery Flow Calculation," ASME Paper No. 82-GT-258, 1982.

7 Deiwert, G. S., "High Reynolds Number Transonic Flow Simulation," *Proc. Fourth Int. Conf. on Num. Methods in Fl. Dynamics*, Lecture Notes in Physics 35, Springer-Verlag, 1975.

8 Baldwin, B., and Lomax, H., "Thin Layer Approximation and Algebraic Model for Separated Turbulent Flows," AIAA Paper No. 78-257, 1978.

9 Steger, J. L., "Implicit Finite Difference Simulation of Flow About Arbitrary Geometries With Application to Air Foils," AIAA Paper No. 77-665, 1977.

10 Rizzi, A., "Computation of Rotational Transonic Flow," *Notes on Num. Fl. Mechs.*, Vol. 3, Vieweg, 1981.

11 McDonald, H., and Briley, W. R., "Computational Fluid Dynamic Aspects of Internal Flows," AIAA Paper No. 79-1445, 1979.

12 Kutler, P., "Supersonic Flow Over Ablated Nose Tips Using an Unsteady Numerical Procedure," AIAA Paper No. 78-213, 1978.

13 Patankar, S. V., and Spalding, D. B., "Heat and Mass Transfer in Boundary Layers," 2nd Edition, Intertext Books, London, 1972.

14 Wilcox, D. C., "Numerical Study of Separated Turbulent Flows," ARL Report No. 74-0133, 1974.

15 Ginder, R. B., "Competition Blade," *I. Mech. E. Conf.*, Computational Methods in Turbomachinery, Birmingham, U.K., Apr. 1984.

On Thermodynamics of Gas-Turbine Cycles: Part 2—A Model for Expansion in Cooled Turbines

M. A. El-Masri
Associate Professor of Mechanical Engineering,
Massachusetts Institute of Technology,
Cambridge, MA 02139

While raising turbine inlet temperature improves the efficiency of the gas-turbine cycle, the increasing turbine-cooling losses become a limiting factor. Detailed prediction of those losses is a complex process, thought to be possible only for specific designs and operating conditions. A general, albeit approximate, model is presented to quantify those cooling losses for different types of cooling technologies. It is based upon representing the turbine as an expansion path with continuous, rather than discrete, work extraction. This enables closed-form solutions to be found for the states along the expansion path as well as turbine work output. The formulation shows the key factor in determining the cooling losses is the parameter scaling the ratio of heat to work fluxes loading the machine surfaces. Solutions are given for three cases: internal air-cooling, transpiration air cooling, and internal liquid cooling. The first and second cases represent lower and upper bounds respectively for the performance of film-cooled machines. Irreversibilities arising from flow-path friction, heat transfer, cooling air throttling, and mixing of coolant and mainstream are quantified and compared. Sample calculations for the performance of open and combined cycles with cooled turbines are presented. The dependence and sensitivity of the results to the various loss mechanisms and assumptions is shown. Results in this paper pertain to Brayton-cycle gas turbines with the three types of cooling mentioned. Reheat gas turbines are more sensitive to cooling losses due to the larger number of high-temperature stages. Those are considered in Part 3.

I Introduction

Raising turbine inlet temperature increases efficiency and specific output of gas-turbine cycles. The surfaces of the components exposed to the hot gas must be maintained below a certain safe working temperature, consistent with mechanical strength and corrosion resistance. The cooling requirements for those components increase with temperature difference between the surfaces and the relative gas temperature. As turbine inlet temperature is raised, this temperature difference increases and a larger proportion of the expansion path requires cooling. The thermodynamic penalties of the cooling process begin to counteract the advantage of the increased inlet temperature. Eventually, an inlet temperature is reached beyond which cycle thermal efficiency falls for further increases. A similar trend occurs with specific power except that cycle efficiency peaks at turbine inlet temperatures which are usually below those for peak specific output.

The temperature for peak thermal efficiency, as well as the difference between its value and that for a similar adiabatic cycle, depend on the machine parameters and the type of cooling technology employed.

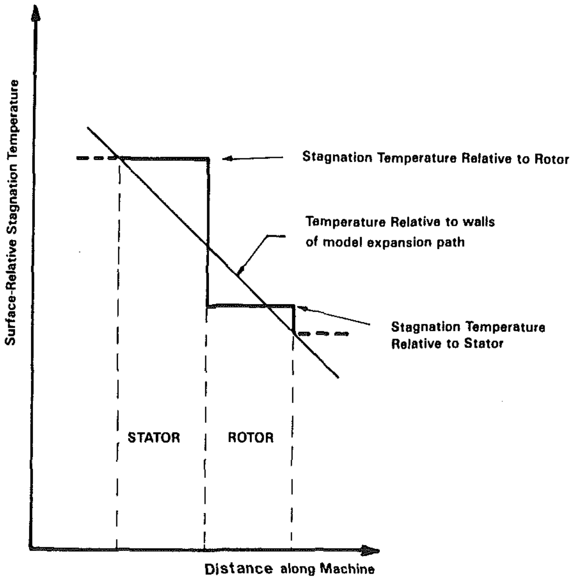

Fig. 1 Schematic representation of the temperature profile in the expansion path with continuous work extraction

---

Contributed by the Gas Turbine Division of The American Society of Mechanical Engineers and presented at the 30th International Gas Turbine Conference and Exhibit, Houston, Texas, March 18-21, 1985. Manuscript received at ASME Headquarters, January 7, 1985. Paper No. 85-GT-130.

A model for the thermodynamic path of expansion in a turbine with cooled walls was developed by Hawthorne [1, 2]. It is based on constant mass flow in the expansion path, which does not suffer losses due to mixing the spent coolant into the gas. The results are presented in terms of a "negative reheat factor" which reduces the exponent on temperature in the pressure–temperature relation along the expansion. Rohsenow applied this model to show the impact of cooling on open cycles [3]. This approach is also presented in [4].

In air-cooled turbines, mixing the spent cooling air into the main flow causes losses in both stagnation temperature and pressure. The thermodynamic penalty due to those losses is usually more substantial than that due to heat extraction through the walls. Since those penalties increase with mass flow of cooling air, minimizing this mass flow is advantageous. This is achieved by improving the internal heat transfer between coolant and blade and by using the spent coolant to shield the blade from the hot gas, essentially reducing the external heat-transfer coefficient. Both those effects could be achieved if a practical transpiration cooling system were developed. They are partially realized by the current technology of film-cooling. The older technology of internal air-cooling does not utilize the spent coolant to reduce the external heat-transfer coefficient. Thus, its performance can be considered a lower bound on film cooling whereas transpiration represents an upper bound. Other methods of reducing cooling-air requirements are currently being developed. One such technology is thermal barrier coatings. Another method proposed recently [5] is to precool the cooling air, use it to cool the nozzles by internal forced convection, then route the same air to the next rotor.

Due to the large number of parameters influencing the cooling losses, precise calculations can only be attempted for specific machines and conditions. Such computations, based on sound modelling and experience, can yield satisfactory predictions for the performance of a particular machine. To obtain a general understanding of the parameters governing cooling losses, and to compare different technologies, one may resort to approximate models based on dimensionless parameters. If the model is sound but oversimplified, it yields the correct dimensionless parameters but cannot provide satisfactory numerical results. Such an approach is briefly presented in [6], and somewhat more extensively applied in [7] to achieve closed-form solutions. A numerical computation based on dimensionless groups derived in the same manner was developed for water-cooled turbines [8], and extended to other cooling systems [9], where results for open-cycle efficiency are presented. Results based on the same model are presented for combined cycles in [10].

The purpose of this paper is to present a model that is sufficiently simplified to enable closed-form solutions, while retaining adequate detail to provide useful numerical results. Thus, the key parameters governing cooling losses can be identified, various technologies may be compared in a common format, and bounds on their performance estimated. The model is based on a representation of the actual turbine by an expansion path with continous work extraction. The algebra is simplified by using an ideal gas with constant properties. Expressions for the local mass flow and state along the expansion path are derived in terms of a temperature coordinate. The key parameter governing cooling losses is shown to be the ratio that scales heat to work fluxes to the expansion path walls.

The model is applied to three cooling systems: internal air cooling, transpiration air cooling, and internal liquid cooling. The first two represent lower and upper bounds for film cooling performance. The solutions are used to estimate the performance of open cycles and combined cycles.

Steam cooling has potential for improving performance over similar air-cooling technology. Calculations presented in [10-14] illustrate its potential. Results presented in Part 3 of this paper indicate an advantage of transpiration with steam over air transpiration in reheat cycles.

II Model of Expansion Path

In the interest of obtaining closed-form and general solutions, the process of work extraction from the expanding gases is modelled as continuous rather than occurring in discrete stages. The turbine is treated as an expander whose walls continuously extract work. The stagnation temperature of the gas relative to those walls is thus approximated by a continuously varying function rather than the actual stepwise variation. This is depicted in Fig. 1 which shows that the assumed temperature profile underestimates the relative gas-to-surface temperature difference for a stator while overestimating it for a rotor. The stage average, however, is essentially preserved.

Nomenclature

A_g = gas flow path cross-sectional area
A_w = wall surface area
b = blowing ratio
c = stage geometry constant
c_p = specific heat at constant pressure
e = polytropic efficiency
h = heat transfer coefficient
I = turbine inefficiency, equation (23)
L_{thr} = throttling loss factor, equation (28)
M = Mach number of gas relative to surface
M_0 = ratio of rotor pitchline velocity to velocity of sound at ambient
m = mass flow rate of gas
n = constant for reduction in Stanton number with transpiration, equation (9)
p = stagnation pressure
δp = loss in stagnation pressure in combustor
Q = heat flow rate
q = dimensionless heat $= Q/m^* c_p T_0$
R = gas constant
S = entropy
s = specific entropy
St = Stanton number
St_0 = Stanton number with impermeable wall
T = absolute stagnation temperature
T_0 = ambient temperature
u = pitchline velocity of rotor
W = work rate
w = dimensionless work $= W/m^* c_p T_0$
Y = stagnation pressure loss factor, equation (24)
α = dimensionless cooling air temperature $= T_a/T_0$
β = dimensionless blade (and wall temperature) $= T_b/T_0$
γ = specific heat ratio
σ = factor scaling heat to work flux, equation (6)
τ = dimensionless gas temperature $= T/T_0$
θ = dimensionless peak temperature
ψ, ϕ = functions
ϵ = effectiveness of blade heat exchange, equation (8)

Subscripts and Superscripts

a = cooling air supply
$a2$ = cooling air leaving blade
0 = ambient
gen = generated
$\tilde{}$ = dimensionless
$*$ = conditions in expansion path at $\tau = \beta$

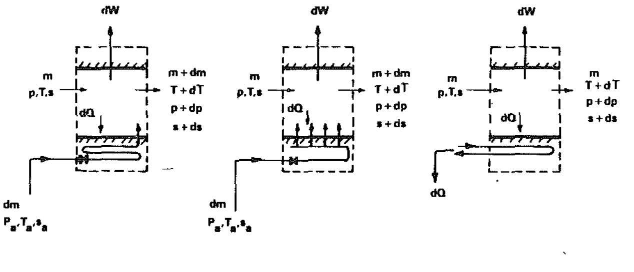

(a) Internally Air-Cooled (b) Transpiration Air-Cooled (c) Internally Liquid-Cooled

Fig. 2 Elements of model of cooled expansion path

The connection between this idealized model of the expansion path and the real machine is accomplished by setting its work flux equal to the machine stage average, i.e.,

$$\frac{dW}{dA_w}=\frac{W_{\text{stage}}}{A_{w,\text{stage}}}. \tag{1}$$

The stage work is proportional to the local gas-flow rate and square of pitchline velocity,

$$W_{\text{stage}}=mcu^2 \tag{2}$$

where the proportionality constant c depends on the stage velocity triangles (geometry) and is typically in the range $(1.0<c<1.5)$.

Consider an element of the expansion path as shown in Fig. 2: The heat flux is[1]

$$\frac{dQ}{dA_w}=h(T-T_w) \tag{3}$$

Assuming the heat-transfer coefficient for the expansion path is the same as the stage average, one may write,

$$h=\text{St}\left(\frac{m}{A_g}\right)c_p. \tag{4}$$

Equations (1) through (4) may be combined and rearranged to give

$$\frac{dQ}{dW}=\sigma(\tau-\beta) \tag{5}$$

where

$$\sigma=\frac{\text{St}(A_{w,\text{stage}}/A_g)}{c(\gamma-1)\text{M}_0^2} \tag{6}$$

is the parameter that characterizes the relative heat to work loadings on the machine surfaces. M_0 is the pitchline Mach number referred to ambient temperature T_0.

Three types of cooled expansion paths are considered in this paper. They are illustrated in Fig. 2 and described briefly below:

(*a*) Internally air-cooled: Cooling air mass dm supplied at T_a and p_a circulates through wall passages. It absorbs the heat load dQ and increases in temperature to T_{a2}, at which it is ejected into the mainflow at the local pressure and with negligible momentum. Thus one may write

$$dQ=c_p(T_{a2}-T_a)\,dm=\epsilon c_p(T_b-T_a)dm \tag{7}$$

where ϵ is a "heat exchanger effectiveness" for the cooling channel configuration

$$\epsilon=\frac{T_{a2}-T_a}{T_b-T_a}. \tag{8}$$

In this system the cooling air is not utilized to reduce the gas-to-surface heat-transfer coefficient and represents turbines where the spent coolant is ejected from blade tips and trailing edges. Its performance may be considered a lower bound for film cooling.

(*b*) Transpiration air-cooling: The cooling air is supplied to a wall cavity from which it transpires uniformly across the porous wall surface, cooling it as well as reducing the heat-transfer coefficient from gas to wall surface. The reduction in heat-transfer coefficient is the maximum that can be achieved for a given coolant flow. Also, due to intimate coolant to wall contact, its exit temperature is the same as the wall, and the effectiveness of equation (8) is essentially unity. This system provides a high upper bound on the performance of film-cooling.

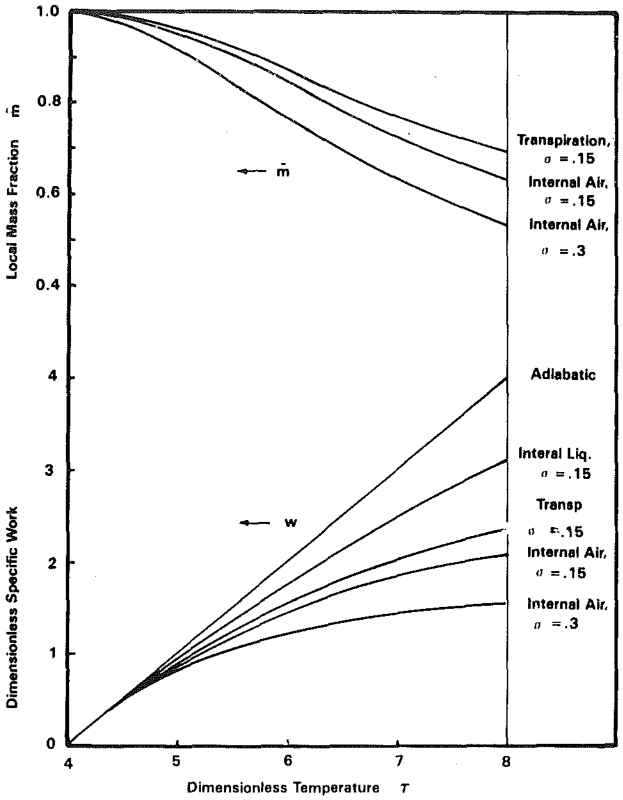

Fig. 3 Work and massflow profiles for examples of cooled expansion

In actual transpiration cooling, the ratio of heat-transfer coefficient to its value with an impermeable wall, (St/St_0), is a function of the parameter (b/St_0), where b is the blowing ratio of transpired to mainflow mass flux. This relation may be linearized in the neighborhood of a projected operating point and expressed as

$$\text{St}=\text{St}_0-nb \tag{9}$$

with n varying from about 1/2 at low transpiration rates to about 1/8 near separation. The theoretical value of n is 1/4 for an infinite Reynolds number [15], and this idealization reasonably approximates the data for the entire range [16]. In this paper n will be idealized as a constant; a value of 1/4 is used in calculations. The final results are not very sensitive to its value.

The blowing ratio b is just

$$b=\frac{dm/dA_w}{m/A_g} \tag{10}$$

Using equation (7) with $\epsilon=1$ for transpiration, together with equations (3) and (4) enables one to rewrite equation (9) as

$$\text{St}=\frac{\text{St}_0}{1+n\left(\dfrac{\tau-\beta}{\beta-\alpha}\right)}. \tag{11}$$

(*c*) Internal liquid cooling: This system is illustrated in

---

[1] The adiabatic wall temperature is assumed equal to the local stagnation temperature.

Fig. 2(*c*). The coolant is circulated in a closed loop within the walls and extracts the thermal loading dQ. The coolant carries the heat out of the expansion path to be utilized elsewhere or wasted. The coolant does not mix with the main flow.

III Solutions

Due to the similarity between the two air-cooled cases, they will be treated together followed by the liquid-cooled case.

Air-Cooled Expansions. Applying the first law to the control volumes of Figs. 2(*a*) and 2(*b*) gives

$$dW=-mc_p dT-c_p(T-T_a)dm. \tag{12}$$

Using this, together with equations (5), (6), (7), and (11), one may explicitly express the local mass-flow rate in terms of local gas temperature as

$$\int_{m^*}^{m}\frac{dm}{m}=-\int_{\tau=\beta}^{\tau}\frac{\sigma(\tau-\beta)d\tau}{(\beta-\alpha)+\{\sigma(\tau-\alpha)+n\}(\tau-\beta)} \tag{13}$$

where m^* is the mass flow in the turbine at and below blade temperature, after all the cooling air has been added. Neglecting leakage, this equals the compressor mass flow. Equation (13) applies to both internal-air and transpiration cooling provided that

$$\left.\begin{array}{l}\sigma=\dfrac{\sigma_0}{\epsilon},\ n=0\ \text{(internal)}\\ \sigma=\sigma_0,\ n\neq 0\ \text{(transpiration)}\end{array}\right\} \tag{14}$$

where σ_0 is given by equation (6) when $\mathrm{St}=\mathrm{St}_0$. Performing the integral of equation (13), the local mass fraction is found as

$$\tilde{m}=\frac{m}{m^*}=\exp\{\sigma\beta\psi_1-\sigma\psi_2\} \tag{15}$$

where the functions ψ_1 and ψ_2 are given in Appendix 1. The work extracted from the expansion path between any gas temperature τ and the location at which $\tau=\beta$ may be obtained from the overall energy balance (or from integrating (12)) as

$$w=W/m^*c_pT_0=\tilde{m}(\tau-\alpha)+(\alpha-\beta). \tag{16}$$

Examples of mass flow and work profiles along air-cooled expansion paths are given in Fig. 3 for $\beta=4$, $\alpha=2.75$. The latter corresponds to delivery from a compressor of polytropic efficiency 0.9 and pressure ratio 24. In those examples $\sigma=0.15$ for transpiration and 0.3 for internal air cooling. To illustrate the effect of transpiration, the internally air-cooled case with $\sigma=0.15$ is also shown. The choice of numerical values is discussed in Appendix II. For an adiabatic turbine $\tilde{m}=1$ and $w=\tau-\beta$ as shown in Fig. 3.

To solve for the pressure-temperature relation along the expansion path, the second law is written for the control volume of Figs. 2(*a*) and 2(*b*) as the entropy balance

$$ms+dm\ s_a+dS_{\mathrm{gen}}=(m+dm)(s+ds) \tag{17}$$

where dS_{gen} is the entropy generated within the control volume. This arises from three mechanisms:

(*a*) Friction and aerodynamic losses in the main gas path. Those may be characterized by the turbine polytropic efficiency e[2] and result in entropy generation

$$dS_{\mathrm{gen,fric}}=\frac{1-e}{e}\frac{dW}{T}. \tag{18}$$

(*b*) Throttling of cooling air from its supply pressure p_a to the local pressure p,

$$dS_{\mathrm{gen,thr}}=dm\ R\ \ln(p_a/p). \tag{19}$$

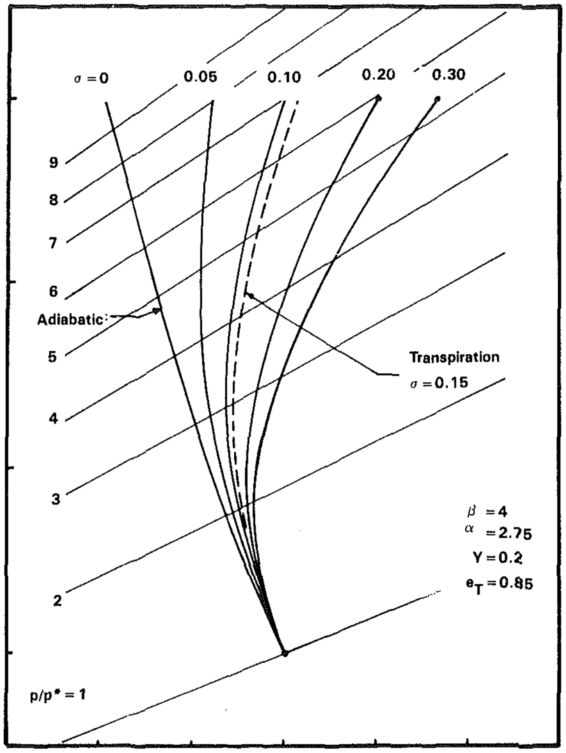

Fig. 4 Temperature-entropy path for air-cooled expansion

(*c*) Irreversible heat transfer from gas to coolant followed by mixing the coolant and gas. This mixing process causes further heat-transfer irreversibility in bringing the mixture to a common temperature, as well as an irreversible loss of stagnation pressure to accelerate the coolant to the main flow velocity, the combined heat transfer and mixing loss is

$$dS_{\mathrm{gen,mix}}=dm\left\{c_p\left[\ln\frac{T}{T_a}+\frac{T_a}{T}-1\right]+\gamma R\mathrm{M}^2\right\}. \tag{20}$$

The first term on the right represents the thermal degradation due to heat-transfer irreversibility and the second the stagnation pressure loss. The former assumes $(\gamma-1)\mathrm{M}^2/2\ll 1$ where M is the Mach number of the flow relative to the surface at the point of coolant ejection [17]. The value of M^2 for the second term should be a weighted average for the points of coolant ejection around the blade profile. profile.

The total entropy generated is found by adding equations (18), (19), and (20),

$$dS_{\mathrm{gen}}=dS_{\mathrm{gen,fric}}+dS_{\mathrm{gen,thr}}+dS_{\mathrm{gen,mix}} \tag{21}$$

which, upon substitution into equation (17), enables one to solve for the change in specific entropy. In dimensionless form this is

$$d\tilde{s}=-I\left[\frac{dm}{m}\left(1-\frac{\alpha}{\tau}\right)+\frac{d\tau}{\tau}\right]+\frac{dm}{m}\left[Y+\frac{\alpha}{\tau}-1\right] \tag{22}$$

where

$$I=\frac{1-e}{e} \tag{23}$$

$$Y=(\gamma-1)\mathrm{M}^2. \tag{24}$$

The first term arises from friction and aerodynamic losses and obtains from combining (12) and (18). The second term accounts for the heat transfer and mixing effects. The throttling term cancels out of the entropy balance of equation (17). Substituting for dm/m from (13) and integrating enables one to find the temperature-entropy path:

---

[2] This includes aerodynamic losses other than mixing.

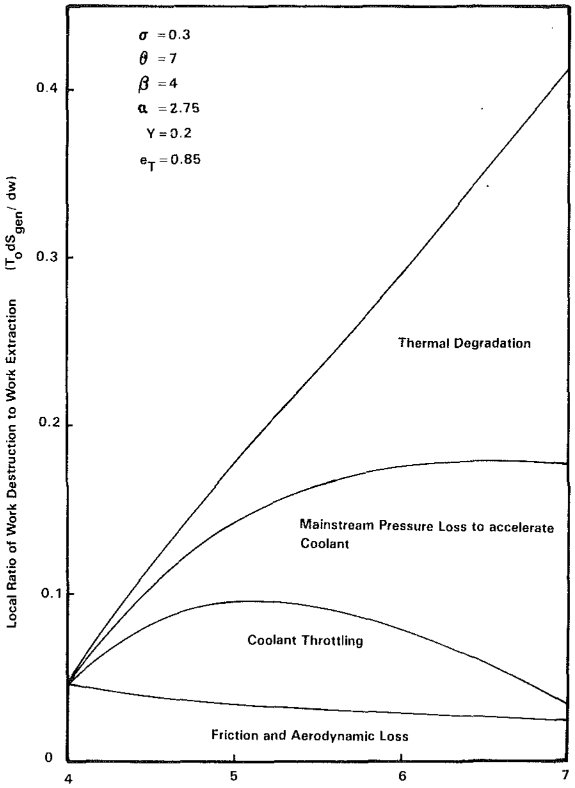

Fig. 5 **Loss distribution in internally air-cooled expansion**

$$(\tilde{s}-\tilde{s}^*)=\int_*^{\tilde{s}} d\tilde{s}=[Y\sigma\beta-\sigma(\beta+\alpha)-nI]\psi_1$$
$$+\sigma[1-Y]\psi_2$$
$$+[\alpha\sigma\beta-I(\beta-n\beta-\alpha)]\psi_3. \qquad (25)$$

ψ_1, ψ_2, ψ_3 are functions of the local temperature and are given in Appendix 1. An example of the $\tau-\tilde{s}$ path of air-cooled expansions is given in Fig. 4 for $\beta=4$, $\alpha=2.75$, $Y=0.2$. Internally air-cooled expansion paths are shown for different values of σ. A transpiration-cooled path for $\sigma=0.15$ is also shown. The pressure ratio across any section of the expansion path may be found from the thermodynamic relation

$$\left(\frac{p}{p^*}\right)=\left(\frac{\tau}{\beta}\right)^{c_p/R}\exp\left\{-\frac{c_p}{R}(\tilde{s}-\tilde{s}^*)\right\}. \qquad (26)$$

Lines of constant pressure are indicated on Fig. 4.

To appreciate the effect of cooling on cycle efficiency, as well as to illustrate the relative magnitude of the loss mechanisms, one may examine the local ratio of available work destruction to work extraction as a function of temperature. From equations (12), (18), (19), (20), and (21) this is found to be

$$\frac{T_0 dS_{\rm gen}}{dW}=\frac{I}{\tau}+\frac{\sigma(\tau-\beta)}{(\beta-\alpha)+n(\tau-\beta)}\left\{\left(\ln\frac{\tau}{\alpha}+\frac{\alpha}{\tau}-1\right)+Y+L_{\rm thr}\right\}. \qquad (27)$$

The first term on the right accounts for frictional and aerodynamic losses. The first of the terms in large parentheses represents heat-transfer irreversibility, the second represents loss in main flow stagnation pressure and the third throttling of cooling air to local pressure.

$$L_{\rm thr}=\frac{R}{c_p}\ln\frac{p_a}{p}. \qquad (28)$$

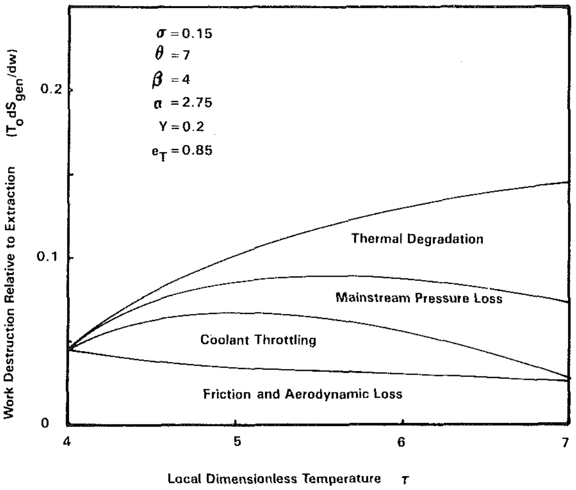

Fig. 6 **Loss distribution in transpiration-cooled expansion**

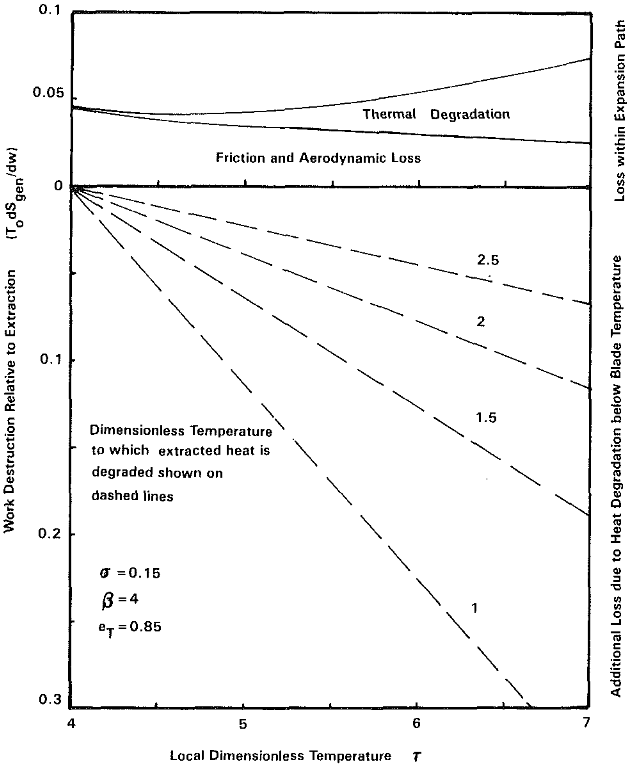

Fig. 7 **Loss distribution in internally liquid-cooled expansion**

Assuming that cooling air is taken from compressor delivery, then

$$p_a=p_\theta(1+\delta_{\tilde{p}}) \qquad (29)$$

where p_θ is the pressure at turbine inlet. Using (26) and (25) enables the throttling loss to be expressed in terms of local temperature only

$$L_{\rm thr}=\ln\frac{\theta}{\tau}+\frac{R}{c_p}\delta_{\tilde{p}}+(\tilde{s}-\tilde{s}_\theta). \qquad (30)$$

Equation (27) is plotted in Figs. 5 and 6 for examples of internally air-cooled and transpiration-cooled expansions for $\theta=7$, $\beta=4$, $\alpha=2.75$. The magnitude of each of the loss mechanisms is shown. The steep rise of losses relative to work for internal air cooling render it impractical for high temperatures. The throttling loss peaks within the expansion since

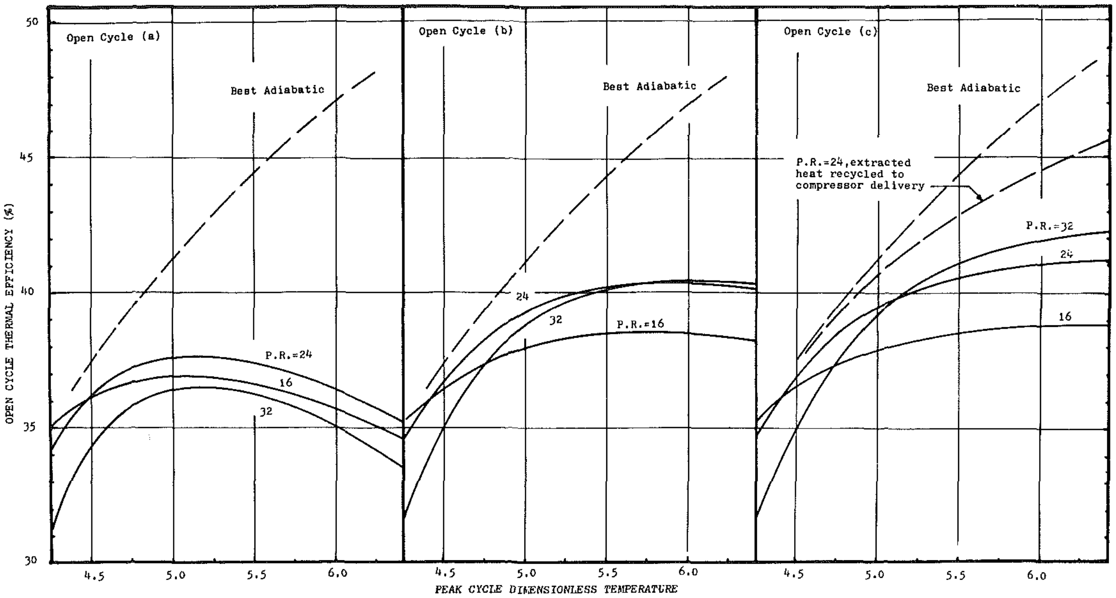

Fig. 8

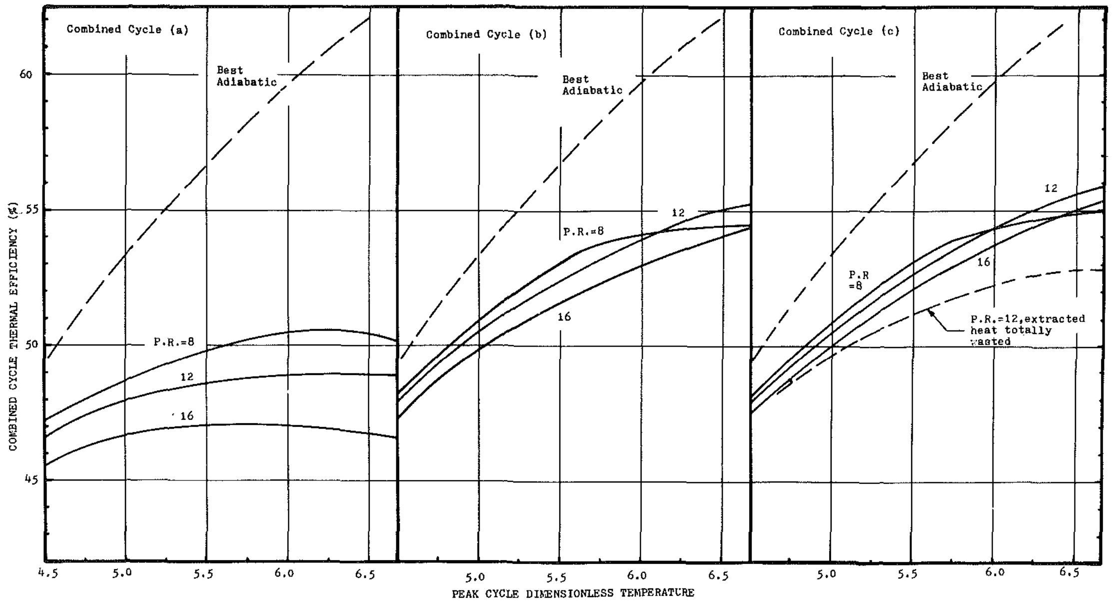

Fig. 9

it is proportional to the product of coolant flow and pressure drop, which goes to zero at either end. It may be reduced by extracting air from intermediate compressor stages, as practiced in some engines.

Internally Water-Cooled Expansion. Applying the first law to the control volume of Fig. 2(*c*) gives

$$dw = -d\tau - dq \tag{31}$$

Also from (5) and (6)

$$\frac{dq}{dw} = \sigma_0(\tau - \beta) \tag{32}$$

Eliminating dq between (31) and (32) the work of expansion for the cooled section of the turbine may be found as

$$w = \int_{\tau}^{\tau^* = \beta} dw = \frac{1}{\sigma_0} \ln[1 + \sigma_0(\tau - \beta)] \tag{33}$$

and the heat extracted by the coolant between any temperature and blade temperature is

$$q = (\tau - \beta) - w. \tag{34}$$

The work profile is illustrated in Fig. 3 for $\sigma_0 = 0.15$. It is above the equivalent transpiration cooled path due to the larger mass flow and lower losses.

If the control volume of Fig. 2(*c*) is taken to surround the expansion path walls at blade temperature β, then the entropy generated within the control volume consists of flow path friction as well as heat transfer from gas to blade temperature

$$d\tilde{s}_{\text{gen}} = I\frac{dw}{\tau} + dq\left(\frac{\tau - \beta}{\beta\tau}\right). \tag{35}$$

The entropy balance for the control volume gives

$$\tilde{s} + d\tilde{s}_{\text{gen}} = (\tilde{s} + d\tilde{s}) + \frac{dq}{\beta}. \tag{36}$$

Substituting (35) in (36), using (32) and (31) to eliminate dq and dw and integrating enables one to find the temperature–entropy path as

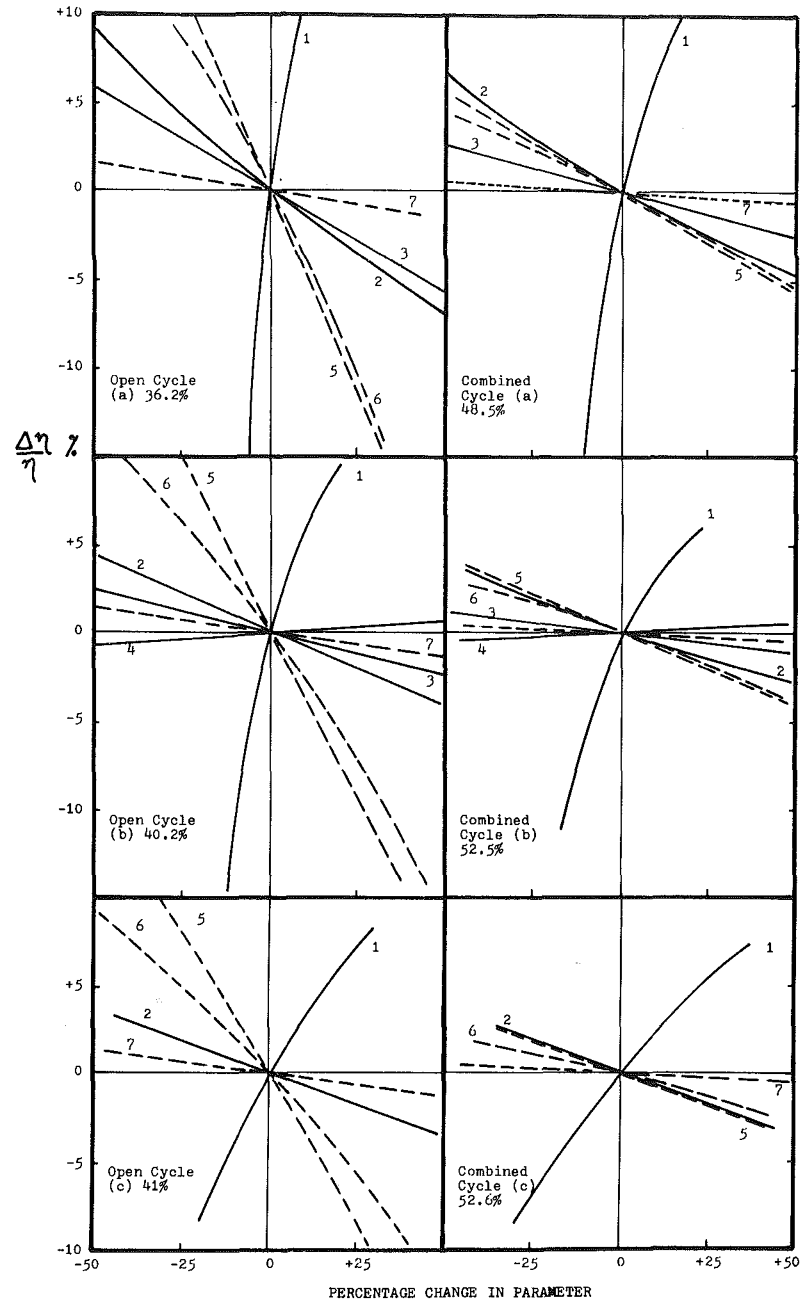

Fig. 10

$$(\tilde{s}-\tilde{s}^*)=\frac{I+\sigma_0\beta}{1-\sigma_0\beta}\ln\left\{\frac{\beta}{\tau}[1+\sigma_0(\tau-\beta)]\right\}+\ln[1+\sigma_0(\tau-\beta)]. \qquad (37)$$

The local pressure may be found by applying equation (26). The $\tau-\tilde{s}$ path of this expansion for $\sigma=0.15$ lies very close to that for transpiration on Fig. 4.

The ratio of availability destruction to work is simply $T_0 ds_{\text{gen}}/dw$ and is plotted in Fig. 7 as a function of temperature. Further availability destruction occurs external to the expansion path control volume depending on the temperature to which the heat extracted dq is degraded before being utilized, if at all. In a real cycle this loss is likely to be more substantial than the expansion path loss as illustrated in Fig. 7.

IV Application to Cycle Calculations

The closed-form expressions for the mass fraction, work, and pressure ratio of cooled expansions may be used to calculate cycle efficiency and specific power for the different cooling system models. For a given peak temperature θ and blade temperature β, the inlet mass fraction is calculated from equation (15) and the work for the cooled section of expansion from equation (16) or (33). The pressure ratio across the cooled section is found from equation (26). Dividing the overall turbine pressure ratio by this gives the pressure ratio across the remaining adiabatic section of the expansion path, whose exit temperature and work are then calculated in the usual manner. The compressor work and combustor heat added are also calculated in the usual manner.

For computation of combined cycle efficiency, the bottoming steam cycle was assumed to recover a certain fraction of the available work in the turbine exit gas which correlates with gas temperature as given in Part 1 of this paper.

Examples of the application of this model are given in Fig. 8 for open cycles and Fig. 9 for combined cycles. The values of the input parameters for those examples are listed in

Appendix II. The sensitivity of the results to the input variables is illustrated in Fig. 10, where each variable is varied around a common point and the percentage change in cycle efficiency computed. The central points selected are described in Appendix II.

The cycles with air cooling, *a* and *b*, present no special problem in describing their performance using the model presented. For the case with internal liquid cooling, however, the results depend on the method of utilizing the heat extracted. In the open-cycle results in Fig. 8(*c*) the heat is assumed wasted. If this heat were transferred to the compressor delivery air, as proposed in [6], the efficiency would improve drastically as the dotted line on Fig. 8(*c*) illustrates. The means for accomplishing this are rather difficult to implement, but are deemed worthy of further consideration in view of the substantial improvement. For the combined cycle results shown in Fig. 9(*c*), the heat extracted is assumed to be utilized with the same efficiency as that of the turbine exit gas. This is somewhat optimistic. The consequences of totally wasting that heat are illustrated by the dotted line on that graph.

V Discussion

Figure 8 shows the best air-cooled open-cycle (transpiration) peaking at about 40.5% with a pressure ratio of about 32 and turbine inlet temperature about 5.5 to 6 times ambient. The dependence of peak efficiency on pressure ratio and inlet temperature is rather slight over a fairly wide range. Peak efficiency is about seven percentage points below that calculated for an adiabatic machine with similar component efficiency. The internally air-cooled cycle peaks at about 37% at a lower pressure ratio and inlet temperature. It is more sensitive to those variables. Film-cooled engines would have performance between those limits. In Fig. 10 the sensitivity of those results to the calculation parameters is shown. The parameters directly related to cooling are indicated by solid lines whereas those depending on other aspects of machine performance are shown as dashed lines. As expected, turbine and compressor polytropic efficiencies, curves 5 and 6, play a leading role in the open cycle. Their role becomes less pronounced as the method of cooling improves as seen by the decreasing slope of those curves from Fig. 10(*a*) to 10(*b*) to 10(*c*). The combustor pressure drop, curve 7, plays a subordinate role.

Of the parameters related to cooling, one may see that blade temperature, curve 1, is an important factor. This is followed by σ, curve 2, then Y, curve 3. The constant n of equation (9) plays a very weak role in transpiration. The sensitivity to all those variables declines with more effective cooling as seen by the reduced slopes in going down the figure from (*a*) to (*b*) to (*c*). It should be noted that blade temperature dependence may be somewhat exaggerated by the figure since the percentage change in β is from absolute zero.

To reduce cooling losses, the ratio σ should be minimized. Inspection of equation (6) shows that this can hardly be accomplished without substantial impact on other design factors. For instance, reducing the wall to gas path area ratio may increase aerodynamic losses and cause a decline in turbine polytropic efficiency, an important factor, it would also decrease turning angle and necessitate more stages. Increasing the value of the constant c of equation (2) can be accomplished by decreasing the reaction effect. For an impulse turbine with axial rotor exit $c=2$. This cuts down cooling loss (in line with Hawthorne's conclusions [2]), but the aerodynamic losses would increase due to the larger nozzle absolute and rotor relative Mach numbers. Increasing rotor pitchline speed (M_0) would decrease cooling loss but this is limited by material strength constraints. Also for given geometry, increasing pitchline speed requires increased relative gas to surface velocity. Thus the parameter Y of equation (24) will increase, and this has a negative impact on air-cooled cycles as seen from curve 3.

For internal-air (or film-cooled) blades σ may be reduced by increasing blade heat exchange effectiveness ϵ. Examination of Fig. 3 shows that the advantage of transpiration over internal air cooling derives substantially from the assumption that $\epsilon=1$ for the former, and less from the reduction in external heat-transfer coefficient. The limit on cooling air supply pressure is a barrier to increasing ϵ.

Figure 9 shows combined cycle efficiency peaking at just over 50% for internal-air (*a*) and about 55% for transpiration (*b*) and internal liquid cooling (*c*). Those peaks occur at turbine inlet temperature substantially above current practice for base-load machines. The calculation assumes fairly sophisticated steam bottoming cycles at the higher temperatures, as discussed in Part 1 of this paper. The best combined cycles have low pressure ratios in the eight to twelve range. As for the open cycle the internally air-cooled case is more dependent on pressure ratio, and has a fairly wide peak with temperature. The transpiration and internally liquid-cooled cases, however, do not peak as broadly and continue to rise with temperature.

Figure 10 shows that the sensitivity to the various parameters for combined cycles is similar in sense but reduced in magnitude from the open cycles.

VI Conclusions

1 The model presented enables closed-form solutions to be found for the impact of cooling on cycle performance.

2 The parameter σ of equation (6), which scales the heat to work loading on the machine surfaces, plays the leading role in determining those losses.

3 Sample results presented show air-cooled cycles peaking at about 40% for simple cycles for conditions thought to represent state of the art. Substantial further progress is thought to be possible either through alternative cooling techniques such as thermosyphons, or through breakthroughs in material technology that would permit higher blade temperatures.

References

1 Hawthorne, W. R., "The Thermodynamics of Cooled Turbines, Part 1: The Turbine Stage," ASME Paper No. 55-A-186.

2 Hawthorne, W. R., "The Thermodynamics of Cooled Turbines, Part 2: The Multistage Turbine," ASME Paper No. 55-A-191.

3 Rohsenow, W. M., "Effect of Turbine Blade Cooling on Efficiency of a Simple Gas Turbine Power Plant," ASME Paper No. 55-A-120.

4 Horlock, J. H., "The Cooled Turbine," in: *Axial Flow Turbines*, Krieger, New York, 1973.

5 Kwalke, K., Kobayashi, N., and Ikeguchi, T., "Effect of New Blade Cooling System with Minimized Gas Temperature Dilution on Gas Turbine Performance," ASME JOURNAL OF ENGINEERING FOR GAS TURBINES AND POWER, Vol. 106, No. 4, Oct. 1984, pp. 756-764; Paper No. 84-GT-89.

6 Kerrebrock, J. L., "Turbines," in: *Aircraft Engines and Gas Turbines*, MIT Press, 1977.

7 El-Masri, M. A., "A Proposed Regenerative Thermosyphon Blade Cooling System for High Efficiency Gas Turbines," *Proc. XIV I.C.H.M.T. Symposium*, Dubrovnik, Yugoslavia, Hemisphere 1983.

8 El-Masri, M. A., Kobayashi, Y., and Louis, J. F., "A General Performance Model for the Open-Loop Water-Cooled Gas Turbine," ASME Paper No. 82-GT-212.

9 Louis, J. F., Hiraoka, K., and El-Masri, M. A., "A Comparative Study of Different Means of Turbine Cooling on Gas Turbine Performance," ASME Paper No. 83-GT-180.

10 Wu, C. S., and Louis, J. F., "A Comparative Study of the Influence of Different Means of Cooling on the Performance of a Combined (Gas and Steam Turbines) Cycles," ASME JOURNAL OF ENGINEERING FOR GAS TURBINES AND POWER, Vol. 106, No. 4, Oct. 1984, pp. 750-755; Paper No. 84-GT-177.

11 Rice, I. G., "Steam-Cooled Blading in a Combined Reheat Gas Turbine/Reheat Steam Turbine Cycle: Part I—Performance Evaluation," ASME Paper No. 79-JPGC-GT-2.

12 Rice, I. G., "Steam-Cooled Blading in a Combined Reheat Gas Turbine/Reheat Steam Turbine Cycle: Part II—Design Considerations."

13 Rice, I. G., "Steam-Cooled Gas Turbine Casings, Struts, and Disks in a Reheat Gas Turbine Combined Cycle: Part I—Compressor and Combustor," ASME JOURNAL OF ENGINEERING FOR POWER, Vol. 105, No. 4, Oct. 1983, pp. 844-850; Paper No. 83-GT-85.

14 Rice, I. G., "Steam-Cooled Gas Turbine Casings, Struts and Discs in a Reheat-Gas-Turbine Combined Cycles: Part II—Gas Generator Turbine and Power Turbine," ASME JOURNAL OF ENGINEERING FOR POWER, Vol. 105, No. 4, Oct. 1983, pp. 851-885; Paper No. 83-GT-86.

15 Kutateladze, S. S., and Leontiev, V. I., "Heat-Mass Transfer and Friction in the Turbulent Boundary Layer," NASA TT F 805, 1974.

16 El-Masri, M. A., "Two-Phase Transpiration Cooling," ASME JOURNAL OF ENGINEERING FOR POWER, Vol. 105, 1983, pp. 106-113.

17 Shapiro, A. H., *The Dynamics and Thermodynamics of Compressible Fluid Flow*, Vol. 1, Ronald Press, New York, 1953.

APPENDIX 1

The temperature functions appearing in equations in the text are:

$$\psi_1(\tau) = \frac{2}{M}\left\{\tan^{-1}\frac{2\sigma\tau+B}{M} - \tan^{-1}\frac{2\sigma\beta+B}{M}\right\}$$

$$\psi_2(\tau) = \frac{1}{2\sigma}\left[\ln\frac{\phi(\tau)}{\phi(\beta)} - B\psi_1\right]$$

$$\psi_3(\tau) = \frac{1}{C}\left[\ln\frac{\tau}{\beta} + \frac{1}{2}\ln\frac{\phi(\beta)}{\phi(\tau)} - \frac{B}{2}\psi_1\right]$$

where

$$\begin{aligned} B &= n-\sigma(\alpha+\beta) \\ C &= (1-n)\beta+\alpha(\sigma\beta-1) \\ M &= (4\sigma C-B^2)^{1/2} \\ \phi(\tau) &= (\beta-\alpha)+[\sigma(\tau-\alpha)+n](\tau-\beta). \end{aligned}$$

APPENDIX II

For a cascade, the ratio of wall area to gas flow path inlet area is

$$\frac{A_w}{A_g} = \frac{l}{s} + 2\frac{x}{L}$$

where l = airfoil perimeter, s = blade circumferential spacing, x = axial breadth, and L = blade height.

If c is the blade chord, typical values are $l = 2.8c$, $s = c$, $x = 0.7c$, $L = 1.25c$ giving $A_w/A_g = 3.92$ for a row and 7.84 for a stage. Allowing for row-to-row spacing gives a total area ratio of about 8 for those conditions.

Stanton numbers based on cascade inlet area are typically about 0.005. Assuming pitchline velocity of 275 m/s gives $M_0 \simeq 0.8$. With $\gamma = 1.4$ and degree of reaction parameter $c = 1.2$, equation (6) gives the estimate of $\sigma_0 = 0.13$. Typically σ_0 will be between 0.1 and 0.2; 0.15 is used for illustration. Assuming $\epsilon = 0.5$ suggests $\sigma = 0.3$ as a typical value for internally air-cooled blades.

The values of the parameters in Fig. 10 are listed below.

Parameter (curve number)	Open cycle			Combined cycle		
	(*a*)	(*b*)	(*c*)	(*a*)	(*b*)	(*c*)
β(1)	4	4	4	3.5	3.5	3.5
σ(2)	0.3	0.15	0.15	0.3	0.15	0.15
Y(3)	0.2	0.2	–	0.2	0.2	–
n(4)	–	0.25	–	–	0.25	–
$1-e_T$(5)	0.15	0.15	0.15	0.15	0.15	0.15
$1-e_c$(6)	0.10	0.10	0.10	0.10	0.10	0.10
$\delta_{\bar{p}}$(7)	0.04	0.04	0.04	0.04	0.04	0.04
P.R.	32.	32	32	12.	12.	12.
θ	5.5	5.5	5.5	5.5	5.5	5.5

On Thermodynamics of Gas-Turbine Cycles:
Part 3—Thermodynamic Potential and Limitations of Cooled Reheat-Gas-Turbine Combined Cycles

M. A. El-Masri
Associate Professor of Mechanical Engineering,
Massachusetts Institute of Technology,
Cambridge, MA 02139

Reheat gas turbines have fundamental thermodynamic advantages in combined cycles. However, a larger proportion of the turbine expansion path is exposed to elevated temperatures, leading to increased cooling losses. Identifying cooling technologies which minimize those losses is crucial to realizing the full potential of reheat cycles. The strong role played by cooling losses in reheat cycles necessitates their inclusion in cycle optimization. To this end, the models for the thermodynamics of combined cycles and cooled turbines presented in Parts 1 and 2 of this paper have been extended where needed and applied to the analysis of a wide variety of cycles. The cooling methods considered range from established air-cooling technology to methods under current research and development such as air-transpiration, open-loop, and closed-loop water cooling. Two schemes thought worthy of longer-term consideration are also assessed. These are two-phase transpiration cooling and the regenerative thermosyphon. A variety of configurations are examined, ranging from Brayton-cycles to one or two-turbine reheats, with or without compressor intercooling. Both surface intercoolers and evaporative water-spray types are considered. The most attractive cycle configurations as well as the optimum pressure ratio and peak temperature are found to vary significantly with types of cooling technology. Based upon the results of the model, it appears that internal closed-loop liquid cooling offers the greatest potential for midterm development. Hybrid systems with internally liquid-cooled nozzles and traditional air-cooled rotors seem most attractive for the near term. These could be further improved by using steam rather than air for cooling the rotor.

I Introduction

It has been shown that the reheat gas-turbine combined cycle possesses fundamental thermodynamic advantages. These derive from carrying out a greater proportion of the combustion and work-extraction processes at elevated temperature, thereby reducing the combustion/heat-transfer irreversibilities. The calculations presented in [1-6] illustrate the potential of this cycle. Since current limitations on working temperature of turbine components necessitate their cooling, the associated thermodynamic losses detract from the benefit of increased gas temperature. This cooling penalty can be considerably larger in a reheat gas turbine, which has several high-temperature stages, than in a conventional Brayton-cycle which has a smaller proportion of its expansion-path exposed to elevated temperatures. Indeed, the effect of turbine cooling may be so large as to result in optimum peak temperatures well below those for a Brayton-cycle of similar cooling technology. Moreover, for some of the less-advanced cooling methods, the optimized reheat cycle may offer little or no advantage over the corresponding Brayton-cycle. Thus, in deciding whether or not to build reheat turbine cycles, it is crucial to integrate the turbine cooling penalties with the cycle thermodynamic optimization.

In what follows, the model for the thermodynamics of cooled turbines presented in Part 2 of this paper is applied to assess the performance of reheat cycles. Due to the limited number of dimensionless parameters which describe the machine construction, cooling technology and cycle parameters, general and unambiguous results are obtained. While some inevitable approximations in this approach are likely to cause slight variations between the results presented and computations based upon the details of specific

---

Contributed by the Gas Turbine Division of The American Society of Mechanical Engineers and presented at the 30th International Gas Turbine Conference and Exhibit, Houston, Texas, March 18-21, 1985. Manuscript received at ASME Headquarters, January 7, 1985. Paper No. 85-GT-131.

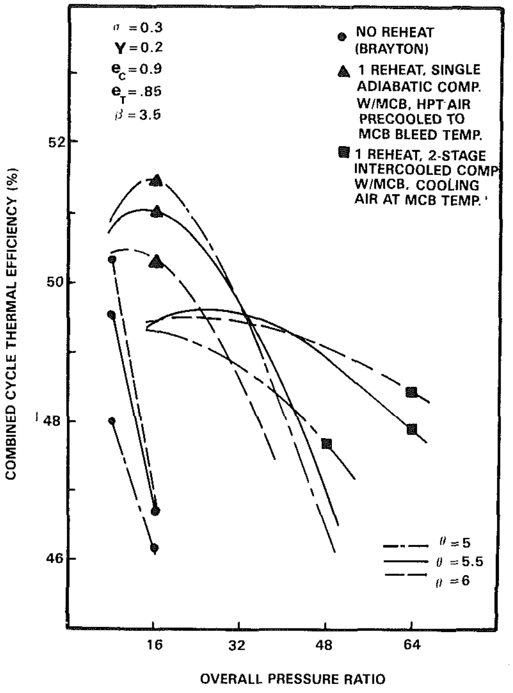

Fig. 1 Internal convection air cooling

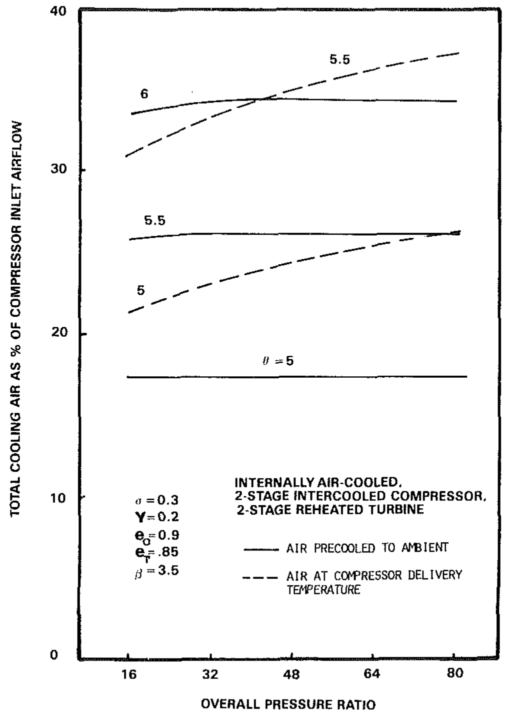

Fig. 2

machines, the generality of this methodology is thought to outweigh this drawback. Moreover, since identical values for the machine dimensionless parameters are used for the different cooling technologies, the results offer a firm basis for comparing those technologies. Examples of the sensitivity of the final results to those assumptions are presented.

The cooling technologies examined start with the well-established method of internal air convection and move on to the more advanced methods, most of which are at an experimental stage such as air-transpiration, internal closed-loop liquid cooling, and open-loop liquid cooling. Two concepts which offer potential for long-term development are also assessed. These are two-phase transpiration cooling and the regenerative liquid-metal thermosyphon. The results obtained for two-phase transpiration illustrate the thermodynamic advantage of using steam rather than air as coolant. The same general conclusion has been drawn in [6–9] as well as from the performance calculations for a steam-injected cycle in [10]. Several design aspects for steam-cooled gas turbines have been given by Rice [11–15].

II Methodology and Results

Three generic types of cooling methods are assessed in this paper:

1 Invasive air cooling, where compressor air is bled, used to cool hot components, and then mixed with the turbine gas. The term "invasive" is used since the spent coolant invades the gas path, causing losses in stagnation pressure and enthalpy.

2 Internal liquid cooling, where a liquid such as water, or perhaps a liquid metal, is used to internally cool the blades and other components. The heat extracted can be used elsewhere in a combined cycle, or in the worst case rejected. The main impact on the gas path is a loss of stagnation enthalpy. The thermodynamic benefit of those methods depends on how effectively this heat can be utilized.

3 Invasive water cooling, in which water is substituted for air, used to cool the walls by evaporation, then mixed into the gas stream. The main advantages are the smaller coolant mass flow and work of compression in the liquid phase. The main disadvantage is rejection of the latent heat of vaporization with the stack gases.

Each of these three types, together with selected examples, is discussed below.

II.1 Invasive Air Cooling. Two limits bracket the range of interest in this type of system: (*a*) where the cooling air is not used to reduce the heat flux to the surface, i.e., internal convection; and (*b*) where the cooling air is utilized to the maximum extent possible to reduce the gas-side heat flux, i.e., transpiration cooling.

System (*a*) described above may be characterized by a "heat-exchanger effectiveness," ϵ, defined in Part 2 of this work. This is the ratio of cooling air temperature rise as it passes through the blade to the thermodynamic maximum of being discharged at blade bulk-metal temperature. The value of ϵ depends on the details of coolant passage layout, leading edge impingement, use of ribs or turbulators, blade-skin thickness and thermal conductivity. Values up to 0.7 for low gas pressures and temperatures were mentioned as feasible by Esgar et al. [16]; the same reference, however, suggests 0.5 as a reasonable practical limit for higher gas pressures and temperatures. The decrease occurs in part by the skin-conduction temperature drop. The value 0.5 is used for the numerical examples in the present work.

Nomenclature

(Symbols not defined in the text or Part 2 of this paper only)

$\bar{c}_{pl}$ = specific heat of liquid water per mole

$\bar{c}_{pv}$ = specific heat at constant pressure for water vapor per mole

$\bar{h}_{fg}$ = latent heat of vaporization per mole of water

M = gas mixture mole flow rate

$\tilde{m}_r$ = ratio of coolant to gas flow rate for a blade row

S_r = $St\,(A_{\mathrm{wall,\,row}}/A_g)$

T_{sat} = saturation temperature

x = steam exit quality from blade tip

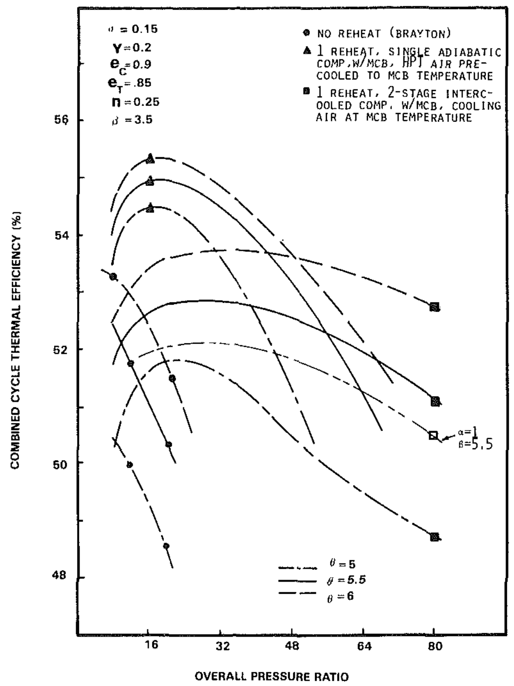

Fig. 3 Transpiration air cooling

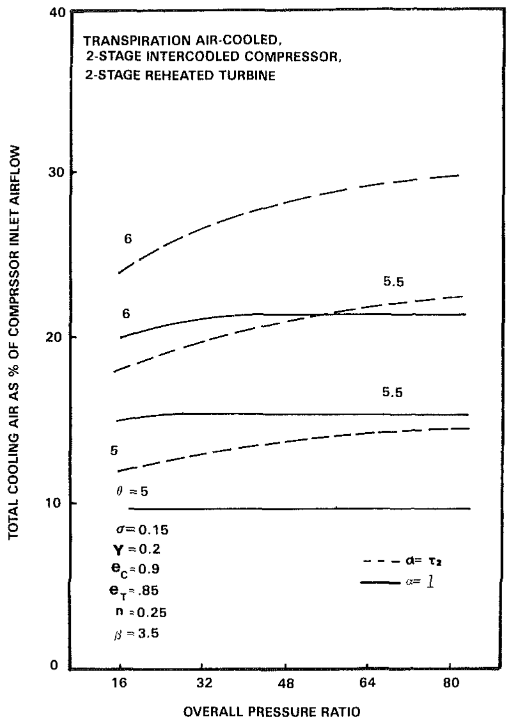

Fig. 4

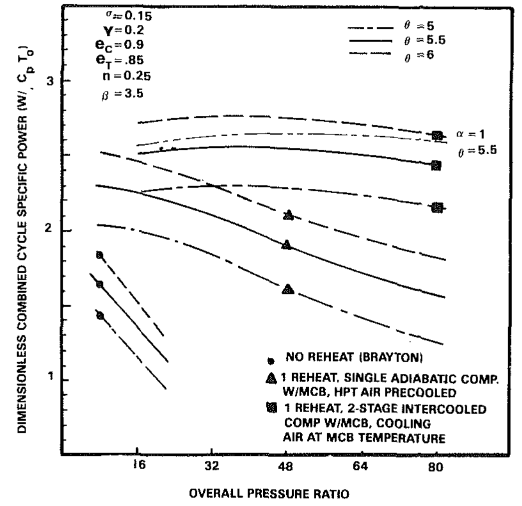

Fig. 5 Transpiration air cooling

System (*b*) described above is characterized by a high value of ϵ, close to unity, due to the intimate coolant-metal contact in porous walls. Another descriptor of this system is the rate of reduction of Stanton number with transpiration mass flux. Although this relationship is typically an exponential function, a simple linear form is used here as discussed in Part 2. It is interesting to note, based on the results shown in Fig. 3 of Part 2 as well as later in this part, that the advantage of transpiration over internal convection derives mostly from the effectiveness being essentially unity and much less from the reduction of Stanton number. Most modern engines employ film cooling, which lies between the two limits (*a*) and (*b*) discussed above. Results for film cooling are likely to lie much closer to those for convection than for transpiration cooling in view of the fact that the heat-exchanger effectiveness cannot be substantially influenced by the film cooling. Rather, the introduction of the film at trouble spots such as the leading edge or transition region can be regarded as a local measure to reduce variations in metal temperature.

A "cooling effectiveness" ϕ defined as

$$\phi = \frac{\tau-\beta}{\tau-\alpha} \qquad (1)$$

is used in the literature. This may be related to the blade heat exchanger effectiveness by

$$\epsilon = \frac{S_r}{\tilde{m}_r}\,\frac{\phi}{1-\phi} \qquad (2)$$

Results given by Waters et al. [17] for the relation between $\tilde{m}_r$ and ϕ for film cooling imply a value of $\epsilon = 0.4$ for $\tilde{S}_r = 0.02$; this further supports the previous statement of the closer similarity between film and convection cooling insofar as bulk average heat balances are applied to determine cooling flow requirements.

The expansion-path model described in Part 2 is applied using typical reference values of the dimensionless parameters listed in Appendix I. Cases with intercoolers or reheats are subdivided into segments of equal pressure ratio. Surface intercoolers are assumed to restore air temperature to ambient whereas reheaters are assumed to boost temperature back to that of the turbine inlet. Heat rejection from surface intercoolers is assumed wasted. The results are displayed in Figs. 1–9. Figure 6 is based upon a single evaporative intercooler. It assumes initially dry air which goes through a process of adiabatic saturation to 100% relative humidity. The subsequent air/vapor mixture is assumed to be a perfect gas with the same molar properties as air. This is consistent with the air-cycle calculations and neglects the minute change of the specific heat ratio in the mixture.

Figure 1 shows internal convection peaking at about 51.7% for a configuration of single adiabatic compressor and one-reheat turbine. It is assumed that one midcompressor bleed (MCB) is used to extract cooling air for the low-pressure turbine. It was found disadvantageous to efficiency to precool this air, even though this would economize in bleed air-mass flow. However, it was found advantageous to precool the HP cooling air to MCB temperature, the resulting economy in air outweighing the heat rejected in its precooling. It is interesting to note that in this configuration the maximum efficiency is achieved with the lowest of the three inlet temperatures shown. That is in contrast with the Brayton-cycle results.

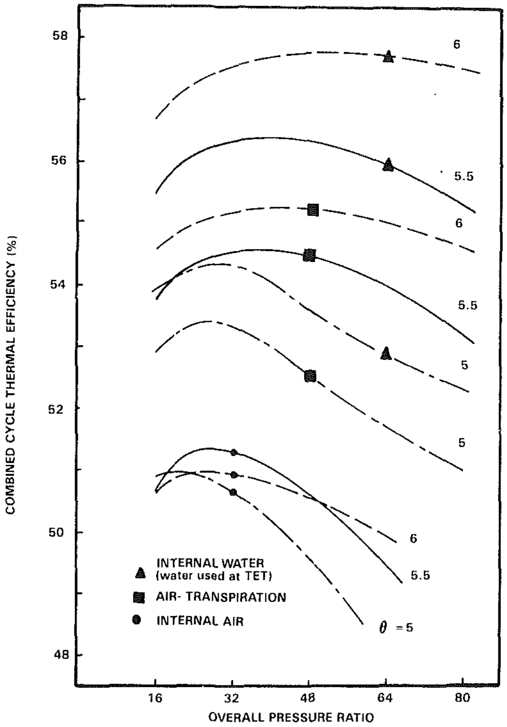

Fig. 6 Effect of a single adiabatic-saturation spray intercooler on cycles with a single turbine reheat

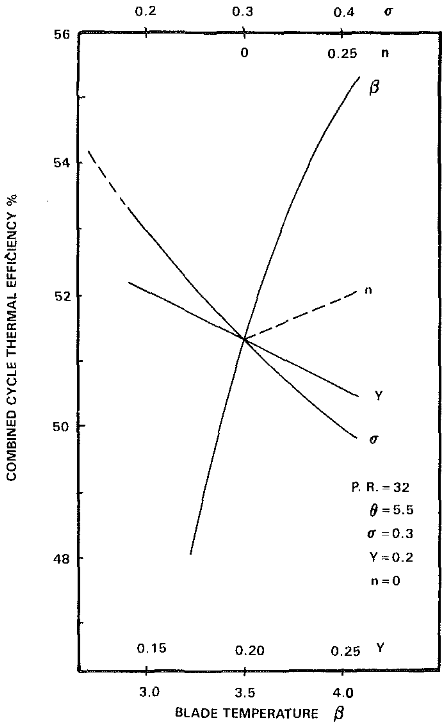

Fig. 7 Effect of cooling parameters on internally air-cooled cycle with single reheat and water-spray intercooler

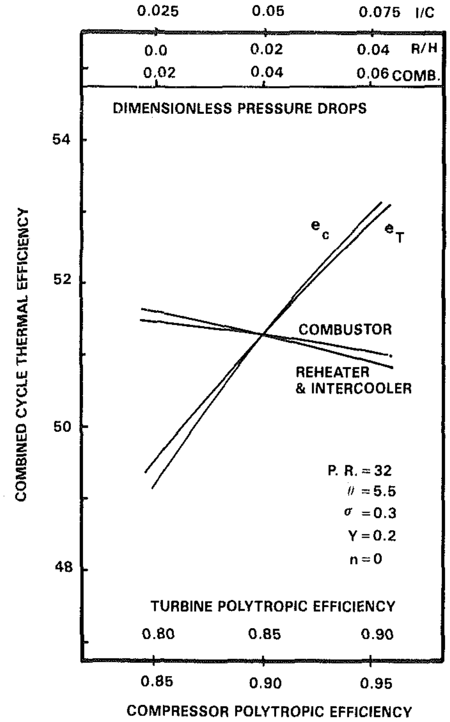

Fig. 8 Effect of component efficiency and pressure drops on internally air-cooled cycle with single reheat and water-spray intercooler

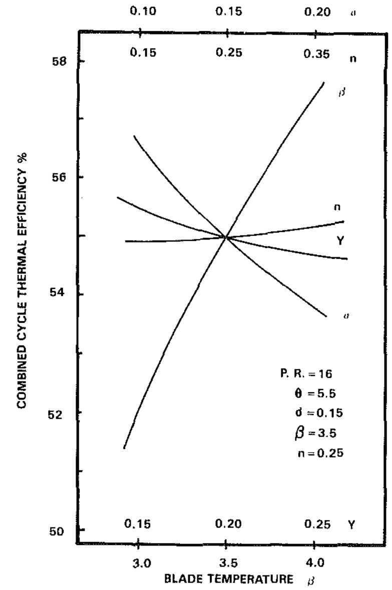

Fig. 9 Effect of cooling parameters on transpiration air-cooled cycle with single adiabatic compressor and one-turbine reheat: cooling air for LP turbine bled from compressor and used at bleed temperature; cooling air for HP turbine precooled to MCB temperature

The surface intercooled cycle results in lower efficiencies as discussed in Part 1 of this paper. However, the evaporative-intercooled cycle peaks at about 51.3% with a higher peak temperature of 5.5 and a pressure ratio around 30. The evaporative intercooler may result in higher heat-rejection losses since the latent heat is ultimately rejected at stack temperature, which is higher than the logarithmic mean temperature of a surface intercooler for the lower pressure ratios. The savings in LP compressor work, however, tend to favor that intercooling option. Partial utilization of the waste heat from a surface intercooler may partially redress this tradeoff. The adiabatic compressor, however, still results in marginally-superior efficiency. It would yield still better efficiency if the heat from the HP cooling air precooler were used in the bottoming cycle.

Figure 2 shows total turbine cooling air as a fraction of compressor inlet for the conditions corresponding to Fig. 1 with the single surface intercooler. The option to precool the cooling air to ambient is found to economize in its amount, but detrimental to overall efficiency.

Figure 3 shows a similar calculation with transpiration

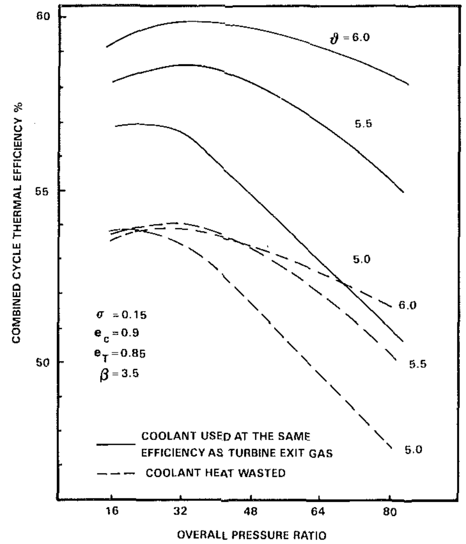

Fig. 10 Internally water-cooled, adiabatic compressor, 2-stage reheated turbine

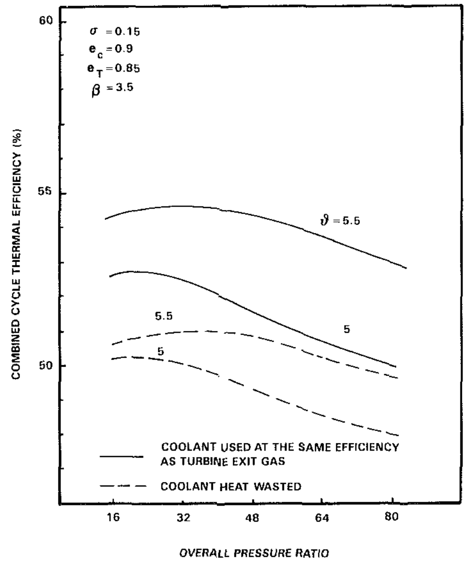

Fig. 11 Internally water-cooled, 2-stage intercooled compressor, 2-stage reheated turbine

cooling. It is worth noting that the peak efficiency case is still the one with adiabatic compression, yielding about 55.4%. This is achieved at the highest of the inlet temperatures shown, in contrast to the convection cooled case. The corresponding cooling-air flows are shown in Fig. 4, and the specific power curves in Fig. 5. Figure 6 shows the cycle with evaporative intercooling peaking at about 55.2%, just below that with adiabatic compression. It must be mentioned that neither of those cycles has been "fine-tuned" and that the heat from the HP cooling air precooler is assumed rejected.

Figures 7-9 illustrate the sensitivity of results to input variables. Figure 7 illustrates the impact of the cooling parameters on the convection-cooled cycle with single evaporative intercooler. Note the steep dependence on blade temperature. The mean value of 3.5, corresponding to about 1015K (1367°F) is considered representative of the current technology; the slope of the curve is about 0.03% cycle efficiency per degree K of metal temperature. The other important parameter is σ; noting that $\sigma = \sigma_0/\epsilon$, one can see from the dashed line that reducing σ to 0.15 which corresponds to hypothetically increasing ϵ from 0.5 to 1.0 at constant $\sigma_0 = 0.15$ provides for most of the gain achieved by transpiration.

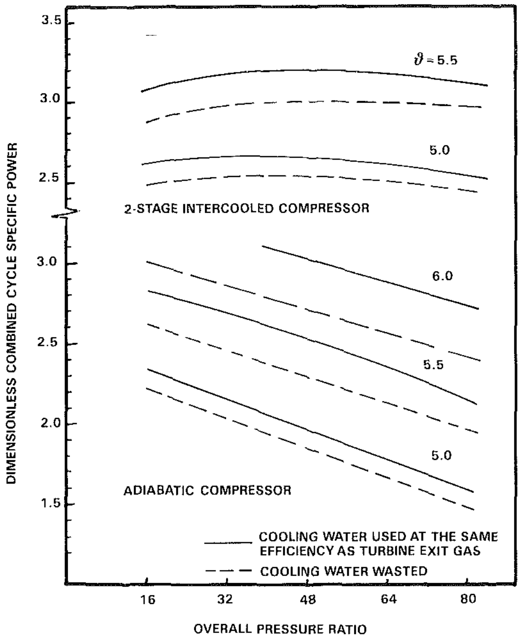

Fig. 12 Internally water-cooled, 2-stage reheated turbine

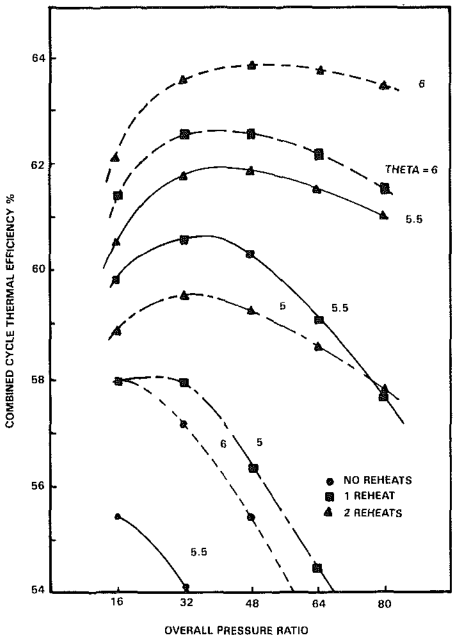

Fig. 13 Regenerative thermosyphon, single adiabatic compressor, $\beta = 3.5$

The dashed line showing the hypothetical increase of n from zero to its transpiration value provides a relatively minor advantage. This reinforces the preceding argument about the importance of the heat-transfer effectiveness ϵ. The impact of the mainstream stagnation pressure loss parameter Y is also illustrated. Figure 8 shows the effect of the non-cooling-related parameters. Whereas component polytropic efficiencies have substantial impact, pressure drops play a minor role. Figure 9 shows that the effects of cooling parameters on transpiration cooling follow the same trends, but with slightly smaller slopes than internal air cooling, similar to the discussion in Part 2 of this paper.

II.2 Internal Liquid Cooling. The methodology of solving for the turbine expansion path is given in Part 2 of this paper. The results for the overall combined cycle performance depend on the disposition of the extracted heat. Figures 10-12 illustrate those results for cases thought to bracket the range of interest. The worst-case analysis, shown in dashed lines,

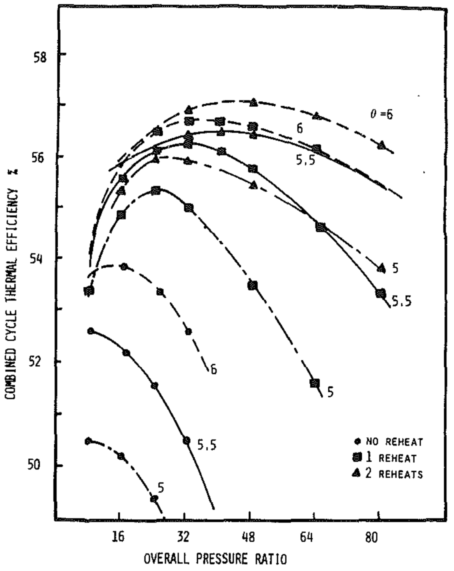

Fig. 14 Two-phase transpiration, single adiabatic compressor, β = 3.5

assumes this heat is totally rejected. Even with this assumption, efficiencies over 54% are achievable, with the results having weak dependence on peak cycle temperature. Figure 11 shows that a surface-intercooled compressor is at a considerable disadvantage.

A reasonable estimate of the upper bound is obtained by assuming that the extracted heat can be converted to work at the bottoming cycle efficiency. This gives the solid lines on Figs. 10–12. In a typical system, the results will be between those bounds depending on the cooling circuit pressure and temperature and whether water or an intermediate high-boiling-point medium is used in the cooling loop.

One concept which might be of long-term interest is the regenerative thermosyphon [18]. The author has shown that due to the difference in radius of rotation between a typical turbine and compressor on the same shaft, a liquid-metal loop can be made to circulate naturally at a high flow rate by centrifugal action, conveying heat from the turbine blades to a rotating preheater between compressor delivery and combustor. The potential for cycle performance is shown in Fig. 13. Despite the great difficulties in implementing this scheme, the author believes it worthy of further consideration due to the exceptionally high efficiencies which would become possible.

II.3 Invasive Water Cooling. Just as with invasive air cooling, two types of systems are considered: (*a*) where the cooling water absorbs the heat load within the blade by partial evaporation and is not used to reduce the external heat load; and (*b*) where the steam generated by boiling the water transpires through the blade and thus serves the additional purpose of reducing the gas-side heat transfer.

System (*a*) constitutes an open-loop water-cooling system such as proposed during a recent development program known as HTTT [19]. Water cools the blade internally, partially evaporates, then exits the blade tip and mixes with the turbine gas. Its cooling-water requirements may be characterized by the tip-exit steam quality x. A value of x = 0.67 has been proposed in that program and is used in subsequent calculations. It must be mentioned, however, that problems of critical heat flux and conduction to the internal water film make the viability of this system unlikely at high gas temperatures and pressures [20, 21].

One method of obtaining system (*b*) is the two-phase transpiration system, proposed by the author [22]. It is characterized by the fact that the exiting steam is at blade temperature and is thus superheated. The major drawback of this system is the requirement of high-purity water. Another method of obtaining system (*b*) is to apply transpiration or film cooling using steam bled from the combined cycle steam turbine. The thermodynamic advantages over air cooling are highlighted by calculations presented in [6–9]. The results given in this paper are a good representation for the performance of a steam transpiration-cooled system.

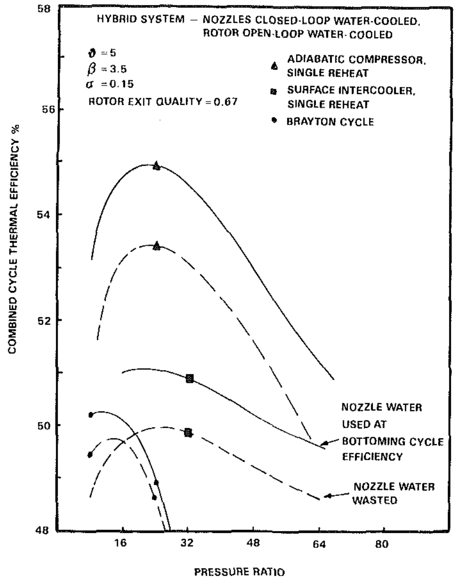

Fig. 15

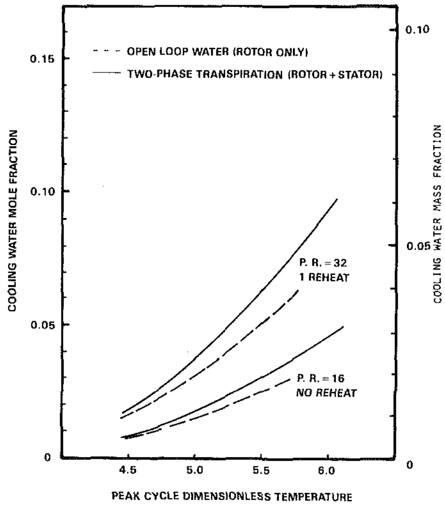

Fig. 16

In order to preserve consistency with the ideal gas analysis used for the other cycles, the air/water-vapor mixture is approximated by an ideal gas of constant molar properties. The error in neglecting the smaller specific-heat ratio of steam is negligible since in all cases the vapor fraction is small. The equations for the expansion-path thermodynamics thus have to be rewritten on a molar basis. Thus, the turbine cooling equation, the first law and the second law of thermodynamics, equations (13), (14), (16), and (22) of Part 2 assume the forms:

$$\frac{dM}{M}=\frac{-\sigma_o(\tau-\beta)\,d\tau}{H+\{\sigma_o\bar{h}_{fg}''+n\}(\tau-\beta)} \quad (3)$$

where

$n=0, H=\bar{h}_{fg}^*$ (internal water)

$n>0, H=\bar{h}_{fg}'$ (two-phase transpiration) (4)

$$dw=-d\tau-\bar{h}_{fg}''\frac{dM}{M} \quad (5)$$

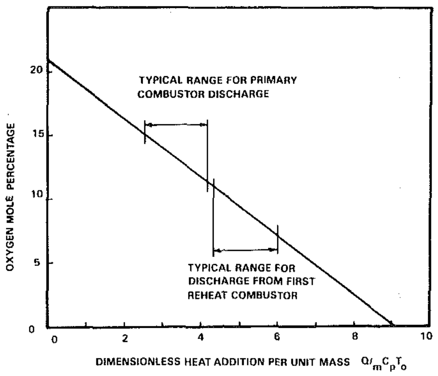

Fig. 17

$$d\bar{s}=I\frac{dw}{\tau}-\frac{\bar{h}_{fg}''}{\tau}\frac{dM}{M}+\frac{Y}{2}\left(\frac{dm}{m}+\frac{dM}{M}\right) \tag{6}$$

The dimensionless latent heat sinks appearing in those equations are defined by:

$$\bar{h}_{fg}'=\bar{c}_{pl}(T_{\text{sat}}-T_o)+\bar{h}_{fg}+\bar{c}_{pv}(T_b-T_{\text{sat}}) \tag{7}$$

$$\bar{h}_{fg}''=\bar{c}_{pl}(T_{\text{sat}}-T_o)+\bar{h}_{fg}+\bar{c}_{pv}(T-T_{\text{sat}}) \tag{8}$$

$$\bar{h}_{fg}^{*}=\bar{c}_{pl}(T_{\text{sat}}-T_o)+x\bar{h}_{fg} \tag{9}$$

and the value of the index n which describes the rate of reduction of Stanton number with transpiration is taken to be the same as with air transpiration; namely 0.25. This is based on the assumption that the critical blowing ratio b_{cr} is proportional to the ratio of molecular weights of transpired to mainstream gases, as discussed in [22].

Unlike the air-cooled cases, the expansion path equations (3-6) cannot be integrated algebraically due to the variation of the heat sink terms of equations (7-9) with pressure and saturation temperature. One must therefore resort to numerical integration. The procedure is to start with one mole of gas, take an increment in temperature $d\tau$ and evaluate the corresponding coolant mole fraction, work done, and change in specific entropy from equations (3, 5, 6). The corresponding pressure increment may then be found from the temperature and entropy and the expansion path states computed.

Figures 14-16 show examples of those results. Figure 14 shows that the two-phase transpiration system has potential of reaching about 57%. The problem of obtaining water of sufficient purity or otherwise designing a blade which would not plug with deposits must be overcome if this system is to be successful.

Figure 15 shows an example for the open-loop water-cooling scheme for $\theta = 5$. Since in a realistic system of this sort it is reasonable to use closed-loop nozzle water cooling, the expansion path equations have been solved by numerically integrating equations (31, 32, 35, 36) of Part 2 together with equations (3-6) given above. Small increments $d\tau$ are used alternating between both sets of equations. The results illustrate excellent thermodynamic potential for this system if a satisfactory method of solving the blade internal heat-transfer problems discussed in [20, 21] could be devised.

Figure 16 shows examples of the overall cooling-water requirements as a fraction of compressor airflow for those systems.

III Discussion

The results show that the use of turbine reheat is generally advantageous over the Brayton-cycle. However, this improvement can be small for systems employing less-advanced cooling systems. In those cases, the optimum peak temperature for the reheat cycle is usually smaller than that for a corresponding Brayton-cycle.

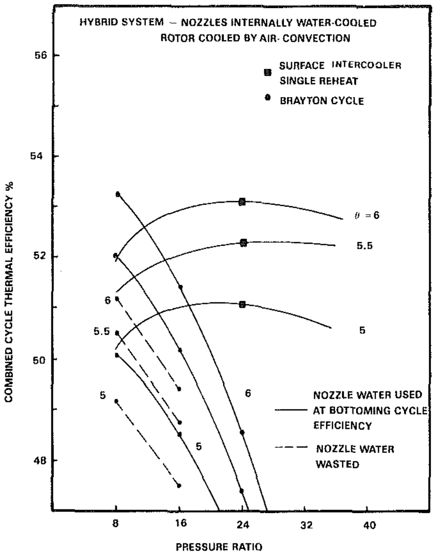

Fig. 18

When some of the more advanced cooling methods are considered, however, considerable benefits are possible with turbine reheats.

A major technical difficulty to be considered with efficient reheat cycles, in addition to turbine cooling, is the design of the reheat combustor(s). One factor is the reduced oxygen content in the gas due to prior combustors. Figure 17 illustrates this fact. This figure, together with the results given in Figs. 15-18 of Part 1 may be used to gauge the effect of the cycle configuration (which determines the dimensionless heat addition per unit mass) on the oxygen content of the gas entering the reheat combustor. Thus, an advanced reheat cycle may require supplementary oxygen supply to the combustion zones. Another difficulty is in cooling the combustor liners without the benefit of the excess relatively low-temperature air available in nonreheat cycles. One solution to this problem may be possible for intercooled cycles since their efficiency exhibits a weak dependence on pressure ratio, as seen in Fig. 6. This allows the concept of a "compound" cycle with a higher mass flow through the low-pressure compressor and turbine than through the high-pressure pair. The air bypassing the high-pressure pair is thus used to cool the reheat combustor liner. The overall consequences to efficiency need not be severe for cycles which exhibit a weak dependence on pressure ratio. However, one must note that the practical difficulties are likely to limit reheat cycles to a single reheat in the foreseeable future.

It should be mentioned that the results presented in this paper are based on system thermodynamics without regard to physical plant layout. The equal-pressure-ratio split in intercooled compressors and reheated turbines used in the present analysis may not lend itself to a simplified mechanical layout in terms of number of shafts, component casings, generator location, and shaft speeds. It is believed, however, that a satisfactory mechanical layout is possible with pressure-ratio splits that do not result in significant departures from the results presented.

Based upon the results of this study, one may rank the thermodynamic attractiveness of the cooling methods considered in this paper in the following ascending order:

- internal convection/film air cooling,
- open-loop water cooling,
- internal liquid cooling; heat wasted,
- air transpiration or steam transpiration,
- two-phase transpiration,
- internal liquid cooling; heat utilized at bottoming cycle effectiveness,
- regenerative thermosyphon.

Based upon the technical feasibility and the amount of research and development required to bring a new system to fruition, it is the author's opinion that the order of increasing difficulty is as follows:

- internal convection/film air cooling,
- internal water cooling,
- air transpiration or steam transpiration,
- open-loop water cooling,*
- two-phase transpiration,
- regenerative thermosyphon.

Simultaneous consideration of those rank orderings leads the author to conclude that a promising medium-term technology is internal liquid cooling. The application to stationary parts such as nozzles need not require major breakthroughs or innovation. Indeed certain prototypes have been successfully tested. One recent example is described in [23]. Turning to internal water cooling for the rotor, a variety of thermosyphon and water-circulation systems have been tested over the past forty years, some with considerable success.** Recent research has shown that the internal heat-transfer and flow stability problems may be overcome [25–28] for water-circulation systems. Some innovation in mechanical and hydraulic design is still needed to construct a reliable and successful system.

Since internal water cooling was found thermodynamically advantageous, and given that development of a successful system for the rotor requires several years of research and development, the author's recommendation for the next step is to develop hybrid machines which use nozzle water cooling and rotor air cooling. This could be further enhanced by applying rotor steam cooling. Figure 18 shows an example of this system. It is interesting to compare the performance of the Brayton-cycles of Fig. 18 with those for internal-air or internal-water alone given in Fig. 9 of Part 2. The hybrid system with nozzle water utilization is only about 1 percentage point below the equivalent internal-water system, but about 2-1/4 points above internal-air alone. With nozzle water wasted, the hybrid system is still roughly 3/4 points above internal air. For the case with intercooling and reheat, the hybrid system with nozzle water utilization and $\theta = 5.5$ peaks at about five points below the equivalent internal-water system but roughly three points above internal-air alone. This illustrates how powerful the influence of cooling technology is on cycles with reheat. For other cycle configurations, similar trends can be found for this hybrid system.

IV Conclusions

1 For current cooling technology, benefits of gas-turbine reheat are moderate, on the order of 3 percentage points.

2 The development of cooling methods which are more benign thermodynamically can allow greater advantage to be taken of reheat cycles.

3 Internal water cooling is thought to be the most attractive option. Potential improvement of about 8 percentage points over current Brayton-cycles is possible with a single-reheat internally water-cooled machine. A hybrid machine where only the nozzles are internally water cooled is a promising next step which can provide about half of this potential improvement. Using steam instead of air as a coolant can also enhance performance.

4 While air transpiration and two-phase transpiration show good thermodynamic performance, the mechanical, material, and coolant supply problems are substantial.

5 The regenerative liquid-metal thermosyphon, if developed, could make thermal efficiencies over 60% possible.

References

1 Rice, I. G., "The Combined Reheat Gas Turbine/Steam Turbine Cycle: Part I—A Critical Analysis of the Combined Reheat Gas Turbine/Steam Turbine Cycle," ASME Paper No. 79-GT-7.

2 Rice, I. G., "The Combined Reheat Gas Turbine/Steam Turbine Cycle: Part II—The LM5000 Gas Generator Applied to the Combined Reheat Gas Turbine/Steam Turbine Cycle," ASME Paper No. 79-GT-8.

3 Hori, A., and Takeya, K., "Outline of Plan for Advance Research Gas Turbine," ASME Journal of Engineering for Power, Vol. 103, No. 4, Oct. 1981; Paper No. 81-GT-28.

4 Rice, I. G., "The Reheat Gas Turbine Combined Cycle," *Turbomachinery International*, July–Aug. 1981.

5 Rice, I. G., and Jenkins, P. E., "Comparison of the HTTT Reheat Gas Turbine Combined Cycle with the HTTT Reheat Gas Turbine Combined Cycle," ASME Journal of Engineering for Power, Vol. 104, No. 1, Jan. 1982; Paper No. 81-GT-69.

6 Rice, I. G., "The Reheat Gas Turbine with Steam Blade Cooling – A Means of Increasing Reheat Pressure, Output and Combined Cycle Efficiency," ASME Journal of Engineering for Power, Vol. 104, No. 1, Jan. 1982; Paper No. 81-GT-30.

7 Rice, I. G., "Steam Cooled Blading in a Combined Reheat Gas Turbine/Reheat Steam Turbine Cycle: Part I—Performance Evaluation" ASME Paper No. 79-JPGC-GT-2.

8 Louis, J. F., Hiraoka, K., and El-Masri, M. A., "A Comparative Study of the Influence of Different Means of Turbine Cooling on Gas Turbine Performance," ASME Paper No. 83-GT-180.

9 Wu, C. S., and Louis, J. F., "A Comparative Study of the Influence of Different Means of Turbine Cooling on the Performance of a Combined (Gas and Steam Turbines) Cycle," ASME Journal of Engineering for Gas Turbines and Power, Vol. 106, No. 4, Oct. 1984, pp. 750–755; Paper No. 84-GT-177.

10 Messerlie, R. L., and Strother, J. R., "Integration of the Brayton and Rankine Cycle to Maximize Gas Turbine Performance—A Cogeneration Option," ASME Paper No. 84-GT-52.

11 Rice, I. G., "Steam-Cooled Blading in a Combined Reheat Gas Turbine/Reheat Steam Turbine Cycle: Part II—Design Considerations," ASME Paper No. 79-JPGC-GT-3.

12 Rice, I. G., "Steam-Cooled Gas Turbine Casing, Struts and Disks in a Reheat Gas Turbine Combined Cycle: Part I—Compressor and Combustor," ASME Journal of Engineering for Power, No. 105, No. 4, Oct. 1983, pp. 844–850; Paper No. 83-GT-85.

13 Rice, I. G., "Steam-Cooled Gas Turbine Casings, Struts and Disks in a Reheat Gas Turbine Combined Cycle: Part II—Gas Generator Turbine and Power Turbine," ASME Paper No. 84-GT-134.

14 Rice, I. G., "The Integrated Gas/Steam Nozzle with Steam Cooling: Part I—Applications," ASME Paper No. 84-GT-134.

15 Rice, I. G., "The Integrated Gas/Steam Nozzle with Steam Cooling: Part II—Design Considerations," ASME Paper No. 84-GT-135.

16 Esgar, J. B., Collady, R. S., and Kaufman, A., "An Analysis of the Capabilities and Limitations of Turbine Air-Cooling Methods," NASA TN D-5992.

17 Gas Turbine Evaluation (GATE) Computer Program, Thermodynamic Cycles, Methods, and Sample Cases. Prepared by Mark Waters and Associates, Inc., EPRI Report AP-2871-CCM, Feb. 1983.

18 El-Masri, M. A., "A Proposed Regenerative Thermosyphon Blade-Cooling System for High-Efficiency Gas Turbines," *Heat and Mass Transfer in Rotating Machinery*, Ed. D. Metzger and N. Afghan, Hemisphere, New York, 1984.

19 Caruvana, A., et al., "Design and Test of a 73-MW Water-Cooled Gas Turbine," ASME Paper No. 80-GT-12.

20 El-Masri, M. A., and Louis, J. F., "On the Design of High-Temperature Gas Turbine Blade Water-Cooling Channels," ASME Journal of Engineering for Power, Vol. 100, No. 4, Oct. 1978, pp. 586–591.

21 Mudawar, I., and El-Masri, M. A., "Thermal Design Constraints in Open-Loop Water-Cooled Turbine Blades," ASME Paper No. 84-WA/HT-68.

22 El-Masri, M. A., "Two-Phase Transpiration Cooling," ASME Journal of Engineering for Power, Vol. 105, No. 1, Jan. 1983, pp. 106–113.

23 Collins, M. F., Muth, M. C., and Schilling, W. F., "Development, Fabrication and Testing of a Prototype Water-Cooled Gas Turbine Nozzle," ASME Journal of Engineering for Power, Vol. 105, No. 1, Jan. 1983, pp. 114–119.

24 Van Fossen, G. J., and Stepka, F. S., "Liquid-Cooling Technology for Gas Turbines: Review and Status," NASA TM 78906, 1978.

25 El-Masri, M. A., "Fluid Mechanics and Heat Transfer in the Blade Channels of a Water-Cooled Gas Turbine," Ph.D. Thesis, MIT, Dept. of Aeronautics and Astronautics, Sept. 1978.

26 El-Masri, M. A., and Louis, J. F., "Design Considerations for the Closed-Loop Water Cooled Turbine," ASME Paper No. 79-GT-71.

27 Motakef, S., El-Masri, M. A., and Louis, J. F., "Critical Heat Flux in the Channels of a Closed-Loop Water-Cooled Gas Turbine," ASME Paper No. 81-HT-74.

28 Ballentine, P., "Stability in the Blade Channels of a Water-Cooled Gas Turbine," S.M. Thesis, Dept. of Mech. Eng., MIT, Feb. 1982.

---

*This is considered less difficult technically for pressure-temperature combinations below those used in the present study [21].

**The review by Van Fossen and Stepka [24] may be consulted for bibliography.

APPENDIX I

The numerical values used in the examples presented are listed below.

Variables	Value used
Machine variables:	
compressor polytropic efficiency	0.9
turbine polytropic efficiency	0.85
intercooler pressure drop	5%
main combustor pressure drop	4%
reheat combustor pressure drop	2%
Cooling parameters:	
mean heat-flux to work-flux scaling factor, σ	0.15
mainstream stagnation pressure-loss factor, Y	0.2
blade heat exchanger effectiveness, ϵ	0.5
factor for reduction of Stanton number, n	0.25
Other:	
ambient temperature for bottoming cycle	290K
gas constant	8314 J/mole-K
specific heat ratio, γ	1.4

APPENDIX I

The numerical values used in the examples presented are listed below.

Variables	Value used
Machine variables:	
compressor polytropic efficiency	0.9
turbine polytropic efficiency	0.85
intercooler pressure drop	5%
main combustor pressure drop	4%
reheat combustor pressure drop	2%
Cooling parameters:	
mean heat-flux to work-flux scaling factor, σ	0.15
mainstream stagnation pressure-loss factor, Y	0.2
blade heat exchanger effectiveness, ϵ	0.5
factor for reduction of Stanton number, n	0.25
Other:	
ambient temperature for bottoming cycle	290K
gas constant	8314 J/mole-K
specific heat ratio, γ	1.4

DISCUSSION

I. G. Rice, P. E.[1]

The author is to be commended on the three-part paper presenting gas turbine cycle analysis based on the Second Law of Thermodynamics. This discussor also wishes to thank the author for including some of the discussor's pertinent papers as references. There are several points of discussion following which are presented for consideration by both the author and readers of the papers. All three parts are covered together in the discussion.

The Second Law can be usefully used to evaluate the availability of heat to do work and is applied extensively to measure both compression and expansion efficiency wherein the work required to compress a gaseous fluid or the work obtained in expanding a gaseous fluid is referenced to the optimum values at constant entropy. The author goes a step further and effectively relates all losses through the Second Law. There is, however, no substitute for the First Law and the conventional heat balance method.

Gas turbine component efficiencies have been improving over the years and firing temperatures have been increasing. Any computer program used in this regard should provide results that agree with actual industrial gas turbines now on the market. Projections can then be made, using this benchmark, for both higher turbine inlet temperatures and cycle pressure ratios (CPRs). A tabulation of published base-load cycle data of five current industrial gas turbines to compare with the data presented by the author is given in Table 1. It can be noted that the LM2500 has the highest base-load firing temperature of any industrial gas turbine on the market – 2214°F (1212°C) – and the highest specific work – 141.4 BTU/lb of air (328.9 kJ/kg). This particular aeroderivative gas turbine also has the lowest excess air in the exhaust gas, as can be noted, and the best state-of-the-art cycle parameters available today for combined cycles. This machine represents a new landmark for combined cycle projections.

The data presented in the papers, particularly in Parts 2 and 3, do not correlate too well with the engine data in Table 1. The simple cycle gas turbine combined cycle efficiency at turbine inlet temperatures of around 2000°F (1093°C) would peak at about a 16 CPR and not at a CPR of about 8 as given in Fig. 9 of Part 2. Likewise, the reheat gas turbine combined cycles peak at much higher CPRs of 50 to 55 and not 16 as shown in Figs. 1 and 3 of Part 3. The Japanese studies and tests of their research reheat gas turbine indicate a peak combined cycle efficiency at a 55 CPR.

Turbine innovations such as already introduced by Rolls-Royce on their RB 211-535 E4 engine whereby the amount of first-stage cooling air required is reduced by placing a ceramic thermal barrier on the pressure side of the rotating blades should be considered. New innovations such as this must be recognized when projecting future cycles. Likewise, as a result of the NASA E^3 program, gas generators now being designed for both the unducted fan jets and the ducted prop jets by General Electric, Pratt & Whitney Aircraft, and Rolls-Royce will have CPRs of 38 to 42 for a base-load turbine inlet temperature of about 2250°F (1232°C) to obtain maximum simple cycle efficiency. Such gas generators will be prime candidates for the industrial reheat gas turbines of the future.

Turbine Inlet Temperatures

When large quantities of cooling air (or steam) are used to cool the first stage stationary nozzle vanes, the coolant acts thermodynamically the same as tertiary combustor liner cooling air – particularly when the cooling air (or steam) is introduced at the vane leading edge where the approach velocity is rather low – being about Mach 0.1. The nozzle exit velocity achieved is dependent upon inlet static pressure, inlet temperature, and static exit pressure wherein inlet static pressure is more dominant than temperature.

Aircraft manufacturers, and also industrial gas turbine makers, for cycle analysis purposes have gone to the term "Turbine Rotor Inlet Temperature" (TRIT) which is the average total temperature with the first-stage nozzle vane cooling air included. Tabla 1 reflects TRIT. There can be a variation of some 150°F (83°C) with this value and the average combustor outlet temperature. When considering water-cooled first-stage nozzle vanes, the gas stream total temperature is not lowered to as great a degree, and therefore there arises a discrepancy in comparing cycles. In any regard, blade metal temperature is the design criterion and not the inlet temperature definition.

Another factor to consider is the type of combustor employed. An annular combustor provides a far more uniform circumferential exit temperature profile and avoids the temperature spikes of a multiple can-type combustor. Therefore, in the opinion of this discussor, the type of combustor assumed should be stipulated for the analysis.

Intercooling

Intercooling can be accomplished without too much difficulty and one stage of intercooling, and possibly two stages, are within reason for the reheat gas turbine combined cycle. Intercooling does, however, degrade combined cycle efficiency. This degradation is shown in Fig. 3 of Part 3. If one stage is used, then the cooling should take place very early in the compression at about a pressure ratio of 2. See this discussion's reference [1]. If a second stage is used, then the second stage should likewise follow the first stage after another compression ratio of about 2. The author does not indicate at what compression ratio intercooling should take place. One stage only of intercooling should not be at the square root of the total pressure ratio for a maximum combined cycle efficiency. As a note of interest, when considering regeneration instead of the combined cycle, the intercooling pressure ratios are indeed higher.

---

[1] Consultant, Spring, TX; Fellow ASME

Table 1 Base-load gas turbine data: iso conditions*

	A	*B*	*C*	*D*	*E*
	General Electric LM2500PE	Rolls-Royce R-B211C	General Electric LM5000A	Westinghouse 501-D	General Electric PG7111E
1 Shaft output**					
HP	29,500	34,000	43,525	138,699	103,682
kW	22,007	25,364	32,469	103,469	77,347
2 Cycle efficiency					
percent LHV	37.0	36.4	37.4	33.4	32.3
3 Cycle pressure ratio	18.7	20.0	30.0	14.0	11.7
4 Air flow					
lb/s	147.5	196.2	265.0	801.0	605.0
kg/s	66.9	89.0	120.2	323.3	274.4
5 Specific work output					
BTU/lb air	141.4	122.6	116.2	122.4	121.2
kJ/kg air	328.9	285.2	270.3	284.7	281.9
6 Turbine rotor inlet temperature					
°F	2214	2133	2113	2025	2019
°C	1212	1162	1156	1107	1104
7 Exhaust temperature					
°F	955	887	797	970	1000
°C	513	475	425	521	538
8 Exhaust excess air					
percent	226	270	302	241	232

---

*Data published by *Gas Turbine International Catalog*, 1984

**Assumed generator loss of 2 percent added as required

Reheating

Reheating, when considering high turbine inlet temperatures, is far more difficult to accomplish than intercooling. The gas exiting the gas generator has a rather high temperature – 1200 to 1400°F (650 to 760°C) – and high velocity – about Mach 0.4 to 0.5 – which accounts for 10 to 15 percent of the total pressure. This high velocity must be fully diffused without separation to a low velocity of about 100 ft/s (30 m/s) combustor reference velocity to avoid an excessive pressure loss and to control the flow to the reheat combustor. Even with the best diffuser, a 1 percent pressure loss will take place. Another 2 to 3 percent is needed for the combustor liner. Another design challenge relates to the rather high temperature encountered to the reheat combustor and the cooling of the reheat combustor liner. Adding a second reheat combustor only compounds these two difficulties. The assumed total value of 2 percent reheat combustor pressure loss given in Part 3 is unrealistic. A more realistic value would be 4 percent.

Reheating cannot readily be done at any particular and desired expansion ratio. A reheat combustor must be placed between turbine stages. This fact can complicate the physical configuration. Reheating, similar to intercooling, should be done early in the expansion for maximum combined cycle efficiency, but this ideal arrangement is impossible to accomplish. There are two basic machine arrangements: the configuration used by the Japanese and the one proposed by the discussor per the references given by the author.

Combined cycle part-load efficiency has not been addressed by the author, which is a decided plus for the reheat gas turbine. The Japanese have now proven that the reheat cycle offers exceptionally good part-load efficiency, even down to 40 percent cycle output. Such part-load efficiency is not possible with the simple cycle gas turbine combined cycle.

Steam Cooling/Injection

Steam cooling/injection falls in an entirely different category from either air cooling or water cooling, and the author does not make any clear distinction. Such steam cooling/injection, in this discussor's judgment, creates not a combined cycle but rather, an integrated gas/steam cycle. The injected steam becomes part of the working fluid of the gas turbine. Steam cooling/injection degradation of combined cycle efficiency does not follow any of the cycles (*a*), (*b*), or (*c*) of Fig. 9, Part 2; and, likewise, Part 3 does not cover the concept of the integrated cycle.

The application of steam cooling/injection makes it possible to drive a high-pressure core compressor (pressure ratio 20) with a single-stage turbine and one disk without excessive expansion losses associated with otherwise transonic blading. Subsonic surface Mach numbers can be realized. Cooling requirements are then reduced by eliminating one complete stage. The additional work for the one stage is accomplished because of the following:

(*a*) All the cooling air is heated in the combustor to do work. Incremental work is obtained.

(*b*) The cooling steam injected at the leading edge of the nozzle vanes provides additional mass flow and more work is realized therefrom.

(*c*) Steam injection in the combustor can augment the cooling steam to provide the required work to drive the high-pressure compressor with the single stage.

Only one turbine stage is required to drive the low-pressure compressor which is normal practice for such gas generators as the LM5000.

In addition to the advantage of one less gas generator turbine stage requiring cooling, the gas generator expansion ratio required is substantially reduced and reheat can be introduced earlier in the overall expansion which increases the power turbine expansion ratio and thus increases output.

If compression intercooling is incorporated, the inlet temperature is reduced to the high-pressure compressor and a reduction of core compression work is realized to further enhance the single stage turbine design.

The high temperature reheat gas turbine is a special machine and there are only a few windows of design opportunities and options open. Generalized studies incorporating 3, 4, 5, etc. stages of intercooling and 2, 3, 4, etc. stages of reheat are of academic interest, but design criteria and practicality must also be considered.

It appears to this discussor that there is no thermodynamic justification for water-cooled first-stage vanes; and the only justification would be for rare occasions where high ash content fuel is burned and a water-soluble ash is formed at a reduced temperature which can be removed by water washing.

The three-part paper does, however, point out the fact that cooling degrades combined cycle efficiency and high cycle pressure ratio gas turbines – particularly reheat gas turbines – are susceptible to excessive cooling losses and these losses should be properly recognized, evaluated and offset by design innovations.

The reheat gas turbine combined cycle efficiency gains are too great to be ignored and Part 3 of the author's paper focuses on and draws deserving attention to this advanced cycle of the future.

References

1 Rice, I. G., "Evaluation of the Compression Intercooled Reheat Gas Turbine Combined Cycle," ASME Paper No. *84-GT-128*.

Author's Closure

The author is appreciative of Mr. Rice's thoughtful and insightful comments. However, the author is unable to agree with some of the discussor's statements, which seem to arise from a misinterpretation of the letter or philosophy of the work.

The author sought to provide a general, compact, and broad-ranging method of analysis that can navigate through and assess the myriad possibilities for future combined cycle developments. The numerical results cited are used as an example of the power and versatility of the model presented. The default values of the three dimensionless parameters (σ, β, Y) used are typical examples. They cannot be used to predict the performance of all existing machines. If the performance of a particular machine were to be modeled, those parameters would have to be calculated for its unique design. The stage design and heat transfer data necessary to calculate σ are proprietary to the manufacturers. Based on publically available information, the author has estimated that the value of this parameter for the AGTJ (moonlight) high-pressure turbine is approximately 0.2. For models of certain older, well-proven machines, the author's estimate is 0.35. The blade temperature β has been estimated at 3.8 for the AGTJ first stage and about 3.6 for the same older model. The cycle performance and optimum pressure ratio depend strongly on those parameters. Therefore, any calibration of the model against existing designs has to be done on a case-by-case basis. The author wishes to report that since this work was completed in early 1984, he has initiated a joint study of future cycles with the General Electric Company and the Electric Power Research Institute. Application of the author's model to calibration test cases on the EPRI GATE program, which provides detailed (but cumbersome) stage-by-stage chemical and thermodynamic calculations, has resulted in remarkably close agreement. The results of those studies are expected to be published in the near future.

Returning to some of Mr. Rice's specific comments, the author would like to elucidate several points:

The author disagrees with the discussor's comment that the optimum pressure ratio for the nonreheat combined cycle at about 1100°C TIT is approximately 16. Such a conclusion might be obtained if one were to do the calculation with a conservative steam cycle without allowing for improvement of steam cycle efficiency with increasing gas turbine exit temperature. Such a calculation was presented by the discussor (ref. [1], Part 3). When one continuously optimizes the steam cycle as turbine exit temperature increases, the optimum pressure ratio obtained is in the 8–12 range. This conclusion has been corroborated by runs on the EPRI GATE program with detailed simulation based upon existing engines and steam cycle technology. In general, the following factors tend to drive the optimization toward higher pressure ratios: (1) lower values of σ; (2) higher values of β; (3) smaller slopes of the curve of steam cycle effectiveness versus turbine exit temperature (Fig. 8, Part 1) which would arise with multipressure steam evaporators.

The discussor's comment on the optimum CPR for the reheat cycle is affected by the same factors. The optimum pressure ratios are in the range 16–25 without intercooling (Figs. 1 and 3, Part 3). The discussor incorrectly compares those to the intercooled Japanese cycle. The latter should be compared with Fig. 6 of Part 3, which shows optima in the range of 30–50 depending on cooling method. With the high value of β (3.8) and low σ (about 0.2) used in the AGTJ, the optimum pressure ratios should be higher (about 50).

On the subject of intercooling, the discussor's own work (ref. [1] of his discussion) is in agreement with the author's conclusion that for optimum efficiency the intercooler pressure ratio should be unity (no intercooler at all). If one assumes its existence, with a finite pressure drop, then the optimum pressure ratio to which the discussor refers is obtained at some low value. Intercooling provides additional specific power output at the expense of efficiency. If one were to optimize for efficiency, intercooling should not be employed at all. For maximum specific output, the intercooler pressure ratio should be at about the square root of the overall value. In general, the intercooler, if used, should be intermediate between those limits, the efficiency falling and specific output increasing as the intercooler pressure ratio increases from unity to the square root of the overall CPR. This tradeoff has to be recognized in deciding whether or not to intercool, and if so at what pressure ratio.

The discussor's comment on the reheat combustor pressure loss is well taken. The author agrees that a total pressure loss of 4 percent is more realistic than the 2 percent used in the examples. Figure 8 of Part 3 shows that the effect of such a change should be a penalty of about ⅓ of a percentage point to the reheat cycle. Notwithstanding, the author wishes to point out some silo-type primary combustors (such as Brown-Boveri's and Kraftwerke Union's) do achieve pressure losses less than 2 percent. Also, the reheat combustor has a smaller fundamental loss than the primary combustor due to the smaller heat addition per unit mass [1].

On the subject of steam cooling, the discussor mentions many advantages but none of the disadvantages. Even though steam cooling requires less coolant massflow, it can be shown that the mole flow rates of coolant are roughly equal for air and steam [2]. The thermodynamic penalties in the gas flow path are essentially a function of the mole fractions of coolant to main gas (equations 3–9 of Part 3). Steam cooling is found to provide modest gains, which derive more from the cycle compounding effect (ref. [10] of Part 3) than from the reduction of the cooling penalty.

References

1 LeFebvre, A. H., "Aerodynamics," *Gas Turbine Combustion*, McGraw-Hill, New York, 1983, Chap. 4.

2 Pourkey, F., and El-Masri, M. A., "Thermal Design Scaling for Turbine Cooling Systems," submitted to ASME 1986 Gas Turbine Conference, Düsseldorf, Germany.

A. Schäffler
Head of Component Testing.
MTU,
Munich, Germany

D. C. Miatt
Manager Compressors Fleet Engines.
RR,
Bristol, England

Experimental Evaluation of Heavy Fan-High-Pressure Compressor Interaction in a Three-Shaft Engine: Part II—Analysis of Distortion and Fan Loading

Analysis of a severe rotating-stall phenomenon encountered in the fan core section of a three-shaft low bypass engine revealed interesting insight into the growth and circumferential extension of the stall cells immediately before surge of the high-pressure compressor was induced. The effect of a rotating distortion in contrast to the usually encountered stationary distortion is highlighted. The rotating distortion changes the time and hence the effectively felt distortion sector angle depending on a co- or contra-rotational arrangement of the distorting and the distorted compressor. The analysis shows that a contra-rotational arrangement provides a more stable and tolerant situation against that type of distortion. Analysis of the fan loading shows the static temperature rise coefficient to be the most descriptive for the fan rotor 1 hub section which initiated the rotating-stall mechanism.

Introduction

The flow phenomenon experienced and described in Part I is quite interesting as it provides an example of a large rotating circumferential distortion in contrast to the usually treated case of a stationary inlet distortion. This rotation of the distortion does modify the reaction of the downstream compressor depending on the direction of rotation relative to the distorted compressor. To develop this statement a short summary of the effects of circumferential distortion on compressors is given.

Summary of Circumferential Distortion Effects

The large amount of experimental results available proves that in compressors operating behind circumferentially distorted inlet flow the rotor blades dominate the behavior. Therefore a stationary sector distortion principally yields an unsteady flow phenomenon comparable to the angle of attack changes seen by oscillating airfoils. As described in the basic work of Melick and Simpkin [1], Korn [2], and Melick [3] the unsteady increase of incidence toward stall shows a time delay as a result of the flow adjustment and the time constant of this process depends on flow velocity and blade chord length. In the work of Roberts, Plourde, and Smakula [4] and Melick and Simpkin [1] the effects of different rotor chord lengths and different distortion sector angles are analyzed with the well-known result that the distortion must be felt long enough by the rotor to become fully effective, i.e., a minimum critical sector angle is required to reduce surge margin by the maximum possible amount. The phenomenon can be described as a unique function of the reduced frequency parameter which appears in two forms in literature.

The usual definition [1, 3, 5] derived from oscillating airfoil aerodynamics is given in equation (1) and used for the determination of critical sector angles.

$$k=\frac{\Omega\cdot c}{2\cdot W}=\frac{1}{2}\cdot\frac{c}{r}\sin\beta \tag{1}$$

Korn [2] developed a modified form including the spoiled sector angle θ or the distortion frequency ω

$$K=\frac{\omega\cdot c}{2\cdot u}=\frac{\pi\cdot\Omega}{\theta}\cdot\frac{c}{r\cdot\Omega}=\pi\cdot\frac{c}{\theta\cdot r} \tag{2}$$

K represents the ratio of the blade chord length to the length of the distorted sector through which the rotor blades pass. Obviously the two definitions are interrelated by the distortion sector angle.

Stall margin reductions due to distorted inlet flow can be predicted by the parallel compressor model.

The parallel compressor theory predicts stall margin reductions due to spoiling reasonably well for narrow chord compressors with reduced frequency parameters $k < 0.1$, but overestimates the loss of surge margin considerably for higher values of the reduced frequency. This effect is illustrated in Fig. 1 which shows the ratio of measured surge margin loss due to spoiling relative to the prediction. Figure 1 is taken

---

Contributed by the Gas Turbine Division of The American Society of Mechanical Engineers and presented at the 30th International Gas Turbine Conference and Exhibit, Houston, Texas, March 18–21, 1985. Manuscript received at ASME Headquarters, January 10, 1985. Paper No. 85-GT-222.

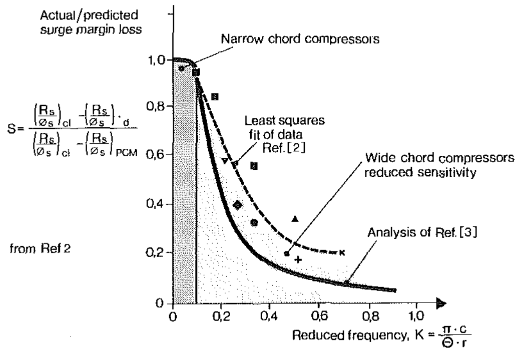

Fig. 1 Circumferential distortion sensitivity

from [2]; the experimental results are underlined by the theoretical model developed in [3]. Higher reduced frequency parameters are obtained either through longer chords or narrower distortion sectors, which both reduce the time for the blades in which they can see the distortion in relation to the time constant of the blade boundary layer.

Effect of Rotating Distortion. The unusual case of a rotating distortion directly affects the reduced frequency parameters. A co-rotating distortion is felt longer and a contra-rotating distortion for a shorter time interval by the rotor blades, thus simulating wider or narrower distortion sectors.

The reduced frequency parameter for rotating distortions can be written in accordance with equation (2):

$$K'=\pi\cdot\frac{c}{r\cdot\theta}\cdot\frac{\Omega_R+\Omega_D}{\Omega_R} \qquad (3)$$

In this equation the angular velocities of the distortion Ω_D and of the distorted compressor rotor Ω_R are defined positive for contra-rotation, as is the case in the RB 199 engine, where fan and IPC rotate clockwise and the HPC counterclockwise.

Table 1

Distortion Type	K; K'	θ sw, crit
co - rotating	0,153	66 deg
stationary	0,208	90 deg
contra - rotating	0,263	114 deg

From equation (3) it can be deduced that in a contra-rotational arrangement the reduced frequency increases and may, depending on the speed of rotation, reduce the effectively felt distortion sector angle to an extent that the surge margin loss is considerably smaller, as can be deduced from Fig. 1.

Analysis of Experienced Pressure Distortion. From isolated HPC rig tests with stationary square wave pressure distortions of 45, 90, and 135 deg circumferential extension a critical sector of about 90 deg was evaluated. From the reduced frequency $k = 0.045$ for the HPC a critical sector angle of $\theta_{crit} = 75$ deg would be expected using the conversion given in [5], which is in reasonable agreement with the experimental result.

In order to evaluate the HPC surge margin loss due to the IPC exit pressure distortion quantitatively, the equivalent critical distortion sectors for co- or contra-rotational distortions can be calculated from the reduced frequency parameters shown in Table 1.

Taking the experimentally determined 90 deg critical sector angle for stationary square wave distortions from rig tests, equivalent critical sectors of 66 deg and 114 deg for co- and contra-rotational distortions are obtained.

The real distortion patterns leaving the fan at probe D and the IPC at probe 230 in the penultimate and last round before surge occurred were analyzed for the highest possible equivalent square wave distortions within the respective sector

Nomenclature

A_j = nozzle area, m^2
c = chord length, m

$$CH = \frac{2c_p\cdot T_{s1}\left[(p_2/p_1)^{\frac{\gamma-1}{\gamma}}-1\right]-(U_2^2-U_1^2)}{2c_p\cdot(T_{t1}-T_{s1})}$$

= loading parameter
c_p = specific heat at constant pressure, J/K
k = reduced frequency (equation 1)
K = reduced frequency (equation 2)
K' = reduced frequency for rot. distortion (equation 3)
M = mass flow, kg/s
N = rotational speed of distorted compressor, min^{-1}
P = total pressure, kPa
p = static pressure, kPa
R = compressor pressure ratio
r = mean radius, m
S = circumferential distortion sensitivity (Fig. 1)

$$SM = \frac{R_s}{R_w}\cdot\frac{\phi_w}{\phi_s}-1 = \text{surge margin}$$

T = temperature, K
t = time, ms
U = circumferential velocity, m/s
Va = axial velocity, m/s
w = relative velocity, m/s
β = relative inlet air angle, deg
γ = ratio of specific heats
Δ = difference
θ = distortion sector angle, deg
λ = bypass ratio

$$\phi = M\sqrt{T}/P = \text{flow function}, \frac{\text{kg}\sqrt{\text{K}}}{\text{s kPa}}$$

$$\Omega = \frac{2\cdot\pi}{60}\cdot N = \text{angular velocity, s}^{-1}$$

$$\omega = \frac{2\cdot\pi}{\Theta}\cdot\Omega = \text{distortion frequency, s}^{-1}$$

Subscripts and Superscripts

cl = clean, undistorted
crit = critical sector angle
d = distorted compressor
D = rotating distortion
L = fan
max = max. value
min. = min. value
PCM = predicted by parallel compressor model
R = distorted compressor rotor
rel = related to design value
s = at surge; static (gas condition)
sw = square wave
t = total
w = at working point
1 = inlet to cascade
2 = outlet of cascade
$\bar{\ }$ = average value
$'$ = relative to cascade

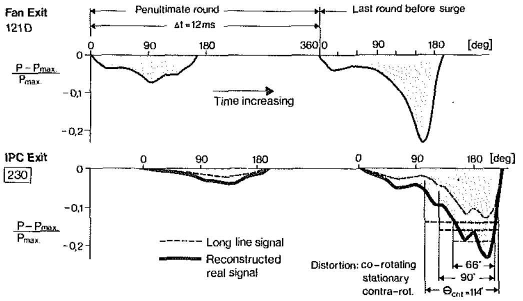

Fig. 2 Distortion increase at fan and IPC exit during last phase before surge

angles. Significant differences emerged due to the essentially triangular shape of the distortions, which resulted in much more severe disturbance amplitudes for the smaller sector angles, as shown in Fig. 2.

As can be seen from Table 2, the IPC attenuates the fan exit distortion up to the penultimate round before surge; however, in the final revolution of the distortion cell a heavy amplification occurs.

From the pressure distortion amplitudes given in Table 2 a surge margin loss of 21 ± 2% (see Nomenclature) can be estimated for the RB 199 HPC, based on rig test results. This ties up reasonably well with the necessary loss in surge margin to explain the HPC surges.

In the case of a co-rotating arrangement a 6% higher surge margin loss would be expected due to the deeper distortion amplitude in the smaller 66 deg sector. The total inlet distortion into the HPC consisted probably of a combined pressure/temperature distortion, the latter being produced by the IPC. Due to the lack of high-response temperature measurements and the fact that during the last round no obvious difference in IPC pressure ratio within and outside the distorted sector was notified, no quantitative assessment of the temperature distortion could be undertaken.

Comparative Engine Testing. Having understood the HPC stall inducing mechanism as a one-cell fan core section rotating stall with its very clear signatures in a power spectral density analysis (see Part I, Fig. 7) a simple method was available for a comparative fan evaluation program.

Using on-line real-time analysis techniques, different fans incorporating modifications such as rotor and stator restaggers were analyzed for the rotating stall areas within their characteristics. Figure 3 shows an example of an improved fan version. The evaluation was coupled with full fan characteristics being taken along lines of constant nozzle area. As soon as the characteristic rotating stall signal was observed, cautious running permitted delineation of the rotating stall areas within the fan characteristics for selection of the most favorable fan variant.

Analysis of Fan Internal Loading Parameters

Basis of the Loading Assessment. In order to understand the origins of the LPC outlet pressure fluctuations an analysis of compressor internal matching and loading was carried out from 80 to 100% design speed. For this, data were used from an equivalent aerodynamic standard rig compressor, which included a better standard of internal instrumentation, that allowed a full analysis to be made. The module was tested to a representative bypass ratio schedule, using a split discharge dual exit throttle system. The overall rig characteristic is given in Fig. 4.

The analyzed engine test points 1 to 6 at 91.6% $N/\sqrt{T}$ (see Part I, Fig. 5) have been overlaid on the figure. Although that engine module demonstrated higher flow at design speed than the rig compressor no flow modification factor has been applied. This is because for a given core the LP compressor matches out along a fixed set of bypass ratio lines (overlaid on Fig. 4) provided there are no gross internal mismatches within the compressor. Analysis of rig tests of varying development module standards confirmed that nondimensional speed and bypass ratio were the dominant factors in compressor matching, hence the decision not to modify flows in Fig. 4.

Table 2

Square wave Distortion	Sector angle / amplitude	penultimate round Fan exit (121 D)	penultimate round IPC exit 230	last round bef. surge Fan exit (121 D)	last round bef. surge IPC exit 230
co-rotating	Θ sw (deg.)	66			
	$\bar{P}-\bar{P}$ min./$\bar{P}$	0,034	0,028	0,114	0,173
stationary	Θ sw (deg.)	90			
	$\bar{P}-\bar{P}$ min./$\bar{P}$	0,032	0,023	0,098	0,148
contra-rotating	Θ sw (deg.)	114			
	$\bar{P}-\bar{P}$ min./$\bar{P}$	0,030	0,016	0,075	0,133

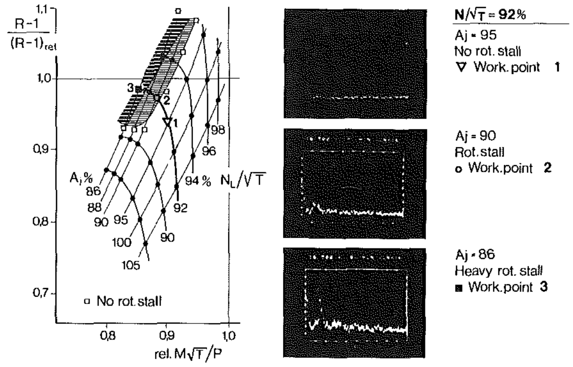

Fig. 3 Power spectral density signals during engine tests

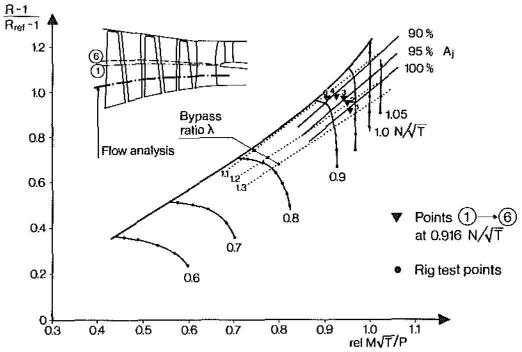

Fig. 4 Fan characteristics used for through-flow analysis

An axisymmetric flow analysis of each rig test point was carried out using a through-flow program. Input data for stator inlet planes were from vane leading edge instrumentation. A stator loss model was used to generate inlet conditions to rotors two and three. The output from the program then provided the basis for further analysis.

In addition to the variation of engine bypass ratio, the loci of constant final nozzle area lines have been plotted in Fig. 4. It can be seen that a reduction in final nozzle area lowers bypass ratio in an essentially linear relationship. The effect of final nozzle area on the location of the splitting streamline between engine section and bypass flow for engine points 1 and 6 is given in the inset diagram in Fig. 4.

Fan Internal Matching and Loading Changes. The analysis of the fan internal matching and loading was aimed at understanding the reason for the observed outlet pressure fluctuations and to explain the limited speed and pressure

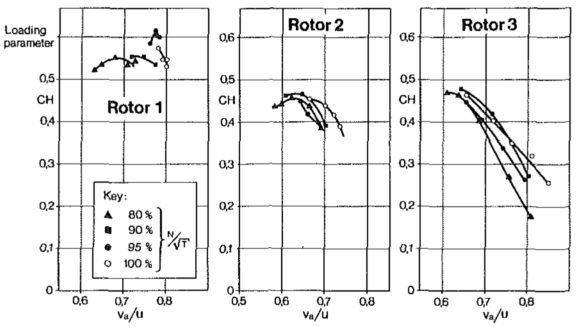

Fig. 5 Fan rotor static enthalpy rise coefficient

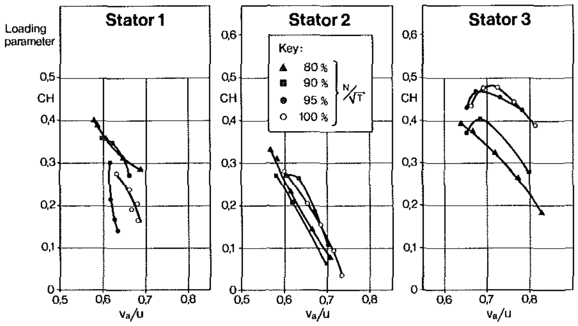

Fig. 6 Fan stator static enthalpy rise coefficient

ratio range over which it occurred. An initial survey of blading diffusion factors failed to show levels that could be expected to produce cascade instability by point 4 on Fig. 4, by which point significant outlet perturbations had become apparent on test. Similarly, calculation of the Dunham criterion [6] for the onset of rotating stall, either for the overall compressor or stage by stage, gave no correlation. The level of analyzed diffusion factor in the critical working region implied that the reason for the outlet perturbations lay in end-wall loadings rather than diffusion or incidence limits of the blade cascades.

Koch [7] used as a basic correlating parameter for the compressor stage stall pressure rise capability an enthalpy-equivalent static pressure rise coefficient. This concept was taken and applied to each blade row in the compressor in view of the stagewise variation of reaction in the compressor design. Values of mean coefficient (CH) were calculated for each blade row at each analyzed rig test point and plotted against a mean engine-section flow coefficient. In the case of a stator the circumferential velocity used in the flow coefficient was that at exit from the rotor directly upstream. Enthalpy-rise coefficients through rotors included a correction for streamline radius change between inlet and exit and the denominator was the relative dynamic head at inlet to the cascade. The results are plotted for rotors in Fig. 5 and stators in Fig. 6.

Through-flow analysis of the stage 1 rotor had shown that it was operating several degrees into stall at 80 and 90% design speed and this is reflected in the almost flat plot of CH against flow coefficient. This is analogous to a diffuser with inlet lip separation—stable although not necessarily working effectively. The rotor hub section is just on stall at 95% and a very high CH is evident in the engine section, with a peak followed by a marked drop as surge is approached. At design speed rotor 1 operates on a virtually unique condition, CH rising on the last test point (very close to surge), but to a lower level than the minimum at 95% speed. The two points that can be seen from the stator plots on Fig. 6 are the generally lower working CH's compared with the rotors, which is a reflection of the reaction choice in the compressor design, and the excessive loading of the exit guide vanes at speed above 90%. Peak level of CH on the EGV is identical to that of rotors 2 and 3.

The conclusions were that the compressor aerodynamic design, with a high reaction first stage, led to a correspondingly heavy "equivalent diffuser" loading in rotor 1. The deep hub blading stall at 80% and 90% was postulated as stabilizing this equivalent diffuser. With the rotor hub just on stall at 95% the loading was sufficiently high to initiate a rotating stall. This was induced by the combination of high back pressure (due to stage matching and level of first stage reaction) and a critical rotor 1 hub incidence.

At design speed compressor-stage matching reduced the level of incidence and loading in rotor 1 so that its stability ceased to be critical. A possible interaction effect between rotor 1 hub and the exit guide vane may exist at 95% due to the positive slope on the stator CH characteristics as surge is approached.

Conclusions

Analysis of a severe fan hub rotating stall in a three-spool low bypass engine revealed the following essential results:

- Severe single-cell rotating stall with pressure deficits of up to 20% against average were encountered in the fan core section stream at high rotational speeds up to 98% $N/\sqrt{T}$, causing surge margin losses in the high-pressure compressor of up to 22%.
- An analytical approach based on the reduced frequency parameter showed that the effect of the rotating distortion depends on the direction of rotation relative to the spoiled compressor. A contra-rotating spool arrangement appears to be less susceptible to this specific type of distortion.
- The high-speed rotating stall mechanism appears to be induced by excessive loading of the rotor 1 hub/endwall junction. This is best described by a static temperature rise loading parameter.

Acknowledgments

The authors wish to thank NAMMA, MTU, and Rolls Royce for the permission to publish this paper. The authors also want to express their gratitude to Messrs. K. Schedl, Dr. K. Ding, G. Sieger, and R. Goehl from MTU for their great help in signal analysis and reconstruction of the long-line system data to their real values.

References

1 Melick, H. C., and Simpkin, W. E., "A Unified Theory of Inlet/Engine Compatibility," AIAA Paper No. 72-1115.

2 Korn, James A., "Estimated Effect of Circumferential Distortion on Axial Compressors Using Parallel Compressor Theory and Dynamic Stall Delay," AIAA Paper No. 74-233.

3 Melick, H. C., "Analysis of Inlet Flow Distortion and Turbulence Effects on Compressor Stability," NASA CR 114577, 1973.

4 Roberts, F., Plourde, G. A., and Smakula, F., "Insight into Axial Compressor Response to Distortion," AIAA Paper No. 68-565.

5 Williams, D. D., and Yost, J. O., "Some Aspects of Inlet/Engine Flow Compatibility," Paper presented at ICAS-Congress, Amsterdam, 1972.

6 Dunham, J., "Non-Axisymmetric Flows in Axial Flow Compressors," *Mechanical Engineering Sciences Monograph No. 3*, Institution of Mechanical Engineers, 1963.

7 Koch, C. C., "Stalling Pressure Rise Capability of Axial Flow Compressor Stages," ASME JOURNAL OF ENGINEERING FOR POWER, Vol. 103, Oct. 1981.

P. Sampath

M. Gratton

Pratt & Whitney Canada,
Mississauga, Ontario, Canada

D. Kretschmer

J. Odgers

Laval University,
Canada

Fuel Property Effects Upon Exhaust Smoke and the Weak Extinction Characteristics of the Pratt & Whitney PT6A-65 Engine

Introduction

Pratt & Whitney Canada (PWC) has recently completed a research program investigating the performance characteristics of small gas turbine combustors with broadened specification and alternate source fuels [1]. As part of this program, tests were conducted using ten different fuels in a PT6A-65 gas generator. The fuels ranged from Jet A1 (taken as baseline) to those derived from Tar Sands.

Two of the performance factors which can be significantly influenced by fuel properties are (*a*) the carbon formation (here indicated by the quantity of exhaust smoke) and (*b*) the weak extinction characteristics. For their part in this work, the Laval University team predicted the performance of the fuels based upon the test result of a standard fuel. This paper presents both the experimental results and the predicted values based upon existing correlation techniques.

Test Vehicle and Fuels

Combustor and Test Equipment

PT6A-65 Engine. The PT6A series of gas turbine engines was developed for application on helicopters and fixed-wing aircraft. Initial power levels of 410 kW were successively increased to 1.03 MW by increasing air mass flows and operating temperatures, and also by adding a second stage power turbine. The PT6A-65 engine, rated at 965 kW, has an overall pressure ratio of 10:1 and a turbine inlet temperature (TIT) of 1330 K (2400 R). It is comprised of a four-stage axial compressor, a single-stage centrifugal compressor, a reverse-flow annular combustor, a single-stage compressor turbine, and a two-stage power turbine (Fig. 1). The PT6A-65 engine weighs approximately 210 kg (464 lb).

PT6A-65 Combustion System. The reverse-flow annular combustor (Fig. 2) is mainly composed of sheet metal panels, although some components located in the dome are of machined construction. Both the inner and outer liners are cooled by splash louver films which insulate the metal from the hot gases. Convective cooling is also achieved outside the combustor by air flowing through the annulus. The combustor is comprised of outer and inner liners bolted at a flange in the dome thus enabling easy access for inspection and repair. Both liners are coated with yttria-stabilized zirconia thermal barrier coatings for enhanced life.

A single recirculating vortex is maintained in the primary zone. It is driven by the cooling films and by a row of trip holes, or jets, located on the inner liner. Combustor air is also introduced through jets in the outer liner and around fuel nozzle sheaths.

Dilution air is introduced through jets on both inner and outer liners and has been optimized to obtain satisfactory exit temperature distributions.

Fourteen tangentially spraying fuel nozzles provide fuel to the primary zone. These are single orifice pressure atomizers with flow numbers (FN) of 2.9×10^{-6}.

PT6A-65 Test Rigs. Test data discussed in this paper were obtained on a PT6A-65 gas generator (Fig. 2), a butterfly valve being used to simulate the restriction of the power turbine. Thus, the gas generator can be run along a full engine running line and all combustor operating parameters remain unchanged.

Engine air mass flow is monitored by measuring the pressure drop across a previously calibrated intake venturi. Fuel flow is recorded using a turbine flowmeter which is corrected for variations in fuel density. Temperatures at various stations within the gas generator are monitored by thermocouples which are connected to a central electronic monitoring system.

Exhaust gas samples are collected by a water-cooled probe which protrudes into the exhaust duct. Samples from 13 sampling points are manifolded and pumped through a heated line (425 K) to the smoke and emission analyzers before being exhausted to atmosphere.

Contributed by the Gas Turbine Division of THE AMERICAN SOCIETY OF MECHANICAL ENGINEERS and presented at the 30th International Gas Turbine Conference and Exhibit, Houston, Texas, March 18–21, 1985. Manuscript received at ASME Headquarters, December 10, 1984. Paper No. 85-GT-27.

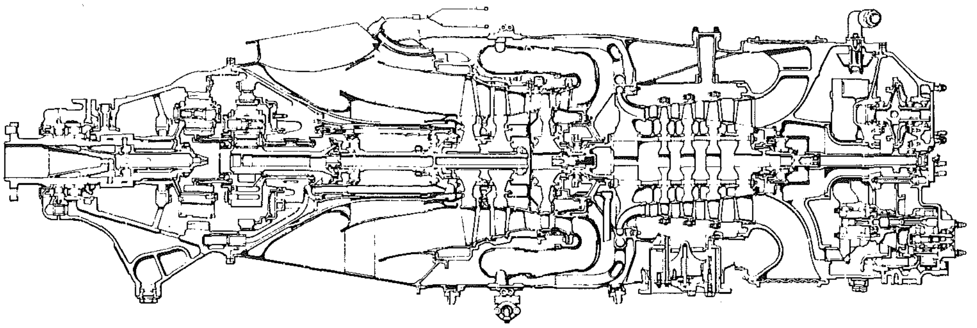

Fig. 1 PT6A-65 engine cross section

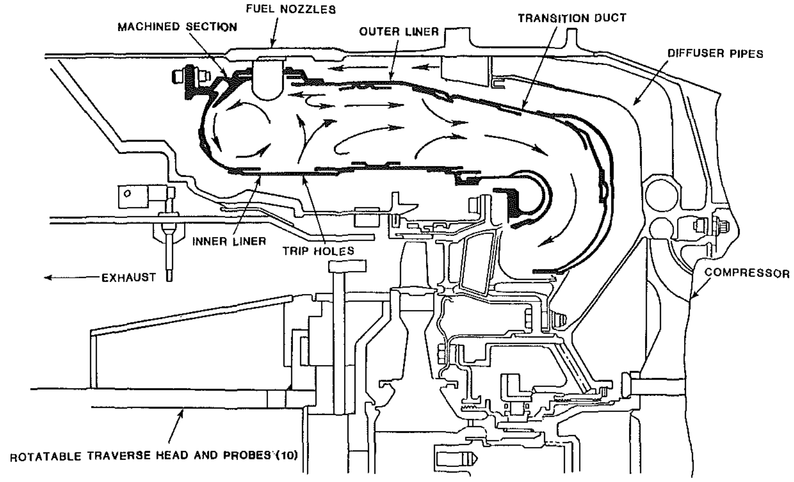

Fig. 2 PT6A-65 combustion system schematic, gas generator rig

The same procedure is adhered to for each test. The gas generator is run at successively increasing power levels from ground idle to 100% power. At each condition, the gas generator is allowed to reach steady state before measurements are taken.

The weak extinction tests were performed on an atmospheric rig (Fig. 3). While the combustion system geometry is the same as in a full engine or gas generator, the operating conditions are considerably different. The atmospheric rig has no rotating components, and air is supplied to the combustor by a blower located upstream, which operates at pressures slightly above atmospheric. This rig represents an ideal vehicle for lean-limit experiments since both the air and fuel flows can be varied to establish flammability limits. Air flows are set to yield the same combustor inlet Mach number in the rig as in the engine. Fuel flow is then slowly reduced until flameout occurs. Repeat blowout tests are always conducted to validate the data.

Test Fuels. The essential properties of the fuels are listed in Table 1. The hydrogen content, which is usually taken as the most important variable, ranged from 10.55% to 14.25%. There was also a wide range of viscosities.

Exhaust Carbon

The measurement of exhaust carbon presents one of the most challenging problems to the combustion engineer. Discussion of the various measurement techniques and their relationship to a proposed "standard" gravimetric technique is given in [2]. Since, in the present work, the only measurement employed is the SAE Smoke Number [3], further discussion will be limited to this technique.

Early in 1968 the SAE organized a committee to introduce a standard technique to quantify the visible obscuration due to smoke. The system was finalized and approved in May 1970.

Smoke emitted from gas turbine exhausts has been shown

Nomenclature

A/F = air/fuel ratio (by mass)
B = mass transfer number
E_i = ignition energy, J
EI_c = emission index, g carbon/kg fuel
FN = flow number of an atomizer, kg s^{-1} Pa$^{-0.5}$
h = hydrogen in fuel (mass fraction)
H/C = hydrogen/carbon, atom ratio
k = constant
LCV = lower calorific value, J/kg
M = molar mass, kg/mol
$\dot{m}$ = mass flow, g/s
O/C = oxygen/carbon, atom ratio
p = pressure, Pa
SMD = Sauter mean diameter, m
T = temperature, K
ΔT = temperature difference, K
ν = kinematic viscosity, m^2/s (cSt)
ρ = density, kg m^{-3} (g/cm^3)
σ = surface tension, N/m (dyne/cm)
ϕ = equivalence ratio

Subscripts

a = air
avg = average
f = fuel
i = at ignition
r = relative to "standard" fuel
st = stoichiometric
0 = ambient
2 = fuel #2
3 = combustor inlet

Table 1 Fuel properties

Fuel No.	ρ kg/m^3 (298 K)	ν cSt (298 K)	σ dyne/cm	Flash point K	Smoke point mm	Heat of combustion net MJ/kg	h Hydrogen mass fraction	Distillation (K)					Molar * mass kg/mol	B Transfer number
								IBP	5%	90%	FBP	T_{avg}		
1†	0.798	1.53	25.4	328.5	22	43.04	0.1376	442	450	492	517	417	0.158	3.79
2	0.760	0.918	22.5	255.0	27	43.82	0.1425	334	361	473	438	427	0.132	4.41
3	0.830	1.14	23.9	259.5	12	41.90	0.1193	331	364	516	541	450	0.137	4.06
4	0.845	1.58	27.0	332.0	12	41.79	0.1204	447	456	511	545	480	0.157	3.69
5	0.796	1.62	25.1	328.5	22	43.30	0.1382	448	457	499	521	475	0.161	3.75
6	0.831	2.35	26.4	339.0	17	42.87	0.1338	444	470	533	556	503	0.176	3.44
7	0.841	2.40	26.2	340.5	14	42.80	0.1303	455	470	538	558	506	0.177	3.41
8	0.834	2.35	27.2	342.0	14	43.07	0.1295	460	470	561	602	507	0.179	3.40
9	0.931	2.97	32.1	325.5	17	42.81	0.1183	451	455	457	469	456	0.129	3.99
10	1.010	7.9	33.7	336.5	8.8	41.99	0.1055	457	461	539	550	507	0.168	3.39

*Predicted
†Jet A1

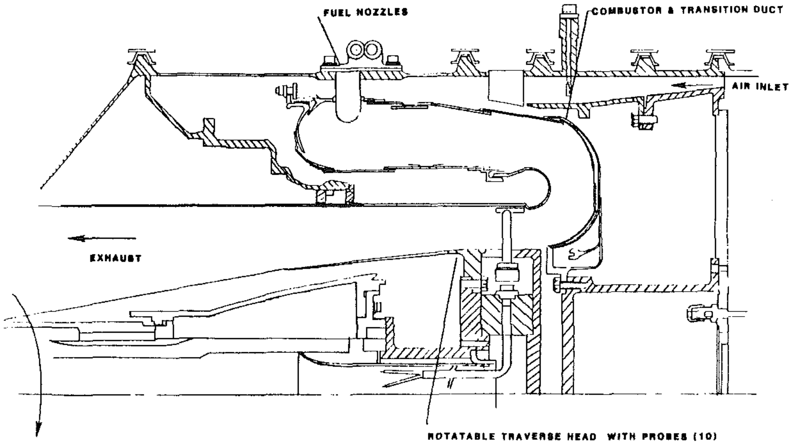

Fig. 3 PT6A-65 atmospheric rig schematic

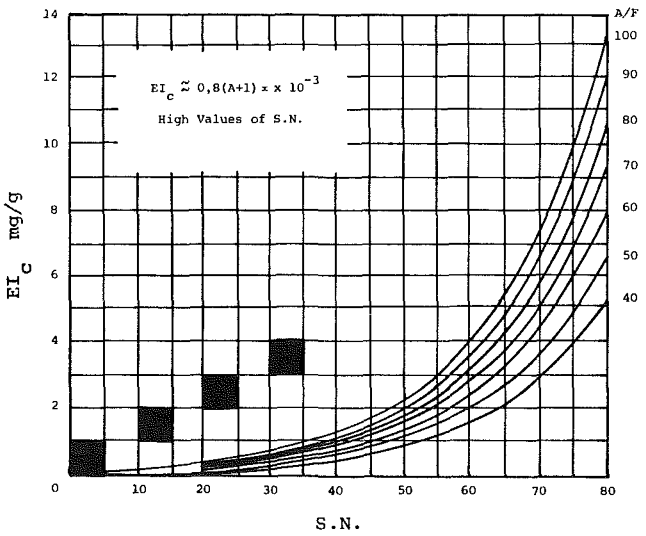

Fig. 4 EI_C**: smoke number relationship at various** A/F

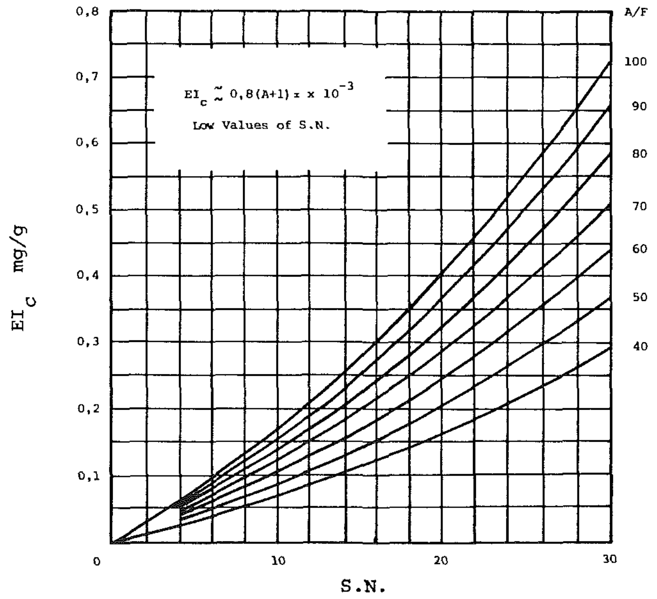

Fig. 5 EI_C**: smoke number relationship at various** A/F

to be a mixture of "small" and "large" particles, and for a conventional gas turbine fuel the proportion was roughly 50/50. (Small is of the order of 0.1 μm and large 1 μm or more.) Any equipment which measures optical smoke density will be more influenced by small particles than by large ones and hence will indicate lower smoke concentrations than a gravimetric measurement, since the large particles will be largely ignored by the optical method. Champagne [4] has given some proof of this, and his curve of smoke density versus SAE smoke number for "total" carbon has been used to establish the relationship between the predicted values (using the correlation technique described below) and the measured SAE smoke numbers.

Figures 4 and 5 illustrate the relation between SN and the carbon emission index (EI_C) for a range of air/fuel ratios. The relationship is based upon:

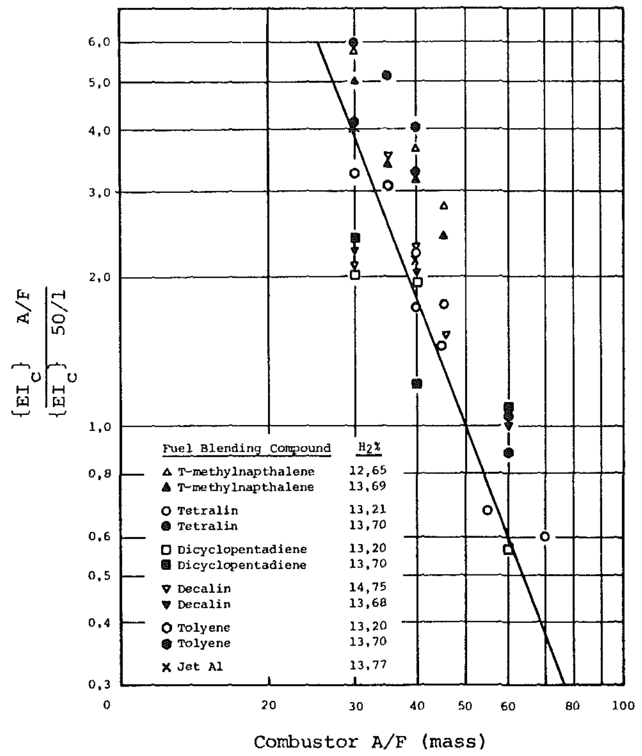

Fig. 6 Soot dependence upon air-fuel ratio data from [5]

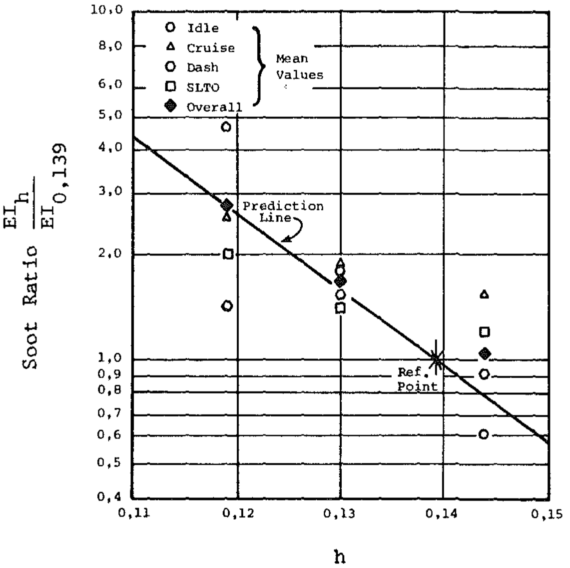

Fig. 7 Effect of hydrogen content upon exhaust soot (data from [6])

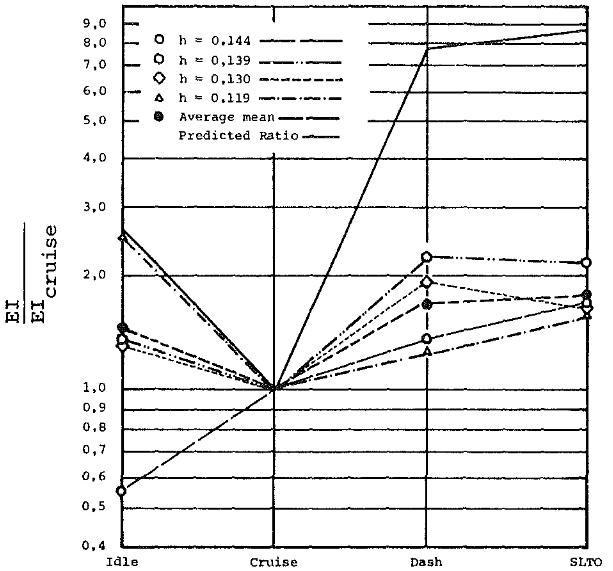

Fig. 8 Effects of operating conditions on exhaust soot T41 combustor [6]

1 g fuel + A g air → $(1+A)$ g products.

Soot (C) $= x$ mg/m^3

EI_c $\equiv g$ carbon/kg fuel

Mproducts ≈ 0.028 kg/mol

This yields: $$EI_c \approx 8 \cdot 10^{-4}(1+A)x \quad (1)$$

The correlation for exhaust carbon derived in [2] has the form:

$$EI \approx 1.08 \times 10^{29} \left(\frac{p}{O/C}\right)^{2.7} (H/C)^{-5.45} T_3{}^{-8.66} \quad (2)$$

Equation (2) has been applied [2] to a number of combustion systems ranging from simple flames, to conventional gas turbine combustors, to "premixed" combustors. The results of these predictions exhibited a high degree of scatter, but it was remarked that for any individual system the scatter was considerably less than the generalized form. The scatter could be further reduced by establishing a "baseline" for the combustor. This was done by selecting a single operating condition and assuming that the measured carbon content was correct. The constant in equation (2) was then altered to agree with the selected value. Predictions at other operating conditions and for other fuels were then made substituting this new constant for that of equation (2).

As an example, the sooting tendencies of Shellsol T blended with various hydrocarbons (reported by Bowden et al. [5]) were treated in this way (p = 0.35 MPa, T_3 = 530 K). The plot of the raw data exhibited a great deal of scatter. A "standard" air-fuel ratio of 50/1 was arbitrarily selected and the carbon content of the other fuels was expressed as the ratio relative to the standard value. Values of (O/C) and (H/C) were then inserted into the equation (p and T_3 were constant) and the results were then plotted as in Fig. 6.

A similar treatment was accorded to the published results of Vogel and Troth [6]. In this instance, the soot contents yielded by the various fuels were averaged and compared with those given by the fuel containing 13.9% hydrogen. The results are expressed in Fig. 7. To demonstrate the effects of operating conditions, the cruise condition was selected as standard and the soot at other conditions expressed as a ratio. Figure 8 shows that the trends were well predicted, although the magnitude of the predictions generally indicated soot ratios which were high in comparison with the measured values.

Possible reasons for the high values are:

(*a*) The correlation requires some adjustment.

(*b*) Overprediction is most noticeable when the carbon has been measured by the SAE smoke number technique. As discussed above, this might be due to particle size effects. This could well be a serious deficiency of the correlation if the soot particle size is a function of fuel composition or structure, or combustor operating conditions and/or combustor geometry.

(*c*) It is possible that combustors will differ in the ratio soot-burnout/soot-formation time. Some idea of this might be obtained by predicting soot within a primary zone and comparing the value with that at the exhaust. From the relative volumes of the zones, it might then be possible to establish a relationship.

Table 2 Baseline smoke data: PWC PT6A-65 gas generator
$14 \times 2.9 \times 10^{-6}$ FN Fuel nozzles Fuel JET A1, $h=0.1376$

Condition	$\dot{m}_a$ kg/s	$\dot{m}_f$ kg/s	A/F	p_3 MPa	T_3 K	Experimental		Predicted	
						SN	EI g/kg	EI g/kg	SN
Ground idle	1.356	1.455×10^{-2}	93.20	0.222	401	3.9	0.068	0.51	24
50% Power	2.930	5.082×10^{-2}	57.65	0.631	545	22.1	0.235	2.18	58
85% Power	3.463	6.959×10^{-2}	49.76	0.816	582	19.4	0.197	3.67	70
100% Power	3.898	7.959×10^{-2}	48.98	0.915	598	15.1	0.140	4.13	73

Table 3 Statistical data

Fuel No.	SN meas.	SN pred.	% Diff.	Fuel No.	SN meas.	SN pred.	% Diff.
1	3.9			6	4.5	5	−11.1
(Baseline)	22.1				25.6	23	10.2
	19.4				24.1	22	8.71
	15.1				23.7	17	28.3
2	4.9	3	38.8	7	4.8	6	−25.0
	18.5	16	13.5		30.2	26	13.9
	19.0	15	21.1		25.4	23	9.45
	21.8	11	49.5		22.4	20	10.7
3	10.2	11	−7.84	8	6.2	6	3.23
	36.1	38	−5.26		42.2	27	37.2
	39.0	37	5.13		36.4	26	28.6
	32.5	32	1.54		34.7	21	39.5
4	7.6	10	−31.6	9	4.7	11	−134
	38.5	34	11.7		35.9	37	−3.06
	35.3	33	6.52		34.1	36	−5.57
	33.3	28	15.9		33.3	31	6.91
5	3.3	4	−21.2	10	12.2	22	−80.3
	16.9	19	−12.4		45.6	51	−11.8
	18.1	13	28.2		41.2	50	−21.4
	16.5	14	15.2		39.7	45	−13.4

	Idle	50%	Load 85%	100%	All conditions	50, 85 and 100% load	
Mean difference	−27.2	5.90	8.29	15.35	1.21	9.86	%
Std. dev.	48.1	14.9	15.3	19.1	31.6	16.5	%

Until the above difficulties are resolved, it will always be necessary to establish a satisfactory baseline for predictions.

Predictions for the Pratt & Whitney PT6A-65 Engine. The baseline smoke data for the engine operating conditions are given in Table 2. The predictions were made using equation (2) and it will be seen that they are much greater than the measured ones and that they do not maximize at the 50% power conditions as do the gas generator tests. The carbon emission index was converted to SN units using Figs. 4 and 5. Because of the high values and the maximum carbon at 50% power, it was decided to use each operating condition as a separate base for predicting the effects of the other fuels. Equation (2) was modified (constant only) and rearranged to suit the specific requirements of the combustor:

$$EI_c = k\left[\frac{p_3(1-h)^3}{(A/F)h^2}\right]^{2.7} T_3^{-8.66} \tag{3}$$

The resulting predicted and measured values are given in Table 3 and Fig. 9.

The agreement between predicted and measured values is generally satisfactory. However, some comments must be made.

(*a*) As indicated in Table 3, the overall accuracy is greatly influenced by the Idle results. If these are discarded the standard deviation reduces to 16.5% from a value of 31.6%.

(*b*) Repeat tests at the four conditions using the base fuel yielded the following values for smoke number:

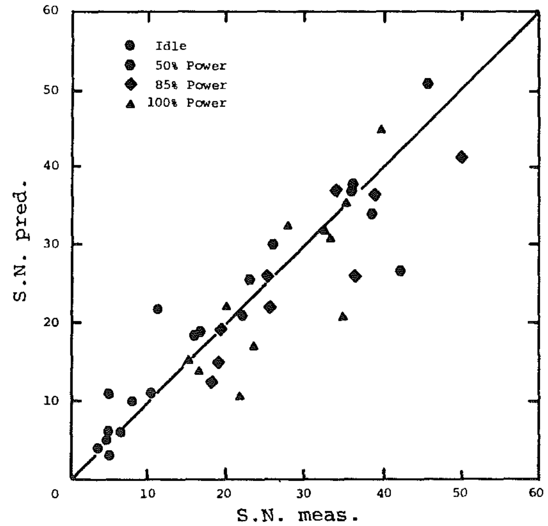

Fig. 9 Exhaust smoke number PT6A-65 engine

	Original Base Line	Test 2
Idle	3.9	0.4
50% Power	22.1	19.9
85% Power	19.4	17.6
100% Power	15.1	14.0

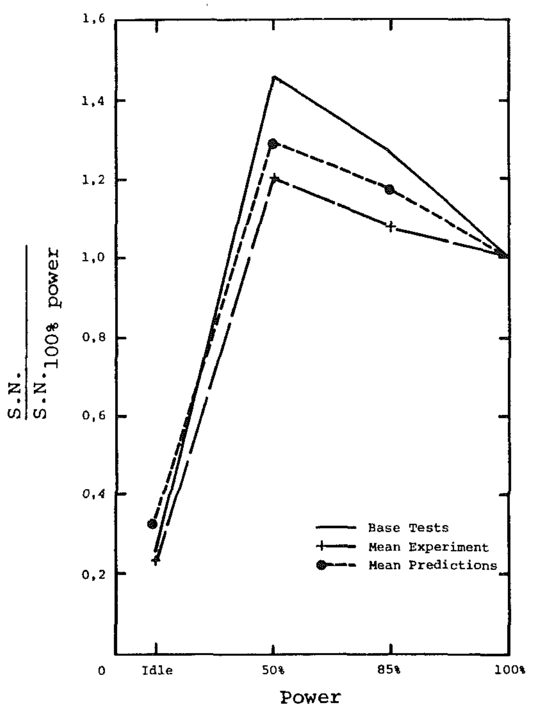

Fig. 10 Carbon formation as a function of engine conditions

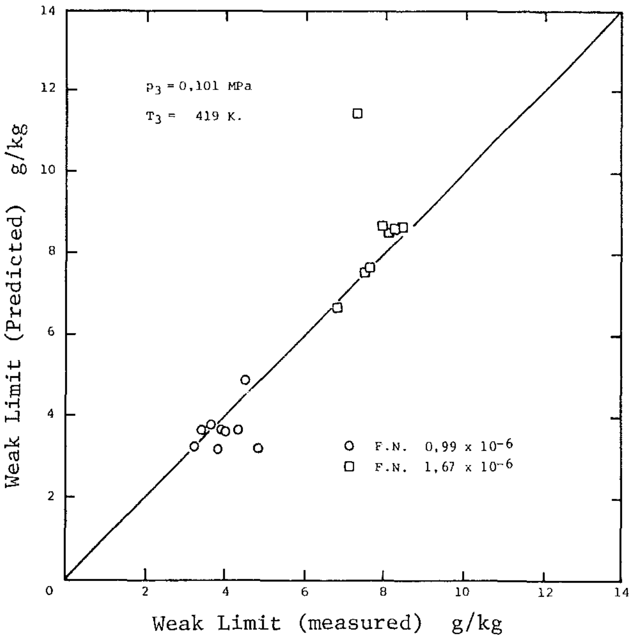

Fig. 11 Weak limit characteristics PT6A-65

These numbers indicate the experimental accuracy and suggest a reason for the poor agreement between prediction and experiment at the idling condition. They also demonstrate the need to establish a firm value upon which to base predictions.

(*c*) As mentioned earlier, and as shown in Fig. 10, the exhaust carbon varies with engine conditions such that (generally) there is a small but significant increase at the 50% and 85% power ratings above the 100% power. The fact that this behavior was generally followed by all the fuels rules out the possibility of experimental error. The explanation is probably due to the geometry and local air-fuel ratio distribution of the combustor. Because of multiport air admittance, all gas turbine combustors comprise regions which may be regarded as carbon formation zones and carbon burnout zones. How closely these can be identified with the usual primary, secondary and dilution zones has not been established, but it is obvious that the dwell time in these zones and their richness (and temperatures) could affect significantly the exhaust carbon at varying operating conditions.

Table 4 Weak extinction characteristics of PT6A-65 engine; pressure = 0.101 MPa, inlet temperature = 419 K

Fuel No.	Lean limits g/kg fuel/air			
	FN = 0.99×10^{-6}		FN = 1.67×10^{-6}	
	Predicted	Measured	Predicted	Measured
1	3.29	3.30	7.69	7.70
2	2.86	3.70	6.69	6.90
3	3.25	4.90	7.60	7.60
4	3.68	4.00	8.61	8.30
5	3.27	3.90	7.64	7.60
6	3.65	4.10	8.54	8.20
7	3.71	4.40	8.67	8.50
8	3.74	3.50	8.74	8.00
9	4.92	4.60	11.49	7.40
10	6.26	ND*	14.62	ND

*ND = no data

(*d*) The need to alter the constant of the equation for different conditions shows that the level of exhaust carbon can be a strong function of the particular combustor. However, most combustors examined to date have not shown this behavior, and generally the functions of pressure, temperature, and hydrogen are satisfactory.

Weak Extinction Characteristics

In [7] Ballal and Lefebvre developed a model for the ignition of heterogeneous fuel-air mixtures. For gas turbines they suggest:

$$E_i = k\left[\frac{\Delta T_{st}}{p_0{}^{0.5}}\;\frac{\rho_f(\mathrm{SMD})^{1.5}\mu^{0.5}}{\phi\;\nu_a 0.5\ln(1+B_{st})}\right]^3 \tag{4}$$

It was thought that this equation might also provide a satisfactory correlation for weak extinction data, and to this end it was transposed as follows:

$$\mathrm{SMD} = k\;\sigma_f{}^{0.6}\nu_f{}^{0.2}FN^{0.8}\dot{m}_f{}^{-0.6}\rho_{st}{}^{0.3}\rho_f{}^{0.5} \tag{5}$$

$$\frac{E_{if}}{E_{i2}} = \left[\frac{\Delta T_{st,f}}{\Delta T_{st,2}}\cdot\frac{\rho_f}{\rho_2}\cdot\left(\frac{\mathrm{SMD}_f}{\mathrm{SMD}_2}\right)^{1.5}\left(\frac{\phi_f}{\phi_2}\right)^{-1}\left(\frac{\ln(1+B_f)}{\ln(1+B_2)}\right)\right]^3 \tag{6}$$

Substituting for SMD from equation (5):

$$\frac{E_{if}}{E_{i2}} = \left[\frac{\Delta T_{st,f}}{\Delta T_{st,2}}\cdot\frac{\rho_f}{\rho_2}\cdot\left(\frac{\sigma_f}{\sigma_2}\right)^{0.9}\left(\frac{\nu_f}{\nu_2}\right)^{0.3}\left(\frac{FN_f}{FN_2}\right)^{1.2}\right.$$

$$\left.\cdot\left(\frac{\dot{m}_f}{\dot{m}_2}\right)^{-0.9}\left(\frac{\rho_f}{\rho_2}\right)^{0.75}\left(\frac{\phi_f}{\phi_2}\right)^{-1}\frac{\ln(1+B_f)}{\ln(1+B_2)}\right]^3 \tag{7}$$

Assuming, for a fixed ignition system, $E_f = E_2$, $FN_f = FN_2$ and accepting

$$\frac{\phi_f}{\phi_2} = \frac{\dot{m}_f}{\dot{m}_2}\left(\frac{\dot{m}_{af}}{\dot{m}_{a2}}\right)^{-1} \tag{8}$$

Then

$$\left(\frac{m_f}{m_2}\right)^{5.7} = \left(\frac{\Delta T_{st,f}}{\Delta T_{st,2}}\right)^3\left(\frac{\dot{m}_{af}}{\dot{m}_{a2}}\right)^3\left(\frac{\rho_f}{\rho_2}\right)^{5.25}\left(\frac{\sigma_f}{\sigma_2}\right)^{2.7}$$

$$\cdot\left(\frac{\nu_f}{\nu_2}\right)^{0.9}\left(\frac{\ln(1+B_f)}{\ln(1+B_2)}\right)^3 \tag{9}$$

$$\frac{\Delta T_{st,f}}{\Delta T_{st,2}} = \left(\frac{f/a_{st,f}}{f/a_{st,2}}\right)\left(\frac{\mathrm{LCV}_f}{\mathrm{LCV}_2}\right) \tag{10}$$

Substitute and rearrange to give:

$$\frac{\dot{m}_f}{\dot{m}_2} = \left[\frac{f/a_{st,f}}{f/a_{st,2}} \bullet \frac{\mathrm{LCV}_f}{\mathrm{LCV}_2} \bullet \frac{\dot{m}_{af}}{\dot{m}_{a2}} \bullet \frac{\ln(1+B_f)}{\ln(1+B_2)}\right]^{0.53} \bullet \left(\frac{\rho_f}{\rho_2}\right)^{0.92} \left(\frac{\sigma_f}{\sigma_2}\right)^{0.47} \left(\frac{\nu_f}{\nu_2}\right)^{0.16} \tag{11}$$

A comparison of the predicted values of extinction and those obtained by experiment is given in Table 4 and Fig. 11. With the exception of a single point (Fuel No. 9) the agreement is considered to be very satisfactory. It is interesting to note that the tests were effected using two different atomizers of the Simplex type having flow numbers 0.99×10^{-6} and 1.67×10^{-6}. This accounts for the grouping of points in Fig. 11. All tests were done at atmospheric pressure and 419 K.

Conclusions

A correlation parameter having the form

$$EI_c = k\left\{\frac{p_3(1-h)^3}{(A/F)h^2}\right\}^{2.7} T_3^{-8.66}$$

has been shown to be capable of predicting the effects of different fuels upon the smoke number of several gas turbine engines. The value of k is a function of the combustor and is required to be determined at a single condition. For greater precision, the value of k should be determined for each individual operating condition of interest.

Weak extinction characteristics may be adequately predicted using the following parameter, which has been derived from a formula proposed by Ballal and Lefebvre:

$$\frac{\dot{m}_f}{\dot{m}_2} = \left[\frac{f/a_{st,f}}{f/a_{st,2}} \bullet \frac{\mathrm{LCV}_f}{\mathrm{LCV}_2} \bullet \frac{\dot{m}_{af}}{\dot{m}_{a2}} \bullet \frac{\ln(1+B_f)}{\ln(1+B_2)}\right]^{0.53} \bullet \left(\frac{\rho_f}{\rho_s}\right)^{0.92} \left(\frac{\sigma_f}{\sigma_2}\right)^{0.47} \left(\frac{\nu_f}{\nu_2}\right)^{0.16}$$

Acknowledgments

The authors express their thanks to the Canadian Departments of National Defence (CDND) and Regional Industrial Expansion (DRIE), the United States Air Force Wright Aeronautical Laboratories (AFWAL) and to Pratt & Whitney Canada who sponsored this work and who have given permission for publication. Thanks are also due to several undergraduate students who gave assistance from time to time.

References

1 Gratton, M., Critchley, I., and Sampath, P., "Alternate Fuels Combustion Research," AFWAL-TR-84-2042, July 1984.

2 Odgers, J., and Kretschmer, D., "Some Fuel Effects on Carbon Formation in Gas Turbines," *Canadian Aero. & Space Journal*, Vol. 28, No. 4, Dec. 1982.

3 "Aircraft Gas Turbine Engine Exhaust Smoke Measurement," Aerospace Recommended Practice, SAE, ARP 1179A, June 15, 1980.

4 Champagne, D. L., "Standard Measurements of Aircraft Gas Turbine Engine Exhaust Smoke," ASME Paper No. 71-GT-88, 1971.

5 Bowden, T. T., and Pearson, J. H., "The Effect of Hydrocarbon Structure Upon Sooting Tendency in a Turbulent Spray Diffusion Flame," ASME Paper No. 83-GT-90, 28th International Gas Turbine Conference and Exhibit, Phoenix, March 27-31, 1983.

6 Vogel, R. E., and Troth, D. L., "Fuel Character Effects on the TF41 Engine Combustion System," *J. Energy*, Vol. 7, No. 3, May-June 1983.

7 Ballal, D. R., and Lefebvre, A. H., "Minimum Ignition Energies in Flowing Kerosene-Air Mixtures," *Combustion and Flame*, Vol. 27, 1976.

J. G. Meier
Mem. ASME

W. S. Y. Hung
Mem. ASME

V. M. Sood

Solar Turbines Inc.,
San Diego, Calif.

Development and Application of Industrial Gas Turbines for Medium-Btu Gaseous Fuels

This paper describes the successful development and application of industrial gas turbines using medium-Btu gaseous fuels, including those derived from biodegradation of organic matters found in sanitary landfills and liquid sewage. The effects on the gas turbine and its combustion system of burning these alternate fuels compared to burning high-Btu fuels, along with the gas turbine development required to use alternate fuels from the point of view of combustion process, control system, gas turbine durability, maintainability and safety, are discussed.

Introduction

Most industrial gas turbines in the United States were originally designed for operation on natural gas, No. 2 distillate oil, or both. Legislative, environmental, and economic factors in recent years have necessitated the development of gas turbines capable of operating on alternate fuels. Expanding gaseous fuel-burning capabilities to alternate gaseous fuels without cumbersome changes in controls or combustion systems requires adequate analyses, design, development, and testing. This paper describes the state-of-the-art methods used in the development of industrial gas turbines for operation on medium-Btu gaseous fuels derived from nontraditional sources, such as:

- Fuel gases from biomass (sanitary landfills, liquid sewage, etc.)
- GOB gas from coal mines
- Fuel gases from oil and gas industry

Table 1 lists the typical composition and heating values of fuels from various sources.

At the authors' company, the development of gas turbines to use alternate medium-Btu gaseous fuels started in the 1960s. The company has since gained field experience with lower heating value (LHV) fuels of 13.0 to 22.84 MJ/nm^3 (320 to 580 Btu/scf) for landfill gas [1, 2], and digester gas [3], respectively.[1] Sample installations are listed in Table 2. An inspection of a Centaur gas turbine running on landfill gas at the Puente Hills site after 4500 hr of operation showed that the combustion system, fuel injection system, and downstream turbine components were free of corrosion, despite the fact that the fuel was not treated before injection into the turbine.

Table 1 Fuel gases from nontraditional sources

Source of Fuel Gas	Typical Composition	LHV MJ/nm^3 (Btu/scf)	Comments
Biomass: Solid wastes in sanitary landfills, liquid sewage, residues from fruit and vegetable canneries, animal & crop wastes, marine plants including macro algae, water hyacinth & sea kelp.	30-50% CH_4, CO_2, N_2, O_2	11.81-21.66 (300-550)	Produced by biodegradation of organic matter
GOB gas from coal mines	30-50% CH_4, N_2, O_2	11.81-17.72 (300-450)	Methane trapped in coal seams mixed with air
Raw natural gas used in gathering and reinjection	20-100% CH_4, C_2H_6, C_3H_8, C_4H_{10}, C_5H_{12} C_6H_{14}, CO_2, N_2, H_e	23.63-53.16 (600-1350)	LHV may vary by reservoir & separator oper. characteristics
Natural gas used in transportation and distribution	70-95% CH_4, C_2H_6, C_3H_8, C_4H_{10}, C_5H_{12} C_6H_{14}, kCO_2, N_2, H_e	33.47-41.35 (850-1050)	LHV variations within the same source are kept below + 10 percent
Process natural gas in nitrogen reject. plants	CH_4/N_2 mixture	11.81-23.63 (300-600)	A waste stream of medium calorific value depending on plant design, operation and rejection efficiency
Refinery Waste Gas	40-90% H_2, CH_4, C_2H_6, C_3H_8, C_4H_{10}, C_5H_{12}	15.75-37.41 (400-950)	Waste gas, from the platforming process, used to increase the H/C ratio in the refining of liquid fuels
Residual Oil Gasification	50-55% CO, 30-40% H_2, CO_2, N_2, CH_4, H_2O	9.85-13.78 (250-350)	Gasification of residual oil into a medium Btu gas of acceptable quality developed by Texaco
Unconventional Natural Gas	Similar to conventional NG	Comparable to conventional NG	Untapped natural gas resources to be recovered from tight sand formation, Devonian shale, aquifiers, hydrate deposits & ultra-deep reservoirs
Abiogenic Gas	—	—	Natural gas of non-biological origin trapped at great depth in northern latitudes where little or no vegetation existed

Combustion and Fuel Injection System Requirements

For industrial gas turbines, the combustor must meet specific design criteria to ensure a long life of satisfactory and reliable operation under a wide range of ambient temperatures, environmental conditions, and fuels. Typical combustor aerothermal performance, heat transfer and mechanical design requirements are presented in Table 3. A successful combustion system meets all of the design requirements in Table 3.

Table 4 lists the interaction of the design requirements with combustor design parameters and their influence on gas turbine operation. Table 5 indicates the impact of major fuel gas characteristics on the design of various combustion system components.

A typical fuel analysis of landfill gases is shown in Table 6. Due to the presence of potentially corrosive compounds

---

[1] Normal cubic meter (nm^3) is defined at 273.15 K and 101.325 kPa. Standard cubic foot (scf) is defined at 60°F and 14.696 psia.

Contributed by the Gas Turbine Division of The American Society of Mechanical Engineers and presented at the 30th International Gas Turbine Conference and Exhibit, Houston, Texas, March 18–21, 1985. Manuscript received at ASME Headquarters, December 18, 1984. Paper No. 85-GT-28.

(organic chlorine) in the gas, the materials selected for the fuel control system, combustion system, fuel injection system, and turbine components must be corrosion resistant to assure a long life of trouble-free operation.

Gas Fuel Control System Requirements

Careful analysis of the operational requirements and possible process-plant startup, transients, and system upset conditions is critical in selecting the appropriate fuel control system. The system must include all components necessary to properly schedule the fuel during starting and operation from idle or no load to full load. A standard fuel gas control system for industrial gas turbines is illustrated in Fig. 1.

Fuel-gas supply pressure to the turbine skid must meet the manufacturer's specification, which is based on standard natural gas fuel. Systems are designed to handle variations in gas Wobbe Index (WI) of ± 10 percent:

$$\text{Wobbe Index} = \frac{\text{LHV of Fuel in MJ/nm}^3\ \text{(Btu/scf)}}{\sqrt{\text{Specific Gravity with Respect to Air}}} \qquad (1)$$

Standard fuel-gas systems can handle gas with lower heating values down to about 23.63 MJ/nm^3 (600 Btu/scf) through minor modifications to fuel injector orifices, valve plugs and/or seats and loader pressure. Multiple fuel control components, manifolds (and fuel injectors) in parallel, may be used to further extend the fuel heating value change down to 11.81 MJ/nm^3 (300 Btu/scf).

A dual-fuel system provides greater flexibility for unconventional or alternative gaseous fuels. Startup and shutdown with a standard backup fuel of consistent heat content, such as natural gas or distillate liquid fuel, is more reliable and has the added advantage of separating the gas turbine startup operation from the fuel generating operation of the process plant. Although it is desirable to have natural gas or distillate liquid fuel for startup, it is not always required. In fact, the Centaur gas turbine installed at the Puente Hills site starts and operates on the landfill gas. If an alternative gaseous fuel is used for gas turbine startup, the extent of modification to fuel handling, control and injection components to provide a dual-fuel system is a function of the difference in WI between the two gases.

A dual-fuel system, involving large variations in heating value, such as a 11.81 MJ/nm^3 (300 Btu/scf) medium-Btu gas (MBG) and a 35.44 MJ/nm^3 (900 Btu/scf) standard natural gas (SNG), requires two different gas manifolds and sets of metering orifices to maintain the gas injector pressure drop that is necessary for good fuel distribution during startup and stable operation under load (free from combustion-driven oscillations).

Table 2 Small industrial gas turbine installations

Type of Gas	Approximate LHV, MJ/nm^3 (Btu/scf)	Model	Number of Units	Year Shipped
CH_4-CO_2-N_2	23.63 (600)	MD-1000	2	1966
Digester Gas	22.84 (580)	GSC-1200	2	1976
Digester Gas	22.84 (580)	GSC-12,000	3	1982
Landfill Gas	13.0 — 15.75 (330 — 400)	GSC-4000	1	1982
CH_4-N_2	23.63 — 35.44 (600 — 900)	CS-4000	2	1982
CH_4-N_2	23.63 — 35.44 (600 — 900)	MD-4000	1	1982
CH_4-N_2	23.63 — 35.44 (600 — 900)	MD-1200R	1	1983
CH_4-CO_2	15.75 — 21.66 (400 — 550)	CS-4000	2	1983

Table 3 Combustor design requirements

• Ambient Temperature Range (Gas Turbine)	220°K (396°R) $< T_0 <$ 335°K (603°R)
• Combustor Pressure Drop	$3.5 \leq \Delta P/P \leq 4.0\%$
• Combustion Efficiency η_c	$\geq$ 99.9% @ Design Point $\geq$ 95.0% @ Idle/No Load
• Exhaust/Emissions	$\leq$ 150 ppmv NO_x @ 15% O_2 $\leq$ 100 ppmv CO @ 15% O_2
• Exit Temperature Distribution	Radial Peak @ 70% Span Circumferential PF $\leq$ .25
• Dynamic Pressure Variations	$\Delta P/P \leq 0.1\%$
• Hot Blow Out (DP)	$\Delta T \leq$ 160°K (288°R)
• Cold Blow Out (Idle)	$\Delta T \leq$ 305°K (549°R)
• Light-Off	$\Delta T \leq$ 220°K (396°R)
• Fuel: Gas — Liquid — Dual	—
• Metal Temperature	$T_m \leq$ 1060°K (1908°R)
• Metal Temperature Gradients	$dT_m/dx \leq$ 25°K/cm (114°F/in)

Table 4 Combustor design and gas turbine performance

Design Requirement	Major Combustor Design Parameters	Impact on Gas Turbine Operation
Ambient Temperature Range (Gas Turbine)	Liner metal temperatures; combustor pressure loading	Liner durability through changes in metal temperatures and gas pressures
Combustor Pressure Drop	Liquid fuel atomization which affects smoke emissions, etc.	Increased sfc and reduced hp with increase in pressure drop
Combustion Efficiency	Primary zone/fuel injector design; residence time	Increased sfc and exhaust emissions
Exhaust Emissions	Primary zone stoichiometry/residence time; water injection	Increased sfc and hp with water injection
Exit Temperature Distribution	Fuel injector design; dilution air mixing and residence time	Reduced turbine life if distribution differs from design
Dynamic Pressure Variations	Fuel injection/stoichiometry/aerodynamics	Combustor and/or turbine failure if excessive
Hot Blow Out	Fuel injection/stoichiometry/aerodynamics/geometry	Affects off-load transients
Cold Blow Out	(Same as hot blow-out)	Affects light off
Light Off	(Same as hot blow-out)	Hot section life
Fuel Type	Fuel injector design	Fuel flexibility
Metal Temperature	Liner cooling method	Liner durability due to oxidation, sulfidation, etc.
Metal Temperature Gradients	Primary zone design; liner cooling method; fuel injection	Liner durability due to thermal stress

Table 5 Impact of fuel characteristics on combustion system design

Fuel Gas Property	Combustor						Fuel Injector	Ignitor
	Primary Zone	Flame Stabilization	Mixing	Secondary Zone	Dilution Zone	Cooling		
LHV (vol)	X*	X	X	X	X	X	X	X
Reaction Rate	X	X	X	X	X	X	X	X
Flame Temperature	X	X		X	X	X	X	X
Molecular Weight			X				X	X
U_{25}/L_{25}	X	X					X	

*X indicates major impact.

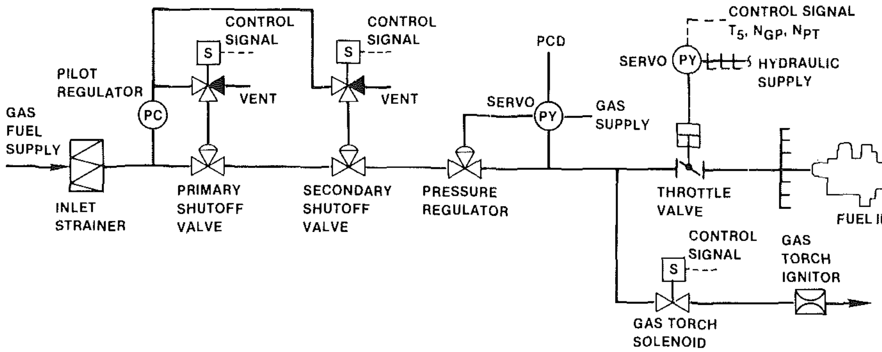

Fig. 1 Typical fuel gas control system

Table 6 Typical landfill gas characteristics

Major Components	Volume Percent
Hydrogen	0.27
Oxygen	0.18
Nitrogen	0.64
Methane	53.3
Carbon Dioxide	45.7
Minor Components	**Part Per Million (V/V)**
Ethane	26
Propane	142
Butanes	104
Pentanes	506
Hexanes	442
Methylene Chloride	1410
Trichloroethylene	638
Benzene	530
Toluene	4147
Tetrachloroethylene	88
Xylenes	354
Styrene	116
C_3 Substituted Benzenes	41
Carbonyl Sulfide	170
Sulfur Dioxide	41
Total Organic Chlorine — 800-1400 mg/L	
Note Expected final gas composition: Methane 40% (V/V) Carbon Dioxide 40% Air 20%	

Table 7 Fuel categories

Class	Category	LHV MJ/nm^3 (Btu/scf)	Combustion System	Start-Up, Shutdown	Load Restriction
1	Natural Gas Liquids (NGL) Liquid Petroleum Gas (LPG)	> 63.0 (1600)	NGL wide range	same	none
2	High Btu Gas (HBG)	23.63-63.0 (600-1600)	Control adj.	same	none
	Standard Natural Gas	31.50-47.26 (800-1200)	Standard		
3	Medium Btu Gas (MGB)	7.88-23.63 (200-600)	Modified combustor New fuel inj. New control	HBG/HBL (same possible)	transients
4	Low Btu Gas (LBG)	2.95-7.88 (75-200)	Modified combustor New injectors New control	HBG/HBL	transients no load
5	Ultra Low Btu Gas (ULBG)	< 2.95 (75)	New system Catalytic com.	same bootstrap	transients slow

Categories of Gaseous Fuels

The volumetric LHV of the gas is used to categorize individual fuels into five distinct classes (Table 7). These classes require different handling, combustion and control systems. As heating values decrease below standard levels, combustion system resizing is necessary and may require standard natural gas for startup/shutdown and restriction in transient load operation.

Fuel Gas Characteristics

Composition. In order to evaluate the suitability of a gas fuel for gas turbine operation, a complete gas analysis is required. Each fuel component, including trace elements, is identified. From the composition and concentration levels, it is then possible to assess the thermodynamic, physical, and chemical characteristics of the fuel gas, and its effects on the aerothermochemistry of the gas turbine energy conversion process. Turbine life and maintenance requirements may be affected by the presence of certain contaminants. Safe handling and reliable operation may also depend on the actual fuel characteristics. Table 8 indicates those characteristics that affect various aspects of turbine operation.

Gas Turbine Fluid Mechanics. Using lower calorific value fuels substantially affects the gas turbine cycle and performance, primarily because of the increased mass flow at the combustor. The mass flow of natural gas, for example, accounts for 1.5 to 2.0 percent of the compressor airflow entering the combustor. Achieving the same firing temperature with a 2222 kcal/kg (4000 Btu/lb$_m$) coal gas requires five times more mass flow, or 7.5–10 percent of the compressor airflow.

In order to properly account for the change in fuel mass flow, the LHV by mass, kcal/kg (Btu/lb$_m$), of the fuel gas is compared with the LHV of the design baseline fuel, which today is a high-Btu fuel, such as natural gas, 11,500 kcal/kg (20,700 Btu/lb$_m$), or distillate fuel oil No. 2, 10,194 kcal/kg (18,350 Btu/lb$_m$). The fuel mass ratio (Rm) is defined as the LHV of methane in kcal/kg (Btu/lb$_m$) divided by the LHV of the subject gas ($Rm \simeq 1$ for natural gas). Increasing Rm without air extraction from the compressor discharge will increase turbine shaft power, reduce heat rate, and reduce the gas turbine compressor stall margin.

In a single-shaft gas turbine, an effective countermeasure is to open the first-stage nozzle area in order to pass the additional fuel-gas mass flow through the turbine and restore the compressor surge margin. In a two-shaft gas turbine, power turbine nozzle area may be opened to correctly match the gas producer output to the power turbine for maximum performance. Turbine nozzle area adjustments can generally accommodate increases in turbine mass flows up to $Rm \simeq 9$, beyond which either the compressor air must be bled off or the turbine nozzles redesigned.

Fluid Mechanics of Fuel Control System. Most modern industrial gas turbines were initially designed to operate on high-calorific value fuel, such as natural gas. Substitution of a fuel with a different molecular weight and heating value requires adequate flow control over the entire operating range without impairing combustor operation. To maintain the same combustion conditions, the fuels must have approximately equal thermal energy release for the same standard fuel injector pressure drop (fixed geometry fuel control) and a similar type of flame (mixing control).

Table 8 Fuel characteristics and gas turbine operation

Gas Turbine Impact / Fuel Properties	Turbine Match Impact	Control System Impact	Cycle Impact	Combustion Process	Exhaust Emissions	Life & Maintenance	Safety & Reliability
Molecular Weight	○	○					○
Lower Heating Value	○	○	○	○			
Ad. Stoich. Temp. Rise		○	○	○	○		
Flammability Limits		○		○	○		○
Reaction Rate				○	○		○
Water Vapor Content		○	○	○	○	○	
Contaminant Level		○			○	○	○
Emission Yield. Comp.					○	○	○
Detonation Limits		○		○			○

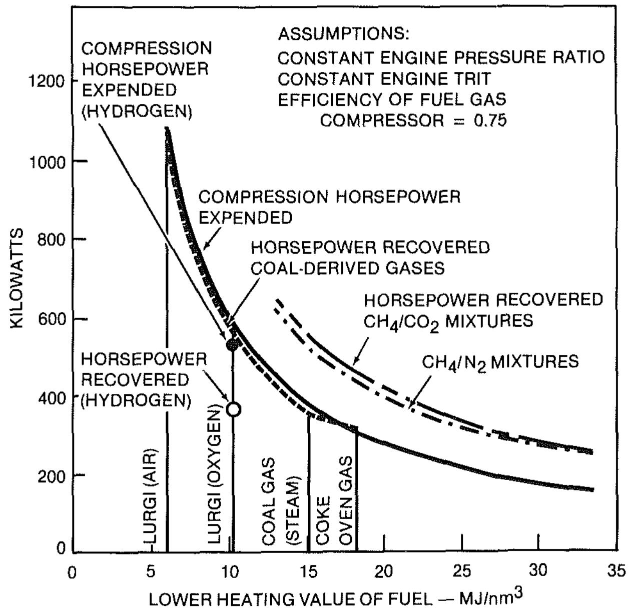

Fig. 2 Required compression to supply alternative fuels

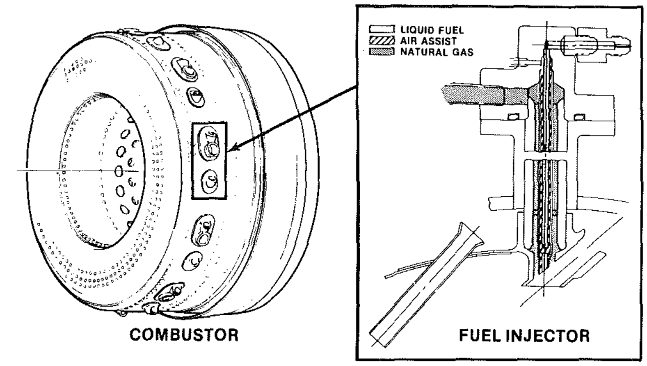

Standard Combustor and Standard Injector

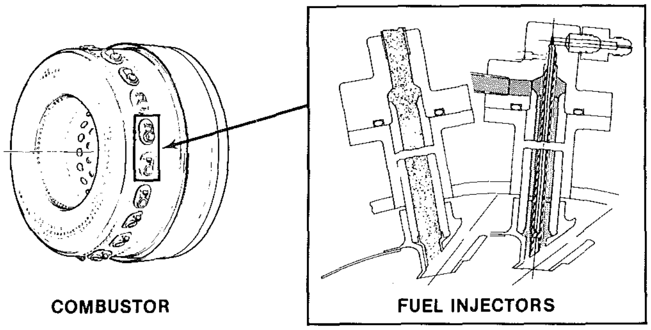

MBG Combustor and MBG Injectors

Fig. 3 Combustor redesigned to restore exit temperature profile

The Wobbe Index is not dimensionless, but has been used extensively throughout the gas industry to account for changes in fuel gas density and heating value. WI relates relative heat input to a burner of fixed geometry at a constant gas supply pressure:

$$\mathrm{WI} = CV/\sqrt{SG} \tag{2}$$

where:

CV = Calorific value in MJ/nm^3 (Btu/scf)
SG = Specific gravity

A more generic way of classifying the interchangeability of fuels is to base the WI on the LHV in MJ/nm^3 (Btu/scf) at standard conditions and on the gas molecular weight (MW)

$$\mathrm{WI} = \mathrm{LHV}/\sqrt{MW_{\mathrm{gas}}/MW_{\mathrm{air}}} \tag{3}$$

In order to more accurately assess the impact of the various fuels on gas turbine control, the WI should be based on the LHV of the fuel at standard pressure, 101.325 kPa (14.696 psia), and temperature, 25°C (77°F), conditions and on the density, kg/m^3 (lb$_m$/cf), ratio of the fuel gas to air at equivalent turbine supply conditions. For the nonazeotropic mixtures of hydrocarbons, which often need to be heated at supply conditions to avoid dropout of liquid fractions, it is advantageous to account for compressibility effects of the gas when computing the density. The revised WI is

$$\mathrm{WI} = \mathrm{LHV}/\sqrt{\rho_{\mathrm{gas}}(p,T)/\rho_{\mathrm{air}}(p,T)} \tag{4}$$

Therefore, if two fuel gases have the same WI, direct substitution of the gases is possible without fuel control adjustment. Dividing the WI for methane by the WI for the fuel gas, the fuel volume ratio (Rv) indicates the anticipated change in pressure drop if no geometric change is made in fuel handling lines, controls, and the injection system. Standard fuel gas control systems are designed to handle ±10 percent variation in WI without adjustments.

Combustion systems usually require a 10 percent pressure drop in the fuel injector at full load to provide stable, high-efficiency combustion with the desired turbine inlet temperature distribution for long operating life. The same pressure drop is required for the fuel control to ensure repeatable, stable operating conditions. Excessive increase in fuel supply pressures beyond the manufacturer's specifications leads to unstable operation and reduced hot section life.

Many fuel gases need to be compressed from ambient pressure to gas turbine supply pressures. As the LHV in kcal/kg (Btu/lb$_m$) decreases, increasing amounts of gas fuel in kg/hr (lb$_m$/hr) are necessary to maintain the heat input in kcal/hr (Btu/hr). When significant amounts of inert gases are present in the fuel, additional heat input is required to attain the rated turbine-inlet temperature. This further increases the fuel-gas mass flow rate and, thus, the compression horsepower requirement. Because of the expansion of the increased

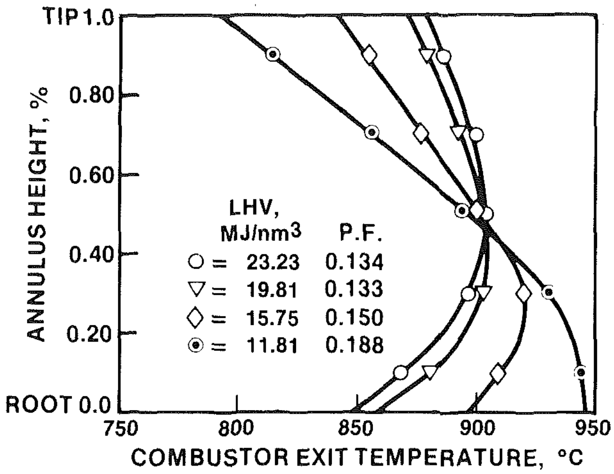

Standard Combustor

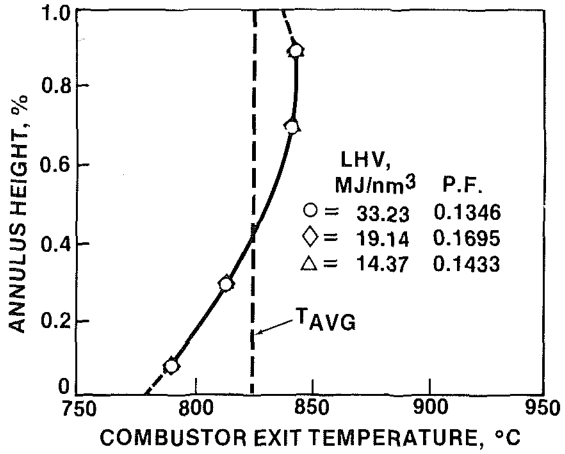

MBG Combustor

Fig. 4 Combustor exit radial temperature profiles for standard and MBG combustors

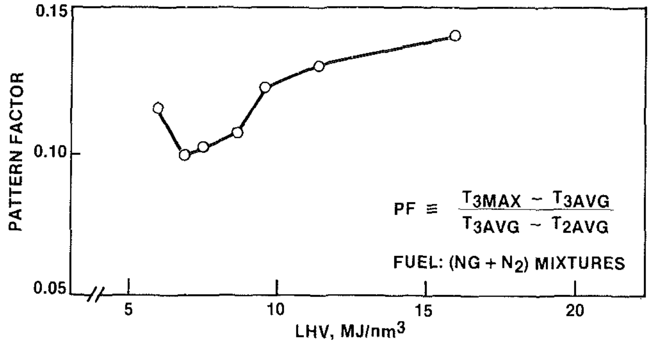

Fig. 5 Variations in MBG combustor pattern factor

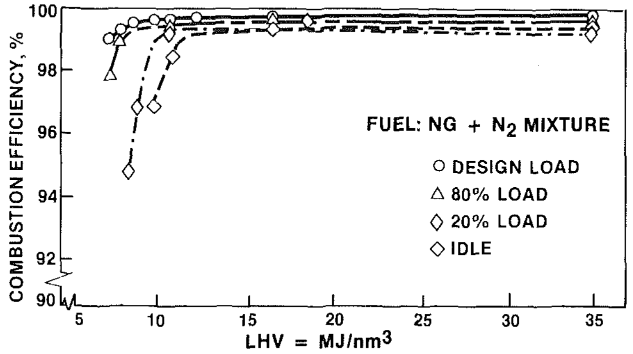

Fig. 6 Variations in MBG combustor efficiency

mass flow through the turbine, the increased output power can be nearly equal to or greater than the compression horsepower expended, depending on the thermal properties of the fuel and the combustion-generated products.

Resizing of fuel handling, control, and injection systems may be necessary to ensure good fuel mixing and stable control at reasonable pressures. Figure 2 compares the compression power required and the horsepower recovered burning typical alternative fuels of various lower heating values in a 3000-kW (4000-hp) ISO gas turbine with 10:1 pressure ratio.

The gas quality throughout the fuel handling, control and injection system must meet the manufacturer's fuel specification to ensure stable, reliable operation of the gas turbine. For single-phase gas, no fuel or water condensation can be tolerated. Fuel gases must be kept a minimum of 5.5°C (10°F) above dew-point temperatures at all operating conditions. In some cases, liquid separators and/or fuel gas preheating may be required. Since process and manufactured gases sometimes exhibit large variations in composition, a stable high-Btu fuel (HBF) may be required for turbine startup/shutdown and during plant transients to simplify the combustion and control systems.

Thermodynamics of Brayton Cycle. The adiabatic temperature rise from stoichiometric combustion (ΔT_{adst})—combustion in which the fuel reacts with a theoretical amount of air so that all the oxygen reacts chemically to appear in the product—measures the degree of difficulty of achieving the desired turbine inlet temperatures. Typically, a minimum adiabatic temperature rise, (ΔT_{ad}) = 778°C (1400°F), is required for simple-cycle gas turbines and 556°C (1000°F) is required for recuperative-cycle gas turbines. No significant problem is expected for fuels which exceed ΔT_{adst} = 1833°C (3300°F).

Through modification of the combustor flow splits, the minimum stoichiometric adiabatic temperature rise requirement for simple-cycle gas turbines may be lowered to about 1500°C (2700°F), using existing fluid mechanic flame stabilization and fuel injection methods. Further reduction in the minimum acceptable adiabatic temperature rise to 1000°C (1800°F) can be achieved by redesigning a conventional mixing controlled diffusion flame combustor to produce a partially premixed flame which will be reaction rate limited. Below 1000°C (1832°F), preheating the fuel and/or air with exhaust heat is necessary to supply adequate energy to the Brayton cycle.

Combustion Process

Mixing of Fuel and Air. The fuel injector pressure drop increases as the lower calorific value of the fuel decreases, and this can reduce overall turbine performance. If a common combustor design is required to handle both MBG and SNG, a tradeoff must be made to ensure sufficient pressure drop on SNG for adequate mixing, fuel metering, and prevention of combustor pressure oscillation feedback without reducing turbine output on MBG. Combustor and fuel injector design changes to improve fuel/air mixing must be made to obtain a combustor exit temperature distribution that does not change with the fuel heating value. Figures 3 and 4 illustrate how changes to combustor design can restore combustor exit temperature distribution [1].

Figures 5 and 6 show the variation in combustion efficiency and pattern factor of the modified MBG combustor with the heating value for a binary mixture of methane-nitrogen [2].

Flame Temperature. In gas turbine combustor diffusion flames, maximum flame temperatures—attained under near

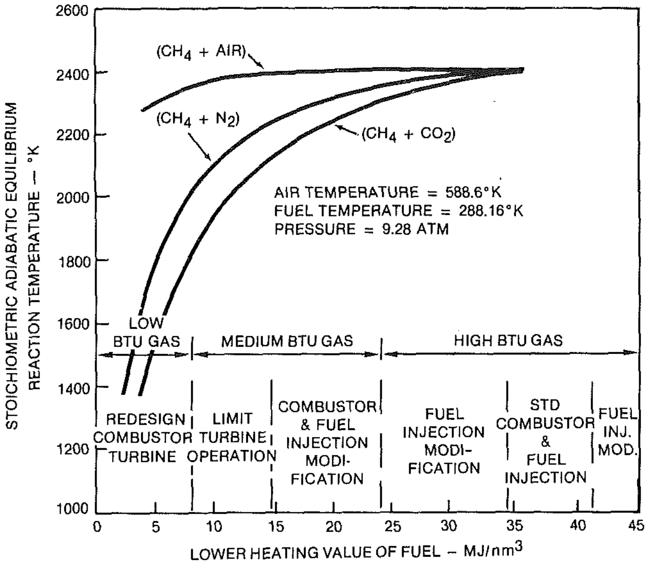

Fig. 7 Adiabatic stoichiometric equilibrium reaction temperature

stoichiometric conditions—occur locally in the primary zone. The highest possible temperature levels depend on the LHV, the composition of the fuel, and the sensible heat in the fuel and in the compressor discharge or combustion air.

To illustrate the effects of various inert constituents on the flame temperature, Fig. 7 shows the adiabatic stoichiometric reaction temperature (taking disassociation into account) as a function of LHV for various mixtures of methane, nitrogen, carbon dioxide, and air.

The adiabatic stoichiometric reaction temperature, which depends on LHV and gas composition, affects the primary zone metal temperatures of the combustor walls. Radiation from a nonluminous gas flame primarily depends on the local concentration of the products of complete combustion—carbon dioxide and water vapor—and the local gas temperature. The amount of heat radiated toward the combustor wall is proportional to the flame emissivity and the fourth-power of gas temperature. In modern, high-pressure ratio ($Rc \leq 20$) industrial gas turbines burning hydrocarbon fuels, emissivities of nonluminous gaseous fuel flames are usually considerably lower than emissivities of luminous flames from burning liquid distillate fuels. Liner cooling may have to be adjusted to reduce local temperature gradients in the combustor walls.

Flammability Limits. In the swirl-stabilized combustor of a gas turbine, an aerodynamically induced recirculation in the primary zone is used to restrict the flame front movement. The stability of the combustion process in this zone depends on the strength of the recirculation, which returns heat and active species to the ignition front, local fuel/air ratio, local gas temperature, and flammability limits of the fuel gas. During gas turbine operation, fuel flow, local fuel/air ratio, and combustion air temperature and pressure changes affect flame stability. The fuel/air ratio typically varies 3:1 across the load range of a simple-cycle gas turbine. Higher turndown ratios are required for startup. The flammability limits of the fuel gas contribute significantly to the stability of the combustion process and depend primarily on the type and concentration of the individual constituents in the gas.

The flammability ratio of the fuel gas is defined as the quotient of the upper flammability limit (U25) divided by the lower flammability limit (L25) at standard conditions of pressure, 101.325 kPa (14.696 psia), and temperature, 25°C (77°F). The flammability limits of the fuel gas can be determined from the concentration of the individual constituents in the gas and the flammability data of individual component gas published by the U.S. Bureau of Mines [4, 5], using LeChatelier's rule.

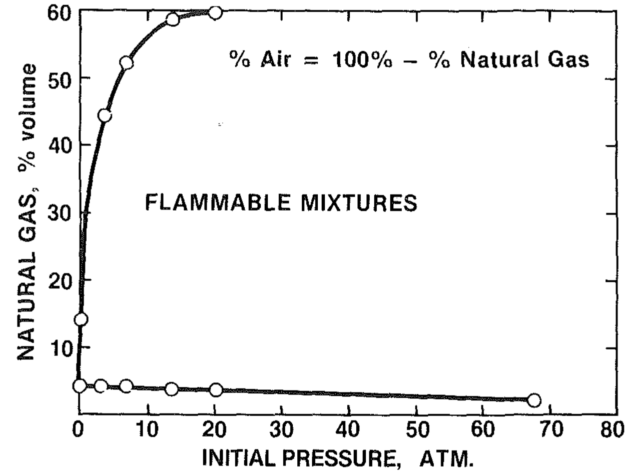

Fig. 8 Pressure effects on flammability limits of natural gas/air mixture

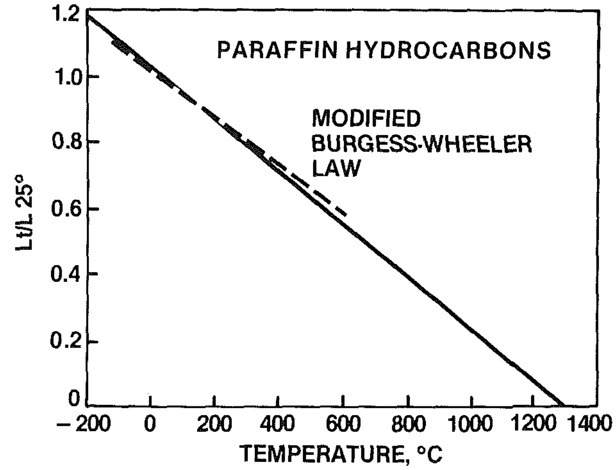

Fig. 9 Temperature effects on lower flammability limits of paraffin hydrocarbons

Although both upper and lower flammability limits broaden with temperature and the upper limits increase with pressure, design evaluation rules can be established using the fuel properties at standard conditions. Figure 8 illustrates the effects of pressure on the flammability limits of natural gas/air mixtures at 25°C (77°F). Figure 9 illustrates the effect of temperature on the lower flammability limit of paraffin hydrocarbons in air at atmospheric pressures.

Based on experimental and empirical data, a flammability ratio greater than 2.8 will give satisfactory gas turbine operation from startup to full load including load transients. Minor adjustments/modifications to the fuel control and/or combustion system will allow satisfactory operation down to a flammability ratio of 2.2. Fuel gas enrichment with wide-range flammability gases, such as higher hydrocarbons (HHC) or hydrogen, may be utilized to handle startup. Alternatively, gas turbine startup may be advantageous with a known and constant standard Btu fuel that also could be used as backup fuel during startup periods of a process plant. Neither of the above two methods improves flame stability during severe load transients, which can only be avoided either through judicious load management or by dumping a part of compressor air overboard.

Flammability limits directly affect combustor light off, turbine cold/hot flameout and combustion efficiency during light off and acceleration. If no alternative enrichment fuels are available and the gas turbine must be started on fuel gases

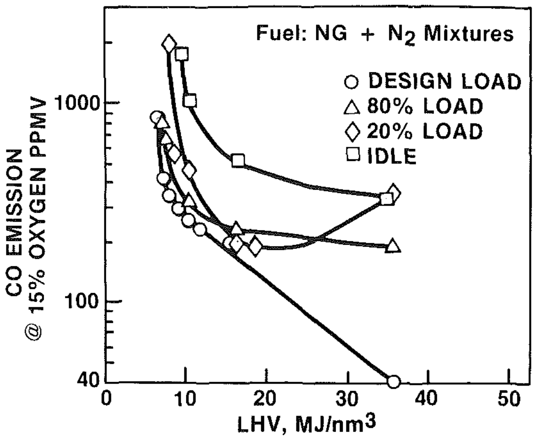

Fig. 10 CO emission from MBG combustor for methane/nitrogen fuel

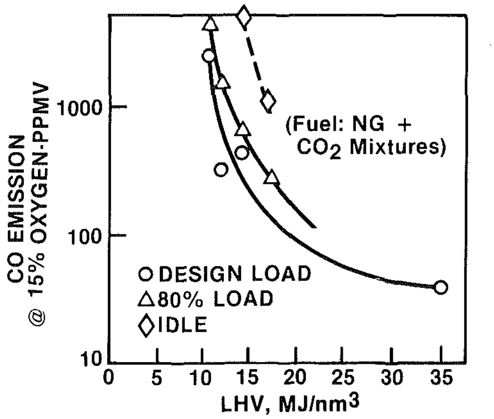

Fig. 11 CO emission from MBG combustor for methane/carbon dioxide fuel

with a flammability ratio less than 2.2, extensive combustor development is required to improve primary zone flame stability.

Reaction Rate. In any combustion process, a number of unstable intermediate species such as O, CO, OH, and H, are formed and actively participate in the reaction process. Oxidation of CO is one of the slowest reactions in the combustion process. Since the residence time in a gas turbine combustor is on the order of 10 ms, any decrease in reaction rate will reduce combustion efficiency, thus emitting additional CO into the exhaust. This behavior is particularly evident when measuring combustor exit emissions close to flameout conditions, where the combustion process becomes reaction limited. CO emissions from the MBG combustor at atmospheric pressure as a function of LHV for binary mixtures of hydrocarbon/inert are illustrated in Fig. 10 for methane/nitrogen and in Fig. 11 for methane/carbon dioxide [2].

Water Vapor Content. Standard gas turbine fuels contain small amounts of water vapor. Liquid water that drops out after fuel compression must be removed. MBG fuels may contain significant amounts of water especially when supplied at elevated temperatures. Figure 12 shows that some amount of water vapor is beneficial to accelerate the CO reaction [6].

Exhaust Emissions. The rate of thermal NO_x formation through fixation of atmospheric molecular nitrogen depends strongly on the peak flame temperature and residence time in the primary zone of the combustor. It is, therefore, not surprising to measure high NO_x emissions when burning fuels that have a high adiabatic stoichiometric flame temperature T_f. Based on a proven NO_x emission model [7, 8], thermal

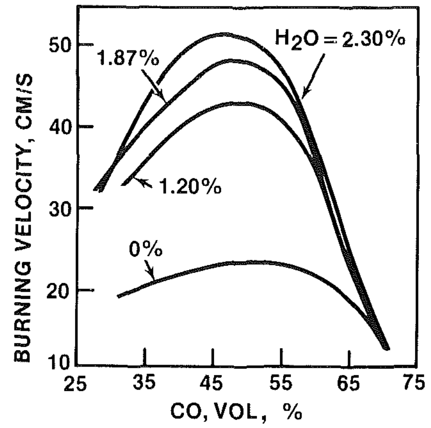

Fig. 12 CO reaction accelerated by water vapor

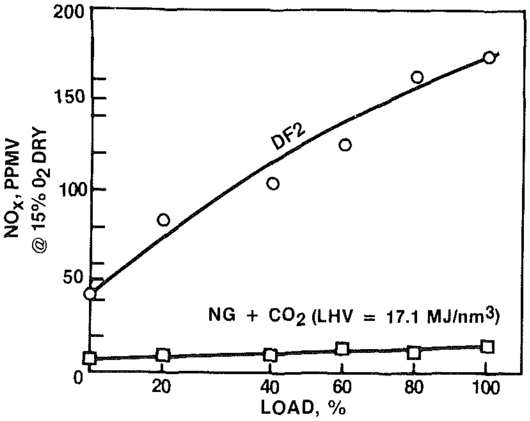

Fig. 13 NO_x emission for MBG and DF No. 2

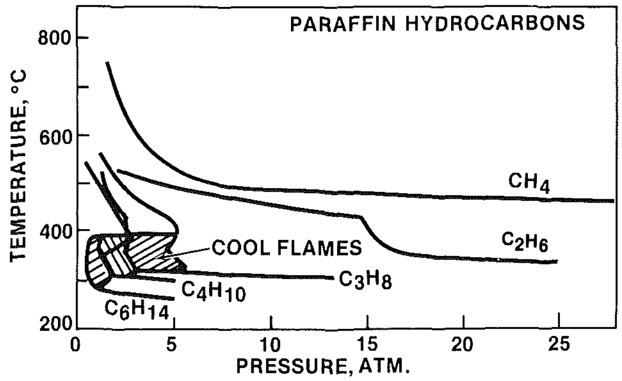

Fig. 14 Pressure influence on paraffin hydrocarbon fuel/air mixture

NO_x emissions from burning MBG or HBG gas relative to that from burning methane can be estimated from the following relationship

$$\frac{NO_x}{NO_{x_{CH_4}}} = 1 + \left[10 \times \ln\left(\frac{T_f}{T_{f_{CH_4}}}\right)\right] \qquad (5)$$

$$\text{for } \frac{T_f}{T_{f_{CH_4}}} > 0.915$$

The thermal NO_x from burning typical LBG is so low (< 10 ppmv) that it is sufficient to indicate its relative thermal NO_x as less than 0.1.

NO_x emissions measured from a 3000-kW (4000-hp) ISO gas turbine burning MBG, CH_4/CO_2 with LHV = 17.09 MJ/nm^3 (434 Btu/scf), and distillate fuel No. 2 over the load range are compared in Fig. 13. Both hydrogen and CO exhibit a high flame temperature, which gives rise to thermal NO_x formation. Hydrogen with LHV = 10.79 MJ/nm^3 (274 Btu/scf) produces about twice as much NO_x as methane with LHV = 35.8 MJ/nm^3 (909.1 Btu/scf). Therefore, it cannot be assumed that MBG will automatically have low NO_x emission levels.

Emission levels of carbon monoxide and unburned hydrocarbons are more difficult to correlate with fuel characteristics, but can be estimated for a combustion system for which experimental data are available on a high-Btu fuel with and without water injection. The natural trend of CO and UHC to increase as flame temperature decreases can be overcome by careful redesign of the combustor's primary zone and the fuel injection system. If the reaction temperature drops significantly below 1600 K (2400°F) at any operating condition, substantial amounts of unreacted CO can be expected [9].

Fuel gases sometimes contain significant amounts of emission yielding compounds, such as nitrogen-bearing compounds (ammonia and hydrogen cyanide), and sulfur-bearing compounds (hydrogen sulfide and sulfur dioxide), which substantially raise NO_x emissions and SO_2/SO_3 emissions, respectively. Fuel gases may need to be cleaned to remove excessive amounts of emission yielding compounds before they can be burned in the gas turbine in order to meet emissions regulations.

In the gas turbine exhaust heat recovery applications, the potential problems of acid corrosion while burning high-sulfur-content natural gas or sulfur-containing MBG must be addressed.

Life and Maintenance. Compliance with the manufacturer's fuel specification generally excludes using heavy liquids and solid particulate-laden gases.

Particulate mass loadings should be kept below 30 ppmw for a standard gaseous fuel, LHV = 11,945 kcal/kg (21,500 Btu/lb$_m$). For lower calorific value gases, this acceptable particulate loading is proportionally reduced by multiplying the quotient of the LHV by weight of the actual fuel gas in kcal/kg (Btu/lb$_m$) divided by 11,945 kcal/kg (21,500 Btu/lb$_m$).

Particulate size must be smaller than 10 microns, with 90 percent below five microns, to protect fuel control and fuel injector gas metering orifices from erosion and plugging. Damaged fuel control systems, distribution orifices, and injectors can adversely affect the turbine inlet temperature profile and reduce hot section life.

Maximum fuel contamination should not exceed the accepted limits for standard liquid fuel, LHV = 10,195 kcal/kg (18,350 Btu/lb$_m$), on the basis of equal mass per kcal (Btu).

- Sulfur (S)

  <1.0% wt ×(LHV)/10,195 or (18,350)
- Vanadium (V)

  <0.5 ppmw ×(LHV)/10,195 or (18,350)
- Alkali (Na + K)

  <1.0 ppmw ×(LHV)/10,195 or (18,350)
- Trace metals (Hg, Pb, Ca, Mg)

  <1.0 ppmw ×(LHV)/10,195 or (18,350)

Since contaminants can come from air and water or steam used for wet NO_x reduction, the total level of contaminants passing through the turbine must be considered. The compressor inlet air may contain trace metal contaminants from:

- Sale-water mist, fly ash, fertilizer dust
- Evaporative cooler carryover
- Industrial process effluents
- Dusts containing Na, K (including desert sand)

Similarly, water or steam injected for NO_x control or power augmentation may contain alkali or other trace metals unless properly removed. A general relationship has been derived to convert the contaminants found in air, water/steam, and fuel to equivalent contaminant levels in the fuel alone:

$$Xe = [(A/F) \times Xa + (S/F) \times Xs + Xf] \tag{6}$$

where:

A/F = air-to-fuel mass flow ratio
S/F = steam/water-to-fuel mass flow ratio
Xf = contaminant concentration in fuel, ppmw
Xa = contaminant concentration in inlet air, ppmw
Xs = contaminant concentration in water/steam injected, ppmw
Xe = equivalent contaminant concentration in fuel, ppmw

Therefore,

$$Xe_i < L_i \tag{7}$$

where:

i = the ith contaminant
L = the equivalent accepted limit on the basis of equal mass per kcal (Btu)

In landfill gases, concentrations of potentially corrosive compounds (organic chlorine) exceed the safe tolerance level of the gas turbine for long life and are usually handled by making appropriate changes to materials used in the control system, combustion system, fuel injection system and turbine.

Safety and Reliability. Potential hazards associated with specific alternate fuels include:

• Flammability limits	- HHC, H_2, CO
• Cool flames and explosion islands	- HHC
• Detonation limits	- H_2, CO
• Negative Joule–Thomson coefficient	- H_2
• Autoignition temperatures	- HHC, H_2
• Toxicity	- CO, H_2S, SO_2, NH_3, HCN
• Molecular weight	- H_2, HHC
• Emissivity	- H_2

Flammability-detonation limits and autoignition temperatures must be considered inside and around the gas turbine in case of unintentional fuel leakages. Premixing fuel with air prior to injection to match the WI is strongly discouraged, particularly for higher hydrocarbons (propane, butane, and heavier). These saturated hydrocarbons exhibit a peculiar behavior of cool flames above 271°C (520°F).

Figure 14 shows the influence of pressure on spontaneous ignition and cool flames of paraffin hydrocarbon fuel/air mixtures [10].

Negative Joule–Thomson coefficients will cause the hydrogen gas temperature to rise during isenthalpic expansion, which may result in an explosion if the autoignition temperature is reached. Certain extremely toxic gases, particularly the odorless ones, such as carbon monoxide, require special safeguards against leakage.

Low-molecular-weight gases rise rapidly and may get trapped in the high "dead spots" of enclosures or buildings. High-molecular-weight gases tend to accumulate on the ground or in the low spots of a package, enclosure or building. Leakage accumulation above the flammability limits must be avoided and corrective measures introduced. Commercial gas detectors that sound an alarm at 25 percent lower flammability limit (LFL) and shut the fuel off at 50 percent LFL are recommended to enhance safe turbine operation. Fire detection may be difficult for nonluminous gases, especially hydrogen, and special care must be taken to safeguard against this type of fire. Standard fire detection sensors are quite useless as protection against hydrogen fires. Ultraviolet sensors are recommended.

Gas Turbine Experience on Medium-Btu Fuels

Approximately 250,000 hr of successful operation have been accumulated on gas turbines in the 746-8952 kW (1000-12,000 hp) range using alternate gaseous fuels. No operational problems directly attributable to the use of medium-Btu fuels have been experienced.

Using the development methods outlined herein, a Centaur gas turbine-driven generator set was developed for operation on medium-heating-value fuels consisting of CH_4, CO_2, and air. This gas turbine has been in service since December 1983 at the Puente Hills landfill site in Southern California. The turbine has demonstrated the capability to successfully start and operate exclusively on medium-Btu fuels, derived from the landfill, down to a heating value of 13.78 MJ/nm^3 (350 Btu/scf). After 4500 hr of trouble-free operation, an inspection of the turbine showed that the combustion system components and the downstream turbine components were free of corrosion, despite the fact that the fuel was not treated before injection into the turbine except for fuel filtration at the inlet of the fuel gas compressor. The compressor used for this application is of the oil flooded screw type and provides a certain degree of gas cleaning due to the intimate oil-gas contact. The percentage of availability of the turbine during this 4500-hr interval was in the high 90s.

Summary

The flexibility of gas turbines to exhibit satisfactory operation and performance on a wide variety of gaseous fuels has been demonstrated in the field. Future availability, production/distribution cost, legislative regulations, and supply of various forms of gaseous fuels, however, are difficult to forecast with certainty. Combustion system designs must, therefore, be adaptable to changing fuel requirements. Combustion systems and fuel controls have been successfully modified in a timely manner using proven modeling and partial simulation techniques, combined with development and verification in existing facilities.

The following presents the current status of alternative gaseous fuel combustion in gas turbines:

1 Various alternative gaseous fuels, including fuels from sanitary landfills and liquid sewage, are suitable for gas turbine operation. This has been widely demonstrated in the field. For operation on landfill gas, the turbine materials must be properly selected to resist corrosion by fuel gas and its products of combustion. This is especially true if the fuel gas is not treated.

2 The major fuel characteristics include calorific value, adiabatic stoichiometric temperature rise (flame temperature), flammability limits, and reaction rates, all of which can be derived from the gas composition of a fuel sample.

3 Medium-Btu fuel gases with lower heating values down to 7.88 MJ/nm^3 (200 Btu/scf) require modifications to fuel handling, control, fuel injectors, and combustion liner, but offer gas turbine startup and operation on a single fuel.

4 On a life-cycle basis, gas turbine systems that can tolerate minimum fuel gas treatment and provide stable, reliable, long-life operation will prove to be economically superior. Separating inert gases from the fuel to increase the gas calorific content can be shown to be uneconomical.

5 Alternative fuels with low calorific content require higher fuel mass flow and must be cleaned up to a proportionately higher degree to meet the limiting concentration levels specified for the combustion products.

References

1 Sood, V. M., "Development of Medium Btu Fuel (365-575 Btu/scf) Combustion System for Centaur Engine," Engineering Report T-5556, Solar Turbines Inc., 1981.

2 Sood, V. M., "Development of Liquid Fuel/Medium Heating Value Fuel Combustion System for Centaur Engine," Engineering Report 2782, Solar Turbines Inc., 1981.

3 Faulkner, R. L., "Mars Atmospheric Rig Testing for Los Angeles Sanitation Combined Cycle Project," Engineering Report T-5552, Solar Turbines Inc., 1981.

4 Jones, G. W., "Inflammability of Mixed Gases," Technical Paper 450, U.S. Bureau of Mines, 1929.

5 Zabetakis, M. G., "Flammability Characteristics of Combustible Gases and Vapors," *Bureau of Mines Bulletin 627*, 1965.

6 Scholte, T. G., and Vaags, P. B., "The Influence of Small Quantities of Hydrogen and Hydrogen Compounds on the Burning Velocity of Carbon Monoxide-Air Flames," *Combustion and Flame* (Quarterly Journal of the Combustion Institute), Vol. III, No. 4, Dec. 1959.

7 Hung, W. S. Y., "A Diffusion Limited Model That Accurately Predicts the NO_x Emissions From Gas Turbine Combustors Including the Use of Nitrogen Containing Fuels," ASME JOURNAL OF ENGINEERING FOR POWER, Vol. 98, July 1976.

8 Hung, W. S. Y., "The NO_x Emission Levels of Unconventional Fuels for Gas Turbines," ASME JOURNAL OF ENGINEERING FOR POWER, Vol. 99, Oct. 1977.

9 Sood, V. M., and Shekleton, J. R., "Ongoing Development of a Low Emission Industrial Gas Turbine Combustion Chamber," ASME JOURNAL OF ENGINEERING FOR POWER, Vol. 102, No. 3, July 1980.

10 Spence, K., and Townend, D. T. A., "The Two Stage Process in the Combustion of Higher Hydrocarbons and Their Derivatives," 3rd Symposium on Combustion and Flame and Explosion Phenomena, The Williams and Wilkins Company, 1949.

High Weber Number SMD Correlations for Pressure Atomizers

J. B. Kennedy
Research Engineer
Aero-Thermal Technology
United Technologies Research Center
East Hartford, Connecticut 06108

Published correlations for the Sauter Mean Diameter (SMD) of sprays produced by pressure atomizing injectors have generally taken the form, $SMD = A\dot{\omega}^B \Delta P^C$. *The system of units and the fuel properties are reflected by the coefficient* A. *The exponent of the flow rate term* (B) *has been found to be approximately 0.20. There has been less agreement relative to the appropriate value of the pressure drop exponent* (C). *Simmons [1] reported the value of the pressure drop exponent to be 0.354, and this value has been widely used. This paper presents recently acquired experimental data that reveal that for We greater than 10.0 a different atomization process occurs, i.e., "shear-type" breakup, which results in much finer atomization than predicted by previously reported correlations. To accurately represent the high We data, a significantly different SMD correlation form is required and is reported in this paper. The effects of large variations in the nozzle size, fuel density, viscosity, surface tension, and fuel temperature have been included in the derivation of the correlations.*

Introduction

Simplex pressure atomizing fuel nozzles are thought to have the most predictable spray characteristics and are the most readily available nozzles in different sizes in the industry. For these reasons, a series of Hago oil burner nozzles were chosen to be used in a NASA-Lewis program [2]. The objective of the program was to investigate the aviation fuel property effects on combustion, independent of the effects of spray pattern and atomization. Based on the recent correlations of droplet size as a function of flow parameters and fuel properties for pressure atomizers, a series of different size nozzles were chosen to give the same drop-size distribution and spray cone angle for the different fuels to be studied. To verify the correlations, ambient spray data were acquired but the existing correlations did not apply at all in the flow range of interest. In analyzing the UTRC data and other published data, it became apparent that for Weber numbers greater than 10.0 the existing correlations significantly overpredicted the drop-size distribution, and a different droplet breakup process existed that required a very different drop-size distribution correlation. Simply trying to extend the old correlations with different exponents was totally unsatisfactory.

Methods of Spray Analysis

The data given in this paper were obtained using the Malvern Droplet Size Distribution Analyzer type ST1800 located at the United Technologies Research Center in East Hartford, Connecticut. The Malvern equipment has previously been described in principle by Swithenbank et al. [5]. It works by analyzing the diffraction pattern produced by a continuous laser beam passing through the spray cloud and fitting the data to a Rosin–Rammler distribution from which the Sauter Mean Diameter (SMD) is calculated.

In addition to droplet size data, photographs and patternation or mass flow distribution data were obtained. The patternation data were obtained using a linear 20 probe system and a timed sample measurement technique. The photographs were obtained using strobe illumination.

The Physical Fuel Properties

Twenty-five different fuel mixtures were used in the test program, and the physical properties of interest for these fuels with regard to atomization are given in Table 1. These fuels and fuel mixtures were chosen to study the effects of the hydrogen weight percent, aromatics, and naphthalene on the combustion process. Rarely have so many different fuels with wide property variations been tested and the atomization levels measured and correlated.

Description of Nozzles

Data are reported here for five Hago nozzles, denoted by flow number or nozzle number (*FN*/*NN* = 12.2/20, 16.5/25, 20/30, 23.4/35, and 31.5/50) and one Delavan Corporation nozzle denoted *FN*/*NN* = 13/18.3. The flow number (*FN*) is a nozzle rating that depends on both the characteristic size and fuel density. The nozzle number (*NN*) indicates the rated volume flow of No. 2 oil (gal/hr) at a differential pressure of

---

Contributed by the Gas Turbine Division of THE AMERICAN SOCIETY OF MECHANICAL ENGINEERS and presented at the 30th International Gas Turbine Conference and Exhibit, Houston, Texas, March 18–21, 1985. Manuscript received at ASME Headquarters, December 18, 1984. Paper No. 85-GT-37.

Table 1 Test fuels

Fuel	Specific Gravity	Viscosity (cst) 253K	Viscosity (cst) 293K	Surf. Tension (dyne/cm) 297K	Hydrogen (wt pct)	Total Aromatics (vol pct)	Naphthalenes (vol pct)	Comments
1 UTRC 2A	0.8618	4.46	1.76	27.54	11.87	34.9	16.0	Parametric for hydrogen
2 EBLS1	0.8524	6.67	2.35	27.46	12.35	38.4	16.6	ERBS/BKS = 79/21 (vol)
3 UTRC 7A	0.8478	4.99	1.91	27.84	12.53	26.2	14.9	Parametric for hydrogen
4 JP7	0.8026	5.80	2.21	25.90	14.39	2.5	0.0	
5 JP4-Shale	0.7649	2.17	1.06	22.96	14.39	15.1	0.3	Derived from oil shale
6 JP4	0.7620	1.85	1.03	23.01	14.57	15.7	0.5	
7 DF2	0.8413	--	5.50	27.90	13.46	22.9	7.9	
8 AFAPL 6	0.8378	--	3.90	27.67	13.41	21.4	6.7	
9 AFAPL 2	0.7852	1.88	0.99	23.96	13.56	31.0	3.6	
10 UTRC 3B	0.8581	5.88	2.19	27.64	12.41	24.9	14.5	Parametric for aromatics
11 UTRC 8A	0.8468	6.31	2.23	27.75	12.84	16.5	13.4	Parametric for aromatics
12 ERBLS2	0.8628	5.83	2.13	27.30	11.89	47.3	20.5	ERBS/BLS=60/40 (vol)
13 UTRC 9A	0.8309	3.71	1.59	26.55	12.89	30.7	1.5	Parametric for naphthalenes
14 UTRC 9B	0.8348	7.42	2.46	27.02	13.10	30.1	7.3	Parametric for naphthalenes
15 Tetralin	0.9712	--	2.30	35.10	9.14	100.0	1.5	
16 Xylene Tower Bottoms (XTB)	0.8602	1.60	0.87	28.20	9.64	100.0	0.1	
17 Blending Stock (BLS)	0.8961	4.30	1.70	29.59	10.36	76.0	29.7	
18 ERBLS3	0 8729	5.22	1.99	28.36	11.38	59.2	26.5	ERBS/BLS=41/59 (vol)
19 ERBS	0.8423	8.05	2.67	27.71	12.94	28.4	13.5	
20 Decalin	0.8877	8.21	3.08	31.00	13.10	0.2	0.0	
21 JP4-A	0.7657	1.76	0.94	22.21	14.16	23.1	0.6	Highly aromatic JP4
22 Jet A	0.8123	4.76	1.91	25.90	13.69	15.9	1.9	
23 JP5	0.8160	6.14	2.23	26.62	13.88	16.5	2.2	
24 Gulf Mineral Seal Oil (GMSO)	0.8217	--	6.08	27.50	14.14	9.9	1.1	
25 UTRC 1	0.7835	12.89	3.37	24.38	14.97	0.0	0.0	

Table 2 Characteristics of simplex nozzles

NN	FN lb/√psi hr	D_o in.	θ deg	t_F μm	ΔP(We=10) psi Jet A	$\dot{\omega}$ pph Jet A
20	12.2	.046	80	733	15.3	47.7
18.3	13.0	.055	45	160	69.8	107
25	16.5	.043	45	260	43.1	108
30	20	.052	45	261	43.0	131
35	23.4	.055	45	290	38.7	146
50	31.5	.063	60	480	23.4	152

0.69 MPa (100 psid). All the nozzles were simplex pressure atomizing hollow cone types; the spray angles were different for the six nozzles and the characteristics of the nozzles are given in Table 2. The table includes values of the liquid film thickness (t_F) and the pressure drop and flow rate of Jet A at which the We equals 10.0. The liquid film thickness was calculated as described in [4] and t_F is equal to

$$t_F = 0.48\, FN/D_o \cos\theta,\ \mu\text{m} \tag{1}$$

where FN = nozzle flow number (lbm/hr$\sqrt{\text{psi}}$)

$$t_F = 71.2\ FN/D_o \cos\theta,\ \mu\text{m in SI Units} \tag{2}$$

where FN = nozzle flow number (kg/hr$\sqrt{\text{kPa}}$). The Weber number (We) is defined as the ratio of inertial forces to surface tension forces and can be defined as

$$\text{We} = \rho_a^2 g_c \Delta P\ t_F/\rho_F \sigma \tag{3}$$

Assuming the entire ΔP is converted to axial velocity and ignoring the tangential component, We can be expressed in terms of the ΔP, FN, orifice diameter (D_o), and half the included spray angle (θ) for air at STP

$$\text{We} = 4.28 \times 10^{-4} \Delta P_F FN/D_o \cos\theta \tag{4}$$

$$= 1.12 \times 10^{-4} \Delta P_F FN/D_o \cos\theta \text{ in SI Units} \tag{5}$$

All nozzles gave acceptable symmetrical sprays free from streaks or voids for all the fuels tested. The spray droplet measurements were made 2.0 in. from the nozzle tip with Malvern ST1800 6-mm-dia laser beam passing through the center of the spray. The spray distribution for these injectors was measured using the 20 probe patternator system 3.0 ins. downstream of the nozzle and the atypical result is shown in Fig. 1. The spray pattern for all nozzles was considered to be hollow for all test conditions.

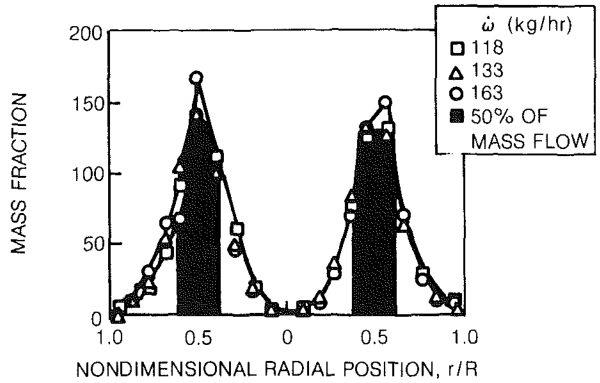

Fig. 1 Fuel spray mass distribution for nozzle No. 35-jet A fuel

Nomenclature

SMD = Sauter mean diameter, μm
ΔP = liquid pressure drop through the nozzle, kPa, psi
ρ_a = air density, g/cm^3
ρ_F = fuel density, g/cm^3
σ_F = fuel surface tension, dynes/cm
$\dot{\omega}$ = mass flow rate, lb/hr
We = Weber number
t_F = estimated film thickness (for calculations of We), μm
T_F = fuel temperature (°C, °F)
D_o = orifice diameter of simplex nozzle, mm, in.
θ = included spray angle/2, deg
FN = flow number, kg/hr • $\sqrt{\text{kPa}}$, lbm/hr $\sqrt{\text{psi}}$
NN = nozzle number, gal/hr
g_c = gas constant, 32.2 lbm-ft/lbf-s^2
μ_F = fuel viscosity, centistokes
V_D = droplet velocity
V_G = gas velocity

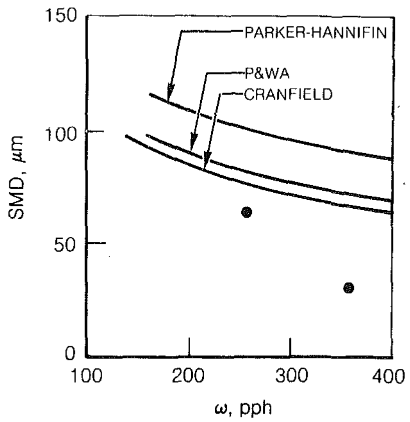

Fig. 2 *Correlations versus experimental data 35 GPH Hago injector*

Test Results

Figure 2 shows the expected trends from the three correlations derived at Parker-Hannifin Corporation [1], Cranfield University [3], and Pratt and Whitney or P&W [6] and the UTRC test results for the $NN = 35$ nozzle. The UTRC data showed a departure from the predictions much greater than the differences between correlations. Additional test data obtained for the $NN = 20$ nozzle are shown in Fig. 3, and the results indicated that the standard correlation predicted the data well up to a Weber number slightly less than 10, but in the range of interest in this study, a different and finer atomization process was taking place. Included in Table 3 is a listing of the previous SMD correlations that have the coefficient of the flow rate term nearly identical (0.205), but the coefficient of the pressure term has changed significantly and increased in the case of the more recent Cranfield data. The increase in the coefficient of the pressure term in Jasuja's correlation occurred when the experimental data were obtained at We greater than 10.0 and the change in the shape of the curve is clearly shown in Fig. 4 in which the test data from the Parker-Hannifin Corporation, Cranfield University, and UTRC are plotted together as a function of We. The result of using a regression analysis and forcing the UTRC data to fit the lower Weber number correlation form, i.e., $\mathrm{SMD} = A\dot{\omega}^B \Delta P^C$, is also included in Table 3. The coefficient of the pressure term (1.36) is approximately four times larger than the Parker-Hannifin term (0.354), and of more importance, the correlation does not accurately predict the droplet size distribution.

Correlation of Results

To develop a correlation for the high Weber number data many correlation forms were used in a regression analysis and the best fit for Jet A was the following

$$\mathrm{SMD} = 168.7 + 1.336\,FN - 16.0\,\sqrt{\Delta P} + 0.3525\,\Delta P,\ \mu\mathrm{m} \qquad (6)$$

$$\mathrm{SMD} = 168.7 + 0.0082\,FN - 41.9\,\sqrt{\Delta P} + 2.422\,\Delta P \text{ in SI units}$$

From the regression analysis the R-squared term was 0.986, and the standard deviation was 4.62 microns. Hence the fit is extremely good. This correlation form is more lengthy, but it only involves the fuel pressure drop and the nozzle flow number.

A similar correlation was developed using the ambient spray data for the 25 different fuels listed in Table 1. The correlation for Weber numbers greater than 10 was the following

$$\mathrm{SMD} = \sigma_F[6.11 + 0.048\,FN - 0.579\,\sqrt{\Delta P} + 0.013\Delta P],\ \mu\mathrm{m} \qquad (7)$$

$$\mathrm{SMD} = \sigma_F[6.11 + 0.00029FN - 1.519\,\sqrt{\Delta P} + 0.0893\Delta P] \text{ in SI units}$$

Table 3 **SMD correlations for pressure atomizers**

- Parker Hannifin (1975) $\mathrm{SMD} = 185\,\dfrac{\dot{\omega}^{0.205}}{\Delta P^{0.354}}$
- P&W (1970) $\mathrm{SMD} = 184.5\,\dfrac{\dot{\omega}^{0.205}}{\Delta P^{0.4}}$
- Cranfield (1979) $\mathrm{SMD} = 185.5\,\dfrac{\dot{\omega}^{0.202}}{\Delta P^{0.43}}$
- UTRC (1982) $\mathrm{SMD} = 5789\,\dfrac{\dot{\omega}^{0.353}}{\Delta P^{1.36}}$

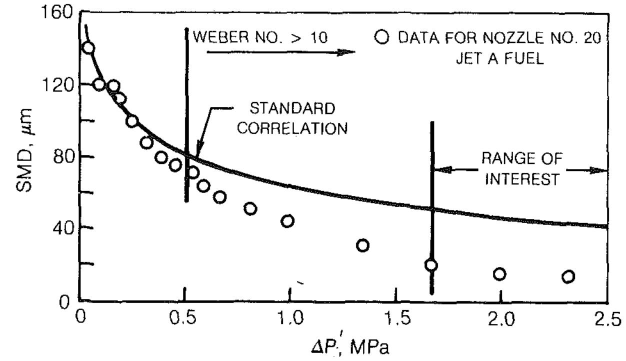

Fig. 3 **Atomization over wide range of Weber number**

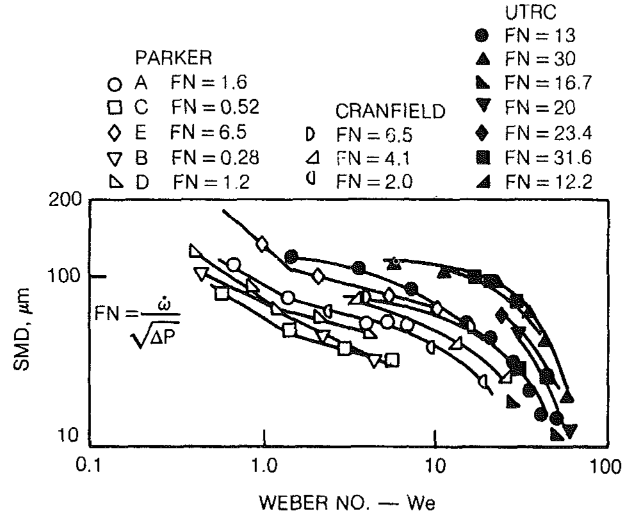

Fig. 4 **Comparison of experimental results**

Again from the regression analysis the R-squared term was 0.96 and the standard deviation was 7.6 microns. The fit is good considering the large variation in the fuel properties listed below

$$0.754 < \rho_F < 0.971 \text{ g/cm}^3$$

$$0.87 < \mu_F < 6.08 \text{ CST}$$

$$25.9 < \sigma_F < 31.0 \text{ dynes/cm}$$

$$299 < T_F < 327 \text{ K}$$

The basic form of the correlation was the same as that derived for Jet A, and the surface tension effect was introduced in a linear fashion. To illustrate the linear surface tension effect, the SMD values are plotted in Fig. 5 for the 25 test fuels. The influence of fuel viscosity on the measured SMD was not

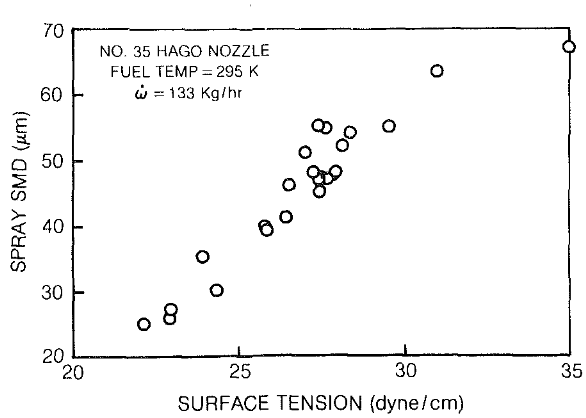

Fig. 5 Influence of fuel surface tension on measured atomization

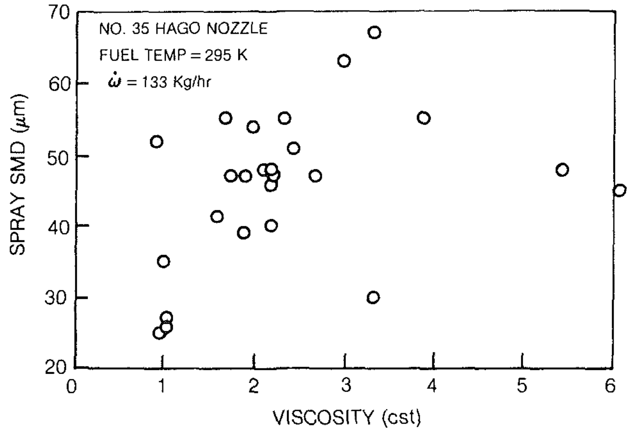

Fig. 6 Influence of fuel viscosity on measured atomization

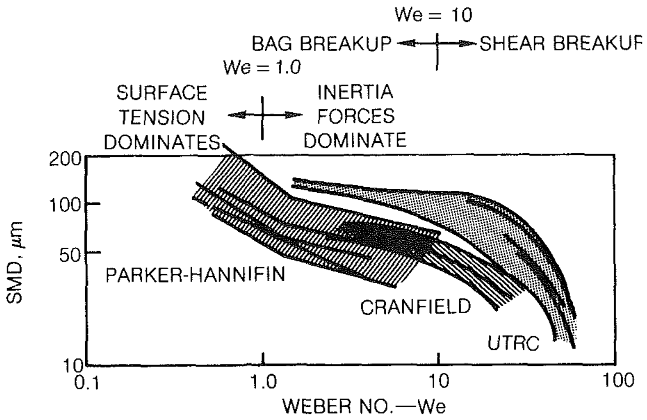

Fig. 7 Weber number regimes

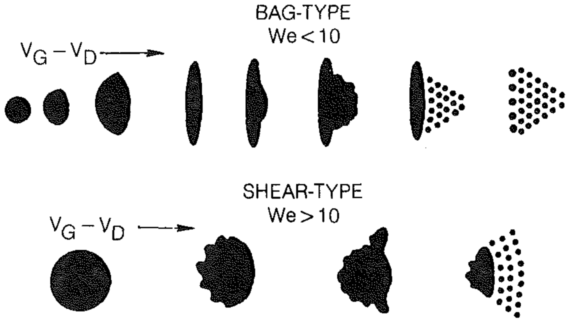

Fig. 8 Droplet breakup mechanisms

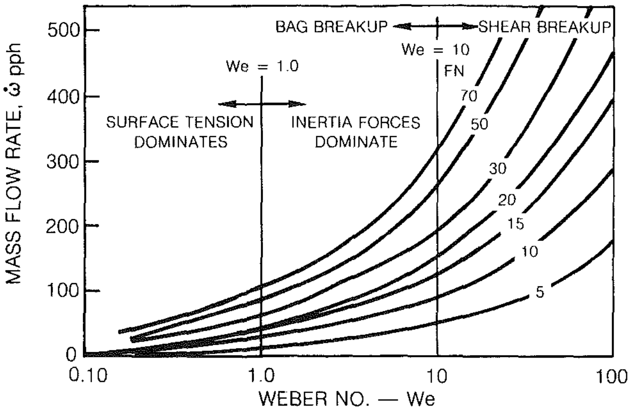

Fig. 9 Nozzle design

apparent as shown in Fig. 6, and no effect was included in the correlation.

Prediction of the Weber Number Effect on the Drop-Size Distribution

The effect of Weber number on the atomization process is not new. In [4], Simmons documented the change in the slope of the SMD at a Weber number of 1.0 (see Fig. 7). For Weber number less than 1.0 the surface tension dominates the atomization process, and for Weber numbers greater than 1.0 the inertial forces dominate. Simmons found that the SMD data for We less than 1.0 could be accurately fitted to a similar expression used at the higher We, but the exponent of the pressure term increased from −0.275 to −0.675. The interpretation of the result by Simmons "is that when the surface tension forces are significantly greater than the inertial forces the process of atomization is terminated earlier, thus giving fewer small-size drops." The low We number data could be fitted to the simple expression since on a log–log plot the SMD varied linearly with injectant pressure drop.

Unfortunately, the We data greater than 10.0 do not fit a straight line when plotted on a log–log plot, and the SMD had to be expressed as a quadratic in terms of the injectant pressure drop in order to yield acceptable predictions. When the We exceeds 10.0, the inertial forces weaken and a "shear-type" breakup occurs. This change in the breakup process is not new to the atomization community, although few experimentalists have encountered or recognized it. The shear-type breakup has been photographed and documented in the rocket nozzle studies [7, 8]. For intermediate We, i.e., 1.0 to 10.0, the atomization was characterized as "hat-type or bag-type" breakup, and this process is artistically represented in Fig. 8. The inertial forces hold the drops together until the drop flattens out, eventually distorting into a hat shape with fine drops breaking out of the thinning center section and a coarser drop breakup from the thicker donut-shape around the outer edge. For We greater than 10.0, shear-type breakup occurs, and the high relative velocities between the initially formed coarse drops and the surrounding medium tear or shear fine droplets from the edge of the coarse drop (see Fig. 8). Pictures of this process clearly showed these differences in [8]. To obtain these high Weber number conditions is not always possible, since it requires high fuel pressure drops or injectant flow rates or high air velocities. However, if fine atomization is required, such as in gas turbines, it might be possible to tailor the injector design to achieve the finer atomization. Figure 9 presents an analytically derived series of curves showing what injector flow numbers and mass flow rates would be required to achieve the high We shear-type breakup.

Summary and Conclusion

It has been shown that for the We greater than 10.0 the atomization from simplex pressure atomizers is significantly greater than would be predicted from previously derived SMD correlations. In fact, a different SMD correlation was required to accurately predict the experimental data. Below We of 10.0 the atomization is dominated by inertial forces and bag-type breakup results. Above We of 10.0 shear-type breakup occurs and results in a very fine spray which can accurately be predicted using a quadratic expression in ΔP. In addition, the correlation was extended to include the fuel property effects and the SMD was found to vary linearly with the fuel surface tension while the influence of the fuel viscosity was not apparent.

Acknowledgments

This work was conducted by United Technologies Corporation under NASA Contract NAS3-23167. The author wishes to thank the NASA Lewis Research Center and the Program Managers Messrs. A. Szaniszlo and J. Biaglow for sponsoring this program and for permission to publish this paper. The testing was conducted at the United Technologies Research Center, and contributing to the technical effort and providing valuable assistance in analyzing and acquiring the data were Dr. J. B. McVey, Dr. T. J. Rosfjord, and S. Russell.

References

1 Simmons, H. C., "Prediction of Sauter Mean Diameter for Gas Turbine Fuel Nozzles of Different Types," ASME Paper No. 79-WA/GT-5, Dec. 1979.

2 Rosfjord, T. J., "Aviation-Fuel Property Effects on Combustion," NASA Contractor Report 168334, Feb. 1984.

3 Jasuja, A. K., "Atomization of Crude and Residual Fuel Oils," ASME JOURNAL OF ENGINEERING FOR POWER, Vol. 101, No. 2, Apr. 1979, pp. 250–258.

4 Simmons, H. C., and Harding, C. F., "Some Effects of Using Water as a Test Fluid in Fuel Nozzle Spray Analysis," ASME Paper No. 80-GT-90, Mar. 1980.

5 Swithenbank, J., et al., "A Laser Diagnostic Technique for the Measurement of Droplet and Particle Size Distribution," University of Sheffield, England, 1976.

6 Koblish, T. R., and Schwartz, H. R., "Reduction of Smoke Emission From an Industrial Gas Turbine Engine," ASME Paper No. 70-GT-103, May 1970.

7 Dickerson, R. A., and Coultas, T. A., "Breakup of Droplets in an Accelerating Gas Flow," AIAA Paper 66-611, June 1976.

8 Wolfe, H. E., and Anderson, W. H., "Kinetics Mechanism and Resultant Droplet Sizes of the Aerodynamic Breakup of Liquid Drops," Report 0395-04(14)SP, Aerojet General Corp., Apr. 1964.

Spatially Resolved Droplet Size Measurements

T. A. Jackson
Research Assistant.

G. S. Samuelsen
Professor of Mechanical Engineering.

UCI Combustion Laboratory,
Department of Mechanical Engineering,
University of California,
Irvine, Calif. 92717

This paper encompasses initial tests of a droplet sizing technique, providing spatially and temporally resolved measurements within a liquid spray from an air assist nozzle. The method utilizes laser interferometry. The primary size measurement is based upon the signal visibility; it is validated by the peak intensity of the scattered light. As the system is based on the Doppler effect, a single component of velocity is extracted concurrent with the size information. The size of the measurement volume is controlled with off-axis light collection. Beam splitting is accomplished with a rotating diffraction grating, allowing the signal to be frequency shifted. Measurements are compared directly to those of a standard diffraction based sizing system (i.e., Malvern). The diffraction information is processed via Rosin-Rammler (2 parameter) and Model Independent (15 parameter) distribution algorithms. Correspondence between diffraction and interferometric results is satisfactory for the Model Independent algorithm. Differences observed using the Rosin-Rammler distribution are attributed to an inadequate representation of the spray by the two parameter model.

Introduction

Development of modern combustion devices is aided by numerical modeling of the combustor aerodynamics and heat release processes. In two-phase systems, the modeling of the dispersed phase is also being attempted [1]. One difficulty in developing a modeling capability in two-phase flows is the absence of detailed experimental measurements within flow fields of interest to verify the model and guide its improvement [2].

Nonintrusive optical methods have been developed to spatially characterize the mean and turbulent motion of the gas phase of complex flow devices [3]. However, techniques to spatially resolve the dispersant phase have been applied neither routinely nor with great success. To support modeling efforts, spatially resolved measurements of both the size and the velocity of the liquid droplet are required.

Laser interferometry has been most recently explored for the point measurement of drop size and velocity. The principal interferometric technique used to date is visibility, first introduced by Farmer [4] and expanded by Bachalo [5]. In this method the size measurement is obtained by measuring the visibility of the light refracted through a droplet as it interacts with a two-laser-beam interference pattern. The visibility function, to be identified later in this paper, is a measure of the modulation of the scattering intensity from the interference pattern. Embedded in this information is also the velocity of the drop, as the refracted light signal is in the form of a standard anemometer Doppler burst.

The visibility technique has been successfully used to size streams of monodispersed droplets, but has encountered difficulty in sizing polydispersed sprays [6, 7]. The principal source of the difficulty can be attributed to the nonuniform and irregular attenuation of the two beams forming the interference fringe pattern. To validate the visibility signal in polydisperse sprays, a second size determination has been proposed [8]. This size validation is made from an analysis of the peak intensity of the pedestal (d-c) component of the Doppler burst. Since the incident laser beams have Gaussian energy profiles, the peak of the scattered intensity varies according to the drop trajectory through the probe volume in addition to the size of the scatterer. As a result, intensity bands are established for each drop size. The two independent size measurements are compared and the visibly determined size is used if the intensity window is matched.

This paper describes the application of visibility with intensity validation (IV) to a spray generated by an advanced air assist nozzle. The utility of the method is evaluated by comparing its performance to two more widely accepted but limited techniques, diffraction scattering and shadowgraph photography. Diffraction measurements are made to give the mean size and size distribution of the spray along a line of sight through the spray. Shadow photographs are taken at selected positions within the spray to provide a visual means of determining drop size. These methods yield information in different forms, but comparisons are possible. This is accomplished in this paper.

Experiment: Measurement Methods

Laser Interferometry (LI). The signal collected from a drop interacting with an interference pattern created in space by intersecting two beams of light with the same phase, wavelength, polarity, and intensity contains both size and velocity information about the scatterer. The velocity information is obtained from the period of the Doppler burst and the known fringe spacing. The size information is encoded in the modulation (visibility) of the intensity (Fig. 1) of the scattered signal. Large diameter drops (relative to the

---

Contributed by the Gas Turbine Division of THE AMERICAN SOCIETY OF MECHANICAL ENGINEERS and presented at the 30th International Gas Turbine Conference and Exhibit, Houston, Texas, March 18–21, 1985. Manuscript received at ASME Headquarters, December 18, 1984. Paper No. 85-GT-38.

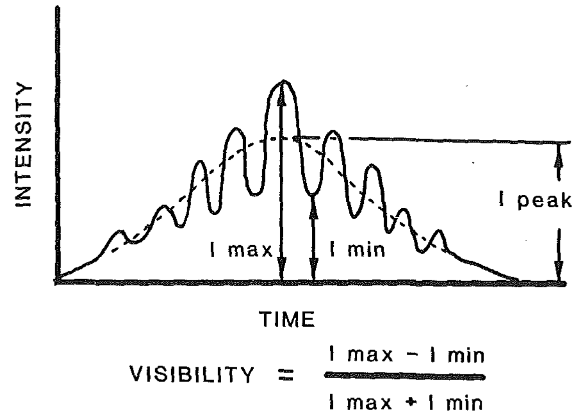

Fig. 1 Visibility function

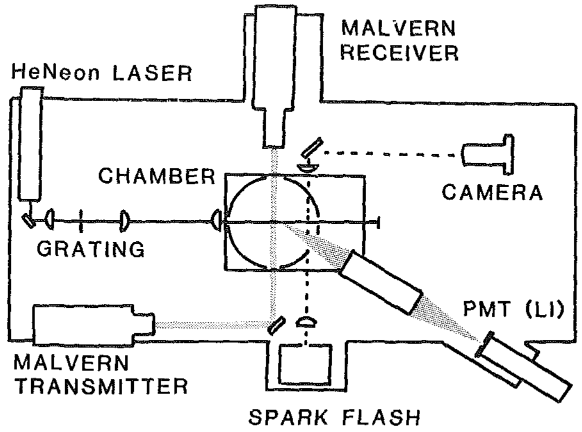

Fig. 2 Optical layout

fringe spacing) yield a signal of low visibility; small drops produce a signal of high visibility.

The visibility sizing method was first applied to sprays utilizing light collected in the forward direction, that is, diffracted light [4]. Size information lost in the required beam stops limited the measurable size range considerably. Also, the shallow angle of intersection of the two laser beams, required to obtain adequate fringe spacing to measure drop diameters of interest ($> 5\ \mu$m), results in a large probe volume when collection is made in the forward direction. This limits the application of this method to low density sprays.

For sprays of nonopaque liquids, Bachalo [5] developed the necessary theory for off-axis light collection using refracted light. The optimal angle for collection is approximately 30 deg off the forward optic axis and out of the plane of interaction of the incident beams. The improvement made it possible to extend the measurable size range of the visibility method to 5 to 2500 μm in discrete steps with a dynamic range typically less than 10:1. Further, the size of the probe volume became more manageable as the collection optics allowed the probe volume to be significantly reduced.

Measurements made in dense sprays using the visibility technique surfaced shortcomings of the method [6, 7]. Accurate sizing from this method can only be accomplished if the fringe visibility (or contrast) is known. In sprays, droplets interacting with the transmitted beams upstream of the probe volume can randomly disrupt the conditions required for perfect fringe contrast at the probe volume (beams of same phase, intensity, polarity, and wavelength). The effect is a reduction in fringe visibility. This results in the measured drop size being larger than the actual size. An increase in the actual visibility is also possible. This can result due to masking of the signal from out-of-focus drops by the pinhole or by the processor's response to a high rise time signal. A signal validating technique was introduced [8] based on the peak intensity of the scattered light to check for incorrect visibilities.

The intensity validation (IV) technique utilizes the amplitude of the pedestal of the Doppler signal to make a second measurement of size, independent of that determined by visibility. Most accurate application of this technique requires that the incident beam intensity be precisely known. Scattering intensity then becomes a direct function of scatterer's diameter (to a power) for a given collection optic arrangement. Two features of the spray environment and the measurement system make the incident light intensity an elusive quantity. First, even if the intensity of the transmitted beam into the spray could be identified, attenuation of the beam by the portion of the spray on the transmitter side of the probe volume would reduce it. Second, the Gaussian nature of the laser beams used in the measurement system provides a situation in which incident intensity is a function of the path of the droplet through the probe volume. Attenuation of the beam by the spray is corrected by automatic adjustment of the photomultiplier tube voltage by the signal processor to yield a signal amplitude consistent with a droplet having a visibility between 47 and 53 percent. The second problem is handled by setting limits on the intensity check such that passage of the droplet within 0.7 of the peak intensity portion of the beams will scatter adequate light to be accepted. Some error is introduced into the measurement because of these concessions. Calibration of the system in conjunction with the spray to be measured is helpful in recognizing influences of the first problem.

The existing laser interferometry system (Fig. 2) utilizes a helium-neon laser, a variable speed rotating grating (Institute of Applied Physics) for beam splitting and frequency shift, and a visibility processor (Spectrum Development Laboratories, Model VP 1001). The visibility processor is equipped to operate either with or without visibility intensity validation.

Laser Diffraction (LD). Laser diffraction provides a measurement of droplet size distribution along a line of sight. Hence the measurement is an integrated or ensemble-averaged measurement, usually across the spray at a given axial location. The technique relies upon light scattered from droplets traversing the laser beam [9, 10]. The Sauter Mean Diameter (SMD) is calculated using a two-parameter size distribution (e.g., Rosin-Rammler) or a model-independent algorithm. The commercial instrument employed for the present experiment, the Malvern ST2200, was operated with a 9-mm, helium-neon beam and a 300-mm, focal length receiving lens. The placement of the instrument relative to the chamber is shown in Fig. 2.

Although the Malvern has a standard alignment procedure, experience has demonstrated that this can be insufficient. A set of Laser Electro-Optics reticle pairs was used to verify alignment [11]. The set corresponds nominally to a Rosin-Rammler size distribution of $D_{\mathrm{RR}} = 53.1\ \mu$m, $N = 2.14$ (12), where D_{RR} is the Rosin-Rammler diameter and N is the distribution parameter. These reticles are used to (*i*) verify alignment, and (*ii*) check the reproducibility of the instrument in order to verify that comparisons of data taken on a spray device over an extended period of time are valid.

Shadowgraph Photography. Shadowgraph photos are produced by collimating the light emitted from a flash source (EGG Micro-flash Model 549-11/21) and directing it across the spray. The scattered light is collected and an image pattern of the drops is formed at a position behind the collection lens dictated by the lens focal length and the object distance. The combination used for the present tests provided a precamera magnification of 2. This image is photographed by a camera (Olympus OM-2) with a bellows for enlarging the image in

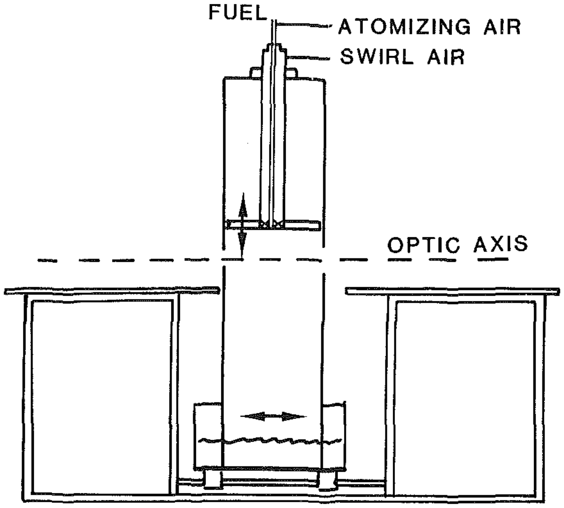

Fig. 3 Spray chamber

varying degrees of magnification in order to document the spray angle, ligament breakup at the nozzle injection plane, and detail the droplet field for a direct verification of the laser diffraction and interferometric results. The duration of each spark flash is approximately 1 μs.

Experiment: Facility

Spray Chamber. The spray facility (Figs. 2 and 3) is designed to characterize a liquid fuel atomizer under non-combusting atmospheric conditions. The chamber consists of the 34.3 cm i.d. × 152 cm long plexiglass tube positioned vertically at the center of the optical platform. The tube rests in a fuel collection basin that is connected to an exhaust system via a fuel vapor trap. The chamber and basin assembly is mounted on a precision platform permitting one degree of freedom movement in the horizontal plane for radial traverses of the spray.

The fuel nozzle is centrally positioned within the large tube in a fixture that permits vertical movement for axial traverses. The fuel nozzle is secured in the end of a 19-mm o.d. fuel delivery tube that is plumbed to supply fuel and air to the nozzle. This is centrally located within a 57-mm o.d. tube that is supplied with metered air and can be fitted with swirl vanes.

The exhaust system draws the air and fuel downward in the chamber. The strength of the exhaust is controlled so as to evacuate at a rate just adequate to prevent the formation of a stagnant droplet cloud in the chamber.

Monodisperse Aerosol Generator. A Berglund Liu Vibrating Orifice Monodisperse Aerosol Generator (TSI Model 3050) is used for checking the final optical arrangement and in setting the photomultiplier tube voltage prior to spray measurement. The Berglund Liu (BL) instrument can be made to dispense a stream of drops of a precisely known size and at a known frequency [13]. Two stable modes of operation are attainable. In the first mode, at relatively low frequencies (25–50 kHz, with a 20 μm orifice and flow rate of 0.177 cc/min) the device puts out several drops of varying sizes per cycle. The drops collide and coalesce into a single drop of a size predicted by the flow rate and frequency of stimulation within about one centimeter of the orifice. In the absence of any dispersion air, these coalesced drops are of very regular size and evenly spaced.

In the second stable mode, at higher frequencies (> 50 kHz) a single drop of a predictable size is emitted per pulse. This can be observed very close to the orifice. In this mode dispersion air can be applied to the stream and a spray of single-size drops is generated. Utilizing both modes, drops from 44 to 63 μm are produced in a stream.

Table 1 Optical parameters for LI

Fringe spacing	14.2 μm
Probe volume diameter	200 μm
Probe volume length	400 μm
Collection angle	30 deg
Collection *F/#*	4.39
PMT aperture	200 μm
Index of refraction (water)	1.33

Table 2 Berglund Liu operating conditions

Fluid	Deionized water filtered to 0.5 μm
Volume flow rate	0.177 cc/min
Orifice diameter	20 μm
Stimulation signal type	Square wave
Stimulation strength	20 V peak-to-peak
Frequency (drop diameters)	25.6 kHz (60 μm) 45.5 kHz (50 μm) 64.5 kHz (44 μm) 23.0 kHz (63 μm)

The BL is positioned over the optic probe volume using a precision, three-directional traverse (spray chamber removed). This precise control of the Berglund Liu position is required for setting the voltage to the PMT.

Air-Assist Nozzle. The air-assist nozzle used in this evaluation was designed by Parker Hannifin Corporation to fill a requirement for a low-flow, two-phase nozzle with a high degree of atomization for use in an atmospheric, laboratory combustor. The nozzle consists of two principal components. The outer body houses a set of swirl vanes and one complete air circuit. Within this, a fuel insert is fitted which contains a hollow tube surrounded by a set of swirler units on the outside surface. In conjunction with a shroud, the insert forms a second air circuit. Fuel is prefilmed on the inner surface of the shroud, separating the two air circuits, by radial injection of fuel through three small ports, located 120 deg apart, in the tip of the hollow fuel insert.

Approach

The optical arrangement used for the evaluation of the Parker Hannifin nozzle was evaluated initially using the Berglund Liu. First, single-size drops were produced to aid in establishing final alignment of the receiver, to observe the effect of grating rotation on the quality of the size measurement, and to set the voltage to be applied to the PMT in the absence of beam attenuation by the spray. Second, the BL was used in conjunction with the Parker Hannifin nozzle to ascertain the effect of spray interference on the size measurement. The nozzle was first positioned on the transmitted beam side of the probe volume, then on the collector side.

The opitcal configuration was then tested using the Parker Hannifin nozzle as the subject. Both LI and LD were utilized, allowing direct quantitative comparison between the techniques. Shadow photographs were also taken for visual confirmation of results.

System Calibration. The optic arrangement for the present experiment is such that resolution of drops with diameters between 8 and 85 microns can be expected. (By using other tracks on the diffraction grating or other collection apertures this range can be extended.) The primary optical parameters are listed in Table 1.

Three BL frequencies were used with a single flow rate and a single orifice size. Conditions are listed in Table 2 (the fourth frequency listed, 23 kHz, was used for the interference tests only). At these three frequencies single-size drops could

Table 3 Calibration of the LI system, results

				Visibility/IV Diameter (μm)				
B-L frequency (kHz)	B-L calculated diameter (μm)	Visibility diameter (μm)	PMT voltage (VDC)	No grating rotation	1200 rpm clockwise	9000 rpm clockwise	1200 rpm counter CW	9000 rpm counter CW
25.6	60	56	385	60	56	57	57	57
45.5	50	45	382	48	47	47	48	48
64.5	44	41	382	38	44	44	47	45

be observed approximately 10 mm from the BL orifice. Using an oscilloscope, the PMT placement could be optimized to most clearly focus the Doppler burst from the drops. The PMT voltage could also be precisely set for Intensity Validation (IV) using tabulated visibility and corresponding intensity values [14, 15]. The procedure was repeated for each of the three frequencies to ascertain whether the optimal PMT voltage changed depending upon where along the visibility curve the calibration was conducted.

At each frequency, once the voltage had been set, the BL drop size was measured using visibility alone, and then using visibility with intensity validation (IV). The visibility/IV system was then used at four settings of the rotating grating to observe the effect of the grating rotation on the size determination.

Interference Test. With the spray chamber removed, the BL was positioned over the probe volume using the three-directional traverse. The Parker Hannifin nozzle was positioned on the transmitter side, halfway between the transmission focusing lens and the BL. The nozzle exit was located 10 mm above the optic axis; the BL discharged at 13 mm above the probe volume. The BL was operated in the stream mode, generating 63 micron diameter droplets. The Parker Hannifin nozzle was operated with deionized water (filtered to 25 μm) at a low rate of 3.2 kg/hr. Two nozzle air:water (A/W) mass ratios were tested, 1.5:1 and 0.75:1. Interference tests conducted on the receiver side were identical except that the Parker Hannifin nozzle had to be raised to 30 mm above the optical axis to clear the solid angle of the receiving optics. The Parker Hannifin spray and the BL both discharged into the collection basin in the absence of confinements.

Nozzle Evaluation. The air assist nozzle was operated at one setting ($\dot{m}_w = 3.2$ kg/hr; $A/W = 1.5$:1) for evaluation of its spray within the spray chamber. The nozzle was checked for axial variation of Sauter Mean Diameter using the Malvern system. Then, at two axial positions, radial traverses of the spray were made, measuring drop size and axial velocity with the LI system. The traverses were in increments of 5 mm.

As many as four separate runs were required to cover the velocities of the droplets observed at a particular location in space. This results from collection limitations imposed by the frequency band filters used on the signal processor to improve the signal-to-noise ratio and to limit rolloff error. A full radial traverse of the spray required 14 (at 30 mm axial), and 15 (at 50 mm axial) data sets. The rotating grating was useful in minimizing the overlap of data collected from two or more band filters.

Data are taken as a velocity-size pair. Up to 3072 pairs can be taken in one run. The raw data are adjusted in two ways before being combined to yield an SMD or a weight distribution. First, the effective probe volume varies as a function of the size of the drop. Due to the Gaussian nature of the laser beams larger drops traversing the edges of the probe volume may scatter enough light to exceed the processor threshold; smaller drops traversing this area may not, however. When using intensity validation, the size of the intensity band also becomes a factor. To compensate for the probe volume variation, correction schemes have been introduced [17, 18] to properly weight the observed counts. Such a correction is applied to each data set. Second, the number of corrected counts must be divided by the velocity associated with each size in order to compare the data to spatial measurements (see ASTM E-799-81 standard, [16]). The velocities used are mean velocities generated for 13 size brackets (each is 6 μm wide) for each data set.

The Sauter Mean Diameter is calculated from the visibility/IV measurements at each spatial location by combining all contributing data sets (as many as four are required). A composite SMD is then determined at two axial positions (30 mm and 50 mm from the nozzle face) by combining all contributing data sets (14 at 30 mm, 15 at 50 mm). The SMD is calculated as

$$\mathrm{SMD} = \frac{\sum_{i=1}^{M} (d_i)^3 \dot{N}_i / \bar{V}_i}{\sum_{i=1}^{M} (d_i)^2 \dot{N}_i / \bar{V}_i}$$

where:

M = the total number of contributing data sets
d_i = the diameter of drop i
$\dot{N}_i$ = the number of corrected counts of drops with diameter d_i per time of collection
$\bar{V}_i$ = the mean velocity associated with the range of drop diameters (6 μm wide) containing diameter d_i

Results

System Calibration. System calibration consisted of aligning the receiver and setting the PMT voltage using the BL in a stable stream mode. Results on determining drop size for three frequencies of the BL using visibility and visibility with IV are presented in Table 3. The PMT voltage levels determined for each of the three drop sizes are within 0.5 percent of their mean value. The effect of rotating the grating on the visibility/IV size measurement of the BL drops has also been evaluated. Results (Table 3) indicate that rotation of the grating has no significant effect on the size measurement.

Interference Measurements. Interference test results are presented in Figs. 4 and 5. Only transmission side interference is illustrated. No effect on the measurement was observed when the interference was on the receiver side. Figure 4 presents data for the worst case, low air:water ratio, where atomization is less effective. Figure 5 presents data for the air:water ratio of 1.5, the condition of primary interest. In the "OFF" condition, the Parker Hannifin nozzle is flowing air only (at the test condition). In the "ON" condition the nozzle is flowing water and air at full operating condition. Figure 4(a) and 5(a) illustrations are visibility only. Figure 4(b) and 5(b) illustrations are visibility/IV measurements. Figure 4 illustrates the broadening of the visibility generated size distribution when the water/air spray is on. The broadening is in the direction of increased size as expected with degradation of the fringe visibility due to nonuniform interference of the P-H drops with the transmitted beams upstream of the probe volume. The IV system corrects the error. The effect of the

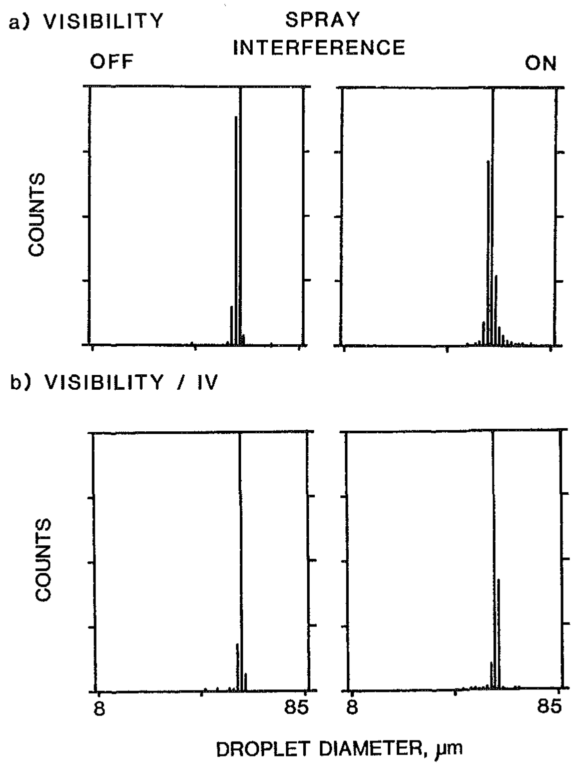

Fig. 4 Spray interference test (interference nozzle @ *A*/*W* = 0.75)

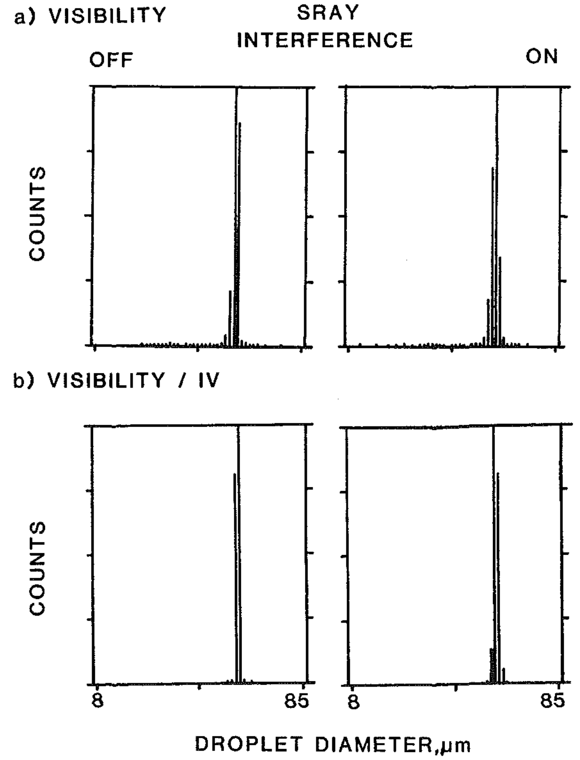

Fig. 5 Spray interference test (interference nozzle @ *A*/*W* = 1.5)

finer spray (higher *A*/*W*, better atomization) on the visibility measurement is illustrated in Fig. 5. No effect is evident although the voltage to the PMT had to be increased to compensate for attenuation of the transmitted beams. The absence of an effect on the visibility data is attributed to a near uniform attenuation to both beams in the finer spray.

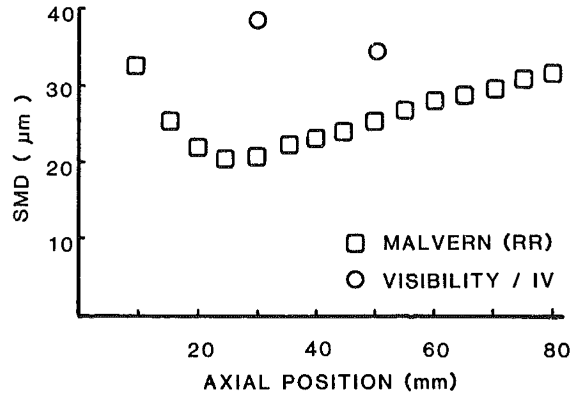

Fig 6 Axial variation of SMD

Spray Measurements. Malvern data were obtained on the air assist nozzle along the spray centerline at 5 mm intervals from 10 mm off the nozzle face to 85 mm. The centerline obscuration of the beam was approximately 20 percent at all positions. The data are presented in Fig 6. The atomization is very fine with the SMD (as determined by a Rosin-Rammler curve fit) varying from 33 to 21 μm. The dip in the curve at about 25 mm off the nozzle face is consistent with other observations [19] and can be attributed to several phenomena. First, the differential in drop velocities in the near vicinity of the nozzle, resulting from the small droplets decelerating more rapidly to terminal velocity established by the surrounding air stream, causes a local biasing of the diffraction data toward smaller sizes. Second, the spreading of a typical spray involves larger drops migrating toward the outer edges of the spray, while the smaller drops remain at the center. Thus, as the measurement is made further from the nozzle, the biasing is also toward small sizes.

Superimposed upon the Malvern axial data are two points from the visibility/IV runs. Each point represents a composite of separate LI data sets as described in the Approach section. The comparison in Fig. 6 is not good at the 30 mm station, but more reasonable (relative to Malvern) at 50 mm from the nozzle.

Figure 7 illustrates the variation of SMD with radial position at the two axial positions of interest. The single Malvern measurement (recall it is a line of sight determination) is also included for reference at both axial stations. At 50 mm, the single Malvern determination is well within the range of the LI determinations. At 30 mm, the Malvern SMD is on the low extreme of the LI SMD's, consistent with the differences observed in Fig. 6.

A good comparison between the two techniques should be expected provided the Malvern SMD is representative of the spray and is in fact spatially resolved and the LI SMD is representative of the spray and is a properly corrected temporal measurement. A poor correspondence between the LD and LI data at 30 mm suggests one of these conditions is not met. Two of the questions will be dismissed with limited discussion. First, the Malvern data were generated using one thousand sweeps per point. It is, therefore, considered spatially resolved (i.e., the spray transients have been averaged). Second, the visibility/IV data are temporal by nature. The corrections applied to the measurement to account for effective variation in the size of the probe volume and to make the data comparable to a spatially resolved measurement are consistent with current practice. The questions remaining concern whether the LD or LI data are representative of the spray.

The lower limit of detection by the Malvern is approximately 6 μm for this test setup (300-mm focal length collection lens and the spray centerline is 250 mm from the lens); it is near 8 μm for the visibility/IV system. The upper

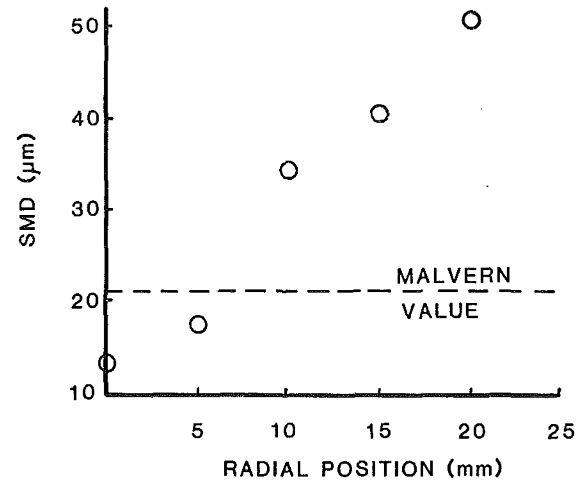

(*a*) 30-mm axial station, composite SMD = 39.6 μm

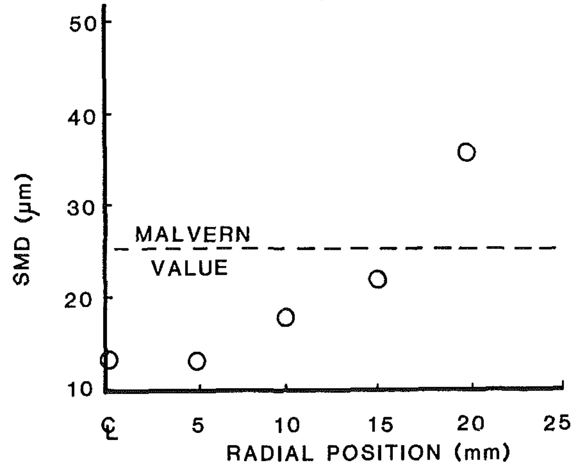

(*b*) 50-mm axial station, composite SMD = 35.8 μm

Fig. 7 Radial variation of SMD, visibility/IV

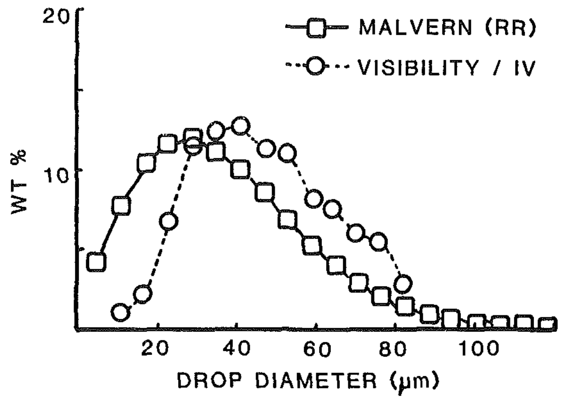

(*a*) 30-mm axial station

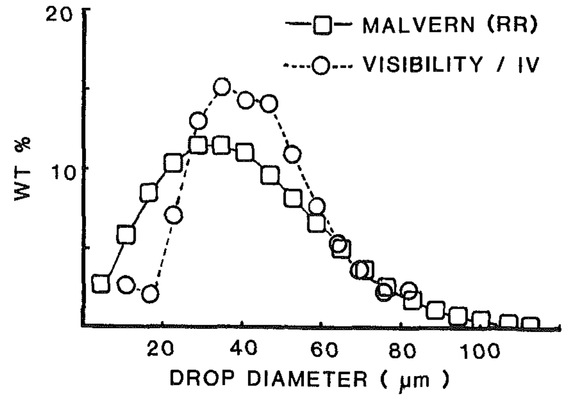

(*b*) 50-mm axial station

Fig. 8 Liquid mass distribution

limit for the LI technique is approximately ten times the lower limit. For this arrangement it is about 85 μm. The Malvern should resolve to 500 μm in its configuration. The mass distributions given by the Malvern's Rosin-Rammler (RR) fit of the data at both 30 mm (Fig. 8(*a*)) and 50 mm (Fig. 8(*b*)) suggest that 99 percent of the spray mass is in drops with diameters below 90 μm, indicating the size limitations of the LI technique encompass most of the spray.

In Figs. 8(*a*) and 8(*b*) the distribution of mass is compared to that measured with LI. The LD distributions are constructed using the Malvern output from the fit of the data directly. The weight percent contained in evenly spaced size intervals (each is 6 μm wide) is plotted against the median value in each interval. The LI determined weight percents are determined by taking the corrected counts, divided by the associated time of collection and mean velocity, and summing them over the same size interval as that of the Malvern. These 13 sums (13 size brackets from 8 to 85 μm) are multiplied by the cube of the median diameter of the size bracket and summed. The weight percent is the ratio of each of these thirteen sums to the total. The LI distribution at 30 mm suggests more mass is contained in larger drops than the observation by the Malvern RR. At 50 mm the two distributions differ in what each sees in the small and medium-size drops.

Figure 9 examines the accuracy with which the Rosin-Rammler curve fit represents the data. Plotted are the weight distributions of the same data points shown in Fig. 8. In Fig. 9, however, both the Rosin-Rammler (2 parameter) algorithm and the Model Independent (15 parameter) algorithm are applied to the same data set. The size intervals used are those output for the Model Independent (MI) algorithm. They are variable, ranging from 1.4 to 101.2 μm wide. At 30 mm, the 2 point fit smoothes over an appreciable amount of the mass contained in larger drops (~ 17 percent). This occurs despite the fact that the fitting error was well within acceptable limits (log error ≅ 4.5) for the Rosin-Rammler model. At 50 mm, the correspondence between the two models is better.

The LI and LD data at the 50-mm axial station show good agreement, both in the spray SMD and in the weight distribution. The variations which are present suggest the LI data are closer to the Malvern Model Independent analysis than to Malvern RR. The poorer match at 30 mm is also expected in light of the Model Independent treatment of the Malvern data. The composite SMD of the LI is appreciably higher than that of the Malvern RR; but the LI SMD is in the direction suggested by the Model Independent distribution. To be effective in providing adequate characterization of the spray at 30 mm the LI size limitation would have had to be broadened. This would have necessitated splicing data to overlap size windows as well as velocity windows. This complication was avoided in this effort.

Typical shadowgraph photos are presented in Fig. 10. In illustration (*a*) the nozzle exit conditions are captured. Liquid ligaments are clearly visible. In this region the visibility/IV technique with off axis collection is not applicable as the drops are not spherical (the LD technique will also experience error if the asphericity is not random). Illustrations (*b*) and (*c*) are shots from within the spray at 30 and 50 mm off the nozzle face, respectively. Along the nozzle centerline the resolution is very poor although some small drops are in focus. Moving away from the centerline the drop images are much more clear. Their spherical shape is apparent. The images also clearly show the presence of drops larger than 90 μm. This is consistent with the LD data when examined with the Model Independent algorithm.

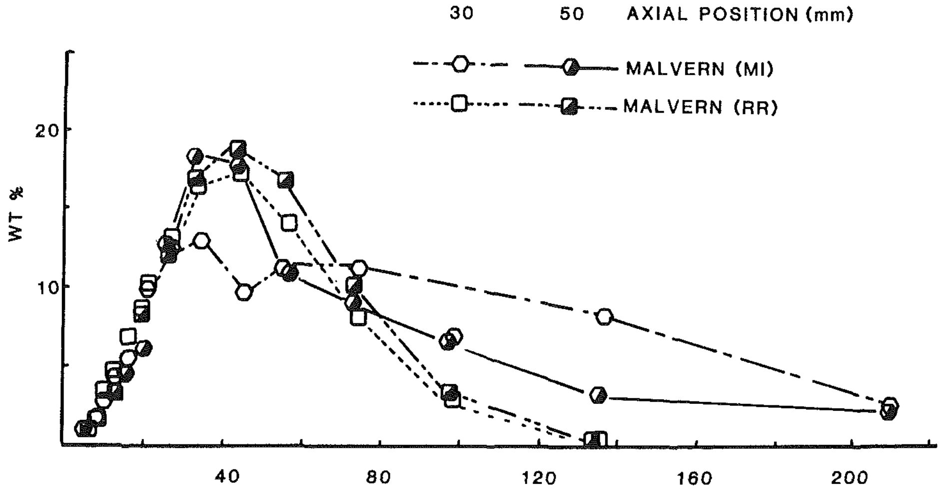

Fig. 9 Comparison of the Malvern's Rosin-Rammler and Model Independent distributions

(a) Nozzle Exit

Scale: 1 Division = 100 µm

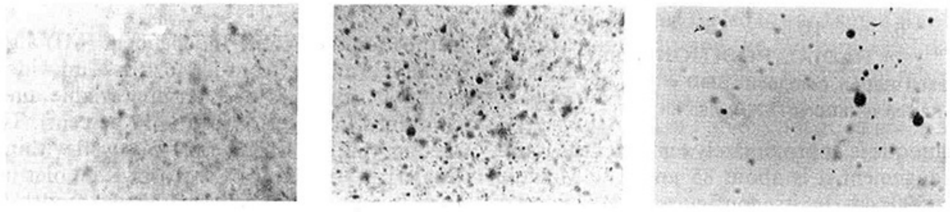

C_L C_L + 10 mm C_L + 20 mm

(b) Axial Position: 30 mm

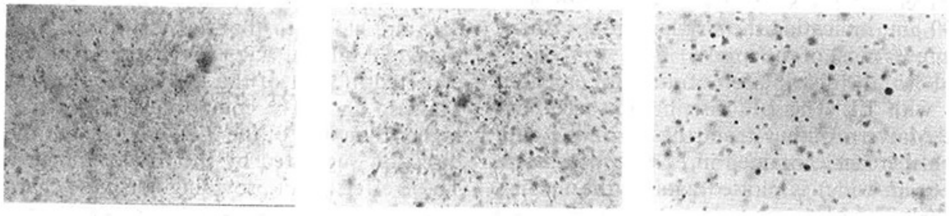

C_L C_L + 10 mm C_L + 20 mm

(c) Axial Position: 50 mm

Fig. 10 Shadow photographs of Parker Hannifin air-assist nozzle ($\dot{m}_w$ = 3.2 kg/hr, A/W = 1.5)

Summary

The investigation demonstrates the application of a nonintrusive technique for obtaining droplet size and velocity information within a practical liquid spray device. Such measurements are useful to hardware designers as well as to those who model two-phase flow fields. Specific results of this paper are as follows:

1 A calibration device such as a single-size droplet generator is indispensable in establishing the capabilities of a given interferometric sizing system. The BL was required to ascertain the PMT voltage, the influences of the rotating grating, and the effect of the spray on the measurement capability of the system. Final receiver alignment is also enhanced.

2 Use of an alternate sizing method to complement and validate the visibility measurement is necessary in a dense spray environment. The IV technique worked satisfactorily in the present case.

3 The rotating grating can be effectively used as a beam splitter for an interferometric sizing system. Further, given the restriction of having to process signals within fairly narrow frequency bands, the variable frequency shift

capability associated with the rotating grating is most appealing. No deterioration of the system's sizing capability was observed.

4 The Malvern SMD was within the extremes of the radial variation of SMD generated by the LI technique.

5 The distribution of the liquid mass within the spray as measured by the LI technique was qualitatively similar to a Rosin-Rammler curve fit of the Malvern data at both axial stations. At 30 mm, however, the LI measurements suggested a higher percentage of the weight existed in larger drops, consistent with the Model Independent treatment of the Malvern data.

6 The utility of a point measurement device in identifying the most representative model for a given spray was established in this work. The interferometric measurements provide an opportunity to actually examine the diffraction based spray measurement. In particular, the interferometric results suggest that the Rosin-Rammler fit of this spray is not an acceptable representation of the liquid mass distribution. Although the Model Independent results are satisfactory, the optical configuration used in making point measurements did not permit a thorough investigation of the 15-parameter algorithm in this spray.

7 Shadow photographs provide a means of visually checking the sizes of drops within the spray and also indicate where LI measurements as well as LD measurements are not possible due to the asphericity of the droplets.

Acknowledgments

This study is supported in part by the Air Force Office of Scientific Research (Grant AFOSR 83-0202), the Air Force Engineering and Service Center, Research and Development Directorate, Environics Division (Air Force Contract FO-8635-83-C-0052), and the Naval Air Propulsion Center (Navy Contract N000140-83-C-9151). The United States Government is authorized to reproduce and distribute reprints for governmental purposes notwithstanding any copyright notation hereon. The authors gratefully acknowledge (*i*) the assistance of Howard Crum, Marilyn Munroe, and Scott Van Vuren in the collection, reduction, and presentation of the data, (*ii*) the assistance of Roger Rudoff, Vince McDonell, and Jack Koency for developing shadowgraphs, (*iii*) the corporation of Parker Hannifin in the provision of the nozzle, (*iv*) the kindness of KVB Engineering, and EER Corporation for providing use of the Malvern droplet analyzer and EGG microflash, respectively, (*v*) the cooperation and technical discussions with Dr. Cecil Hess, Spectron Development Laboratories, in developing the LI system at UCI, and (*vi*) Janice Johnson for the preparation of the manuscript.

References

1 Crowe, C. T., "Review—Numerical Models for Dilute Gas-Particle Flows," *J. of Fluids Engineering*, Vol. 104, 1982, pp. 297-303.

2 Mostafa, A. A., and Elghobashi, S. E., "Prediction of a Turbulent Round Gaseous Jet Laden with Vaporizing Droplets," Western States Section/CI, 1983.

3 Brum, R. D., Ikioka, L. A., and Samuelsen, G. S., "Assessment of Candidate Combustor Configurations as Test Beds for Modeling Complex Flow," presented at the AIAA/ASME Fluids, Plasma, Thermophysics, and Heat Transfer Conference, St. Louis, MO, 1982; ASME Paper No. 82-HT-36.

4 Farmer, W. M., "Measurement of Particle Size, Number Density, and Velocity Using a Laser Interferometer," *Applied Optics*, Vol. 11, No. 11, 1972.

5 Bachalo, W. D., "Method for Measuring the Size and Velocity of Spheres by Dual-Beam Light-Scatter Interferometry," *Applied Optics*, Vol. 19, 1980, p. 363.

6 Seeker, W. R., Clark, W. D., and Samuelsen, G. S., "The Influence of Scale and Fuel Properties on Fuel-Oil Atomizer Performance," *Proceedings of the 1982 Joint Symposium on Stationary Combustion* NO_x *Control*, Vol. 2, Electric Power Research Institute Report, EPRI CS-3182, V2, July 1982.

7 Ferrenberg, A. J., "Liquid Rocket Injector Atomization Research," ASTM Symposium on Liquid Particle Size Measurement Techniques, 1983.

8 Hess, C. F., "A Technique Combining the Visibility of a Doppler Signal with the Peak Intensity of the Pedestal to Measure the Size and Velocity of Drops in a Spray," AIAA-84-0203, AIAA 22nd Aerospace Science Meeting, Reno, Nev., 1984.

9 Dobbins, R. A., Corcco, L., and Glassman, I., "Measurement of Mean Particle Sizes of Sprays from Diffractively Scattered Light," *AIAA Journal*, Vol. 1, 1963, pp. 1882-1886.

10 Swithenbank, J., Beer, J. M., Taylor, D. S., Abbot, D., and McCreath, G. C., "A Laser Diagnostic Technique for the Measurement of Droplet and Particle Size Distribution," in *Experimental Diagnostics in Gas Phase Systems*, edited by B. T. Zinn, Progress in Astronautics and Aeronautics, Vol. 53, 1977, pp. 421-447.

11 Hirlemen, E. D., "On-Line Calibration Technique for Laser Diffraction Droplet Sizing Instruments," presented at the 28th International Gas Turbine Conference, ASME Paper No. 83-GT-232, 1983.

12 Dodge, L. G., "Change of Calibration of Diffraction-Based Particle Sizes in Dense Sprays," *Optical Engineering*, Vol. 23, No. 5, Sept.-Oct., 1984, pp. 626-630.

13 Berglund, R. N., and Liu, B. Y. H., "Generation of Monodisperse Aerosol Standards," Environmental Science and Technology, Vol. 7, 1973, pp. 147-153.

14 Spectron Development Laboratories, Inc., "Visibility/Intensity Manual," SDL No. 83-51030, Feb. 1983.

15 Hess, C. F., "Development and Implementation of Advanced Diagnostic Techniques," SDL No. 83-2263-13M, May 1983.

16 ASTM STD E 799-81, (1982), "Data Criteria and Processing for Liquid Drop Size Analysis."

17 Roberds, D. W., Brassier, C. W., and Bomar, B. W., "Use of a Particle Sizing Interferometer to Study Water Droplet Size Distribution," *Optical Engineering*, Vol. 18, No. 3, May-June 1979.

18 Spectron Development Laboratories, Inc., "Integrated Particle Sizing System Operator's Manual: Data Management System," Vol. IV, SDL No. 82-51029, Sept. 1982.

19 Risk, N. K., and Lefebvre, A. H., "Influence of Atomizer Design Features on Mean Drop Size," *AIAA Journal*, Vol. 21, 1983, pp. 1139-1142.

Semiempirical Analysis of Fuel-Air Ratio Distribution Downstream of a Plain Orifice Injector Under Nonuniform Crossflow

J. S. Chin
Visiting Professor,
Purdue University,
West Lafayette, Ind.

W. M. Li

M. H. Cao

Beijing Institute of Aeronautics
and Astronautics,
People's Republic of China

The present paper is a step further and a modification of the semiempirical analysis of liquid fuel distribution downstream of a plain orifice injector proposed previously [*1*]. *It has been improved from the previous paper in two aspects:* (*i*) *the use of experimental data of plain orifice atomization under crossflow obtained by the present authors instead of using Ingebo's correlation* [*2*], *and* (*ii*) *consideration taken of the effect of a nonuniform crossflow. The agreement between the calculated results and the experimental data on fuel-air ratio distribution is quite good. In particular the model is capable of predicting the maximum value of the fuel-air ratio distribution and its position. The model has been used for the calculation of fuel-air ratio distribution under nonuniform crossflow with different average flow velocities. Thus the authors are able to predict how the position of maximum fuel-air ratio changes with average velocity for the same profile. The results are in good agreement with the experimental data. From the results of present research the authors conclude that for fuel-air ratio prediction in afterburners or ramjets, it is necessary to consider the effects of nonuniform crossflow. The present semiempirical analysis provides a good design tool for combustor development.*

Introduction

In a previous paper [1], the authors presented an improved flat fan spray model for the semiempirical analysis of the liquid fuel distribution downstream of a plain orifice injector under cross-stream air flow. The present paper represents a step beyond that theory and a modification of that analysis. It has been improved in two aspects: (*i*) the use of experimental data on plain orifice injection under crossflow obtained by the present authors instead of using Ingebo's correlation [2], and (*ii*) consideration taken of the effect of a nonuniform crossflow. Thus the analysis has been extended from a uniform flow field to a nonuniform one.

The flat fan spray model for crossflow spray dispersion has been used in various situations; for instance, in [3], it is used for the prediction of the distribution of liquid fuel and fuel vapor concentration. In [4, 5] the flat fan spray model has been used for the analysis of fuel spray capture on a V-gutter flame holder. Based on previous research, it is certain that the flat fan spray model constitutes a workable analysis. However, one limitation of the previous analysis that should be removed is that it is suitable only for a uniform flow field. Actually, most flow fields in afterburners and ramjets are nonuniform. For simplification, the flow field in the present research is assumed to be axisymmetric or two dimensional. The problem to be resolved is the analysis of fuel-air ratio distribution downstream of a plain orifice injector under two-dimensional, nonuniform air flow. Since the air flow is nonuniform, instead of using fuel concentration (percentage of fuel injected per unit cross-section area), we shall use the fuel-air ratio directly to express the distribution, which is defined as the fuel flow rate per unit cross-section area divided by the air flow rate for the same area. The limitation of the present research is that it neglects the evaporation of fuel droplets, which means the analysis is suitable for airflow of low temperature such as the fan air flow path in afterburner or the air flow in ramjet.

Analytical Model

The authors assume the fuel injected through the orifice is exposed to the aerodynamic force of a high-velocity, nonuniform crossflow and immediately forms a flat fan liquid sheet in the YOZ-plane (see Fig. 1). The flat fan liquid sheet so formed is perpendicular to the crossflow with a fan angle of $2\psi_o$. The initial fuel allocation with respect to the fan angle ψ is assumed to be distributed as a normal probability density distribution, which is expressed as [1]

$$\frac{dQ_\psi}{d\psi} = \frac{3}{\sqrt{2\pi}\psi_o}\exp\left(-\frac{4.5\psi^2}{\psi_o{}^2}\right) \qquad -\psi_o < \psi < \psi_o \tag{1}$$

Contributed by the Gas Turbine Division of THE AMERICAN SOCIETY OF MECHANICAL ENGINEERS and presented at the 30th International Gas Turbine Conference and Exhibit, Houston, Texas, March 18-21, 1985. Manuscript received at ASME Headquarters, December 18, 1984. Paper No. 85-GT-32.

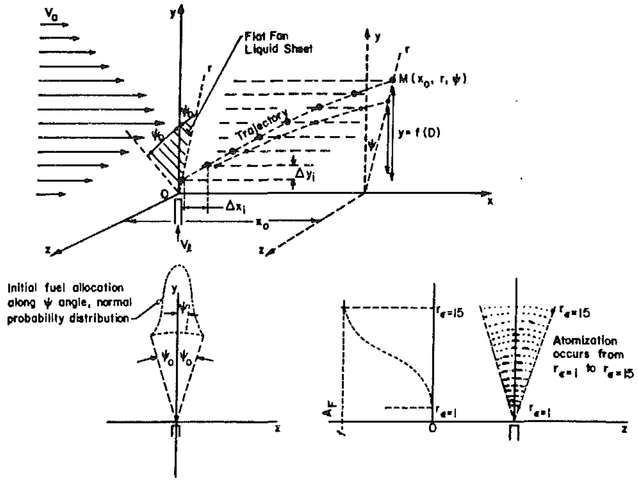

Fig. 1 Coordinate system and explanation of flat fan model

and ψ_o is determined by

$$\psi_o = \mathrm{arctg}\left[4.87\sqrt{\frac{\rho_g}{\rho_l}\left(1+\frac{V_g^2}{V_l^2}\right)}\right] \tag{2}$$

The liquid flat fan sheet is atomized under aerodynamic force into droplets within a certain distance. The atomization fraction is a function of a nondimensional jet breakup parameter ϵ [6], which is

$$A_F = 1 - [1 + 0.00392(7.68\epsilon - 1)(\epsilon - 1)^{2.34}]^{-1} \tag{3}$$

$$\epsilon = \frac{\rho_g}{\rho_l}\left(1+\frac{V_g^2}{V_l^2}\right)\frac{r^2}{d_o^2} \tag{4}$$

It can be assumed that at $\epsilon = 15$ the liquid fuel has been fully atomized. All the droplets start to move at different initial positions in the YOZ-plane at different radial distances r away from the x-axis and with a different fan angle ψ with respect to the XOY-plane. The drop-size distribution obtained by the present authors is used [7]. After the droplets have formed, their trajectories determine the liquid fuel distribution downstream. Since the flow field is nonuniform, it is divided into a series of stream tubes. Within each stream tube, the flow is assumed to be uniform and the average velocity is taken as the uniform flow velocity. Droplet trajectory equations for uniform crossflow can be used within each stream tube to determine the position of a droplet when it reaches the boundary of the stream tube. The final position and velocity of the droplet in a previous stream tube is taken as the initial position and velocity of the droplet in the next stream tube. Thus, step by step, the final position of the droplet when it reaches the desired downstream distance can be determined. Based on the droplet trajectories, fuel–air ratio distributions for various operational conditions can be predicted.

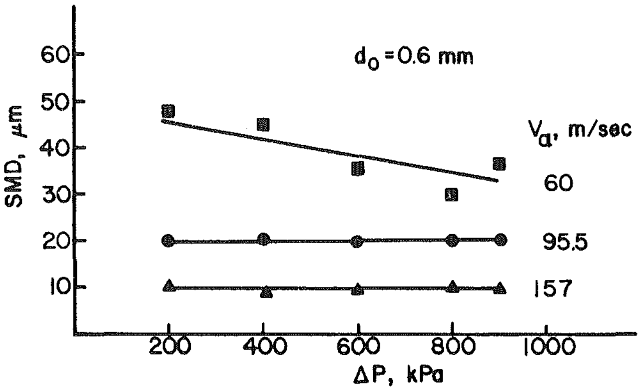

Fig. 2 SMD variations with air velocity and injector pressure drop

The analysis makes use of several simplifications. These are:

1 Fuel evaporation is neglected. As this analysis is mainly for the fan air flow path of an afterburner, this simplification is allowable.

2 Turbulent droplet diffusion is neglected. For high velocity and cross-stream air flow, the turbulent droplet diffusion is considered unimportant.

Atomization Data

The authors conducted a separate research program on the atomization of a plain orifice injector under crossflow using a Malvern particle sizer [7]. The experimental data obtained were compared with Ingebo's correlation [2]. Ingebo's correlation is shown to underestimate the effect of air velocity on mean drop size. In [7], the Rosin–Rammler distribution function is used, which is

$$Q_v = \exp\left[-0.693\left(\frac{D}{MMD}\right)^N\right] \tag{5}$$

where MMD is mass median diameter, and N is the drop size distribution parameter. A typical result is shown in Fig. 2. Based on the experimental data obtained, the following modified correlation for MMD is proposed

$$\frac{MMD}{d_o} = 9.837 \cdot 10^{10}\left(\frac{\mathrm{We}}{\mathrm{Re}}\right)^{0.25} \cdot \mathrm{M}^{-1} \tag{6}$$

where d_o is the orifice diameter in cm, and MMD is in μm. Also,

Nomenclature

A_F = atomization fraction
B_2, B_3, B_4 = combination parameters in droplet trajectory equation
C_D = droplet drag coefficient
D = droplet diameter
d_o = orifice diameter
F = area
f = fuel–air ratio
M = Mach number
M_f = fuel mass flow rate
MMD = mass median diameter
N = drop-size distribution parameter in R-R distribution
P = pressure
Q_v = volume fraction of drops having diameter larger than D
Q_ψ = fuel distribution along the flat fan angle ψ (expressed in percentage of fuel flow rate)
$\frac{dQ}{dF}$ = fuel concentration per unit area
Re = Reynolds number
r = radial distance
T = temperature
t = time
V = velocity
$\bar{V}$ = average velocity
V_R = relative velocity
We = Weber number
X, Y, Z = coordinates
ϵ = nondimensional jet breakup parameter
ρ = density
μ = viscosity
ψ = flat fan angle

Subscripts

a = air
g = gas
l = liquid

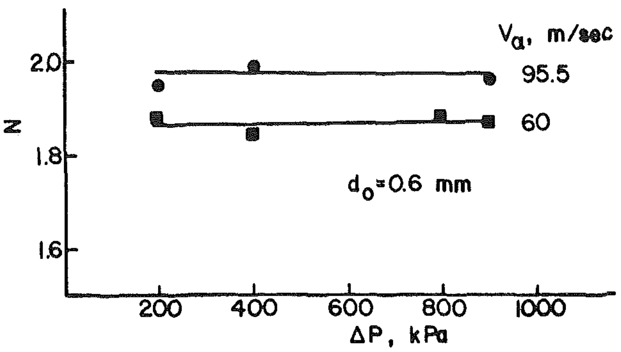

Fig. 3 Drop size distribution parameter N

We $= \dfrac{\sigma}{\rho_g d_o V_R{}^2}$, σ in dyne/cm, ρ in g/cm^3, V_R in cm/s

Re $= \dfrac{d_o V_R}{\nu}$, ν in cm^2/s

M = relative Mach number

In comparison with Ingebo's correlation, equation (6) has one more item, that is, M^{-1}. It shows a stronger dependence on air flow velocity.

A typical experimental result for the drop-size distribution parameter N is shown in Fig. 3. These correlations and data are used in the present study, although ideally atomization data in a nonuniform flow field are needed. No such data are available at the present time, so in order to use equation (6) for the calculation of mean drop size, the authors use an averaged velocity within the atomization distance as estimated from equation (4) by setting $\epsilon = 1$ and $\epsilon = 15$.

$$V_g = \int_{r_{\epsilon=1}}^{r_{\epsilon=15}} \frac{V_a \bullet dr}{r_{\epsilon=15} - r_{\epsilon=1}}$$

Also when using equation (3) to calculate the atomization fraction along the radial distance the authors divide the radial atomization distance into several elements, using the air velocity V_a in each individual element to calculate ϵ (instead of V_g) and the increment of atomization fraction ΔA_F, then the total atomization fraction A_F.

Droplet Trajectory Equation

The droplet trajectory equations used in the present study are as follows [1]

$$\Delta X_i = V_a \bullet \Delta t_i - (V_a - V_{\text{xoi}}) \int_0^{\Delta t_i} \frac{V_R}{V_{\text{Roi}}} dt$$

$$\Delta y_i = V_{\text{yoi}} \int_0^{\Delta t_i} \frac{V_R}{V_{\text{Roi}}} dt \qquad (7)$$

$$\Delta Z_i = V_{\text{zoi}} \int_0^{\Delta t_i} \frac{V_R}{V_{\text{Roi}}} dt$$

where

x_i, y_i, z_i = increments of droplet trajectory within the ith stream tube
Δt_i = time element of droplet movement in ith stream tube
V_{Roi} = initial relative velocity of the droplet in ith stream tube
$V_{\text{xoi}}, V_{\text{yoi}}, V_{\text{zoi}}$ = initial velocity of the droplet in ith stream tube

When the droplet drag coefficient equation

$$C_D = \frac{24}{\text{Re}} \left(1 + \frac{1}{6} \text{Re}^{2/3}\right) \qquad (8)$$

is used, the integration term is [1]

$$\int_0^{\Delta t_i} \frac{V_R}{V_{\text{Roi}}} dt = \frac{12\sqrt{6}}{B^2 B_3{}^3} \left\{ \frac{B_3}{\sqrt{6}} - \frac{1}{B_4} + \text{arctg} \frac{\sqrt{6}}{B_3} - \text{arctg}\, B_4 \right\} \qquad (9)$$

where

$$B_2 = 12 \bullet \mu_g / \rho_l \bullet D^2$$

$$B_3 = \left(\frac{\rho_g \bullet V_{\text{Roi}} D}{\mu_g} \right)^{1/3} \qquad (10)$$

$$B_4 = \left[\left(1 + \frac{6}{B_3{}^2}\right) \exp(B_2 \bullet \Delta t_i) - 1 \right]^{1/2}$$

When the droplet drag coefficient equation

$$C_D = a \bullet \text{Re}^{0.217} \qquad (11)$$

is used, the integration term will be

$$\int_0^{\Delta t_i} \frac{V_R}{V_{\text{Roi}}} dt = C_1 \bullet \frac{\rho_l}{\rho_g} \bullet D \bullet \left(\frac{\rho_g V_{\text{Roi}} D}{\mu_g} \right)^{-0.217} \bullet \left\{ \left[1 + C_2 \frac{\rho_g}{\rho_l} \bullet \frac{1}{D} \left(\frac{\rho_g \bullet V_{\text{Roi}} D}{\mu_g} \right)^{-0.217} \Delta t_i \right]^{0.178} - 1 \right\} \qquad (12)$$

where C_1, C_2 are constants dependent on the value of a in equation (11).

Fuel-Air Ratio Equation

At any point $M(X_o, y, z)$ or (X_o, r, ψ) downstream of a plain orifice injector, at an area element $y \bullet \Delta y \bullet \Delta \psi$, the fuel mass flow (expressed as percentage of fuel injection) per unit area can be written as [1]

$$\frac{dQ}{dF_{(x_o, y, z)}} = \int_{r_{\epsilon=1}}^{r_{\epsilon=15}} \frac{dQ_v}{dD} \bullet \frac{dD}{dy} \bullet \frac{d(A_F)}{dr} \bullet dr \bullet \frac{1}{y} \bullet \frac{dQ_\psi}{d\psi} \qquad (13)$$

where $\dfrac{dQ_v}{dD}$ is determined from equation (5)

$\dfrac{dQ_\psi}{d\psi}$ is determined from equation (1)

$\dfrac{d(A_F)}{dr}$ is determined from equation (3)

The only unknown in equation (13) is dD/dy, which is determined from the droplet trajectory equation.

The fuel-air ratio f is determined as

$$f = \frac{\left(\dfrac{dQ}{dF} \right) \bullet M_f}{\rho_a \bullet V_a} \qquad (14)$$

where M_f is the fuel mass flow rate.

Calculation Results and Comparison With Experimental Data

The droplet drag coefficient equation suggested in [1] has a drawback in that it has discontinuity at Re = 350; in the present study the following droplet drag coefficient equations are used

$$C_D = \frac{24}{\text{Re}} \left(1 + \frac{1}{6} \text{Re}^{2/3}\right) \quad \text{Re} \le 350$$

$$0.178\, \text{Re}^{0.217} \qquad \text{Re} > 350 \qquad (15)$$

In order to determine dD/dy it is necessary to calculate the

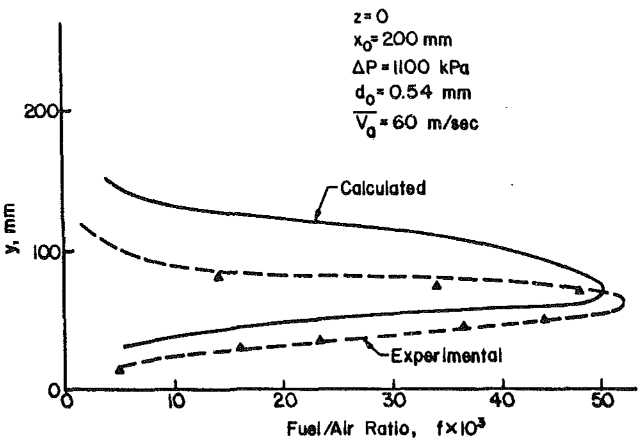

Fig. 4 Calculated and experimental fuel-air ratio distribution downstream of a plain orifice injector under nonuniform crossflow

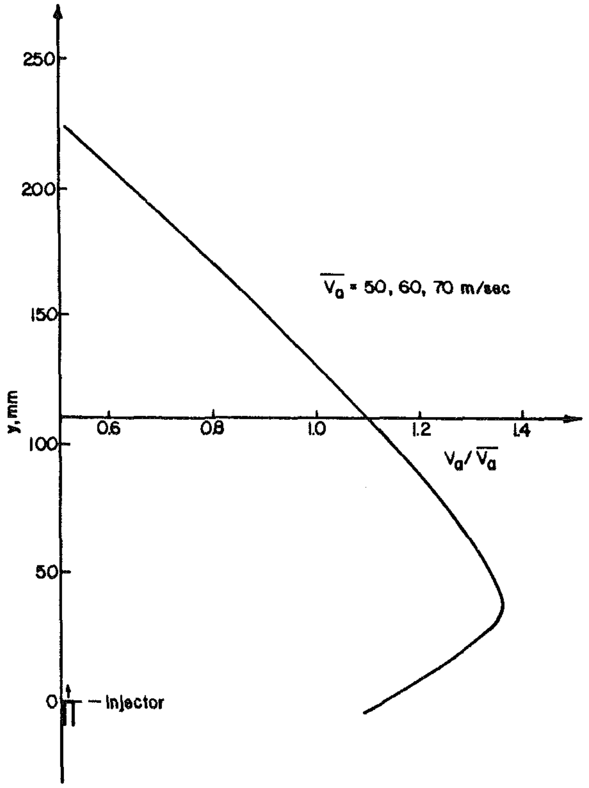

Fig. 5 Velocity profile

droplet trajectory, that is, at $x = x_o$, the y value for different droplet diameters with different initial positions, and so obtain $y = f(D)$. Then the derivative dD/dy can be obtained.

After many calculations, the authors found that in a nonuniform flow field, it is always possible to obtain the function $y = f(D)$, but it may not be a unique function; also at some points dD/dy appears as a negative value, which is meaningless physically. In order to overcome this difficulty, the authors calculate the trajectory and obtain the curve $y = f(D)$, then divide the $y = f(D)$ curve into several sections, using polynomials for curve fitting, to obtain dD/dy from the polynomial expression.

For the purpose of comparing the calculated results with existing experimental data, three types of calculation were carried out:

1 Calculation of fuel-air ratio distribution downstream of a plain orifice injector under nonuniform cross air flow. The results are shown in Fig. 4. The fuel-air ratio distribution is measured and calculated at symmetrical plane, that is, $z = 0$ plane. It can be seen from Fig. 4, that the agreement is fairly good. In particular, the model can predict the maximum fuel-air ratio and its position very well. The velocity profile for the fuel-air ratio measurement and calculation is shown in Fig. 5. The parameters used in the calculations are listed below (which are consistent with experiments)

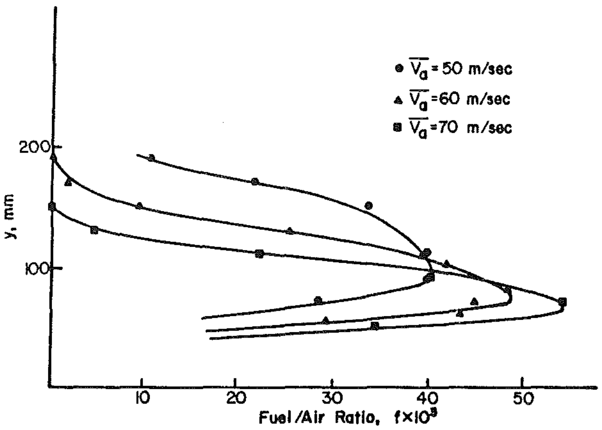

Fig. 6 Calculated fuel-air ratio distributions under nonuniform cross flow with different average velocities

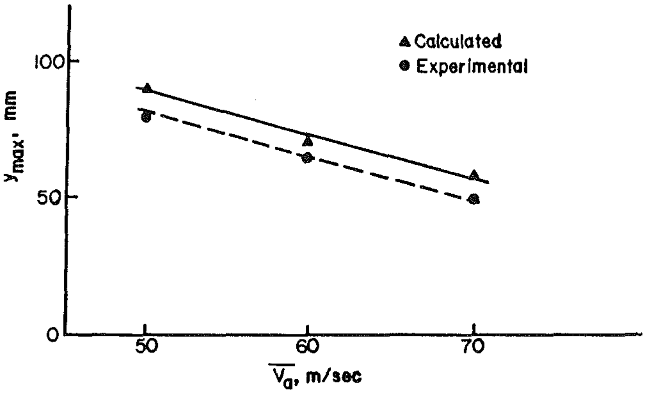

Fig. 7 The position of maximum fuel-air ratio Y_{max} for nonuniform crossflow. Comparison between prediction and experiment.

P_a = 102 kPa, $T_a = 291.5$k, $\mu_a = 1.81 \cdot 10^{-5}$ N•s/M²
ρ_l = 774.7 kg/M³, $\mu_l = 1.45 \cdot 10^{-3}$ N•s/M²
σ = $2.53 \cdot 10^{-2}$ N/M, $\Delta p = 1100$ kpa
d_o = 0.54 mm, $Z = 0$, $X_o = 200$ mm
V_a = 60 M/s

The experimental data were taken in the Thermal Power Research Institute of Beijing Institute of Aeronautics and Astronautics, People's Republic of China, using Chinese kerosine RP-2 as fuel, and a gas analysis system with traverse gear for fuel-air ratio measurement. The fuel-air ratio measurement system has been calibrated for maximum error less than 5 percent.

2 The authors calculated the fuel-air ratio distribution for different average velocities using the same velocity profile. The results are shown in Fig. 6. Thus the position of maximum fuel-air ratio Y_{max} can be obtained for different average velocities as shown in Fig. 7, where they are compared with experimental results under the same conditions. The agreement is very good. Also it is clear that with higher average velocity the maximum fuel-air ratio increases and its position moves downstream. This trend is true both for prediction and for experiments. So the analysis presented is capable of predicting the maximum value and position of the fuel-air ratio distribution.

3 It is also interesting to see the change of fuel-air ratio

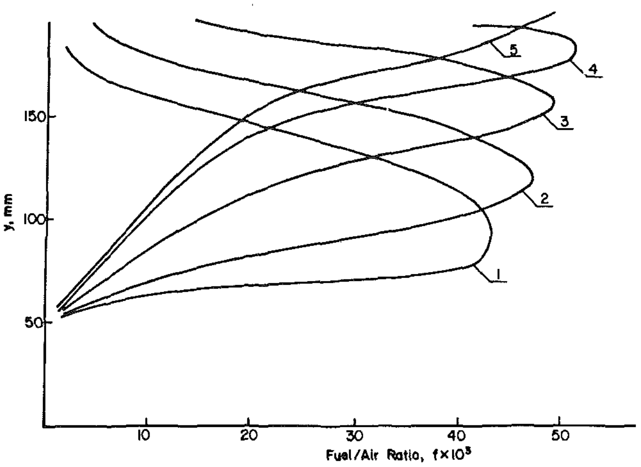

Fig. 8 Calculated fuel-air ratio distributions for different velocity profiles for the same average velocity as shown in Fig. 9

distribution curve for the same average velocity but different velocity profiles. In this case the effect of velocity profile on the fuel-air ratio distribution is clearly shown. The authors calculate the fuel-air ratio distributions for the same average velocity but different profiles (as shown in Fig. 9). The results are shown in Fig. 8. The effect of velocity profile on the fuel-air ratio distribution is very important. In afterburners and ramjets the flow velocity is never uniform, so combustion modeling combustor development purpose must take into consideration the effects of nonuniform flow velocity.

Discussion

1 Although the analysis is successful for engineering applications, further improvement must rely on new experimental data on crossflow atomization under nonuniform flow velocity conditions.

2 Droplet drag coefficient data for nonuniform flow velocities are also urgently needed.

Conclusion

Combustion modeling for afterburner or ramjet combustion development must take into consideration the effects of nonuniform velocity profile on fuel-air ratio distribution.

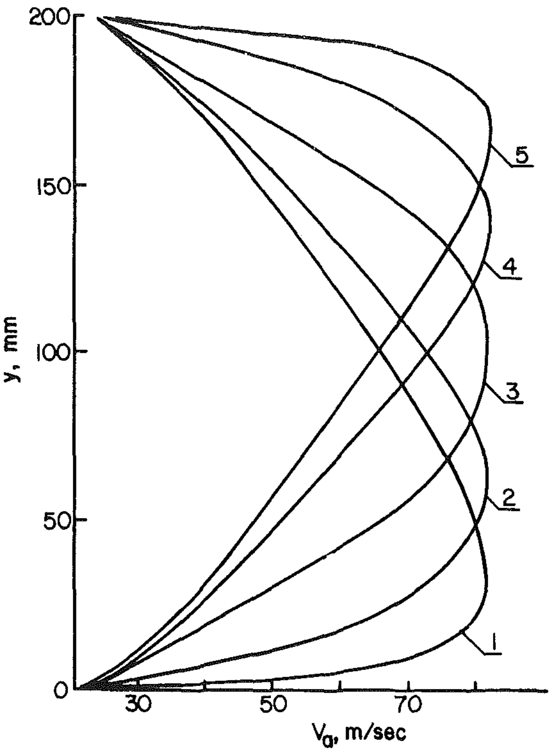

Fig. 9 Velocity distributions of nonuniform crossflow for calculation of fuel-air ratio distribution in Fig. 8

References

1 Cao, M. H., Jiang, H. K., and Chin, J. S., "Semiempirical Analysis of Liquid Fuel Distribution Downstream of a Plain Orifice Injector Under Cross Stream Air Flow," ASME JOURNAL OF ENGINEERING FOR POWER, Vol. 104, No. 4, Oct. 1982.

2 Ingebo, R. D., and Foster, H. H., "Drop-Size Distribution for Cross-Current Breakup of Liquid Jets in Airstreams," NACA TN 4087, 1957.

3 Chin, J. S., Durrett, R., and Lefebvre, A. H., "The Analysis of Liquid Fuel and Fuel Vapor Distribution Downstream of a Plain Orifice Injector Under Cross-Stream Air Flow," *Proceedings of National Engineering Thermophysics Conference* (Chinese Universities), Sept. 1983.

4 Chin, J. S., and Cao, M. H., "Prediction of Fuel Spray Capture by V-gutter Downstream of a Plain Orifice Injector Under Uniform Cross Air Flow," AIAA Paper No. 83-0153, 1983.

5 Chin, J. S., and Cao, M. H., "Further Study on the Prediction of Liquid Fuel Spray Capture by V-gutter Downstream of a Plain Orifice Injector Under Uniform Cross Air Flow," *Proceedings of the Sixth International Symposium on Air Breathing Engines*, Paris, France, June 1983.

6 Clark, B. J., "Breakup of a Liquid Jet in a Transverse Flow of Gas," NASA TND-2424, 1964.

7 Chin, J. S., Hou, M. H., and Zhao, Y. H., "Further Study on Drop Size Distribution," Submitted to 7th ISABE, Sept. 1985.

Effect of Elevated Temperature and Pressure on Sprays From Simplex Swirl Atomizers

L. G. Dodge
Senior Research Scientist.
Southwest Research Institute,
San Antonio, TX

J. A. Biaglow
Project Manager.
NASA Lewis Research Center

The effects of air temperature and air pressure on spray quality of a moderately high capacity pressure swirl atomizer (127 kg/h $\sqrt{MPa}$ *or 23.3 lbm/h* $\sqrt{psid}$*) spraying jet-A and No. 2 diesel fuel have been examined. Drop-size distributions, in terms of both Sauter mean diameter (SMD) and the width of the distribution as given by the Rosin–Rammler* N *parameter, and cone angle as measured close to the nozzle (10-mm distance) have been determined over a variety of air conditions. A new correction procedure was developed to extend diffraction-based drop-size measurements in dense sprays from maximum optical opacities of 50% to maximum opacities of 96%, equivalent to an increase in spray density of a factor of five. Drop-size measurements are reported for a temperature range of room temperature (297K) to 589K and air pressures of atmospheric (101 kPa) to 597 kPa. Cone angle data are reported for temperatures to 589K and pressures to 1318 kPa. The maximum operating temperature was limited to the occurrence of autoignition. Close to the nozzle (25 mm), limited data suggest that the SMD's were a strong function of air density,* $SMD \sim \rho^{-0.53}$*, but independent of air temperature (which affects air viscosity). The width of the distribution narrowed slightly with increasing density,* $N \sim \rho^{0.15}$*, at 25-mm distance. Trends of SMD and* N *are also shown as a function of distance from the nozzle at all conditions. These trends indicate some of the evaporation characteristics of fuel sprays. Pressure drop across the nozzle had an unusually large effect on SMD with* $SMD \sim (\Delta P)^{-0.86}$*. At 10 mm from the nozzle exit, the cone angle of the nominal 80 deg cone angle nozzle was* $\phi = 79.8\text{–}0.918\ (\rho/\rho_0)$ *where* ρ *is the air density at the test condition and* ρ_0 *the density at atmospheric conditions.*

Introduction

Fuel-spray performance has traditionally been determined using small-capacity spray nozzles (flow numbers of 4 to 26 kg/h $\sqrt{MPa}$ or 0.7 to 5 lbm/h $\sqrt{psid}$) at atmospheric conditions, and resulting correlations for fuel-property effects and other variables affecting performance have been used for large capacity nozzles used in combustor tests. Fuel-spray tests are not conducted with large-capacity nozzles because diagnostics for nozzle peformance such as spray-drop sizes can be applied more easily and accurately to small-capacity nozzles. Measurements of drop sizes are usually made at atmospheric conditions because experiments at elevated temperatures and pressures are much more difficult than at atmospheric conditions, and indeed special technqiues have been developed for these measurements.

This program was directed toward taking measurements of a larger-capacity (128 kg/h $\sqrt{MPa}$ or 23.3 lbm/h $\sqrt{psid}$) pressure atomizer spraying into air at elevated temperature and pressure.

Drop-size measurements of large-capacity nozzles at high air densities require special diagnostic techniques for two reasons. First, the high fuel capacities sprayed into dense air produce very optically dense sprays, making it difficult to apply optical diagnostics. Second, at elevated temperatures, the temperature and fuel-vapor concentration gradients cause the laser beam used in the drop-sizing instrument to be steered and fluctuate in intensity and direction in traversing the spray. These obstacles have required the development of modifications to both the instrument and the data-reduction procedures used in the standard instrument.

In addition to the drop-size measurements, cone-angle measurements have been made using back-lit strobe photography.

Experimental Apparatus

Unvitiated compressed air is supplied to the test cell by three compressors and a gas-fired preheater which provide up to 1.1 kg/s at pressures ranging from 138 kPa (1.36 atm) to 1620 kPa (16.0 atm) and temperatures up to 1090K.

The test section consists of a type 316 stainless steel pipe, 16.83 cm o.d., 12.50 cm i.d., 2.17 cm wall thickness, with 2.5-

---

Contributed by the Gas Turbine Division of The American Society of Mechanical Engineers and presented at the 30th International Gas Turbine Conference and Exhibit, Houston, Texas, March 18–21, 1985. Manuscript received at ASME Headquarters, December 21, 1984. Paper No. 85-GT-58.

Table 1 Fuel properties

	Jet A (AL-10112F)	I.H. Cat Reference No. 2 Diesel (AL-12370-F)
Viscosity at 40°C (cS)	1.72	3.10
Viscosity at 100° (cS)	0.83	1.25
Surface Tension at 24°C (dynes/cm)	26.9	29.0
Specific Gravity (60°F/60°F)	0.8049	0.8509
Heat of Combustion (MJ/kg)		
Gross	46.904	45.491
Net	43.899	42.729
Hydrogen Content	14.15%	13.02%
Flash Point (°C)	82	85
Boiling Point Distribution (°C)	(by GC)	(by D-86)
10%	195	234
20%	211	247
30%	217	257
40%	221	266
50%	229	274
60%	233	282
70%	237	293
80%	245	307
90%	254	324

Table 2 Test conditions and results for drop-size measurements

Fuel	Pres. (kPa)	Temp. (K)	Dens. (kg/m^3)	Visc. (cS)	ΔP (kPa)	Obsc.	Dist. (cm)	SMD$_m$ (μm)	N$_m$	SMD$_o$ (μm)	N$_o$
1	101.4	297.	1.191	2.26	1027.	.85	1.3	60.8	1.63	69.8	1.81
1	101.4	297.	1.191	2.26	1027.	.74	2.5	54.9	1.54	61.1	1.66
1	101.4	297.	1.191	2.26	1027.	.68	3.8	47.5	1.47	52.5	1.57
1	101.4	297.	1.191	2.26	1027.	.65	5.1	42.7	1.46	47.2	1.56
1	101.4	297.	1.191	2.26	1027.	.62	6.4	37.6	1.53	41.6	1.63
1	101.4	297.	1.191	2.26	814.	.58	6.4	48.9	1.63	52.3	1.71
1	101.4	297.	1.191	2.26	1538.	.78	6.4	24.0	1.39	30.7	1.59
1	199.3	414.	1.733	2.13	1027.	.86	2.5	35.7	1.48	45.7	1.72
1	199.3	414.	1.733	2.13	1027.	.81	3.8	34.8	1.49	43.0	1.70
1	199.3	414.	1.733	2.13	1027.	.77	5.1	34.5	1.56	41.5	1.75
1	199.3	414.	1.733	2.13	1027.	.74	6.4	31.9	1.60	38.0	1.78
1	448.2	417.	3.751	2.26	1027.	.96	2.5	16.6	1.49	29.8	1.99
1	448.2	417.	3.751	2.26	1027.	.95	3.8	16.0	1.46	28.4	1.93
1	448.2	417.	3.751	2.26	1027.	.95	5.1	18.7	1.53	31.7	2.00
1	448.2	417.	3.751	2.26	1027.	.95	6.4	19.0	1.62	32.0	2.12
1	786.0	414.	6.626	2.26	1027.	1.00	5.1	15.5	1.73	0.0	0.00
1	786.0	414.	6.626	2.26	1027.	1.00	6.4	17.5	1.83	0.0	0.00
1	199.3	589.	1.180	1.63	1027.	.85	2.5	44.1	1.60	53.7	1.82
1	199.3	589.	1.180	1.63	1027.	.80	3.8	47.0	1.68	54.9	1.87
1	199.3	589.	1.180	1.63	1027.	.73	5.1	49.2	1.80	55.2	1.95
1	199.3	589.	1.180	1.63	1027.	.70	6.4	51.8	1.82	57.2	1.95
1	597.1	589.	3.538	1.63	1027.	.98	2.5	17.7	1.62	0.0	0.00
1	597.1	589.	3.538	1.63	1027.	.97	3.8	21.4	1.73	35.9	2.27
1	597.1	589.	3.538	1.63	1027.	.97	5.1	23.9	1.81	38.7	2.35
1	597.1	589.	3.538	1.63	1027.	.96	6.4	26.8	1.90	41.2	2.42
1	689.5	589.	4.085	1.63	1027.	1.00	2.5	17.8	1.68	0.0	0.00
1	689.5	589.	4.085	1.63	1027.	1.00	3.8	20.3	1.79	0.0	0.00
1	689.5	589.	4.085	1.63	1027.	1.00	5.1	21.6	1.87	0.0	0.00
1	689.5	589.	4.085	1.63	1027.	.99	6.4	24.1	1.93	0.0	0.00
2	101.4	297.	1.191	4.50	1048.	.87	1.3	64.6	1.57	74.0	1.75
2	101.4	297.	1.191	4.50	1048.	.70	2.5	62.7	1.55	67.8	1.65
2	101.4	297.	1.191	4.50	1048.	.65	3.8	54.6	1.48	59.0	1.57
2	101.4	297.	1.191	4.50	1048.	.60	5.1	45.7	1.46	49.4	1.54
2	101.4	297.	1.191	4.50	1048.	.60	6.4	43.6	1.46	47.3	1.54
2	101.4	297.	1.191	4.50	834.	.50	6.4	56.1	1.53	58.6	1.58
2	101.4	297.	1.191	4.50	1558.	.70	6.4	28.5	1.35	33.6	1.49
2	199.3	417.	1.722	5.50	1048.	.80	2.5	40.3	1.47	48.3	1.65
2	199.3	417.	1.722	5.50	1048.	.73	3.8	41.1	1.42	47.2	1.55
2	199.3	417.	1.722	5.50	1048.	.65	5.1	36.3	1.48	40.7	1.59
2	199.3	417.	1.722	5.50	1048.	.61	6.4	40.0	1.65	43.8	1.75
2	448.2	417.	3.753	4.50	1048.	.95	2.5	22.0	1.48	35.4	1.91
2	448.2	417.	3.753	4.50	1048.	.93	3.8	22.8	1.50	35.2	1.90
2	448.2	417.	3.753	4.50	1048.	.90	5.1	24.2	1.67	35.3	2.05
2	448.2	417.	3.753	4.50	1048.	.87	6.4	24.5	1.68	34.3	2.02
2	786.0	414.	6.626	4.50	1048.	1.00	2.5	14.5	1.44	0.0	0.00
2	786.0	414.	6.626	4.50	1048.	1.00	3.8	17.9	1.50	0.0	0.00
2	786.0	414.	6.626	4.50	1048.	1.00	5.1	22.4	2.74	0.0	0.00
2	786.0	414.	6.626	4.50	1048.	1.00	6.4	21.4	1.99	0.0	0.00
2	199.3	589.	1.181	2.90	1048.	.86	2.5	54.1	1.48	63.7	1.67
2	199.3	589.	1.181	2.90	1048.	.80	3.8	55.9	1.50	63.6	1.65
2	199.3	589.	1.181	2.90	1048.	.66	5.1	54.6	1.58	59.2	1.67
2	199.3	589.	1.181	2.90	1048.	.57	6.4	54.8	1.65	58.1	1.72
2	597.1	589.	3.538	2.90	1048.	.98	2.5	18.3	1.40	0.0	0.00
2	597.1	589.	3.538	2.90	1048.	.97	3.8	22.5	1.54	37.2	2.01
2	597.1	589.	3.538	2.90	1048.	.95	5.1	24.3	1.62	38.0	2.07
2	597.1	589.	3.538	2.90	1048.	.94	6.4	26.6	1.68	39.9	2.11
2	689.5	589.	4.086	2.90	1048.	1.00	2.5	17.3	1.48	0.0	0.00
2	689.5	589.	4.086	2.90	1048.	1.00	3.8	20.4	1.57	0.0	0.00
2	689.5	589.	4.086	2.90	1048.	1.00	5.1	23.3	1.67	0.0	0.00
2	689.5	589.	4.086	2.90	1048.	1.00	6.4	26.0	1.74	0.0	0.00

cm-thick quartz windows on each side having a clear aperture of 9.2 cm × 6.7 cm. A smooth transition section 5.5 cm long is provided on each end of the windows to reduce recirculation zones. Each window is purged by air on both top and bottom. Air is supplied to each window by a total of 10 tubes of nominal 0.635 cm o.d. and then diffused and exhausted by a convergent section parallel to the window surface.

The fuel nozzle is mounted about even with the upstream edge of the windows. The nozzle is supported with a 12.7 mm o.d. stainless steel tube which follows the test section centerline for a distance of about 250 cm upstream from the nozzle and then makes a right angle bend and exits from the test section. The 12.7 mm o.d. tube carries cooling water and a separate parallel 6.35 mm o.d. stainless steel tube is the water return line. Another 6.35 mm o.d. stainless steel tube is mounted inside the 12.7 mm water cooling tube and carries fuel to the nozzle. Fuel temperature is regulated by controlling the water-cooling temperature.

The nozzle was supplied by NASA-Lewis Research Center and is a Hago 127 kg/h $\sqrt{\text{MPa}}$ (23.3 lbm/h $\sqrt{\text{psid}}$) 80 deg cone angle pressure atomizer.

Drop-size data were obtained with a Malvern Model 2200 Particle Sizer based on the diffraction angle produced by drops when illuminated by a beam of monochromatic, coherent, collimated light from a HeNe laser. All data were reduced assuming a Rosin–Rammler distribution. A 300-mm focal length *f*/7.3 lens was used to collect the scattered light. The laser beam diameter was 9 mm with a Gaussian intensity distribution truncated at the edge by the 9-mm aperture.

When drop-size measurements are conducted at elevated temperatures with the laser diffraction-based instrument, the thermal and fuel-vapor concentration gradients cause the laser beam to be diffused resulting in erroneous data. A standard instrument cannot be used in these circumstances. Modifications necessary to overcome this problem have been described by Dodge and Cerwin [1].

In addition, it was necessary to calibrate the Malvern particle sizer. Athough the manufacturer claims the instrument does not need to be calibrated, it has been determined at this laboratory that the variation in relative response of the 30 optical detectors varies with different instruments, and this results in different answers using the same standard calibration reticles.The procedure is described by Dodge [2].

Cone-angle measurements were determined from backlit strobe-illuminated photographs of the fuel spray. The fuel spray motion was "frozen" with a GenRad Strobatac operating with a flash duration of about 3 μs. Pictures were recorded on Polaroid Type 52 film at a magnification of 1.43:1 using a bellows camera with a 135-mm focal length lens.

Some of the significant fuel-property data for the two fuels are given in Table 1.

Results

Drop-Size Measurements. The matrix of test conditions and results is summarized in Table 2. At air temperatures of 617K (650°F) spontaneous ignition occurred, so the maximum temperature was limited to 589K (600°F). At room temperature, the compressors produced a fine mist of oil or water vapor in the air stream which was recorded by the drop-sizing instrument and produced a large background in addition to the fuel spray signal. This mist disappeared with preheat, but this limited the minimum temperature at elevated pressures to the minimum stable preheat temperature of about 415K (287°F). Maximum pressures for drop size measurements were limited to about 600 kPa (6 atm), beyond which the density of the spray was so great that the multiple scattering of the laser beam produced errors beyond correction. In fact, at almost all of the conditions the spray density with this moderately large-capacity nozzle was beyond the range recommended for diffraction-based drop sizers, and it was necessary to develop a correction procedure for this effect, as discussed below, and in detail by Dodge [3]. Air velocities in the test section were moderately high (15 to 26 m/s) to somewhat limit the spray density at elevated pressures.

The results of the drop-size measurements are summarized in Table 2, where each entry is the result of at least two measurements. The columns can be explained as follows. "Fuel" contains a "1" for jet-A and a "2" for No. 2 diesel. "Pres." is the air pressure, and "Temp." the air temperature, which define "Dens." the air density. Viscosity is labeled "Visc.," while ΔP is the pressure drop across the nozzle. The fractional attenuation or obscuration is labeled "Obsc.," and the distance from the nozzle exit to the point of measurement is "Dist." The measured drop-size values for the Sauter mean diameter (SMD$_m$) and the Rosin-Rammler N parameter

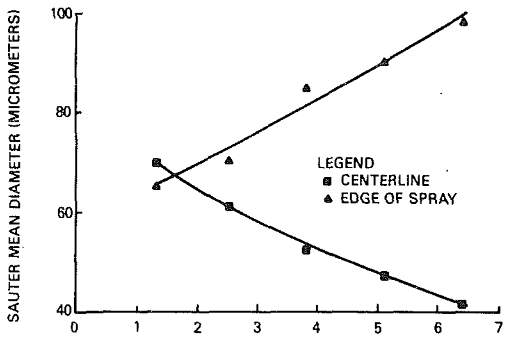

Fig. 1 **Comparison of SMD on centerline and edge of spray**

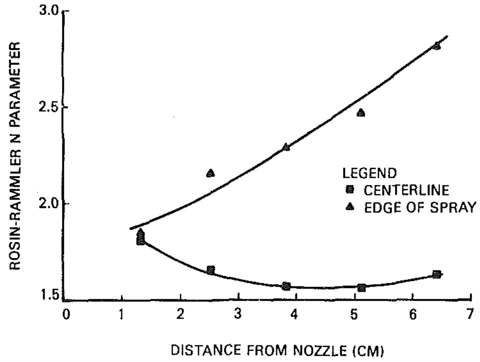

Fig. 2 **Comparison of Rosin-Rammler N parameter on centerline and edge of spray**

(N_m) are included, as well as the same values corrected to zero obscuration, SMD_0 and N_0.

The guidelines for normal use of the Malvern require that the obscuration (attenuation) of the laser beam always be less than 50% to avoid problems with multiple scattering. An examination of Table 2 indicates that if all data were rejected where the obscuration exceeded 50%, the data analysis task would have been extremely brief. For that reason, another set of experiments was conducted to develop a technique to correct the data in Table 2 for multiple scattering. Seven essentially identical nozzles were selected and a manifold designed to accept and test from one to seven nozzles at a time. The nozzles were arranged linearly and aligned with the laser beam axis so that the beam would be scattered successively by each nozzle spray. At the measurement location, the sprays did not overlap. For an ideal measuring system, the results would be independent of the number of nozzles, but for a diffraction-based instrument the measured average size decreases and distribution width increases as more nozzles are added. By varying the number of nozzles and the nozzle pressure drop, an empirical correction procedure was developed to cover the range of SMD's from 20 to 60 μm. The data shown in the last two columns of Table 2 are for the measured values corrected to zero obscuration, i.e., to a level unaffected by multiple scattering.

The correction equations, which are limited to SMD's (after correction) of approximately 20 to 60 μm and N values (after correction) on the order of 2, are as follows:

$$\mathrm{SMD}_0 = \mathrm{SMD}_m/(1-0.9456\exp(-3.811\,T)\exp(-0.0204\,\mathrm{SMD}_0)) \quad (1)$$

$$N_0 = N_m/(1-0.4264\exp(-3.672T)\exp(-0.0130\,\mathrm{SMD}_0)) \quad (2)$$

where the subscript 0 refers to the value after correction to zero attenuation, i.e., dilute spray, the subscript m refers to measured value, and T is the transmission of the undiffracted laser beam. Since SMD_0 appears to both sides of equation (1), an iterative technique must be used for solution. Some of the SMD's of Table 2 are slightly larger than the range indicated, but the corrected values probably represent an improvement over the uncorrected values.

All data given in Table 2 were for drop-size measurements made through the centerline of the spray. Atmospheric pressure measurements were also made through the edge of the spray, 40 deg off the nozzle centerline. The obscuration problem on centerline had been anticipated and measurements were made at the edge of the spray to see if the problem was less severe, but the obscuration values were comparable. Therefore, all remaining drop-size measurements were performed along the centerline to provide a more representative sample of the whole spray.

A comparison of the spray data on centerline and at the edge of the spray is instructive in understanding the features of fuel sprays from swirl nozzles. As noted above, the attenuation of the laser beam by the edge of the spray is about comparable to that for the beam passing through the center of the spray, although the path length in the spray through the edge is much shorter than the center. This can be understood by considering that in swirl atomizers, the majority of the fuel goes into larger drops along the outer edge of the cone, with an inner core composed of smaller drops which are more easily entrained by the airflow into the core. Figure 1 shows a comparison of the average drop sizes, represented by the Sauter mean diameter (SMD), measured along the edge of the spray and the centerline (both after correction for multiple-scattering errors). These results are consistent with the above description of the spray in that near the nozzle, the measurements are close to the same place (considering the 9-mm diameter of the measuring beam), and the SMD's are similar, while further downstream the edge measurements are weighted toward the large drops and the centerline measurements toward the small drops. Further evidence for this view of the spray structure is shown in Fig. 2 which compares the Rosin-Rammler N parameter for the edge and centerline measurements. The N parameter is defined by [4, 5]:

$$R = \exp(-((d/X)^N)) \quad (3)$$

where R is the cumulative volume fraction of drops larger than size d, X is a size parameter, and N measure the width of the distribution. Large values of N imply narrow distributions and vice versa. Thus, Fig. 2 shows that close to the nozzle, the measurements converge to a single value, as they should, while further from the nozzle the edge measurements show a much narrower distribution consisting of just the larger drops (from Fig. 1), while the distribution through the centerline remains relatively broad since both larger drops on the edges and smaller drops in the center of the cone are being sampled. For completeness, it should also be noted that the SMD is computed from the two Rosin-Rammler parameters by [5]:

$$\mathrm{SMD} = X/\Gamma(1-1/N) \quad (4)$$

where Γ is the gamma function.

One further effect should be mentioned regarding trends in SMD and N in moving downstream from the nozzle. At elevated temperatures, the fuel evaporates in going downstream, and the small drops are preferentially evaporated due to the d^2 law. This causes the average drop size remaining in the distribution, measured by the SMD, to actually increase initially for broad size distributions such as those observed here. Also, the increase in drop temperature decreases the density and causes the drops to expand about 7% for the highest temperature conditions present in these experiments. These effects can be observed by comparing the atmospheric temperature and pressure data for jet-A in Fig. 3 with the

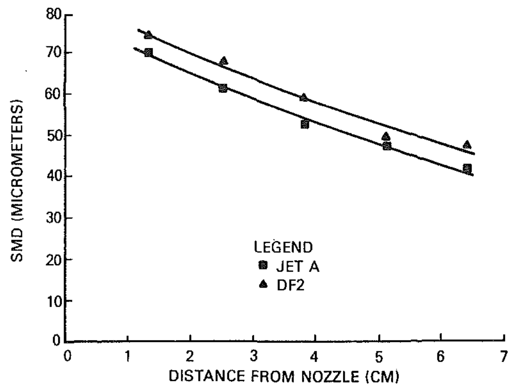

Fig. 3 Comparison of SMD's for jet-A and DF2 at atmospheric conditions, 101 kPa, 297K

414K data in Fig. 4 and the 589K data in Fig. 5. Air densities in Figs. 4 and 5 represent densities close or slightly above atmospheric, and about 3 times atmospheric. The jet-A data in Fig. 3 are the same as the centerline data of Fig. 1, but plotted on the same scale as Figs. 4 and 5. The steep decrease in SMD in Fig. 3 is moderated in Fig. 4 and even more in Fig. 5. Preferential evaporation of the small drops also causes a narrowing of the drop-size distribution, and thus, an increase in the Rosin-Rammler *N* parameter going downstream from the nozzle. This can be seen in Table 2 where the largest *N*'s and largest relative increase in *N* with distance from the nozzle occur at the highest temperatures and densities.

Besides affecting evaporation rates, air density has another strong effect, obvious from Figs. 3-5. Density strongly affects the initial atomization near the nozzle. Increasing density causes better atomization and reduces the SMD. These results show the fallacy of using drop-size data obtained at atmospheric conditions in computer models for spray behavior in high-pressure combustors. Similarly, altitude relight at reduced densities must be performed with larger drops than those measured at atmospheric pressure. This point will be discussed quantitatively following the discussion of the correlation of the spray data.

Fuel effects typical of those observed for all tests are shown in Fig. 3. The higher viscosity and surface tension of No. 2 diesel resulted in larger drops throughout the test matrix, as can be seen in Table 2. With only two fuels, there were insufficient data to independently determine the effects of viscosity, density, and surface tension. However, since the surface tensions differed by only 7.6% and the densities by 5.7% for these fuels, while the viscosity of No. 2 diesel was about twice that of jet-A, it is a reasonable assumption that the differences observed for these two fuels were due primarily to viscosity differences. Using the room-temperature data, it was determined that SMD $\sim \nu^{0.136}$, and this exponent is close to the value of 0.16 suggested by Jasuja [6]. Correlating all the data in Table 2 for the initial atomization SMD at 2.5 cm with the viscosities corrected for fuel temperature gave a similar exponent for viscosity of 0.118. Thus, viscosity was a reasonable correlating parameter for these two fuels, and the exponent on viscosity was slightly lower than accepted values.

A multiple linear regression analysis computer program was used to examine the SMD values (after correction for multiple scattering) at 2.5 cm from the nozzle for all data in Table 2. This location was picked to represent the initial SMD upon atomization before evaporation significantly affected the results. Reasonable data closer to the nozzle could not be obtained for these spray densities. The SMD's at 2.5 cm represent a limited data set of 10 values consisting of the 8 data shown in Table 2, plus 2 more data extrapolated from the SMD's measured further from the nozzle at the 597 kPa/589K condition. Each of these data resulted from an average of two experimental measurements. Examining the different variables revealed that all the SMD's at 2.5 cm could be correlated with air density and fuel viscosity. Interestingly, air temperature, which affects air viscosity, was insignificant with a *T*-ratio (coefficient/standard deviation of coefficient) of 0.14 while air density and fuel viscosity had *T*-ratios of −11.84 and 2.11, respectively. Absolute values in excess of 2 are significant parameters. For initial SMD's at 2.5 cm, the following equation provided a good fit with an R^2 (correlation coefficient squared) of 0.952,

$$\mathrm{SMD}_{2.5} = 58.5\,\rho^{-0.528}\nu^{0.118} \tag{5}$$

where the units are the same as those in Table 2. The parameter R^2 represents a "goodness-of-fit" with $R^2 = 1.0$ indicating a perfect fit. Certainly data further downstream correlate with the air temperature as increased temperature causes increased relative SMD as discussed for Figs. 3-5. To perform a simple correlation of these values is meaningless as they can only be compared with a detailed spray model which predicts drop evaporation.

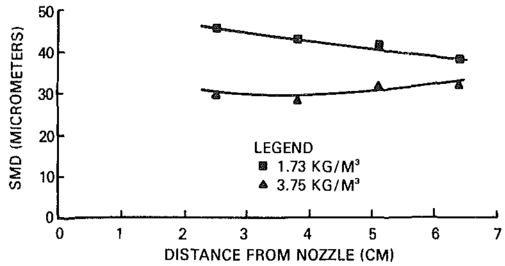

Fig. 4 Effect of air density on SMD's for jet-A, 414K

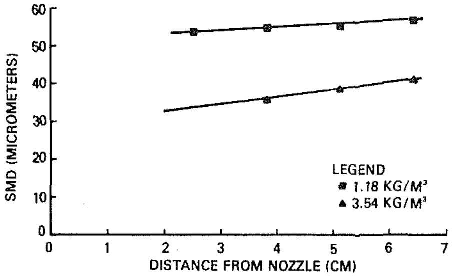

Fig. 5 Effect of air density on SMD's for jet-A, 589K

The exponent relating SMD to density given in equation (5) is large relative to previous values measured at this laboratory for smaller nozzles, which have ranged from 0.25 to 0.40. This is partly due to the convection chosen to correlate all data at 2.5 cm from the nozzle. Figure 3 shows the SMD decreasing with increasing distance from the nozzle, and this curve should reach a minimum at about 10 cm, after which it would slowly increase due to evaporation, and a slowing down of the large drops which increases their relative concentration in the sample volume. As the air density increases, this curve is not only shifted downward to smaller SMD's, but the minimum SMD as a function of distance occurs closer to the nozzle. Thus, for nonevaporating sprays, it might be possible to correlate this minimum SMD with density and the exponent would probably be smaller than that reported here. However, in evaporating sprays, the SMD near the nozzle is required as a beginning point for spray models. For that reason, a fixed distance of 2.5 cm was used for these correlations.

It is also worthwhile to include that the width of the drop-size distribution at 2.5 cm, as measured by the Rosin-Rammler *N* parameter, can be correlated with the air density ρ and the fuel viscosity ν in the form

Table 3 Cone angle measurements

Fuel	Air Pressure		Air Temperature		Air Density		Air Velocity		Cone Angle
	(psia)	(kPa)	(F)	(K)	(lbm/ft^3)	(kg/m^3)	(ft/sec)	(m/sec)	
Jet A	29.4[1]	203	68	293	.151	2.41	3.3	1.0	77
	29.4	203	67	293	.151	2.41	3.4	1.0	75
	29.4[2]	203	67	293	.151	2.41	3.4	1.0	77
	82.3	567	65	292	.424	6.78	3.4	1.0	75
	191.1	1318	70	294	.974	15.59	3.7	1.1	68
#2	29.4[3]	203	50	283	.156	2.49	3.3	1.0	78
Diesel	29.4	203	55	286	.145	2.47	3.3	1.0	78
	82.3	567	55	286	.432	6.91	3.4	1.0	73
	191.1	1318	72	296	.970	15.53	4.9	1.5	61
Jet A	29.4	203	82	301	.147	2.35	20	6.1	81
	82.3	567	83	302	.409	6.55	20	6.1	77
	191.1	1318	83	302	.950	15.21	20	6.1	72
#2	29.4	203	78	299	.147	2.36	20	6.1	78
Diesel	82.3	567	77	298	.414	6.63	20	6.1	77
	191.1	1318	78	299	.960	15.36	20	6.1	70
Jet A	28.9	199	600	589	.074	1.18	20	6.1	81
	86.6	597	600	589	.221	3.53	20	6.1	75
	160.8	1108	600	589	.410	6.56	20	6.1	75
#2	28.9	199	600	589	.074	1.18	20	6.1	78
Diesel	86.6	597	600	589	.221	3.63	20	6.1	77
	160.8	1108	600	589	.410	6.56	20	6.1	73

For all tests except those noted by 1, 2, and 3, the pressure drop across the nozzle was 1027 kPa (149 psid) for jet-A and 1047 kPa (152 psid) for #2 diesel.

[1] P = 814 kPa (118 psid)

[2] P = 1538 kPa (223 psid)

[3] P = 834 kPa (121 psid)

$$N = 1.81\ \rho^{0.152} \nu^{-0.100} \tag{6}$$

using units as given in Table 2, with an R^2 of 0.894.

The effect of pressure drop across the nozzle (measured only at atmospheric conditions and a distance of 6.4 cm) had the usual effect on flow rate, with $\dot{w} \sim \sqrt{\Delta P}$, but an abnormally large effect on SMD with SMD $\sim (\Delta P)^{-0.86}$.

Cone Angle Determination. The matrix of test conditions is shown in Table 3 with the corresponding cone angles in the last column. The cone angles are not constant at higher air pressures but tend to decrease further from the nozzle. Cone angles were measured at 10 mm from the nozzle. No effect on cone angle was observed for the nozzle ΔP. Air temperature was insignificant with a T-ratio (coefficient/standard deviation of coefficient) of -0.22, if density was accounted for. Air density is very significant with a T-ratio of -5.4. There is no statistically significant difference in cone angles between the fuels, as the T-ratio based on fuels is -1.1. The cone angle was defined as twice the half-angle where the half-angle was calculated from the total width of the spray at 10 mm divided by 2 divided by the distance from the nozzle (10 mm) plus the effective origin of the spray which was 1.1 mm upstream of the nozzle tip. The cone angle ϕ is thus

$$\phi = 2 \cdot \arctan\left(\frac{\text{Spray width}/2}{10+1.1}\right) \tag{7}$$

where spray width is measured in millimeters at 10 mm.

The air density appears to be the controlling parameter for cone angle. Two forms may be used to correlate cone angle with air density, where density is made dimensionless by taking the ratio of the actual density to the density at 298K (76°F) and 1 atm (1.185 kg/m^3) to get

$$\phi = 79.8 - 0.918\left(\frac{\rho}{\rho_0}\right) \quad R^2 = 0.73 \tag{8}$$

or

$$\phi = 81.3\left(\frac{\rho}{\rho_0}\right)^{-0.062} \quad R^2 = 0.63 \tag{9}$$

Judging by the R^2 values, the first form appears preferable for the limited data set examined.

Discussion

Comparison of drop-size observations by different workers is complicated by the fact that different analyzers, even if performing correctly, can give very different results in sprays. This is due to the fact that different types of instruments sample different characteristics of the spray, and average the results differently. For instance, a temporal average results when the sampling process describes observations in the traffic through a fixed area during intervals of time. Examples of temporal averaging are collecting drops on a stationary slide, or a counter/sizer counting drops going by a set of photocells. On the other hand, a spatial average results if the sampling process describes the population of drops in a volume of space, independent of the velocity of the particles. Examples would be strobe photography and laser-diffraction sizing instruments, although the photography samples only a narrow depth of field, and the laser-diffraction instruments sample a line of sight through the spray. Thus, temporal averaging measures a flux of drops past an area, while spatial averaging measures a population within a volume.

Consider the implications of these sampling effects for measurements of drop sizes in a simplex swirl atomizer. In most calibration applications, the initial spray velocity is on the order of 20 m/s ($\Delta P \simeq 700$ kPa) while the air velocity is stagnant or less than 1 m/s. The small drops decelerate to the air velocity rapidly while the large ones maintain their momentum. The result is that a spatially averaging instrument will measure a higher ratio of small/large drops than a temporally averaging instrument. As pointed out previously, there are also spatial inhomogeneities within the spray. This makes the understanding and comparison of drop-size measurements from different instruments and laboratories difficult.

One further difficulty is the different air (or nitrogen) velocities used to remove the spray from the sampling area. The experimental arrangement of using vertically downward spraying nozzles and negligible air velocities along with laser-diffraction (e.g., Malvern) type instruments is in most common use today, but represents an unfortunate combination of sampling biases. From the above discussion, it can be seen that the extremely low air velocities will "trap" the small drops while the larger ones maintain their initial velocity much longer and then their velocity remains significant due to the effects of gravity. Since the laser diffraction instruments measure a spatial average, or population within a volume, these small drops that are floating slowly through the sampling area result in a significant bias toward smaller sizes. Since a laser-diffraction instrument was used for the measurements reported here, relatively higher velocities (when compared with standard practice) of 4 m/s were used for atmospheric pressure tests and 15 to 26 m/s for elevated pressure tests to minimize this sampling bias. The initial axial component of the spray velocity can be calculated to be about 16 m/s for these experiments, so air velocities approximately matching the initial axial spray velocity would alleviate some of these sample problems. Even higher air velocities were used for this program in some cases to reduce the effective spray density in the spray volume. Thus, although it is possible to compare results from different laboratories, the interpretation is difficult.

Much of the early work on effects of elevated air densities on sprays was done with diesel nozzles using very high fuel injection pressures. Giffen and Lamb [7] found a decrease in drop size with increasing gas density with a fuel pressure drop (ΔP) of 12.4 MPa (1800 psid) for air densities of 1.22 to 51.2 kg/m^3 (0.076 to 3.20 lbm/ft^3). Lee [8, 9] reported negligible effect of ambient gas density on drop sizes at a fuel ΔP of 28.4 MPa (4120 psid) and air densities of 4.96 to 25.0 kg/m^3 (0.31 to 1.56 lbm/ft^3). Retel [10] reported a decrease in drop sizes with increasing air density up to densities of 4 kg/m^3 (0.25 lbm/ft^3), but then an increase at higher air densities. All of these tests were with diesel nozzles using very high injection pressures and are not directly comparable with simplex swirl atomizers used in gas turbine nozzles.

DeCorso [11] examined a simplex swirl atomizer operating at fuel ΔP's of 172 to 689 kPa (25 to 100 psid) and gas densities of 0.041 kg/m^3 (0.0025 lbm/ft^3), 1.17 kg/m^3 (0.073 lbm/ft^3), and 9.27 kg/m^3 (0.579 lmb/ft^3). Increasing the density from 0.041 kg/m^3 (subatmospheric) to 1.17 kg/m^3 (atmospheric) led to a significant reduction in SMD. A further increase to 9.27 kg/m^3 led to a slight increase in SMD, but also resulted in an almost complete collapse of cone angle (nominally 80 deg) from about 80 deg at atmospheric density to 28 deg at 9.27 kg/m^3 (nozzle ΔP = 689 kPa). This would probably be regarded as an unacceptable collapse of cone angle with pressure, and therefore not suitable to use for evaluating the effects of elevated densities on drop sizes. The data were taken photographically, representing a spatial average, but also converted to a temporal average based on the average spray velocity in different parts of the spray. A more optimum conversion between spatial and temporal averaging would be based on average drop velocities as a function of both size and spatial location, but that was not available in DeCorso's experiment. It should also be pointed out that DeCorso's measurements were made at 184 mm (7.24 in.) downstream of the nozzle, far enough for a significant amount of coalescence and evaporation to occur.

Rizk and Lefebvre [12] also examined the effect of air density on swirl atomizers, but using a laser-diffraction instrument spraying into stagnant pressurized nitrogen. (As discussed above, this can lead to a small-drop sampling bias.) At air densities up to 4.1 kg/m^3 (0.26 lbm/ft^3), increasing air densities reduced SMD's measured 125 mm from the nozzle by SMD $\sim \rho^{-0.1}$, while at densities greater than 4.1 kg/m^3, the effect was stronger with an exponent of -0.28. At 38 mm from the nozzle the effect was apparently similar. Rizk and Lefebvre [12] suggest that an exponent of -0.25 be used overall.

Abou-Ellail et al. [13] studied swirl atomizers using a sliding sampling method, which results in a temporal sample rather than the spatial sampling reported here. At constant air temperature, they report a dependence of SMD on pressure of SMD $\sim P^{-0.26}$ at a distance of 60 mm from the nozzle. Since these were at constant temperature, this pressure dependence could also be interpreted as an air density dependence.

The experiments reported here also indicate a reduction of SMD with increasing air density, but with an exponent of -0.53 for the 25-mm location. As is obvious from Figs. 3, 4, and 5, the density effect is less pronounced further downstream of the nozzle. However, the elevated temperature data also included some evaporation effects further downstream of the nozzle, complicating the interpretation at those locations. For that reason, and the need for drop-size data close to the nozzle for computer modeling efforts, the density correlations were performed for the 25-mm location. The stronger density dependence reported here is due in part to the location chosen for the correlation.

Air temperature could affect atomization for a number of reasons. At constant pressure it affects the density, which is corrected for by correlating results with density rather than pressure. The air viscosity increases roughly as $\sqrt{T}$, which could affect atomization. For constant air density, the Weber number is unaffected by changes in air temperature, except for changes in liquid temperature which affect surface tension. Increases in liquid temperature due to heat transfer to the nozzle cause a large decrease in viscosity and a small decrease in surface tension, with improved atomization resulting. To correct for heat transfer to the nozzle, the fuel temperature was monitored at the nozzle inlet for these experiments, and after correcting for the effect on viscosity, air temperature had no statistically significant impact on initial atomization as measured at 25 mm.

Abou-Ellail et al. [13] also examined the effect of air temperature on the size distribution as measured 60 mm from the nozzle. At constant pressure, they report a decrease in SMD proportional to $T^{-0.56}$. These results are contrary to those reported here, which would predict an increase in SMD at constant pressure due to the reduction in air density as the temperature is raised. Abou-Ellail et al. [13] do not indicate if the fuel feed lines and spray nozzle were cooled to maintain constant fuel temperature, and hence viscosity. If the fuel temperature is allowed to increase with air temperature, the drop-size distribution will be shifted to smaller sizes. Also considerable evaporation of the spray had occurred at the 60-mm location used by Abou-Ellail et al. [13] at the elevated air temperatures.

Summary and Conclusions

1 Fuel-spray nozzle calibrations which are used to predict or interpret results for elevated pressure gas-turbine combustors or reduced-pressure altitude relight conditions should either be performed at the air conditions of interest or, if performed at atmospheric conditions, corrected for the effects of density on atomization. For the nozzle and conditions of this experiment, the SMD close to the nozzle (25 mm) depended strongly on air density:

$$\mathrm{SMD} \sim \rho^{-0.53}.$$

The Rosin-Rammler N parameter increased with density according to:

$$\mathrm{N} \sim \rho^{0.15}.$$

2 Air temperature had no effect on the initial SMD close to the nozzle if density rather than pressure was used to correlate the data, and if viscosity changes due to fuel heating were accounted for.

3 Air temperature had a very significant effect on SMD's downstream of the nozzle as increasing temperatures increase evaporation rates which cause increases in SMD's due to the preferential evaporation of the smaller drops. Also droplet heatup causes a reduction in fuel density and a small increase in diameter of about 7% for the maximum temperature conditions.

4 Fuel effects on atomization could be correlated with the viscosity differences between jet-A and No. 2 diesel. Two fuels were insufficient to evaluate the relative importance of surface tension, specific gravity, and viscosity to the atomization performance.

5 Pressure drop across the nozzle had an unusually large effect on SMD at 64 mm from the nozzle,

$$\mathrm{SMD} \sim (\Delta P)^{-0.86}$$

Pressure drop had the usual effect on flow rate,

$$\dot{w} \sim \sqrt{\Delta P}$$

6 Cone-angle data correlated with air density, independent of air temperature and air velocity at the location chosen for measurements (10 mm from nozzle). Air velocity may have an effect further downstream.

7 An empirical correlation scheme has been developed for diffraction-based drop-size data suffering errors from multiple scattering and recorded at opacities up to 96 percent. The accuracy of this technique has not been established, but it is an attempt to extend the applicability of these instruments from attenuation limits of approximately 50% to 96%, equivalent to an increase in spray density of more than a factor of five.

Acknowledgments

This work was funded by NASA Lewis Research Center under Contract No. NAS3-24090. The technical assistance of Mr. R. C. Haufler is gratefully acknowledged.

References

1 Dodge, L. G., and Cerwin, S. A., "Extending the Applicability of

Diffraction-Based Drop Sizing Instruments," in: *Liquid Particle Size Measurement Techniques*, ASTM STP 848, ed. J. M. Tishkoff, R. D. Ingebo, and J. B. Kennedy, ASTM, 1984, p. 72.

2 Dodge, L. G., "Calibration of the Malvern Particle Sizer," *Applied Optics*, Vol. 23, 1984, p. 2415.

3 Dodge, L. G., "Change of Calibration of Diffraction-Based Particle Sizers in Dense Sprays," *J. Optical Eng.*, Vol. 23, No. 5, 1984, p. 626.

4 Allen, T., *Particle Size Measurements*, Third Edition, Chapman and Hall, 1981, pp. 139–140.

5 Mugele, R. A., and Evans, H. D., "Droplet-Size Distribution in Sprays," *Ind. Eng. Chem.*, Vol. 43, 1951, p. 1317.

6 Jasuja, A. K., "Atomization of Crude and Residual Oils," ASME Paper No. 78-GT-83, 1978.

7 Giffen, E., and Lamb, T. A. J., "The Effect of Air Density on Spray Atomization," The Motor Industry Research Association Report No. 1953/5, Great Britain.

8 Lee, D. W., "Fuel Spray Formulation," *Trans. ASME*, Vol. 54, 1932, p. 63.

9 Lee, D. W., "The Effect of Nozzle Design and Operating Conditions on the Atomization and Distribution of Fuel Sprays," NACA Report No. 425, 1932.

10 Retel, R., "Contributions à l'Etude de l'Injection Dans les Moteurs Diesel," *Min de Air (France) Bull. Serv. Techn.*, No. 81, 1938.

11 DeCorso, S. M., "Effect of Ambient and Fuel Pressure on Spray Drop Size," ASME JOURNAL OF ENGINEERING FOR POWER, Vol. 82, 1960, p. 10.

12 Rizk, N. K., and Lefebvre, A. H., "Spray Characteristics of Simplex Swirl Atomizers," presented at the Central States Section/Combustion Institute, Paper No. 82-19, Dec. 1982.

13 Abou-Ellail, M. M. M., Elkotb, M. M., and Rafat, N. M., "Effect of Fuel Pressure, Air Pressure, and Air Temperature on Droplet Size Distribution in Hollow-Cone Kerosene Sprays," *1st International Conference on Liquid Atomization and Spray Systems*, 1978, p. 85.

Gan Xiao-Hua

Zhao Qi-Shou

Jet Propulsion Lab,
Beijing Institute of Aeronautics
and Astronautics,
Beijing, People's Republic of China

An Expression of Liquid Film Thickness Inside Prefilming Atomizers

In the present paper, the characteristics of liquid film thickness inside prefilming airblast atomizers are investigated. An expression of liquid film thickness in three-dimensional axisymmetric coordinates is presented. The film thickness of kerosene and water is measured by using special techniques. It is found that the predictions of liquid film thickness agree well with experiments.

Introduction

Since Rizkalla and Lefebvre [1] indicated a correlation of SMD α $h^{0.4}$ for prefilming atomizers, predictions of h have been tried by several researchers. Rizk and Lefebvre [2] obtained a correlation to predict h at the lip of their two-dimensional atomizers by analyses and experiments. Zhao Qi-Shou and Yin Xin-Liang [3] obtained two semiempirical expressions for water and kerosene separately to predict h along the prefilming surface of two-dimensional atomizer.

In the present paper this problem of the three-dimensional atomizer is treated by analyses and experiments.

Basic Equations

The atomizer employed in the paper is shown in Fig. 1. Liquid flows through eight equispaced tangential ports of the liquid swirler piece into prefilming surface before being discharged at the atomizing lip. The axisymmetric flow of a viscous incompressible fluid is considered. The cylindrical coordinates X and Y are employed and each component velocity is denoted by U and V, as shown in Fig. 2.

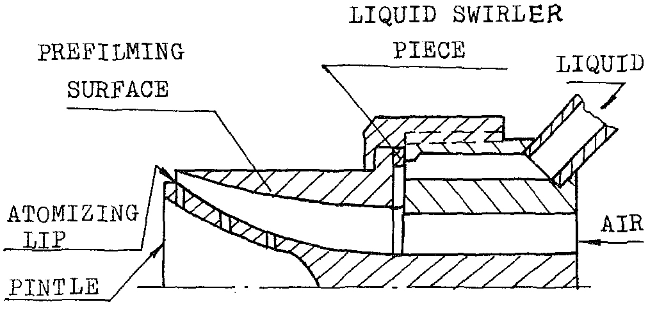

Fig. 1 Atomizer

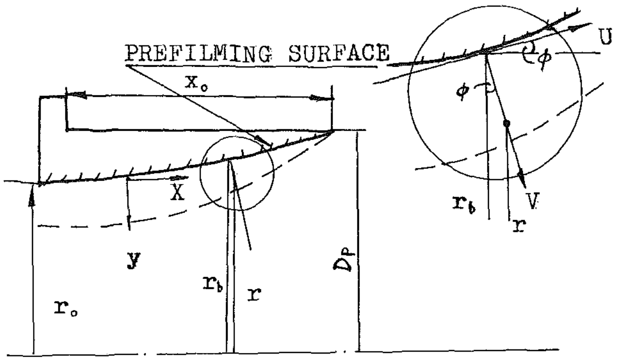

Fig. 2 Liquid flowing scheme

Assumptions in the Analyses

1 Inside the atomizer, the swirling of liquid sheet along the prefilming surface will not be considered.

2 $A_a \gg A_L$

3 The liquid flow is considered laminar.

Using the shear layer equation [4] to describe the liquid flowing along the prefilming surface, the momentum and continuity equations are expressed as follows

$$U_l \frac{\partial U_l}{\partial x} + V_l \frac{\partial U_l}{\partial y} = -\frac{1}{\rho_l} \frac{dP_l}{dx} + \frac{1}{\rho_l} \frac{\partial}{r\partial y} \left[r\mu_l \frac{\partial U_l}{\partial y} \right] \tag{1a}$$

$$\frac{\partial P_l}{\partial y} = 0 \tag{2}$$

$$\frac{\partial}{\partial x}(rU_l) + \frac{\partial}{\partial y}(rV_l) = 0 \tag{3}$$

where

$$r(x) = r_b(x) - y\cos\phi(x) \tag{4}$$

Each variable in equation (1) is compared by parameters at the atomizing lip. We have $U \sim U_{lp}$, $X \sim L$, $Y \sim h$, $V \sim U_{lp}h_p/l$ (it is obtained from equation (3)).

The following relation is now introduced.

$$U_l \frac{\partial U_l}{\partial x} + V_l \frac{\partial U_l}{\partial y} = \frac{1}{\rho_l} \frac{\partial}{r\partial y} \left(r\mu_l \frac{\partial U_l}{\partial y} \right) - \frac{1}{\rho_l} \frac{dP_l}{dx} \tag{1b}$$

$$\frac{U_{lp}^2}{L} \qquad \frac{U_{lp}^2}{L} \qquad \frac{\mu_l U_{lp}}{\rho_l h^2} \qquad \frac{\rho_a U_{ap}^2}{\rho_l 2L}$$

If

Contributed by the Gas Turbine Division of The American Society of Mechanical Engineers and presented at the 30th International Gas Turbine Conference and Exhibit, Houston, Texas, March 18–21, 1985. Manuscript received at ASME Headquarters, December 27, 1984. Paper No. 85-GT-110.

$$\frac{U_{lp}^2}{L} \ll \frac{U_{ap}^2 \rho_a}{2L\rho_l}$$

there is

$$\frac{dP_l}{dx} = \frac{\mu_l}{r} \frac{\partial}{\partial y} \left(r \frac{\partial U_l}{\partial Y} \right) \tag{5}$$

Because $y\cos\phi \ll r_b$, $r \approx r_b$ equation (5) becomes

$$\frac{\partial^2 U_l}{\partial y^2} = \frac{1}{\mu_l} \frac{dP_l}{dx} \tag{6}$$

Integrating equation (6) along y, we have

$$U_l = \frac{1}{\mu_l} \frac{dP_l}{dx} \frac{y^2}{2} + C_1(x) y + C_2(x) \tag{7}$$

Substituting the following boundary conditions into equation (7)

$$y = 0, \quad U_l = 0 \tag{8}$$

$$y = h, \quad \mu_l \frac{\partial U_l}{\partial y} = \tau_{wa} \tag{9}$$

We obtain

$$C_2 = 0 \tag{10}$$

$$C_1 = \frac{\tau_{wa}}{\mu_l} - \frac{1}{\mu_l} \frac{dP_l}{dx} h \tag{11}$$

$$U_l = \frac{1}{\mu_l} \frac{dP_l}{dx} \frac{y^2}{2} + \frac{1}{\mu_l} \left(\tau_{wa} - \frac{dP_l}{dx} h \right) y \tag{12}$$

According to the continuity equation, we have

$$W_l = \rho_l \int_0^h 2\pi (r_b - y) U_l dy \tag{13}$$

From equation (12), we integrate equation (13) and rearrange the equation derived. We have

$$\left(-\frac{dP_l}{dx} \right) \frac{h^3}{3} + \frac{\tau_{wa}}{2} h^2 - \frac{W_l \mu_l}{2\pi P_l r_b} = 0 \tag{14}$$

where

$$-\frac{dP_l}{dx} = C_3 \left(-\frac{dP_a}{dx} \right) \tag{15}$$

$$\tau_{wa} = \frac{\lambda_i}{4} \frac{\rho_l U_a^2}{2} \tag{16}$$

From [5], we employ

$$\lambda_i = \frac{\lambda_a}{2} \left(1 + \frac{300h}{2\, r_b} \right) \tag{17}$$

where λ_a is a friction factor. From [6], $\lambda_a = 0.0176$ can be found. Therefore, we have

$$\tau_{wa} = \frac{\tau_a}{2} + \frac{150}{60} \frac{\lambda_a h}{r_b} \rho_a U_a^2 \tag{18}$$

Where $\tau_a = (\lambda_a/4)\, \rho_a U_a^2/2$, substituting equation (15), (16), (17) into equation (14), we obtain

$$\left(-\frac{1}{3} \frac{dP_l}{dx} + \frac{150}{32} \frac{\lambda_a}{r_b} \rho_a U_a^2 \right) h^3 + \frac{\tau_a h^2}{4} - \frac{W_a \mu_l}{2\pi \rho_l r_b} = 0 \tag{19}$$

Let

$$a = -\frac{1}{3} \frac{dP_l}{dx} + \frac{150}{32} \frac{\lambda_a}{r_b} \rho_a U_a^2, \quad b = \frac{\tau_a}{4}, \quad c = \frac{W_a \mu_l}{2\pi \rho_l r_b} \tag{20}$$

Equation (19) can be rearranged as follows.

$$(ah^3)^{2/3} = \left[c \left(1 - \frac{bh^2}{c} \right) \right]^{2/3} \tag{21}$$

Using Taylor's expansion, equation (21) becomes

$$\left(\frac{a}{c} h^3 \right)^{2/3} = 1 - \frac{2}{3} \frac{bh^2}{c} - \frac{1}{9} \left(\frac{bh^2}{c} \right)^2 - \frac{1}{3} \left(\frac{bh^2}{c} \right)^3 + \ldots \tag{22}$$

We employ the first two terms of the right side of equation (22) and rearrange them. We have

$$h = \left[\left(\frac{a}{c} \right)^{2/3} + \frac{2}{3} \frac{b}{c} \right]^{-1/2} \tag{23}$$

At an arbitrary cross-sectional area inside the atomizer, there are

$$U_a = \frac{U_{ap} A_p}{A} \tag{24}$$

$$\frac{dP_a}{dx} = -\rho_a U_a \frac{dU_a}{dx} = \frac{\rho_a U_a^2}{A} \frac{dA}{dx} \tag{25}$$

Substituting equations (20), (25) into equation (23), we have

$$h = \left\{ \frac{\pi c_3}{3} \left(-\frac{dA}{Adx} \frac{D_b}{A} \frac{W_a}{W_l} \frac{\rho_l}{\mu_l} U_a + \frac{0.518}{A} \frac{W_a}{w_l} \frac{\rho_l}{\mu_l} U_a \right)^{2/3} + 0.0012 \frac{D_b}{A} \frac{\rho_l}{\mu_l} \frac{W_a}{W_l} U_a \right\}^{-1/2} \tag{26}$$

where C is determined by experiments. Equation (26) represents the relation of h and other relevant parameters.

Experiments

For verifying the availability of equation (26), the experiments have been done in practical operating conditions with swirling liquid flow. Techniques called capacitance method and resistance method are employed to measure h. In the capacitance method, a change of kerosene film thickness inside the atomizer will result in a change of capacitance between the prefilming surface and the pintle of the atomizer correspondingly. In the resistance method, a needle probe with an electric circuit break with the prefilming surface or water film will result in obvious changes of resistance. Measuring errors in both are less than ±4 percent.

The atomizers employed in experiments are the same type as shown in Fig. 1. The prefilming cup and pintle can be changed independently for the variations in geometrical parameters of D_p/A and $(-dA/Adx)$. The diameters of the atomizing lip are of 32, 36 and 48 mm. In practical working processes, the wave will be made at liquid film surface due to interaction of the airflow, while the data in the figures shown below are average thicknesses of liquid film.

From the experiments, we obtain

$$C_3 = 1 - \left(\frac{\rho_a}{\rho_l} \right)^{0.019} \tag{27}$$

Several curves from experiments and equation (26) are shown in Figs. 3-7. $(A_o - A)/A \cdot l$ in Fig. 7 represents

Nomenclature

SMD = Sauter mean diameter (m)
$h(H)$ = liquid film thickness (m)
ρ = density (kg/m^3)
μ = dynamic viscosity (kg/ms)

W = mass flow (kg/s)
P = pressure (N/m^2)
A = passage area (m^2)
——— = experiment
---- = prediction

Subscripts

a = air
l = liquid
p = at atomizing lip

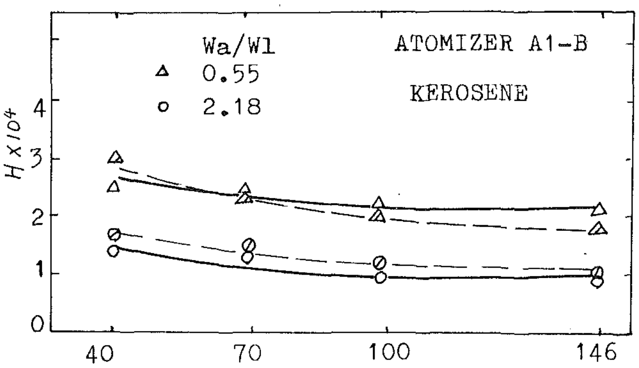

Fig. 3 Variation of H with U_a

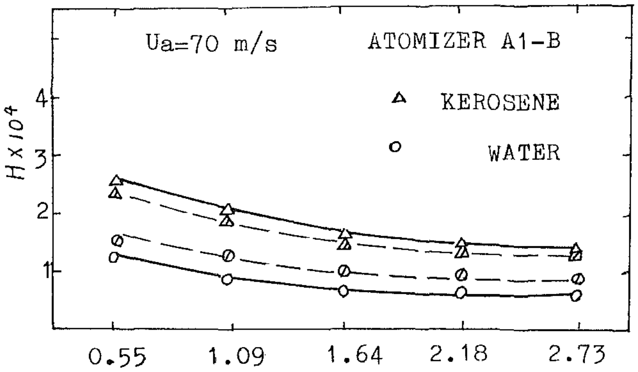

Fig. 4 Variation of H with W_a/W_l

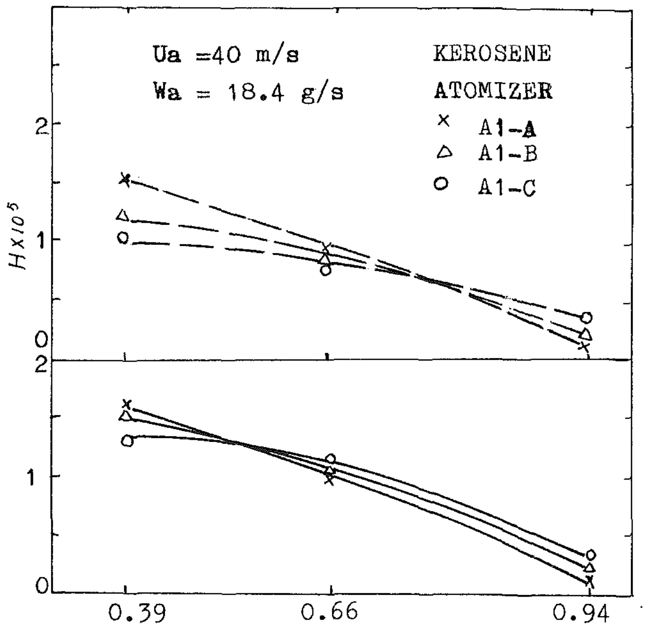

Fig. 5 Variation of H with X/L

($-dA/Adx$). It is a mean parameter of ($-dA/Adx$) for an atomizer. The data in all figures except Fig. 5 are measured at the atomizing lip. The deviations between measured and predicted values in the figures are less than ± 20 percent. The experiments also show that there are few effects of the liquid swirl speed out from the swirler piece on the film thickness, if the swirl speed is great enough. Details of experiments will be described in another paper to be published later. This result and the agreement of theoretical analyses results with the experiments show that assumption 1 is appropriate.

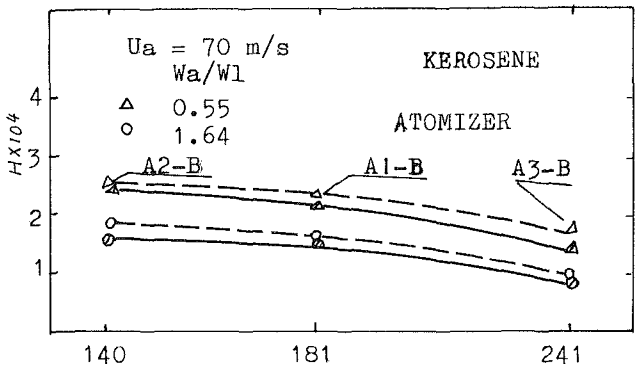

Fig. 6 Variation of H with D_p/A

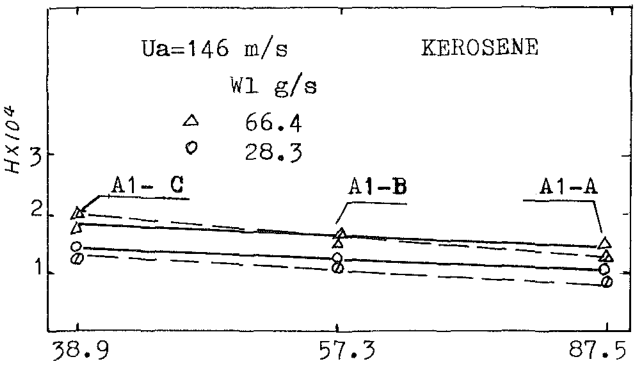

Fig. 7 Variation of H with $\frac{A_0 - A}{A \cdot L}$

Conclusions

From the foregoing predictions and experiments, we have drawn the following main conclusions:

1 Liquid film thickness h inside a prefilming atomizer is mainly related to the parameters of U_a, W_a/W_l, D_b/A, ($-dA/Adx$) and ρ_l/μ_l.

Increases of the parameters will lead to the decrease of h.

2 When $U_a > 100$ m/s or $W_a/W_l > 2 \sim 3$, h hardly changes with U_a or W_a/W_l.

3 h decreases with the increase of X/L in the atomizers.

4 Equation (26) may be used to predict the liquid film thickness inside the atomizers employed in the experiments.

Acknowledgments

Acknowledgment is made to Prof. Ning Huang, Mr. Liu Tao, and Huo Bao-Ging. They have made important contributions in the paper.

References

1 Rizkalla, A. A., and Lefebvre, A. H., "The Influence of Air and Liquid Properties on Airblast Atomization," ASME *Journal of Fluids Engineering*, Vol. 97, 1975, pp. 316–320.

2 Rizk, N. K., and Lefebvre, A. H., "Influence of Liquid Film Thickness on Airblast Atomization," paper presented at Winter Annual Meeting of ASME, Atlanta, Gas Turbine Combustion and Fuels Technology Conference, 1977, pp. 37–42.

3 Zho Qi-Shou, Yin Xing Liang, and Hou Muyu, "Investigation on Two-Dimensional Airblast Atomizer," *Acta Aeronautica et Astronautica Sinica*, Vol. 4, No. 3, 1983, pp. 47–55.

4 Cebeci, T., and Bradshaw, P., *Momentum Transfer in Boundary Layers*, Hemisphere, Washington, D.C., 1977.

5 Cheng Zi-Hang, "Double Flows and Heat Transfer of Air and Liquid," *Mechanical Industry*, China, 1983, pp. 68–73.

6 Moody, L. F., "Friction Factors for Pipe Flow," ASME *Trans.*, Vol. 66, 1944, pp. 671–684.

J. S. Chin
Visiting Professor.

D. Nickolaus
Graduate Student.

A. H. Lefebvre
Reilly Professor of
Combustion Engineering.

School of Mechanical Engineering,
Purdue University,
West Lafayette, IN 47907

Influence of Downstream Distance on the Spray Characteristics of Pressure-Swirl Atomizers

An analytical study is made of the factors that are responsible for the observed changes in fuel spray characteristics with axial distance downstream of a pressure-swirl nozzle. To simplify the analysis the effect of fuel evaporation is neglected, but full account is taken of the effects of spray dispersion and drop acceleration (or deceleration). Equations are derived and graphs are presented to illustrate the manner and extent to which the variations of mean drop size and drop-size distribution with axial distance are governed by such factors as ambient air pressure and velocity, fuel injection pressure, initial mean drop size, and initial drop-size distribution.

Introduction

In [1], Rizk and Lefebvre showed how the measured values of the mean drop sizes produced by simplex swirl atomizers varied with downstream distance. Their results indicate that mean drop sizes are relatively large close to the nozzle but decrease with increase in downstream distance, x, attaining a minimum value at a distance of around 50 mm from the nozzle. Beyond this distance the mean drop size increases continuously, but the rate of increase declines with increase in x. This pattern of variation of drop size with downstream distance is very similar to previous observations on both simplex and airblast fuel injectors [2, 3].

In [4], Chin et al. showed how the value of q in the Rosin–Rammler parameter varied with x for airblast atomizers. They found that once the atomization process is complete the value of q always increases with increase in axial distance from the nozzle.

Measurements carried out by Dodge and Moses [5] at different distances downstream of a pressure-swirl atomizer revealed that an increase in x causes the mean drop diameter to increase at the edge of the spray and to decline along the centerline of the spray. At the same time the value of q at the edge of the spray increases with x (indicating a smaller range of drop sizes) while the value of q falls at the centerline as x increases. These results suggest that when a light-scattering technique (such as the Malvern particle analyzer) is used to measure mean drop size and drop-size distribution, the observed variations of these properties with change in downstream distance should be less through the centerline of the spray than at the edges. This is due to the fact that when a laser beam is directed through the centerline of a spray, at right angles to the spray axis, the smaller drops at the center of the spray and the larger drops at the edges are both included in the measurement.

Spray characteristics are known to have a strong influence on many important aspects of gas-turbine combustion performance [6]. It was decided therefore to investigate analytically the variation in spray properties with downstream distance from the nozzle, and to assess the manner and extent to which these variations are influenced by the fuel injection pressure and the ambient air properties of pressure and flow velocity.

Variation of Drop-Size Distribution With Downstream Distance

Once the atomization process is complete, there are three main factors that influence the change of drop-size distribution of a spray with axial downstream distance. They are:

1. The effect of evaporation. As reported in [7], for $q < 4$, which is the range of interest for practical atomizers, the mean drop diameter and the distribution parameter, q, always increase as evaporation proceeds. Thus, this aspect will not be discussed further.
2. The effect of spray dispersion. In the present context the term "dispersion" is intended to denote the spatial volume occupied by the spray. According to one definition [6], the degree of dispersion may be stated as the ratio of the volume occupied by the spray (air plus fuel) to the volume of fuel contained within it.
3. The effect of drop acceleration (or deceleration). In most practical combustion systems burning liquid fuels, the fuel is sprayed into a coflowing air stream whose velocity is usually different from the initial velocity of the fuel drops. The effect of this air stream is either to accelerate or decelerate the fuel drops, depending on whether the air velocity is higher or lower than the

---

Contributed by the Gas Turbine Division of The American Society of Mechanical Engineers and presented at the 30th International Gas Turbine Conference and Exhibit, Houston, Texas, March 18–21, 1985. Manuscript received at ASME Headquarters, January 7, 1985. Paper No. 85-GT-138.

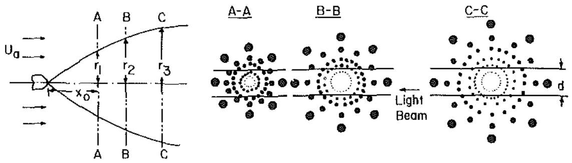

Fig. 1 Diagram illustrating influence of axial distance on radial drop-size distribution

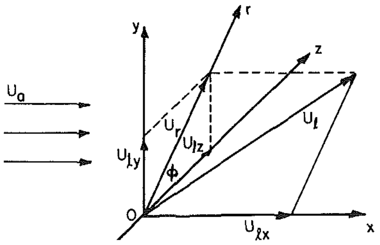

Fig. 2 Coordinate system employed to describe initial drop motion

initial axial velocity of the spray. In either case, beyond a certain axial distance, which is usually between 300 and 500 mm, substantially all of the fuel drops attain the same velocity as the air.

Effect of Spray Dispersion

As illustrated in Fig. 1, when a spray is formed at the outlet of a pressure-swirl atomizer, it first expands radially before finally assuming a fully axial direction. As predicted by calculations, and confirmed experimentally by Dodge [5], the larger drops penetrate farther radially than the smaller droplets. This causes the drops to be distributed radially from smaller drops at the center of the spray to larger drops at the edge. As the spray expands, the liquid-volume fraction becomes distributed in a larger circle, as shown in Fig. 1 (see sections A-A, B-B, C-C). The diameter of a light beam for measuring drop-size distribution is constant, as shown by d in Fig. 1. Thus, at different axial stations the number of drops of any given size in the sampling volume will be different. If the liquid is fully atomized at the outlet of the nozzle, the volume fraction in a unit drop-size range of mean diameter D will be

$$\frac{q\,D^{q-1}}{(\mathrm{MMD})^q}\bullet\exp\left[-0.693\left(\frac{D}{\mathrm{MMD}}\right)^q\right] \tag{1}$$

At station A-A, not all of these droplets will be sampled; actually only $2d/2\pi r_1 = d/\pi r_1$ will be sampled. At station B-B, by the same reasoning, only $d/\pi r_2$ will be sampled. At station C-C only $d/\pi r_3$ will be sampled. So at any axial distance, the sampled fraction having drop size D will be:

$$\frac{dQ}{dD}\bullet\frac{d}{\pi r}$$

where r is a function of D. Thus, the drop-size distribution of the spray as indicated by the particle sizer will be

$$\frac{dQ'}{dD}=\frac{\dfrac{dQ}{dD}\bullet\dfrac{d}{\pi r}}{\displaystyle\int_0^{D_{\max}}\frac{dQ}{dD}\bullet\frac{d}{\pi r}\bullet dD}$$

or

$$\frac{dQ'}{dD}=\frac{\dfrac{dQ}{dD}\bullet\dfrac{1}{r}}{\displaystyle\int_0^{D_{\max}}\frac{dQ}{dD}\bullet\frac{1}{r}\,dD} \tag{2}$$

For the purpose of analysis it is convenient to consider only one variable at a time. Thus, in order to eliminate any possible effects of fuel spray evaporation on drop-size distribution, the assumption is made that the air temperature is so low that evaporation can be neglected. Also the air flow velocity U_a is assumed equal to the axial component of the drop velocity U_{lx}, i.e., $U_a = U_{lx}$, so that the drops suffer neither acceleration nor deceleration in the axial direction. Thus, the only factor to be analyzed is the effect of spray dispersion.

The injection velocity components are U_{lx}, U_{ly}, and U_{lz}, as shown in Fig. 2. If we use a cylindrical coordinate system U_{lx} and U_{ly} can be combined to form U_r. As all the drops are formed at the outlet of the nozzle, it is reasonable to assume that they all have the same initial velocity. The circumferential distribution of drops may also be considered uniform. The air velocity is one dimensional (in x direction) and equal to U_{lx}.

The initial relative velocity is given by

$$\begin{aligned}W_0&=\sqrt{(U_a-U_{lx})^2+U_{ly}^2+U_{lz}^2}\\&=\sqrt{U_{ly}^2+U_{lz}^2}\\&=U_r\end{aligned}$$

If a coordinate system moving at the air velocity is used, the drops will have an initial velocity relative to the air W_0 (or U_r), which later on becomes W. Since all the drops are distributed uniformly circumferentially, it is only necessary to analyze their radial trajectories.

For the moving coordinate system, the equation of motion of a drop is given by

$$m\bullet\frac{dW}{dt}=-C_D\bullet\frac{\rho_a W^2}{2}\bullet\frac{\pi}{4}D^2 \tag{3}$$

Integration of equation (3) gives

$$\frac{W}{W_0}=\left[\left(\frac{\mathrm{Re}_0}{24}+1\right)\exp\left(\frac{18\,\rho_a W_0}{\mathrm{Re}_0\rho_l D}\bullet t\right)-\frac{\mathrm{Re}_0}{24}\right]^{-1} \tag{4}$$

where $\mathrm{Re}_0=\dfrac{\rho_a W_0 D}{\mu_a}$

Nomenclature

C_D = drag coefficient = 1 + (24/Re)
D = drop diameter
d = diameter of laser beam
MMD = mass median diameter
m = mass of fuel drop = $(\pi/6)\,\rho_l\bullet D^3$
Q = fuel volume fraction of drops having diameter smaller than D
q = drop-size distribution parameter in Rosin-Rammler equation
Re = Reynolds number = $\rho_a\bullet WD/\mu_a$
r = radial coordinate
t = time
U_a = air velocity
U_{lx} = component of fuel velocity in x direction
U_{ly} = component of fuel velocity in y direction
U_{lz} = component of fuel velocity in z direction
U_r = initial radial fuel velocity
W = relative velocity
x = downstream distance
μ = viscosity
ρ = density

Subscripts

a = air
l = liquid
max = maximum value
0 = initial value

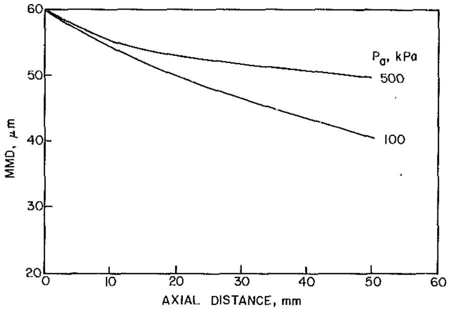

Fig. 3 Influence of ambient air pressure on variation of MMD with axial distance

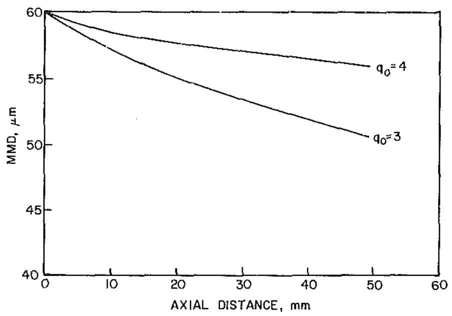

Fig. 4 Influence of initial drop-size distribution parameter on variation of MMD with axial distance

The drop velocity at a downstream distance x is:

$$U_{lx}{}' = U_{lx} = U_a$$

$$U_r{}' = U_r \bullet \frac{W}{W_0}$$

or
$$U_r' = U_r \bullet \left[\left(\frac{\mathrm{Re}_0}{24}+1\right) \bullet \exp\left(\frac{18\,\rho_a W_0}{\mathrm{Re}_0 \rho_l D} \bullet t\right) - \frac{\mathrm{Re}_0}{24}\right]^{-1} \tag{5}$$

The trajectory of the drop will be:

$$x = \int_0^t U_{lx}' dt = U_a t \tag{6}$$

$$r = \int_0^t U_r' dt = U_r \int_0^t \frac{dt}{\left(\frac{\mathrm{Re}_0}{24}+1\right)\exp\left(\frac{18\,\rho_a W_0}{\mathrm{Re}_0 \rho_l D} \bullet t\right) - \frac{\mathrm{Re}_0}{24}}$$

$$= U_r \bullet \frac{4}{3} \bullet \frac{\rho_l D}{\rho_a W_0} \bullet \left[\left(\frac{\mathrm{Re}_0}{24}+1\right) - \frac{\mathrm{Re}_0}{24}\exp\left(-\frac{18\,\rho_a W_0}{\mathrm{Re}_0 \rho_l D}\, t\right)\right] \tag{7}$$

As $U_r = W_0$, and $t = x/U_a$, equation (7) may be rewritten as

$$r = \frac{4}{3} \bullet \frac{\rho_l D}{\rho_a} \ln\left[\left(\frac{\mathrm{Re}_0}{24}+1\right) - \frac{\mathrm{Re}_0}{24}\exp\left(-\frac{18\,\rho_a U_r}{\mathrm{Re}_0 \rho_l D} \bullet \frac{x}{U_a}\right)\right] \tag{8}$$

In equation (8), at a certain downstream distance where $x = x_0$, the values of U_a, U_r, ρ_a, ρ_l, and Re_0 are known, so this equation shows the relationship $r = f(D)$ at that station. Combining equations (2) and (8), we can calculate the change of drop-size distribution with axial distance. By substituting equation (8) and (1) into equation (2), we have

$$\frac{dQ'}{dD} = \frac{\left[D^{(q_0-2)} \bullet \dfrac{\exp\left[-0.693\left(\dfrac{D}{\mathrm{MMD}_0}\right)^{q_0}\right]}{\ln\left[\left(\dfrac{\mathrm{Re}_0}{24}+1\right) - \dfrac{\mathrm{Re}_0}{24}\exp\left(-18 \bullet \dfrac{\rho_a U_r}{\mathrm{Re}_0 \rho_l D} \bullet \dfrac{x}{U_a}\right)\right]}\right]}{\left[\displaystyle\int_0^{D_{\max}} D^{(q_0-2)} \dfrac{\exp\left[-0.693\left(\dfrac{D}{\mathrm{MMD}_0}\right)^{q_0}\right]}{\ln\left[\left(\dfrac{\mathrm{Re}_0}{24}+1\right) - \dfrac{\mathrm{Re}_0}{24}\exp\left(-\dfrac{18\,\rho_a}{\mathrm{Re}_0 \rho_l}\dfrac{U_r}{D} \bullet \dfrac{x}{U_a}\right)\right]} dD\right]} \tag{9}$$

If the initial values of q_0 and MMD_0 are known, at a certain distance x, given a series of D values, we may obtain $dQ'/dD = f_1(D)$ and then calculate $Q' = \int_0^D dQ'/dD \bullet dD = f_2(D)$. The downstream drop-size distribution can be expressed by the Rosin-Rammler parameter

$$Q' = 1 - \exp\left[-0.693\left(\frac{D}{\mathrm{MMD}'}\right)^{q'}\right] \tag{10}$$

where MMD′ and q' will generally be different from the initial values MMD_0 and q_0. From equation (10), we have

$$\ln D = \ln(\mathrm{MMD}') + \frac{1}{q'}\ln\left[\frac{1}{0.693}\ln\left(\frac{1}{1-Q'}\right)\right] \tag{11}$$

By using the data obtained as $Q' = f_2(D)$, and the least-squares method, we obtain values of ln (MMD′) and $1/q'$, so the value of MMD′ and q' at the downstream distance x can be determined. The calculated results are shown in Figs. 3 to 12. In all these figures, unless otherwise stated, the relevant fuel and air properties are as listed below.

Air temperature	300K
Air pressure	100 kPa
Fuel density	780 kg/m^3
MMD_0	60 μm
q_0	3.0
Axial air velocity	20 m/s
Axial fuel droplet velocity	20 m/s
Radial fuel droplet velocity	20 m/s

The influence of ambient air pressure on the change of MMD with axial distance is illustrated in Fig. 3. It is clear from this figure that the effect of spray dispersion on mean drop size is lower at higher air pressures. This is because high air pressures impede the radial penetration of the larger drops.

The change of MMD with axial location also depends on the initial distribution parameter q_0. As shown in Fig. 4, the higher the q_0 value (i.e., the more monodisperse the spray), the smaller is the change of MMD with axial distance.

The effect of varying the radial fuel velocity is shown in Fig. 5. As might be expected, the change of MMD is larger for higher radial velocities, but the effect of radial fuel velocity is generally quite small.

The effect of variation in axial velocity is shown in Fig. 6, for the case where $U_a = U_{lx} = U_r$. Here a lower axial velocity gives a longer residence time that allows more radial spreading of the spray. This results in a larger change of MMD with axial distance.

The change of drop-size distribution parameter q with axial distance is shown in Fig. 7. This figure shows that q gradually declines with increase in axial distance. The two curves

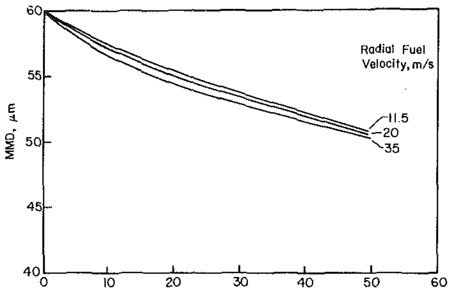

Fig. 5 Influence of radial fuel velocity on variation of MMD with axial distance

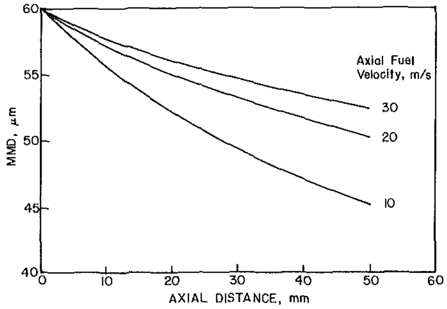

Fig. 6 Influence of axial fuel velocity on variation of MMD with axial distance

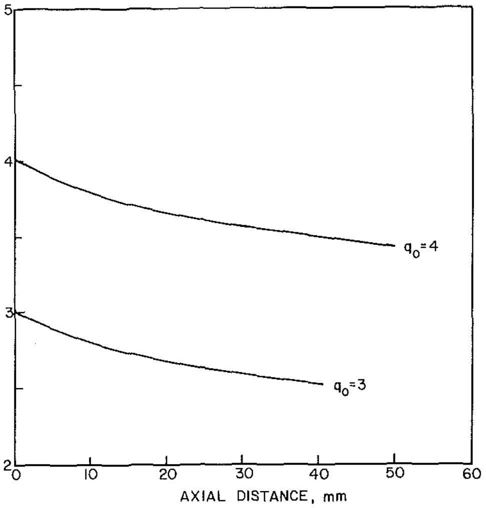

Fig. 7 Influence of initial *q* value on subsequent change of *q* with downstream distance

representing q_0 values of 3 and 4 exhibit the same trends, although the variation of q with x is less significant for $q_0 = 4$ (i.e., the relative change is smaller). The effect of axial distance on q is stronger for a finer spray, as shown in Fig. 8.

Calculations carried out over wide ranges of test conditions show that the effects of ambient air pressure and axial air velocity on the variation of q with downstream distance are both quite small.

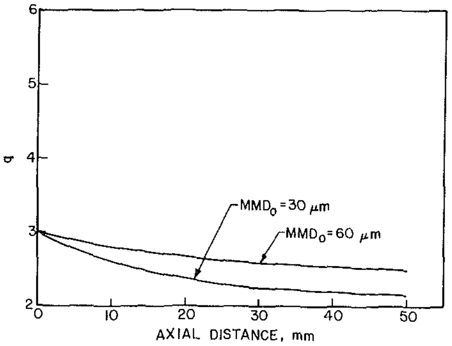

Fig. 8 Influence of initial MMD on variation of *q* with axial distance

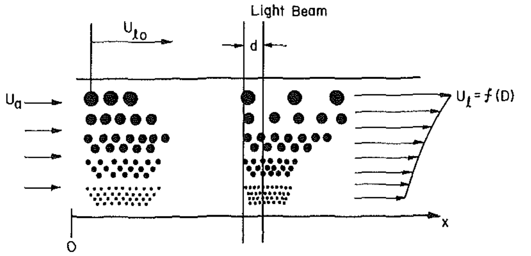

Fig. 9 Diagram to illustrate change in drop-size distribution with axial distance due to drop acceleration or deceleration

Effect of Drop Acceleration or Deceleration

In order to investigate the effect of drop acceleration (or deceleration), it is assumed that the air temperature is low enough for evaporation to be neglected, and that all the drops have axial velocity only (as produced, for example, by injection from a plain-orifice pressure atomizer). The air velocity U_a is also considered as axial and uniform, as shown in Fig. 9. U_a may be greater or smaller than the initial liquid velocity, U_{l_0}. If U_a exceeds U_{l_0} the drops are all accelerated, but if U_{l_0} exceeds U_a the drops slow down. The drop-size distribution varies with axial distance downstream of the nozzle, because small drops can accelerate or decelerate more rapidly than large drops. In a typical spray the smallest drops (i.e., the vast majority) attain the air velocity almost instantaneously, whereas the largest drops approach the air velocity more gradually. Thus, at any downstream location the velocity of any individual drop is a function of its diameter.

The time required for a drop to pass through the light beam of diameter d is inversely proportional to its velocity, V_l. This means that if the volume increment for a given size range is dQ/dD, then the volume increment actually observed by the light beam will be

$$\frac{dQ}{dD}\cdot\frac{d}{U_l}$$

The total observed liquid volume is given by

$$\int_0^{D_{\max}}\frac{dQ}{dD}\cdot\frac{d}{U_l}\,dD$$

Since there will be the same proportional constant for both formulae above, the measured drop-size distribution will be:

$$\frac{dQ'}{dD}=\frac{\dfrac{dQ}{dD}\cdot\dfrac{d}{U_l}}{\displaystyle\int_0^{D_{\max}}\frac{dQ}{dD}\cdot\frac{d}{U_l}\,dD}$$

$$=\frac{D^{(q_0-1)}\cdot\exp\left[-0.693\cdot\left(\dfrac{D}{\mathrm{MMD}_0}\right)^{q_0}\right]\cdot\dfrac{1}{U_l}}{\displaystyle\int_0^{D_{\max}}D^{(q_0-1)}\exp\left[-0.693\left(\dfrac{D}{\mathrm{MMD}_0}\right)^{q_0}\right]\cdot\frac{dD}{U_l}}\tag{12}$$

The problem that remains is how to determine U_l as a function of D. This can be achieved by considering droplet motion in a moving coordinate system in which the drop velocity is equal to the air velocity.

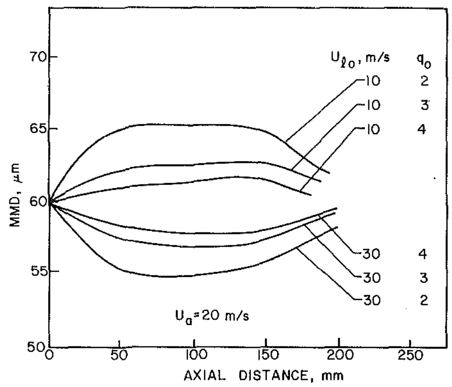

Fig. 10 Effects of drop acceleration and deceleration on spray MMD

We have:

$$m\cdot\frac{dW}{dt}=-C_D\frac{\rho_a W^2}{2}\cdot\frac{\pi}{4}D^2 \tag{3}$$

If $C_D = (24/\mathrm{Re}) + 1$ is used, the same equation as equation (4) is obtained,

$$\frac{W}{W_0}=\left[\left(\frac{\mathrm{Re}_0}{24}+1\right)\exp\left(\frac{18\,\rho_a W_0}{\mathrm{Re}_0\rho_l D}\cdot t\right)-\frac{\mathrm{Re}_0}{24}\right]^{-1} \tag{4}$$

Here $W_0 = U_{l0} - U_a$.

The drop velocity U_l at a downstream location is simply

$$U_l=U_a+W=U_a+(U_{l0}-U_a)$$
$$\cdot\left[\left(\frac{\mathrm{Re}_0}{24}+1\right)\exp\left(\frac{18\,\rho_a W_0}{\mathrm{Re}_0\rho_l D}\cdot t\right)-\frac{\mathrm{Re}_0}{24}\right]^{-1} \tag{13}$$

The downstream distance the drop has traveled can be written as:

$$x=\int_0^t U_l dt=U_a t+(U_{l0}-U_a)\cdot\frac{4}{3}\cdot\frac{\rho_l D}{\rho_a W_0}$$
$$\cdot\ln\left[\left(\frac{\mathrm{Re}_0}{24}+1\right)-\frac{\mathrm{Re}_0}{24}\exp\left(-18\frac{\rho_a W_0}{\mathrm{Re}_0\rho_l D}\cdot t\right)\right] \tag{14}$$

where $\mathrm{Re}_0=\dfrac{\rho_a W_0 D}{\mu_a}$

From equation (13), we obtain t as

$$t=\frac{\mathrm{Re}_0\rho_l D}{18\,\rho_a W_0}\ln\left[\frac{\dfrac{U_{l0}-U_a}{U_l-U_a}+\dfrac{\mathrm{Re}_0}{24}}{1+\dfrac{\mathrm{Re}_0}{24}}\right] \tag{15}$$

Substituting equation (15) into equation (14) gives

$$x=U_a\cdot\frac{\mathrm{Re}_0\rho_l D}{18\,\rho_a W}\cdot\ln\left[\frac{\dfrac{U_{l0}-U_a}{U_l-U_a}+\dfrac{\mathrm{Re}_0}{24}}{1+\dfrac{\mathrm{Re}_0}{24}}\right]$$
$$+\frac{4}{3}\cdot\frac{\rho_l D}{\rho_a}\ln\left[\frac{1+\dfrac{\mathrm{Re}_0}{24}}{1+\dfrac{\mathrm{Re}_0}{24}\,\dfrac{U_l-U_a}{U_{l0}-U_a}}\right] \tag{16}$$

At a certain downstream distance $x = x_0$, equation (16) defines the relationship $U_l = f(D)$.

Combining equations (16) and (12), and following the same procedure as before, we can calculate $dQ'/dD = f_1(D)$, $Q' = f_2(D)$, MMD, and q for the measured drop-size distribution as functions of downstream location. The results of such calculations are shown in Figs. 10 and 12.

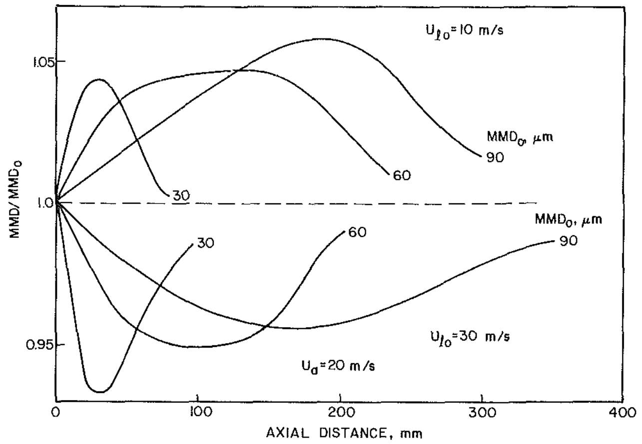

Fig. 11 Effects of initial MMD on variation of MMD with downstream distance due to drop acceleration or deceleration

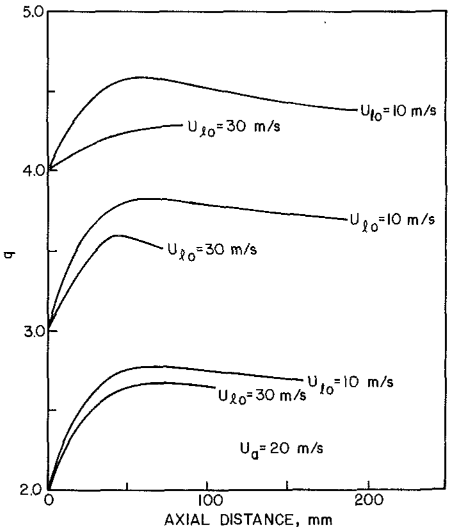

Fig. 12 Illustration of effects of drop acceleration and deceleration on variation of q with downstream distance

Figure 10 shows that for $U_{l0} > U_a$, MMD decreases with axial distance. After reaching a minimum it slowly increases again to approach its initial value. For $U_{l0} < U_a$, the trend is just the opposite. MMD first increases and then declines toward its initial value. As q_0 increases from 2 to 4, the change of MMD with axial distance becomes much less pronounced. The change of MMD with axial distance for sprays having different initial values of MMD$_0$ is shown in Fig. 11. For a finer spray, say MMD$_0$ = 30 μm, the effect of acceleration or deceleration diminishes after a short distance (around 100 mm), but for a coarser spray (MMD$_0$ = 90 μm), the effect of acceleration (or deceleration) persists for a longer distance (around 300 mm). It is interesting to note, for the conditions studied, the maximum effect of acceleration on MMD is as follows:

for $q_0=4$, 3% ~ 4%
$q_0=3$, 5% ~ 6%
$q_0=2$, 10% ~ 12%

Figure 12 shows the variation of q with axial distance for two values of axial fuel velocity. The variation of q is clearly less marked for the higher fuel velocity. The change of q with axial distance is also lower for higher initial values of q. In all cases q is observed to increase initially with downstream distance before declining toward its initial value.

The analysis presented above provides a useful understanding of the factors that influence the change of mean drop size and drop-size distribution downstream of the fuel nozzle for conditions where spray evaporation may be neglected.

Conclusions

For low ambient temperatures, where the effects of fuel evaporation may be regarded as negligibly small, it is shown that when fuel is injected from a pressure atomizer into a coflowing air stream, the values of mean drop size and drop-size distribution, as measured by light-scattering techniques in the region downstream of the atomizer, may be appreciably different from the true values as would be measured in a plane fairly close to the nozzle where the atomization process is just complete. Unfortunately, in practice, this plane is very difficult to determine with any degree of precision, since it is very dependent on nozzle design features, as well as fuel flow rate, fuel injection pressure, and ambient air properties.

The equations derived herein predict the deviations from the initial values of mean drop size and drop-size distribution that occur with variation in downstream distance from the nozzle. The parameters included in the calculation procedures comprise ambient air pressure and velocity, and also the initial values of fuel spray velocity, mean drop size, and drop-size distribution.

The results of calculations show that the effect of spray dispersion is to make the measured value of MMD lower than the actual initial one. Generally, an increase in air or fuel velocity will decrease the effect of dispersion. Also a more uniform spray (higher q) or a higher initial MMD will exhibit less variation of MMD with changing axial location. Increasing the air pressure decreases slightly the impact of dispersion. Where droplet acceleration or deceleration is present, the effect on spray measurement is to increase or decrease respectively the measured values of MMD. Far downstream of the nozzle (the distance depending on the air velocity and initial MMD), all the drops attain a sensibly uniform velocity, regardless of size, so the measured MMD again approaches the initial value.

Generally, for both acceleration and deceleration, the same trends are evident regardless of initial MMD. However, for both acceleration and deceleration, a wider drop-size range (lower q) will significantly increase the maximum deviation of the measured MMD from the initial MMD.

These findings indicate that measurements of nozzle spray characteristics in a flowing air stream should ideally be carried out well downstream of the nozzle (200 to 300 mm), using air at low temperature (<300K) in conjunction with liquids of low volatility.

References

1 Rizk, N. K., and Lefebvre, A. H., "Influence of Downstream Distance on Simplex Atomizer Spray Characteristics," presented at 1984 ASME Winter Annual Meeting, New Orleans, Dec. 1984.

2 El-Shanawany, M. S. M. R., and Lefebvre, A. H., "Airblast Atomization: The Effect of Linear Scale on Mean Drop Size," *Journal of Energy*, Vol. 4, No. 4, 1980, pp. 184-189.

3 Rizk, N. K., and Lefebvre, A. H., "Spray Characteristics of Simplex Swirl Atomizers," presented at the Ninth International Colloquium on Dynamics of Explosions and Reactive Systems, Poitiers, France, July 1983.

4 Chin, J. S., Zhao, Y. H., Hou, M. H., and Kong, Y. Z., "Investigation on Drop-Size Distribution," AIAA Paper No. 84-1314, 1984.

5 Dodge, L. G., and Moses, C. A., "Mechanisms of Smoke Reduction in the High Pressure Combustion of Emulsified Fuels," South West Research Institute Report No. 6287/4, May 1984.

6 Lefebvre, A. H., *Gas Turbine Combustion*, McGraw-Hill, 1983.

7 Chin, J. S., Durrett, R., and Lefebvre, A. H., "The Interdependence of Spray Characteristics and Evaporation History of Fuel Sprays," ASME JOURNAL OF ENGINEERING FOR GAS TURBINES AND POWER, Vol. 106, No. 3, July 1984, pp. 639-644.

cases q is observed to increase initially with downstream distance before declining toward its initial value.

The analysis presented above provides a useful understanding of the factors that influence the change of mean drop size and drop-size distribution downstream of the fuel nozzle for conditions where spray evaporation may be neglected.

Conclusions

For low ambient temperatures, where the effects of fuel evaporation may be regarded as negligibly small, it is shown that when fuel is injected from a pressure atomizer into a coflowing air stream, the values of mean drop size and drop-size distribution, as measured by light-scattering techniques in the region downstream of the atomizer, may be appreciably different from the true values as would be measured in a plane fairly close to the nozzle where the atomization process is just complete. Unfortunately, in practice, this plane is very difficult to determine with any degree of precision, since it is very dependent on nozzle design features, as well as fuel flow rate, fuel injection pressure, and ambient air properties.

The equations derived herein predict the deviations from the initial values of mean drop size and drop-size distribution that occur with variation in downstream distance from the nozzle. The parameters included in the calculation procedures comprise ambient air pressure and velocity, and also the initial values of fuel spray velocity, mean drop size, and drop-size distribution.

The results of calculations show that the effect of spray dispersion is to make the measured value of MMD lower than the actual initial one. Generally, an increase in air or fuel velocity will decrease the effect of dispersion. Also a more uniform spray (higher q) or a higher initial MMD will exhibit less variation of MMD with changing axial location. Increasing the air pressure decreases slightly the impact of dispersion. Where droplet acceleration or deceleration is present, the effect on spray measurement is to increase or decrease respectively the measured values of MMD. Far downstream of the nozzle (the distance depending on the air velocity and initial MMD), all the drops attain a sensibly uniform velocity, regardless of size, so the measured MMD again approaches the initial value.

Generally, for both acceleration and deceleration, the same trends are evident regardless of initial MMD. However, for both acceleration and deceleration, a wider drop-size range (lower q) will significantly increase the maximum deviation of the measured MMD from the initial MMD.

These findings indicate that measurements of nozzle spray characteristics in a flowing air stream should ideally be carried out well downstream of the nozzle (200 to 300 mm), using air at low temperature (<300K) in conjunction with liquids of low volatility.

References

1 Rizk, N. K., and Lefebvre, A. H., "Influence of Downstream Distance on Simplex Atomizer Spray Characteristics," presented at 1984 ASME Winter Annual Meeting, New Orleans, Dec. 1984.

2 El-Shanawany, M. S. M. R., and Lefebvre, A. H., "Airblast Atomization: The Effect of Linear Scale on Mean Drop Size," *Journal of Energy*, Vol. 4, No. 4, 1980, pp. 184–189.

3 Rizk, N. K., and Lefebvre, A. H., "Spray Characteristics of Simplex Swirl Atomizers," presented at the Ninth International Colloquium on Dynamics of Explosions and Reactive Systems, Poitiers, France, July 1983.

4 Chin, J. S., Zhao, Y. H., Hou, M. H., and Kong, Y. Z., "Investigation on Drop-Size Distribution," AIAA Paper No. 84-1314, 1984.

5 Dodge, L. G., and Moses, C. A., "Mechanisms of Smoke Reduction in the High Pressure Combustion of Emulsified Fuels," South West Research Institute Report No. 6287/4, May 1984.

6 Lefebvre, A. H., *Gas Turbine Combustion*, McGraw-Hill, 1983.

7 Chin, J. S., Durrett, R., and Lefebvre, A. H., "The Interdependence of Spray Characteristics and Evaporation History of Fuel Sprays," ASME JOURNAL OF ENGINEERING FOR GAS TURBINES AND POWER, Vol. 106, No. 3, July 1984, pp. 639–644.

DISCUSSION

S. M. DeCorso[1]

I found the paper to be an interesting and informative exposition on spray behavior. I wish to raise a point which will help to explain the observation that large drops predominate at the outer surface of the spray. In the section on the *Effect of Spray Dispersion*, this effect is attributed to the penetration of the larger drops farther radially in the spray.

I want to point out an additional effect which preferentially moves smaller drops toward the center of the spray, leaving the larger drops at the outer portion of the spray. This effect is a strong ambient gas flow induced by the spray action itself. This ambient gas flow moves directly across and through the spray surface from the outside of the spray in toward the spray axis, transporting the smaller drops with the gas flow, as noted in [8, 9].

References

8 DeCorso, S. M., and Kemeny, G. A., "Effect of Ambient and Fuel Pressure on Nozzle Spray Angle," Trans. ASME, Vol. 79, No. 3, Apr. 1957.

9 Jasuja, A. K., "Dual-Orifice Atomizer Performance Under Varying Air Density Conditions," ASME Paper No. 85-GT-44.

Author's Closure

There is little doubt that the strong air currents generated by the spray itself, as first noted by DeCorso and Kemeny, have a pronounced effect on many spray characteristics, including the radial distribution of drop sizes. Although our paper was concerned solely with the influence of drop penetration on radial drop-size distribution, some reference to the role of these air currents should have been made, and we are grateful to Dr. DeCorso for repairing this omission on our part.

---

[1] Manager, Energy Program Development, Westinghouse Electric Corporation, Concordville, PA 19331

Journal of
Engineering
for Gas Turbines
and Power

Discussion

Evaluation of Polytropic Calculation Methods for Turbomachinery Performance[1]

N. S. Nathoo[2] and W. G. Gottenberg.[2] The paper begins by discussing the shortcomings of the established Schultz [7] method (incorporated in ASME PTC 10-1965) and Mallen's [8] method for evaluating the thermodynamic performance of turbomachinery, specifically compressors. In certain cases of high-pressure compression of gases, the paper shows that the results of calculated work by two above methods differ by 3 percent. It then shows that the primary deficiency in the Schultz procedure is the assumption that n (polytropic volume exponent) is a constant. Further, if n is not assumed to be a constant, then the resulting differential equation is difficult to solve and the numerical computation limits the accuracy of the solution. The paper then develops a "reference" method whose results fall between those calculated by Schultz and Mallen.

All of the above points, with the notable exception of difficulty with the integration procedure, were published in "A New Look at Performance Analysis of Centrifugal Compressors Operating with Mixed Hydrocarbon Gases" by N. S. Nathoo and W. G. Gottenberg [9]. In that paper the following were established:

1 A unified experimental approach to acquire accurate pressure, temperature, flow, and gas sample data from field installations.

2 Solution of the fundamental differential equation

$$\eta_p dH = VdP$$

by coupling it with an equation of state characterization of gas properties and using a robust and accurate integration scheme. The above paper [9] was not referenced in the subject one.

Specific points to be noted are

1 The present author's "reference" method and the method previously reported in [9], as "exact," produce the same deviation when compared to Schultz and Mallen. The comparison is shown in Tables 1-3 for ethylene at two discharge pressures and Freon-12.

We define

$W_{so} \equiv$ Schultz work as computed in [9]
$W_{mo} \equiv$ Mallen work as computed in [9]
$W_e \equiv$ "exact" work as computed in [9]
$W_{sl} \equiv$ Schultz work as computed by RAH
$W_{ml} \equiv$ Mallen work as computed by RAH
$W_r \equiv$ "reference" work as computed by RAH

As may be seen, the ratios of work W_{sl}/W_r and W_{ml}/W_r are essentially the same as W_{so}/W_e and W_{mo}/W_e.

2 Computational difficulty was not encountered in [9] while solving the differential equations describing the process, unlike that reported in the subject paper. The process is an extremely smooth, well-behaved function and a robust Runge-Kutta or similar scheme will produce accurate results.

3 Because of 1 and 2 above, there is no need for an alternate method which requires development of functional forms for $Z(P)$ as reported in the subject paper. Although this may produce accurate results for some gases, no indication is provided in the paper that they are applicable to general petrochemical industry gas mixtures which are occasionally comprised of 20 or more constituents.

Finally, this question must be raised: How does one know whether any reference method is accurate and that it represents the actual performance of a machine? One approach would be the verification of a computation scheme by actual field measurement. This was done for work reported in [9]. Furthermore, since that paper was published, calculation of compressor work by the reported exact method has been validated in the field against a calibrated torquemeter installed between the driver and driven machines. The results indicated differences between predicted and measured values to be less than 1.5 percent; this after taking into account the very careful procedures that have to be followed in obtaining field data.

Based upon the above, there appears to be no need to change the accepted method of Schultz. If more accuracy is required, then the equations defining compressor work can be coupled with equation-of-state representations of real gases and the resulting differential equations solved as shown in [9].

References

7 Schultz, J. M., "The Polytropic Analysis of Centrifugal Compressors," ASME Journal of Engineering for Power, Jan. 1962, pp. 69-82.

8 Mallen, M., and Saville, G., "Polytropic Processes in the Performance Prediction of Centrifugal Compressors," I. Mech. E. Conference Publications, 1977.

9 Nathoo, N. S., and Gottenberg, W. G., "A New Look at Performance Analysis of Centrifugal Compressors Operating With Mixed Hydrocarbon Gases," ASME Journal of Engineering for Power, Vol. 105, Oct. 1983.

Author's Closure

I should first thank Mssrs. Nathoo and Gottenberg for their interesting discussion. I also regret that their paper [9] was not referenced in the body of the subject paper. Their paper presents a comparison of the "approximate" Schultz and Mallen & Saville compressor performance calculation methods to a numerically precise method and supports the preliminary conclusions of the subject paper – specifically that for some cases, the errors associated with these approximate methods may be 1.5 percent or more. However, in contrast to [9], during the preparation of the subject paper we found the accuracy of these methods to be inconsistent with our increasing trend to tighten compressor performance guarantees required for new compressors. This dissatisfaction with the capabilities of these methods led us to develop the new polytropic calculation method that is presented in the

---

[1] By R. A. Huntington, published in the October 1985 issue of the Journal of Engineering for Gas Turbines and Power, Vol. 107, No. 4, pp. 872-879.

[2] Shell Development Company, Houston, TX 77001

Table 1 Comparison of compressor work and efficiency as computed by methods of discussed paper and [7–9]

	Polytropic work, kJ/kg (ft-lb/1bm)	Efficiency	Ratio of computed work
Schultz's method as computed by RAH	$W_{sl} = 350.66$ (117,313)	0.796	$W_{sl}/W_r = 0.983$
Mallen and Seville's method as computed by RAH	$W_{ml} = 359.61$ (120,309)	0.816	$W_{ml}/W_r = 1.008$
Huntington's "reference" method	$W_r = 356.77$ (119,357)	0.810	
Schultz's method as computed in [9]	$W_{so} = 359.71$ (120,276)	0.799	$W_{so}/W_e = 0.984$
Mallen and Seville's method as computed in [9]	$W_{mo} = 367.89$ (123,077)	0.817	$W_{mo}/W_e = 1.007$
"Exact" method of [9]	$W_e = 367.89$ (123,077)	0.812	

Gas: ethylene
Suction pressure, MPa/psia: 2.5/362.5; suction temperature, K/°F: 310.0/98.3
Discharge pressure, MPa/psia: 50.0/7250.0, discharge temperature, K/°F: 570.0/566.3

Table 2 Comparison of compressor work and efficiency as computed by methods of discussed paper and [7–9]

	Polytropic work, kJ/kg (ft-lb/1bm)	Efficiency	Ratio of computed work
Schultz's method as computed by RAH	$W_{sl} = 269.33$ (90,104)	0.738	$W_{sl}/W_r = 0.984$
Mallen and Seville's method as computed by RAH	$W_{ml} = 275.49$ (92,167)	0.755	$W_{ml}/W_r = 1.007$
Huntington's "reference" method	$W_r = 273.57$ (91,525)	0.750	
Schultz's method as computed in [9]	$W_{so} = 275.17$ (92,058)	0.745	$W_{so}/W_e = 0.984$
Mallen and Seville's method as computed in [9]	$W_{mo} = 281.33$ (94,119)	0.762	$W_{mo}/W_e = 1.006$
"Exact" method of [9]	$W_e = 279.61$ (93,545)	0.757	

Gas: ethylene
Suction pressure, MPa/psia: 2.5/362.5; suction temperature, K/°F: 310.0/98.3
Discharge pressure, MPa/psia: 30.0/4351.2; discharge temperature, K/°F: 535.0/503.3

Table 3 Comparison of compressor work and efficiency as computed by methods of discussed paper and [7–9]

	Polytropic work, kJ/kg (ft-lb/1bm)	Efficiency	Ratio of computed work
Schultz's method as computed by RAH	$W_{sl} = 51.67$ (17,288)	0.754	$W_{sl}/W_r = 1.0019$
Mallen and Seville's method as computed by RAH	$W_{ml} = 51.62$ (17,268)	0.753	$W_{ml}/W_r = 1.00075$
Huntington's "reference" method	$W_r = 51.58$ (17,255)	0.753	
Schultz's method as computed in [9]	$W_{so} = 51.84$ (17,342)	0.755	$W_{so}/W_e = 0.99931$
Mallen and Seville's method as computed in [9]	$W_{mo} = 51.91$ (17,368)	0.757	$W_{mo}/W_e = 1.00081$
"Exact" method of [9]	$W_e = 51.87$ (17,354)	0.756	

Gas: Freon-12
Suction pressure, kPa/psia: 68.9/10.0; suction temperature, K/°F: 250.0/ – 10.0
Discharge pressure, kPa/psia: 986.3/130.0, discharge temperature, K/°F: 372.0/210.0

paper and recommended for incorporation into PTC-10. This new method, which is the major focus of the subject paper, is shown to be at least an order of magnitude more accurate than the previous approximate methods and is no more difficult to apply than the Schultz technique.

In comparison to the numerical integration methods presented in the subject paper and in [9], this new method exhibits a high level of accuracy, ranging from essentially zero error for routine compression calculations to 0.05 percent error for the most difficult compression example presented. In light of this, application of a numerical integration technique (whose results may be extremely difficult for a customer to verify) to a PTC-10 performance test seems to be unjustified. On the other hand, the new method is accurate, simple to apply and verify, and appears to be better suited to inclusion in a performance test code.

In response to the specific points raised by Mr. Nathoo are the following comments:

1 I agree that the "reference" method and the "exact" method of [9] can produce virtually identical results. Both numerically integrate the polytropic path equations to calculate head; the reference uses a predictor-corrector technique while the exact uses a Runge–Kutta or similar technique. The differences noted between these methods are most likely due to the equations of state and gas data used in the integration procedures.

As noted by Mr. Fozi in his discussion of the subject paper (October 1985), numerical integration of the polytropic equations has been used before. It was suggested by Schultz [1] and has been applied in various forms by compressor vendors and users to perform stage-by-stage compressor simulations for the past 15 to 20 years. The reference and exact methods discussed are simply refinements of these previous methods to take advantage of present computer capabilities and improve overall accuracy.

2 The "computational difficulty" noted in the discussion was not a difficulty at all but simply an acknowledgment that all numerical integration techniques, in contrast to closed-form integral solutions, are subject to computational errors. These are well known and are related to integration step size and computational precision. Because of this fact, the

reference and exact methods are just two more "approximate" head calculation techniques unless their error magnitudes are demonstrated. In the subject paper, the accuracy of the reference calculation was demonstrated to be much better than the accuracies of the other methods that were compared to it. The level of accuracy of the exact method was not discussed in [9] but could easily be evaluated in a similar fashion.

3 The advantages of the new method are discussed in the opening paragraphs of this Closure.

It is anticipated that the assumed function for compressibility factor given by equation (20) along a polytropic path will be generally applicable and will not require alteration. The excellent fit of this function is demonstrated in Fig. 2.

While no mixed hydrocarbon examples were presented in the paper, nothing in the development of the new method precludes its application to these or any other gases. Generally, limits are only imposed indirectly by the applicability of equations of state and gas data. To demonstrate this, the mixed-hydrocarbon compression example (with 21 gas components) given in Tables 2 and 3 of [9] has been calculated with the new method and the reference method. The polytropic heads calculated were 75.121 and 75.124 kJ/kg, respectively – an error of 0.004 percent.

Finally, I must disagree with the assertion that polytropic head calculations can be quantitatively verified by field measurements. Polytropic head is strictly a calculated quantity and cannot be measured. The results of accurate field measurements of compressor flow rate, power, and heat dissipation will provide verification of the enthalpy rise of the gas and thus verify the calculated polytropic head divided by efficiency. However, the head and efficiency cannot be independently verified from field measurements. As present, the only way known to this author to check the accuracy of polytropic head and efficiency calculation methods is to compare them to a precise numerical integration method as was done in [9] and in the subject paper.